The History and Evolution of Young and Distant Radio Sources

Jordan Collier

A thesis submitted for the degree of
Doctor of Philosophy
at
Western Sydney University

September 2016

Dedication

This thesis is dedicated to my wife, Emily, whose love and support throughout the long journey of my PhD never ceased to amaze me. Emily, I could not have done this without you.

Acknowledgements

Personal acknowledgements

I'd like to acknowledge and thank my supervisors

- Miroslav Filipović, for always supporting me in such a way that I always knew you had my best interests at heart, not just in my research, but also in my life. Thanks also for the coffee!
- Ray Norris, for imparting your wisdom and experience and teaching me so many crucial lessons in writing papers, proposals, and doing research in general.
- Nick Tothill, for taking the time to commit your mind to and talking me through difficult problems, and for the baby clothes and accessories!

Each of you always made time for me and had my best interests in mind, and I count you all as mentors and friends. This thesis would not have been possible without your constant supervision, support and guidance.

I'd like to acknowledge and thank my colleagues

- Tim 'Galvination Sensation' Galvin
- Andrew 'α Male' O'Brien
- Kevin 'Kevy Wevy' Grieve
- Quentin 'Quintin' Roper
- Perica 'Perrrrro'[1] Manojlovic
- Nick 'Nike' Patkovic
- Graeme 'Wong Lab' Wong

You guys have always created a fun and relaxed environment that is great to be a part of. Special mention to Tim and Andrew for teaching me so much about computing and giving me constant help. And thank you Tim and Kevin for alleviating my discomfort while I was writing my thesis and my air con was broken – Tim for letting me crash your place and Kevin for letting me borrow your portable air con! And thanks Tim for staying friends with me despite that script I installed and ran on your computer!

[1] This may also be represented as Pe$[\prod_{i=1}^{5} r_i]$o

Thanks also to my past and present colleagues Miranda, Evan, Ain, Luke, Danica, Alex, Chris, Nathan, David, Darren, David, Raelene, Elaina, Niyas and Ros for being a great group to work with, and for letting me be involved at our wonderful observatory!

I'd like to acknowledge and thank my office partners Ron, Tri and Syed for mixing up our office with a bit of Engineering and Construction Management!

I'd also like to acknowledge and thank the following people

- Frank Stootman, for constantly mentoring, encouraging and supporting me in my writing and general life.
- Susan Henley, for always being on the ball and assisting me in so many ways with travel, funding and any problems only vaguely related to her job!
- Both of my examiners, who provided very detailed and insightful feedback that improved the general quality of the thesis.

Lastly, I'd like to acknowledge and thank my family

- John & Kate Collier, my parents, for constantly loving, encouraging and supporting me financially throughout my PhD, babysitting, and much more.
- Lynda & Andrew Robinson, for going out of your way to support me in so many ways, such as mowing the lawn, looking after Emily & Archie when I was busy, cooking us meals, babysitting, and much more.
- Emily Collier, my wife, for constantly supporting me and loving me and going above and beyond to serve me so sacrificially, for which I am eternally grateful.
- Archer Collier, my son, for being such a delight!

Thank you all for your constant support, prayer and understanding while I had an extremely large document to produce!

Scientific acknowledgements

I'd like to thank Joe Callingham for the code to perform the spectral modelling for the GPS and CSS sources, and for the stimulating discussions we had over their nature. I'd also like to thank Steve Tingay giving up his valuable time to reduce the LBA data.

I gratefully acknowledge the people and institutes that contributed to the NVSS and FIRST surveys. This publication makes use of data products from the *Wide-field Infrared Survey Explorer*, which is a joint project of the University of California, Los Angeles, and the Jet Propulsion Laboratory/California Institute of Technology, funded by the National Aeronautics and Space Administration. The National Radio Astronomy Observatory is a facility of the National Science Foundation operated under cooperative agreement by Associated Universities, Inc.

ATD acknowledges support from an NWO Veni Fellowship. The National Radio Astronomy Observatory is a facility of the National Science Foundation operated under cooperative

agreement by Associated Universities, Inc. This work made use of the Swinburne University of Technology software correlator, developed as part of the Australian Major National Research Facilities Programme and operated under licence.

Funding for SDSS-III has been provided by the Alfred P. Sloan Foundation, the Participating Institutions, the National Science Foundation, and the U.S. Department of Energy Office of Science. The SDSS-III web site is http://www.sdss3.org/.

SDSS-III is managed by the Astrophysical Research Consortium for the Participating Institutions of the SDSS-III Collaboration including the University of Arizona, the Brazilian Participation Group, Brookhaven National Laboratory, Carnegie Mellon University, University of Florida, the French Participation Group, the German Participation Group, Harvard University, the Instituto de Astrofisica de Canarias, the Michigan State/Notre Dame/JINA Participation Group, Johns Hopkins University, Lawrence Berkeley National Laboratory, Max Planck Institute for Astrophysics, Max Planck Institute for Extraterrestrial Physics, New Mexico State University, New York University, Ohio State University, Pennsylvania State University, University of Portsmouth, Princeton University, the Spanish Participation Group, University of Tokyo, University of Utah, Vanderbilt University, University of Virginia, University of Washington, and Yale University.

This scientific work makes use of the Murchison Radio-astronomy Observatory, operated by the Commonwealth Scientific and Industrial Research Organisation (CSIRO). We acknowledge the Wajarri Yamatji people as the traditional owners of the Observatory site. Support for the MWA comes from the U.S. National Science Foundation (grants AST-0457585, PHY-0835713, CAREER-0847753, and AST-0908884), the Australian Research Council (LIEF grants LE0775621 and LE0882938), the U.S. Air Force Office of Scientific Research (grant FA9550-0510247), and the Centre for All-sky Astrophysics (an Australian Research Council Centre of Excellence funded by grant CE110001020). Support is also provided by the Smithsonian Astrophysical Observatory, the MIT School of Science, the Raman Research Institute, the Australian National University, and the Victoria University of Wellington (via grant MED-E1799 from the New Zealand Ministry of Economic Development and an IBM Shared University Research Grant). The Australian Federal government provides additional support via the CSIRO, National Collaborative Research Infrastructure Strategy, Education Investment Fund, the Australia India Strategic Research Fund, and Astronomy Australia Limited, under contract to Curtin University. We acknowledge the iVEC Petabyte Data Store, the Initiative in Innovative Computing and the CUDA Center for Excellence sponsored by NVIDIA at Harvard University, and the International Centre for Radio Astronomy Research (ICRAR), a Joint Venture of Curtin University and The University of Western Australia, funded by the Western Australian State government. SJT acknowledges support from the Western Australian Government via a Premier's Research Fellowship.

The Australia Telescope Compact Array is part of the Australia Telescope National Facility which is funded by the Commonwealth of Australia for operation as a National Facility managed by CSIRO. The Parkes Radio Telescope is part of the Australia Telescope National Facility which is funded by the Commonwealth of Australia for operation as a National Facility managed by CSIRO. *Facilities:* ATCA, MWA, Parkes.

The work presented in this thesis is, to the best of my knowledge and belief, original except as acknowledged in the text.

I hereby declare that I have not submitted this material, either in full or in part, for a degree at this or any other institution.

Jordan Collier September 30, 2016

Contents

List of Tables

List of Figures

Abstract

We study two classes of object to gain a better understanding of the evolution of Active Galactic Nuclei (AGN): Infrared-Faint Radio Sources (IFRSs) and Gigahertz Peaked Spectrum (GPS) / Compact Steep Spectrum (CSS) sources.

IFRSs are a recently discovered rare class of object, which were found to be strong in the radio but undetectable in extremely sensitive infrared observations from the Spitzer Space Telescope, even in stacked images with $\sigma < 1\,\mu$Jy. IFRSs were found to exhibit a relatively high sky density, and were thought to represent AGN at $z > 3$. Therefore, IFRSs may significantly increase the number of known high-redshift galaxies. However, their non-detections in the optical and infrared prevented confirmation of their nature.

Previous studies of IFRSs focused on very sensitive observations of a few small regions of the sky, and the largest sample consisted of 55 IFRSs. However, we follow the strategy of combining radio data with IR and optical data for a large region of the sky. Using these data, we discover a population of >1300 brighter IFRSs which are, for the first time, reliably detected in the infrared and optical. We present the first spectroscopic redshifts of IFRSs and show that the brightest IFRSs are at $z > 2$. Furthermore, we rule out that IFRSs are Star Forming Galaxies, hotspots, lobes or misidentifications. We find the first X-ray counterparts of IFRSs, and increase the number of known polarised IFRSs five-fold. We present an analysis of their radio spectra and show that IFRSs consist of GPS, CSS and ultra-steep-spectrum sources. We follow up >50 of these using VLBI observations, and confirm the AGN status of IFRSs.

We conclude that IFRSs represent a new population of high-redshift radio galaxies, which, for the faintest IFRSs, may have redshifts as high as $z = 7$ and consist of a few hundred thousand objects across the μJy sky.

GPS and CSS sources are compact radio sources with a convex radio spectrum. They are widely thought to represent young and evolving radio galaxies that have recently launched their jets. However, good evidence exists in individual cases that GPS and CSS sources are one of the following: 1) frustrated by interactions with dense gas and dust in their environment; 2) prematurely dying radio sources; 3) recurrent radio galaxies. Their convex spectrum is generally thought to be caused by Synchrotron Self Absorption (SSA), an internal process in which the same population of electrons is responsible for the synchrotron emission and self-absorption. However, recent studies have shown that the convex spectrum may be caused by Free-Free Absorption (FFA), an external process in which an inhomogeneous screen absorbs the synchrotron emission. The majority of GPS and CSS samples consist of Jy-level and therefore, high-luminosity sources. VLBI images show that GPS and CSS sources typically have double-lobed, edge-brightened morphologies on mas scales, appearing as scaled down versions of Fanaroff-Riley Class II (FR II) galaxies. Recently, two low-luminosity GPS sources were found to have jet-brightened morphologies, which appeared as scaled down versions of Fanaroff-Riley Class I (FR I) galaxies. From this, it was proposed that there exists a morphology-luminosity

break analogous to the FR I/II break and that low-luminosity GPS and CSS sources are the compact counterparts of FR I galaxies. However, this hypothesis remains unconfirmed, since very few samples of low-luminosity GPS and CSS sources exist.

We have observed the faintest population of GPS and CSS sources to date, consisting ∼150 sources, many of which are low-luminosity. We use high-resolution radio observations to determine their linear size, resolve their jets and observe their small-scale morphology. We combine these data with a large number of radio observations at other frequencies to model their radio spectra using SSA and FFA models. In particular, we use very low frequency observations that have only recently become available to constrain their spectral peaks. We follow up eight of the most compact sources with VLBI and detect six of them.

We find that our GPS and CSS sources are well modelled by an inhomogeneous FFA model (hereafter 'FFA'). Furthermore, we find a number of very compact GPS and CSS sources that are inconsistent with SSA theory. We show that a single inhomogeneous SSA model fits poorly to the majority of radio spectra, predicting far too steep a slope below the peak. We resolve all of the sources with VLBI and derive their kinematic ages based on the jet sizes. Even when assuming more complex SSA models, we derive magnetic field strengths several orders of magnitude too high for one source. A few sources are well modelled by an FFA model in which the inhomogeneous absorption is dominated by clouds of high density, consistent with the frustration hypothesis. However, the majority of sources are well modelled by FFA models with low-density clouds. These models suggest that an inhomogeneous and clumpy medium surrounds the sources, implying they may undergo recurrent activity. Furthermore, the spectral model of one CSS source suggests it is a prematurely dying radio galaxy whose jets have been switched off for ∼600 years. However, we find no evidence of restarted radio galaxies within our high resolution observations. The kinematic and spectral ages we derive are consistent with the hypothesis that GPS and CSS sources are young and evolving. We find tentative evidence that at mJy-levels, the fraction of CSS sources is smaller than the fraction estimated for Jy-level sources. This may be accounted for as a selection effect or if a smaller fraction of mJy-level GPS sources evolve into CSS sources as compared to the Jy-level GPS sources. We find a few GPS sources with low luminosities, which we will follow up with VLBI to test whether they are the compact counterparts of FR I galaxies.

We conclude that, despite being historically favoured, single inhomogeneous SSA is not the dominant form of absorption amongst a large fraction of GPS and CSS sources. We find that FFA provides a good model for the majority of the spectra with observable turnovers, suggesting an inhomogeneous and clumpy ambient medium. Furthermore, we conclude that the majority of our GPS and CSS sources are young and evolving and may undergo recurrent activity over small time scales. We conclude that a very small fraction of GPS and CSS sources consists of frustrated, dying or restarted radio galaxies.

List of Abbreviations

$\boldsymbol{\alpha}$	Spectral Index: given by $S_\nu \propto \nu^\alpha$
$\boldsymbol{\sigma}$	r.m.s.: the r.m.s. noise level of an observation
ΛCDM	Λ Cold Dark Matter: the standard model of Big Bang Cosmology
AGN	Active Galactic Nuclei
ASKAP	Australian Square Kilometre Array Pathfinder
AT20G	Australia Telescope 20 GHz
ATCA	Australia Telescope Compact Array
ATLAS	Australia Telescope Large Area Survey
CABB	Compact Array Broad-band Backend
CDFS	*Chandra* Deep Field South
COINS	CSOs Observed In the Northern Sky
CSIRO	Australian Commonwealth Scientific and Industrial Research Organisation
CSO	Compact Symmetric Object
CSS	Compact Steep Spectrum
ECDFS	Extended *Chandra* Deep Field South
ELAIS-S1	European Large Area *ISO* Survey-South 1
EMU	Evolutionary Map of the Universe
FFA	Free-Free Absorption
FIR	Far Infrared
FIRST	Faint Images of the Radio Sky at Twenty Centimeters
FR I	Fanaroff-Riley Class I
FR II	Fanaroff-Riley Class II
FITS	Flexible Image Transport System
FWHM	Full Width Half Maximum
G	gauss: a unit of magnetic flux density

GB6 Green Bank 6 cm survey

GLEAM Galactic and Extragalactic All-sky MWA Survey

GMRT Giant Metrewave Radio Telescope

GPS Gigahertz Peaked Spectrum

HERG High-Excitation Radio Galaxy

HFPs High Frequency Peakers

HPBW Half Power Beam Width

HyLIRG Hyper-Luminous Infrared Galaxy

HzRGs High-z Radio Galaxies

IDR2 Internal Data Release 2: the 2nd GLEAM catalogue

IFRS Infrared-Faint Radio Source

IGM Intergalactic Medium

IR Infrared

ISM Interstellar Medium

Jy jansky: 1 Jy $\equiv 10^{-26}$ W m^{-2} Hz^{-1}

LBA Long Baseline Array

LERG Low-Excitation Radio Galaxy

LF Luminosity Function

LINER Low-Ionisation Nuclear Emission-line Region

LIRG Luminous Infrared Galaxy

LLS Largest Linear Size

LOFAR Low-Frequency Array for Radio astronomy

LSO Large Symmetric Object

MOST Molonglo Observatory Synthesis Telescope

MPS Megahertz Peaked Spectrum

MRC Molonglo Reference Catalogue

MSO Medium-sized Symmetric Object

MWA Murchison Widefield Array

NVSS NRAO VLA Sky Survey

PA Position Angle

pc parsecs: 1 pc $\simeq$ 3.26 light-years $\simeq 3.09 \times 10^{16}$ m

PMN Parkes-MIT-NRAO

QSO Quasi-Stellar Object

RFI Radio Frequency Interference

RG Radio Galaxy

RM Rotation Measure

r.m.s. root mean squared: also known as σ for a gaussian distribution

S/N signal-to-noise

SDSS Sloan Digital Sky Survey

SED Spectral Energy Distribution

SERVS *Spitzer* Extragalactic Representative Volume Survey

SF Star Formation

SFG Star Forming Galaxy

SMBH Supermassive Black Hole

SMC Small Magellanic Cloud

SSA Synchrotron Self Absorption

SWIRE *Spitzer* Wide-area InfraRed Extragalactic Survey

ULIRG Ultra-Luminous Infrared Galaxy

URC Unified Radio Catalog

USS Ultra-Steep Spectrum

VLA Very Large Array

VLBA Very Long Baseline Array

VLBI Very Long Baseline Interferometry

VLSS VLA Low-Frequency Sky Survey

WENSS Westerbork Northern Sky Survey

WISE *Wide-field Infrared Survey Explorer*

Chapter 1

Introduction

Many galaxies within our universe contain very bright and active radiation sources at their centres, which we refer to as Active Galactic Nuclei (AGN). AGN are powered by Supermassive Black Holes (SMBHs) many millions of times more massive than the Sun, but are only found in a few percent of galaxies. Less than ∼10% of AGN are detectable within typical radio observations, which we refer to as 'radio-loud AGN', and which are thought to have a major role in the evolution of the most massive galaxies and SMBHs (Alexander and Hickox, 2012). Radio-loud AGN are generally observed in two different forms: (1) quasars; and (2) Radio Galaxies (RGs). The 'unified model' (Barthel, 1989; Norris, 1992; Antonucci, 1993) reveals that orientation affects the appearance and observational characteristics of AGN (see Fig 1.1), in which radio galaxies are viewed edge-on, quasars are viewed face-on, and Blazars are viewed directly down the jet.[1]

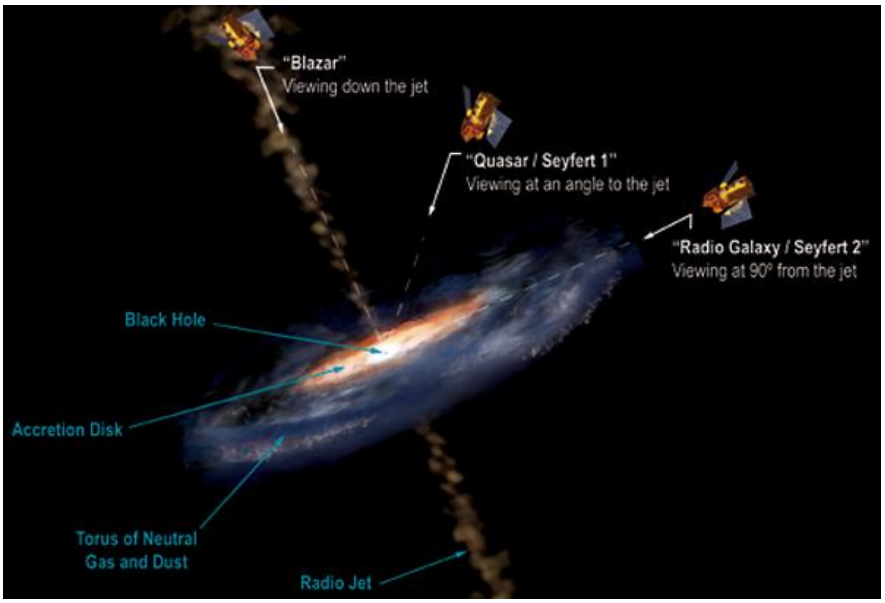

Figure 1.1: The unified model, in which an AGN is launching radio jets from the SMBH, which is surrounded by an accretion disc and dense torus. Radio galaxies are viewed edge on, quasars are viewed end-on, and Blazars are viewed directly down the jet. *Image credit —Aurore Simonnet / Sonoma State University.*

[1]Historically, there was a distinction between quasars, which were detected in the radio, and Quasi-Stellar Objects (QSOs), which were not. In this thesis, I refer to these as radio-loud and radio-quiet quasars / QSOs.

Quasars are the brightest galaxies in the universe, with a typical brightness of several hundred to several thousand times that of a normal galaxy contained just within the core, which can often outshine the host galaxy. The brightness of the core is a product of the large amounts of material being accreted onto the SMBH, within a region referred to as the *accretion disc*. Due to being oriented face-on, quasars are much more compact in the radio than RGs, and are often significantly variable in brightness.

RGs arise from material being ejected away from the SMBH at large angles to our line of sight. The ejecta are concentrated into thin radio jets, which usually emanate out of both sides of the accretion disc, perpendicular to the plane of accretion. The most powerful jets can carry material well beyond the galaxy, sometimes several million parsecs (pc). When the ejected material collides with the surrounding medium, it appears as two symmetric, compact and bright hotspots, which disperse into large diffuse radio lobes. These structures appear strong in the radio-continuum and hence we call these objects *radio galaxies*. An example of this is Centaurus A, which is illustrated in Figure 1.2. Since the data analysed in this thesis come primarily from the radio-continuum, radio galaxies are of particular interest.

The jet-hotspot-lobe structure of the largest classical double radio sources was first characterised by Fanaroff and Riley (1974) and divided into two distinct populations. Fanaroff-Riley Class I (FR I) galaxies have low luminosity and less well-defined lobes powered by a bright but lossy jet, and hotspots contained within $<50\%$ of the source extent. As these low-powered radio galaxies expand, their outer structure becomes a flaring and meandering plume that is typically brightest close to the core. Fig 1.3 shows a typical FR I source, 3C31, with its prominent inner jet and plumes extending out to 300 kpc. Fanaroff-Riley Class II (FR II) galaxies have high luminosity and well-defined lobes surrounding faint jets, a faint core and very prominent hotspots, which are contained within $>50\%$ of the source extent, and are hence referred to as having *edge-brightened* morphologies. Fig 1.3 shows a typical FR II source, Cygnus A, which reveals two symmetric lobes extending out to 160 kpc, characterised by bright hotspots, and faint jets and a faint core. These classifications relate to the ability of a jet to transport and deposit momentum and energy at the leading edge of the lobe (An and Baan, 2012).

1.1 Formation and evolution of AGN

It has long been suggested that the AGN and Star Formation (SF) within a galaxy are closely related and play a significant role in the evolution of galaxies. A typical scenario (e.g. Best et al., 2006; Croton et al., 2006; Hardcastle et al., 2007) involves the merger of a gas-rich spiral with another spiral or elliptical, causing an intense burst of SF together with "quasar-mode accretion" onto a central SMBH. The SMBH grows both through coalescence and through the accretion of cold disc gas from the host galaxies, producing a rapid growth of the SMBH mass. The outflows driven by the resulting powerful quasar winds quench SF activity (Malbon et al., 2007; Antonuccio-Delogu and Silk, 2008; Hopkins et al., 2008), and clear the central regions of fuel, starving the AGN, which begins accreting hot gas inefficiently ("radio mode accretion"). A dramatic example of this process can be found in the Ultra-Luminous Infrared Galaxy (ULIRG) F00183-7112 (Norris et al., 2012), in which a starbursting merger hosts a hidden powerful radio-loud AGN, whose jets have not yet broken through the shroud of dust and gas, and so is invisible at optical/NIR wavelengths. F00183 also appears to be in a transitionary stage between Gigahertz Peaked Spectrum (GPS) and Compact Steep Spectrum (CSS), which are generally thought to represent the youngest AGN (see section 1.3).

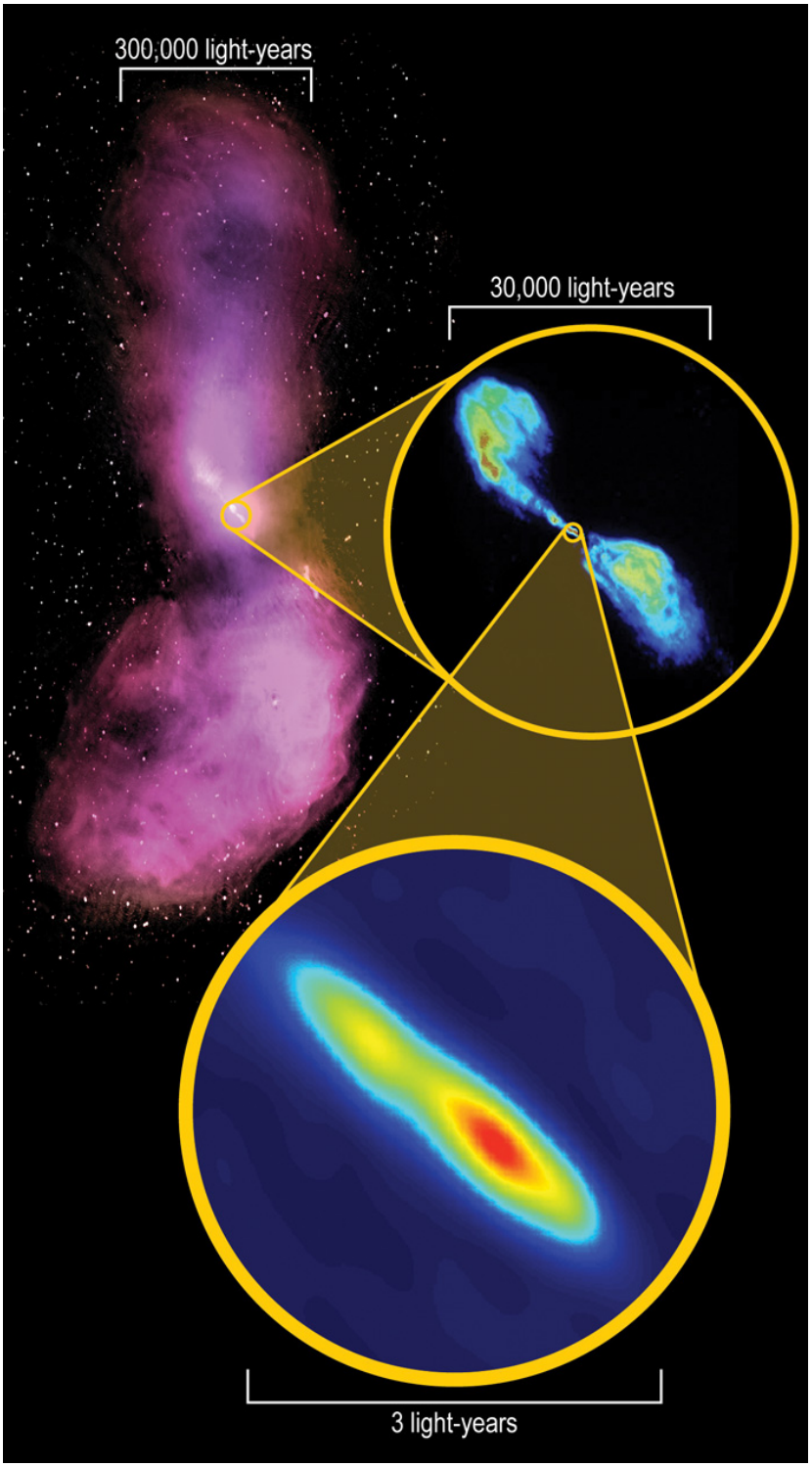

Figure 1.2: Centaurus A, one of the largest RGs in the sky. The radio lobes can be seen in pink, within which the jets and can be seen, within which the AGN can be seen.
Image credit —Whole galaxy: I. Feain, T. Cornwell & R. Ekers (CSIRO/ATNF); ATCA northern middle lobe pointing courtesy R. Morganti (ASTRON); Parkes data courtesy N. Junkes (MPIfR). Inner radio lobes: NRAO / AUI / NSF. Core: S. Tingay (ICRAR) / ICRAR, CSIRO and AUT.

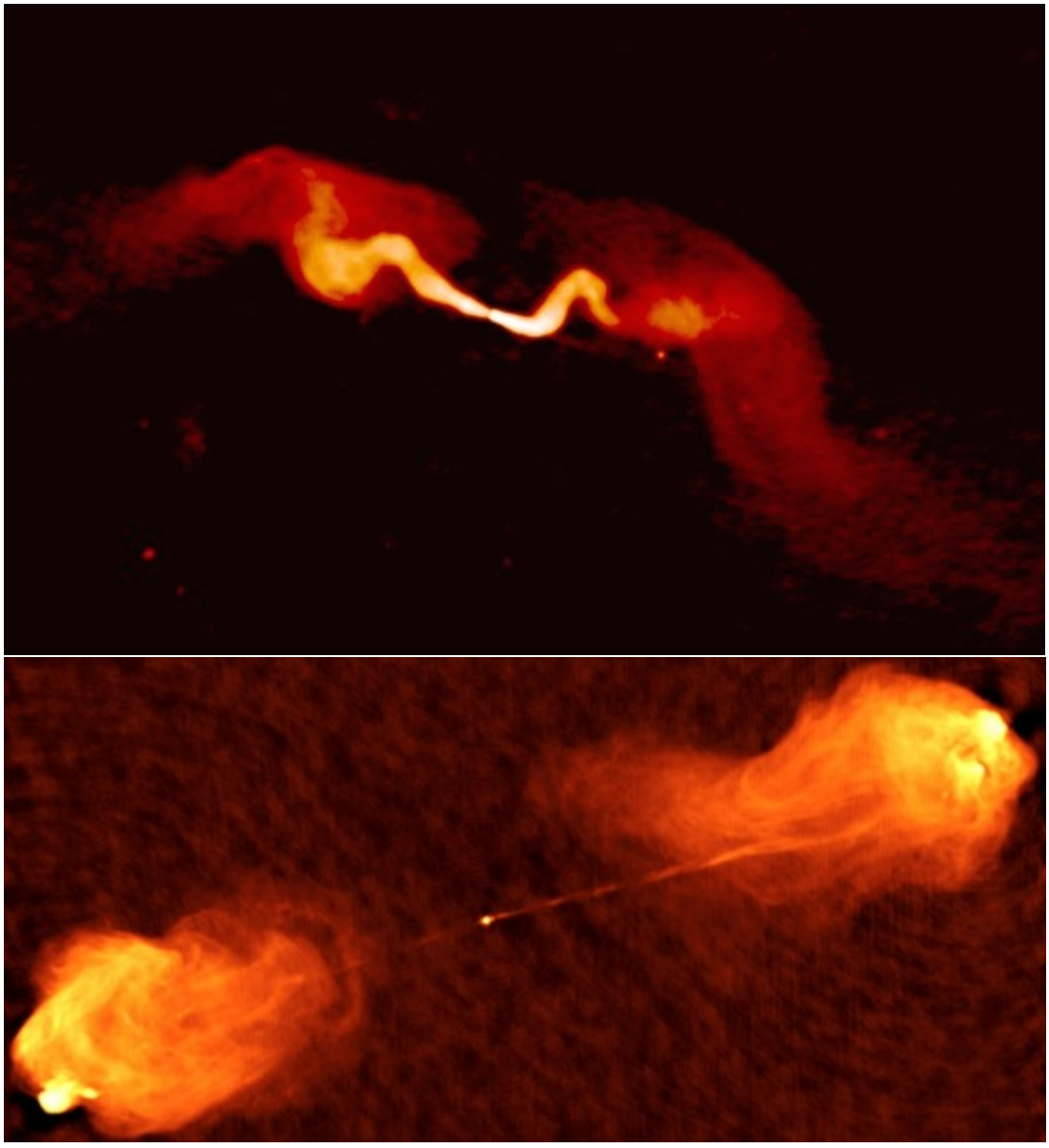

Figure 1.3: The FR I galaxy 3C31 (top), spanning 300 kpc, and FR II galaxy Cygnus A (bottom), spanning 160 kpc. Image courtesy of NRAO/AUI.

Best and Heckman (2012) proposed that the physical processes causing an AGN give rise to a fundamental dichotomy between High-Excitation Radio Galaxies (HERGs), in which the accretion is radiatively efficient within a classical accretion disc, and Low-Excitation Radio Galaxies (LERGs), in which the accretion is radiatively inefficient and therefore the accretion rate is significantly lower. These can be differentiated spectroscopically: HERGs have a classical accretion disc surrounding the SMBH, which causes excitation that can be observed in optical emission lines; LERGs lack a strong accretion disc and therefore have weak or no optical emission lines, but can still power radio jets.

Powerful radio sources ($L_{1.4\mathrm{GHz}} > 10^{25}$ W/Hz) represent only a small fraction of the AGN (Orienti, 2016). This suggests that the radio activity represents a transient phase in the life of these galaxies, or that the majority of AGN do not have a radio-loud phase. The typical lifetime of radio-loud phases, referred to within the context of galaxy evolution as the *duty cycle*, is $\sim 10^7 - 10^8$ years, followed by a relic phase that is roughly an order of magnitude shorter (Parma et al., 2007; Orienti, 2016). However, some young radio galaxies have been proposed to go through short-lived phases of activity of the order of $\sim 10^4 - 10^5$ years (Orienti, 2016; Kunert-Bajraszewska, 2016, and references therein). It has even been suggested that the whole lifetime of AGN is made up of many short phases, each typically lasting for $\sim 10^5$ years, which alternate between high and low accretion rates (Schawinski et al., 2015; Kunert-Bajraszewska, 2016, and references therein).

AGN are often triggered by mergers, which provide the fuel to the central AGN and star-bursting regions (Orienti, 2016). Chiaberge et al. (2015) find evidence that mergers are involved in triggering radio-loud AGN at all redshifts. However, as discussed by Alexander and Hickox (2012), other large-scale processes may be responsible for triggering AGN, such as secular evolution (either internal secular evolution or external secular evolution via galaxy interactions), and hot halo accretion. The latter of these is caused by the cooling and infalling of gas from the galaxy's halo and in thought to dominate SMBH growth for LERGs.

Shabala et al. (2012) present the timescales over which the starburst and AGN are triggered for a sample of dust lane early-type galaxies, including the delay of $100 - 150$ Myr between these two phases. However, these timescales are not known in general, nor whether the starburst always precedes the AGN. Furthermore, no studies investigating the co-triggering of the AGN and SF have been done at high-redshift.

It is clear that there is still much to be understood about the formation and evolution of AGN, particularly during the early stages of evolution and at high redshift. What is clear is that in order to gain a complete understanding of AGN evolution, the SF and AGN must be considered simultaneously. Here, we test this general model of AGN formation and evolution by studying GPS and CSS sources, which are thought to represent very young AGN (section 1.3), and Infrared-Faint Radio Sources (IFRSs), which are thought to represent very distant AGN (section 1.4).

1.2 Radio Astronomy

Radio astronomy involves observing and analysing radiation from one extreme end of the electromagnetic spectrum – namely that of very long wavelengths λ, ranging from about 0.3 mm — 30 m, and hence very low frequencies ν, as opposed to a typical optical wavelength of 0.6 μm. Radio waves, unlike other electromagnetic radiation such as X-rays and Gamma Rays, are transparent to our atmosphere over much of the radio range, through the earth's 'Radio Window', allowing the majority of radiation between ∼15 MHz – 300 GHz to

reach the ground. This emission comes from a number of astronomical sources, such as RGs, pulsars, quasars and Supernova Remnants.

1.2.1 Radio Telescopes

Radio emission is typically observed by radio dishes, such as in Fig. 1.5 and 1.6, which are most commonly large parabolic or spherical dishes which focus radio waves onto the feed of an antenna, where the signal is amplified and converted into a digital signal that can be analysed on a computer. The power received by radio telescopes from astronomical sources is extremely small and is measured in units of radio flux density ('flux' for short[2]) called the jansky (Jy), named after Karl Jansky, a pioneer in radio astronomy. This unit is equal to 10^{-26} W m^{-2} Hz^{-1}.

Single dish radio telescopes, such as the Parkes radio telescope, Mopra and Green Bank, are typically between 20 — 100 m in diameter, allowing a relatively large amount of energy to be reflected and combined in the antenna feed at once. Radio interferometers, such as the Australia Telescope Compact Array (ATCA), and the Very Large Array (VLA), combine a number of smaller radio dishes in a technique called radio interferometry.

1.2.1.1 The Resolution of a Radio Telescope

Any image of the sky captured with a radio telescope is the true sky image convolved with the telescope's response. The telescope's response to an object is caused by diffraction, which is a property of light, whereby light rays expand outwardly at an angle determined by the 'slit' they are being viewed through. If the light is viewed by a circular aperture, which is usually the case in radio astronomy (i.e. a dish), the pattern formed by a point source convolved with the telescope's response is an 'Airy disc', like that seen in Fig. 1.4.

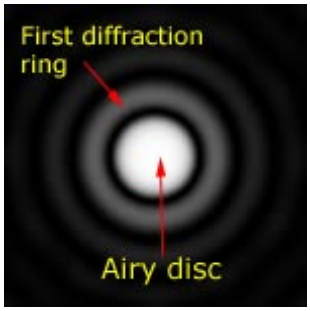

Figure 1.4: An Airy disc, showing the main lobe and diffraction fringes (or side lobes) formed by a circular aperture. Image provided by Brian Burton, Boston University.

An instrument is said to be diffraction limited if its resolution matches that of its theoretical resolution limited by diffraction. Two sources closer than the angular resolution of a telescope will not be resolved, due to their diffraction fringes (or side lobes) overlapping. All instruments with circular apertures are diffraction limited to an angular separation θ, given in radians by (Marr et al., 2015)

$$\theta = 1.22\frac{\lambda}{D}, \tag{1.1}$$

where λ is the wavelength of radio emission, and D is the diameter of the radio dish.

[2]'Flux' is technically defined as W m^{-2}, but since this unit is not used here, flux density is referred to as 'flux' at various points throughout the thesis

We equate the resolution of the telescope to the Full Width Half Maximum (FWHM) of the Airy disc pattern formed by a point source, which is the angular separation of the main lobe at half of its maximum. In the case of a circular aperture, the FWHM is given in radians by (Marr et al., 2015)

$$\theta_{\mathrm{FWHM}} = 1.02\frac{\lambda}{D} \tag{1.2}$$

Since the wavelength λ is such a relatively large value in radio astronomy, the aperture's diameter D must be large in order to achieve good resolutions. This is the reason for building such large radio telescopes, such as the 64 m Parkes radio telescope shown in Fig. 1.5.

As we can see from the equations above, only very high frequency radio waves can be observed with reasonable resolution with smaller dishes. In order to achieve resolutions more like that of optical telescopes, a much larger aperture is needed, especially in the case of low frequency radio waves. Hence the technique of interferometry is made incredibly useful, allowing massive apertures to be synthesised.

Figure 1.5: The 64 m Parkes radio telescope. Image courtesy of CSIRO.

1.2.2 Radio Interferometry

Radio interferometry, a technique first used in the 1940s, makes use of an array of radio dishes, such as in Fig. 1.6, in order to overcome limits of a single dish collecting area. To increase the diameter D of the aperture's collecting area, such that the diffraction limit becomes a much smaller angular size, we must combine an array of smaller apertures in order to synthesise such an area. We term the *baseline length* as the distance between two telescopes within an array. The resolution of the interferometer is synthesised to the resolution that a dish with a diameter

equal to the largest baseline would have. The resolution is now given in radians by (Marr et al., 2015)

$$\theta_{\mathrm{FWHM}} = \frac{\lambda}{b} \tag{1.3}$$

where b is the interferometric baseline length. However, the sensitivity of the interferometer is only the equivalent of a dish with a collecting area of the sum of the collecting areas within the array. Furthermore, arrays can suffer from what is referred to as 'missing flux', due to the fact that they have no 'zero spacing' and are not sensitive to large-scale emission. This problem is only significant for extended objects, and can be partially overcome by using an array configuration that contains short baselines.

Figure 1.6: The Australia Telescope Compact Array (ATCA), an interferometer in Narrabri, northern NSW. Image courtesy of CSIRO.

1.2.3 Very Large Baseline Interferometry

Very Long Baseline Interferometry (VLBI), as the name suggested, takes the idea of interferometry and applies it to very long baselines that stretch across vast distances. Given equation 1.3, if we have an extremely large baseline b that stretches over hundreds or thousands of kilometres, the resolution will be sub-arcsec, or in most cases, milliarcsec (mas $-$ $\sim$1 / 3 600 000 of a degree). Due to only using extremely large baselines, the missing flux problem is very extreme within VLBI observations, and therefore only very compact sources can be reasonably observed with VLBI, such as AGN, given that the emission will be resolved out for more extended sources. The VLBI network which will be considered in this project is the Australian Long Baseline Array (LBA; Tzioumis, 2010), shown in Figure 1.7.

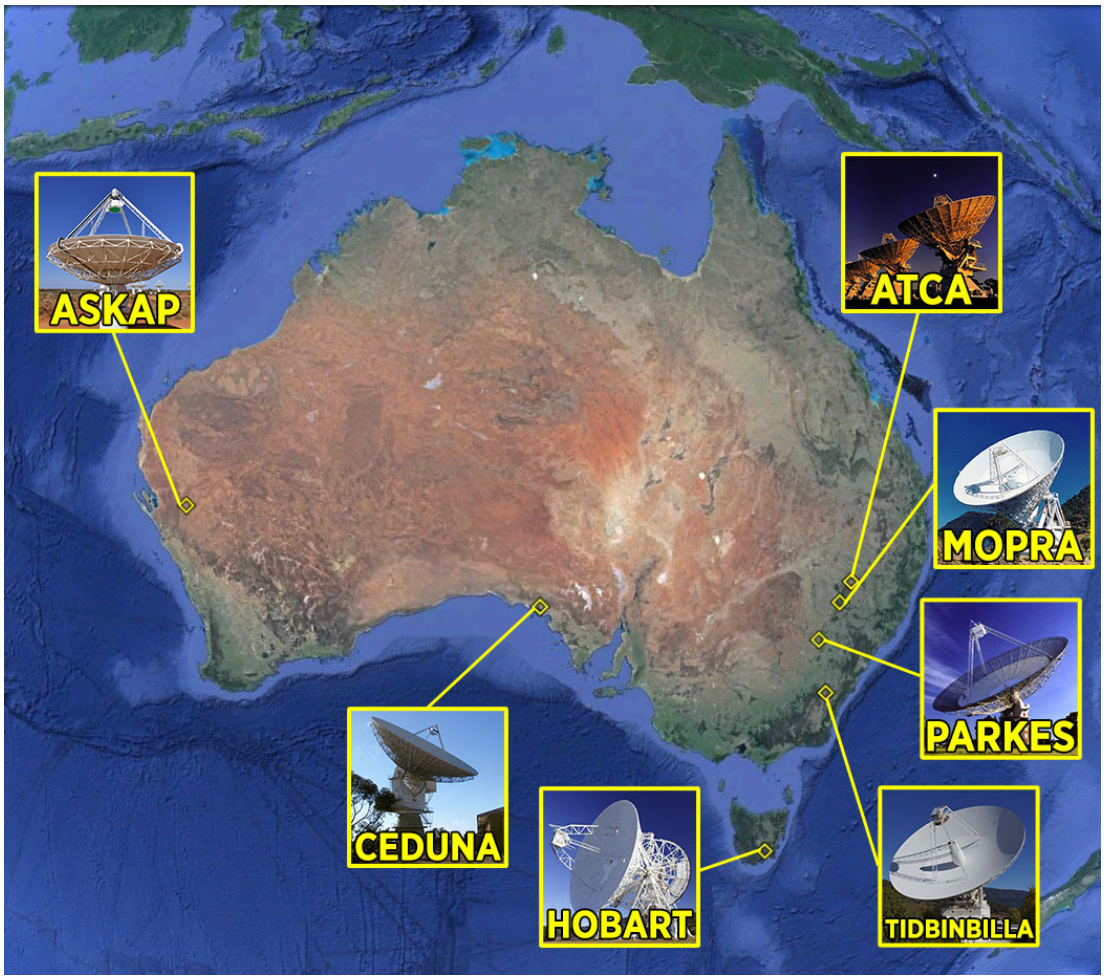

Figure 1.7: The VLBI telescopes within Australia belonging to the LBA. *Image credit: A. O'Brien.*

1.2.4 Spectral Index

Radio telescopes have historically had small bandwidths of a few to a few hundred MHz, so typical observations would only capture an object's radio emission over a small range of frequencies. Therefore, an object's radio spectrum has usually been modelled by a power law, given by

$$S_\nu = S_0 \nu^\alpha, \tag{1.4}$$

where α is referred to as the 'spectral index' of an object, which is a measure of how the flux density changes as a function of frequency, and S_0 is the normalisation flux density. Performing a least-squares fit allows for S_0 and α to be solved. Most radio sources are dominated by synchrotron emission (see section 1.3.1) at GHz frequencies, with $\alpha = -0.7$.

Modern radio telescopes have large bandwidths of a few GHz, across which a power law often inadequately describes an object's radio spectrum, many of which show curvature. Therefore, more complex models are needed to model the radio spectrum, particularly in the case of GPS and CSS sources.

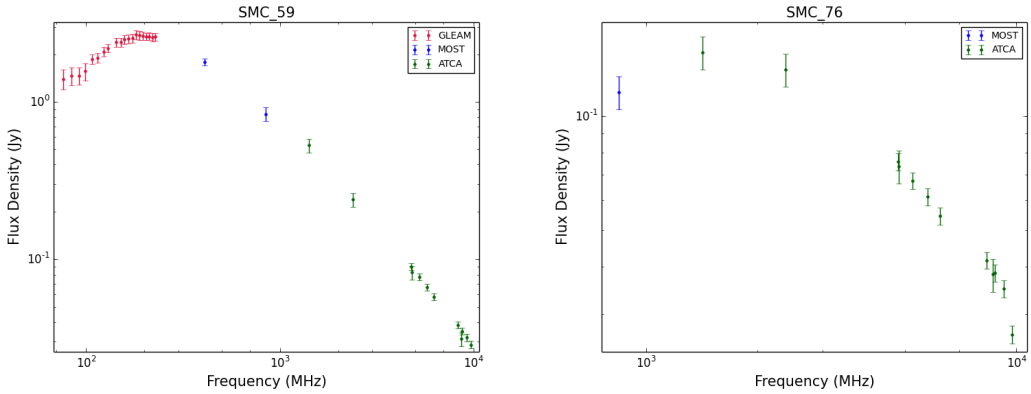

Figure 1.8: Radio spectrum of a CSS (left) and GPS (right) source from this thesis, respectively turning over at ∼200 MHz and ∼1.5 GHz. The colours denote the telescopes or surveys each flux density comes from.

1.3 GPS and CSS sources

Orienti (2016) provides an excellent summary of GPS and CSS sources, much of which is summarised throughout this section.

GPS and CSS sources are small but powerful AGN that have a convex radio spectrum with a characteristic turnover (see Fig. 1.8), and are hosted in quasars, RGs or Seyfert galaxies (Gelderman and Whittle, 1994; de Vries et al., 1997; Stanghellini, 2003).[3] They are widely thought to represent the earliest stages of radio-loud AGN evolution (e.g. Fanti et al., 1995; O'Dea, 1998; Polatidis and Conway, 2003; Tinti and de Zotti, 2006; Fanti, 2009a; Randall et al., 2011; Orienti, 2016). GPS sources turn over at a few GHz, or above a few GHz in the subclass of High Frequency Peakers (HFPs) defined by Dallacasa et al. (2000), and are typically < 1 kpc in size. CSS sources turn over at a few hundred MHz, have steep ($\alpha < -0.7$) spectral indices across the GHz range, and are typically $1 - 10$ kpc in size. It is generally considered that most GPS sources evolve into CSS sources, some of which gradually evolve into FR I and FR II galaxies. If GPS/CSS sources are the youngest RGs, then they are ideal objects for investigating the birth and early lives of AGN, including any associated SF and its effect on the AGN.

'Classical' GPS and CSS sources have radio powers $P_{1.4\mathrm{GHz}} > 10^{25}$ W/Hz and angular sizes not exceeding $1-2$ arcsec (Orienti, 2016). However, as the class as a whole has been unravelled, many GPS and CSS sources have been found with radio powers lower than this (e.g. Fig. 1.12), many of which would have sizes exceeding $1 - 2$ arcsec at any redshift (e.g. even at $z = 1.5$, most of the CSS sources in this figure would be $> 2''$).

GPS and CSS sources represent a large fraction ($15 - 30\%$, depending on frequency) of the radio sky, at least at the mJy levels in which they have been well sampled (O'Dea, 1998; Orienti, 2016). In fact, there is a significant excess of compact sources compared to what is predicted by evolutionary models, even if it is assumed that: 1) they decrease in luminosity throughout their growth; and 2) their growth is initially confined via interactions between the ambient medium and expanding jet. The excess is confirmed by the distribution of linear sizes within GPS and CSS samples.

[3]Within this thesis, as in the literature, I refer to quasar-type GPS / CSS sources as those hosted by quasars whose jets are oriented toward us, and galaxy-type GPS / CSS source as those hosted by radio galaxies whose jets are oriented at large angles to our line of sight.

It is generally accepted that GPS and CSS sources are young and evolving radio sources that are developing into large-scale radio sources (Fanti et al., 1995; Alexander, 2000; Snellen et al., 2000; Orienti, 2016). Evidence for this *youth* hypothesis includes their appearance as scaled-down versions of FR I/II galaxies, kinematic age estimates via proper motion measurements of their hotspot expansion speeds (Polatidis and Conway, 2003; Polatidis, 2009; Giroletti and Polatidis, 2009) and models of their radio spectra and spectral ages (Murgia et al., 1999; Murgia, 2003). However, as stated by Callingham et al. (2015), this hypothesis is still disputable, since statistical studies of the Luminosity Functions (LFs) have revealed an over-abundance of the most compact sources relative to the number of large-scale radio galaxies (Readhead et al., 1996; O'Dea and Baum, 1997; An and Baan, 2012).

An alternative interpretation of the compactness of GPS and CSS sources is that they are frustrated by interactions with dense gas and dust in their environment, which halts the expulsion of the jets (van Breugel et al., 1984; Baum et al., 1990). Furthermore, some GPS and CSS sources have been interpreted as: (1) prematurely dying radio sources (Fanti, 2009b; Orienti et al., 2010b); (2) recurrent radio galaxies (Baum et al., 1990; Shulevski et al., 2012). In the evolutionary model presented by An and Baan (2012), they consider each of these scenarios to exist amongst the GPS and CSS population, with an estimate of only $\sim$30% of sources being those which will evolve into large scale radio galaxies.

Orienti (2016) state that the *frustration* hypothesis was not supported by multi-frequency observations, which showed that the host galaxies contained gas similar to FR II hosts (Fanti et al., 1995, 2000; Siemiginowska et al., 2005). However, many observational studies of individual GPS sources have provided good evidence for the frustration scenario (e.g. Tingay and Edwards, 2015; Callingham et al., 2015). As noted by Callingham et al. (2015), one reason these hypotheses are still under debate is because the absorption mechanism responsible for the peaked spectra is still under debate.

1.3.1 Radio spectra and absorption models

The spectra of GPS and CSS sources are dominated by synchrotron emission, which is the radiation caused when a charged particle accelerates along a path that is curved by a magnetic field. Electrons travelling at relativistic velocities produce a continuum of synchrotron emission, which typically gives a spectral index, based on the electron energy spectrum, of $\alpha = -0.7$. However, the spectra of GPS and CSS sources are affected by absorption at lower frequencies, and can also be affected by a spectral break (see section 1.3.1.3), which typically occurs at high frequencies.

The various absorption mechanisms responsible for the shape of GPS and CSS spectra and the associated models are well outlined in Callingham et al. (2015), which presents each of these with respect to the spectrum of GPS source PKS B0008-421, and which we summarise below.

1.3.1.1 Synchrotron Self Absorption

Historically, the turnover in the spectra of GPS and CSS sources has been generally thought to be caused by SSA, related to the compact dimension of the sources (Snellen et al., 2000; Orienti and Dallacasa, 2008a; Fanti, 2009a; Orienti, 2016). SSA is an internal process in which the same population of electrons is responsible for the synchrotron emission and self-absorption, which contrasts other models in which the absorption is external. In this model, the turnover occurs at a frequency where the low-energy photons associated with synchrotron emission are likely to be absorbed, which occurs in the optically-thick region and increases toward lower frequencies.

Therefore very low frequency emission is only visible within a thin shell at the surface of the source, and as the frequency increases, photons begin to emerge from deeper within the source, which increases the total flux that is observed, until the optically-thin region is reached and the spectrum turns over. If we assume the region emitting (and absorbing) the synchrotron photons is homogeneous, we can model the spectrum as

$$S_\nu = a \left(\frac{\nu}{\nu_m} \right)^{-(\beta-1)/2} \left(\frac{1 - e^{-\tau}}{\tau} \right), \tag{1.5}$$

where a is the normalisation parameter of the intrinsic synchrotron spectrum, ν_m is the turnover frequency, β is the power-law index of the electron energy distribution, and τ is the optical depth given by $(\nu/\nu_m)^{-(\beta+4)/2}$. In this model, ν_m is the frequency at which the source becomes optically-thick, defined as the point at which the mean free path of electron-photon scatterings is approximately the size of the source. This model predicts an optically-thick spectral index of 2.5, which is characteristic of a homogeneous opaque synchrotron source (Kellermann and Pauliny-Toth, 1981). Spectral indices shallower than this are generally attributed to inhomogeneity of the SSA regions.

Tingay and de Kool (2003) point out that the radio spectrum of unresolved sources represents the sum of the two dominant components, which are the mini-lobes. Therefore, equation 1.5 assumes self-similarity between the two lobes and their environments, which is likely for symmetric sources. However, assuming self-similarity doesn't exist (e.g. asymmetric sources), Tingay and de Kool (2003) suggest that the spectra of GPS and CSS sources can be modelled by the sum of two separate instances of SSA, each with a separate non-thermal distribution of electrons, given by

$$S_\nu = \sum_{i=1,2} a_i \left(\frac{\nu}{\nu_{m,i}} \right)^{-(\beta_i-1)/2} \left(\frac{1 - e^{-\tau_i}}{\tau_i} \right). \tag{1.6}$$

In the SSA model, the turnover frequency and peak flux density should relate to one another and provide constraints on the magnetic field. In previous studies of bright sources, this relation has suggested a differentiation between galaxy-type sources, which yield an anti-correlation between these properties, and quasar-type sources, which do not appear to follow this relation (Orienti, 2016).

In the homogeneous SSA model, the magnetic field strength B in gauss (G) is given by

$$B \sim f(\beta)^{-5} \theta^4 S_p^{-2} \nu_m^5 (1+z)^{-1}, \tag{1.7}$$

where $f(\beta)$ is a function that depends only weakly on β from equation 1.5 and is $\sim$8, θ is the maximum angular size of the source in mas, S_p is the peak flux density in Jy, ν_m is the turnover frequency in GHz, and z is the redshift (Kellermann and Pauliny-Toth, 1981). Alternatively, the magnetic field strength can be estimated by assuming that the minimum energy of the radio source is equipartitioned between the magnetic field and the radiating particles. For sources with low-frequency turnovers, the magnetic field calculated from the spectrum is not in agreement with those derived from equipartition (Scott and Readhead, 1977; Readhead, 1994), whereas some studies indicate that these two are in good agreement for HFPs (e.g. Orienti and Dallacasa, 2008a). The estimated magnetic field strengths range from 0.1 milli-gauss (mG) in the lobes of CSS sources to a few hundred mG in the most compact components of HFPs (Orienti, 2016, and references therein.), which generally follows the trend of what is expected from a source that is adiabatically expanding.

1.3.1.2 Free-Free Absorption

The other dominant model used to account for the spectra of GPS and CSS sources is FFA, which results from emission being attenuated by an ionised screen external to the emitting electrons, which has a homogeneous or inhomogeneous structure. In the homogeneous case, assuming that the screen surrounds the entire region of synchrotron emission, the spectrum is modelled by

$$S_\nu = a\nu^\alpha e^{-\tau_\nu}, \tag{1.8}$$

where α is the synchrotron spectral index, τ_ν is the optical depth, parameterised by $\tau_\nu = (\nu/\nu_0)^{-2.1}$, where ν_0 is the frequency at which $\tau_\nu = 1$.

As in the case of the double SSA model (equation 1.6), Tingay and de Kool (2003) suggest that we can model the radio spectrum with two separate homogeneous free-free absorbing screens, each with two different electron populations, given by

$$S_\nu = \sum_{i=1,2} a_i \nu^{\alpha_i} e^{-\tau_{\nu,i}}. \tag{1.9}$$

Another model, proposed by Bicknell et al. (1997), assumes the screen is inhomogeneous, which is modelled by clouds with a power-law distribution of optical depths parameterised by p, such that the spectrum is given by

$$S_\nu = a(p+1)\gamma\left[p+1, \tau_\nu\right]\left(\frac{\nu}{\nu_0}\right)^{2.1(p+1)+\alpha}, \tag{1.10}$$

where γ is the lower incomplete gamma function of order $p+1$, given by

$$\int_0^{\tau_\nu} e^{-x} x^p dx, \tag{1.11}$$

and $\tau_\nu = (\nu/\nu_0)^{-2.1}$. Since γ and the last term, $(\nu/\nu_0)^{2.1(p+1)+\alpha}$, scale differently as a function of ν, ν_0 does not represent the observed turnover frequency ν_m, but will usually be lower, except for large values of α or small values of p.

1.3.1.3 Spectral breaks

Another feature of the spectra of GPS and CSS sources is the steepening of the spectral index at high frequencies, referred to as a spectral break (see Fig 1.9). This effect is due to synchrotron and inverse-Compton cooling in the jets and lobes, in which higher-energy electrons deplete more quickly, since their energy is expelled faster. Kardashev (1962) models the spectral break in a system in which the jets are continually switched on, injecting electrons into a volume with a constant magnetic field. In this model, there is an abrupt change in the spectrum at the break frequency, at which point the synchrotron spectrum steepens from α to $\alpha - 0.5$, where α is the injection spectral index (i.e. the synchrotron spectral index of fresh electrons, which is typically -0.7). Murgia (2003) show that this model more accurately describes the spectrum of a GPS or CSS source as a whole, integrated over all of its components.

In an alternative model, proposed by Jaffe and Perola (1973), the jet has switched off and the radio source has become a relic, and therefore no new particles have been injected. In this model, the Kardashev (1962) spectral break may be found at lower frequency below the turnover, as in Callingham et al. (2015), and a second break frequency exists at even higher frequency, above which there is a smooth exponential drop. This spectral break is a multiplicative term

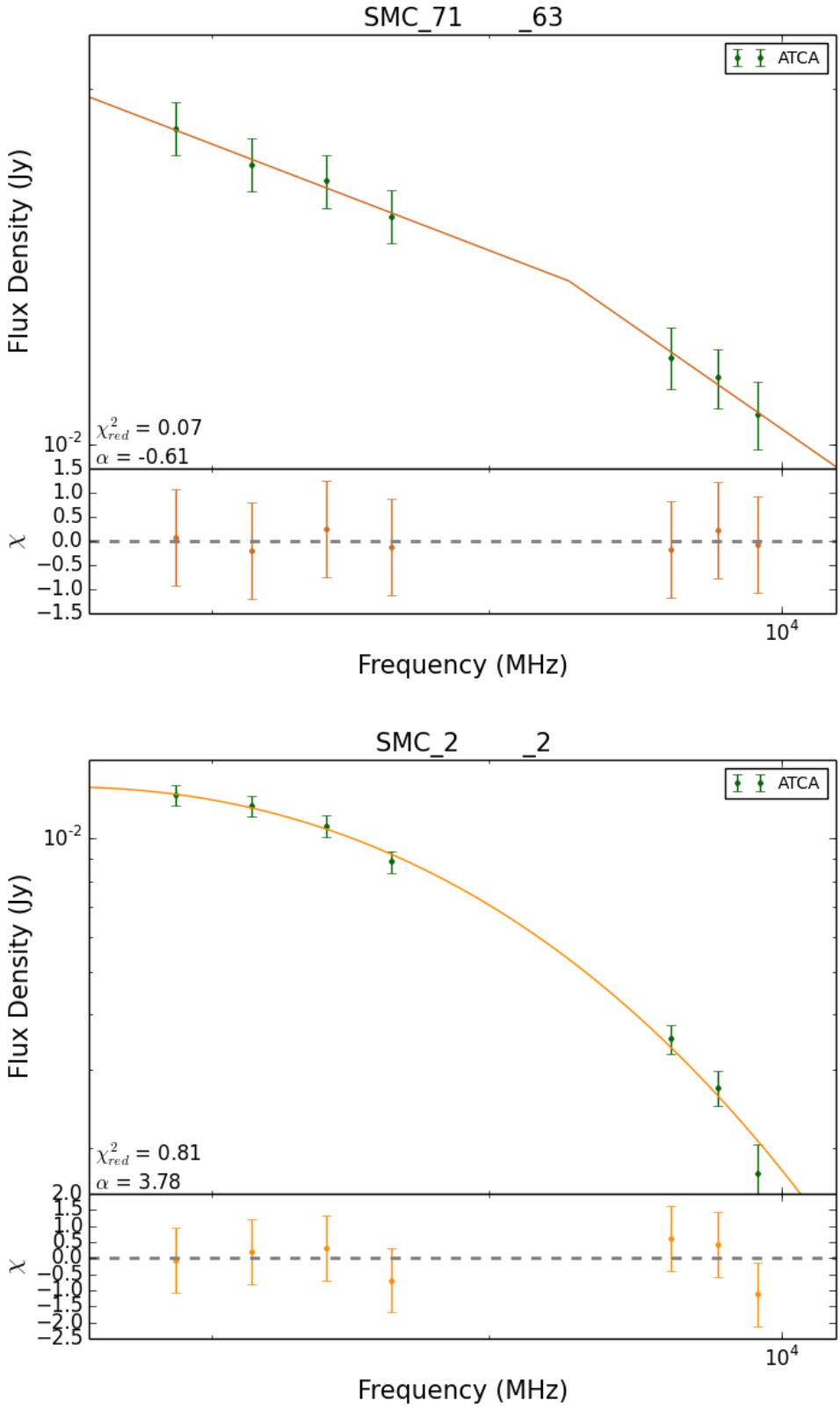

Figure 1.9: Two spectral breaks in the high-frequency, optically-thin regions of two sources from this thesis (see section 4.1): a Kardashev break (top) and an exponential break (bottom).

in the absorption model given by $e^{-\nu/\nu_{\rm br}}$, where $\nu_{\rm br}$ is the break frequency. Therefore, unlike the Kardashev (1962) break, this term significantly affects the shape of the spectrum even below the spectral break. Murgia (2003) suggest that this model more accurately describes the spectrum of sources which have ceased injecting electrons for a significant fraction of their lifetime, or in the lobes of high-resolution images, in which the regions where the electrons age can be differentiated from the regions where they are injected.

Murgia (2003) derive the spectral age (t) based on the electron lifetime, which is given by

$$t_s = 5.03 \times 10^4 \cdot B^{-1.5}[(1+z)\nu_{\rm br}]^{-0.5} \text{ years}, \tag{1.12}$$

where B is the strength of the magnetic field in mG and $\nu_{\rm br}$ is the break frequency in GHz. In a model with an exponential break, its frequency ($\nu_{br_{\rm exp}}$) relates to the (Kardashev) break frequency (ν_{br}) via

$$\nu_{br_{\rm exp}} = \nu_{br}\left(\frac{t_s}{t_{\rm off}}\right)^2, \tag{1.13}$$

where $t_{\rm off}$ is the turnoff time, since the jet ceased injecting new electrons (Parma et al., 2007). The break frequency is often difficult to observe, and can be hidden below the turnover, so detailed observations and modelling of the radio spectra are necessary to provide a sufficient estimate of the spectral age. Where a spectral break is hidden below the turnover, as in Callingham et al. (2015), an injection spectral index of $\alpha+0.5$ is expected, where α is the optically-thin spectral index. Murgia (2003) states that in sources dominated by jets or hotspots, the spectral age represents the age of these dominant components, which is expected to be significantly less than the source age and perhaps completely unrelated. In lobe-dominated systems, all of the electrons produced over the lifetime of the source have been accumulated together in the lobes, and therefore the spectral age is likely to represent the source age.

1.3.2 Radio Morphology

Radio imaging not only reveals the spectra of GPS and CSS sources, but also their compact jets, cores, hot spots and lobes. The high-resolution imaging required to reveal such compact details is usually limited to Very Large Baseline Interferometry (VLBI), but can also be achieved with high-frequency short-baseline observations. The radio morphologies of GPS and CSS sources divide into three main classes of morphology: 1) symmetric; 2) core-jet; 3) complex.

The most commonly-observed morphologies are symmetric, in which a two-sided structure is observed that resembles a scaled-down FR II source, consisting of steep-spectrum mini-lobes and hotspots, sometimes with a weak inverted or flat-spectrum core and weak jets. These are further sub-divided into Compact Symmetric Objects (CSOs), which have linear sizes $l < 1$ kpc, and Medium-sized Symmetric Objects (MSOs), which have $l > 1$ kpc. They form the family of radio galaxies together with Large Symmetric Objects (LSOs), which have $l \gtrsim 100$ kpc, and which consist of FR Is and FR IIs (An and Baan, 2012). CSOs are generally hosted by low-redshift galaxies (Wilkinson et al., 1994; de Vries et al., 2009). Although we label them as symmetric, a large fraction of CSOs and MSOs have asymmetric morphologies (see Fig 1.10), in which one side is significantly brighter (Saikia et al., 2003; Rossetti et al., 2006). In the case that a core is detected, the brighter lobe is typically located closer to the core, which is the opposite to what we expect from the effects of Doppler-boosting and path delay (Orienti, 2016, – see section 1.3.2.1), suggesting that this is due to the interaction of the jet and ambient medium. In CSOs and MSOs, the core typically represents only a few % of the flux density.

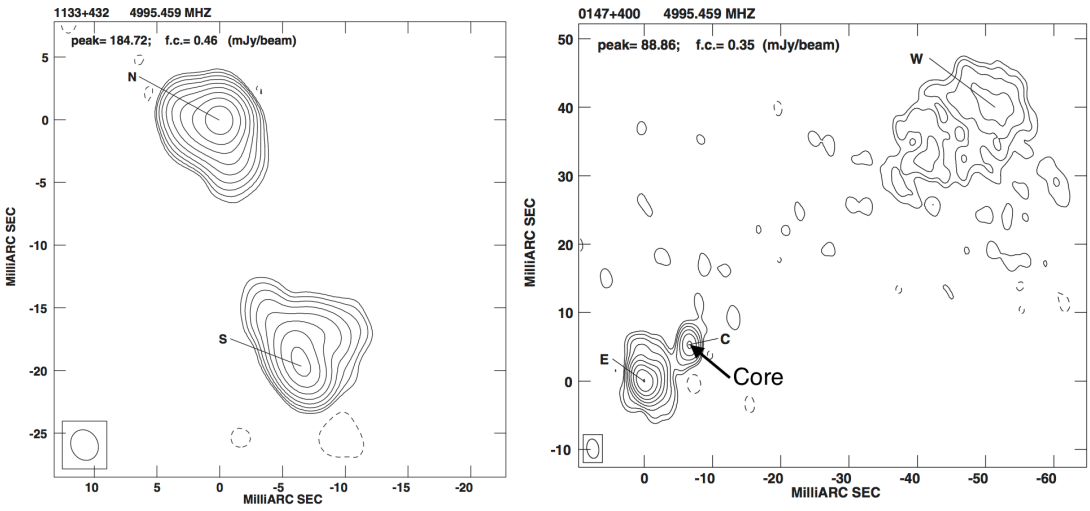

Figure 1.10: An example of a symmetric (left) and an asymmetric (right) CSO, taken from Orienti et al. (2004). The asymmetric source shows a core very close to the hotspot and lobe from one side, which are much brighter than the opposing hotspot and lobe.

Contrarily, the core in sources with a core-jet or complex morphology dominates the radio emission, suggesting that significant Doppler-boosting occurs in these cases.

1.3.2.1 Projection effects

Doppler-boosting, also referred to as *relativistic beaming*, is an effect in which a source of radiation is moving toward an observer at relativistic speeds and therefore an increased luminosity is observed. In radio galaxies, this is caused when a jet is oriented at small angles to the line of sight, which causes a bright relativistic jet and a weak or undetectable counter-jet. Geometrical foreshortening can also be present alongside Doppler-boosting, whereby an object appears smaller due to being inclined toward or away from an observer's line of sight. These effects account for core-jet morphologies, which are one-sided and shortened.

Core-jet sources are typically hosted by high-redshift quasars (Stanghellini et al., 1997; Rossetti et al., 2005; Orienti et al., 2006), giving further evidence for projection effects. The most luminous sources with a complex morphology appear to be affected by boosting effects, while many of the low-luminosity complex sources appear to be intrinsically distorted and contain weak extended emission (Orienti, 2016, and references therein).

Fanti et al. (1990) investigated whether foreshortening could cause the compact sizes of GPS and CSS sources, but concluded that this was unlikely and that $< 25\%$ could appear compact due to projection effects.

1.3.3 Variability and contamination

GPS and CSS sources have low variability in general on time scales of hours to decades (O'Dea et al., 1991; Callingham et al., 2015; Orienti, 2016), in which the variations are due to the evolution of the jet that has originated from the black hole and accretion disc system (Tingay and Edwards, 2015). As these objects are compact, the jet contributes to a small fraction of the total flux density, which results in low variability.

The spectral and flux-density variability of GPS and CSS sources has been studied over many epochs of multifrequency observations, which are near-simultaneous where possible. This

long term-monitoring has revealed that most CSS sources are not variable, while some objects with a GPS or HFP spectrum are variable. In particular, many quasars have been found to adopt a peaked spectrum only during a flaring event, when beaming components of the jet dominate the radio emission, whilst maintaining a flat spectrum during their normal state (Tinti et al., 2005; Torniainen et al., 2005). A peaked spectrum can also result from non-simultaneous observations of variable flat spectrum quasars. In both of these cases, the peaked spectrum is not related to the evolution of radio galaxies, and therefore these objects 'contaminate' samples of HFPs/GPS/CSS sources. These sources can be detected through large variability above the turnover alongside small variability below the turnover, which is indicative of a quasar in which the jet is pointed along our line of sight.

Torniainen et al. (2007) found that at least 30% of galaxy-type GPS sources retained their classification after undergoing long-term monitoring and simultaneous measurements of their radio spectra, with another possible 30% that could not be confirmed due to lack of data. Comparatively, Orienti et al. (2010a) found that $\sim$56% of HFPs retain their classification after long-term monitoring. Furthermore, most of the quasar-type GPS, CSS and HFPs show significant spectral and flux-density variability (Orienti et al., 2007). Less than 10% of the quasar-type GPS sources in literature retain their classification (Torniainen et al., 2005). For both types, the contamination rate increases with increasing turnover frequency.

However, variability does not always imply contamination. Tingay and de Kool (2003) show that source expansion may result in spectral or flux-density variability. In the youngest sources, these evolutionary timescales can be over a few tens of years, which are observable over epochs of $5 - 10$ yr (Orienti, 2016). In the SSA model, source expansion will cause the turnover to shift to lower frequency, the flux density to decrease in the optically-thin region and increase in the optically-thick region and at the turnover.

Therefore, depending on the turnover frequency, sources identified as HFPs or GPS sources can be contaminated by up to 60% by quasars or other sources temporarily adopting a peaked spectrum that isn't related to galaxy evolution. Therefore, any candidate GPS or CSS sources must be confirmed via a low level of variability, at the level of $\lesssim$10%, particularly above the turnover, where the most variability is expected. Such a step is necessary to justify the use of multi-frequency, multi-epoch data to model the radio spectrum.

1.3.4 Jet and luminosity evolution

Many evolutionary models have been put forward to describe how the luminosity, linear size and jet velocity of GPS and CSS sources evolves (e.g. Fanti et al., 1995; Readhead et al., 1996; Snellen et al., 2000; An and Baan, 2012). Most of these models predict an increase in luminosity alongside a decrease in the velocity of the jet during the stages when the radio emission is still contained within the dense narrow-line region (NLR), and then a decrease in luminosity alongside a roughly constant jet velocity once the jet emerges from the NLR.

Orienti and Dallacasa (2014) investigated a sample of 51 *bona fide* young radio sources spanning linear sizes from a few pc to tens of kpc to determine their evolution. To minimise projection effects, only objects optically identified as galaxies were considered. In agreement with the evolutionary models, Orienti and Dallacasa (2014) found that sources increased in luminosity until a few kpc, after which the sources decreased in luminosity. This can be explained by the smallest sources residing within the innermost region of the host galaxy, amongst the dense and inhomogeneous ambient medium where radiative losses dominate, resulting in more radio emission. As the radio source expands beyond a few kpc, it begins to enter a less

dense ambient medium and adiabatic losses dominate, resulting in less radio emission. Kunert-Bajraszewska et al. (2010) performed the same analysis for a sample of CSS sources with low luminosities comparable to FR I galaxies. They found that high-power sources seemed to follow the expected evolutionary path, but that low-power sources fell short of this path, suggesting they may be prematurely dying sources.

It is still unknown why and when the radio emission within GPS and CSS sources switches off. As mentioned in section 1.3, there is an excess of compact objects compared to what is predicted by evolutionary models. This suggests the existence of a large fraction of short-lived objects, which are unable to become FR I/II galaxies. This idea is also supported by statistical studies of CSO ages, which reveal a sharp peak in the age distribution under 500 years (Gugliucci et al., 2005), and by low-luminosity CSS sources (Kunert-Bajraszewska et al., 2010). These sources would quickly fade from flux-limited catalogues, since, without the supply of new relativistic particles, the radio emission rapidly fades and steepens due to significant electron depletion, as in the Jaffe and Perola (1973) model. This is also consistent with the fact that few of these "faders" have been observed so far, based on steep spectral indices across the whole source and the absence of active regions (Kunert-Bajraszewska et al., 2005, 2006; Orienti et al., 2010b).

However, not all of these dying radio galaxies are destined to fade. Recurrent activity had been observed in some of these, in which active regions like a core and hotspots are found within the fossil of radio galaxy having undergone a previous cycle of activity. A clear example is presented by B0925+420, which is an intermittent FR II galaxy in which three cycles of radio activity have been observed (Brocksopp et al., 2007). Other examples include the GPS galaxy J0111+3906 and CSS galaxy B2 0258+35, which have been observed within remnants respectively a few kpc and 160 kpc in size, estimated to have occurred $\sim 10^8$ years ago (Orienti, 2016, and references therein). In the example of HFPs J1511+0518 and OQ208, a relic was found $\sim$50 pc from the reborn jet, suggesting that for some radio galaxies, the duty cycle is $10^3 - 10^4$ years (Orienti, 2016, and references therein). When it comes to modelling the spectra for these intermittent and recurrent sources, the assumptions of continuous injection in the Kardashev (1962) model may not hold. If no recent nuclear activity has occurred, the Jaffe and Perola (1973) model will more suitably model the spectra that is dominated by synchrotron cooling / electron ageing across the whole electron population.

Hence, Orienti (2016) proposes a model for the life-cycle of radio emission within radio galaxies (see Fig 1.11). The evolutionary models predict CSOs should evolve into FR II galaxies within $10^7 - 10^8$ years before entering the relic phase. However, not all CSOs become FR II galaxies, but there exists a population of short-lived and fading objects which are under-represented in flux-limited catalogues. If the activity ceases only temporarily and the emission restarts, the source may again appear as a CSO before the radio spectra significantly steepens, and the source may still evolve into a FR II. However, if no new activity occurs, the fading source will emit at lower frequencies until it disappears below the MHz band altogether.

1.3.4.1 A detailed evolutionary model

An and Baan (2012) state that the morphological and spectral characteristics of radio sources are determined from their power, local environment and evolutionary stage, and can be characterised by observables such as the kinetic power, the source extent, the hotspot expansion speed, and the density gradients of the ambient medium along the path of the jets and lobes. In particular, the morphology of all members of the family of radio galaxies reveals not only their

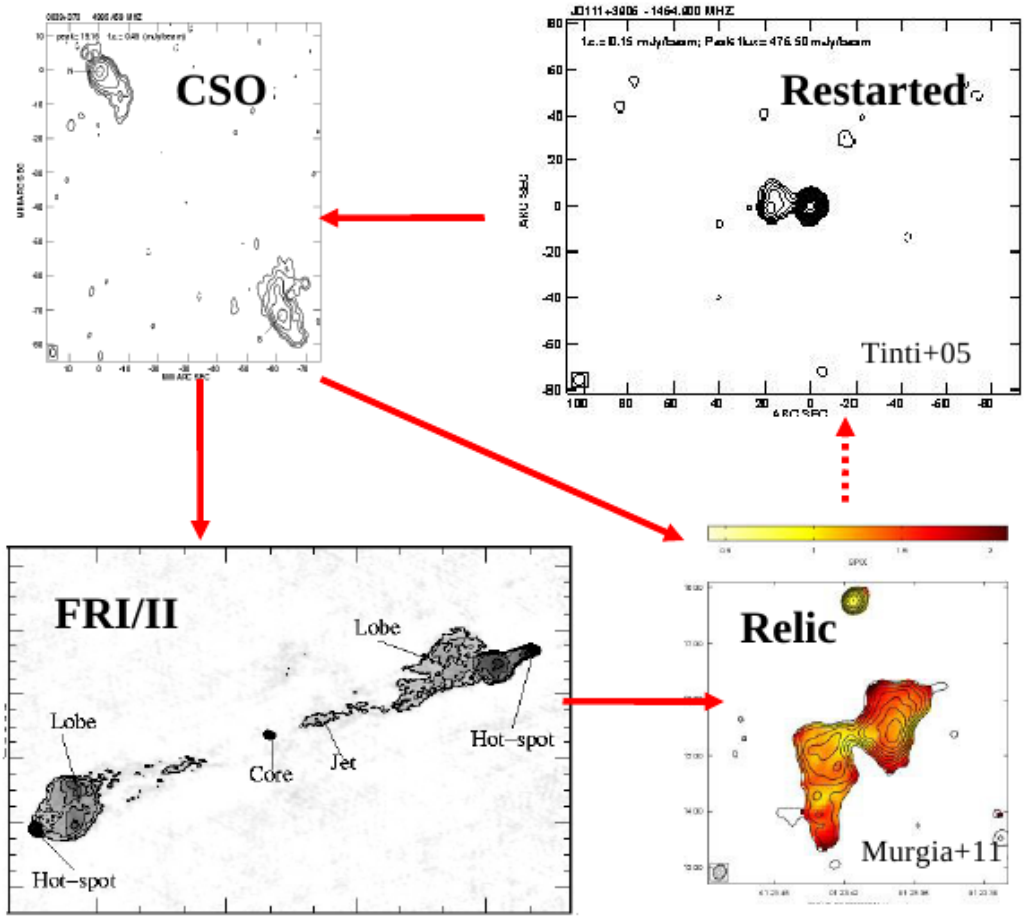

Figure 1.11: The life-cycle of radio galaxies proposed by and adapted from Orienti (2016). Young CSOs (top left) may evolve into FR IIs (bottom left) or, if the activity terminates shortly after its onset, a relic (bottom right). If the AGN becomes active again, a restarted object may be observed within the relic of previous activity (top right), essentially becoming a new-born CSO.

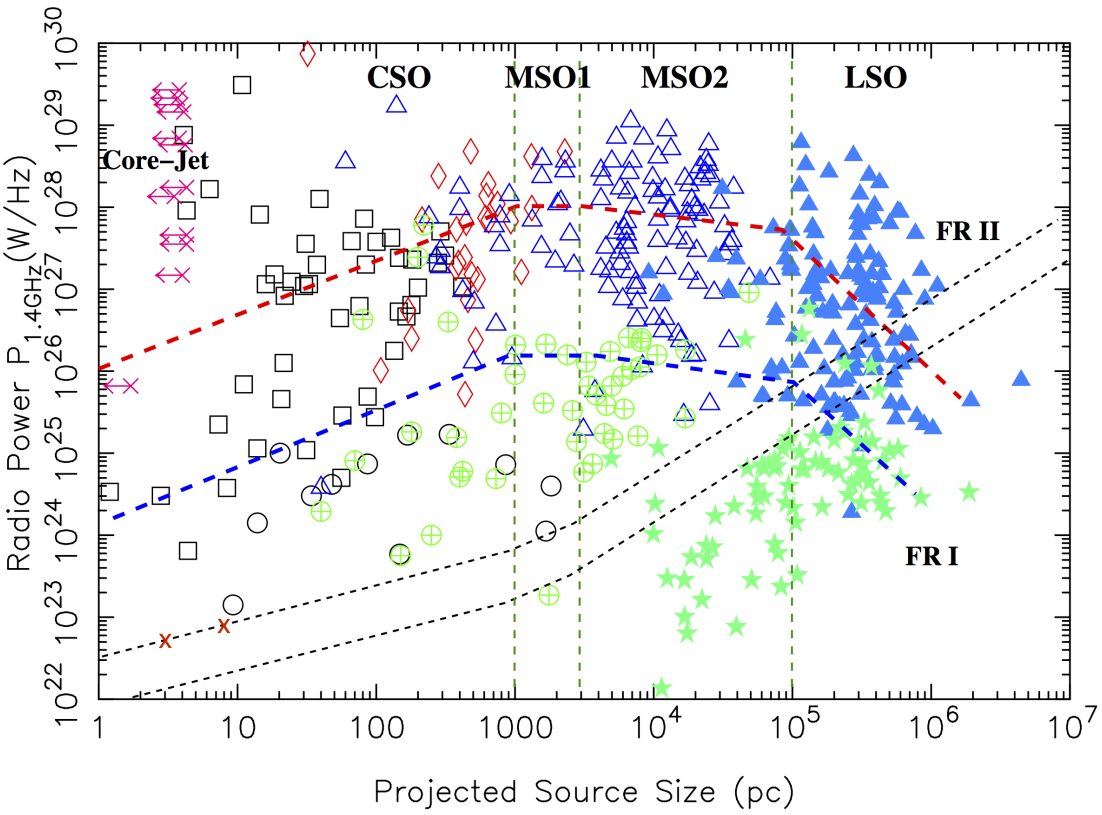

Figure 1.12: The radio power ($P_{\rm rad}$) as a function of linear size (l) for compact, medium-sized and large symmetric objects, adapted from An and Baan (2012). The thick red and blue dashed lines respectively represent the evolutionary tracks of a high-power and low-power radio galaxy, which are given by $P_{\rm rad} \propto l^{2/3}$, $P_{\rm rad} \propto l^{0}$, $P_{\rm rad} \propto l^{-0.2}$ and $P_{\rm rad} \propto l^{-1.6}$, respectively during the CSO, MSO1, MSO2 and LSO stages. The symbols represent different classes of radio galaxies from the literature (An and Baan, 2012, and references therein): purple crosses - HFPs; black squares - CSOs; black circles - low-power GPS; red diamonds - high-power GPS; green circles - low-power CSS; blue open triangles - high-power CSS; blue filled triangles - FR IIs; green filled stars - FR Is. The thin black dashed lines represent the approximate boundary between a stable (above the lines) and unstable (below the lines) jet. The two red crosses have been added to show the positions of the sources NGC 1052 and PKS 2254-367 from Tingay and Edwards (2015) (see section 1.3.4.2).

evolutionary stage, but also indicates survival or demise. An and Baan (2012) state that the advancing motion of the hotspots and lobes is determined in full by the momentum of the jets, locations of shocks, and the density structure of the Interstellar Medium (ISM) and Intergalactic Medium (IGM). They present a dynamical model for the evolutionary stages beginning with CSOs and ending with LSOs.

Earlier modelling of FR II sources assumed self-similarity in their shape and a constant hotspot separation velocity, but more recent analytic modelling has shown that a deceleration is experienced between the CSO and MSO stages, after which an acceleration is experienced between the MSO and LSO stages (An and Baan, 2012, and references therein). An and Baan (2012) also use self-similarity predictions to model their evolution, using the $P_{\rm 1.4GHz} - l$ diagram (see Fig 1.12) for the entire family of radio galaxies as a strong indicator of their evolutionary characteristics.

The radiative properties, which determines $P_{\rm rad}$, are given by the balance between adiabatic losses, synchrotron losses and inverse-Compton losses. The adiabatic losses result from the

expansion of the source into lower-pressure regions. The synchrotron losses are determined by the particle energy distribution, and during later states, the evolving energy density of the magnetic fields in the hotspots and lobes. The inverse-Compton losses are relevant during later stages when the jet has reached the IGM, and are determined by the energy density of the cosmic microwave background. Unlike with previous modelling, a constant hotspot separation velocity is not assumed, but the changing density gradient along the jet path, which has a dominant role during the early stages, is accounted for and modelled as $\rho(z) = \rho_0(a_0/z)^\beta$, where ρ_0 is reference density of the ISM, a_0 is the scale length of the IGM, z is the distance from the AGN assumed to be at the centre of the distribution, and β is the 'density parameter' (Kaiser and Best, 2007; An and Baan, 2012, and references therein). Observations have suggested a double-β model with an innermost region of roughly constant density and then beyond a_0, a steepening density profile, where $a_0 \sim 1$ kpc marks the transition between the ISM ($\beta \sim 0$) and the IGM ($\beta \sim 1.5$) (An and Baan, 2012, and references therein).

Based on the literature, An and Baan (2012) identify four distinct stages during the evolution of radio doubles, which have the following properties:

1. CSO phase − includes compact GPS sources up to $\sim 1 - 3$kpc; flat density profile with $\beta = 0$; dominated by adiabatic losses since B-fields not yet strong enough; radio power increasing with time as $P_{\rm rad} \propto t^{2/5}$ and size as $P_{\rm rad} \propto l^{(8-7\beta)/12} = l^{2/3}$; steep spectrum ($\alpha = -1.0$).

2. MSO-1 phase − includes extended GPS sources and compact CSS sources in the ISM-IGM transitionary region ($a_0 = 1 - 3$ kpc and $\beta \sim 1$); balance between adiabatic and synchrotron losses; constant power $P_{\rm rad} \propto l^0$; steep spectrum ($\alpha = -1.0$).

3. MSO-2 phase − includes mostly CSS sources but also some FR Is and FR IIs; dominated by synchrotron losses; steep density profile ($a_0 \geq 3$ kpc and $\beta \geq 1.5$); steady decrease of radio power $P_{\rm rad} \propto l^{(8-7\beta)/12} = l^{-0.2}$; relatively flat spectrum ($\alpha = -0.5$).

4. LSO phase − includes fully developed FR I and FR II galaxies larger than ~ 100 kpc; steep density profile ($\beta \geq 1.5$); dominated by inverse-Compton losses; sharp decrease of radio power $P_{\rm rad} \propto l^{(-4-\beta)/(5-\beta)} = l^{-1.6}$; $l \propto t^{3/(5-\beta)} = t^{0.86}$ (Kaiser and Best, 2007); steep spectrum ($\alpha = -1.0$).

These phases and the $P_{\rm rad} - l$ relations between them yield a luminosity-dependent evolutionary track along the $P_{\rm 1.4GHz} - l$ diagram, which An and Baan (2012) represent by two representative tracks at high-power (between $\sim 10^{26} - 10^{28}$ W/Hz) and low-power (between $\sim 10^{24} - 10^{26}$ W/Hz).

An and Baan (2012) identify that FR I-like flaring sources have similar properties to FR II-like sources during the flaring stage, but follow a downward trend in radio power due to their lower radio power and the cooling of their expanding structures. They identify a size-dependent boundary in the $P_{\rm rad} - l$ diagram below which jets cease to supply sufficient energy and momentum to the lobes, which become diffuse and undefined as in FR I sources. The curve predicts that low-power CSOs and MSOs, or any source experiencing a decrease or halting of jet power could evolve to an FR I-like source, with jet stagnation or disruption and flaring lobe structures. This boundary in association with the above evolutionary tracks indicate that FR II galaxies will naturally evolve into FR I galaxies since they eventually reach the region of jet instability.

If a radio galaxy is to continue evolving, the nuclear activity must continue and the jet must remain persistent. The jets of a radio galaxy powered by a short-lived outburst of nuclear

activity are not able to escape the host galaxy unless it is active for $> 10^4$ years, which is the typically required time for a lobe to successfully pass the ISM-IGM boundary (An and Baan, 2012, and references therein). This discontinuity has been associated with FR I-like CSS sources and CSOs that die before reaching the MSO stage.

The above relations during each of the four evolutionary stages assumes the jet power stays constant during the whole evolutionary lifetime until the LSO stage. However, if the jet power reduces, the hotspot will recede from the leading edge of the lobe, the jet will become more lossy and the lobe will become unstable and meandering and steepen its spectrum, all analogous to FR I galaxies. If the jet power is further reduced or completely terminated, the source will become a low-power relic and eventually die in its current phase.

Recurrent activity will result in many FR I-like sources depending on the jet power and the time interval between adjacent events. Between active events, the lobes will become diffuse and the hotspot expansion velocity and luminosity will reduce. After re-ignition, the hotspot may again move to the leading edge of the lobe. If the source is powerful, its jet will expand into the excavated channel and may still become FR II-like. If the jet re-ignites along a different axis, an X-shaped sources will result. If the time-delay between recurrent events is large compared to the cooling lifetime, the source will begin again as FR II-like source.

Based on these physical processes, An and Baan (2012) classify seven morphological types (Mtype) of radio galaxies (see Fig 1.13).

1. Mtype 2 double sources have powerful and stable jets with prominent hotspots at the leading-edge of well-defined lobes, yielding an edge-brightened morphology, and a weak core and jet structure. These sources have abundant and enduring jet power and are present among CSOs, MSOs and LSOs, following the evolutionary tracks defined above up until they become an FR II.

2. Mtype 1 flaring sources have a lossy and prominent jets with diffuse and less-well-defined or flaring lobes, with hotspots located closer to the bright core. These exist among the low-power CSOs, MSOs and LSOs below the jet-stability boundary and include FR I sources, which have followed the evolutionary tracks up until passing below the boundary during the LSO stage. Any source that began its life as a different Mtype and falls below the jet-stability boundary is destined to become an Mtype 1.

3. Mtype 3 dying sources experience an interruption or reduction of jet power, which causes the hotspots to disappear and continual adiabatic expansion of the radio structure, causing the source to become an expanding diffuse relic unless the nuclear activity restarts and the jet re-forms. During the CSO stage, the short-lived nature of these sources results in an unstable jet-flow before reaching the ISM-IGM boundary and the ultimate dissipation of the lobe. During the MSO and LSO stages, these sources will reserve their shape within the IGM but without a hotspot, where they will continually expand and radiate away their energy. Since the nuclear activity is able to reduce or terminate at any point during a radio galaxy's life, these sources are present amongst CSOs, MSOs and LSOs, which may follow the evolution tracks up until the point of jet termination or reduction, at which point they will move rapidly downward in luminosity.

4. Mtype 4 restarted sources are Mtype 3 sources that experience a restarting or intermittence of nuclear activity and a kickstarting of jet power into channels already excavated. If powerful enough, the hotspot will advance through this channel until reaching the leading edge of the lobe, where is sets up a new shock-confined lobe within the larger and

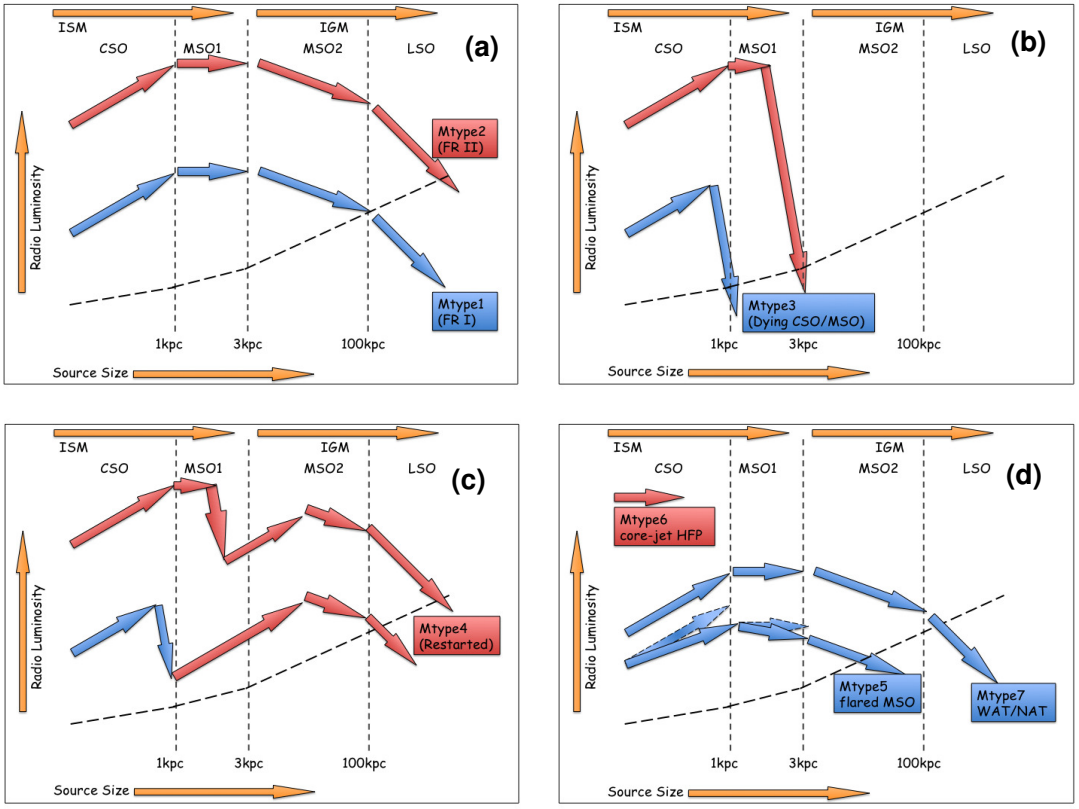

Figure 1.13: The suggested evolutionary tracks across the $P_{\rm rad} - l$ diagram for seven morphological types of radio galaxies, taken from An and Baan (2012).

older lobe. If the time delay is sufficient, the new lobe will be distinct from the relic lobe. If the source experiences regular intermittence, a series of shock fronts will be spread throughout the lobe. If the source restarts along a different jet axis, the source will appear X-shaped. Mtype 4 sources can appear amongst CSOs, MSOs and LSOs, moving up and down in luminosity during restarting phases. Restarting sources with sufficient jet-power may follow the evolutionary tracks and become an Mtype 2 again.

5. Mtype 5 obstructed sources have jets with lower power that interact with a dense medium, as in the frustration scenario, resulting in hotspots within 1 kpc and misaligned plume-like diffuse structures beyond 1 kpc. These exist amongst the low-power CSOs and MSOs.

6. Mtype 6 core-jet sources have a small angle between the jet-axis and the line of sight, which appear as one-sided jets with elevated radio emission due to Doppler boosting. These exist amongst HFPs and do not follow the evolutionary track due to projection effects.

7. Mtype 7 trail sources are tailed radio galaxies located in clusters whose lobes are bent outside the ISM-IGM boundary due to ram pressure arising from host galaxy's motion through the intra-cluster medium. These follow the evolutionary tracks but with warped linear sizes.

An and Baan (2012) used a sample of 24 CSOs with known redshifts and linear sizes and proper motion measurements, which allowed for a statistical study of their kinematic properties. Since the sources span such a large range of jet powers and environments, they differentiate

between trends yielded by each class as a whole, and trends yielded by sources of a given jet power. The physical properties of these CSOs are generally consistent with their self-similar modelling, which assumes a constant jet power and predicts individual sources with a given power will have $P_{\rm rad} \propto l^{2/3}$, $P_{\rm rad} \propto \nu_{\rm HS}^{-1}$, $\nu_{\rm HS} \propto l^{-2/3}$, $P_{\rm rad} \propto T_{\rm kin}^{2/5}$, $\nu_{\rm HS} \propto T_{\rm kin}^{-2/5}$, and $l \propto T_{\rm kin}^{3/5}$, where $\nu_{\rm HS}$ is the hotspot separation velocity (equal to twice the hotspot advance velocity assuming both jets are ejected with the same velocity), and $T_{\rm kin}$ is the kinematic age derived from l and $\nu_{\rm HS}$. Furthermore, they find a slow decrease in spectral index as a function of projected linear size or kinematic age, which is probably due to the turnover shifting to lower frequencies as the source adiabatically expands. As a whole (i.e. over all radio powers), the CSOs follow the trends $P_{\rm rad} \propto l^4$ and $l \propto T_{\rm kin}^{1.5}$. In general, more powerful sources are larger, have higher expansion velocities, and are older.

The distribution of kinematic ages of the CSO sample from An and Baan (2012) shows a steady decrease with a half-width of 1100 years, suggesting a significant fraction of CSOs will not become old. Similarly, the distribution of source sizes shows a decrease toward larger sizes, with a half-width of 100 pc. An and Baan (2012) rule out projection effects as playing a major role, suggesting that not all CSOs will grow in CSS sources. These results suggest that sources older than ∼1100 years and larger than ∼100 pc have a greater chance of survival and are able to evolve beyond CSOs. This suggests a significant fraction of CSOs are short-lived sources with a typical lifetime of < 1000 years, as compared to the long-term AGN duty cycle of $10^7 - 10^8$ years, which is generally considered to be triggered by major mergers and long-term accretion events. This depletion of CSOs may be the result of a reduction of jet power or a complete termination of nuclear activity after a short active phase, which may even suggested a different triggering mechanism.

Inspection of the source morphologies in the An and Baan (2012) CSO sample suggests that only ∼30% of the CSOs are Mtype 2 doubles with hotspots at the leading edge of the lobe, while those remaining show signs of decay, such as prominent jets, hotspots closer to the core, and diffuse or disrupted lobes, some of which may even be Mtype 3 relics.

An and Baan (2012) state that the dynamic processes and evolutionary behaviours of their sample of CSOs represent both the youth and frustration scenarios, since CSOs are naturally young radio sources, but that those with short-lived or intermittent activity or with low power can be regarded as frustrated sources that will not evolve into large scale double sources.

1.3.4.2 Possible luminosity-morphology relationship

Hancock et al. (2009) and Tingay and Edwards (2015) have suggested the existence of a luminosity-morphology relationship in GPS radio galaxies analogous to that of the larger scale FR I and FR II galaxies. Tingay and Edwards (2015) used VLBI observations of PKS 2254-367, the second closest GPS source known (D ∼21 Mpc), and compare its high-resolution morphology to the only other two GPS sources known within 100 Mpc, NGC 1052 (∼17 Mpc) and PKS 1718-649 / NGC 6328 (∼59 Mpc), both of which are CSOs. The observations were taken at frequencies of 1.66, 2.27, 4.98 and 8.42 GHz, which were approximately beam-matched with a synthesised beam of 3.5 mas, and which reached root mean squared (r.m.s.) values of $\sigma = 0.8 - 1.1$ mJy/beam. Based on the VLBI morphology, Tingay and Edwards (2015) classify PSK 2254-367 as a CSO. However, the source's morphology appears to contain a strong core, and strong double sides jets (see Figure 1.14), as compared to typical CSOs, which predominantly contain strongly edge-brightened lobes with weak or absent jets and core. Amongst the CSO candidates and CSS objects respectively found in the COINS (CSOs Observed In the

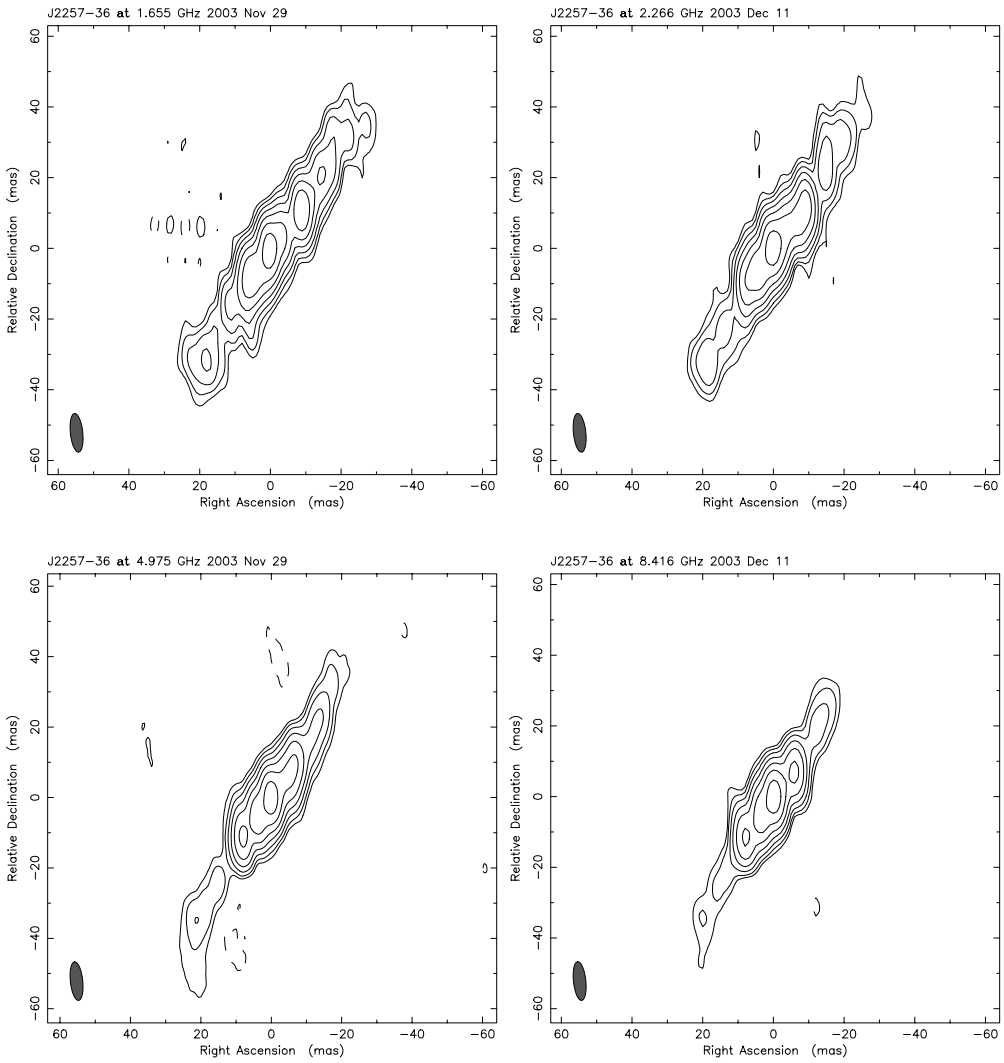

Figure 1.14: The VLBI morphology of PKS 2254-367 at 1.7, 2.3, 5.0 and 8.4 GHz, taken from Tingay and Edwards (2015). The contours represent −1 (dashed) and 1, 2, 4, 8, 16, 32 and 64% of the image peak. All images are restored with a synthesised beam of 11×3.5 mas at a position angle of 6 degrees, which is represented by the ellipse in the bottom left corner.

Northern Sky) survey (Peck and Taylor, 2000) and by Orienti et al. (2004), a small minority of sources contain similar morphologies.

Both NGC 1052 and PKS 2254-367 have counter-rotating cores, Low-Ionisation Nuclear Emission-line Region (LINER) spectra, are compact and have peaked spectra, and are hosted by cluster-dominant elliptical galaxies, all of which supports the idea that they are compact due to a dense nuclear environment and merger activity. Both contain strong evidence for free-free absorption (Vermeulen et al., 2003; Tingay et al., 2015). Both have similarities on pc scales, with highly symmetric bi-directional jets which appear to be oriented in the plane of the sky. The jets of NGC 1052 are ∼3 pc across and are moving at $\sim 0.38c$, while those of PKS 2254-367 are ∼8 pc across. The integrated monochromatic 5 GHz luminosities for NGC 1052 and PKS 2254-367 are $\sim 5 \times 10^{22}$ W Hz^{-1} and $\sim 7 \times 10^{22}$ W Hz^{-1}, respectively. Comparatively, PKS 1718-649 has classic double morphology with a hotspot expansion speed of $< 0.08c$ and a monochromatic 5 GHz luminosity of $\sim 2 \times 10^{24}$ W Hz^{-1}. Similarly, most of the known GPS population contains sources more luminous than $\sim 10^{23}$ W Hz^{-1} with classic double structures

(e.g. Snellen et al., 2004).

Therefore, Tingay and Edwards (2015) speculated of the existence of a sub-class of GPS sources which are compact, low in luminosity and are jet-dominated, differentiated from the general GPS population by their lack of powerful and compact lobes. They suggest a break analogous to the FR I/II luminosity-morphology break, in which sources like NGC 1052 and PKS 2254-367 are the analogs of FR I galaxies and sources like 1718-649 are the analogs of FR II galaxies, and perhaps even the progenitors. On the $P_{\rm rad} - l$ from An and Baan (2012), these sources sit just below the upper bound of the jet-stability boundary, which denotes an FR I-like morphology (see Fig 1.12).

Since detecting such low-luminosity sources beyond ∼50 Mpc is only possible in very deep observations, Tingay and Edwards (2015) suggest it is important to find more nearby GPS sources, suggesting we target weak radio sources in nearby ($\sim 10 - 70$ Mpc) elliptical galaxies, at levels of $10 - 100$ mJy, corresponding to luminosities of 10^{21-22} W Hz^{-1}. Using deep surveys such as the Australia Telescope Large Area Survey (ATLAS; see Section 2.2.2.1) makes this possible out to even more substantial distances.

1.3.4.3 Turnover-linear size relation

O'Dea and Baum (1997) present a relation between the projected linear size (l) of the radio source and the intrinsic turnover frequency (ν_m), which is revised by Orienti and Dallacasa (2014) using a sample of *bona fide* young radio sources spanning a large range of linear sizes as

$$\log \nu_m = -0.21(\pm 0.04) - 0.59(\pm 0.05) \log l \ . \tag{1.14}$$

The minimal scatter around this linear fit (see Fig 1.15) shows that the there is a continuous rather than bimodal distribution, which implies that GPS sources are simply scaled-down CSS sources. This is consistent with the great deal of overlap that exists between GPS and CSS sources, which are chosen arbitrarily from their turnover frequencies. This relation indicates that the mechanism causing the peaked spectra is related to the source dimension. In the SSA model, as the source expands, adiabatic expansion occurs in the mini-lobes that dominate the radio emission, which causes their opacity to decrease, causing less SSA and therefore a lower-frequency turnover. Therefore, in the SSA model, this relation is well justified and indicates that the turnover frequency and linear size are both related to the age.

However, if FFA via a dense, confining medium is causing the peaked spectrum (i.e. the 'frustration scenario'), the variables in equation 1.14 may not be related to the source age. The simple FFA models cannot replicate this relation (O'Dea, 1998). However, in the Bicknell et al. (1997) FFA model, the electron density within the external inhomogeneous medium decreases with distance from the core, allowing for the relation. Alternatively, the relation may be explained by dense ionised clouds that coexist with the relativistic electrons and cause FFA (Callingham et al., 2015, and references therein). Within the frustration scenario in general, the dense medium will prevent significant adiabatic expansion and confine the jets. If the medium is sufficiently dense, or if the jets are low in power or intermittent, both variables in equation 1.14 will not vary significantly and therefore will not significantly relate to the source age, but may relate closely to one another. Therefore if frustration plays a significant role, we may expect the kinematic age to be underestimated and lower than the spectral age of the source.

Some of the most compact and asymmetric sources depart from the turnover-linear size relation. Orienti (2016) state that this is likely to be due to several components that contribute to the overall spectrum, such as a bright hotspot that dominates the spectrum.

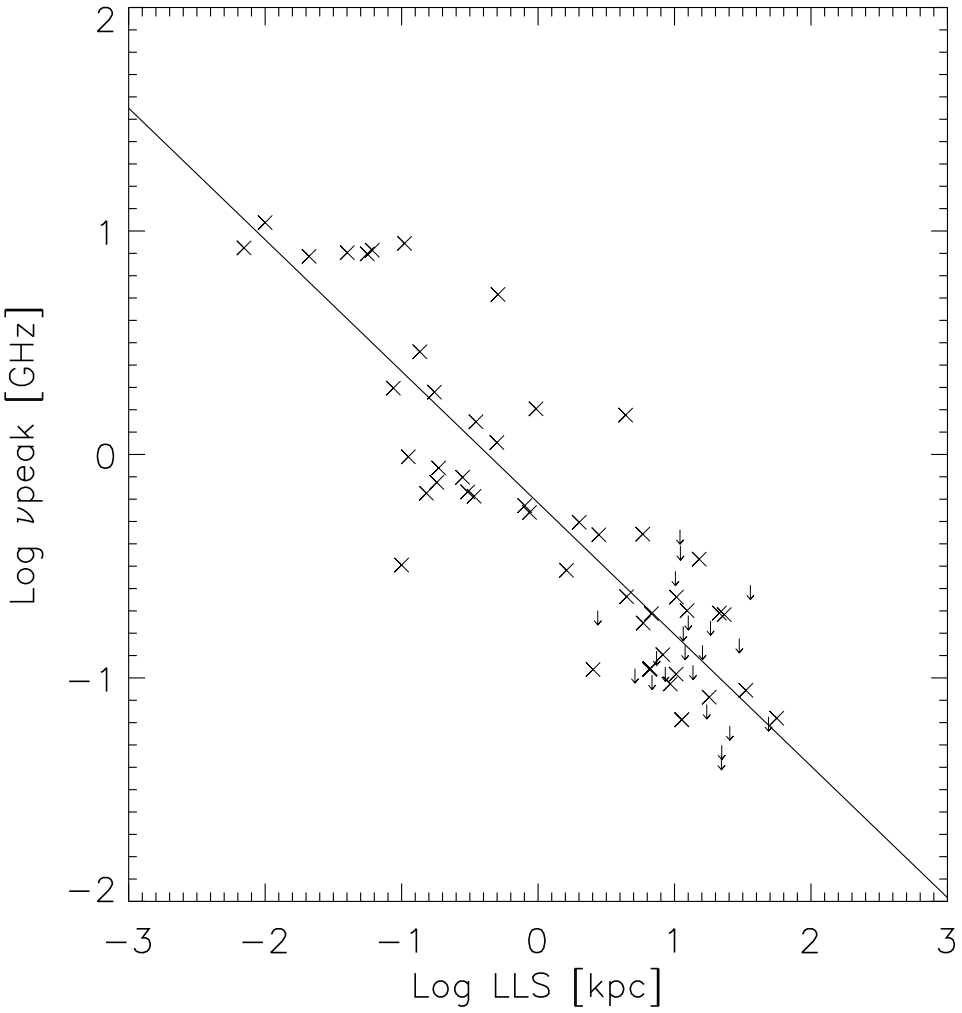

Figure 1.15: The rest-frame turnover frequency as a function of the linear size for a sample of *bona fide* young radio sources, taken from Orienti and Dallacasa (2014). The arrows represent upper limits on the turnover frequency.

1.3.5 Ambient medium

GPS and CSS sources are typically hosted by gas-rich galaxies. Support for the existence of vast amounts of gas comes from the higher occurrence of HI absorption (Vermeulen et al., 2003; Pihlström et al., 2003; Gupta et al., 2006; Allison et al., 2015) compared to older and larger sources. The dense medium responsible for this absorption most likely resulted from a merger that triggered the radio source (Morganti et al., 2004). The structure of the gas within the ambient medium is critical for understanding the innermost environment in which compact radio sources evolve.

Pihlström et al. (2003) found an anti-correlation between the linear size and the HI column density for a sample of GPS and CSS sources, which suggests the HI gas is settled in a circumnuclear disk or torus which decreases in density radially and only the receding lobe experiences absorption (Orienti, 2016). This model of the ambient medium is supported by VLBI observations of atomic and ionised gas and by deep observations of molecular gas (Orienti, 2016, and references therein).

However, not all systems are expected to contain a circumnuclear structure. Due to the merger or accretion activity experienced by the host galaxy, the existence of unsettled and clumpy gas is expected, distributed inhomogeneously as clouds throughout the ambient medium, and increasingly so toward the core. These clouds may interact with the jet and temporarily confine its expansion. Some observations indicate that jet-cloud interactions do occur within these systems and may be responsible for the asymmetric morphologies (Orienti, 2016, and references therein). The trend in asymmetric sources that the closer lobes are brighter (see section 1.3.2) generally supports the existence of an inhomogeneous medium in which the jets are piercing through different environments. The interactions that take place may enhance the luminosity due to radiative losses dominating adiabatic losses, and should be more dominant during the earliest stages while the jet is still confined to the innermost regions. This enhancement may account for some of the excess of GPS and CSS sources in flux-limited catalogues. Studies of the flux density ratio between the lobes as a function of the linear size has revealed that sources larger than $\sim$15 kpc are more symmetric than smaller ones (Orienti and Dallacasa, 2008b). Interestingly, sources at $\sim$1 kpc are the most asymmetric, and are significantly less so below 1 kpc. The significant fraction of sources with brighter and closer lobes suggests that jet-cloud interactions are common and cause an underestimate in the age.

1.3.6 GPS and CSS samples

Until recently, our understanding of GPS and CSS sources was limited to very bright (Jy-level) samples. Even still, their properties at faint levels are generally unknown. In particular, very few faint CSS sources have been observed (Orienti, private communication), which is most likely a selection effect. Identifying GPS and CSS sources requires combining data from several different surveys with different frequencies, which dramatically drop in sensitivity or area either side of 1.4 GHz, particularly at low frequency where CSS sources are identified (Sadler, 2016). Existing samples are therefore biased toward finding GPS sources that turn over around 1 GHz, since they will be easier to find than those turning over at higher or lower frequency. Furthermore, existing samples contain more luminous sources, such as those in O'Dea (1998), which have a median luminosity of $L_{5\mathrm{GHz}} > 10^{27}$ W Hz^{-1}, and even those in the 'low luminosity' sample from Kunert-Bajraszewska et al. (2010), which have typical luminosities of $L_{1.4\mathrm{GHz}} = 10^{25-26}$ W Hz^{-1} (Sadler, 2016). Using a sample crossmatched between the AT20G survey and the 6dF spectroscopic survey, Sadler (2016) identified a population of radio sources

that spanned radio luminosities $L_{20\mathrm{GHz}} = 10^{22-26}$ W Hz^{-1}, with more than a quarter of the sample below 10^{24} W Hz^{-1} at 1.4 GHz. Sadler (2016) concluded that there is indeed a large population of less-luminous GPS and CSS sources, which have so far eluded detailed study, due to the lack of large-area surveys at multiple frequencies, and the large time-requirement for characterising their morphologies with VLBI. Kunert-Bajraszewska (2016) also identified a sample of low-luminosity compact sources, with luminosities down to $L_{1.4\mathrm{GHz}} = 10^{23}$ W Hz^{-1}. These are broken into as HERGs and LERGs, which were found to occupy distinct regions in the radio-X-ray luminosity diagram. Like Tingay and Edwards (2015), Kunert-Bajraszewska (2016) concluded that GPS and CSS sources start to resemble FR Is at low luminosity, which are the missing precursors of large-scale FR Is, but that their sample is *'the tip of the iceberg and much larger population[s] of short-lived low power radio sources are still waiting to be explored with high sensitivity radio surveys.'*

As summarised by Orienti (2016), bright samples of GPS and CSS sources have been selected from the 3C, PW and 1-Jansky catalogues (Spencer et al., 1989; Fanti et al., 1990; Stanghellini et al., 1998). Faint samples were selected from B3, FIRST, WENSS and AT20G (Snellen et al., 1998; Fanti et al., 2001; Kunert et al., 2002; Hancock et al., 2010), which are typically brighter than a few hundred mJy. Other samples were compiled via selecting GPS and CSS sources based on their radio morphology or compactness, optical counterparts (COINS sample, Peck and Taylor (2000); CSS-VIPS samples, Tremblay et al. (2009); CORALZ, Snellen et al. (2004)) and polarisation (Cassaro et al., 2009).

Randall et al. (2012) and Hancock et al. (2010) have compiled catalogs of sub-mJy and mJy-level GPS and CSS sources, which are amongst the faintest. Until now it has not been plausible to study their properties at even fainter (μJy) levels across a large sample.

1.3.6.1 AT20G samples of HFPs

Hancock (2009) compiled a sample of HFPs selected from near-simultaneous flux-density measurements at three frequencies from the AT20G survey, which covers the entire sky south of the equator. The candidate HFPs were selected from the subset of 4404 sources that were measured at all three frequencies, and selected to have an inverted spectrum between the 4.8 and 8.6 GHz or between 8.6 and 20 GHz (i.e. $\alpha_{4.8}^{8.6} > 0.2$ or $\alpha_{8.6}^{20} > 0.2$) and be greater than 2.5 deg away from the Galactic plane. The resulting sample consisted of 656 GPS sources that turnover above 5 GHz, which have typical 20 GHz flux densities of a few hundred mJy.

Ancillary data was found for each source in the sample by crossmatching to SUMSS, NVSS, NED, 6dF and SuperCOSMOS. 466 sources contained B magnitudes in SuperCOSMOS and were separated into galaxies and quasars using the class ID flag, which is based solely on the optical morphology. These were treated separately in analysis since the origin of their spectra is thought to be intrinsically different. 104 redshifts were gathered from NED, almost all of which were from 6dF. The turnovers of each of the sources were binned into 8-15 GHz, 15-30 GHz and $>$ 30 GHz.

As expected, the quasars were found to have systematically higher redshifts than the galaxies, as well as radio powers two orders of magnitude higher. Furthermore, the quasars had a much higher 20 GHz flux density on average, but had hosts with similar B magnitudes.

Hancock (2009) compared the properties of their sample of HFPs to the updated GPS master list from Labiano et al. (2007), which was the most complete listing of GPS and HFP sources known, consisting of 79 galaxies and 57 quasars. Compared to the Hancock (2009) sample, those from the master list were found to typically peak much lower ($1 - 5$ GHz), have

a higher fraction of galaxies, were typically at higher redshift and typically had higher radio powers. Stanghellini (2003) noted that the fraction of galaxies in a GPS sample increases as the turnover frequency decreases, supporting the idea that the radio emission from galaxies and quasars are intrinsically different, respectively coming from the lobes or hotspots and the core. The lower typical radio powers in the Hancock (2009) suggest that the AT20G sample consists of GPS sources that are typically in earlier stages of radio evolution.

Hancock et al. (2009) compiled a subsample from the previous sample of HFPs, selected as those identified as a galaxy in SuperCOSMOS and with $z < 0.15$. All had radio powers $P_5 < 10^{24.5}$ W/Hz and turned over above 8 GHz. Ten of these, which were typically a many tens of mJy at 5, 8 and 20 GHz, were observed with e-VLBI using the LBA, reaching a typical r.m.s. level of 1 mJy/beam and a typical angular resolution of ∼100 mas. All ten sources were unresolved on scales of ≤ 200 mas, corresponding to linear sizes of $\lesssim 260$ pc down to < 15 pc. Based on the VLBI to AT20G flux density ratio measurements, which were taken three years apart, Hancock et al. (2009) found good evidence that nearby AT20G sources are compact, with ∼90% of their 4.8 GHz emission coming from scale smaller than $100 - 200$ pc, most of which are only very modestly variable on time-scales of $1 - 3$ yr. They show that even for a source that evolves very slowly, with a hotspot expansion rate of 0.1c, a linear size of < 100 pc gives an age of < 3000 yr, which they suggest supports the youth hypothesis for GPS sources.

Interestingly, one source was identified as the core of a Giant Radio Galaxy spanning ∼750 kpc, classified as FR I and consisting of a core-jet morphology at high resolution, suggesting that the source is a restarting radio jet within relic lobes. Another source is identified as a shell galaxy, which are generally thought to be the result of the merger of two gas-poor galaxies. Another source contains two compact components in AT20G within another large double-lobed radio source observed at low resolution and spanning ∼90 kpc, which may also be a recently restated radio galaxy. These are interesting sources since they show evidence of more than one cycle of radio galaxy evolution and may be inherently different from those HFPs that have just begun their first phase of evolution. If we could determine the history of mergers and star formation in such sources, the processes they have undergone to restart could be investigated.

Hancock et al. (2009) concluded that the e-VLBI observations were sufficient to reveal the compact nature of their sample of GPS source, but insufficient in resolution to differentiate between different morphologies, which is needed to confirm if a luminosity-morphology relationship exists for GPS sources. A better way to select targets for VLBI would be to estimate their angular size based on equation 1.14 and their redshift, and select those with angular sizes larger than the angular resolution.

Hancock et al. (2010) selected a similar sample of HFPs from AT20G, selected as those which had a rising spectrum ($\alpha_{4.8}^{20} > 0.2$) their either remained inverted or appeared to turn over above 10 GHz, resulting in a sample of 148 sources. 21 of these were followed up with 20, 40 and 95 GHz observations from the ATCA, using the H75 array and resulting in FWHM synthesised beam sizes of 31, 15 and 7 arcsec. The 20 GHz observations were taken to detect variability. Optical data from SuperCOSMOS was found in a similar way, but using a more strict search criteria of 2.5 arcsec, which gave a optical ID to all but two of the sources, one of which was added despite being $> 2.5''$ away since its radio centroid was still within the extent of the optical source. All of these were assigned redshifts, either estimated from the B magnitude, or measured from spectroscopic observations taken from the ANU 2.3-m telescope or the 3.58-m ESO New Technology Telescope. Using the 20 GHz observations over two epochs spanning $1 - 3$ yr, they found 11 of the 20 sources to be <10% variable. Interestingly, no significant difference was found between the variability of the galaxies and quasars, which were

found to vary between $10 - 12\%$ on average, typical of GPS sources.

Using a homogeneous SSA model from Snellen et al. (1998), in which the spectral indices in the optically thick and thin regions are free parameters, Hancock et al. (2010) modelled the radio spectra of their sample of 21 sources observed from $5 - 95$ GHz. The median value of the observed (rather than intrinsic) turnover frequencies in those identified as galaxies and quasars were 84.5 ± 8.9 GHz and 20.5 ± 9.4 GHz, respectively, which they attribute in part to the difference in redshift.

Hancock et al. (2010) studied the optical colours of the candidate HFPs and found each of them to have an excess of blue emission which, when compared with the available optical spectra, was found to be consistent with an AGN component. They showed evidence of a relation between the optical and radio luminosity, which they attribute to an expected correlation between the radio emission above the self-absorbed turnover, which is most likely synchrotron emission from the core, and the optical emission, which is dominated by stellar emission up until the source becomes radio loud, at which point the optical luminosity increases along with the radio luminosity. They state that this relation is consistent with a scenario in which the luminosities are correlated in the radio-loud regime, but unrelated in the radio-quiet regime.

Hancock et al. (2010) re-classified each of their 21 sources based on all the information gathered. 75% of the GPS sources identified as galaxies were re-classified as genuine or likely GPS sources, while only 25% of the GPS sources identified as quasars were re-classified as this. Hancock et al. (2010) suggest that one simple way to remove contaminating sources is to exclude those identified as quasars in SuperCOSMOS. Of these 21 sources, three showed evidence of being restarted, with typical GPS radio cores but with extended emission, hotspots or jets. Hancock et al. (2010) state that if these numbers are indicative of the larger population of high-frequency radio sources, then in AT20G there are as many as 400 genuine GPS sources, and up to $\sim$100 being restarted. This tells us that while GPS sources may be young and evolving radio galaxies, if the population of HFPs is indicative of the GPS population in general, a significant number of them have previously undergone many stages of radio galaxy evolution.

1.3.6.2 ATLAS DR1 CSS sample

Randall et al. (2012) compiled an initial complete sample of faint CSS sources from ATLAS DR1 (Norris et al., 2006; Middelberg et al., 2008a), drawn from both fields, which reached r.m.s. values of 30 μJy. The sample only includes 1.4 and 2.3 GHz flux density measurements. The sources were chosen based on being unresolved, single sources and a spectral index cut of $\alpha_{1.4}^{2.3} < -0.95$, with an additional cut of $\alpha_{1.4}^{2.3} < -0.9$ for a supplementary sample. These cuts were chosen to avoid selecting Star Forming Galaxies (SFGs), which have typical synchrotron spectral indices of -0.7 and which begin to dominate at μJy flux densities. Applying these criteria resulted in selecting 86/975 sources and 5 supplementary sources. Of the 86 sources, 5 contain 843 MHz measurements, which is added to the catalogue, but not used in the analysis. From the main and supplementary sample of 91 sources, 22 spectroscopic and 17 photometric redshifts were found, with respective means of 0.37 and 1.21.

The mean 1.4 and 2.3 GHz flux densities of the sample are 1.68 and 1.08 mJy, respectively. The spectral indices are between -4 and -0.9, with a very steep mean of -1.58. The rest-frame 1.4 and 2.3 GHz luminosities were between 10^{21} and 10^{27} W/Hz, with a mean around $10^{23.5}$ W/Hz. The spectral indices and luminosities are indicative of AGN, as expected. However, the majority of the sample falls in the region occupied by SFGs in the radio-FIR correlation, many of which are also spectroscopically classified as SFGs, suggesting that the sources are

dominated by active SF, consistent with other studies of CSS sources (O'Dea, 1998; Labiano et al., 2008; Holt, 2009; Morganti et al., 2009). Furthermore, the q_{24} ratios as a function of redshift are closest to the SED tracks of Arp 220 and Mrk 273, two nearby ULIRGs. These CSS candidates which show strong evidence of being hosted by a SFG and which make up the majority of the sample, present an interesting case for exploring the effect of AGN feedback on the SF.

1.3.6.3 Limitations of these samples

The AT20G HFPs and ATLAS CSS sample are amongst the faintest samples of GPS and CSS sources to date. However, neither reach sensitivity levels of tens of μJy, typical of today's deep surveys. The AT20G samples are huge in size, but are typically many tens to hundreds of mJy, contain flux density measurements from seven frequencies at most. Furthermore, they contain high-frequency turnovers and are therefore more subject to contamination by flat-spectrum quasars. The ATLAS CSS sample is much fainter, reaching sub-mJy levels, with a mean of $\sim$1 mJy, but only contains flux density measurements at two frequencies. To probe GPS and CSS sources in an unexplored regime, one needs to observe them at faint μJy levels across seven or more frequencies, which gives one or more degrees of freedom in the absorption models described above.

1.3.7 Summary

1.3.7.1 Sub-classes of compact, peaking radio sources

Based on radio spectra alone, we define the following classes:

- HFPs $-$ $\nu_m \gg 1$ GHz;
- GPS sources $-$ $\nu_m \sim 1$ GHz;
- CSS sources $-$ $\nu_m \ll 1$ GHz.

Based on the morphologies, we have the following classes:

- symmetric;
- core-jet;
- complex.

Based on the linear sizes (l) of the symmetric objects, we have the following classes:

- CSOs $-$ $l < 1$ kpc;
- MSOs $-$ $1 < l \lesssim 100$ kpc;
- LSOs $-$ $l \gtrsim 100$ kpc.

As shown in An and Baan (2012) (e.g. Fig 1), most HFPs are core-jet, most GPS sources are CSOs, most CSS sources are MSOs, and most FR I and FR II galaxies are LSOs, which is generally consistent with equation 1.14.

1.3.7.2 SSA vs. FFA

Orienti (2016) state that SSA is responsible for the turnover in GPS and CSS sources, but that an additional contribution from FFA is detected in the most compact sources. Callingham et al. (2015) state that the main reason that the debate between SSA and FFA remains unresolved is because the previous studies lacked broad coverage of the spectra below the turnover, where the distinction between models is most significant. Only now, with low-frequency telescopes becoming operational such as the Murchison Widefield Array (MWA; Tingay et al., 2013) and Low-Frequency Array for Radio astronomy (LOFAR; van Haarlem et al., 2013), is it possible to perform a comprehensively study of the optically-thick spectra in GPS and CSS sources. Furthermore, with radio telescopes such as ATCA allowing for larger bandwidths to be observed, significant frequency coverage within the GHz range has now become plausible, which is critical for observing any spectral features in the optically-thin spectra, such as spectral breaks.

Now that it has become feasible to study the spectra of GPS and CSS sources over a large range of radio frequencies and particularly at low frequency, the Bicknell et al. (1997) inhomogeneous FFA model has been found to accurately represent the radio spectrum of compact GPS sources. Examples include Tingay et al. (2015) and Callingham et al. (2015), in which the model not only accurately describes their spectrum, but is also consistent with their spectral variability and accurately describes their physical properties, such as the dense and inhomogeneous ambient medium.

1.3.7.3 The nature of GPS and CSS sources

The existence of a clumpy and inhomogeneous medium in the innermost regions of the host galaxies of GPS and CSS sources arising from recent mergers or large accretion events, causing jet-cloud interactions and confining the growth of the most compact sources, fits in well with the Bicknell et al. (1997) FFA model of the radio spectrum and the frustration scenario. However, as summarised above, good evidence exists that the majority of GPS and CSS sources are young and evolving, which is now generally accepted. Therefore, it is extremely unlikely that the jet-cloud interactions frustrate the expansion of the source indefinitely and account for the majority of GPS and CSS sources. However, it is possible that in most sources, these interactions are able to temporarily confine the jet and severely slow down its growth, which is only able to probe through the clumpy medium after some time. As noted by An and Baan (2012) and references therein, both scenarios relate to the power level and duration of the nuclear activity, and therefore both scenarios may account for CSOs and GPS sources, in which young sources with persistent long-term nuclear activity continue growing and become LSOs, while others deteriorate due to intermittent nuclear activity. In other words, young sources may be initially confined to small spatial scales due to the dense ambient medium, but those with constant nuclear activity could eventually break through this medium given enough time, while those with intermittent nuclear activity may stagnate.

During these early stages, the Bicknell et al. (1997) FFA model is a good description of the physical conditions in place, and should therefore accurately model the radio spectrum, provided that the FFA dominates over the SSA. However, beyond the ISM-IGM boundary, it seems unlikely that significant FFA will occur within the less dense IGM, and therefore, SSA should accurately model the radio spectrum. As previously stated, many observational studies of individual GPS sources with CSO morphologies (i.e. the most compact sources) have provided good evidence for the frustration scenario, in which FFA is responsible for the turnover (e.g. Peck et al., 1999; Kameno et al., 2000; Marr et al., 2001; Tremblay et al., 2008; Marr et al.,

2014; Tingay and Edwards, 2015; Callingham et al., 2015). In the case of Orienti and Dallacasa (2008a), FFA is invoked as an additional contribution to SSA, since the optically-thick spectral index is steeper than the SSA limit of 2.5. As noted by Fanti (2009a), SSA is present by default.

Furthermore, good evidence exists in individual cases for systems that are dying or restarted (e.g. Baum et al., 1990; Kunert-Bajraszewska et al., 2005, 2006; Brocksopp et al., 2007; Orienti et al., 2010b; Hancock et al., 2010; Shulevski et al., 2012). These are well modelled and accounted for across all sub-classes of compact, peaking radio sources by An and Baan (2012).

1.4 Infrared-Faint Radio Sources

Infrared-Faint Radio Sources (IFRSs) are a rare class of object that was first discovered by Norris et al. (2006), many of which are GPS and CSS sources. IFRSs were identified as radio sources which were detected at $\lambda = 20\,\mathrm{cm}$ ($\nu = 1.4$ GHz) in the deep radio observations of the Australia Telescope Large Area Survey (ATLAS) *Chandra* Deep Field South (CDFS; Rosati et al., 2002), but which were not detected in the *Spitzer* Wide-area InfraRed Extragalactic Survey (SWIRE; Lonsdale et al., 2003) at 3.6, 4.5, 5.8, 8 and 24 μm (see Fig 1.16). A total of 22 IFRSs were identified by Norris et al. (2006), which were undetected at 3.6 μm down to a 3σ level of 3 μJy. At the time, this was an unexpected discovery since it was believed that SWIRE would detect all AGN or SFGs that were observable at radio frequencies. Similarly, Middelberg et al. (2008a) identified a sample of 31 IFRSs when cross-matching the ATLAS radio observations of the European Large Area ISO Survey South 1 (ELAIS-S1; Oliver et al., 2000) field with the co-spatial SWIRE observations, which had similar Infrared (IR) sensitivities to the SWIRE CDFS observations.

Most of these sources were found to have flux densities at 20 cm of a few hundred μJy, but some were as bright as 20 mJy. All 53 IFRSs discovered in ATLAS also lacked optical counterparts. Therefore, IFRSs may be extreme counterparts of the Optically Invisible Radio Sources (OIRS) identified by Higdon et al. (2005), which are compact radio sources undetected in the optical up to an R-band magnitude of $\sim$25.7. Higdon et al. (2008) show that 34% of their OIRS are not detected at 3.6 μm, and conclude that these undetected sources appear to embody a sample of powerful radio galaxies at $z > 2$. We refer to the IFRSs discovered in ATLAS which lacked optical and IR counterparts as *first generation* IFRSs. Since IFRSs were originally discovered, eight IR and nine optical counterparts have been potentially detected (Garn and Alexander, 2008; Huynh et al., 2010), all of which are extremely faint.

The nature of IFRSs remains unconfirmed, given their non-detections at optical and infrared wavelengths. Putative explanations of their nature have included: (1) high-redshift radio-loud galaxies; (2) extremely obscured radio galaxies at moderate redshifts ($1 < z < 2$); (3) lobes or hotspots of nearby unidentified radio galaxies; (4) very obscured, luminous starburst galaxies; (5) AGN or starburst galaxies in a transitory phase; (6) high-latitude pulsars; (7) misidentifications; (8) an unknown type of object; (9) a combination of these (Norris et al., 2011a, and references therein). The study of IFRSs has been almost entirely limited to their properties at radio frequencies.

The first steps taken toward probing the nature of IFRSs were the Very Long Baseline Interferometry (VLBI) observations undertaken by Norris et al. (2007) and Middelberg et al. (2008b), who respectively observed two and four IFRSs originally identified in ATLAS. Norris et al. (2007) detected an AGN within one of the IFRSs at a flux density of 5.0 mJy, implying a core size of < 0.03 arcsec, corresponding to a linear size of ≤ 260 pc at any redshift. Norris et al. (2007) suggested that if such an AGN were at a redshift of $z = 1$, it would be detected

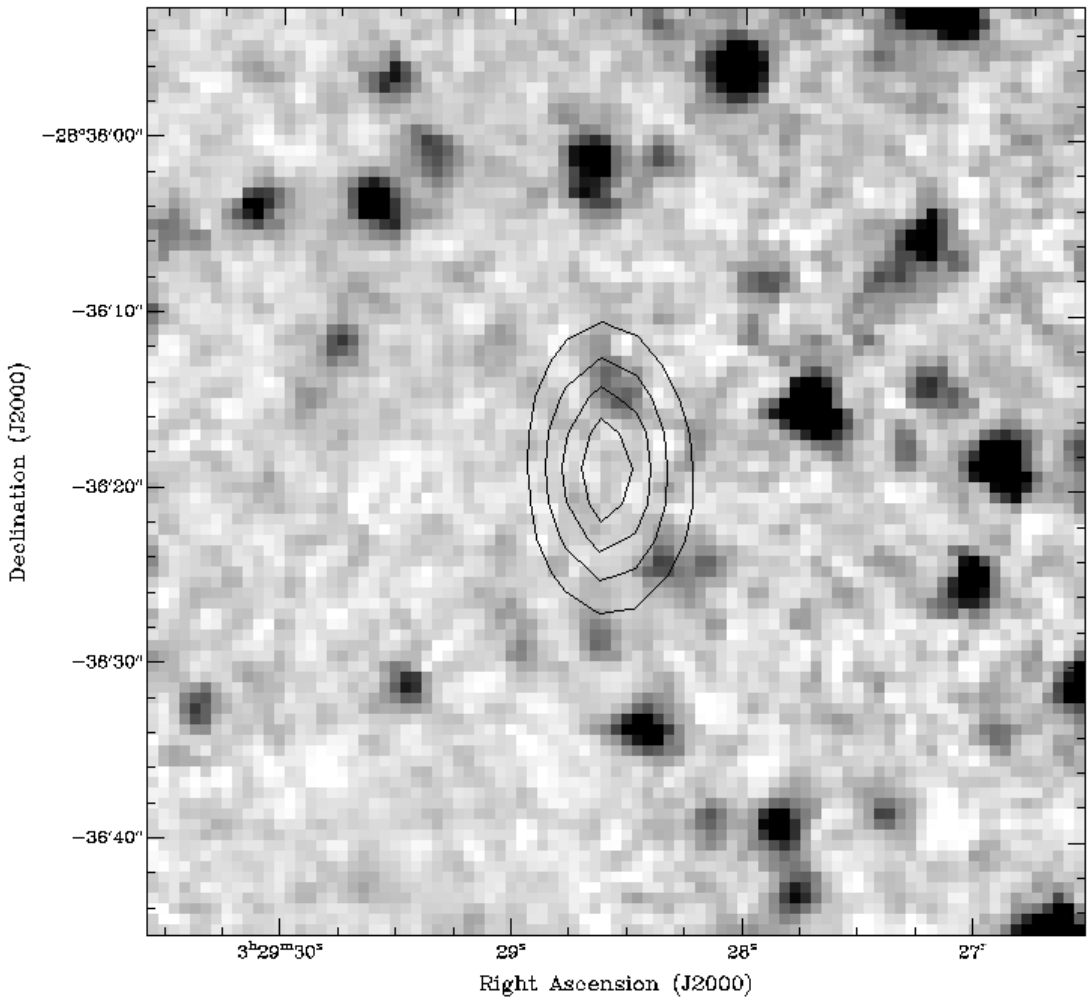

Figure 1.16: An IFRS from ATLAS, taken from Norris et al. (2011a). The grayscale is the deep 3.6 μm *Spitzer* Extragalactic Representative Volume Survey image, and the contours represent 1, 2, 3, 4 and 5 mJy/beam of the 1.4 GHz image.

by SWIRE. However, they proposed that at a redshift of $z = 7$, an AGN like this would most likely elude deep infrared detection, but could still be detected in deep radio observations.

Middelberg et al. (2008b) detected only one IFRS with VLBI. The detected source had a flux density on the longest baselines of 7 mJy, which they inferred corresponded to a brightness temperature of $T_{\rm B,min} = 3.6 \times 10^6$ K, indicating non-thermal emission from an AGN. They showed that the detected IFRS had properties consistent with that of a high redshift ($z > 1$) CSS source.

A further study of IFRSs was conducted by Garn and Alexander (2008), who analysed 14 IFRSs in the *Spitzer* First Look Survey (FLS) field, using the *Spitzer* Infrared Array Camera (IRAC; Fazio et al., 2004) and Multiband Imaging Photometer (MIPS; Rieke et al., 2004) data, as well as 20 cm VLA data from Condon et al. (2003). Their sample is complementary to that of the previous samples of ATLAS IFRSs, since their 3.6 μm 3σ sensitivity is $\sim 9\,\mu$Jy. Eight optical detections with a median AB magnitude of $R_{\rm AB} = 24.4$ suggest that the sample is a much brighter population of IFRSs, and may be at lower redshift. Garn and Alexander (2008) suggested that since they did not see an increase in the population of IFRSs at low flux densities (~ 1 mJy), at which point the contribution of SFGs becomes significant, their sources were unlikely to be obscured SFGs. Additionally, upper limits of the flux density ratio $q_{\rm IR} = \log_{10}(S_{\rm IR}/S_{1.4})$ (Appleton et al., 2004) were calculated to be $q_{24} < -0.7$ and $q_{70} < 1$, well below the typical values derived for SFGs. Through source stacking in the four IRAC bands, Garn and Alexander (2008) showed that six sources had possible infrared counterparts below the detection threshold. Using a stacked image of the remaining eight sources that are not identified as having a potential counterpart, they found an upper limit of the median 3.6 μm flux density of $3\sigma/\sqrt{8} = 3.1$ μJy. Garn and Alexander (2008) showed that IFRSs are made up of a population of flat, steep and Ultra-Steep Spectrum (USS) sources, from which they suggested that IFRSs ought not to be treated as a single source population. By modelling the Spectral Energy Distributions (SEDs) of the IFRSs from each of these three classes of radio spectra separately, and by placing upper limits on their linear size, they showed that all their IFRSs could be modelled as well-known Fanaroff and Riley Type II (FR II; Fanaroff and Riley, 1974) radio galaxies which are less luminous and placed at high redshift.

Possible infrared detections of two ATLAS IFRSs were made by Huynh et al. (2010), who found 3.6 μm flux densities of 5.5 ± 0.3 and 6.6 ± 0.3 μJy for the two sources, using ultra-deep *Spitzer* imaging of the Extended *Chandra* Deep Field South (ECDFS). The fainter of these sources also contained an optical Advanced Camera for Surveys (ACS; Giavalisco et al., 2004) counterpart at $V_{\rm AB} = 26.27$ and $z_{\rm AB} = 25.62$ magnitudes. Huynh et al. (2010) conducted detailed modelling of the SEDs of these two IFRSs, and two others that were undetected. Huynh et al. (2010) found that the data could be reproduced by a 3C 273-like object which, when detected in the infrared, was redshifted to $z = 2$, and when not detected in the infrared, was redshifted to $z > 4$. Furthermore, no non-detected IFRSs could be explained by any SED template at redshifts smaller than $z = 4$. Huynh et al. (2010) concluded that their four IFRSs lie well beyond the radio-infrared correlation, since none of them was detected at 24 μm, down to a 5σ level of 50 μJy. Hence, their radio emission cannot be accounted for by star formation and must be due to the presence of an AGN.

The deepest *Spitzer* imaging to date of the larger regions of the CDFS and ELAIS-S1 fields comes from the *Spitzer* Extragalactic Representative Volume Survey (SERVS; Mauduit et al., 2012), which has a 3σ noise level of ~ 1.5 μJy, and which mostly overlaps with the ATLAS regions where the first IFRSs were identified. Using the 3.6 μm SERVS data, Norris et al. (2011a) found three candidate detections of IFRSs at levels of ~ 2 μJy. However, they concluded

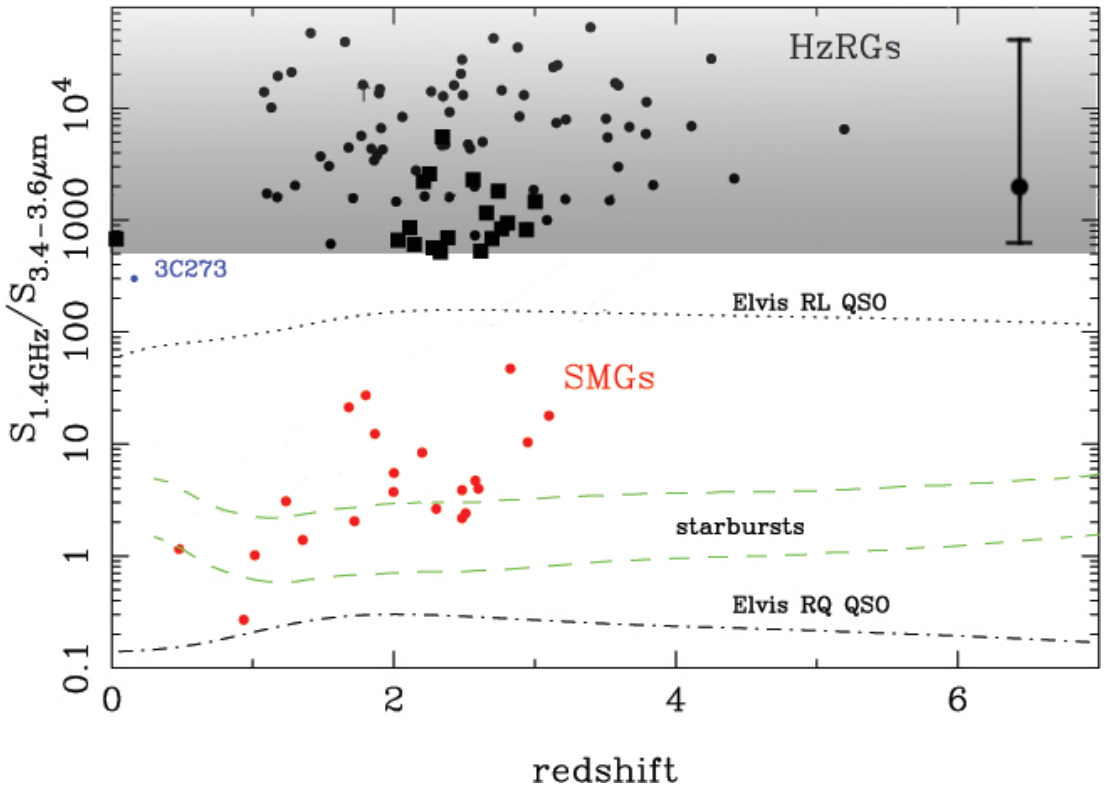

Figure 1.17: The flux density ratio between 20 cm and 3.4−3.6 μm as a function of redshift, for a number of different models, adapted from Norris et al. (2011a). The area in grey represents the ratio range above 500 which all IFRSs occupy. The black squares represent the IFRSs with redshifts from this thesis (see § 2.1.3 and 3.1.6). The filled circles within the grey area are the HzRGs from Seymour et al. (2007). The large black dot and error bar on the right marks the likely range of the first generation IFRSs. The area defined by the dashed green lines either side of the label "starbursts" represents the expected loci of Luminous Infrared Galaxies (LIRG) and Ultra-Luminous Infrared Galaxies (ULIRG) (using the SED template from Rieke et al. 2009) and the dotted and dot-dashed lines respectively indicate the loci of a classical radio-loud and radio-quiet QSOs (from Elvis 1994). The red dots show the locations of classical submillimetre galaxies.

that 2−3 of these detections could be spurious detections due to confusion. After producing a stacked infrared image, they found a median flux density of ∼0.2 μJy or less, attributing very extreme radio to infrared flux density ratios to these objects. Norris et al. (2011a) found no evidence of a cross-identification for the two candidate detections from Huynh et al. (2010), which would have appeared at ∼11σ and ∼13σ in SERVS. However, new radio data with greater positional accuracy from Miller et al. (2013) has revealed that while one of the Huynh et al. (2010) IR counterparts is probably due to confusion, the other coincides well with the updated radio position and consequently, we consider it to be a reliable match.

Maini et al. (2016) identified a further 21 IFRSs using more recent SERVS data, which went down to an even deeper 3σ level of ∼1 μJy at 3.6 μm, and which extended to the Lockman Hole. They also found a number of new candidate IR detections, and showed that these IFRSs are well modelled as quasars at $3 < z < 5$, based on their 3.6 and 4.5 μm tracks as compared to the SED tracks of other classes of object. Using median stacking, Maini et al. (2016) found that the undetected IFRSs had flux density upper limits of 0.3 and 0.4 μJy, respectively at 3.6 μm and 4.5 μm.

Norris et al. (2011a) showed that IFRSs span a range in flux density ratio $S_{20\mathrm{cm}}/S_{3.6\mu\mathrm{m}}$ that

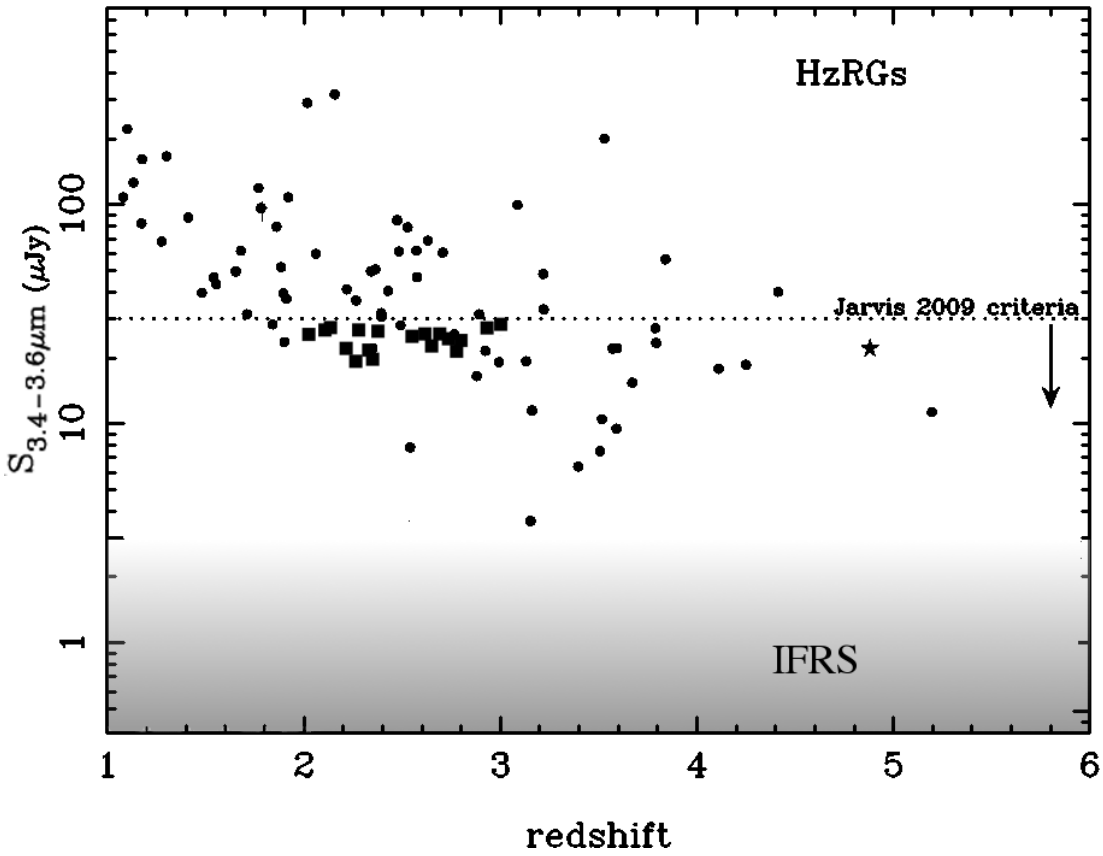

Figure 1.18: The 3.4−3.6 μm flux density as a function of redshift for our IFRSs and the HzRGs from Seymour et al. (2007), adapted from Norris et al. (2011a). The area in grey represents the range of upper limits on the flux density for the IFRSs discussed in Norris et al. (2011a), as indicated by the IFRS label. The black squares represent the IFRSs with spectroscopic redshifts discussed in this thesis (see § 2.1.3 and 3.1.6). The black dots are the HzRGs from Seymour et al. (2007). The star represents the $z = 4.88$ radio galaxy discovered by Jarvis et al. (2009), and the line represents the $S_{3.6\mu m} < 30$ μJy criterion they used to select their candidate HzRGs, which is also adopted by Zinn et al. (2011) to select IFRSs.

is unoccupied except for HzRGs, as illustrated in Fig. 1.17. They showed that if IFRSs follow the observed relation for HzRGs between $S_{3.6\mu m}$ and redshift, similar to the well-known $K - z$ relation that holds for other radio galaxies (Willott et al., 2003), then all first generation IFRSs occupy a place in the relation at $z \sim 5$, as illustrated in Fig. 1.18. Norris et al. (2011a) concluded that while there is a possibility that more than one class of object may represent IFRSs, the evidence suggests that a significant fraction, if not all of them, are radio-loud AGN at $z \gtrsim 3$, but could also be made up of a new class of radio-loud AGN at lower redshift ($1 < z < 3$), in which the IR luminosity of the entire host galaxy must be reduced by several magnitudes ($A_V \geq 10$ mag) of dust extinction.

Middelberg et al. (2011b) studied the high-resolution characteristics, spectral indices and polarisation properties of a sample of 17 IFRSs identified in the ATLAS ELAIS-S1 field. They concluded from the high resolution 4.8 and 8.6 GHz radio-continuum data that the observed sources are smaller than 4.5 kpc × 2.1 kpc, much smaller than the projected linear sizes of classic high redshift radio galaxies, which range from a few to many hundreds of kiloparsecs. Middelberg et al. (2011b) suggested that these IFRSs could therefore be intrinsically much smaller, or have their extended emission resolved out, even at lower resolution. None the less, the hypothesis that IFRSs are simply radio lobes of nearby galaxies was ruled out for these

particular sources, since they were too compact to be lobes. Middelberg et al. (2011b) found a median radio spectral index of $\alpha = -1.4$ for their sample of IFRSs, with no indices larger than -0.7, as compared to the respective medians of -0.86 and -0.82 for the general source population and the AGN source population in the ATLAS ELAIS-S1 field. Additionally, they found a curvature in the radio spectra as seen in GPS and CSS sources, rather than the power-law spectra of classical AGN. This implies that some IFRSs are very young and evolving AGN with very small jets, which is in good agreement with their observed sizes.

Middelberg et al. (2011b) also showed that the properties of their IFRSs are strikingly similar to those of a sample of HzRGs from Seymour et al. (2007), which had a median radio spectral index of -1.02. Furthermore, the flux density ratio $S_{20cm}/S_{3.6\mu m}$ of the IFRSs from Middelberg et al. (2011b) significantly overlapped with this sample of HzRGs, both of which had values of several hundred up to several tens of thousands, at the very tail end of the general source population, which peaked at $S_{20cm}/S_{3.6\mu m} \approx 5$. Middelberg et al. (2011b) also found three of the sources to be significantly polarised at 20 cm, with fractional polarisations between 7 – 12% . Given the evidence, Middelberg et al. (2011b) classified 10 of their sources as AGN and the other 7 as most likely AGN based on their 24 μm non-detections alone.

Banfield et al. (2011) found similar spectral indices and fractional polarisations for a sample of 18 IFRSs in the ELAIS-N1 field. They found a median spectral index of $\alpha = -1.1$ for five sources which had detectable polarisations, ranging from about 6 – 16% fractional polarisation. Banfield et al. (2011) found a steeper median spectral index of $\alpha = -1.5$ for the 13 unpolarised sources. Additionally, four of the polarised sources showed structure on arcsecond scales, while only two unpolarised sources showed resolved structure.

Cameron et al. (2011) observed 16 IFRSs to test the hypothesis that IFRSs are pulsars. After searching for short-term radio pulsations coming from the IFRSs, it was found that pulsed emission could not account for their observed flux densities. Cameron et al. (2011) concluded that it is unlikely that any IFRSs are simply pulsars.

Zinn et al. (2011) showed that the X-ray radiation from IFRSs may contribute significantly to the Cosmic X-ray Background. They estimated the X-ray emission of IFRSs and showed that it is consistent with the missing unresolved components of the Cosmic X-ray Background.

Despite the significant work undertaken in uncovering the nature of IFRSs, prior to this thesis, it still remains unconfirmed exactly what they are. However, good progress has been made toward ruling out some explanations of what makes up their majority, including pulsars, radio-lobes, and obscured SFGs. Additionally, it has been shown that it is not necessary for some new type of object to explain the existence of IFRSs. The evidence is mounting up that suggests the majority, if not almost all IFRSs are high-redshift ($z > 3$) radio-loud AGN. While it is possible that they could be suffering from significant dust extinction, such extinction is not necessary to explain the observed data. However, a minority of what we are calling IFRSs could be made up of several types of objects, given their non-uniform characteristics such as their radio spectral index. The most likely such objects include: (1) very obscured radio galaxies at moderate redshifts ($1 < z < 2$); (2) hotspots of nearby unidentified radio galaxies; (3) misidentifications. In this thesis we address these possibilities and whether they can explain IFRSs.

1.4.1 New IFRSs selection criteria

Norris et al. (2006) defined an IFRS as 'a radio source with no detectable IR counterpart'. Zinn et al. (2011) proposed a new set of selection criteria to enhance searching for IFRSs, since the

previous selection criterion was survey-specific. They defined IFRSs as sources that have:

1. a flux density ratio $S_{20\,\mathrm{cm}}/S_{3.6\,\mu\mathrm{m}} > 500$
2. a $3.6\,\mu$m flux density $< 30\,\mu$Jy

Although these limits are somewhat arbitrary, they encompass all known IFRSs. The first criterion ensures that the selected sources are outliers in the radio-IR correlation, minimising contamination from SFGs and foreground stars. The second criterion reduces the chance of selecting low-redshift AGN, although it does not rule out the possibility of selecting low-redshift AGN obscured by heavy dust extinction. Using these criteria, Zinn et al. (2011) compiled a catalogue of 55 known IFRSs from four deep radio surveys (CDFS, ELAIS-S1, FLS, and COSMOS), which remains until now the largest catalogue of IFRSs.

1.5 Aim of the Thesis

I aim to construct an evolutionary sequence for the early stages of AGN development, with a particular focus on faint GPS and CSS sources and IFRSs. Two ageing effects are present amongst AGN:

1. the evolutionary age of the AGN, as measured since it was triggered;
2. the cosmic age of the AGN, as measured from its redshift.

As discussed in sections 1.3 and 1.4, GPS and CSS sources are thought to represent AGN during an early evolutionary stage (i.e. young AGN), while IFRSs are thought to represent AGN during an early cosmic age (i.e. distant AGN), but these remain open questions. Studying IFRSs gives us an advantage for disentangling these effects, since many of them are also GPS and CSS sources.

1.5.1 GPS and CSS sources

The typical place of GPS and CSS sources within an evolutionary sequence is not well understood, particularly at faint levels, since many of them appear to be dying or restarting before evolving into large-scale radio galaxies. I test the hypothesis that GPS and CSS sources generally represent the youngest RGs, place them into an evolutionary sequence along with a number of other AGN, and search for evidence of the evolving accretion mode and its relationship to SF, in order to gain a more complete understanding of AGN evolution (see section 1.1). I study faint GPS/CSS sources from radio through to X-rays over a large sample size in order to detect meaningful indicators of their age.

1.5.1.1 Age Indicators

The indicators we use to derive independent estimates of the AGN age include the:

- jet sizes and kinematic ages
- spectral ages
- separation of nuclei (where available)
- colours, Spectral Energy Distributions (SEDs) and optical spectra of the host galaxy

The main age indicator we use is the jet size, as measured from high resolution radio observations. We use the jet sizes as input for dynamical models such as An and Baan (2012), which allows us to estimate the kinematic age. Another age indicator we use is the break frequency, obtained from the radio spectrum. We fit a power law, SSA and FFA models with and without a break frequency to all available radio flux density measurements, and derive the turnover and break frequencies from the best fit model. Where break frequencies are derived, the spectral age is estimated. The host colours, SEDs and spectra are obtained using all available IR and optical data.

Combining these age indicators enables us to identify if there is any evolutionary correlation between these properties, if they can be assembled into a self-consistent model, and if this is consistent with the currently accepted model (see section 1.1).

1.5.2 IFRSs

The Zinn et al. (2011) criteria enable the selection of a larger, brighter population of IFRSs with detectable infrared and optical emission. Therefore, while previous studies focused on very sensitive observations of a few small regions on the sky, we followed the strategy of combining radio data with IR data from the *Wide-field Infrared Survey Explorer* (*WISE*; Wright and WISE Team, 2009) for a large region of the sky, albeit at poorer sensitivity, and selecting detectable IFRSs from these data using the Zinn et al. (2011) criteria. With this data set we can not only study a statistically significant number of sources, we can learn how the brighter *WISE* IFRSs connect to the first generation of IFRSs.

1.6 The research problem(s)

1.6.1 GPS and CSS sources

As discussed in section 1.3.7, it is generally accepted that the majority of GPS and CSS sources are young and evolving, but good evidence exists in individual cases for frustrated, prematurely dying and restarted systems. As also discussed, it is still under debate whether SSA or FFA accounts for the radio spectra of GPS and CSS sources. Therefore, we aim to answer:

1. Are the majority of GPS and CSS sources are young and evolving?
2. Is there a significant fraction of GPS and CSS sources that are frustrated, dying or restarted?
3. Can SSA account for the spectra of GPS and CSS sources?
4. Can FFA account for the spectra of GPS and CSS sources?
5. What are the properties of faint GPS and CSS sources?

1.6.2 IFRSs

As discussed in section 1.4, it is generally thought that IFRSs are AGN either at low-redshift and with significant obscuration, or at high-redshift without significant obscuration. This remains an open question, since, prior to this thesis, no redshifts have so far been measured. Furthermore, the hypotheses that IFRSs are misidentifications, hotspots or lobes has not been ruled out. Therefore, we aim to answer:

1. Are IFRSs misidentifications?
2. Are IFRSs hotspots or lobes?
3. Are IFRSs nearby AGN?
4. Are IFRSs distant AGN?
5. How do the brightest IFRSs compare to the faintest IFRSs?
6. What is the nature of IFRSs?

1.7 Significance of thesis

1.7.1 GPS and CSS sources

GPS and CSS sources are difficult to study comprehensively. In order to characterise them sufficiently and unambiguously, we would ideally observe them simultaneously over many frequencies that sample below and above the turnover, and over many epochs to ensure minimal variability, alongside high-resolution observations (VLBI for the most compact sources) to characterise their morphologies. Furthermore, if we wish to study their properties at faint levels, we must use deep observations.

As noted above, we are in an unprecedented age for observing objects over a large range of radio frequencies, especially in the MHz range. In particular, using Murchison Widefield Array (MWA) observations allows for us to cover 20 frequencies between $70 - 230$ MHz, as described in section 2.2.1.3. This will allow us to characterise CSS sources in a way that has never been done before. Furthermore, using ATLAS will enable us to identify the faintest GPS and CSS sources yet.

Out to $z = 0.5$, all objects with $L_{1.4\mathrm{GHz}} \geq 7 \times 10^{23}$ W Hz^{-1} will be detectable in ATLAS DR3 down to the 5σ sensitivity limit of $\sim$75 μJy. Combining this with the μJy-level radio observations of the ATLAS fields at other frequencies enables us to identify low-luminosity GPS and CSS sources at distances beyond a Gpc, far beyond the nearby GPS sources proposed for investigation by Tingay and Edwards (2015). Therefore, from the existing radio data covering the ATLAS fields alone, we can identify a population of distant GPS and CSS sources which have $L_{1.4\mathrm{GHz}} = 10^{22-23}$ W Hz^{-1}, below the break luminosity proposed by Tingay and Edwards (2015) for identifying the compact counterparts of FR I galaxies. These low-luminosity sources will enable us to directly test this hypothesis with subsequent VLBI observations.

As shown from the An and Baan (2012) model above, the evolution of low-luminosity radio sources is significantly different from those of high-luminosity, which has since been proposed to differentiate accretion type, in which the lower-luminosity evolution is followed by LERGs (Kunert-Bajraszewska, 2016). However, since low-luminosity compact objects are still poorly sampled, this remains an open question. Therefore studying sources that are low in luminosity and amongst the earliest stages of radio galaxy evolution will unveil a population of objects critical for understanding galaxy evolution that has so far eluded observation. Furthermore, since the *Chandra* Deep Field South (CDFS), covered by ATLAS, is arguably the best-studied field in the sky, we can investigate the properties of GPS and CSS across deep observations at virtually all wavelengths. This multi-wavelength data gives valuable information about the environment, revealing how AGN properties such as size, luminosity and duty cycle depend on environment. For some sources, we have independent measurements of the star-formation rate (e.g. Herschel and Hα), which allows us to study the mechanisms of the co-triggering of the

AGN and the SF (see section 1.1) and the effect the expanding jet has on these, none of which has been done at $z > 0$. ATLAS enables this research to take place on such a faint sample of such size for the first time, which will pave the way for the science that will come out of the Evolutionary Map of the Universe (EMU; Norris et al., 2011b). The study of GPS and CSS sources at such faint levels will give great insight into the genesis and evolution of powerful radio galaxies.

1.7.2 IFRSs

IFRSs are also difficult to study, since the majority are undetected in IR and optical observations. However, we have used the Zinn et al. (2011) selection criteria to select a sample of brighter IFRSs which are detectable in both optical and IR, enabling us to comprehensively study their properties and draw comparisons between these and previous samples of IFRSs. This enables us to draw conclusions about this poorly understood class of galaxy as a whole, in particular, by measuring their redshifts. We present the first spectroscopic redshifts of IFRSs, as well as the first X-ray counterparts of IFRSs. Additionally, we examine the properties of all IFRSs with detectable polarisation, significantly increasing the number of known polarised IFRSs.

Chapter 2

Data, Sample Selection and Observations

The data used throughout this thesis consists primarily of radio and IR data, used to select the samples, as well as ancillary optical and X-ray data that were not used during selection. These come from catalogued data (see sections 2.1.1, 2.2.1.1 and 2.2.2.1), as well as new radio data which I collected, reduced and analysed for this thesis (see section 2.2.4 and 2.3). The different samples presented here make use of different datasets, which cover different areas of the sky. Therefore we must differentiate between the data used to select the different samples, before introducing their selection. The IFRS sample (see section 2.1.3) covers most of the northern sky, while the GPS and CSS samples (see section 2.2.3) cover the Small Magellanic Cloud (SMC) and ATLAS fields. For each of these samples, Appendix B lists the work completed by me and by others that I have used for this thesis.[1]

2.1 IFRS sample

2.1.1 Catalogued data

2.1.1.1 Unified Radio Catalog

The 20 cm radio data used for the IFRS sample come from the Unified Radio Catalog (URC) compiled by Kimball and Ivezić (2008). This radio catalogue combines data from the NRAO VLA Sky Survey (NVSS; Condon et al., 1998), Faint Images of the Radio Sky at Twenty Centimeters (FIRST; Becker et al., 1995), Green Bank 6 cm survey (GB6; Gregory et al., 1996), the Westerbork Northern Sky Survey (WENSS; Rengelink et al., 1997), and the Sloan Digital Sky Survey (SDSS) Data Release 6 (DR6; Adelman-McCarthy et al., 2008). We use updated NVSS and FIRST data from the URC version 2.0 (Kimball and Ivezic, 2014), which includes a number of new sources as well as updated positions and flux densities.

2.1.1.2 Infrared data

The IR data used for the IFRS sample come from the *Wide-field Infrared Survey Explorer* (*WISE*; Wright and WISE Team, 2009), which is an all-sky survey centred at 3.4, 4.6, 12, and 22 μm (referred to as bands W1, W2, W3 and W4), with respective angular resolutions of 6.1″, 6.4″, 6.5″, and 12.0″ (FWHM), and typical 5σ sensitivity levels of 0.08, 0.11, 1, and 6 mJy,

[1]The descriptions in Appendix B will make more sense after having read the chapters they concern.

with sensitivity increasing towards the ecliptic poles. The majority of our sources fall in these strips of greater sensitivity, because we require their 3.4μm flux density to be $< 30\,\mu$Jy. To convert *WISE* magnitudes to flux density in Jy, $S_{\rm band}$, we used

$$S_{\rm band} = F_{\rm band}({\rm iso}) \times 10^{(-M_{\rm band}/2.5)}\,{\rm Jy}\,, \tag{2.1}$$

where $F_{\rm band}$(iso) is the flux correction factor at the given *WISE* band from Jarrett et al. (2011) and $M_{\rm band}$ is the observed magnitude at the corresponding *WISE* band.

Additionally, we need to apply a colour correction, which depends on the assumed SED, which we don't know in detail. Hence, we initially assume the correction factor of 0.991 in band W1 given by Jarrett et al. (2011) for a source that scales as $F_\nu \propto \nu^0$, which is generally suitable for galaxies, and which results in the conversion

$$S_{3.4\mu{\rm m}} = 309.540 \times 10^{(-M_{3.4\mu{\rm m}}/2.5)}\,{\rm Jy} \tag{2.2}$$

We initially selected the IFRSs using this conversion factor. We then measured the *WISE* colours of this pre-selection in order to determine if our colour correction was suitable. Band W4 was not considered in this calculation, and therefore nor was the colour [W3 − W4], since only seven sources were detected at $\geq 5\sigma$ in band W4. The respective median colours were [W1 − W2] = 1.376 and [W2 − W3] = 4.277. According to Wright et al. (2010), these colours are closest to that of a source that scales as $F_\nu \propto \nu^{-2}$, which gives an SED with *WISE* colours [W1 − W2] = 1.3246 and [W2 − W3] = 3.9225, and for which there is no colour correction. Hence, when converting 3.4 μm from mags to Jy, we use no colour correction factor, which results in the conversion

$$S_{3.4\mu{\rm m}} = 306.682 \times 10^{(-M_{3.4\mu{\rm m}}/2.5)}\,{\rm Jy} \tag{2.3}$$

The 30 μJy cutoff therefore corresponds to a lower limit in band W1 of ∼17.5 magnitudes. Using this more appropriate conversion, we then reselected the IFRSs, adding less than 5% to the original.

2.1.2 Ancillary data

Ancillary data for the IFRS sample were searched for in the Parkes-MIT-NRAO (PMN; Griffith et al., 1995), VLA Low-Frequency Sky Survey (VLSS; Lane et al., 2008), *Spitzer* and SDSS DR9 (Ahn et al., 2012) catalogues. Misidentification rates were estimated for these using the same procedure as outlined in § 2.1.4. Table 2.1 summarises the ancillary data gathered for our sample of IFRSs from these various surveys. The ancillary data can be found within the full table, available in the electronic version of Collier et al. (2014).

There are 31 IFRSs that have a counterpart in one of the following surveys from the *Spitzer Space Telescope*: SWIRE (9); FLS (5); *Spitzer* Deep Wide-Field Survey (SDWFS) (1); the '*Spitzer* Enhanced Imaging Products Explanatory' from the NASA/IPAC Infrared Science Archive (IRSA)[2] (16) (Lonsdale et al., 2003; Ashby et al., 2009). The aperture and colour corrected 3.6 μm flux densities from *Spitzer* are consistent with our 3.4 μm flux densities from *WISE*, since only nine sources lay outside the 1σ uncertainty, as expected by chance.

There are 230 SDSS matches to our IFRSs, which yield a cross-match rate of ∼17% . SDSS DR9 has a 95% completeness for point sources, to AB magnitude limits of 22.0, 22.2, 22.2, 21.3 and 20.5, respectively in bands *ugriz*. The optical magnitudes quoted refer to the SDSS model

[2] `http://irsa.ipac.caltech.edu/cgi-bin/Gator/nph-scan?submit=Select&projshort=SPITZER`

magnitudes, which are measured using a weighting function as determined from the object's brightness in band r.

SDSS DR9 was also queried for spectroscopic redshifts, which were searched for within a 2 arcsec radius of the FIRST positions of our sample. 19 spectra were returned. No flags were given in the field zWarning, and all had reduced χ^2 spectral fit values of < 2, apart from three which had values of 2.06, 3.19 and 7.06. All spectra were 'science primary', which ensured they were the best spectra available at each location.

2.1.2.1 Searching NED

To search for additional spectroscopic redshifts, NED was queried for each IFRS to within 2 arcsec. Of the 1317 IFRSs, 1007 were matched to 1137 unique NED sources, where some IFRSs had multiple matches. For the sake of simplicity, we simply kept the closest match from NED.

Six of the 19 spectroscopic redshifts from SDSS were returned from NED, which contained SDSS data only as recent as DR4, but no additional spectroscopic redshifts were found. Furthermore, 16 photometric redshifts were found (Verkhodanov et al., 2002; Richards et al., 2004; Abazajian et al., 2004, 2005; Hsieh et al., 2005; Adelman-McCarthy et al., 2006; Tinti and de Zotti, 2006; Schmidt et al., 2006; Rowan-Robinson et al., 2008; El Bouchefry, 2009), but we do not use these photometric redshifts in our analysis as it is unlikely that the SED templates used match those of our IFRSs.

2.1.2.2 Survey fields

A number of our IFRSs were found within deep survey fields that have a large amount of multi-wavelength coverage. Table 2.2 lists the number of sources from our sample that were identified to be within the approximate boundaries of several deep fields. The sources located within these deep fields can be found in the full table, available in the electronic version of Collier et al. (2014).

Table 2.1: Cross-Identifications of Ancillary Data for IFRS sample

Survey	Telescope	Reference	Mean Resolution (arcsec)	Astrometric Precision (arcsec)	Search Radius (arcsec)	Misidentification Rate	Matches
Various	*Spitzer*	–	1.66	0.2	5	∼1%	31
SDSS DR9	Sloan	Ahn et al. (2012)	1.3	0.1	2	3%	230
PMN	Parkes	Griffith et al. (1995)	300	∼10	120	10%	19
VLSS	VLA	Lane et al. (2008)	80	< 8	15	3%	214

Table 2.2: IFRSs within deep fields

Deep Field	Reference	Matches
All-Wavelength Extended Groth Strip International Survey (AEGIS)	Davis et al. (2007)	1
Bootes1	Murray et al. (2005)	2
European Large Area ISO Survey-North 1 (ELAIS-N1)	Oliver et al. (2000)	5
European Large Area ISO Survey-North 2 (ELAIS-N2)	Oliver et al. (2000)	1
SDSS Stripe 82	Abazajian et al. (2009)	12
VLA First Look Survey (FLS)	Condon et al. (2003)	1
XMM Large Scale Structure (XMM-LSS) SWIRE Boundaries	Lonsdale et al. (2003)	22

2.1.3 Sample Selection

Our sample of 1317 IFRSs was selected with the following criteria:

- Single NVSS source with $S_{20\mathrm{cm}} > 7.5$ mJy
- At least one FIRST counterpart within $30''$ of NVSS source
- *WISE* counterpart within $5''$ from FIRST position
- *WISE* $S_{3.4\,\mu\mathrm{m}} < 30\,\mu$Jy
- The NVSS to *WISE* flux ratio, $S_{20\,\mathrm{cm}}/S_{3.4\,\mu\mathrm{m}} > 500$
- signal-to-noise (S/N) at $3.4\,\mu$m is ≥ 5
- Visually do not appear as radio lobe matched to IR source

We now discuss the selection criteria in detail.

2.1.3.1 $S_{20\mathrm{cm}} > 7.5$ mJy

To maximise completeness and minimize polarisation bias, we applied a 7.5 mJy cutoff to our NVSS sources from the URC. This flux density corresponds to a 5-sigma detection in the *WISE* $3.4\,\mu$m band and a flux ratio $S_{20\,\mathrm{cm}}/S_{3.4\,\mu\mathrm{m}} = 500$, assuming the best *WISE* noise level is 3 μJy (see Fig. 4.43). At this level, *WISE* is far from complete (see Fig. 2.2), due to its non-uniform depth across the sky.

2.1.3.2 FIRST counterparts

We extracted from the URC all NVSS radio sources with at least one FIRST counterpart. The angular resolution of NVSS is $45''$, while the angular resolution of FIRST is $5.4''$ at 20 cm, making the FIRST position more accurate than the NVSS position when matching with counterparts in other surveys. We use the higher angular resolution data of FIRST for the accurate positional information, whilst using the NVSS flux density as a measure of the total integrated flux density of all of the FIRST components, which generally number between 1 and 3. Using NVSS data also allows us to match sources from the NVSS rotation measure (RM) catalogue (Taylor et al., 2009), which consists of RMs for 37 543 polarised sources from the NVSS catalogue, from which we extracted 41 matches.

After applying an NVSS radio flux density cutoff at 7.5 mJy and selecting only sources with at least one FIRST counterpart in the URC, we had 312 514 radio sources.

2.1.3.3 *WISE* counterpart within $5''$ of FIRST position

When matching the radio sources to *WISE*, we want to ensure that at $z > 0.5$, the corresponding linear separation is $\lesssim 30$ kpc, smaller than the size of large spiral galaxies. This limit reduces confusion and is consistent with the observed limits on the projected sizes of previous IFRSs. Therefore, *WISE* counterparts were searched for in a $5''$ radius from the FIRST positions. Of the 312 514 preselected radio sources, 137 154 *WISE* matches detected at $\geq 5\sigma$ in band W1 were found.

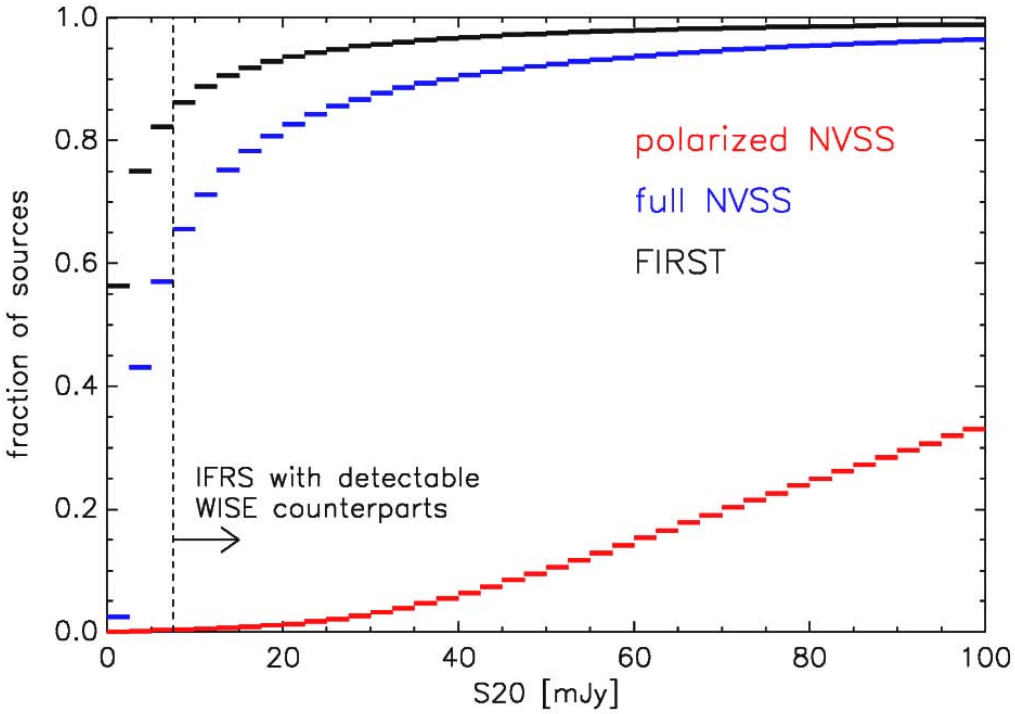

Figure 2.1: Cumulative distribution of flux densities for three different radio surveys at 20 cm. An IFRS could have a radio counterpart as faint as 7.5 mJy, if *WISE* detected it at 5σ at 3.4 μm and the flux density ratio $S_{20\mathrm{cm}}/S_{3.4\mu\mathrm{m}} = 500$ (assuming the best *WISE* noise level of 3 μJy). At these flux densities the catalogue of polarised NVSS sources (red) is far from complete, while the other two catalogues contain many faint radio sources.

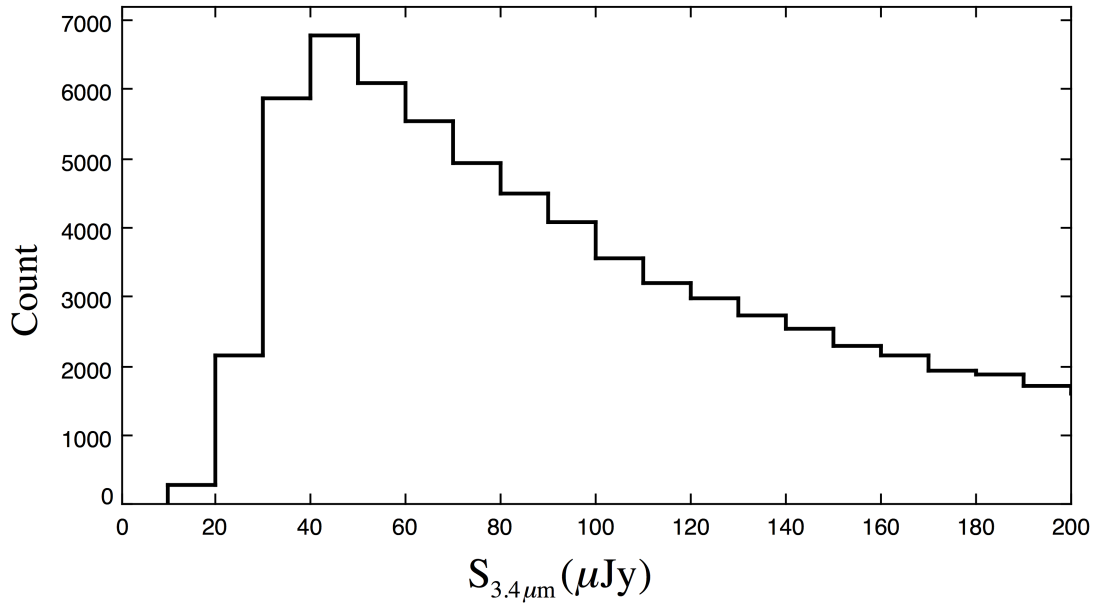

Figure 2.2: Histogram of the *WISE* 3.4 μm flux density for all *WISE* sources detected at $\geq 5\sigma$ with FIRST/NVSS radio counterparts (from the URC) above 7.5 mJy. The sharp drop in the number of sources below 40 μJy signifies that the catalogue is far from complete below this level.

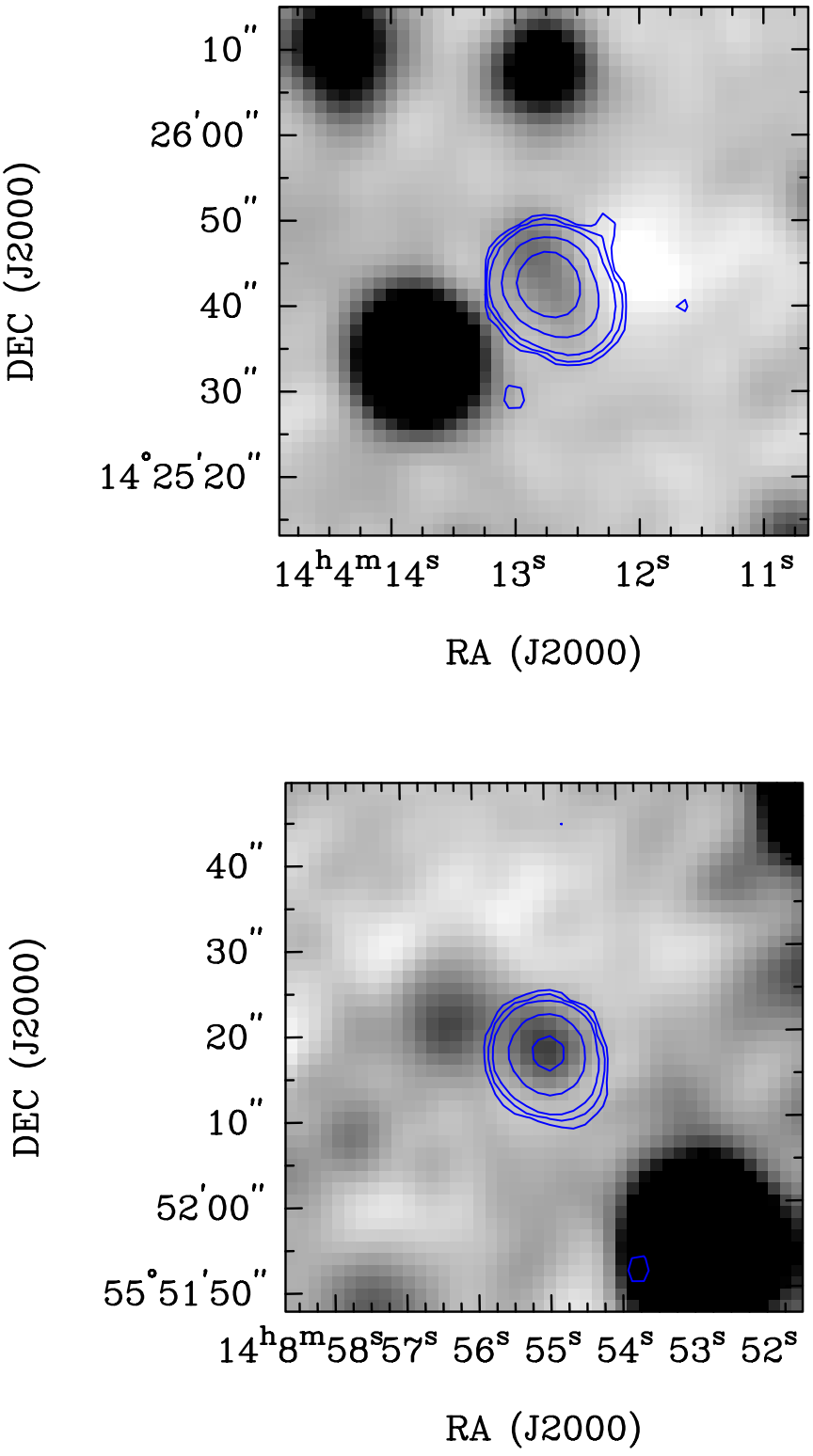

Figure 2.3: Polarised NVSS sources detected by *WISE* and classified as IFRSs. These two sources were found to have cataloged redshifts of 0.99 (top image) and 2.56 (bottom image). The background image shows the *WISE* 3.4 μm detection, and the contours mark the FIRST source at 20 cm. Contour levels are: 3, 6, 12, 64, 256, 1024 times the local noise level. The *WISE* sources are detected at the 5.5–6$\sigma_{\rm WISE}$ level, while their total intensity counterparts in NVSS are detected at the 33$\sigma_{\rm NVSS}$ level.

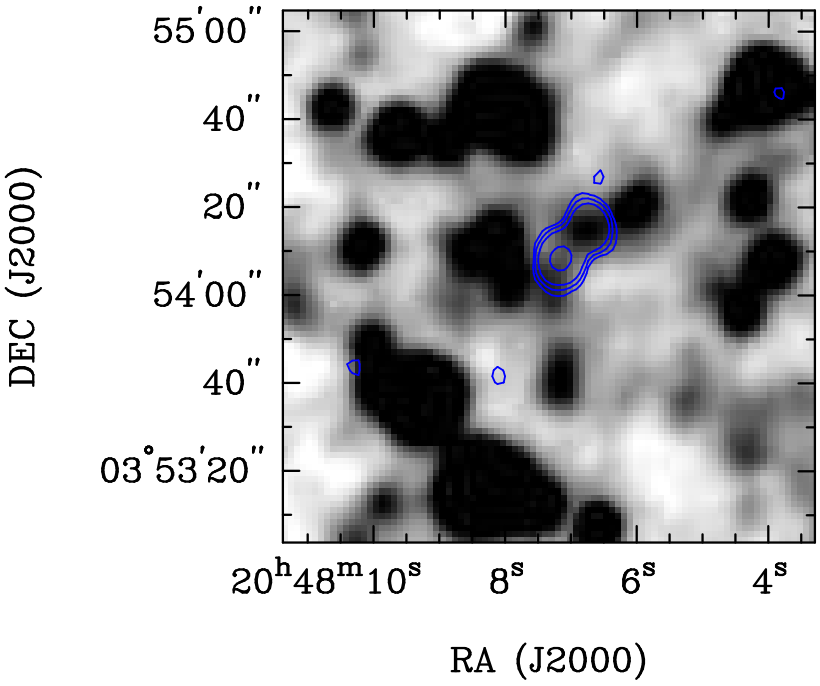

Figure 2.4: An example of an IFRS candidate that was discarded during visual inspection. The background image shows the *WISE* 3.4 μm intensity, and the contours mark the FIRST source at 20 cm. Contour levels are: 3, 6, 12, 64, 256, 1024 times the local noise level.

2.1.3.4 IFRS selection

We then applied our IFRS selection, using the Zinn et al. (2011) criteria (i.e. $S_{3.4\,\mu\mathrm{m}} < 30\,\mu$Jy and $S_{20\,\mathrm{cm}}/S_{3.4\,\mu\mathrm{m}} > 500$), as well as the criterion that the S/N at 3.4 μm is ≥ 5. This resulted in a total of 1471 candidate IFRSs.

2.1.3.5 Visual inspection

As the radio emission can originate from the the lobes or the central area of the host galaxy, the candidate IFRSs were visually inspected, to ensure that no radio lobes from a nearby source were spuriously matched to a *WISE* source. In many cases, the IFRSs were resolved into several FIRST components, which could be identified as nuclei or lobes when overlaid as contours on a *WISE* greyscale image. If the radio emission came from the lobe of the radio source and overlapped with a *WISE* galaxy, this was not considered an IFRS, and so was discarded from the sample, to reduce the number of misidentifications. 154 sources were discarded during the visual inspection. Fig. 2.3 shows two detected IFRSs and Fig. 2.4 shows a discarded IFRS.

2.1.3.6 Final IFRS catalogue

The final IFRS catalogue consists of 1317 sources, 41 of which have matches in the Taylor et al. (2009) RM catalogue. Table 2.3 lists the FIRST RA and DEC, the radio and infrared flux densities and their ratio ($\mathrm{S_{20cm}/S_{3.4\mu m}}$), the bias corrected fractional polarisation and RM, and the radio spectral index for the 41 polarised IFRSs. The full table of 1317 IFRSs is available in the electronic version of Collier et al. (2014), which includes a number of additional columns.

Table 2.3: The 41 IFRSs which have matches in the Taylor et al. (2009) RM catalogue. Listed is the FIRST RA and DEC, the NVSS 20 cm flux density, the *WISE* 3.4 μm flux density, the radio-IR flux density ratio, the bias corrected fractional polarisation and RM from the Taylor et al. (2009) RM catalogue, and the radio spectral index, calculated using flux densities at 92, 20 and 6 cm, as discussed in § 3.1.4.

FIRST RA (J2000)	FIRST DEC (J2000)	$S_{20\,\mathrm{cm}}$ (mJy)	$S_{3.4\,\mu\mathrm{m}}$ (μJy)	$S_{20\,\mathrm{cm}}/S_{3.4\,\mu\mathrm{m}}$	Fractional Polarisation	Rotation Measure (rad m^{-2})	α
02:16:36.78	−00:24:51.36	44.47 ± 1.40	28.10 ± 5.90	1583 ± 393	11.57%	19.3 ± 11.9	
02:17:06.19	+05:31:09.58	131.66 ± 4.65	29.05 ± 5.30	4533 ± 1016	5.35%	−20.6 ± 9.7	
02:25:45.07	−06:37:53.99	23.81 ± 0.83	25.60 ± 5.38	930 ± 235	12.19%	−11.5 ± 16.7	
02:29:29.97	+04:53:19.90	72.70 ± 2.22	28.67 ± 5.23	2536 ± 554	8.63%	−17.9 ± 10.1	
02:31:52.06	−02:26:47.48	60.19 ± 2.24	28.70 ± 5.61	2097 ± 504	6.92%	13.7 ± 15.8	
11:13:54.32	+35:12:33.97	45.00 ± 1.73	26.78 ± 5.57	1680 ± 427	9.78%	50.7 ± 15.1	
11:44:06.17	+56:54:39.63	171.63 ± 5.16	30.00 ± 5.44	5721 ± 1241	3.92%	9.4 ± 9.3	−0.69
13:25:13.02	−05:48:10.59	94.28 ± 2.86	28.44 ± 5.63	3315 ± 776	4.25%	4.3 ± 15.8	
13:54:03.81	+05:05:44.21	91.31 ± 3.30	27.97 ± 5.35	3264 ± 765	5.28%	−17.5 ± 13.2	
13:55:02.25	+16:10:23.64	197.37 ± 5.93	25.94 ± 5.13	7610 ± 1780	3.02%	7.3 ± 13.3	
14:04:12.73	+14:25:42.47	137.28 ± 4.14	26.86 ± 4.96	5111 ± 1126	6.37%	−8.6 ± 5.5	
14:08:54.99	+55:52:17.62	62.86 ± 1.93	26.42 ± 4.99	2380 ± 537	5.51%	−9.5 ± 15.4	−0.69
14:12:22.77	+28:54:02.20	127.16 ± 4.36	27.11 ± 5.48	4691 ± 1142	5.64%	13.3 ± 9.2	−0.98
14:24:21.25	+20:14:55.25	186.60 ± 5.61	22.90 ± 4.94	8148 ± 2055	3.21%	8.8 ± 10.9	
14:29:33.30	+12:26:01.06	66.54 ± 2.04	22.90 ± 4.61	2905 ± 691	6.94%	12.8 ± 12.3	
14:30:18.96	+08:26:12.22	96.19 ± 2.91	26.91 ± 5.29	3575 ± 833	3.85%	16.0 ± 15.0	
14:36:53.44	+42:44:16.99	276.94 ± 9.81	25.94 ± 4.93	10678 ± 2480	3.59%	−0.1 ± 6.9	
14:38:32.97	+29:33:54.70	290.19 ± 8.71	28.00 ± 4.59	10365 ± 2064	1.77%	35.4 ± 12.0	−0.77
14:41:57.04	+41:51:01.80	72.62 ± 2.22	25.04 ± 5.29	2900 ± 719	6.08%	−10.9 ± 12.9	−1.01
14:48:55.62	+53:52:10.43	109.01 ± 3.29	22.86 ± 4.80	4768 ± 1176	3.49%	53.1 ± 14.9	−0.87
14:54:13.84	+53:38:04.11	135.50 ± 4.08	28.54 ± 4.68	4747 ± 946	2.81%	29.5 ± 13.8	−0.90

Continued on next page

FIRST RA (J2000)	FIRST DEC (J2000)	$S_{20\,\mathrm{cm}}$ (mJy)	$S_{3.4\,\mu\mathrm{m}}$ (μJy)	$S_{20\,\mathrm{cm}}/S_{3.4\,\mu\mathrm{m}}$	Fractional Polarisation	Rotation Measure (rad m^{-2})	α
15:01:36.29	+05:27:25.64	248.49 ± 7.47	27.61 ± 5.16	9000 ± 2003	2.73%	−17.2 ± 9.4	
15:02:51.14	+60:09:41.68	128.96 ± 3.89	28.46 ± 3.98	4531 ± 789	5.59%	−4.8 ± 8.1	−0.91
15:04:22.70	−05:58:16.47	127.94 ± 3.86	29.80 ± 5.93	4292 ± 1009	5.10%	−8.4 ± 10.8	
15:08:46.27	+41:27:50.23	407.60 ± 14.38	27.36 ± 3.82	14898 ± 2681	6.25%	6.9 ± 2.8	−0.82
15:09:04.89	−03:09:17.66	49.32 ± 2.13	25.44 ± 5.46	1939 ± 517	13.69%	16.1 ± 11.2	
15:10:04.47	+60:29:24.64	77.46 ± 2.36	23.89 ± 4.00	3242 ± 658	4.99%	6.5 ± 17.0	−1.02
15:10:20.14	+35:40:43.09	28.28 ± 0.93	28.15 ± 3.49	1005 ± 162	13.98%	−3.5 ± 16.5	−0.61
15:28:21.90	+21:14:59.25	39.52 ± 1.25	23.44 ± 4.53	1686 ± 390	8.01%	27.6 ± 20.0	
15:30:22.57	+06:44:07.97	293.14 ± 8.80	28.49 ± 5.04	10289 ± 2186	3.35%	5.2 ± 5.8	
15:40:43.74	+46:44:48.06	116.36 ± 3.51	18.81 ± 3.35	6188 ± 1322	2.76%	9.9 ± 16.8	−1.23
15:51:28.21	+64:05:37.28	683.19 ± 20.50	16.82 ± 3.37	40612 ± 9587	2.95%	−45.3 ± 7.6	−0.35
15:56:48.48	+55:39:05.80	61.22 ± 1.88	20.72 ± 3.09	2955 ± 545	5.85%	30.1 ± 16.4	−0.89
16:11:39.63	+46:18:51.12	47.67 ± 1.48	26.81 ± 3.30	1778 ± 281	7.01%	4.0 ± 17.0	−0.83
16:13:34.76	+45:46:54.40	97.08 ± 2.94	24.20 ± 3.38	4011 ± 699	3.16%	53.8 ± 15.4	−0.89
16:14:19.24	+59:59:33.77	273.78 ± 8.22	29.91 ± 3.65	9152 ± 1425	1.36%	21.8 ± 17.3	−0.82
16:22:31.98	+41:23:22.62	113.66 ± 3.43	29.80 ± 4.80	3813 ± 747	4.09%	32.8 ± 14.2	−1.10
16:52:01.27	+47:05:01.96	110.82 ± 3.35	29.56 ± 5.17	3749 ± 789	3.96%	2.0 ± 11.9	−0.90
17:04:21.92	+41:54:35.88	116.46 ± 3.52	28.62 ± 6.04	4069 ± 1008	6.32%	29.6 ± 7.9	−0.97
17:04:32.08	+54:56:42.91	34.96 ± 1.12	21.32 ± 3.87	1640 ± 359	10.23%	14.1 ± 15.6	−0.61
17:16:25.50	+33:05:50.64	176.16 ± 6.24	27.94 ± 5.19	6304 ± 1436	6.46%	24.2 ± 6.0	−0.94

2.1.4 Positional Uncertainties and Confusion

The FIRST survey has an astrometric precision of $\lesssim 1''$ (Becker et al., 1995). *WISE* has an astrometric precision of $< 0.15''$ with a further error of $\sim$FWHM/(2 $\times$ S/N) added in quadrature (Wright et al., 2010). Since we require a 5σ detection, all *WISE* positions in our sample are accurate to $< 1''$. The mean sky separation between the *WISE* positions and the FIRST positions is 1.5 arcsec, with the mean ΔRA and ΔDEC both < 1 arcsec, and a standard deviation of $\sigma = 1.4$ arcsec for both the RA and DEC. We find 65% of our sources have a FIRST/*WISE* separation < 1.5 arcsec. The sky separation for all of our IFRSs is shown in Fig. 2.5.

Since the *WISE* 3.4 μm data approach the confusion limit, it is necessary to estimate the misidentifications that are due to confusion. We do so by taking an unbiased subsample of 312 (0.1%) of the NVSS sources with FIRST positions from the URC, which are located all across the sky. We then shift their radio positions by an amount (typically $\sim 15''$) that is greater than the beam size of both the radio and IR data, but smaller than the scale of the variations in the image sampling. We then apply our matching and selection procedure (see § 2.1.3), to estimate the confusion. This process was repeated eight times, each time shifting the radio positions by a different amount. It was found that a mean of 25.5 ± 4.8 ($\sim$8%) of the shifted radio sources contained *WISE* counterparts. Of these, a mean of 0.75 ± 0.83 matched the criteria of being an IFRS, giving a misidentification rate of our final sample of 0.24 ± 0.27% . Hence, the vast majority of our sample are genuine cross-matches, with an expectation of about 3 false-positives in our total of 1317 IFRSs.

2.2 GPS and CSS samples

2.2.1 SMC sample

2.2.1.1 Catalogued Radio Data

The close proximity of the SMC has resulted in extensive studies of its foreground emission during the past few decades, with particular interest in its Planetary Nebulae, Supernova Remnants and H II regions. The SMC has been the target of many deep observations from space-based telescopes, such as the SAGE survey from the *Spitzer Space Telescope*, deep *XMM-Newton* observations in the X-ray, and deep *Herschel* observations in the Far Infrared (FIR).

Radio observations of this region were originally undertaken to map the large-scale structure of the SMC. Since then, however, it has been probed in the radio at higher resolutions, often to find compact supernova remnants or planetary nebulae, or even to target background polarised AGN to determine the magnetic field structure across the SMC via Rotation Measure (RM) Synthesis (Mao et al., 2008). Since radio observations are able to penetrate through the foreground dust and gas, this has resulted in making the SMC a large region of sky (> 20 square degrees) that contains data for thousands of background sources at mJy levels, most of which are AGN.

The combination of multiple datasets of the SMC in the radio has allowed for even more detailed pictures at several frequencies in the GHz range, which are sensitive to both large- and small-scale structure, allowing foreground and background objects to be disentangled (Filipović et al., 2002; Wong et al., 2011a; Crawford et al., 2011). This has enabled many background RGs to be identified, many of which are GPS and CSS sources.

The radio data covering the SMC come from radio continuum mosaics created using Molonglo

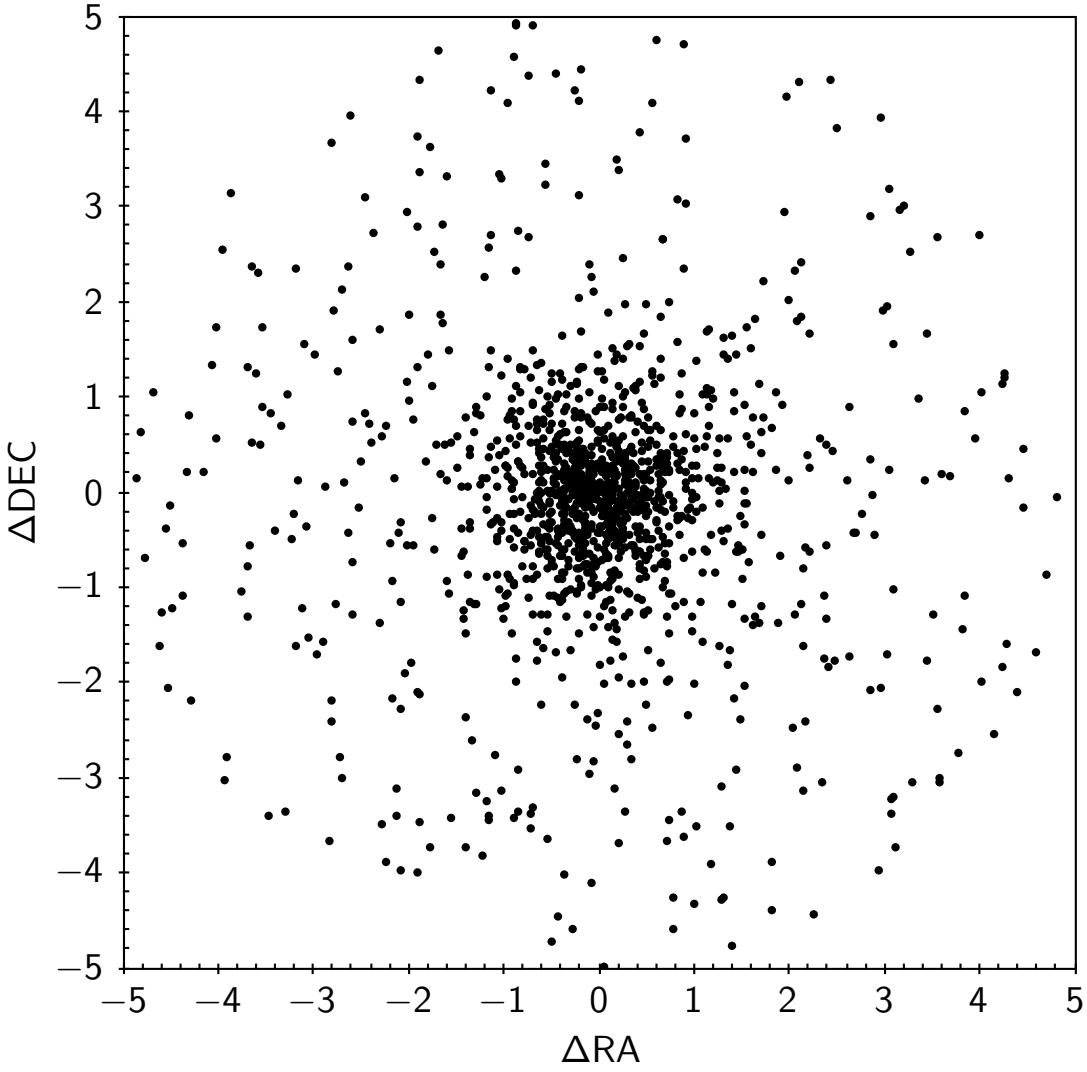

Figure 2.5: The sky separation between the FIRST and *WISE* positions for our 1317 IFRSs, where ΔRA and ΔDEC are in arcseconds. The standard deviation of both ΔRA and ΔDEC is 1.5 arcsec.

Observatory Synthesis Telescope (MOST) observations at $\lambda = 36$ cm ($\nu = 0.84$ GHz) and ATCA observations at $\lambda = 20$, 13, 6 and 3 cm ($\nu = 1.35$, 2.37, 4.80 and 8.64 GHz), compiled by Turtle et al. (1998), Filipović et al. (2002), Wong et al. (2011a) and Crawford et al. (2011), covering between $20 - 36$ square degrees of the SMC, with respective beam sizes of $20''$, $30''$, $40''$, $14.8'' \times 12.2''$ and $43'' \times 43\,\mathrm{cosec}\,\delta''$, and r.m.s. sensitivities of 0.8, 0.7, 0.4, 0.7 and 0.7 mJy beam^{-1}.

The 3 and 6 cm data from which the Crawford et al. (2011) mosaics are compiled primarily come from ATCA project C1207 (Dickel et al., 2010), which makes use of array configurations EW352 and EW367. These mosaics also combine observations taken from projects C1604, C882, C859 and C634, which contain a few pointings taken with the array configurations 6A, 6B, 6D, 1.5G, 750C, 375, EW367, and EW352.[3] The 13 cm mosaic from Filipović et al. (2002) combines data taken from ATCA and Parkes, and the 20 cm mosaic from Wong et al. (2011a) combines ATCA data from project C1288 (Mao et al., 2008) with Parkes data from Filipovic et al. (1997). The 36 cm mosaic was compiled by Turtle et al. (1998) using MOST.

We make use of catalogues of these images compiled by Wong et al. (2011b, 2012), which respectively consist of 457, 601, 743, 1560, and 1689 point-like background sources at these frequencies, with no significantly extended sources included. These observations complement the ATLAS observations, since they are wider, shallower and cover higher frequencies, targeting stronger, rarer and presumably younger AGN.

2.2.1.2 SMC pre-CABB Radio Spectral Index Catalogue

In order to make use of these data and select sources based on their radio spectra, we combined the 3, 6, 13, 20 and 36 cm data from the Wong et al. (2011b, 2012) catalogues together, in one master spectral index catalogue. We refer to these data as the '*pre-CABB data*', in contrast to the '*CABB data*' we later collected using the Compact Array Broad-band Backend (CABB; Wilson et al., 2011) from ATCA (see section 2.2.4).

To begin with, we looked for duplicates and blended sources by individually matching each catalogue to itself and the other catalogues to within 10 arcsec. We found 16 duplicates in the 20 cm catalogue, and two and three duplicates respectively in the 13 and 36 cm catalogues, all of which were discarded. A total of 3 unique sources were found to be blended, all of which were two-component sources at 20 cm and single-component sources at the other frequencies. These were flagged as blended sources in the combined catalogue.

Following this step, we cross-matched the catalogues at each frequency to one other using a 10 arcsec search radius, in this order: 20, 3, 6, 13, and 36 cm. During each step, we listed the best RA and DEC value, in the same order of preference. The resulting catalogue had 2714 radio sources, 219 of which were detected at all five frequencies. The positions of eight additional sources of interest were manually added to our spectral index catalogue, since they were not listed in any of the catalogues from individual frequencies, which consisted primarily of point sources. This gave a total of 2722 radio sources in our pre-CABB spectral index catalogue.

To reduce the amount of extended emission being resolved out, and therefore fit better radio spectral indices, we created a supplementary set of beam-matched mosaics at 3, 6, 13 and 20 cm. This was done using the data summarised above, and matching the resolution to that of the MOST mosaic, which had the lowest resolution. The first part of this step occurred during deconvolution, when the dirty map was created using the MIRIAD (Sault et al., 1995) task `invert`, by selecting only the visibilities below 6 kλ, such that the data sampled the same

[3] For an idea of how much sensitivity each pointing contributes, see the r.m.s. maps in figures 5 and 6 of Crawford et al. (2011).

(u, v) space as the MOST mosaic. Since the C1288 (Mao et al., 2008) data used a 6 km array, very few visibilities existed at $< 6\,\mathrm{k}\lambda$. Therefore, we excluded these data, resulting in the beam-matched image at 20 cm being much smaller in area. We also excluded the Parkes data at 13 cm. The beam-matched images at 3 and 6 cm data were quite poor, since these frequencies were sufficiently high that few visibilities existed at small (u, v) distances, and therefore the data only very sparsely sampled the (u, v) space between $0 - 6\,\mathrm{k}\lambda$. During the second part of this step, we set the FWHM and Position Angle (PA) of the gaussian that was convolved to the CLEAN model using the task `restor`. Since the MOST mosaic didn't have a fixed beam size $(43'' \times 43\,\mathrm{cosec}\,\delta'')$, we simply set the FWHM to be matched to the MOST beam size roughly in the middle of the SMC, which was $44.88'' \times 43.00''$ with position angle 0.

For consistency, we used the MIRIAD task `imsad` to extract the sources from each of these beam-matched images down to 5σ, using a similar approach to Wong et al. (2011b, 2012). From each catalogue returned from `imsad`, we accepted matches in which the gaussian fit converged, and the deconvolution didn't fail (i.e. column flag = C and column dflag $\neq$ F). These were then matched to the non-beam-matched catalogue in the same way as summarised above. Fewer beam-matched flux density measurements were available compared to the non-beam-matched images, due to several issues: 1) some images were smaller, particularly at 20 cm; 2) the r.m.s. was higher; 3) we used a more conservative criterion for accepting flux measurements than Wong et al. (2011b, 2012).

We derived the compactness of each of the sources in the beam-matched images based on the integrated flux density (S_{int}) and the peak flux density (S_{peak}) from `imsad`, both of which are read from the fitted gaussians. We considered a source to be resolved if

$$\log \frac{S_{\mathrm{int}}}{S_{\mathrm{peak}}} > 0.1 \quad . \tag{2.4}$$

For resolved sources, we stored the integrated flux density, and for unresolved sources, we stored the peak flux density. Using these, we derived the spectral index of each source using a least-squares power-law fit. The *pre-CABB* spectral index catalogue processed up until this point (which includes some components at one frequency listed as a separate row at another frequency - see below) can be found in table F.1 in Appendix F.

The difference in flux density measured from these beam-matched images can be seen in Fig. 2.6. It can generally be seen that the low-resolution beam-matched images detected more of the flux, since they don't include the longer spacings. The effect is less pronounced at 13 cm, since the non-beam-matched fluxes already include the zero-spacing information from the Parkes data. At 3 and 6 cm, the sparse (u, v) sampling results in the fluxes reducing even further and the r.m.s. increasing significantly.

When we selected our sample of 72 GPS and CSS sources (see section 2.2.3), we performed further processing for the 72 sources only, since we were interested in using their total flux to model their radio spectra. Firstly, we visually inspected the sources and gave a unique identifier to all rows (i.e. components) in the pre-CABB catalogue that appeared to belong to the same source of interest. In a few rare cases, the flux corresponding to a source at one frequency was listed in a separate row (i.e. separate component) to the flux from another frequency, due to being separated by $> 10''$ and therefore not being matched during the cross-matching procedure described above. Once all rows belonging to one source were identified, we added all of the fluxes from one frequency together, to give the integrated flux of all components of the source. Lastly, we estimated the uncertainty of the flux. IMSAD did not output a fitting uncertainty or the local r.m.s. However, these will be much smaller than the systematic uncertainty for the

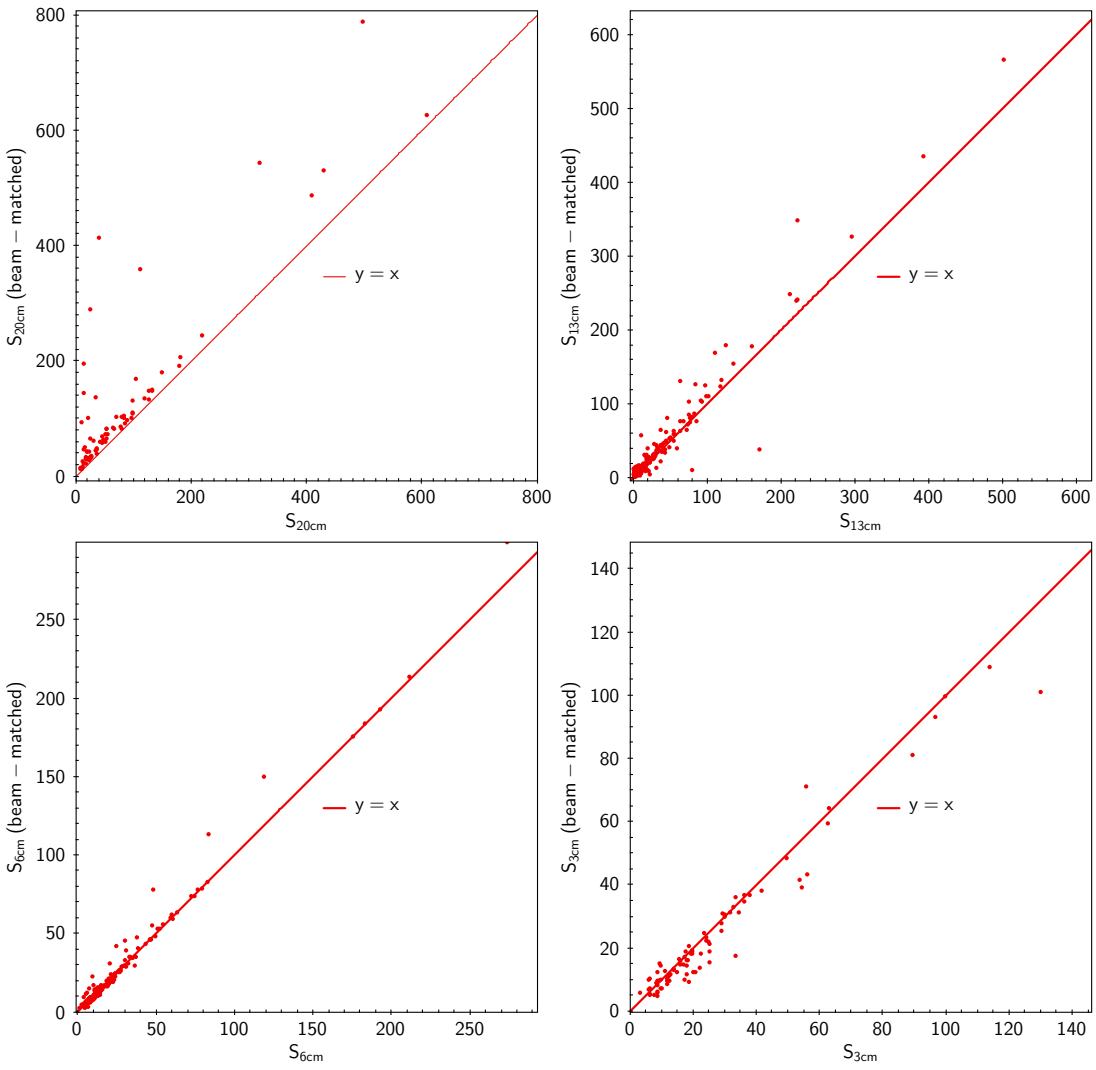

Figure 2.6: The flux densities in mJy found in Wong et al. (2011b, 2012) compared to the flux densites found in the beam-matched images from this thesis. It can generally be seen that the low-resolution beam-matched images detect more of the flux, since they don't include the longer spacings, which resolve out flux from the extended sources.

majority of sources $> 10\sigma$. Therefore, we simply estimated an uncertainty of 10%.

2.2.1.3 Ancillary data

We made use of MWA data from the Galactic and Extragalactic All-sky MWA Survey (GLEAM) survey (Wayth et al., 2015) for the GPS and CSS samples. The GLEAM observations were gathered from the MWA over a total of 254 hours, spanning two semesters in 2013 and 2014 (project ID G0008; PI: Staveley-Smith). Over four observing sessions, the sky south of $\delta = 30$ degrees was surveyed from $72 - 231$ MHz. The Internal Data Release 2 (IDR2) Catalogue (Hurley-Walker et al., 2016, in prep.) was produced using AEGEAN (Hancock et al., 2012), which excluded areas with poor S/N near bright sources as well as areas that were highly confused due to extended foreground emission. Therefore the inner ∼1.5 degrees of the SMC was excluded from IDR2. The IDR2 catalogue was created by forming a deep image covering $170 - 231$ MHz, and source finding to produce a reference catalogue. Each source within this reference catalogue was then remeasured in 20 sub bands with 8 MHz bandwidth, using AEGEAN's priorised fitting feature[4], by which the position stays fixed, and only the gaussian axes and flux density are allowed to vary during the fitting. Therefore, all rows contain measurements at all 20 sub-bands, although many are very low in S/N and therefore have a significant contribution of noise.

We found that ∼40 of our SMC sample (see section 2.2.3) were located inside the region excluded from IDR2. Since the deep reference catalogue of this region existed before it was filtered out in IDR2, we obtained a catalogue of the SMC (hereafter 'GLEAM SMC catalogue') in which the priorised fitting had been re-run for all 20 sub-bands within this region, and which included the same information as in IDR2 (Paul Hancock, Joseph Callingham, private communication). We found ∼70 sources common to both the GLEAM SMC and IDR2 catalogues in an overlapping region. For these common sources, we found that most of the values between the two catalogues differed from each other, sometimes quite significantly (e.g. Fig. 2.7), most likely due to the high level of confusion. Since IDR2 followed a procedure of quality assurance testing and science verification, we used the IDR2 entry for common sources.

Therefore, the GLEAM data used in this thesis come from the GLEAM SMC catalogue within the inner ∼1.5 degrees of the SMC, the IDR2 catalogue outside this region. We also made use of MOST 408 MHz observations from the Molonglo Reference Catalogue (MRC; Large et al., 1981).

We also made use of 20 GHz data from the AT20G survey (Murphy et al., 2010), which covers the whole southern sky down to a sensitivity limit of ∼50 mJy/beam. Since our GPS and CSS sources are so faint, only four sources had matches. For two of these sources, the AT20G data were able to differentiate between an exponential and Kardashev break. For these four sources, we also made use of the AT20G high-angular-resolution catalogue (Chhetri et al., 2013), which uses the 6 km baselines that were filtered out of the main survey and is therefore able to resolve extended sources at the 0.15 arcsec scale.

2.2.2 ATLAS sample

2.2.2.1 Catalogued Radio Data

We made use of 1.4, 1.7 and 2.3 GHz observations from ATLAS (Norris et al., 2006; Middelberg et al., 2008a; Zinn et al., 2012; Franzen et al., 2015), which is the widest deep radio survey,

[4] `https://github.com/PaulHancock/Aegean/wiki/Priorized-Fitting`

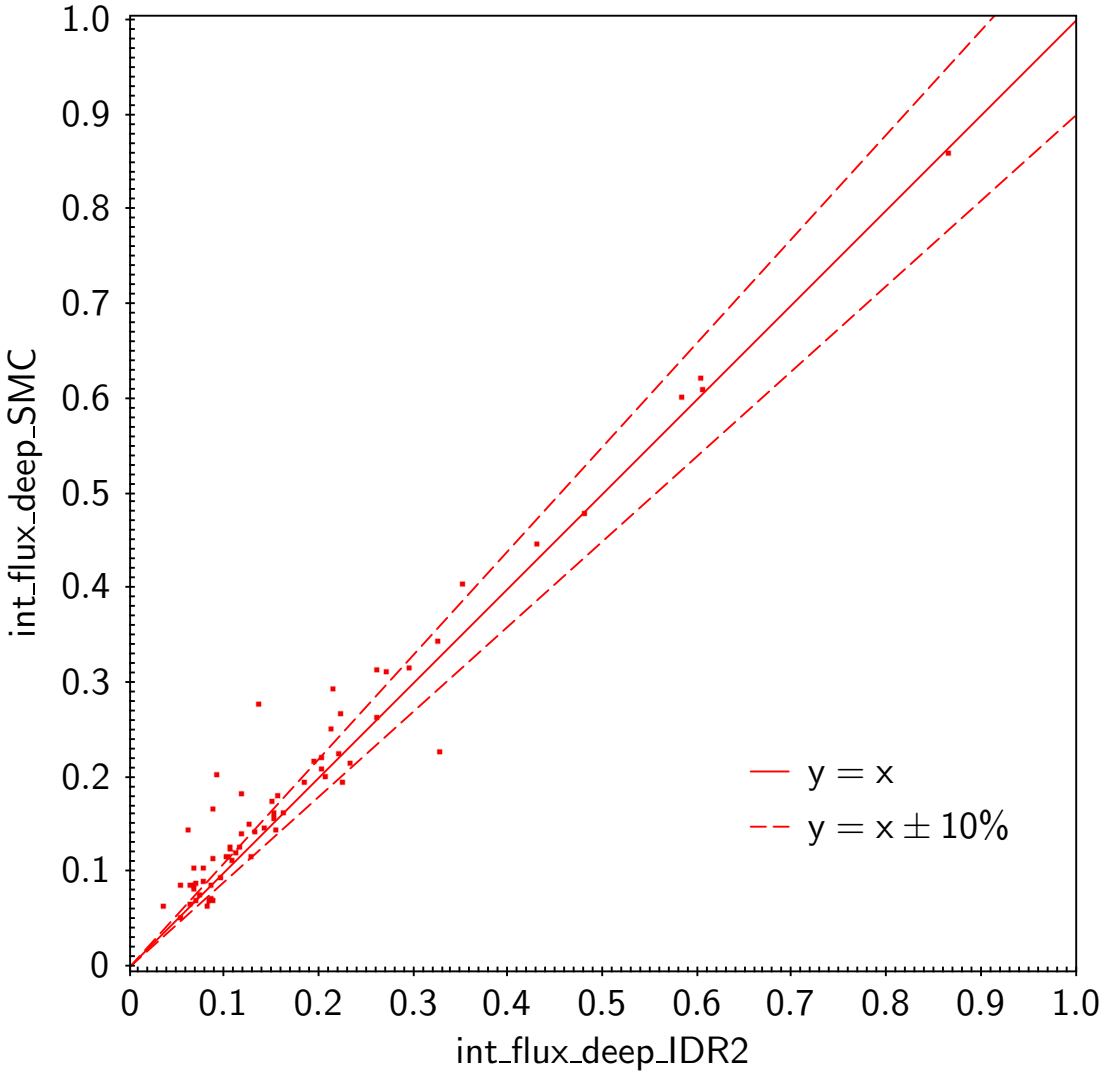

Figure 2.7: The integrated flux density in Jy from the GLEAM IDR2 catalogue compared to the integrated flux density in Jy from the GLEAM SMC catalogue. The difference is most likely due to the high level of confusion, which has not been corrected for in the SMC catalogue.

covering ∼7 square degrees in the CDFS and the European Large Area *ISO* Survey-South 1 (ELAIS-S1) fields down to an r.m.s. of ∼15 μJy beam^{-1} at 1.4 GHz. ATLAS overlaps with deep observations in the X-ray, optical and IR, including those from *Chandra*, *Spitzer*, *Herschel* and *VIDEO*. The third data release (DR3; Franzen et al., 2015) contains more than 5 000 galaxies, about half of which are AGN. ∼30% of the DR3 sources have spectroscopic redshifts within 2″ of the radio positions, primarily from OzDES (Yuan et al., 2015), ATLAS (Mao et al., 2012), and PRIMUS (Coil et al., 2011), compiled together in the OzDES Global Reference Catalogue (Uddin et al. in prep.). The ECDFS, which covers 0.25 deg^2 of the CDFS, has also been observed with MOST at 843 MHz (PI: Hunstead; Crawford et al., in prep.) and ATCA at 5.5 GHz (Huynh et al., 2012, 2015) and 9.0 GHz (Huynh et al., in prep), 18 and 20 GHz (Franzen et al., 2014), and 34 GHz (project ID C2317; PI: Beelen).

The ATLAS DR3 catalogue (Franzen et al., 2015) consists of a 1.4 GHz flux density and a spectral index, derived between two sub-bands at 1.4 and 1.7 GHz. We derive the 1.7 GHz flux density and uncertainty as:

$$S_{1.71\mathrm{GHz}} = S_{\nu_{\mathrm{obs}}} x^{\alpha}, \text{and} \tag{2.5}$$

$$dS_{1.71\mathrm{GHz}} = \sqrt{(x^{\alpha})^2 + (S_{\nu_{\mathrm{obs}}} \ln(x) x^{\alpha} d\alpha)^2}, \text{where} \tag{2.6}$$

$$x = \frac{1.71 \text{ GHz}}{\nu_{\mathrm{obs}}}. \tag{2.7}$$

Due to its relatively small bandwidth, for some sources, the 1.7 GHz sub-band flux density contains a large uncertainty, while the full-band 1.4 GHz flux density contains small uncertainty due to its relatively large bandwidth.

2.2.2.2 Ancillary Data

In addition to these data, the ATLAS fields have been observed across many other low radio frequencies where CSS sources turn over, including 843 MHz observations from MOST (Randall et al., 2012), Giant Metrewave Radio Telescope (GMRT) observations at 150, 325 (Sirothia et al., 2009; Intema et al., 2016, Intema et al., in prep) and 610 MHz (Magnelli et al., 2015, Intema et al., in prep).

Our ATLAS sample also made use of the GLEAM IDR2 catalogue. As part of the GLEAM survey, in addition to the 'deep' image, stacked images were created at 72-103, 103-134 and 139-170 MHz, which have much greater sensitivity than the sub-bands. We used these to extract our own fluxes using AEGEAN's priorised fitting for faint ATLAS sources from IDR2 whose sub-band fluxes were too faint to give any useful spectral information.

Furthermore, for a handful of ATLAS sources, we made use of the AT20G deep pilot survey of the CDFS (Franzen et al., 2014), which is 90% complete at $S > 2.5$ mJy. As part of the survey, follow up observations were collected at 5.5, 9.0 and 18 GHz, separated by more than 3 years. The 18 GHz data were close enough to the 20 GHz that the variability of each source was measured. A strip within the ECDFS was also observed at 34 GHz with ATCA (project ID C2317; PI: Beelen).

2.2.3 Selection Criteria

We followed the basic strategy of selecting unresolved GPS and CSS candidates to be observed at higher resolution, and then selecting those that remained unresolved, to be observed with VLBI. Our GPS and CSS candidates were selected according to the following criteria:

1. Has a GPS radio spectrum with an identifiable peak; or
2. Has a CSS radio spectrum with $\alpha < -0.8$; and
3. Is unresolved at highest available ATCA resolution ($\sim 5-10''$; $l \sim 30-60$ kpc at $z = 0.5$).

The first two criteria were based on visual inspection of plots of the radio spectrum (e.g. Figure 1.8), which used all available flux densities (including our new observations where available – see section 2.2.4), which were measured from beam-matched images where possible. The third criterion gave an upper limit on the angular size of the source, ensuring that higher-resolution observations would yield a high enough signal-to-noise.

The five samples we selected are summarised in Table 2.4. Sources from samples (1), (2) and (5) were selected to be unresolved at 1.4 GHz (i.e. $\lesssim 10$ arcsec) in ATLAS and the SMC. Sources in sample (5) were selected to be outside the ECDFS, which had already been observed (Huynh et al., 2012, 2015). Sources from sample (3) were selected to be unresolved at 9 GHz from sample (1) (i.e. < 1 arcsec). Sample (5) had not been observed when sample (4) was selected, and therefore these sources were selected slightly differently. One source from sample (4) was selected to be unresolved at 5.5 GHz in the ECDFS (i.e. < 5 arcsec). The other two sources from sample (4) were outside the 0.25 deg^2 of the ECDFS, and since their redshifts were known, the expected angular size (which we used to essentially replace the third criterion) was estimated based on the linear size derived from equation 1.14, which used a turnover frequency estimated from the radio spectrum. Sources in sample (4) were also selected to be not observed or detected with VLBI by Middelberg et al. (2011a).

In the SMC, since our resulting targets were relatively bright, we were able to select a handful of additional targets without losing much sensitivity across the sample. Therefore, we also selected sources that were resolved at the $\sim 10''$ resolution, to be used as a reference sample of more extended RGs, which are presumably older FR I and FR II galaxies. These correspond to the eight sources manually added to the *pre-CABB* spectral index catalogue (see section 2.2.1.2).

The combined samples consist of 144 GPS and CSS candidates and RGs selected from ATLAS and the SMC, including the ECDFS source that was unique to sample (4).

2.2.4 New Radio Observations

We undertook high-resolution observations using the new 4 cm receiver on the ATCA (project ID: C2730 and C2768) of the faintest GPS/CSS sample to date (samples (1), (2) and (5) from Table 2.4). These observations made use of the ATCA in 6A and 6B configurations, which used a 6 km baseline and gave a resolution at 9 GHz of $\sim 1''$. Our data consisted of 2 GHz CABB observations at 5.5 and 9.0 GHz, centred on the selected sources. Therefore, we refer to these data as the '*CABB data*', in contrast to the '*pre-CABB data*' we described in section 2.2.1.2.

We observed the ATLAS targets down to r.m.s. levels between $\sim 10-100$ μJy beam^{-1}, and the SMC targets down to r.m.s. levels between ~ 50 -150 μJy beam^{-1}, depending on the strength of each source. The on-source time we scheduled for each pointing was chosen based on achieving a target S/N of 5σ in each beam at 9 GHz. We expected the CSS sources to have

a discontinuous jet morphology spanning < 10 kpc, which for a typical redshift of 0.5, gives an angular size of $\lesssim 3$ arcsec, spanning $\lesssim 3$ beams at 9 GHz. To estimate the S/N, we used the measured 8.64 GHz flux densities for SMC sources, and an estimated 9 GHz flux density extrapolated from the spectral index for ATLAS sources.

After taking these new observations, we typically had radio flux density measurements at a minimum of 10 frequencies in ATLAS and 6 frequencies in the SMC, and typically up to ~ 30 or more if the source had a high enough S/N to enable the use of sub-band measurements.

Additionally, we undertook LBA observations (project ID: V506) of the most compact sources selected from ATLAS (samples (3) and (4) from Table 2.4). For V506a, the array consisted of the Australian Commonwealth Scientific and Industrial Research Organisation (CSIRO) telescopes of Australian Square Kilometre Array Pathfinder (ASKAP), ATCA, and Parkes, in addition to the University of Tasmania telescopes of Hobart and Ceduna (At-Ak-Pa-Ho-Cd). For V506b, the CSIRO telescope Mopra (Mp) was added to the array. This gave resolutions as high as $\sim$15 mas. In both cases, observations were made at a central frequency 1.634 GHz with a 64 MHz bandwidth at each of the two circular polarisations (left and right; L and R) and were obtained over 10 hour periods (V506a on 2013 November 21; V506b on 2014 February 21). The observations were structured to cycle between the targets and nearby calibrators, with scan lengths of 90 seconds. We plan to select further targets in ongoing VLBI observations, and present the results in Collier et al. (in prep.).

Table 2.4: A summary of the ATCA and LBA observations (see section 2.2.4) undertaken in this thesis, sorted by date.

Sample	Telescope	Project Number	Date	Array Configuration	Frequency	Time	Field	$N_{\rm sources}$
(1)	ATCA	C2730	Dec 2012	6B	5.5/9 GHz	39 h	ELAIS-S1	49
(2)	ATCA	C2768	Feb 2013	6A	5.5/9 GHz	12 h	SMC	72
(3)	LBA	V506a	Nov 2013	At-Ak-Pa-Ho-Cd	1.6 GHz	10 h	ELAIS-S1	5
(4)	LBA	V506b	Feb 2014	At-Ak-Pa-Ho-Cd-Mp	1.6 GHz	10 h	CDFS	3
(5)	ATCA	C2730	Apr 2014	6A	5.5/9 GHz	11 h	CDFS	22

2.3 Data Reduction

2.3.1 ATCA observations of SMC sources

2.3.1.1 Calibration

The data reduction of the SMC observations was performed using MIRIAD (Sault and Killeen, 2011). Our calibration and flagging procedure can be seen in Fig. 2.8. We used the PKS 1934-638 as the bandpass and flux calibrator, and PKS 2353-686 as the phase calibrator. We found the default flagging procedure using the task `pgflag` and command=<b first for stokes=xx and then for stokes=yy to work sufficiently during flagging the calibrators. However, this was found to flag a huge percentage of the data when performed for the sources, particularly at 9.0 GHz. Originally, we set the parameter flagpar = 10,3,1,3,5,3,20 and flagged the sources using 4 iterations of `pgflag`, one iteration on each polarisation, beginning with the cross-polarisations, and following the order: "xx,yy,yx,xy", "xy,xx,yy,yx", "yx,xy,xx,yy", "yy,yx,xy,xx". This step was performed a second time for just less than half of the sources, since Radio Frequency Interference (RFI) was still clearly seen in the amplitude plots. However, following this, 21 of the sources were found to have >30% of their data flagged, with some as high as 50%. Additionally, the images were found to have elongated synthesised beams when they were imaged. For these 21 sources, we unapplied the previous flagging and ran through four iterations of `pgflag`, but with flagpar = 7,1,1,3,3,3,20 and stokes=i. Following this, we manually flagged the data using `blflag`, usually removing entire channels that were affected by RFI. Following this, it was found that all sources had <30% of their data flagged.

2.3.1.2 Imaging

The imaging of the 72 GPS and CSS candidates was done using my own custom python script that made use of MIRIAD (Sault et al., 1995). Each pointing was reduced separately, since no joint-deconvolution method that considers a large bandwidth yet exists in MIRIAD.

Because very few pointings overlapped and the r.m.s. across the pointings was non-uniform, two approaches were made to creating the final images. Firstly, we imaged each pointing separately, and created two images for each pointing: one which had the best resolution (`invert` parameter robust = -2), and one which had the best S/N (robust = 2), roughly corresponding to natural and uniform weighting, respectively. This allowed the `invert` task full freedom to choose the best pixel size and FWHM for each weighting scheme. Secondly, we set the pixel size and FWHM to a fixed number that matched what `invert` chose by default for a pointing roughly in the centre of the SMC ($0.41''$ at 5.5 GHz & $0.26''$ at 9.0 GHz for robust = 2), and then mosaicked the pointings together in `linmos`. This second approach allowed for more sensitivity in those pointings which slightly overlapped (see Fig 2.9). The full 72-pointing mosaic at 5.5 GHz can be seen in Fig. 2.9.

During the first approach, two sets of images were produced at both 5.5 and 9.0 GHz: a broadband image with 2 GHz bandwidth and four sub-band images with 512 MHz bandwidth. We split the full-bandwidth data into 512 MHz sub-bands using the task `uvsplit` and imaged them individually, ensuring that the cell size and the FWHM of the synthesised beam were the same for each sub-band, and equal to that of the lowest resolution sub-band. This reduced the chance that flux was missing at higher frequencies when we later derived the radio spectra. This resulted in five sets of visibilities that were reduced one by one.

Beginning with robust=2 weighting, a dirty map two times the primary beam size was created using the `invert` task. If the fractional bandwidth was less than 10% , the dirty map

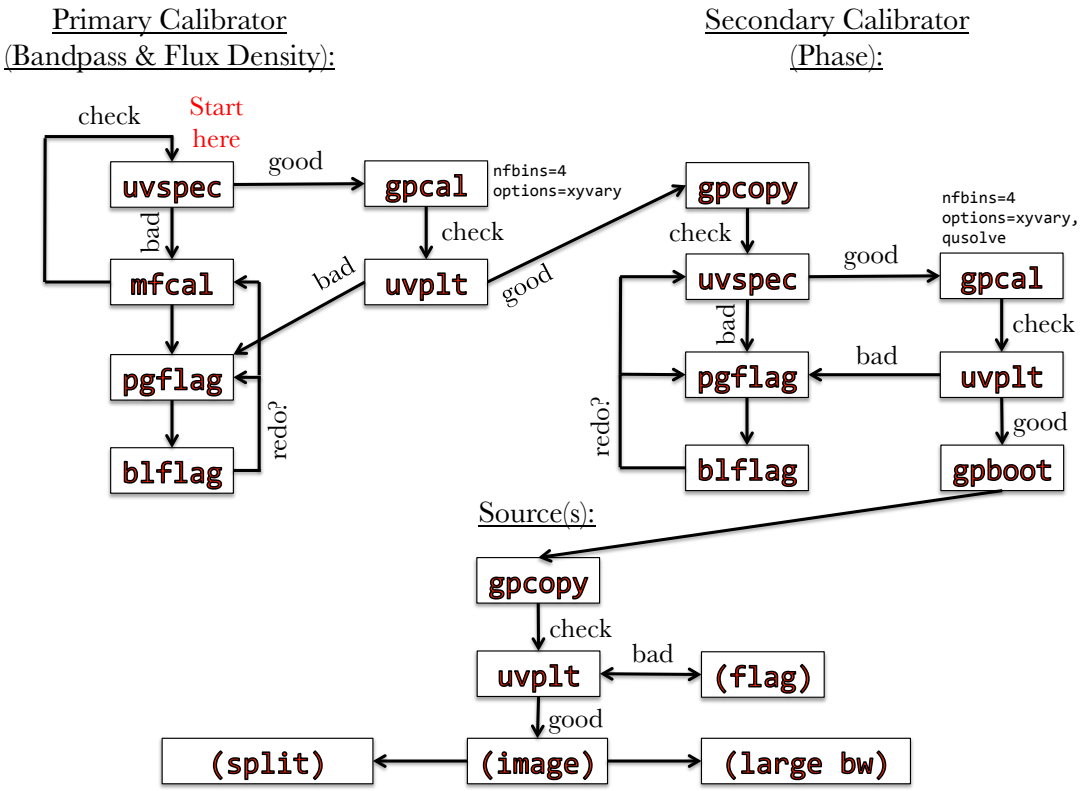

Figure 2.8: Calibration flow chart showing the process by which we calibrated the ATCA data from this thesis in MIRIAD. The task names in the boxes (e.g. `mfcal`) are the MIRIAD tasks that were executed during each step, while those in brackets (e.g. (split)) denote the process that was followed in general during that step.

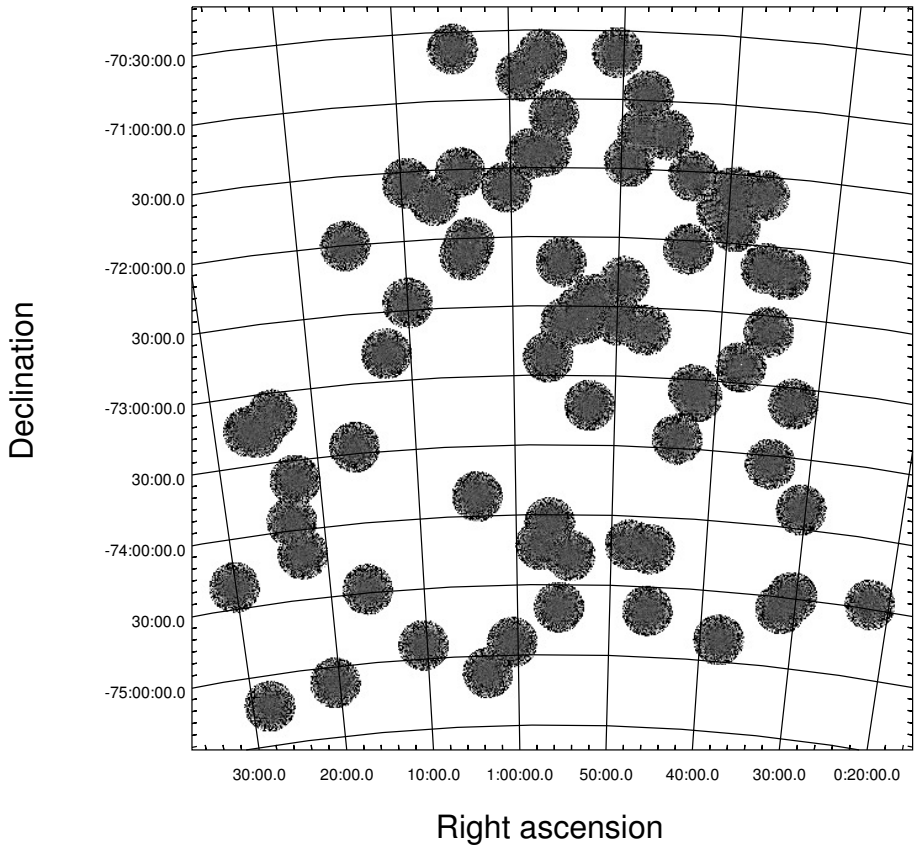

Figure 2.9: A 72-pointing mosaic of the SMC at 5.5 GHz, imaged with natural weighting and consisting of over 2 billion pixels. This shows the region of sky from which our GPS/CSS candidates were selected.

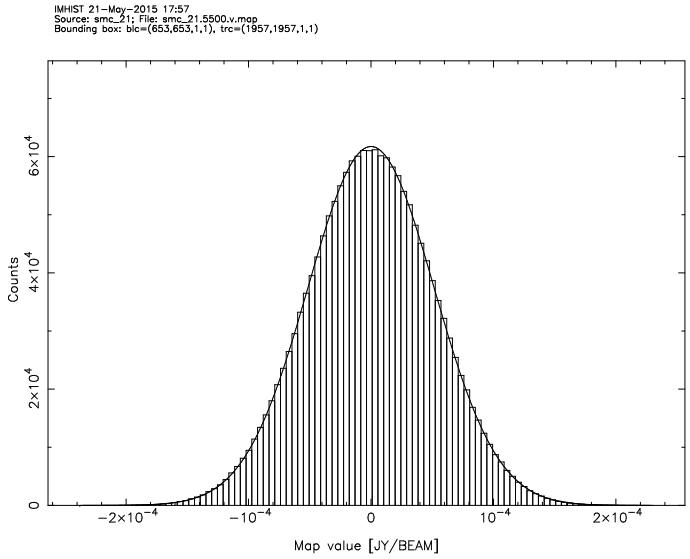

Figure 2.10: The gaussian noise distribution of pixel values measured in the stokes v map of source smc_21, output from MIRIAD task `imhist`. In our imaging pipeline, σ was read from the stokes v image using this task.

was decolvolved using the standard CLEAN algorithm. If the fractional bandwidth was greater than 10% (in particular, the full 2 GHz-wide data), the dirty map was deconvolved using a multi-frequency CLEAN algorithm from the task `mfclean`. The chosen CLEAN algorithm was executed down to a cutoff level of the maximum flux in the residual image (i.e. the cutoff parameter) of 20σ, where σ is the r.m.s. as read out from the Stokes v map using task `imhist` (e.g. Fig. 2.10). This ensured that only the brightest sources were CLEANed at this point. After applying the calibration tables to the visibility data using the task `uvaver`, we then self-calibrated the phases using these visibilities and the CLEAN-component map as a model input into the task `selfcal`. Solutions were derived at intervals equal to one scan of the source (30 or 40 seconds). These new visibilities were then used as input to another iteration of CLEAN. This process was repeated two more times, self-calibrating using the CLEAN model down to 15σ and then 10σ, after which CLEAN was executed on the thrice-self-calibrated visibilities down to a cutoff of 5σ. No amplitude self-calibration was performed, since this was found to give an unreliable flux scale.

The data were then restored and corrected for primary beam attenuation, using a cutoff radius equal to the Half Power Beam Width (HPBW). After this step, `imsad` was executed and sources $\geq 10\sigma$ were extracted. Around these sources, 15 arcsec boxes were drawn. We then CLEANed the self-calibrated dirty map again, but down to 3σ at the locations of the clean boxes (since we were CLEANing real emission), followed by a general CLEAN down to 5σ. We then restored and corrected the primary beam attenuation of these second set of images that used clean boxes. The second set of images was used during source extraction (see section 2.3.1.3) in almost every case, apart from a handful in which using the clean boxes caused imaged artefacts. A few examples of individual sources are shown in Fig. 2.11.

The images with robust$=-2$ weighting followed the same procedure, except the initial dirty map was created using the visibilities that were already self-calibrated beforehand, and no further self-calibration was performed. At this point we visually inspected the images to check their general quality and dynamic range. Most of the images at each weighting were found to have a good dynamic range following this procedure. However, some images were found to have

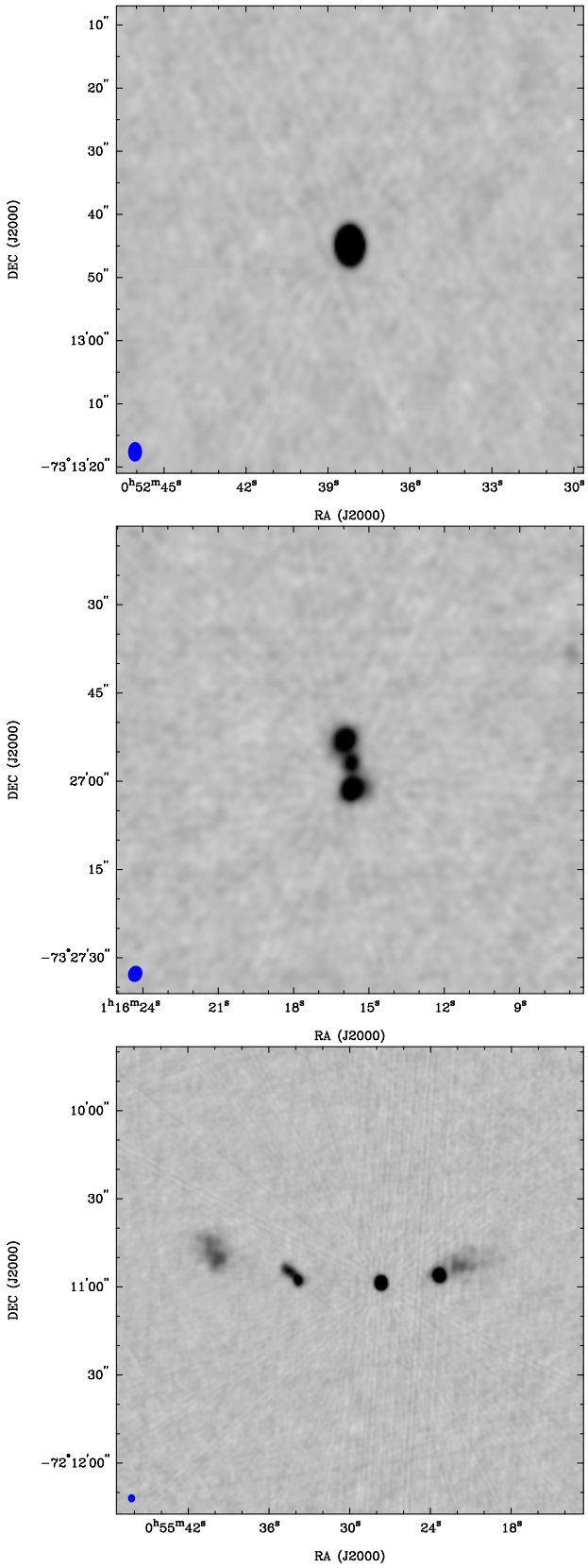

Figure 2.11: An example of an unresolved and resolved GPS/CSS candidate from the SMC, compared to one of the resolved RGs, all observed at 5.5 GHz and imaged with robust=2 weighting during this thesis. The synthesised beam is shown by the blue ellipse in the bottom left corner.

poor dynamic range, either due to strong sources that were outside two primary beams and therefore weren't CLEANed, or due to the CLEAN algorithm deconvolving part of the diffraction pattern rather its main lobe. In the former case, we created dirty maps at more than two times the primary beam size, until the strong source had been CLEANed. In the latter case, we used extremely tight clean boxes around the central source, as small as several pixels for the sources most badly affected, which we used while performing self-calibration. For a few sources, this was done using the image with robust=−2 weighting. These steps substantially improved the dynamic range of the affected sources, with the result that only three sources ended up with moderate dynamic range.

During inspection of the sources, it was found that some of them were only detected very faintly, or not at all. We re-imaged these sources with robust=2 weighting and excluding the 6th antenna baselines, which gave a lower resolution and for sources previously resolved, a higher S/N. A handful of these remained undetectable.

The sub-bands were imaged in the same way (i.e. for the same sources as above, at more than two times the primary beam, using tight clean boxes and excluding the 6th antenna baselines), and only with robust=2 weighting. For faint sources, we split the data into sub-bands using the visibilities already self-calibrated over 2 GHz. For bright sources, we self-calibrated each sub-band on its own, since this was found to perform better.

During the second (mosaicking) approach, we created a dirty map four times the size of the primary beam and used a common pixel offset roughly equal to the centre of the SMC (RA=00:55:00; Dec=-73:20:00).

As well as these total intensity Stokes I maps, spectral index maps were created for each pointing. These were created between $4.5 - 6.5$ and $8.0 - 10.0$ GHz using the spectral index plane of the full 2 GHz data as input to the task `mfspin`.

Ideally, we would have created images that have the same resolution so that we could reliably trace the radio spectrum of each source without suffering the loss of flux from missing short spacings. However, very few short spacings exist in the 6A array configuration that was used, with the shortest spacing being 337 metres. Furthermore, these observations were undertaken to inspect the high-resolution morphologies of the selected sources. Therefore, we use the high-resolution data primarily to give information about the high-resolution morphologies, components and positions, while using the *pre-CABB* beam-matched spectral index catalogue primarily to give information about the radio spectrum of each source. However, we do use the high-resolution data to model the radio spectrum for sources that have a spectrum consistent with that derived from the beam-matched catalogue (see section 4.1.2).

2.3.1.3 Source extraction

Source extraction was performed using PYBDSM (Mohan and Rafferty, 2015). PYBDSM calculates the background r.m.s. and mean maps, identifies islands of emission, fits multiple gaussians to each island, derives the residuals, groups gaussians into sources, and performs source extraction on lower resolution images generated by processing the residual images with an *á trous* wavelet transformation, at the end of which gaussian and source catalogues are written. Since we were interested in the total sum of fluxes over all components, we grouped all gaussians belonging to an island into one source, and used an island threshold of 2.0, allowing PYBDSM to flood-fill adjacent pixels down to 2σ. Additionally, we used an adaptive r.m.s. box, which allowed for higher r.m.s. values close to strong sources due to artefacts.

The source extraction performed well for most sources using these parameters. However,

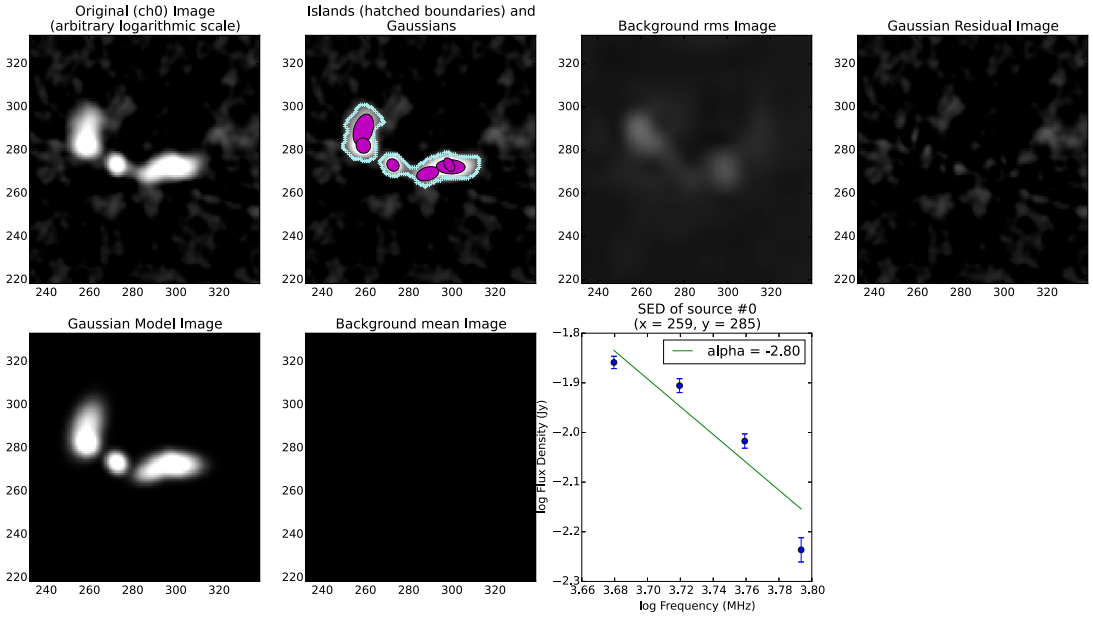

Figure 2.12: An example of using PYBDSM to perform source extraction on a cube with four 512 MHz sub-band 'channels'. Starting from the top-left, we can see the averaged image, the island boundaries (blue) and FWHM of the fitted gaussians (purple), the background r.m.s. image, the gaussian residual image, the gaussian model image, the background image, and the radio spectra across the sub-bands.

some sources needed to be treated manually due to poor models being derived, generally because artefacts were treated as real emission or some faint extended emission was missed. In most of these cases, we used some or all of the following parameters: a user-set r.m.s. box size (typically 100 pixels with a step size of 25 pixels), a fixed r.m.s. value across the entire map, a constant or zero mean map, a higher island threshold, and a wavelet scale typically equal to one or two. Each of the images that excluded the sixth antenna used three or four wavelet scales.

Source extraction for the sub-band images was performed differently. Firstly, a subsection of each sub-band image was derived by taking the inner 150 pixels from the reference pixel using the MIRIAD task `imsub`, and these were combined into a cube using the MIRIAD task `imcat`. This allowed us to input a cube into PYBDSM, which was then averaged together into a single channel, upon which the source extraction was performed, allowing for a better S/N. This also allowed the flux in each channel to be written to the catalogue, which we used in the modelling of the radio spectra (see Fig 2.12).

2.3.1.4 Visual Inspection

We visually inspected each of the SMC sources by looking at four images in separate frames at once in ds9: the GLEAM 200 MHz "deep" image, the Wong et al. (2011a) 1.4 GHz image, a higher-resolution 1.4 GHz image (Grieve et al., in prep.), and the 5.5 and 9.0 GHz images from this work.

During visual inspection, we gave a unique identifier to all entries in the 5.5 GHz PYBDSM source catalogue that appeared to correspond to our source of interest, for later processing. For each source, we also marked the island that appeared to be closest to that of the nucleus, to

use as the source position when we later derived our own source catalogue. We labelled the morphology of each source, manually measured angular sizes for extended sources resolved out at 5.5 GHz, and added notes, such as noting where sources were located in the dusty, confused region of the SMC.

We labelled the morphology for each source as unresolved, double-lobed, or resolved with an unknown or complex morphology, based on their visual appearance. For the double-lobed sources, we labelled them as having no core when the source was resolved enough to identify a core, but where none was detected. Where a core was present, we labelled the sources as core-dominated or lobe-dominated. For each double-lobed source we also labelled them as FR I or FR II like.

We found four extended sources that had been resolved out at 5.5 GHz, but which were more strongly detected at 1.4 GHz. These sources were smc_3, smc_14, smc_47 and smc_61, and we manually measured their angular sizes by drawing a line across the approximate extent of the source in ds9.

2.3.1.5 Component catalogue

We produced what we call a component catalogue by simply concatenating together all rows from the PYBDSM source catalogues from different frequencies (including the sub-bands) that we had identified above as belonging to the sources of interest, which gave a total of 407 rows. There were two primary reasons for this. Firstly, there was no straightforward way to cross-match each of the source components/islands to each other. For example, performing a nearest-neighbour match between $2 - 5''$ only matched $70 - 80\%$ of the components to each other, despite the resolution being $\sim 1''$. Secondly, we present this as a catalogue in which no subjective decisions have been made, apart from filtering out sources that didn't appear to correspond to our sources of interest.

Using this, we add several columns for each component:

1. the value of the robust weighting that was used to create the image, either 2 or -2;
2. the frequency, derived from the Flexible Image Transport System (FITS) header;
3. the total uncertainty in the flux density;
4. the flux ratio, defined as $\log(S_{\rm int}/S_{\rm peak})$.

The total flux uncertainty was derived at each frequency, which we express as

$$\sigma S_\nu = \sqrt{[S_\nu(\sigma_{gain} + \sigma_{other})]^2 + \sigma_{rms}^2 + \sigma_{fit}^2}\ , \tag{2.8}$$

where S_ν is the flux density at frequency ν, σ_{gain} is the uncertainty in the telescope gain, σ_{rms} is the local r.m.s., σ_{fit} is the uncertainty in the gaussian fitting, and σ_{other} is a factor that accounts for other more complex errors such as instrument instabilities, CLEAN errors, imaging artefacts and the uncertainty in the absolute flux calibration.

σ_{rms} and σ_{fit} are reported by PYBDSM for each source, the former of which we take as the local r.m.s. in the residual image, rather than from the r.m.s. map. Since the source extraction for our sub-bands was performed on an averaged image that combines all "channels", the r.m.s. level reported corresponded to the r.m.s. in the averaged image. Therefore, we estimated the local r.m.s. in each of the four 512 MHz-wide sub-bands as $\sigma_{sub} = \sigma_{avg}/\sqrt{1/4}$, where σ_{avg} is the r.m.s. in the averaged image.

We estimate σ_{gain} by taking the standard error in the amplitude of the phase calibrator over one scan, since the source gains are interpolated between bracketing scans of the phase calibrator and any variation in its amplitude cannot be attributed to the source itself but to the uncertainty in the gain. This was done by first outputting the calibrated visibilities to file using MIRIAD task `uvdump`, allowing the task to frequency average across all 2048 channels. For each two minute scan of the phase calibrator, we derived the mean amplitude in Jy across all 15 baselines and all 10 second integrations. After deriving mean amplitudes for each of the 32 scans, we derive the standard deviation, giving us the standard error in the amplitudes. Figure 2.13 shows the calibrated frequency-averaged amplitudes measured for each of the 32 scans at 5.5 and 9.0 GHz. The flux was found to be 1.304 ± 0.001 at 5.5 GHz and 1.197 ± 0.001 at 9.0 GHz. Therefore we attribute a 0.1% to σ_{gain}. Lastly, we estimate 5% for σ_{other}. The component catalogue is shown in table D.1 in Appendix D.

2.3.1.6 Source catalogue

We produced a source catalogue to be used for modelling the integrated radio spectrum of each source. To do this, we added all of the fluxes from all islands in our component catalogue identified as belonging to one source, as well as adding their total flux uncertainties from equation 2.8 in quadrature. For each source position, we list the RA and Dec of the component we identified as closest to the nucleus during visual inspection. This catalogue lists the number of islands and gaussians that each source is made up from. For all sources made up from one island, we also included the PYBDSM measurements of the angular sizes. The source catalogue is shown in table E.1 in Appendix E.

2.3.1.7 Measuring angular sizes

From our PYBDSM source catalogue, we had measurements of the angular sizes for all sources comprised of one island, in particular, the FWHM of the deconvolved major and minor axes from PYBDSM (DC_Maj and DC_Min from here on in), which are set to 0 when no extension is found. However, in cases where we identified more than one island belonging to one source, these values were not representative of the source as a whole. Therefore we measured the angular size of multi-island sources by finding the two gaussians from the PYBDSM gaussian catalogue that were the furthest apart, when also considering the extent of each gaussian. In order to do this, we first matched the gaussian catalogue to our visually-inspected source catalogue, to ensure that we only selected gaussians belonging to islands that we identified as part of the 72 SMC sources of interest. We iterated through each of these gaussians and derived the separations between all gaussians belonging to the source, storing the maximum separation and the position angle subtended between these two gaussians. We took the maximum separation to be

$$\Theta + \theta_{\rm gauss1} + \theta_{\rm gauss2} - \theta_{\rm psf}, \tag{2.9}$$

where Θ was the separation between the gaussians derived from their RA and Dec, and $\theta_{\rm gauss1}$, $\theta_{\rm gauss2}$ and $\theta_{\rm psf}$ were respectively the radii of the first and second gaussians and the synthesised beam at the position angle subtended between the two gaussians ($\rm PA_{sky}$), defined as

$$\theta = \sqrt{(a\cos(\rm PA_{sky} - PA_{gauss}))^2 + (b\sin(\rm PA_{sky} - PA_{gauss}))^2}, \tag{2.10}$$

where a, b and $\rm PA_{gauss}$ were respectively the FWHM of the major and minor axes, and the position angle of the gaussian, either the PYBDSM gaussian, or the synthesised beam.

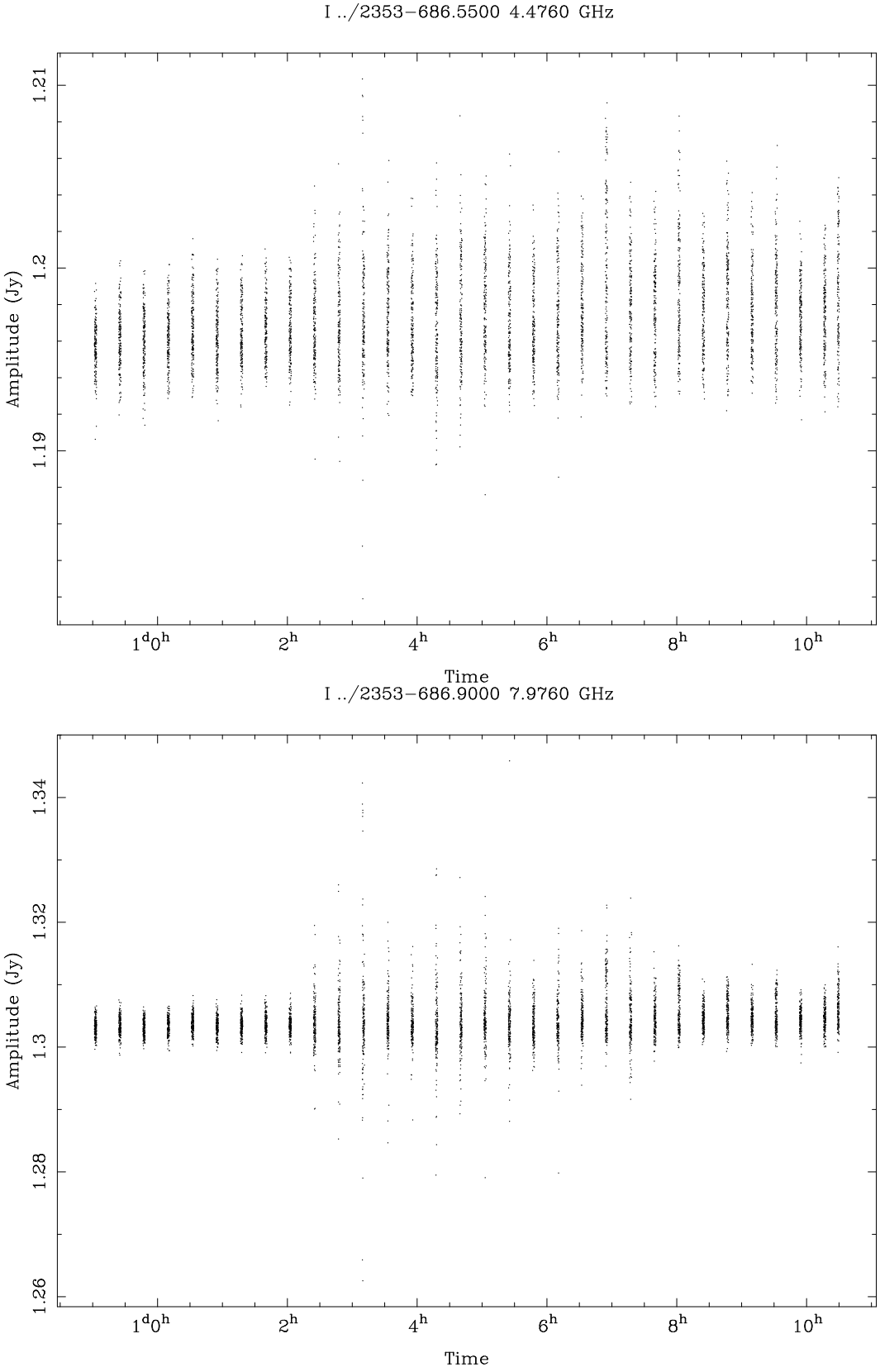

Figure 2.13: The calibrated frequency-averaged amplitudes for project C2768 phase calibrator 2353-686 at 5.5 (top) and 9.0 GHz (bottom) for all 15 baselines across all 32 scans that span the observations.

We compare the DC_Maj values to the integrated to peak flux density ratio. Williams et al. (2013), who use PYBDSM on data from a Monte Carlo simulation, use the following criterion to determine whether a source is likely to be resolved:

$$S_i/S_p = 1 + \sqrt{(0.01 \pm 0.02)^2 + (3.58 \pm 0.10)^2(\sigma_L/S_p)^2}, \tag{2.11}$$

where S_i is the integrated flux, S_p is the peak flux, and σ_L is the local r.m.s., which we adopt from the residual image. From the component catalogue of 407 sources, a total of 353 sources were considered resolved according to this criterion, while 329 sources have a non-zero DC_Maj value, which are therefore considered resolved by PYBDSM. We find six sources that are unresolved according to the Williams et al. (2013) criterion at 5.5 or 9.0 GHz, but which have DC_Maj > 0. We make no corrections to the values of the integrated flux, nor the deconvolved axes, but simply flag which sources are resolved according to equation 2.11. We found that the smallest value of $\theta_{\mathrm{DC,maj,9GHz}}/\theta_{\mathrm{PSF,maj,9GHz}}$ (i.e. the ratio between the DC_Maj and the FWHM of the major axis of the synthesised beam from 9 GHz) was $\sim$0.16, and therefore we attribute

$$0.16 \times \theta_{\mathrm{PSF,maj,9GHz}} \tag{2.12}$$

as an upper limit to sources considered as uresolved by PYBDSM (i.e. with DC_Maj = 0).

Therefore, we attribute the following angular sizes to our sources in the following order:

1. where the source was resolved out at 5.5 GHz, our measurement of the 1.4 GHz extent from visual inspection (4 sources);
2. where only one island was identified to be part of a source at 5.5 GHz, the DC_Maj value, or where this was zero, the value derived from equation 2.12 (46 sources);
3. when more than one island was identified to be part of a source, equation 2.9 (22 sources).

2.3.1.8 Preparing the catalogue

In order to model the radio spectra for our GPS/CSS candidates, we wanted to ensure the total flux of all components was used in the fitting routine. We also wanted to use all available flux densities that were considered reliable. We anticipated the following issues that could have caused the flux densities to be unreliable:

1. Variability between the different observing epochs
2. Resolving out some of the flux at high resolution
3. Blending of components or sources between the different instrument resolutions ranging from $< 1''$ and $\sim 3'$

As discussed in section 1.3.3, for genuine GPS/CSS sources, we expect very minimal variability over the timespan of these observations, of the order of $< 10\%$. Since the pre-CABB and CABB frequencies overlap, we are also able to estimate the variability that has occurred between different epochs by comparing their fluxes. We estimate this by taking the ratio between the pre-CABB and CABB fluxes. This also enables us to identify whether much of the flux has been resolved out in the high resolution CABB observations. If the flux between the overlapping frequencies agrees within 2σ, and since the MWA and CABB observations were taken roughly during the same epoch, we consider the effect between these first two issues to be

minimal and we therefore use all available frequencies. Where these do not agree within 2σ, we use the pre-CABB beam-matched fluxes, since these are low resolution ($\sim 45''$) and are much less subject to the second issue.

For the third issue, we identify blended sources between the MWA and pre-CABB catalogues, as well as those between the pre-CABB and CABB catalogues. While it's possible to attempt to correct for the former of these by extrapolating their spectral indices to MWA frequencies and subtracting their flux, we make no attempt at this, since we have no idea of which of these may be turning over at low frequency. The same is assumed for the latter of these, since we have no way of estimating the variability of the blended sources. Instead, we flag which sources suffer from significant blending and choose not to analyse these absorption models. We define blended sources between pre-CABB and MWA as pre-CABB sources within the minor axis of the MWA beam (i.e. 140 arcsec) that have an estimated MWA "deep" flux extrapolated from the spectral index ($S_{200,\mathrm{est}}$) that is greater than 10% of the MWA flux (S_{200}) plus its uncertainty of the source of interest. We define blended sources between CABB and pre-CABB as CABB sources within the pre-CABB beam that have a flux (S_{CABB}) at the same frequency greater than 10% of the pre-CABB flux ($S_{\mathrm{pre-CABB}}$) of the source of interest.

To determine the blended sources between the GLEAM and pre-CABB catalogues, we performed a nearest neighbour match between all 2722 sources in the pre-CABB spectral index catalogue, and the 63 GLEAM sources we matched to our data, and accepted all matches within 140 arcsec. A total of 38 sources were found during this crossmatch that did not correspond to the source of interest. For pre-CABB sources with fewer than two fluxes, we derived an estimate of the 200 MHz deep MWA flux by assuming a typical spectral index of -0.7. We found nine blended sources according to the criteria above. However, we visually inspected these and found three that were detected only at 3 cm, which were spurious sources within the noise. Therefore, we concluded that six sources between the MWA and pre-CABB images are blended, which range between $0.1 < S_{200,\mathrm{est}}/S_{200} < 0.6$, and which are listed as blended in the source catalogue (see table E.1 in Appendix E).

To determine the blended sources between the pre-CABB and CABB catalogues, we performed a nearest neighbour match between all sources in the combined PYBDSM source catalogue (i.e. before we filtered out sources that weren't of interest) and the 72 sources from the pre-CABB spectral index catalogue, and accepted all matches within 30 arcsec. A total of 13 sources were identified during this crossmatch that did not correspond to the source of interest. From these, only one source matched the criteria from above, which has ($S_{\mathrm{CABB}}/S_{\mathrm{pre-CABB}} = 0.1$), and which is listed as blended in the source catalogue (see table E.1 in Appendix E). Inspecting this source in the image and the model produced from PYBDSM, we deduce that it is an artefact and not a real source.

2.3.1.9 Cross-matching to ancillary radio data

We crossmatched our 72 GPS and CSS sources to ancillary radio data via a nearest neighbour search using the 5.5 GHz positions from our source catalogue. Table 2.5 summarises the ancillary radio data.

Table 2.5: Cross-identifications of ancillary radio data for SMC GPS and CSS sample.

Data	Reference	Beam size (arcsec)	Astrometric Precision (arcsec)	Search Radius (arcsec)	$N_{\rm matches}$
GLEAM	Hurley-Walker et al., in prep. (2016)	140×170	10	50	62
AT20G	Murphy et al. (2010)	11×11^a	1	2.5	4
MRC	Large et al. (1981)	157×223^b	$\sim 10^c$	40	5

[a] AT20G mostly consisted of observations using ATCA configuration H214, which gives a 20 GHz beam size of $10.8'' \times 10.8''$, but also included observations using the H168 configuration, which gives a beam size of $13.9'' \times 13.9''$.

[b] The MRC had a beam size of $2.62 \times 2.86/\cos(\delta - \lambda)$ arcmin, where δ is the declination and λ is the effective latitude of -35.5 degrees. At $\delta = -75$, where the SMC is located, this gives 2.62×3.71 arcmin, or 157×223 arcsec.

[c] The typical astrometric precision for a 1 Jy source (all SMC sources > 1 Jy) observed as a single zenith transit and not near the edge of the primary beam was $5''$ is RA and $6''$ in Dec. See Large et al. (1981) for more details.

Table 2.6: The mean number of GLEAM matches to the shifted ATCA data ($N_{\rm matches,shifted}$), the number of GLEAM matches to the unshifted ATCA data ($N_{\rm matches}$), and the fraction of misidentifications derived from these.

Search Radius	$N_{\rm matches,shifted}$	$N_{\rm matches}$	Mis-ID fraction
$40''$	13 ± 4	445	0.03 ± 0.01
$50''$	21 ± 5	454	0.05 ± 0.01

2.3.1.10 Positional Uncertainties and Confusion

GLEAM has an astrometric precision of $5''$ within $-75 < \delta < 20$. However, this increases to $10''$ at $\delta = -80$, where the lower portion of the SMC is located. The positional error of our ATCA radio data is expected to be of the order $\theta_{\rm FWHM}/{\rm SNR}$, where SNR is the signal-to-noise ratio (Condon, 1997; Norris et al., 2006). For each source, we required a 5σ detection, and the worst resolution at 5.5 GHz is $\theta_{\rm FWHM} = 5.4''$. Therefore, we estimate the ATCA 5.5 and 9.0 GHz sources have an astrometric precision of $\lesssim 1''$. The mean sky separation between the ATCA positions from our source catalogue and the GLEAM positions is $14''$, with a mean ΔRA of $6''$ and ΔDEC of $1''$, and standard deviations of $11''$ and $12''$, respectively. The sky separation for all 62 GPS and CSS candidates matched to GLEAM is shown in Fig. 2.14.

Within the SMC, GLEAM has a FWHM synthesised beam size of $140 \times 170''$. Since the FWHM of our ATCA data ranges from $< 1''$ to several tens of arcsec, we expect some misidentifications due to confusion when crossmatching to GLEAM. To estimate this, we use the same procedure as outlined above, by shifting the positions of the *pre-CABB* ATCA data by random amounts and then crossmatching GLEAM to a catalogue containing these shifted positions. We used two different search radii in order to ensure we had used an optimum search radius of $50''$. We expect larger search radii to have a higher completeness, but also a higher fraction of false-detections, and hence a lower reliability. We shifted the radio positions by random amounts between $250 - 500''$, encoding a 50% chance of the shift being a negative number for both the RA and Dec. We repeated this procedure 1000 times for each search radius in order to find the mean number of matches to the shifted positions. Table 2.6 summarises the misidentification fraction found for each search radius. At $50''$, the mean misidentification faction is 0.05 ± 0.01, and we expect $\sim$30% of these to be GPS or CSS sources (O'Dea, 1998; Orienti, 2016). Therefore we estimate a misidentification rate of 1.5 ± 0.3%, resulting in $\sim$1 false-positive in our sample of 62 GLEAM cross-matches.

2.3.2 ATCA observations of ATLAS sources

The data reduction of the ATCA observations of the ATLAS sample was done in a very similar way to that of the SMC observations, using the same python script that calls MIRIAD tasks. The five days of observations are summarised in table 2.7. Each of the observations used PKS 1934-649 as the bandpass and flux density calibrator.

2.3.2.1 Calibration

During calibrating the ATLAS observations, we followed the same calibration procedure as shown in Figure 2.8. During flagging the sources, `pgflag` was generally performed using the second approach discussed in section 2.3.1.1 (i.e. one iteration of `pgflag` using flagpar = 7,1,1,3,3,3,20 and stokes=i). After this step, very few sources were $\geq$ 20% flagged, but RFI

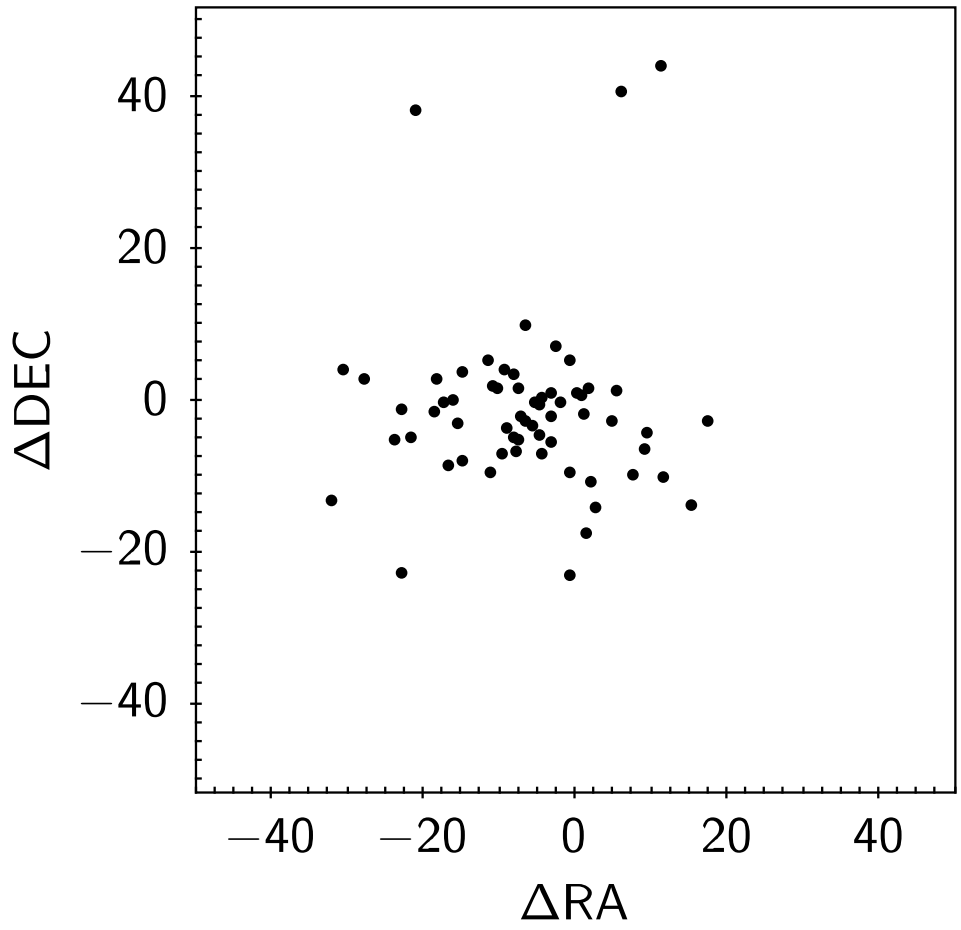

Figure 2.14: The sky separation between the ATCA 5.5 GHz and GLEAM 200 MHz positions for the 62 sources from our SMC sample that were matched to GLEAM, where ΔRA and ΔDEC are in arcseconds. The standard deviation of ΔRA and ΔDEC is respectively 11″ and 12″. The mean ΔRA is 6″, suggesting there may be a systematic uncertainty in the RA of the order of GLEAM's astrometric precision. Two of the three outliers are sources which have no detectable nucleus and therefore the ATCA position represents one of the lobes, while the third is a very extended GLEAM source. All matches have been visually inspected.

Table 2.7: A summary of the individual days of ATLAS observations undertaken in this thesis, sorted by date.

Field	Date	Time	N_{sources}	Phase calibrator
ELAIS-S1	5 Dec 2012	8 h	10	PKS 0022-423
ELAIS-S1	6 Dec 2012	10 h	12	PKS 0022-423
ELAIS-S1	7 Dec 2012	10.5 h	11	PKS 0022-423
ELAIS-S1	8 Dec 2012	10.5 h	16	PKS 0022-423
CDFS	21 Apr 2014	11 h	22	PKS 0327-241

was still present and clearly visible in the amplitude plots for a few sources at 5.5 GHz and for all sources at 9.0 GHz. These were dealt with in the same way as above, by manually running `blflag`, sometimes flagging out entire channels affected by RFI.

2.3.2.2 Imaging

The imaging was performed in the same way as for the SMC observations, except that only individual pointings were imaged, and no mosaicking was performed. The self-calibration interval was set to 20 minutes, which ensured that each solution used one entire scan of a source. Furthermore, the number of sub-bands that were imaged varied between $2 - 16$ depending on the S/N of each source. Since all sources were point sources or very close to point sources, we did not beam-match the sub-bands, but allowed `invert` to choose the optimal FWHM, which gave a better S/N.

For the ECDFS source unique to sample (4) from table 2.4 (ID CI0020), we were given data (Minh Huynh, private communication) collected as part of the 5.5 and 9.0 GHz observations of the ECDFS (Huynh et al., 2012, 2015). At 5.5 GHz, we used the 512 MHz sub-band images created as part of the investigation of the radio spectra in Huynh et al. (2015). At 9.0 GHz, we used the self-calibrated visibilities from Huynh et al. (in prep) and for consistency, also created 512 MHz sub-bands, imaged in the same way as for our own observations.

2.3.2.3 Source extraction

The source extraction was performed using PYBDSM in the same way as described for the SMC in section 2.3.1.3, but for sub-band images only, which used a cube as input. Since they varied, the beam dimensions were input for each channel. Furthermore, we used PYBDSM to perform source extraction on the ancillary radio data from GMRT at 150, 325, 610 MHz, MOST at 843 MHz and ATCA at 34 GHz. We also used PYBDSM to perform source extraction on the ATLAS 2.3 GHz images for a few sources which had not been included in the Zinn et al. (2012) catalogue. In the ELAIS-S1 field, PYBDSM had already been used to perform source extraction on the 610 MHz mosaic (Intema et al., in prep.).

For sources CI0020, s415 and s895, which were detected weakly in the GLEAM 200 MHz deep image, the GLEAM sub-band measurements were extremely noisy, and therefore we performed source extraction on the three stacked bands. We used AEGEAN to do this, since it was also used to create IDR2, which enabled us to use the priorised fitting feature of AEGEAN. To do this, we first used the BACKGROUND AND NOISE ESTIMATOR (BANE) program featured in AEGEAN, to create background and noise images for each of the three stacked images. These were then fed into AEGEAN, which was performed using priorised fitting, in which the flux, position and gaussian shapes were allowed to vary. The 155 MHz stacked band fluxes were found to be within uncertainty of the 150 MHz GMRT fluxes and therefore we considered these faint measurements as reliable.

2.3.3 VLBI observations of ATLAS sources

The calibration, imaging and source extraction were performed by Steve Tingay[5], and are summarised below.

[5]International Centre for Radio Astronomy Research, Curtin University, Bentley, WA 6102, Australia.

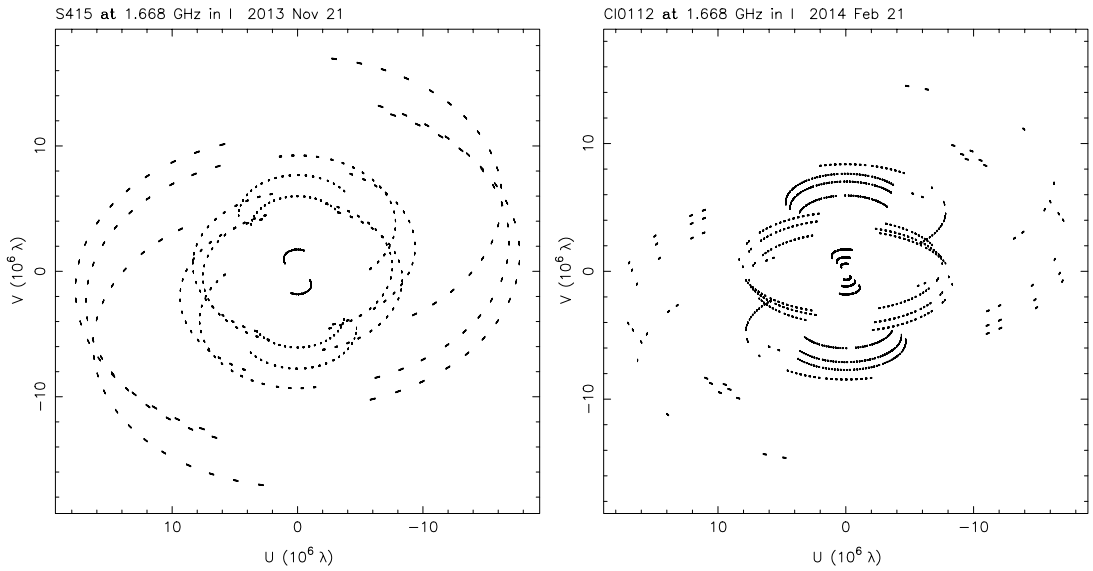

Figure 2.15: The typical (u, v) coverage achieved during the first (left) and second (right) days of our LBA observations.

2.3.3.1 Calibration

The LBA data for all eight sources were correlated at Curtin University using the DiFX software correlator (Deller et al., 2007, 2011) using 128 channels across the 64 MHz band and 2 s integration times. Only parallel hand polarisations were correlated (RR and LL). The typical (u, v) coverage achieved on the first and second observing runs are shown in Figure 2.15. The visibility data were imported into AIPS for standard processing, as described briefly below.

The visibility data were calibrated in amplitude using measured system temperatures for each telescope from the time of observation, as well as known gains for each telescope. The resulting amplitudes for the calibrators (which were unresolved) were then compared to flux densities measured from the ATCA. Adjustments to the telescope gains were made, with a subsequent refinement of the calibrated amplitudes. We estimate the flux densities are known to approximately 10% uncertainty.

The visibilities for the calibrator sources were then fringe-fitted in order to solve for delays and phases for each antenna, interpolated to the times of the target observations, and applied to the target visibilities. This standard phase referencing step calibrates the visibility phases for the target sources, allowing imaging to proceed.

2.3.3.2 Imaging and source extraction

The target visibility data were exported from AIPS into DIFMAP for further analysis. Two sources yielded no detections in the (u, v) plane, and were not imaged. For the remaining six, due to the relatively sparse nature of the measurements, a model-fitting approach was adopted, using the task `MODELFIT` in DIFMAP. For each target source, a model for the source structure was generated using the smallest number of simple components required to fit the visibilities. The models were iteratively fit to the data and used for self-calibration (when the sources were detected with high enough signal to noise). Four sources were imaged with a pixel size of $\sim$3 mas, while the other two were imaged with a pixel size of $\sim$6 mas.

Chapter 3

Infrared-Faint Radio Sources

3.1 All-sky IFRS sample

As outlined in section 1.4, IFRSs are a recently discovered rare class of object detected strongly in the radio, but with very faint or undetectable IR counterparts in very deep surveys. Earlier studies were unable to confirm their nature since they were almost entirely focussed on the radio, although they were found to exhibit a high sky density, and were thought to represent AGN at $z > 3$. Therefore, IFRSs may significantly increase the number of known high-redshift galaxies. As outlined in section 2.1.3, we selected a sample which met the same IFRS selection criteria from Zinn et al. (2011), but which was significantly detected at $\geq 5\sigma$ at 3.4 μm in *WISE*. We refer to this as the 'all-sky IFRS' or 'WISE IFRS' sample. This sample is presented in Collier et al. (2014), the results of which we present here.

3.1.1 Sky density

Our final sample consists of 1317 IFRSs in ∼11 000 deg^2, although the area where *WISE* is sensitive enough to find IFRSs is much smaller. This implies a lower limit to the sky density of ∼0.1 per deg^2 for $S_{20cm} > 7.5$ mJy. Comparatively, Norris et al. (2011a) estimated a sky density of ∼7 per deg^2 for $S_{20cm} > 0.1$ mJy. Additionally, the four sources in their sample with $S_{20cm} > 7.5$ mJy have a sky density of ∼0.5 per deg^2.

3.1.2 WISE and NVSS detections

3.1.2.1 NVSS 20cm flux density

Because of our 7.5 mJy cutoff, the 20 cm flux densities found for our sample are much greater than those found for the first generation IFRSs from ATLAS, which were not detected in the IR. The distribution in the NVSS 20 cm flux density from 0 – 100 mJy for our IFRSs can be seen in Fig. 3.1.

3.1.2.2 NVSS 20cm polarisation

We matched our IFRS source list to the Taylor et al. (2009) RM catalogue, which lists 37 543 polarised NVSS sources down to $8\sigma_{QU}$. We accepted as polarised those sources with a match to our IFRS source list and a percentage polarisation greater than 1% ($\Pi = p/S \times 100\%$), since below this level, the instrumental off-axis polarisation becomes significant. This resulted in 41 polarised IFRSs, which increases the number of known polarised IFRSs five-fold. Fig. 3.2

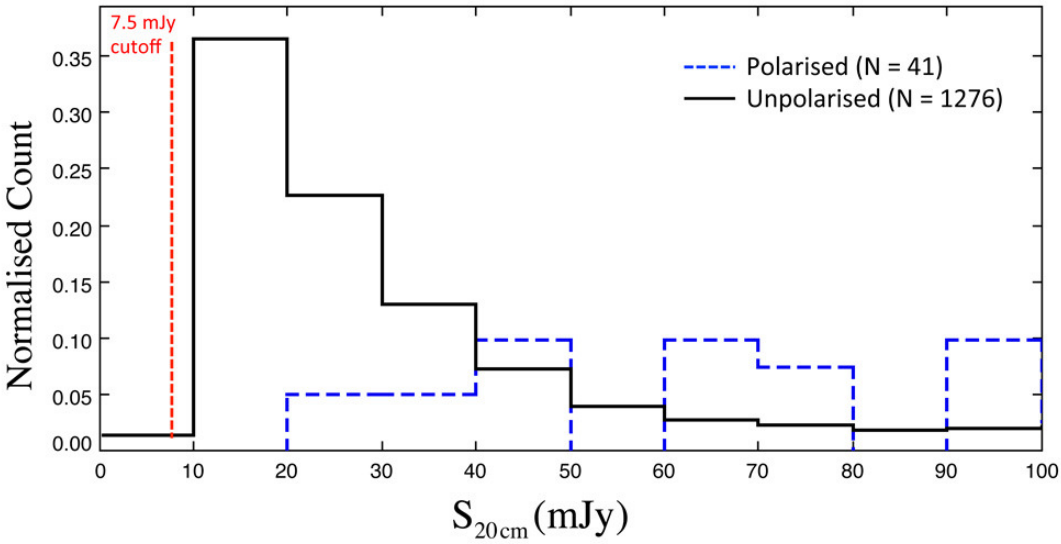

Figure 3.1: The normalised NVSS 20 cm flux density distribution from $0 - 100$ mJy for our sample of IFRSs. The dotted red line indicates our 7.5 mJy cutoff. However, since the *WISE* catalogue is far from complete below $\sim$40 μJy, and since we require $S_{3.4\,\mu\mathrm{m}}/S_{20\,\mathrm{cm}} > 500$, the radio sources are highly incomplete below $\sim$20 mJy. Sources polarised at levels of $8\sigma_{\mathrm{QU}}$ and above are shown by the dotted blue line, while those with no polarisation detected at this level are shown by the solid black line.

shows the distribution of fractional polarisation and RMs for our polarised IFRSs, which have fractional polarisations between 1% and 14% , and a median of 5.4% . This is consistent with the findings of Middelberg et al. (2011b) and Banfield et al. (2011), who respectively found fractional polarisations ranging from $7 - 12\%$, and $\sim 6 - 16\%$ for their samples of IFRSs.

The RMs values of our polarised IFRSs range from $-45.8 \leq \mathrm{RM} \leq 53.8$ rad m^{-2} and have a mean at 9.3 rad m^{-2}. If we neglect how the Galactic σRM varies with Galactic latitude, since our IFRSs happen to be located more than 20 degrees away from the Galactic plane, then based on Schnitzeler (2010), the polarised NVSS sources will show a σRM of 14 rad m^{-2}, where σRM ≈ 6 rad m^{-2} is the scatter in intrinsic RMs of polarised NVSS sources. This is close to the σRM $= 16$ rad m^{-2} estimated using robust statistics from the binned RMs in Fig 3.2. Therefore, the RMs for our polarised IFRSs are similar to those of typical polarised NVSS sources.

However, the distribution of the properties of our polarised IFRSs cannot be effectively compared to the general population of polarised sources, since we have not corrected our sample for incompleteness. Banfield et al. (in prep.) will investigate the radio polarisation properties of a sample of IFRSs not suffering from incompleteness.

3.1.2.3 *WISE* flux densities

Fig. 3.3 shows a colour-colour diagram of the IFRSs detected at 3.4, 4.6, and 12 μm, as compared to those from Cutri et al. (2011). This figure reveals that the majority of our IFRSs have *WISE* colours similar to those found for obscured AGN, quasars and Seyferts (Jarrett et al., 2011; Assef et al., 2013).

The distribution in the *WISE* flux densities for our IFRS sample is listed in Table 3.1. We show the number of IFRSs detected at $\geq 5\sigma$ in the *WISE* bands that are polarised at 20 cm compared to the IFRSs with no detectable polarisation. The numbers are consistent in both groups indicating that the polarised IFRSs are similar to the unpolarised IFRSs in the infrared.

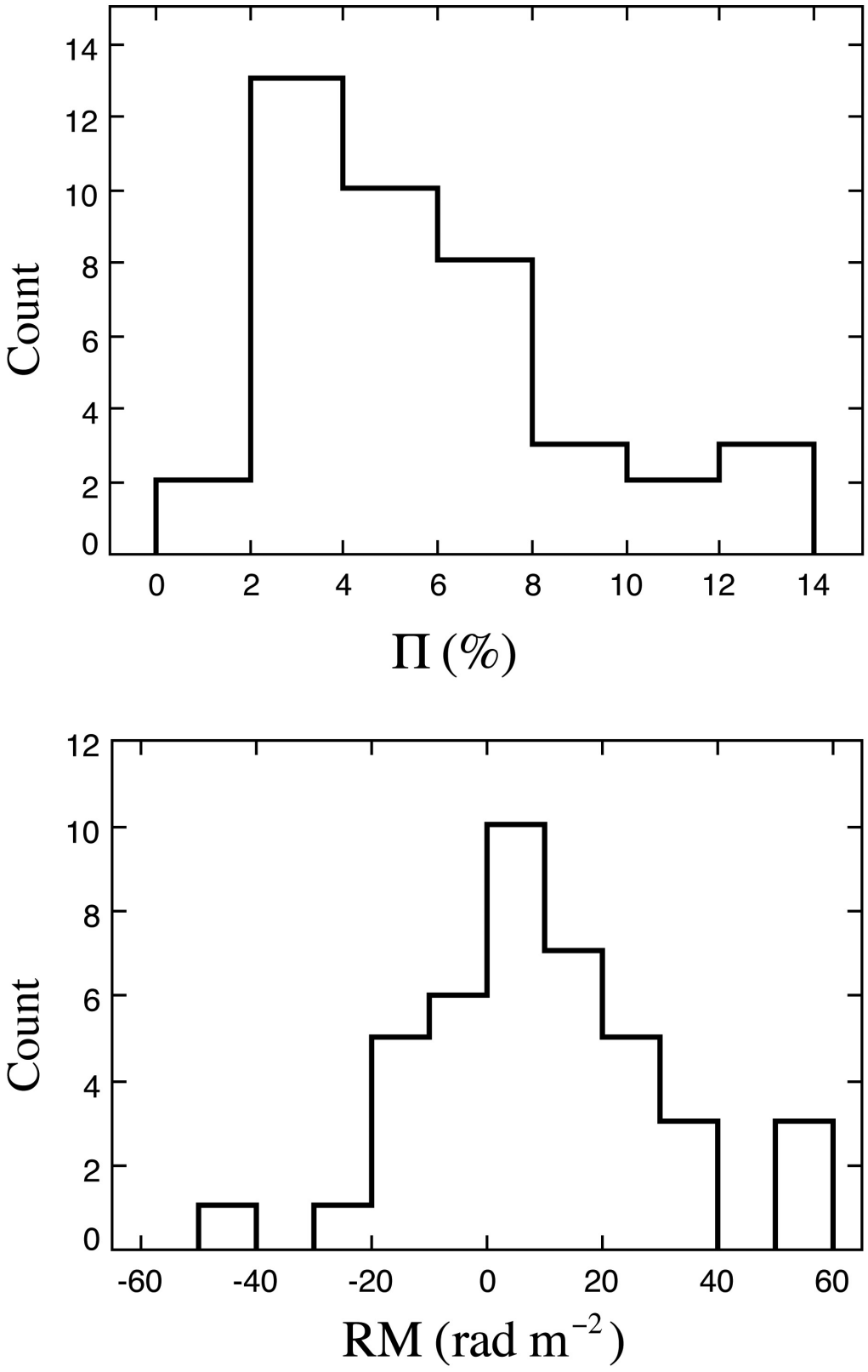

Figure 3.2: Fractional polarisation (top) and rotation measure (bottom) histograms for the 41 polarised IFRSs. The fractional polarisation values range from $1\% < \Pi < 14\%$, with the peak of 4% and a median of 5.4% . The RMs range from $-45.8 \leq \mathrm{RM} \leq 53.8$ rad m^{-2} and have a mean at 9.3 rad m^{-2}.

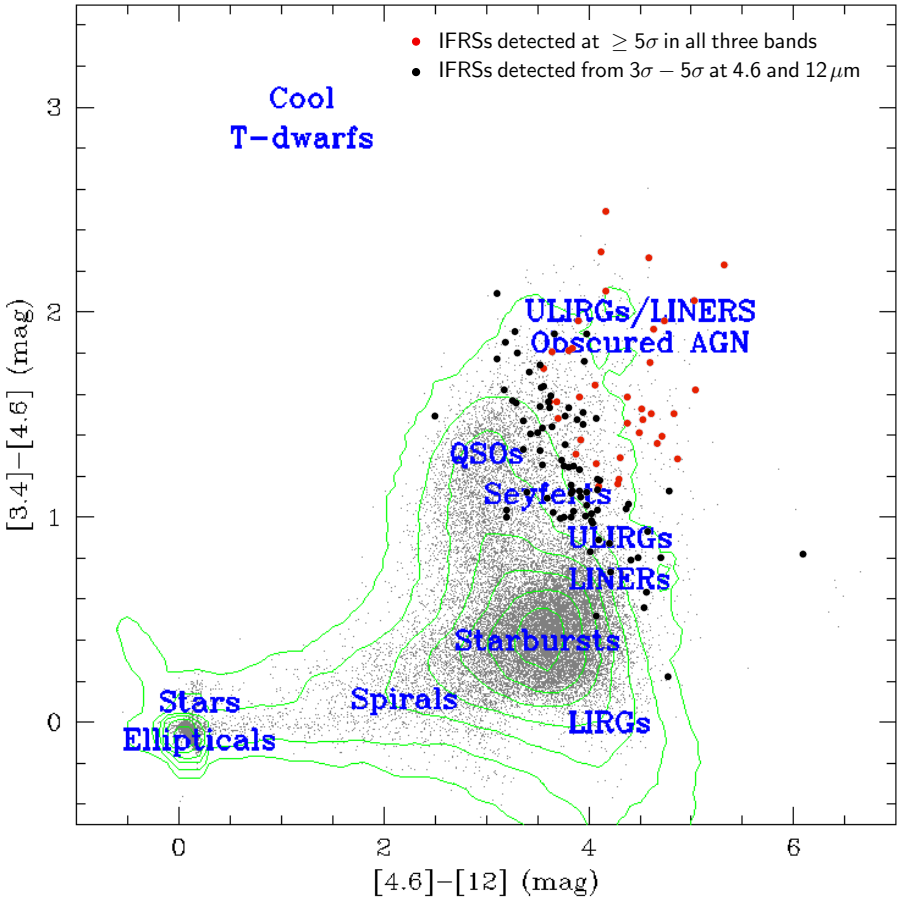

Figure 3.3: *WISE* colour-colour diagram of the 3.4, 4.6, and 12 μm magnitudes for our sample of IFRSs compared to the sample from Cutri et al. (2011). The red dots are the 37 IFRSs that were detected at $\geq 5\sigma$ in all three bands, the black dots are the 107 IFRSs that were detected at $\geq 5\sigma$ at 3.4 μm and between $3\sigma - 5\sigma$ at 4.6 or 12 μm, and the grey points are the sources from Cutri et al. (2011). Image adapted from Cutri et al. (2011).

Table 3.1: The *WISE* flux density distribution, showing the number of IFRSs detected at $\geq 5\sigma$ in the different *WISE* bands that are polarised at 20 cm compared to the IFRSs with no detectable polarisation. The percentages in the brackets indicate the percentage of total sources detected in each band. The percentage error is given by $\frac{N_{\rm band}}{N_{\rm TOT}}/\sqrt{N_{\rm band}}$.

	$N_{3.4}$	$N_{4.6}$	N_{12}	N_{22}
Unpolarised	1276	458 ($35.9 \pm 1.7\%$)	47 ($3.7 \pm 0.5\%$)	8 ($0.6 \pm 0.2\%$)
polarised	41	17 ($41.5 \pm 10.1\%$)	1 ($2.4 \pm 2.4\%$)	0 ($0.0 \pm 0.0\%$)
All Sources	1317	475 ($36.1 \pm 1.7\%$)	48 ($3.6 \pm 0.5\%$)	8 ($0.6 \pm 0.2\%$)

However, from the 20 cm flux densities, we conclude that our sample of polarised IFRSs are AGN, as Grant et al. (2010) determined that polarised sources with $S_{20\,\rm cm} \geq 1.0$ mJy are mainly lobe-dominated AGN. As can be seen in Table 3.1, the number of sources detected in the infrared decreases with increasing wavelength, partly because of the lower sensitivity of *WISE* at longer wavelengths, and partly because the sources typically follow a power-law SED.

3.1.2.4 Radio-IR flux density ratios

Fig. 3.4 shows the radio to infrared flux density ratio $\rm S_{20cm}/S_{3.4\mu m}$ for all of our sources. This is similar to the distribution in $\rm S_{20cm}/S_{3.4\mu m}$ for the sample from Middelberg et al. (2011b), although peaks slightly lower, since our sources are brighter in the infrared. The polarised sources have a much higher flux density ratio, but this is a selection effect, since no polarisation is detected in the weaker radio sources, due to low S/N.

We also calculate the radio to far-infrared (FIR) ratio $\rm q_{22} = \log(S_{22\mu m}/S_{20cm})$, using 22 μm flux densities for 31 sources detected at 3σ and above, and 22 μm 3σ upper limits for the remaining 372 sources that had reliable r.m.s. noise (σ) estimates. Those detected all have values $\rm q_{22} < -0.23$, while those with upper limits all have values $\rm q_{22} < -0.30$. From the 31 sources with *Spitzer* counterparts, four had detected counterparts at 24 μm, for which we found $\rm q_{24} < -1.28$. These values of $\rm q_{22}$ and $\rm q_{24}$ are all well below those seen for SFGs, which are typically $\rm q_{24} \sim 1$ (Appleton et al., 2004), suggesting that the vast majority of our sources are AGN.

3.1.3 Radio morphology

The number of resolved and compact IFRSs from our sample was determined using two different methods: flux density ratios and visual inspection. We use a stricter criterion for the definition of a source that is unresolved in FIRST, adopted from Kimball and Ivezić (2008). We consider a source as unresolved if the ratio between its peak flux density $S_{\rm peak}$ and integrated flux density $S_{\rm int}$ is

$$\log \frac{S_{\rm int}}{S_{\rm peak}} < 0.05 \; . \tag{3.1}$$

The number of resolved and unresolved IFRSs that were found using these two methods is given in Table 3.2. The compactness of our sources can be used as a proxy for their projected linear size, since in Λ Cold Dark Matter (ΛCDM), at $z > 1$, the angular size corresponding to a fixed linear size varies only weakly with z. Sources that are unresolved in FIRST have linear sizes $\lesssim 30$ kpc at any redshift > 0.5.

From the 946 IFRSs that appeared resolved from visual inspection, 157 had uncertain morphologies, and 214 had double-lobed morphologies (most likely FR II galaxies with strong hotspots), which included sources with a single catalogued FIRST component that could still

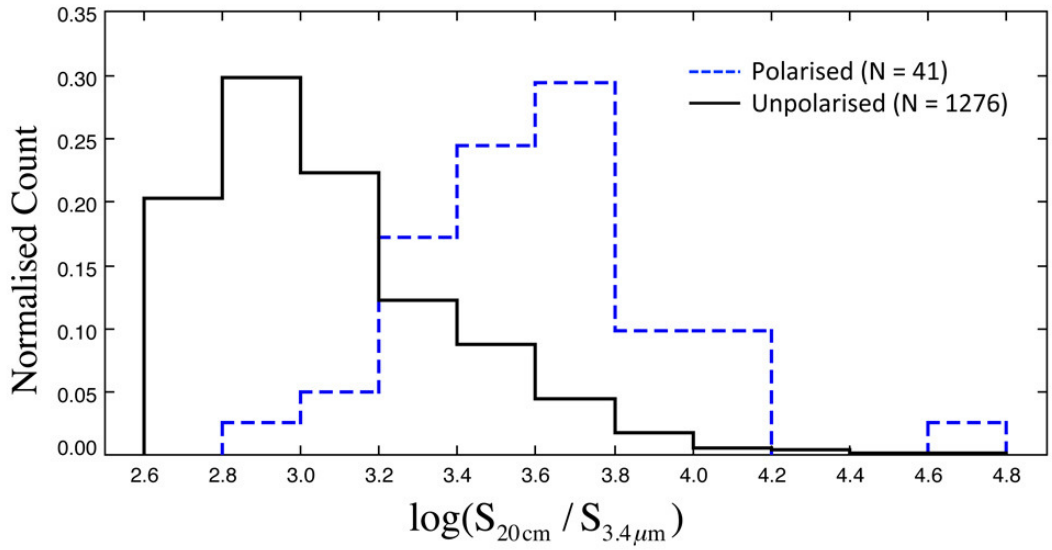

Figure 3.4: Normalised histogram of $\log(S_{20cm}/S_{3.4\mu m})$ for sources with polarisation detected $\geq 8\sigma_{QU}$ (dotted blue line) and for sources with no detected polarisation at this level (solid black line). The drop-off at 2.6 corresponds to our selection criterion $S_{20cm}/S_{3.4\mu m} > 500$, since $\log(500) \approx 2.7$.

Table 3.2: The total number of resolved and unresolved IFRSs (polarised IFRSs in brackets) found using the flux density ratio and visual inspection methods.

	Flux Density Ratio	Visual Inspection	Both
Unresolved	845 (13)	946 (12)	760 (5)
Resolved	472 (28)	371 (29)	286 (21)

be identified as a double-lobed galaxy (e.g. Fig. 3.5 (top)). Of the 41 polarised sources, 23 had morphologies of a double-lobed galaxy, 6 appeared resolved with unknown morphologies, while the remaining 12 sources appeared unresolved. Fig. 3.5 shows some examples of IFRSs with double-lobed morphologies with one, two and three catalogued components in FIRST. The double-lobed morphologies are consistent with previous hypotheses about IFRSs, which have found that IFRSs are well represented by high-redshift FR II galaxies. However, the majority of our sources are unresolved, like the IFRSs from Middelberg et al. (2011b), suggesting they may be younger radio galaxies with smaller jets.

A much larger fraction of polarised IFRSs have resolved morphologies ($\gtrsim 70\%$), compared to the unpolarised IFRSs that have resolved morphologies ($\lesssim 35\%$). This is consistent with Banfield et al. (2011), who found that $\sim$80% of their polarised sources and $\sim$15% of their sources with no detected polarisation were resolved. It is also consistent with the number of lobe-dominated AGN we expect for polarised sources with $S_{20\mathrm{cm}} \geq 1.0$ mJy (Grant et al., 2010).

3.1.4 Radio spectra

From the URC, we extracted flux densities at $\nu = 326$, 1400 and 4850 MHz ($\lambda = 92$, 20 and 6 cm), respectively from WENSS, NVSS, and GB6. In order to derive the spectral shape and spectral indices, we used the flux densities from two or three of these frequencies. Because it was not possible to match the beamsizes and epoch of observation of the various surveys, the flux density at a particular frequency was used only if the source:

1. was unconfused;
2. was unresolved (according to equation 3.1, except at 6 cm);
3. was the only match within $30''$ of NVSS source;
4. had no error flags;

3.1.4.1 Spectral shape

Although upper limits of the flux densities cannot be effectively used to determine the spectral index, they are effective in constraining the shape of the radio spectra. Therefore, we measure the shape of the radio spectrum for our IFRSs using all the flux densities available ($S_{20\mathrm{cm}}$ always available) and where this is unavailable, upper limits. Where the detection is not significant, a 5σ upper limit is attributed to the source. Where no detection is made within the WENSS or GB6 footprint (i.e. when the source does not appear in the WENSS or GB6 catalogue, but is still in its footprint), an upper limit of 18 mJy is attributed to the source, since this is the sensitivity limit of both the WENSS and GB6 surveys. To identify GPS sources, we use the flux densities and limits from all three frequencies, since at least three points are needed to identify a peak. We define a GPS source as a source that:

1. is unresolved in FIRST;
2. contains a positive spectral index between 92 and 20 cm and a negative spectral index between 20 and 6 cm;
3. has a minimum 20 cm flux density of $\mathrm{S_{20cm}} - 3\Delta\mathrm{S_{20cm}}$ greater than the expected value at 20 cm as extrapolated from the spectral index fit between the two points $\mathrm{S_{92cm}} + \Delta\mathrm{S_{92cm}}$ and $\mathrm{S_{6cm}} + \Delta\mathrm{S_{6cm}}$, where ΔS is the 1σ error in the flux density.

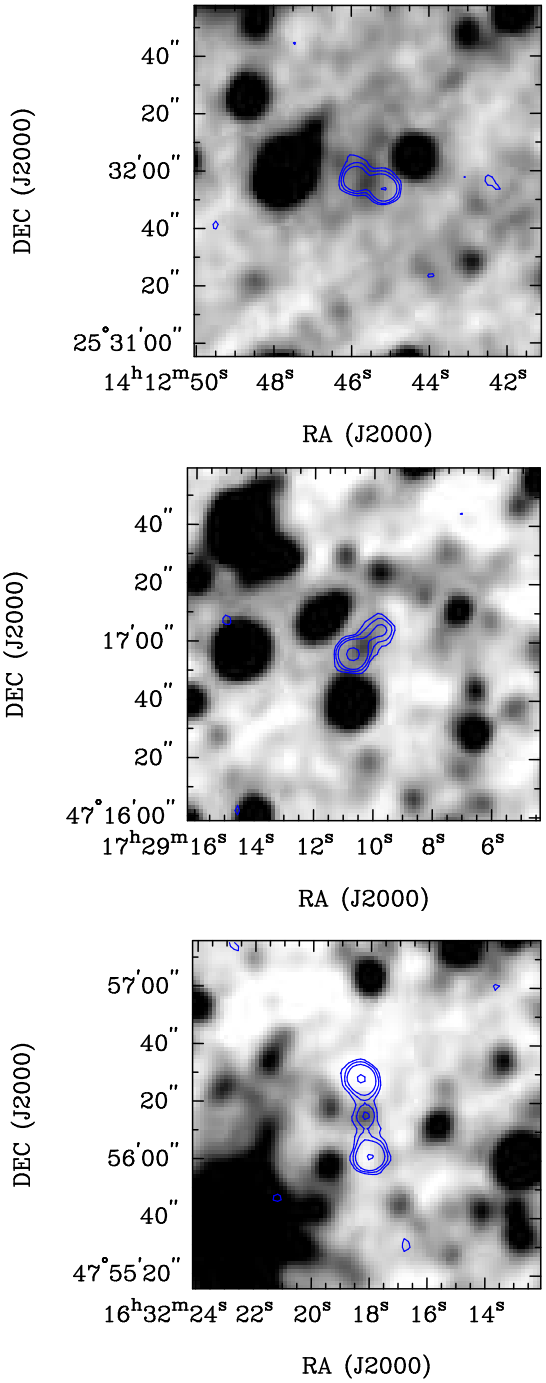

Figure 3.5: Examples of a source with a double-lobed morphology with one (top), two (middle), and three (bottom) catalogued FIRST components. The background image shows the *WISE* 3.4 μm detection, and the contours mark the FIRST source at 20 cm. Contour levels are: 3, 6, 12, 64, 256, 1024 times the local noise level.

The last of these criteria ensures that the peak lies outside the uncertainty in the spectral index, separating the GPS sources from the flat-spectrum sources. We also use this criterion to identify curvature in other radio spectra. We define a CSS source as a source that:

1. is unresolved in FIRST;

2. has a spectral index of $\alpha < -0.8$.

To identify CSS sources, we use flux densities from two or three frequencies, and upper limits on the flux density only at 20 cm and 6 cm, since we expect all CSS sources with $S_{20cm} > 7.5$ mJy to be detected in WENSS.

We find that 208 of our IFRSs have a steep spectrum of $\alpha < -0.8$, while 32 have a gigahertz-peaked spectrum. All of these GPS candidates and 124 of the CSS candidates are considered compact in FIRST according to equation 3.1, and we therefore respectively define them as GPS and CSS sources. Fig. 3.6 shows the radio spectra of a GPS and a CSS source from our sample. These findings are consistent with Middelberg et al. (2008b) and Middelberg et al. (2011b), who found that their IFRS sample consisted of GPS and CSS sources, based on finding compact AGN cores and curvature in the radio spectra. This implies that a substantial fraction of our IFRSs are young and evolving AGN, with jets that have not broken out far beyond the galaxy.

Of the 13 polarised sources that are compact according to equation 3.1, six are CSS sources, and one is a GPS source.

3.1.4.2 Spectral indices

We derived spectral indices using a least squares fit in the log-log domain for the same selection of sources described in section 3.1.4, and also required that they: (1) had a signal-to-noise ratio ≥ 5; (2) did not show a GPS spectrum. Therefore, we don't use upper limits to derive spectral indices. Given the 18 mJy sensitivity limits at 92 and 6 cm, sources close to the median 20 cm flux density of 25.5 mJy will not be detected at 92 cm if they are shallower than $\alpha = 0.24$, nor at 6 cm if they are steeper than $\alpha = -0.28$. Hence there is a large bias on our spectral indices, with the 6 cm data tending to give shallower spectral indices, and the 92 cm tending to give steeper spectral indices.

The median values of the spectral index for three different groupings of frequencies are listed in Table 3.3, and their distributions are shown in Fig. 3.7. We find that our sample is made up of USS, steep, flat and inverted sources, as shown in Fig. 3.8. Banfield et al. (2011) and Middelberg et al. (2011b) found much steeper median spectral indices of -1.07 and -1.01 (with the majority of sources having $\alpha < -1.0$) when they studied the ELAIS-N1 and ATLAS fields respectively. Those from Banfield et al. (2011) were measured from the flux densities at 92 and 20 cm. However, the spectral indices from Middelberg et al. (2011b) were calculated primarily from the flux densities at 20, 13, 6 and 3 cm, and in some cases, also from the 36 cm flux densities. Therefore a GPS source will appear to be steeper when measured at the frequencies used by Middelberg et al. (2011b) than at the frequencies measured in this paper.

Inverted sources with $\alpha > 0$ are possibly very young GPS sources that peak above 4850 MHz, like those seen by Hancock (2009). These could also be variable sources with varying flux densities across the different epochs, or Blazars.

Objects with steep radio spectra are more likely to be found at high redshifts than objects with flatter radio spectra, and the USS criterion ($\alpha \lesssim -1.0$) has been employed to discover most of the known radio galaxies at $z > 3.5$ (Norris et al., 2013, and references therein). Most

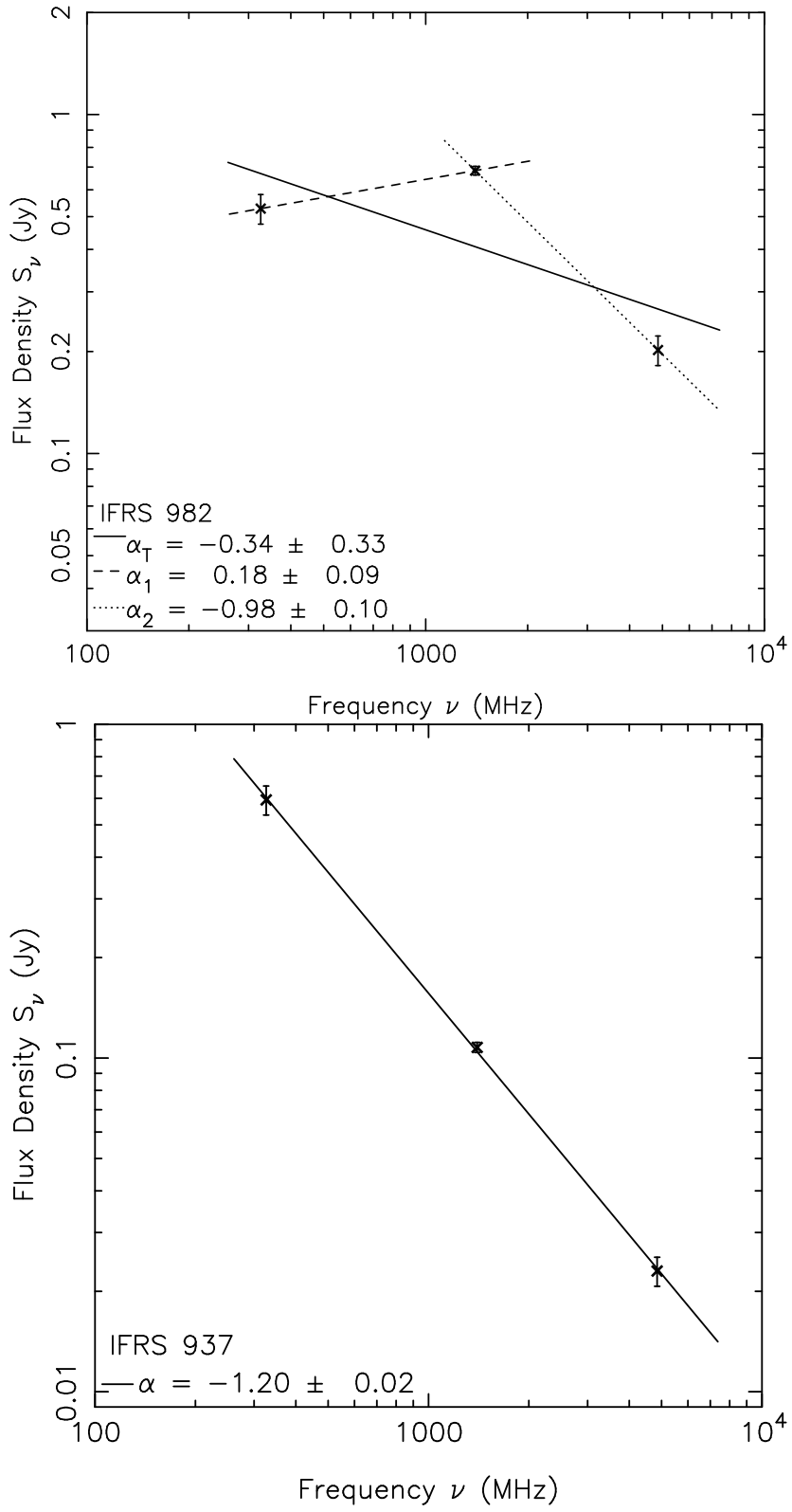

Figure 3.6: The radio spectra of a GPS (top) and a CSS (bottom) source from our sample of IFRSs. The dashed and dotted lines respectively denote the spectral index below and above the turnover frequency of the GPS source.

Table 3.3: The median spectral indices of our IFRSs. The first row contains sources with available flux densities at 92, 20 and 6 cm, while the second row has only flux densities at 92 and 20 cm, and the third row only at 20 and 6 cm. Sources in the first row are also in the second and third row. $N_{\rm USS}$ signifies the number of USS ($\alpha < -1.0$) sources.

Wavelengths used to fit α	$N_{\rm total}$	$\alpha_{\rm total}$	$N_{\rm polarised}$	$\alpha_{\rm polarised}$	$N_{\rm unpolarised}$	$\alpha_{\rm unpolarised}$	$N_{\rm USS}$
92, 20 & 6 cm (α_3)	136	−0.82	12	−0.90	124	−0.82	16
92 & 20 cm (α_{20}^{92})	570	−0.82	18	−0.88	552	−0.81	84
20 & 6 cm (α_{6}^{20})	249	−0.80	23	−0.91	227	−0.79	55

of our IFRSs have steep spectral indices (see Table 3.3), and many are USS, suggesting that a significant fraction of them are likely to be located at high redshifts.

3.1.5 Optical matches

Most of our IFRSs are undetected in SDSS to the limiting magnitude of $r = 22.2$, which is consistent with previous studies of IFRSs, in which few optical counterparts were found. The distribution of the SDSS r magnitudes for the 230 detected sources is shown in Fig. 3.9 (bottom), which shows an increase up to a magnitude of 22.2, beyond which SDSS becomes highly incomplete. This shows that at least a fraction of our IFRSs are also optically brighter than first generation IFRSs. The *WISE* sources studied by Yan et al. (2013) peak at an SDSS r magnitude of 20, and these sources lie almost entirely at $z < 1$. This suggests that most of our IFRSs are likely to lie at redshifts of $z > 1$, but could also be at $z < 1$ and suffer from more obscuration than typical *WISE* galaxies.

3.1.6 Redshifts

Table 3.4 lists the 19 sources which have spectroscopic redshifts in SDSS DR9[1]. Their spectra and postage stamps are shown in Fig. 3.11. 18 of these sources are identified as quasars in the range $2 < z < 3$, 14 of which contain broad emission lines. Their strong radio emission means that they are necessarily radio-loud quasars.

One source is identified as a SFG at a redshift of $z \approx 0.02$, which clearly hosts an AGN, because of its high flux density ratio $\rm S_{20cm}/S_{3.4\mu m}$ and its GPS spectrum. This source is probably either a misidentification, or a composite galaxy with a radio-loud AGN embedded within a SFG, similar to F00183-7112 (Norris et al., 2012).

Because these sources with spectroscopy are much brighter than first generation IFRSs, they probably represent the closer and brighter tail end of the IFRS population. This is also suggested by the distribution in 3.4 μm flux density for these sources (Fig. 3.9), which ranges from $20 - 30\,\mu$Jy and has a higher median of $26.7\,\mu$Jy, as compared to the rest of the sample, which ranges from $10 - 30\,\mu$Jy and has a median of $25.9\,\mu$Jy. Fig. 3.9 demonstrates that the sources with spectroscopic redshifts are taken from the upper half of the infrared and optical brightness distribution, implying that the fainter half is located at higher redshift. Despite being brighter in the optical and infrared, these 18 sources are still classified as IFRSs and share the same region in $\rm S_{20cm}/S_{3.4\mu m}$ space as HzRGs (Fig. 1.17).

Fig. 1.18 shows where our *WISE* IFRSs with spectroscopy appear in the diagram adapted from Norris et al. (2011a). Our sources are very densely concentrated around $S_{3.4\mu\rm m} \approx 30\mu$Jy in this figure and do not have sufficient range in IR flux density to show the observed $S_{3.4\mu\rm m} - z$

[1]The cosmological parameters used throughout this section are $\Omega_\Lambda = 0.7$, $\Omega_{\rm M} = 0.3$, and $H_0 = 70\ \rm kms^{-1}\ Mpc^{-1}$.

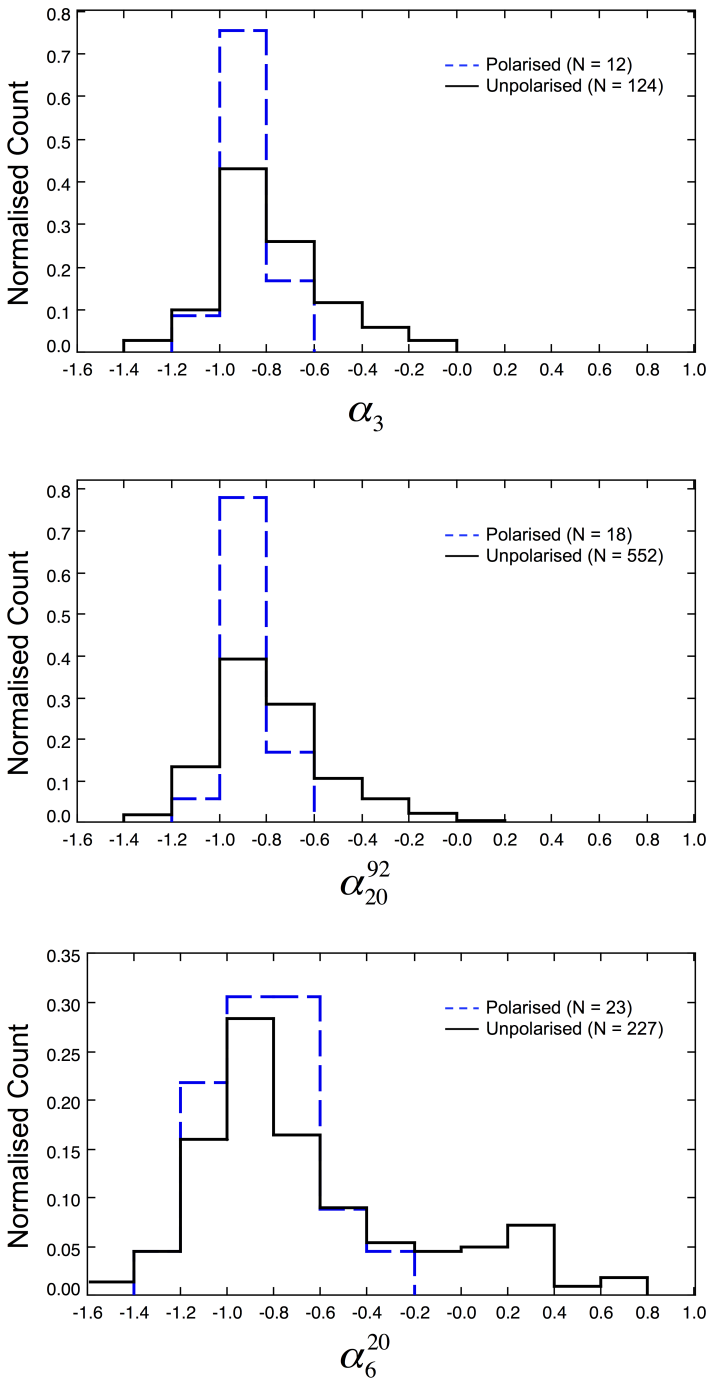

Figure 3.7: Normalised histogram of the spectral indices of the compact non-GPS IFRSs as found respectively between frequencies one (92 cm), two (20 cm) and three (6 cm) (α_3: top), frequencies one and two (α_{20}^{92}: middle) and frequencies two and three (α_6^{20}: bottom). Sources polarised at $8\sigma_{\rm QU}$ and above are shown by the blue dotted line, and sources with no detectable polarisation at this level are shown by the solid black line.

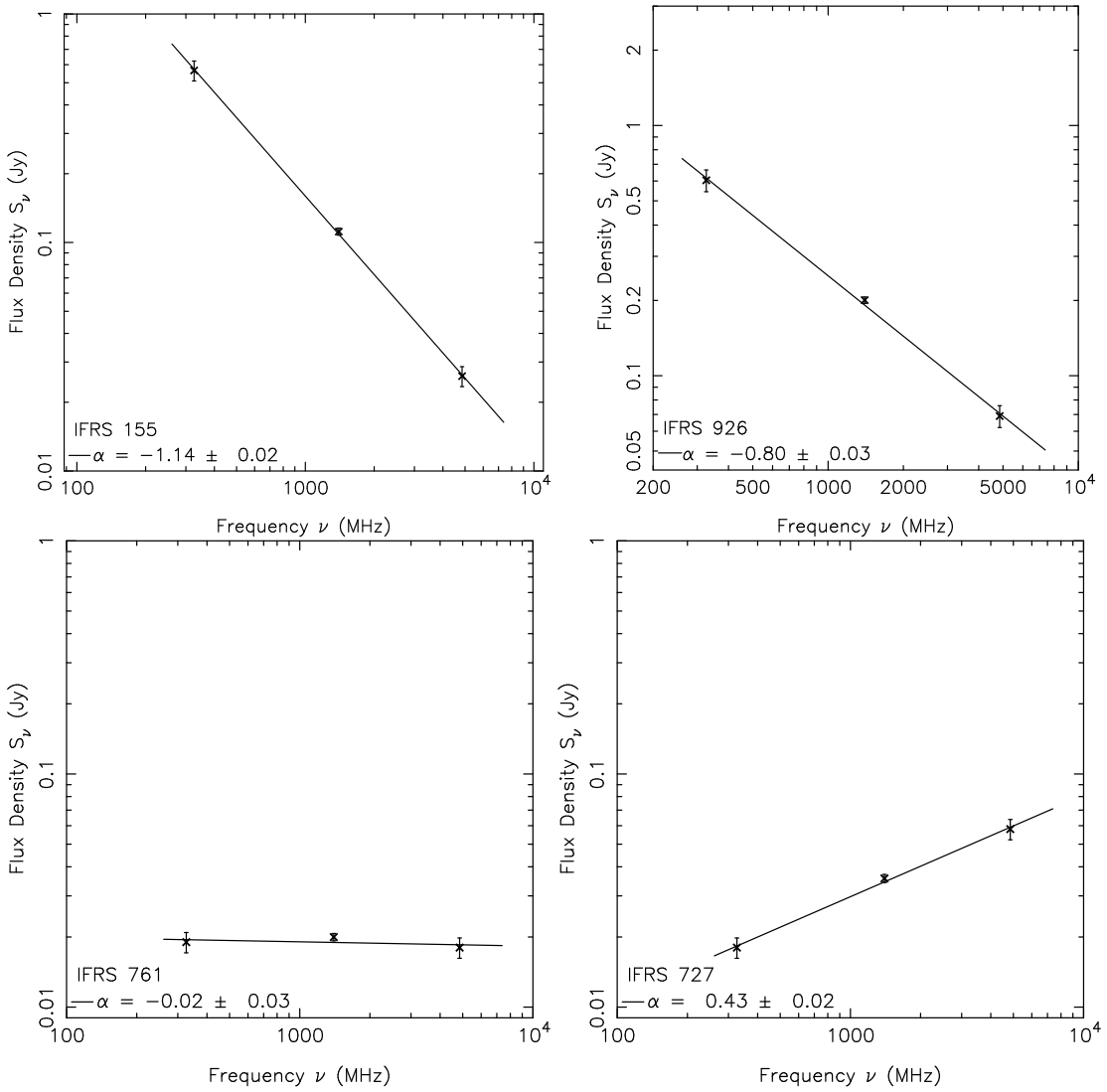

Figure 3.8: The radio spectra of some IFRSs from our sample with a USS (top left), steep (top right), flat (bottom left) and inverted (bottom right) spectral index.

relation, although they are consistent with it. From this we conclude that distance, rather than dust obscuration, is likely to be the main mechanism for the infrared-faintness of our sample of IFRSs. Furthermore, Fig. 1.17 and 1.18 confirm our hypothesis that at least a fraction of IFRSs are indeed high-redshift radio-loud AGN.

3.1.6.1 Supplementary sample

Given that a very small fraction of the IFRSs within our sample had spectroscopic redshifts, we were unable to find sources that occupy a large enough range of IR flux densities to significantly test the $S_{3.4\mu\mathrm{m}} - z$ relation for IFRSs. This is because our selection criteria included an IR-faintness criterion ($S_{3.6\mu\mathrm{m}} < 30$ μJy) and very few *WISE* sources are this faint, with no sources in our sample having $S_{3.6\mu\mathrm{m}} < 10$ μJy. Therefore, we compiled a supplementary sample of objects selected in the same way as our IFRSs, except for the IR-faintness and visual inspection criteria, enabling us to test the relation over a sufficient range of IR flux densities (i.e. with $S_{3.6\mu\mathrm{m}} > 30$ μJy). Matching these with SDSS, we found > 1000 sources with spectroscopy. Fig. 3.10 shows the 3.4 μm flux density as a function of redshift for the supplementary sample alongside the IFRS sample. This shows that the objects in our supplementary sample do indeed follow the $S_{3.4\mu\mathrm{m}} - z$ relation. Since the IR-faintness criterion is set at an arbitrary flux density, the supplementary sample should consist of very similar objects, and therefore, we conclude that IFRSs follow the $S_{3.4\mu\mathrm{m}} - z$ relation, and that the *first generation* IFRSs are therefore located at higher redshifts.

Table 3.4: Sources from our sample with matching spectroscopic redshifts from SDSS DR9. Listed is the SDSS RA and DEC, spectroscopic redshift and uncertainty, the NVSS flux density at 20 cm, the luminosity at 20 cm, the *WISE* flux density and luminosity at 3.4 μm, the flux density ratio between 20 cm and 3.4 μm, the sky separation between the FIRST and SDSS positions, and the class (and subclass) of the spectra as labelled by SDSS. Notes: (1) 'BL' stands for broadline. (2) The luminosities are given at the observed frequency and have not been K-corrected.

RA	DEC	Spectroscopic	S_{20}	L_{20}	$S_{3.4}$	$L_{3.4}$	$S_{20}/S_{3.4}$	Sky Separation	Class
J2000.0		redshift	[mJy]	[W Hz^{-1}]	[μJy]	[W Hz^{-1}]		[arcsec]	
02:06:22.45	−00:43:20.68	2.3767 ± 0.0005	19.9 ± 0.7	8.8 $\times10^{26}$	28.3 ± 5.8	1.2 $\times10^{24}$	703 ± 175	0.124	BL QSO
11:35:41.11	+45:40:42.85	2.1420 ± 0.0007	17.3 ± 0.7	5.9 $\times10^{26}$	29.1 ± 5.5	9.9 $\times10^{23}$	594 ± 140	0.797	BL QSO
11:36:34.93	+61:06:20.53	2.0296 ± 0.0005	18.3 ± 0.7	5.5 $\times10^{26}$	27.3 ± 5.5	8.2 $\times10^{23}$	670 ± 164	1.360	BL QSO
12:27:43.49	+36:42:55.74	2.1151 ± 0.0015	24.1 ± 0.8	8.0 $\times10^{26}$	28.8 ± 6.2	9.5 $\times10^{23}$	836 ± 216	0.205	QSO
13:29:22.21	+05:20:14.38	2.9943 ± 0.0004	44.5 ± 1.4	3.4 $\times10^{27}$	29.9 ± 6.4	2.3 $\times10^{24}$	1487 ± 374	0.251	QSO
13:55:04.58	+36:38:02.00	2.2817 ± 0.0006	15.9 ± 0.6	6.4 $\times10^{26}$	28.8 ± 5.6	1.1 $\times10^{24}$	555 ± 133	0.184	BL QSO
14:08:55.02	+55:52:17.96	2.5526 ± 0.0002	62.9 ± 1.9	3.3 $\times10^{27}$	26.4 ± 5.0	1.4 $\times10^{24}$	2380 ± 537	0.393	BL QSO
14:19:18.81	+39:40:35.87	0.0196 ± 0.0000	18.5 ± 1.0	1.6 $\times10^{22}$	26.7 ± 4.4	2.3 $\times10^{19}$	695 ± 159	0.500	SFG
14:29:48.64	−02:59:21.28	2.6837 ± 0.0005	18.7 ± 0.7	1.1 $\times10^{27}$	27.4 ± 5.8	1.6 $\times10^{24}$	682 ± 175	0.115	BL QSO
14:38:21.80	+34:40:00.94	2.3452 ± 0.0010	10.7 ± 0.5	4.6 $\times10^{26}$	20.4 ± 4.3	8.7 $\times10^{23}$	526 ± 141	0.324	QSO
14:52:51.72	+52:39:56.05	2.3372 ± 0.0005	126.1 ± 3.8	5.3 $\times10^{27}$	22.7 ± 4.7	9.6 $\times10^{23}$	5551 ± 1349	0.131	BL QSO
14:55:06.54	+06:40:18.92	2.2183 ± 0.0003	51.5 ± 1.6	1.9 $\times10^{27}$	23.0 ± 5.0	8.6 $\times10^{23}$	2237 ± 574	0.081	BL QSO
15:16:09.85	+22:25:07.80	2.7756 ± 0.0008	20.1 ± 0.7	1.3 $\times10^{27}$	23.1 ± 4.5	1.5 $\times10^{24}$	871 ± 207	0.036	QSO
15:17:03.80	+24:01:27.51	2.9306 ± 0.0005	18.1 ± 0.7	1.3 $\times10^{27}$	29.2 ± 4.4	2.1 $\times10^{24}$	620 ± 120	0.260	BL QSO
15:20:44.37	+27:06:36.38	2.7324 ± 0.0003	46.8 ± 1.5	2.9 $\times10^{27}$	25.9 ± 4.7	1.6 $\times10^{24}$	1803 ± 393	0.218	BL QSO
15:33:17.30	+12:18:00.89	2.7974 ± 0.0016	23.3 ± 0.8	1.5 $\times10^{27}$	25.0 ± 4.3	1.6 $\times10^{24}$	932 ± 197	0.261	BL QSO
15:38:26.90	+14:55:05.29	2.6189 ± 0.0002	15.1 ± 0.6	8.4 $\times10^{26}$	27.1 ± 5.2	1.5 $\times10^{24}$	558 ± 134	1.428	BL QSO
15:43:14.72	+32:51:38.19	2.2652 ± 0.0003	50.3 ± 1.6	2.0 $\times10^{27}$	20.2 ± 4.2	7.9 $\times10^{23}$	2495 ± 617	0.759	BL QSO
17:26:16.51	+32:16:20.01	2.6405 ± 0.0008	28.4 ± 0.9	1.6 $\times10^{27}$	24.2 ± 4.5	1.4 $\times10^{24}$	1175 ± 267	0.203	BL QSO

3.1.7 X-ray data

El Bouchefry (2009) identified an X-ray counterpart in the *Chandra* XBoötes survey for one of the IFRSs from our sample (IFRS ID 545 in full catalogue). The source respectively has a soft (0.5−2 keV), hard (2−7 keV) and full-band (0.5−7 keV) X-ray flux of 0.44, 0.46 and 0.99 $\times 10^{-15}$ erg s^{-1} m $^{-2}$. This gives a hardness ratio (HR)[2] of $-0.60^{+0.23}_{-0.29}$, from which El Bouchefry (2009) concludes that the source is a type 1 (unobscured) AGN. The IFRS has an X-ray to optical flux ratio of $\log(f_{\rm X}/f_{\rm opt}) = -0.29$, which El Bouchefry (2009) states is well within the expected locus for a typical AGN (0 ± 1), rather than that for a SFG or a low luminosity AGN, which typically have $\log(f_{\rm X}/f_{\rm opt}) \leq -1$. The source is fitted with a photometric redshift of $z = 0.605^{+0.727}_{-0.499}$. However, this is an incorrect photometric redshift, since we find the SDSS source at this positions has a spectroscopic redshift of $z = 2.3452 \pm 0.0010$ (row 10 in Table 3.4). At this distance, the source has a full-band X-ray luminosity of $L_{\rm X} = 4.22 \times 10^{36}$ W.

Further cross-matches from the *Chandra* and *XMM-Newton* X-ray Telescopes were searched for within a 5″ radius of the FIRST radio positions for our entire sample using the *Chandra* Data Archive[3] and the *XMM-Newton* Science Archive (XSA)[4]. No additional matches were found.

The *ROSAT* All-Sky Survey (RASS) bright and faint source catalogues (Voges et al., 1999, 2000) were searched for matches within 10″ of the FIRST radio positions, and only one match from the faint source catalogue was returned, which had RXS designation J144102.9+534040. These represent the first X-ray counterparts of IFRSs yet found.

3.2 Discussion

3.2.1 How our sample relates to the original IFRSs

Our sample consists of much brighter IFRSs than the original first generation IFRSs discovered in ATLAS, since the radio and infrared flux densities are much larger. We suggest that this is due to them being lower-redshift counterparts of the first generation IFRSs. Both generations of IFRSs have ratios of $S_{20\rm cm}/S_{3.4\mu\rm m} > 500$ and flux densities $S_{3.4\mu\rm m} < 30\,\mu$Jy, so they are likely to be from the same parent population. Our IFRSs are brighter, and have lower $S_{20\rm cm}/S_{3.4\mu\rm m}$ ratios. Our sample has a lower sky density than the first generation IFRSs, which is consistent with them being brighter (and probably closer) versions of the same object.

We find a higher fraction of resolved IFRSs compared to Middelberg et al. (2011b), who found no resolved IFRSs. AGN may appear compact in the radio either because (1) their jets are small, suggesting they are quite young (O'Dea, 1998), or (2) they are oriented with their lobes pointed along the line-of-sight of the observer. We find a number of GPS and CSS sources, which is consistent with the first scenario. This suggests that the more compact first generation IFRSs may be more representative of younger radio galaxies than our IFRSs, possibly located at higher redshift in the younger universe.

The optical magnitudes of our sample are also consistent with this interpretation. Norris et al. (2011a) studied a very deep sample of IFRSs and found a median 3.6 μm flux density of $\sim$0.2 μJy, while Garn and Alexander (2008) studied a moderately deep sample and found an upper limit on the median 3.6 μm flux density of $\sim$3.1μJy, which is approximately 10 times

[2]The HR is defined as HR $= h - s/h + s$, where h and s are respectively the number of counts detected in the $2-7$ keV and $0.5-2$ keV bands.

[3]http://hla.stsci.edu/hlaview.html

[4]http://xmm.esac.esa.int/xsa/index.shtml

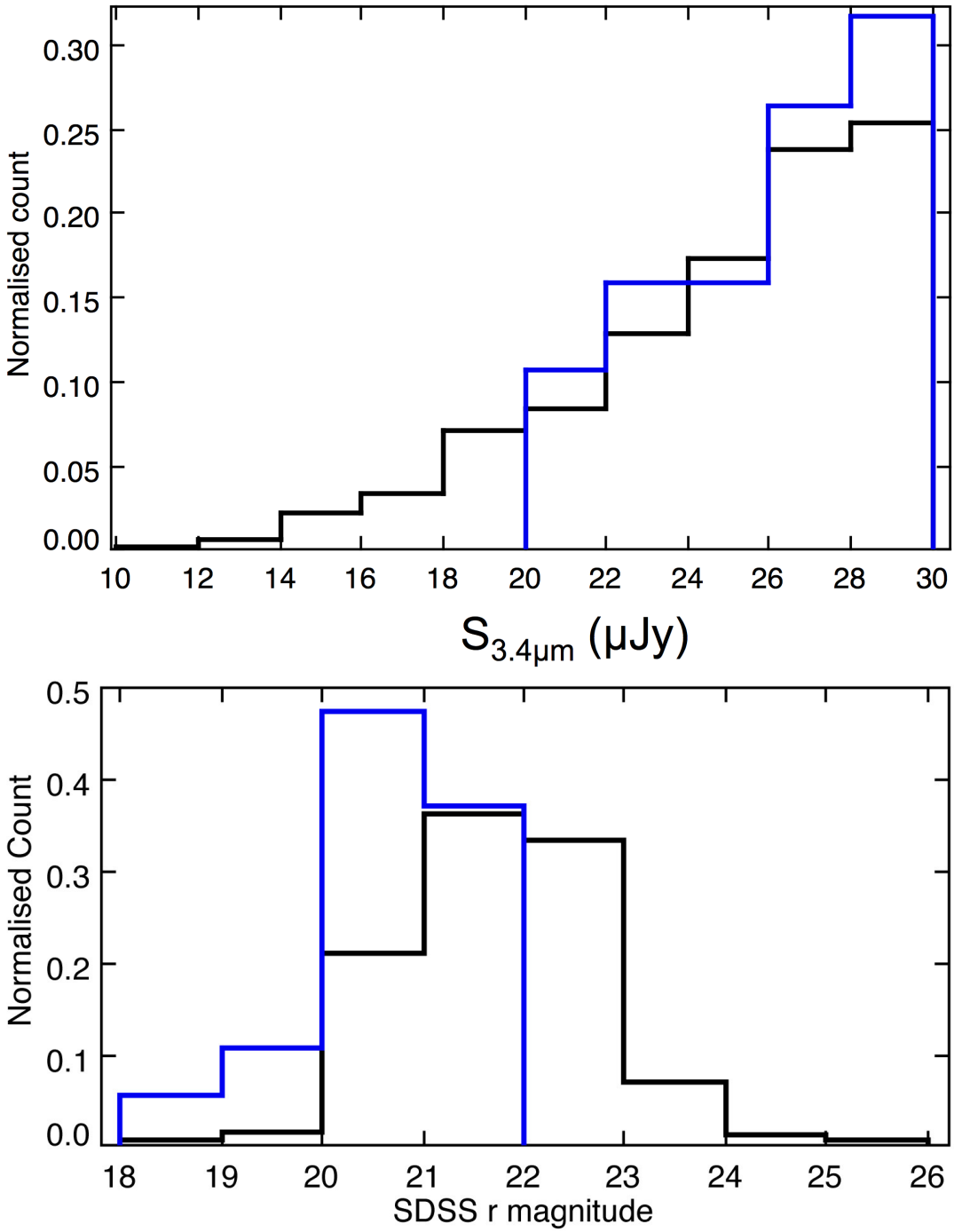

Figure 3.9: Normalised histogram of the 3.4 μm flux density (top) and the SDSS r magnitudes (bottom) for the 19 IFRSs with spectroscopic redshifts (blue) and the IFRSs without redshifts (black). It can be seen that the sources in blue are more representative of the bright end of the distribution at both wavelengths. The distribution of r magnitudes becomes highly incomplete above the SDSS limiting magnitude of 22.2.

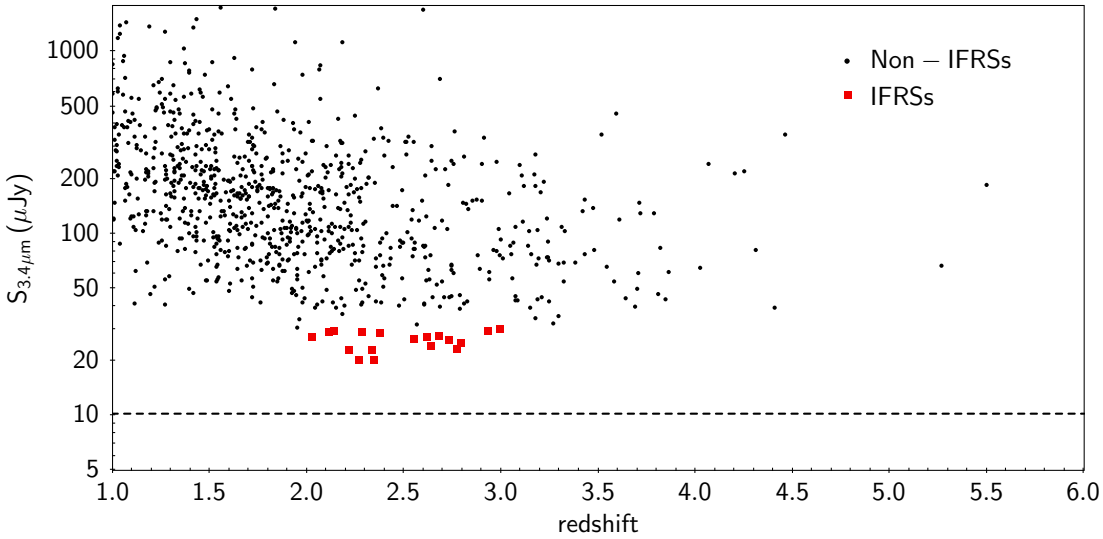

Figure 3.10: The 3.4 μm flux density as a function of redshift within the range $1 < z < 6$ (as in Fig. 1.18). The 833 sources plotted in black are from the supplementary sample (non-IFRSs) that was selected in the same way as our IFRS sample, excluding the infrared-faintness ($S_{3.6\mu m} < 30$ μJy) and visual inspection criteria. These sources strongly follow the same $S_{3.6\mu m} - z$ relation as seen for HzRGs. The red boxes show the 18 IFRSs with redshifts of $z > 1$ from our final sample of 1317 IFRSs, only 19 of which have measured redshifts. The dotted line indicates the flux density of the weakest source from our final sample.

brighter. We studied a bright sample of IFRSs and found a median 3.4 μm flux density of ∼26 μJy, approximately 10 times brighter still. If this difference is simply due to cosmic distance, rather than obscuration, we expect the optical brightness to scale in the same way. If the Huynh et al. (2010) optical magnitudes are representative of the population as a whole, the faintest IFRSs selected from the deepest surveys have typical optical magnitudes of about $z_{\rm AB} = 26$, while the brighter Garn and Alexander (2008) IFRSs have typical magnitudes of $r_{\rm AB} = 24.4$, for which we expect a typical colour $z - r = -0.6$, giving $z_{\rm AB} \sim 23.8$. Our median SDSS magnitude of $z_{\rm AB} = 21$ is 100 times brighter than those from Huynh et al. (2010), the same factor brighter as for the infrared emission. This suggests that obscuration is not the dominant effect in reducing the infrared flux density for these IFRSs, since the optical and IR magnitudes scale in the same way.

Furthermore, the spectroscopic redshifts from our sample suggest that the brighter IFRSs are found at $2 < z < 3$ and form a continuous population with the faintest IFRSs which are believed to be at $z > 3$. The distribution of redshifts we find is consistent with the results from Huynh et al. (2010), who found that IR-detected IFRSs cannot be explained easily at $z < 2$, but can be modelled at $z \geq 2$. Huynh et al. (2010) find that the radio-loud quasar 3C 273 at $z \geq 2$ accurately models the SEDs of the IFRSs from their sample. Similarly, all our IFRSs in Table 3.4 are radio-loud quasars.

The place occupied by our IFRSs in $S_{20\rm cm}/S_{3.4\mu m}$ space (Fig. 1.17) suggests that HzRGs, first generation IFRSs and *WISE* IFRSs are all from the same parent population of radio galaxies.

3.2.2 Are IFRSs misidentifications?

WISE sources are dominated by low-redshift, low-luminosity objects at $z < 1$ (Yan et al., 2013).

So objects mistakenly identified with *WISE* sources should have low redshifts, whereas all of our objects with spectroscopy except one have $z > 2$. This result cannot therefore be attributed to misidentifications. Furthermore, our misidentification rate is estimated to be $0.24 \pm 0.27\%$ (see section 2.1.4), so $\sim$3 of our sources are false-positives.

3.2.3 Are IFRSs hotspots or lobes?

The VLBI detections from Norris et al. (2007) and Middelberg et al. (2008b) suggest that at least a third of IFRSs are not radio lobes. Additionally, the majority of IFRSs are unresolved at high resolution. Middelberg et al. (2011b) find the vast majority of sources are unresolved on scales of $\sim$2 arcsec. From our sample, 845 (64%) of our sources are unresolved at the 5 arcsec FIRST resolution, which puts an upper limit of $\sim$ 30 kpc on their projected linear size at $z > 0.5$.

Werner et al. (2012) found *Spitzer* observations of hotspots in the radio lobes of FR II galaxies, ranging in IR flux density from $< 1\,\mu$Jy up to $\sim$70 μJy. It is therefore possible that our sample consists of a number of hotspots. However, 213 of our sources are identified as double-lobed galaxies which have hotspots that are not coincident with the corresponding faint IR source (e.g. Fig. 2.4). Additionally, careful inspection was carried out to ensure that the faint *WISE* sources did not coincide with an identifiable lobe or hotspot. Furthermore, if they were hotspots, the redshifts shown in Table 3.4 would reflect the overall distribution of the radio galaxy population, very few of which are at $z > 2$. We therefore conclude that they are not hotspots.

3.2.4 Are IFRSs nearby AGN?

18 out of the 19 spectroscopic redshifts from our sample are $z \geq 2$. This shows that the brightest members of our sample are not nearby AGN. Additionally, we find steep radio spectral indices for most of our sample, as well as many USS sources. This shows that our IFRSs are more likely to be taken from a higher redshift population, particularly in the case of the USS sources. However, we cannot rule out the possibility that some small fraction of our sample is located at low redshift and is suffering from significant dust extinction.

3.2.5 The nature of IFRSs

In § 3.1.2.4, we showed that most of our IFRSs are not SFGs. We have also ruled out the hypotheses that their majority is made up of misidentifications, hotspots, lobes or nearby AGN. Furthermore, it has been ruled out that IFRSs are pulsars (Cameron et al., 2011). The radio spectra, *WISE* colours and many other properties of our sample are consistent with the IFRSs being high-redshift radio-loud AGN. Above all, we have shown that the brightest IFRSs have spectroscopic redshifts > 2, and so we conclude that the IFRSs are most likely high-z radio-loud AGN.

Previous studies of IFRSs have been almost entirely unsuccessful in detecting their emission in the infrared and optical bands, resulting in speculations about their nature based only on their radio detections and upper limits in the infrared and the optical. We have shown that there exists a significant population of IFRSs that can be detected in the infrared and optical, which show similar properties to these first generation IFRSs. IFRSs seem to span a continuous population of high-redshift AGN which are from the same parent population of AGN from which HzRGs and their lower redshift versions come.

If IFRSs are high-redshift AGN and follow the relation between redshift and 3.4 μm flux density, where those with lower infrared flux densities are found at even higher redshifts, then we have found a very effective way to find HzRGs using their 3.4 μm emission, a technique parallel to using the K-z diagram (Willott et al., 2003). Therefore *WISE* provides a great new all-sky method to find many HzRGs, which will be valuable in studying cosmic AGN evolution.

3.3 Conclusion

We have compiled the first detectable sample of IFRSs, consisting of 1317 sources generated by cross-correlating the NVSS, FIRST and *WISE* surveys. Below we summarise and discuss our results.

- Our sample is brighter and has a lower sky density than first generation IFRSs, while retaining the same values of distance-independent measures such $S_{20cm}/S_{3.4\mu m}$. This suggests that our sample consists of a lower-redshift, brighter population of IFRSs.
- The 403 sources that have reliable measurements or upper limits of the 22 μm flux density all have $q_{22} < -0.23$, which is strong evidence that they are AGN, rather than SFGs.
- The *WISE* colours of our sources significantly detected at 3.4, 4.6 and 12 μm are similar to those of obscured AGN, QSOs and Seyferts.
- 41 IFRSs are polarised at levels $\geq 8\sigma_{QU}$, with fractional polarisations ranging between $1 < \Pi < 14\%$, and RMs ranging from -45 to 54 rad m^{-2}.
- There are 213 sources that contain double-lobed radio morphologies. The majority of our sources are unresolved, suggesting that most of them are either beamed radio sources or young radio sources with small jets.
- We derive radio spectra for a significant fraction of our sample and find that the majority have steep spectral indices, and many have USS, suggesting that they are more likely to be located at high redshift than low redshift. We also find 32 GPS sources and 124 CSS sources, which is consistent with some of our IFRSs being young radio sources with small jets.
- Amongst our brightest IFRSs, we find 19 spectroscopic redshifts from SDSS DR9, 18 of which are quasars located at $2 < z < 3$, giving strong evidence that our IFRSs are high-redshift radio-loud AGN.
- One of these sources at $z = 2.3452$ has an X-ray detection, at which redshift it has a luminosity of $L_X = 4.22 \times 10^{36}$ W. The X-ray hardness ratio suggests that the source is an unobscured AGN.
- The properties of our large sample of IFRSs imply that they are radio-loud AGN at $z \geq 2$. We suggest that the fainter IFRSs that are undetectable in the infrared represent a population of radio sources at even higher redshift.
- Searching for IFRSs is an effective all-sky method for finding HzRGs and investigating cosmic AGN evolution.

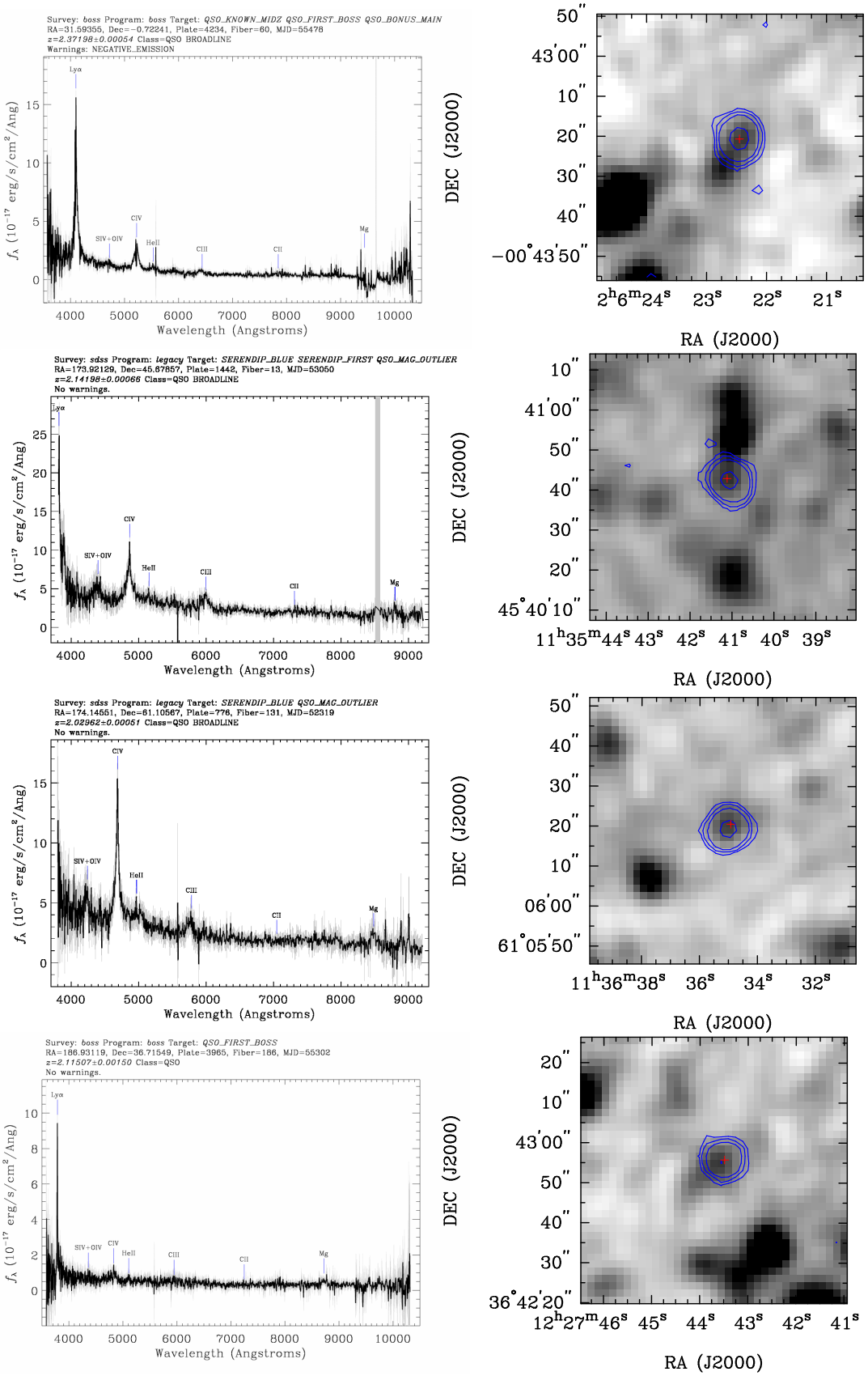

Figure 3.11: Spectra and postage stamps of the 19 IFRSs with spectroscopy in SDSS DR9, appearing in the same order as in Table 3.4. On the right, the background image shows the *WISE* 3.4 μm detection, the red cross represents the position of the SDSS spectroscopy, and the contours mark the FIRST source at 20 cm, at levels of 3, 6, 12, 64, 256 and 1024 times the local noise level. On the left, the grey spectra represent the errors per pixel, and any vertical grey bands represent the masked pixels.

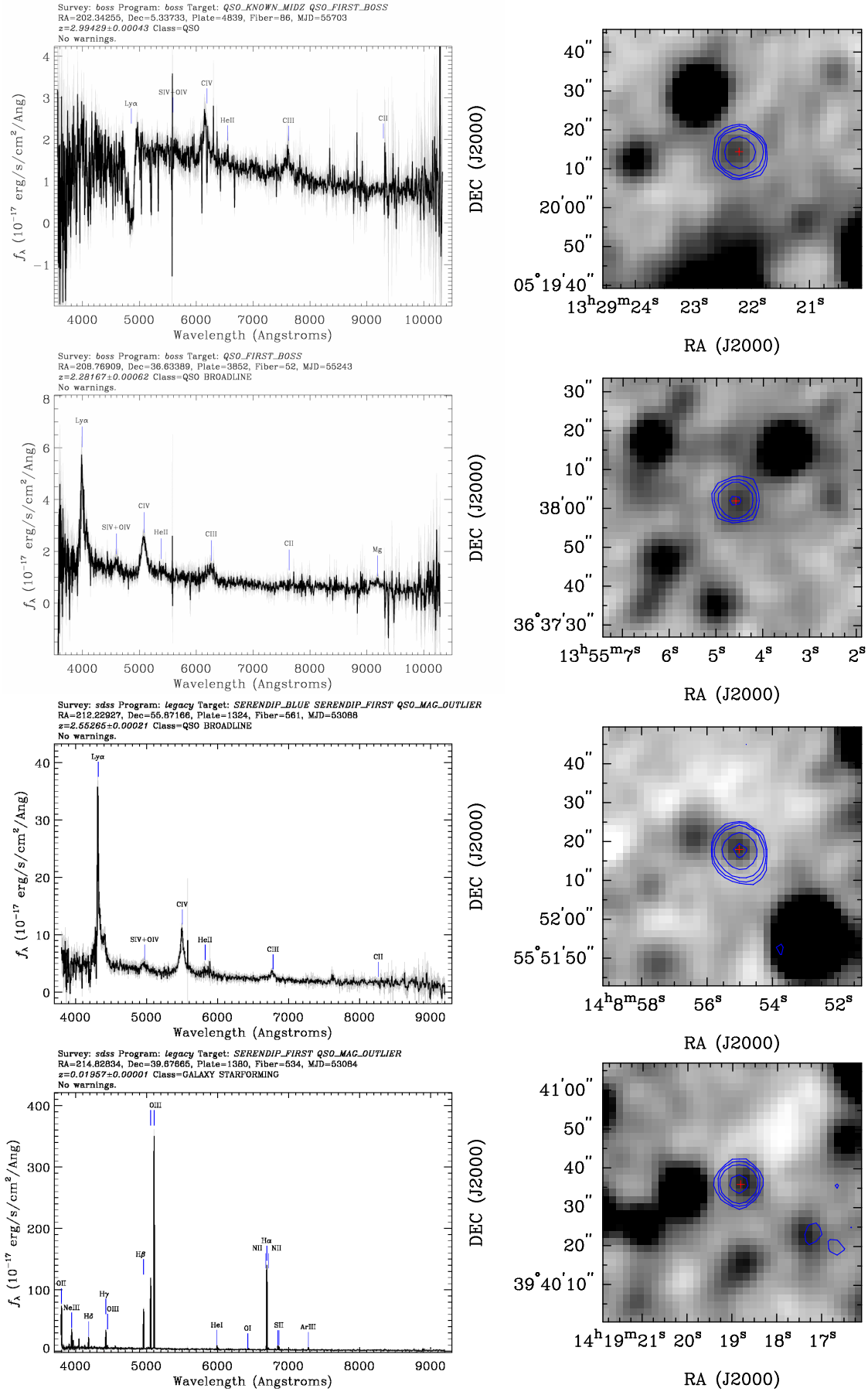

Fig. 3.11. (continued)

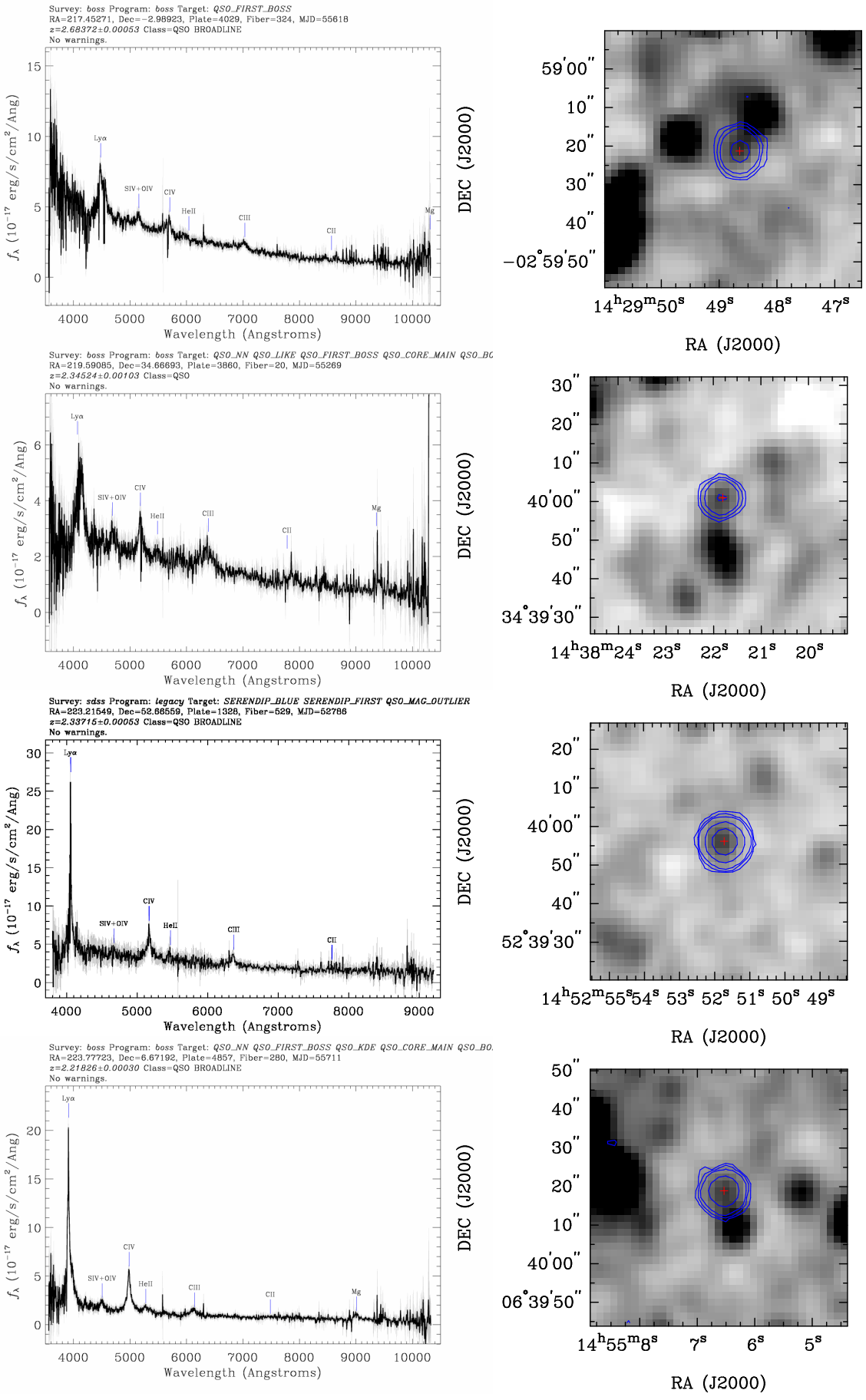

Fig. 3.11. (continued)

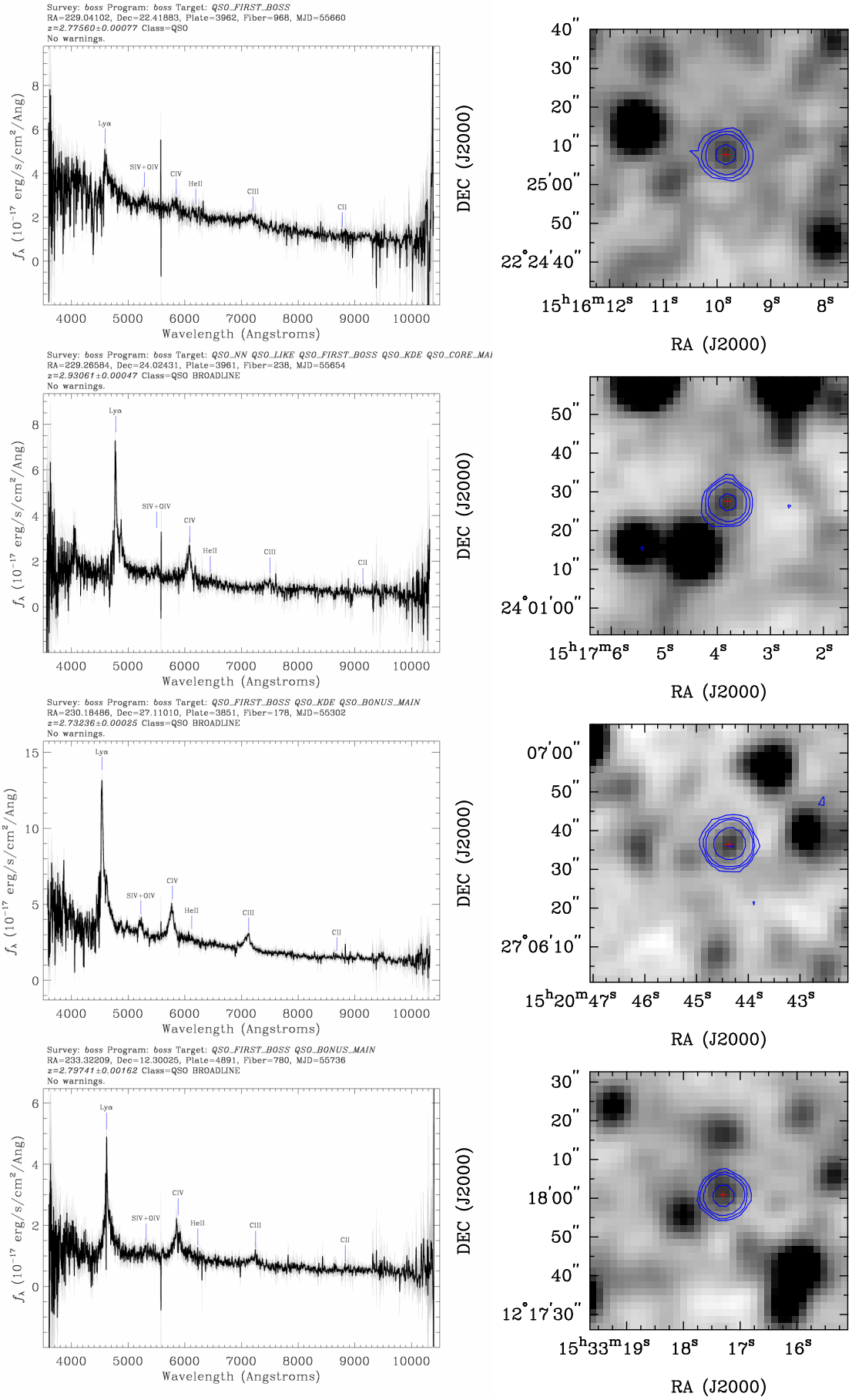

Fig. 3.11. (continued)

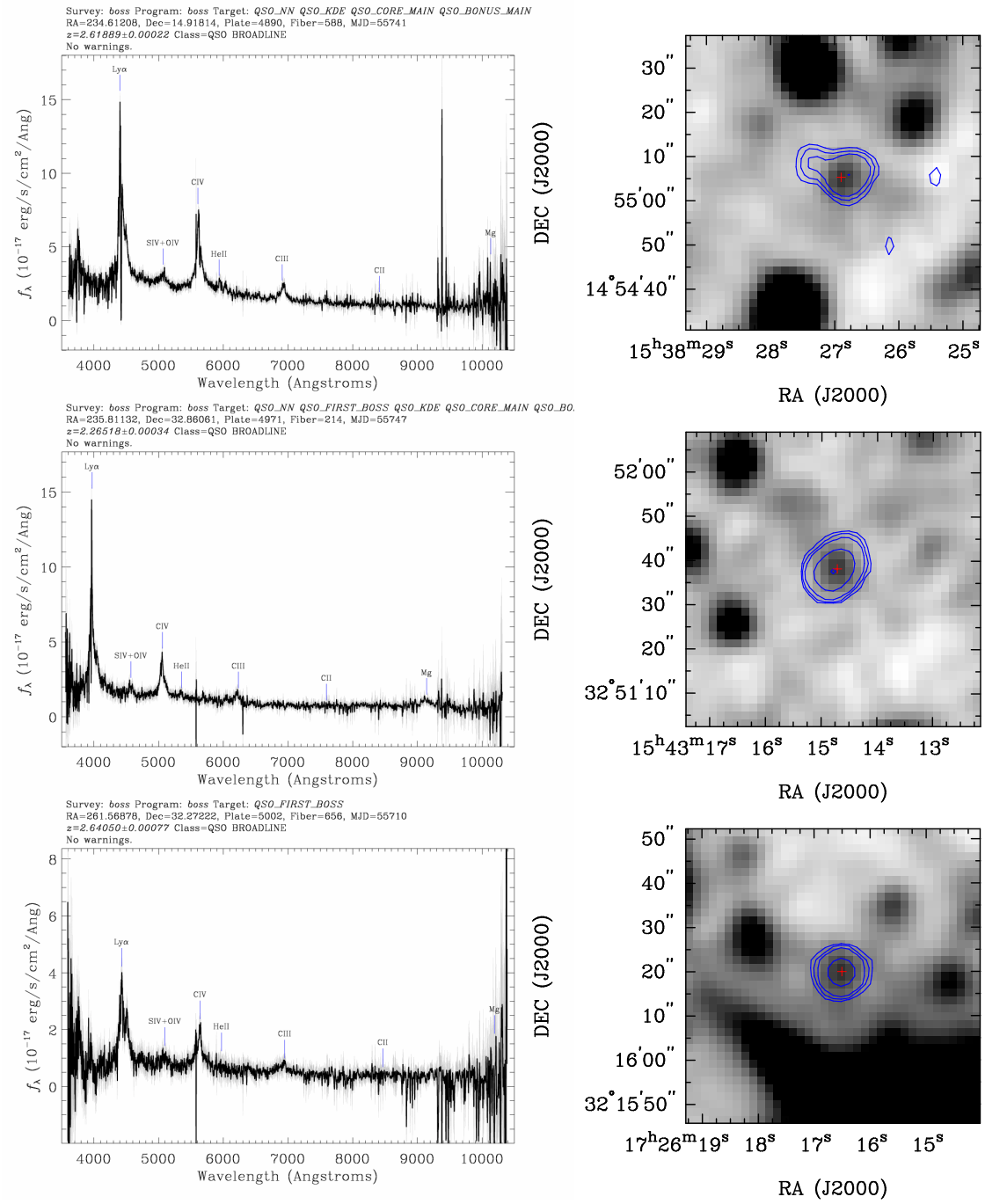

Fig. 3.11. (continued)

Section 3.4 is taken from Herzog et al. (2015a), to which I contributed ∼10%, which included originally providing a master catalogue, guidance throughout the project, and giving comments on the paper. The text covering their results remains the same except for formatting and minor editorial changes.

3.4 Follow-up VLBI observations of IFRS sample

In this paper, we test the AGN content in IFRS based on VLBI observations with the Very Long Baseline Array (VLBA) of a large number of sources taken from the all-sky catalogue of IFRS (Collier et al., 2014). Whereas the high redshifts of IFRS have been recently confirmed based on spectroscopic data, the evidence for the presence of AGNs in IFRS is mainly indirect. So far, only two AGNs have been unquestionably confirmed in IFRS based on VLBI observations. In this work, we test the hypothesis that IFRS contain AGNs in a large sample of sources using VLBI.

Throughout this paper, we use flat ΛCDM cosmological parameters $\Omega_\Lambda = 0.7$, $\Omega_\mathrm{M} = 0.3$, $H_0 = 70$ km s^{-1} Mpc^{-1} and the calculator by Wright (2006). We quote 1σ confidence intervals of binomial population proportions based on the Bayesian approach, following Cameron (2011).

3.4.1 Sample and observations

We selected all IFRS from the catalogue from Collier et al. (2014) which were located within 1 deg of a VLBA calibrator. This low angular separation between source and calibrator ensured the phase coherence required for VLBI observations. Since 1.4 GHz VLBI observations of the calibrators were not available, we required the calibrators to have a 2.3 GHz flux density of at least 0.2 Jy on a baseline of 5000 km. Out of the 1317 IFRS presented by Collier et al. (2014), 110 were found to provide a calibrator which fulfills the given conditions.

A VLBI detection provides unambiguous evidence for an AGN because compact radio emission in AGNs is a non-thermal process and results in brightness temperatures of more than 10^6 K to which our observations are sensitive. In contrast, compact radio emission in starburst galaxies, which is usually dominated by thermal free-free emission, is represented by brightness temperatures of around 10^4 K (e.g. Condon et al., 1991). Although brightness temperatures of 10^6 K can also be produced by very luminous radio supernovae (SNe; Huang et al., 1994; Smith et al., 1998), Kewley et al. (2000) showed that the probability for a VLBI-detected radio SN in a galaxy sample is very low. Therefore, a VLBI detection provides strong evidence for an AGN. However, it should be noted that the reverse is not true, i.e. the non-detection of a source in a VLBI observation does not imply the non-existence of an AGN. Instead, a VLBI non-detection implies significant extended emission compared to the compact core. The ratio of extended emission to core emission depends on beaming which can boost or suppress the compact core emission, AGN age, and the surrounding medium, affecting the brightness and extent of the diffuse radio lobes.

Since this is a detection experiment, the (u, v)-coverage is not critically important and a minimum number of six out of ten VLBA antennas was requested. Since the individual observations were short and independent of the weather conditions because of the observing frequency of 1.4 GHz, the observations were scheduled in filler time. Although the maps resulting from the data will be of rather poor quality, they will unambiguously resolve potential compact components.

Out of 110 proposed objects, 57 IFRS were observed in semester 14A in project BH197. The 57 observed IFRS were randomly selected based on the IFRS positions and available filler time at the VLBA. These observed sources have 1.4 GHz integrated flux densities between 11 mJy and 183 mJy in the NRAO VLA Sky Survey (NVSS; Condon et al., 1998). The VLBA observations were set to a bandwidth of 32 MHz in each of the eight basebands which were observed in dual polarisation at 1.4 GHz, resulting in a total data rate of 2048 Mbps.

Each of the 57 epochs had a total observing time of one hour. We decided to use two different approaches for the scan settings, depending on the distance between source and calibrator. If the separation between source and calibrator was less than $25'$, we continuously pointed at the position in between IFRS and calibrator to prevent unnecessary nodding between the two sources. If the separation was more than $25'$, we alternately observed the calibrator for 60 s and the source for 225 s, starting and ending with a scan on the calibrator. The resulting observing time on the IFRS was around 45 min. The data were correlated using the VLBA Distributed FX (DiFX) software correlator (Deller et al., 2007, 2011).

3.4.2 VLBA data calibration, optical properties, and redshifts

3.4.2.1 Data calibration, imaging, and flux measurement of the VLBA data

Calibration and imaging of the individual epochs was carried out based on a ParselTongue script. ParselTongue (Kettenis et al., 2006) is a Python-based interface to the Astronomical Image and Processing System[5] (AIPS). The calibration and imaging strategy used here is very similar to the procedure described by Deller and Middelberg (2014). However, we calibrated the amplitudes using the technique suggested by VLBA Scientific Memo #37 (R. Craig Walker; Dec 15, 2014).

In the pipeline, we loaded the data into AIPS and applied a priori flags and manual flags. We then corrected for ionospheric effects using the task `TECOR`, applied the latest earth orientation parameters, and corrected for parallactic angles, in the latter cases using the task `CLCOR`. Amplitudes were calibrated based on autocorrelation data using the task `ACCOR`. We corrected for primary beam effects using the task `CLVLB`, following the procedure outlined by Middelberg et al. (2013). Delay correction was carried out based on the calibrator, using the task `FRING` and a solution interval of 2 min. We applied a bandpass correction using the task `BPASS`. The new task `ACSCL`, implemented in AIPS in consequence of the flux density calibration errors described in the VLBA Scientific Memo #37, kept the calibrated autocorrelation values at unity. The flux density calibration was completed by using `APCAL`, calibrating the amplitudes based on system temperatures and gains. We used the AIPS/ParselTongue implementation of Pieflag (Middelberg, 2006), *dynspec-flagger*, to automatically flag data affected by interference. Using the task `CALIB`, we performed one iteration of phase and amplitude self-calibration on the calibrator and applied the solution on the target. Finally, we imaged the (u, v) data based on the task `IMAGR` into a map of 2048×2048 pixels with a pixel size of 1 milliarcsecond (mas)—matching the angular resolution of ~ 5 mas—using uniform weighting. In this step, we cleaned the dirty image in a given box, down to a flux of three times the rms or up to 500 iterations.

The mean synthesised beam size in our observations is $14.3 \times 4.7\,\mathrm{mas}^2$. Because the linear scale is limited in a ΛCDM cosmology at redshifts $0.5 \leq z \leq 12$ between 4 kpc/″and 8.5 kpc/″, we were able to convert this beam size over this redshift range to an area of between 57 pc×19 pc and 122 pc × 40 pc. The rms in the final maps is around $60\,\mu\mathrm{Jy\,beam}^{-1}$, depending on the number of antennas. Of the 57 observations, 31, 21, 4, and 1 were carried out with 10, 9, 8, and

[5] `http://www.aips.nrao.edu/`

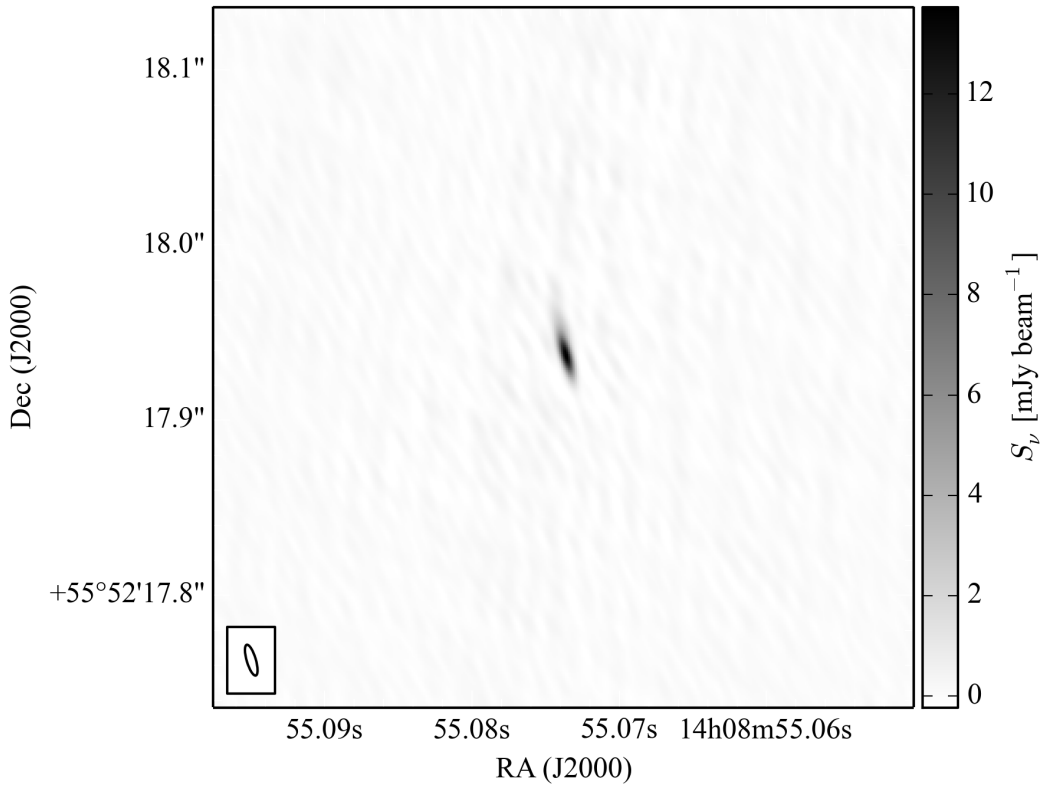

Figure 3.12: VLBA map of IFRS F0398. The source is slightly resolved with a peak flux density of 13.7 mJy beam^{-1} and an integrated flux density of 17.2 mJy.

7 antennas, respectively. Since the longest VLBA baseline of 8611 km—between the stations Mauna Kea and St. Croix—was available in all observations, the east-west angular resolution of around 5 mas is similar for all 57 observations, whereas the north-south angular resolution varies slightly because of changing antenna availability. As an example, Fig. 3.12 shows the final map of IFRS F0398.

We measured the flux density of each component using the AIPS task `JMFIT`, setting a box of size of 40 pixels around the components. For a few sources, image artefacts resulted in unreasonable fluxes. In these cases, we manually measured flux densities using the task `TVSTAT`. Checks on control sources resulted in consistent flux measurements based on `TVSTAT` and `JMFIT`. For the brighter component in IFRS F0030, we measured the flux density using the `blobcat` package (Hales et al., 2012) because of the complex structure of this source. Following Deller and Middelberg (2014), we set a 6.75σ detection limit for all sources, corresponding to a mean detection sensitivity of around 450 μJy beam^{-1}. Most of our sources are slightly resolved, but insufficiently resolved to determine the morphology. The resulting flux densities und flux density upper limits are summarised in Table 3.5.

Table 3.5: Component catalogue of 57 IFRS observed with the VLBA. Listed is the identifier, the NVSS ID, the FIRST position, the NVSS peak and integrated flux densities, the VLBA peak flux density and integrated flux density, the VLBA S/N, and the VLBA beam size. If a source is found to be composed of several components in the VLBA observations, we list the components individually. In case of a non-detection, we quote a 6.75σ peak flux density upper limit. The identifier follows the numbering by Collier et al. (2014). NVSS and FIRST data are taken from Collier et al. (2014).

Identifier	NVSS ID	RA_{FIRST} J2000.0	Dec_{FIRST} J2000.0	$S_{NVSS,\,peak}$ [mJy beam^{-1}]	$S_{NVSS,\,int}$ [mJy]	$S_{VLBA,\,peak}$ [mJy beam^{-1}]	$S_{VLBA,\,int}$ [mJy]	S/N	$\Theta_{maj} \times \Theta_{min}$ [mas × mas]
F0013	NVSS J014418–092158	01:44:18.196	–09:21:54.77	13.3	13.3	<0.3	–	–	–
F0030_1	NVSS J021557–082517	02:15:57.080	–08:25:17.55	70.7	75.6	4.1	21.8	54.9	14.0 × 4.4
F0030_2	NVSS J021557–082517	02:15:57.080	–08:25:17.55	70.7	75.6	3.5	6.0	45.7	14.0 × 4.4
F0037	NVSS J022022–011017	02:20:22.049	–01:10:16.49	30.0	30.6	1.3	4.8	27.9	13.4 × 4.6
F0052	NVSS J023033–030909	02:30:33.435	–03:09:08.37	49.7	50.5	<0.6	–	–	–
F0072	NVSS J024150–032011	02:41:50.196	–03:20:12.17	19.2	19.2	6.5	11.1	64.4	13.7 × 4.7
F0076	NVSS J024346–050737	02:43:46.908	–05:07:36.51	42.1	43.3	5.5	21.2	74.8	20.7 × 4.7
F0081	NVSS J024700+062831	02:47:00.457	+06:28:34.34	28.7	29.3	<0.3	–	–	–
F0100	NVSS J090337+515142	09:03:37.302	+51:51:42.90	19.7	19.7	10.3	11.2	263.8	14.0 × 4.2
F0106	NVSS J093243+521400	09:32:43.626	+52:13:59.53	13.0	13.3	0.7	1.1	17.4	13.7 × 4.8
F0127	NVSS J104946+531947	10:49:46.291	+53:19:50.81	10.9	15.5	<0.4	–	–	–
F0146	NVSS J112624+375323	11:26:23.726	+37:53:34.75	8.4	16.1	3.6	3.9	74.8	12.4 × 6.0
F0149	NVSS J113330+585506	11:33:29.982	+58:55:05.01	39.4	39.6	24.0	29.3	93.3	16.8 × 4.6
F0154	NVSS J114333+582209	11:43:33.395	+58:22:07.59	15.7	16.5	3.7	7.1	83.6	13.2 × 4.5
F0167	NVSS J115544+495437	11:55:44.856	+49:54:36.55	53.8	54.2	<0.4	–	–	–
F0169	NVSS J115900+474005	11:59:00.500	+47:40:05.26	17.5	17.7	<0.2	–	–	–
F0173	NVSS J120221+482514	12:02:21.184	+48:25:13.80	58.4	59.9	26.4	40.4	248.7	19.8 × 4.7
F0187	NVSS J121731+485954	12:17:31.830	+48:59:53.73	43.9	44.1	<0.4	–	–	–
F0189	NVSS J121814+590516	12:18:14.097	+59:05:16.16	26.9	27.1	0.7	1.0	15.2	15.8 × 4.1
F0194	NVSS J122524+433439	12:25:24.786	+43:34:38.92	25.7	25.7	<0.3	–	–	–

Continued on next page

Identifier	NVSS ID	RA_{FIRST} J2000.0	Dec_{FIRST} J2000.0	$S_{NVSS,\,peak}$ [mJy beam^{-1}]	$S_{NVSS,\,int}$ [mJy]	$S_{VLBA,\,peak}$ [mJy beam^{-1}]	$S_{VLBA,\,int}$ [mJy]	S/N	$\Theta_{maj} \times \Theta_{min}$ [mas × mas]
F0197	NVSS J122743+364252	12:27:43.502	+36:42:55.83	23.8	24.1	<0.3	–	–	–
F0209	NVSS J123952+604958	12:39:52.632	+60:49:55.77	18.9	19.5	3.0	7.1	71.2	14.3×6.1
F0222	NVSS J125148–064218	12:51:48.680	–06:42:17.01	11.6	23.9	<0.3	–	–	–
F0241	NVSS J130316+481558	13:03:16.442	+48:15:57.70	13.8	13.9	6.9	8.1	137.8	12.8×5.7
F0244	NVSS J130748+555452	13:07:48.324	+55:54:50.53	14.2	14.5	1.0	1.3	22.4	13.8×5.0
F0251	NVSS J131322+322105	13:13:22.589	+32:21:10.13	36.1	37.6	<0.4	–	–	–
F0257_1	NVSS J131551+512710	13:15:51.150	+51:27:10.01	36.0	36.7	2.5	5.7	77.3	14.2×4.4
F0257_2	NVSS J131551+512710	13:15:51.150	+51:27:10.01	36.0	36.7	1.2	2.1	35.9	14.2×4.4
F0273	NVSS J132804+431418	13:28:04.382	+43:14:17.27	18.1	18.5	2.2	2.3	39.3	12.7×4.2
F0277	NVSS J133024+221800	13:30:24.695	+22:18:00.36	177.0	179.6	7.8	20.3	104.4	12.3×4.8
F0283	NVSS J133431+543930	13:34:31.807	+54:39:32.23	13.5	14.4	<0.3	–	–	–
F0293	NVSS J133733+591837	13:37:33.098	+59:18:37.68	44.7	45.4	13.6	21.2	214.3	18.3×4.1
F0319	NVSS J134921+081217	13:49:21.396	+08:12:15.75	27.2	27.9	<0.4	–	–	–
F0334	NVSS J135248+093020	13:52:48.328	+09:30:16.60	16.9	17.4	<0.4	–	–	–
F0351	NVSS J135601–012539	13:56:01.445	–01:25:38.70	34.9	35.3	3.0	4.2	51.0	13.0×4.7
F0382	NVSS J140707+285558	14:07:07.241	+28:55:56.39	66.7	68.8	<0.3	–	–	–
F0385	NVSS J140730+040234	14:07:30.593	+04:02:34.61	16.3	16.5	3.1	4.8	55.8	18.1×4.2
F0398	NVSS J140855+555218	14:08:54.995	+55:52:17.62	62.4	62.9	13.7	17.2	184.1	18.1×5.2
F0406	NVSS J141004+024051	14:10:04.764	+02:40:49.82	30.0	32.9	19.3	21.9	219.2	13.6×4.7
F0471	NVSS J142228+264716	14:22:28.909	+26:47:16.63	19.8	19.8	5.1	5.0	136.9	12.5×4.8
F0472	NVSS J142241+363956	14:22:41.669	+36:39:57.74	17.1	18.2	0.7	0.6	14.2	13.4×4.5
F0509	NVSS J143110+360317	14:31:10.868	+36:03:17.05	16.3	18.3	<0.2	–	–	–
F0588	NVSS J144500+624605	14:45:00.769	+62:46:05.55	16.7	17.2	<0.4	–	–	–

Continued on next page

Identifier	NVSS ID	RA_{FIRST} J2000.0	Dec_{FIRST} J2000.0	$S_{NVSS,\,peak}$ [mJy beam^{-1}]	$S_{NVSS,\,int}$ [mJy]	$S_{VLBA,\,peak}$ [mJy beam^{-1}]	$S_{VLBA,\,int}$ [mJy]	S/N	$\Theta_{maj} \times \Theta_{min}$ [mas × mas]
F0611	NVSS J144924+085628	14:49:24.799	+08:56:32.59	36.1	36.8	<0.4	–	–	–
F0633	NVSS J145334–014513	14:53:34.184	–01:45:13.48	18.0	18.1	0.4	2.6	9.5	13.0 × 4.9
F0726	NVSS J150623+103048	15:06:23.301	+10:30:47.54	49.0	50.0	20.8	32.0	317.8	12.4 × 4.3
F0732	NVSS J150649+422059	15:06:49.247	+42:20:59.02	101.8	103.6	9.1	25.5	167.3	13.8 × 5.1
F0787	NVSS J151557+201248	15:15:57.840	+20:12:47.13	17.5	18.0	2.6	3.2	56.6	12.8 × 4.3
F0807	NVSS J151817+042327	15:18:17.648	+04:23:26.84	77.5	78.8	6.5	13.5	58.8	15.8 × 4.2
F0838	NVSS J152348+321541	15:23:48.347	+32:15:43.79	96.5	98.8	<0.3	–	–	–
F0912	NVSS J153826+145505	15:38:26.812	+14:55:05.91	14.7	15.1	<0.6	–	–	–
F1037	NVSS J160235+310832	16:02:35.685	+31:08:33.12	13.9	14.2	1.3	1.4	25.6	16.0 × 4.1
F1111	NVSS J161910+483709	16:19:10.025	+48:37:13.21	12.2	12.6	8.5	10.9	199.4	14.0 × 4.3
F1268	NVSS J172102+333445	17:21:02.788	+33:34:47.29	25.7	26.7	<0.3	–	–	–
F1286	NVSS J172923+390532	17:29:24.122	+39:05:31.52	11.6	11.6	<0.3	–	–	–
F1287	NVSS J173019+460128	17:30:19.022	+46:01:28.48	43.4	43.9	18.4	28.5	309.9	14.5 × 3.9
F1301	NVSS J173517+474300	17:35:17.371	+47:42:59.30	180.0	183.8	0.9	2.6	14.2	12.0 × 6.6
F1305	NVSS J173703+494446	17:37:02.943	+49:44:46.26	23.0	23.4	5.7	7.9	71.3	14.9 × 3.9
F1313	NVSS J174243+621908	17:42:43.642	+62:19:08.65	79.6	82.5	9.2	29.9	176.2	15.2 × 3.7

Table 3.6: Redshift information for those IFRS with SDSS DR10 detections. Listed is the IFRS ID, the u band model magnitude from SDSS DR10, the photometric redshift measured in this work using *EAZY*, and the spectroscopic redshift from SDSS DR10. The SED fitting for F0277 failed.

IFRS ID	u [mag]	z_{phot}	z_{spec}
F0146	20.21 ± 0.05	$1.26^{+0.29}_{-0.25}$	–
F0194	23.82 ± 0.95	$0.78^{+0.42}_{-0.34}$	–
F0197	22.83 ± 0.32	$2.54^{+0.14}_{-0.22}$	2.1150 ± 0.0014
F0273	20.84 ± 0.08	$1.65^{+0.20}_{-0.18}$	–
F0277	24.16 ± 0.86	–	–
F0293	22.94 ± 0.33	$3.02^{+0.09}_{-0.08}$	–
F0398	20.49 ± 0.06	$2.24^{+0.07}_{-0.08}$	2.55265 ± 0.00021
F0726	23.21 ± 0.52	$3.07^{+0.26}_{-0.24}$	–
F0732	22.88 ± 0.27	$2.26^{+0.27}_{-0.28}$	–
F0912	21.55 ± 0.10	$2.47^{+0.06}_{-0.06}$	2.61873 ± 0.00023
F1037	25.14 ± 0.79	$0.39^{+3.77}_{-0.08}$	–

Since observations and data calibration are very similar to the approach taken by Deller and Middelberg (2014) who targeted more than 20 000 sources in their mJy Imaging VLBA Exploration (mJIVE) survey, we expect our flux densities to be of similar accuracy of 20%.

3.4.2.2 Optical properties and redshifts

Our sample was taken from the all-sky IFRS catalogue from Collier et al. (2014) who cross-matched their sources with the Sloan Digital Sky Survey (SDSS) DR9 (Ahn et al., 2012). For the purpose of this work, we cross-matched our sample of VLBA-observed IFRS to the recent SDSS DR10 (Ahn et al., 2014). 53 (93^{+2}_{-5}%) out of our IFRS are covered by SDSS DR10. Eleven (21^{+7}_{-4}%) out of these 53 IFRS provide photometric counterparts which are all close to the sensitivity limit of SDSS.

We used the software *EAZY* (Brammer et al., 2008) with the standard template set to derive photometric redshifts for our sources. Since most IFRS in the catalogue from Collier et al. (2014) are only detected in the WISE bands W1 (3.4 μm) and W2 (4.6 μm)—apart from the radio detections which are not used in the redshift fitting—measuring photometric redshifts is impossible for most of the IFRS in our sample. However, measuring photometric redshifts is possible for those IFRS with SDSS counterparts. For these eleven IFRS in our sample with SDSS counterparts, we obtained ten photometric redshifts using *EAZY*. As examples, we show the resulting fits for IFRS F0197 and F0273 in Fig. 3.13. The fitting of IFRS F0277 failed. Table 3.6 summarises the photometric redshifts and—where applicable—spectroscopic redshifts for our subsample of IFRS with SDSS DR10 counterparts. Fig. 3.14 shows the photometric redshifts as a function of the spectroscopic redshifts for the three IFRS in our sample for which SDSS DR10 provides spectroscopic redshifts.

Based on the SEDs resulting from the fitting of photometric redshifts, we find that most of our fitted IFRS are very blue. These characteristics can be explained by a type I AGN in the optical. However, we stress that we might be significantly affected by selection bias since these IFRS are very close to the detection sensitivity of SDSS and SDSS is more sensitive to blue objects. Nevertheless, this study shows that at least some IFRS are very blue, non-dusty

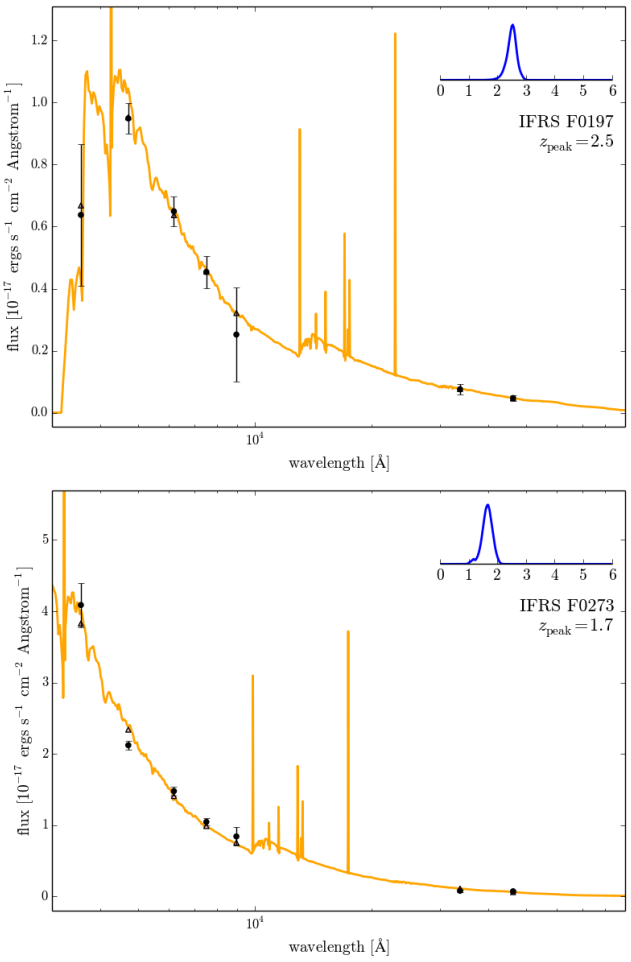

Figure 3.13: Resulting photometric redshift fit from *EAZY* for IFRS F0197 (left) and F0273 (right). The SED (orange line) shows the best fit template based on the peak redshift in the observer's frame. Black dots with error bars represent photometric data points of the IFRS, whereas black triangles show the flux density of the fitted SED at the same wavelengths. The subplots in the upper right of both plots show the redshift-probability distribution. The redshift of the peak in the probability distribution is quoted below each subplot.

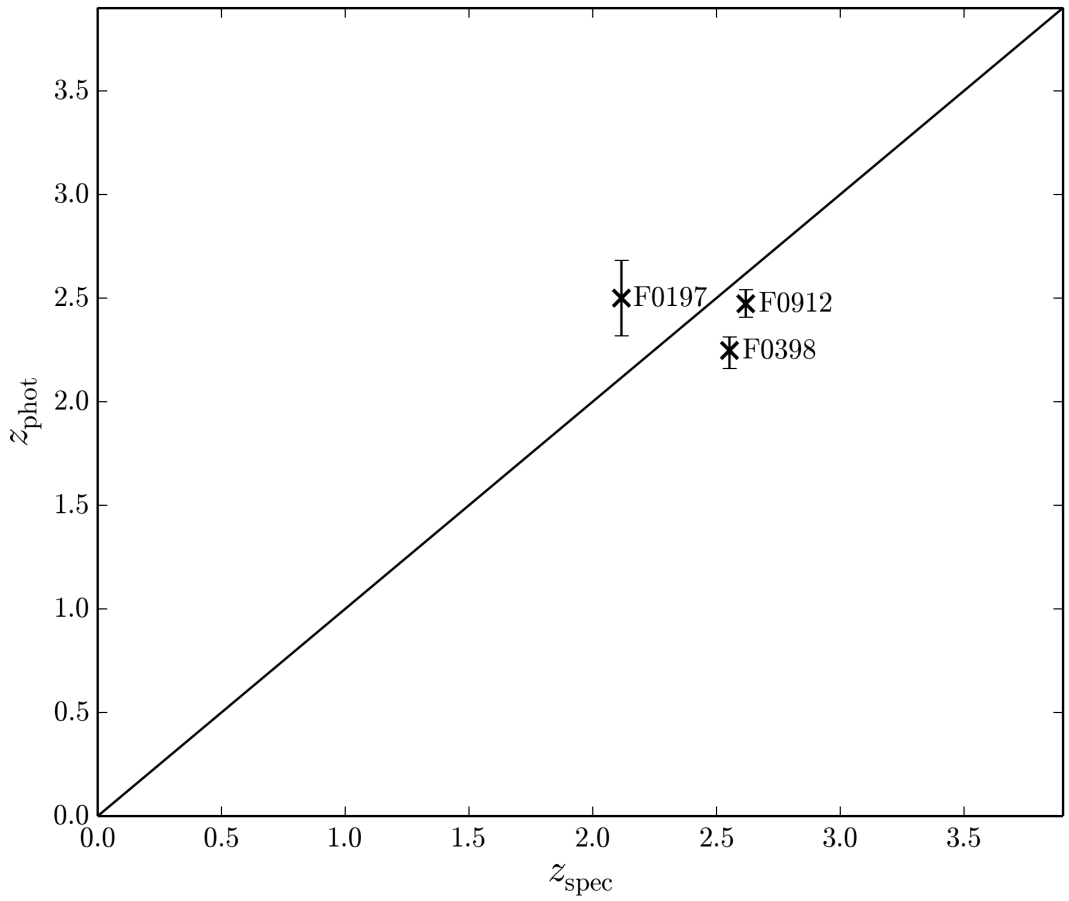

Figure 3.14: Comparison of the photometric redshifts obtained from *EAZY* and the spectroscopic redshifts from SDSS DR10. The error bars show the 1σ uncertainties in the photometric redshifts as determined by *EAZY*. The solid line represents the positions of exact agreement between photometric and spectroscopic redshifts.

galaxies.

3.4.3 Analysis

3.4.3.1 VLBI detection fraction

In our VLBA observations, we detected 35 (61^{+6}_{-7}%) out of 57 observed IFRS, showing peak flux densities between 0.4 mJy beam^{-1} and 26.4 mJy beam^{-1} and integrated flux densities between 0.6 mJy and 40.4 mJy as listed in Table 3.5.

The detection of a source in VLBI observations with brightness temperatures above 10^6 K—which is reached for our VLBA observations—is an unambiguous sign for an AGN as discussed in Sect. 3.4.1. However, we note that the reverse is not true, i.e. the non-detection of a source in VLBI observations does not exclude the existence of an AGN. The detection of 35 out of 57 IFRS in our VLBA observations provides strong evidence that most—if not all—IFRS contain AGNs.

VLBI detection fraction compared to other samples:

The detection fraction in our VLBA observations of 61^{+6}_{-7}% down to a 6.75σ detection limit of ~ 0.45 mJy beam^{-1} is significantly higher than the detection fractions found by Garrington et al. (1999) or Deller and Middelberg (2014) who targeted large samples of sources from the Faint Images of the Radio Sky at Twenty centimetres (FIRST; Becker et al., 1995) survey in VLBI observations and detected 35% and 20%, respectively. However, the sensitivity of the respective VLBI observations and the sample selection criteria were different. Garrington et al. (1999) had a detection sensitivity between 1 mJy and 2 mJy and targeted FIRST sources with 1.4 GHz peak flux densities above 10 mJy, whereas Deller and Middelberg (2014) targeted all kinds of FIRST sources without any preselection at a varying detection sensitivity. In order to compare their detection fraction with that of Garrington et al. (1999), Deller and Middelberg (2014) cut their catalogue to FIRST sources with $S_{1.4\,\mathrm{GHz}} > 10$ mJy beam^{-1} and to the VLBI detection sensitivity from Garrington et al. (1999). Deller and Middelberg (2014) found a detection fraction of 36% in that subsample, in agreement with the number from Garrington et al. (1999).

We followed the approach from Deller and Middelberg (2014) and compiled a subsample of our IFRS sample by including only those sources with an arcsec-scale 1.4 GHz flux density above 10 mJy beam^{-1}, ending up with 56 IFRS. Setting our detection sensitivity to 1.5 mJy, we would have detected 25 (45^{+7}_{-6}%) out of these 56 IFRS, i.e. a slightly higher fraction than those from Garrington et al. (1999) and Deller and Middelberg (2014). Using a *Fisher's exact test* (e.g. Wall and Jenkins, 2012), we found a probability of 0.88 that our sample has a higher VLBI detection fraction than the sample from Deller and Middelberg (2014).

It is known that the radio source population at 1.4 GHz with flux densities above 1 mJy consists almost exclusively of AGNs (e.g. Condon et al., 2012, Fig. 11). This implies that the VLBI-observed subsamples from Garrington et al. (1999) and Deller and Middelberg (2014) and the sample presented in this work—all cut to 10 mJy and matched to the same sensitivity as discussed above—contain virtually only AGNs. Thus, based on the numbers given above, we find a tendency of a higher VLBI detection fraction for IFRS compared to the general AGN population.

Collier et al. (2014) discarded all objects from their IFRS catalogue which provided a spurious WISE counterpart to one of the radio lobes. It is unclear whether this selection criterion can explain the higher VLBI detection fraction of IFRS compared to the general AGN popula-

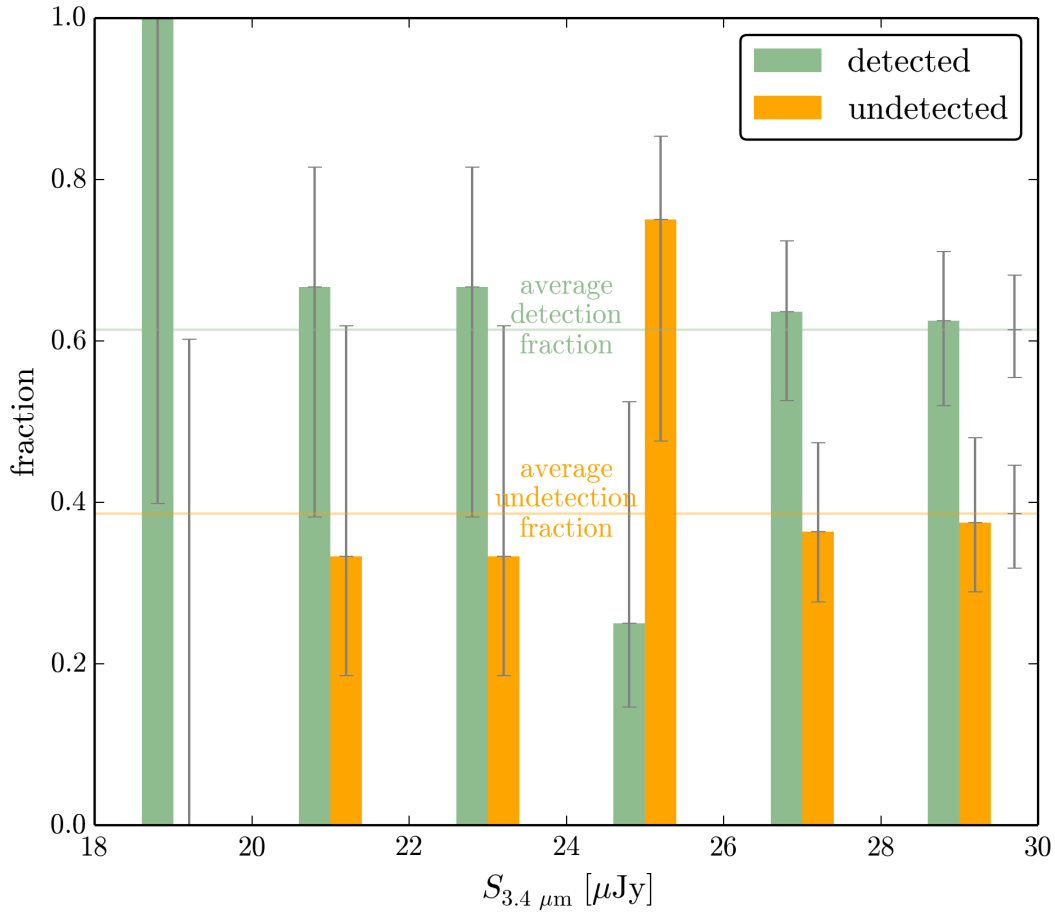

Figure 3.15: Histogram of the VLBA detection and non-detection fraction, binned by the flux density at 3.4 μm. The horizontal lines show the overall detection and non-detection fraction of the observations presented in this work. 1σ confidence intervals are shown in grey.

tion. Apart from that, the only difference in selecting the objects of the general AGN sample and the IFRS sample is the application of the IFRS selection criteria from Zinn et al. (2011) mentioned in Sect. 1.4.

Figure 3.15 shows the VLBA detection fraction binned in the 3.4 μm flux density for our sample of IFRS. We do not find any evidence for a dependence of the VLBI detection fraction on the 3.4 μm flux density. We also tested the detection fraction against the arcsec-scale 1.4 GHz flux density, the radio-to-IR flux density ratio, and the WISE colour [W1-W2] and found no significant correlation.

Compact radio cores are detected in eight (73^{+9}_{-16}%) of the eleven IFRS with SDSS counterpart and in 24 (57^{+7}_{-8}%) of the 42 IFRS covered by SDSS without SDSS counterpart. However, we do not consider this a significant difference (a) because these two subsamples are not flux-complete, (b) because of the non-uniform sensitivity of SDSS, and (c) because SDSS is biased towards detecting blue objects as discussed above.

Three out of the eleven IFRS with SDSS counterpart are classified as "galaxy" in SDSS. We detected two (67^{+14}_{-28}%) of these three galaxy-type IFRS in our VLBA observations. The other eight IFRS with SDSS counterpart are classified as "star" in SDSS. We note that this photometry-based classification is based on the extension of the object, i.e. objects classified as star are point-like, whereas extended objects are classified as galaxy. Out of these eight IFRS classified as star, we detected six (75^{+9}_{-19}%) in our VLBA observations. Deller and Middelberg

(2014) found a higher VLBI detection fraction for sources classified as star-like in SDSS. Our results are in agreement with this finding.

Dependence of the VLBI detection fraction on radio properties:

Based on data at 6 cm, 20 cm, and 92 cm, Collier et al. (2014) classified 124 of their IFRS as CSS sources and 32 as GPS sources. Out of the 57 IFRS observed with the VLBA, five IFRS were classified as CSS sources and two as GPS sources. In our VLBA observations, we detected four out of five IFRS which were classified as CSS sources and both IFRS which were classified as GPS sources so that CSS/GPS sources have a higher detection rate (85^{+5}_{-21}%) than the non-classified sources (58^{+6}_{-7}%).

Collier et al. (2014) used the lower-resolution data of NVSS for the flux densities in their IFRS catalogue. They also listed the number of sources in the higher-resolution FIRST survey associated with the NVSS source. IFRS detected with more than one FIRST component are clearly extended radio galaxies and not GPS or CSS sources. Out of the 57 IFRS observed with the VLBA, 47 are associated with exactly one FIRST source, while ten IFRS are associated with two or three FIRST sources. Out of these ten IFRS with two or three FIRST counterparts, we detected one (10^{+17}_{-3}%) in our VLBA observations, whereas 34 (72^{+5}_{-7}%) out of 47 IFRS with exactly one FIRST counterpart were detected with the VLBA. We found a statistically significantly higher VLBA detection fraction for IFRS with exactly one FIRST counterpart compared to the detection fraction of IFRS with more than one FIRST counterpart.

We also compared our VLBA detection fraction of IFRS with exactly one FIRST counterpart to the detection fraction found by Deller and Middelberg (2014) for the general radio source population. As described above, we matched the arcsec-scale radio flux density and the VLBA detection sensitivity to 10 mJy beam^{-1} and 1.5 mJy beam^{-1}, respectively. We found a detection fraction of 54^{+7}_{-7}% for those IFRS with exactly one FIRST counterpart, compared to a detection fraction of 36% for the general radio source population above 10 mJy beam^{-1} measured by Deller and Middelberg (2014). Thus, our sample of IFRS with exactly one FIRST counterpart is statistically different to the general radio source population, based on a probability of 0.01 in a *Fisher's exact test* (e.g. Wall and Jenkins, 2012) that the two samples are taken from the same parent population.

3.4.3.2 Compactness

We determined ratios of the integrated mas-scale flux density in the VLBA observations at 1.4 GHz to the integrated arcsec-scale flux density in NVSS at 1.4 GHz to fall between 0.86 and 0.014 for the IFRS detected in our VLBA observations. On average, this ratio, which we refer to as compactness, was 0.33 ± 0.23. Figure 3.16 shows the number of detections binned by the compactness.

The mean compactness of our detected IFRS of 0.33 ± 0.23 is lower than that of the two former VLBI detections of IFRS where Norris et al. (2007) and Middelberg et al. (2008b) detected 88% and 58%, respectively, of the arcsec-scale flux density. This discrepancy may be due to small-number statistics or because our fluxes are measured on smaller scales than those from Norris et al. (2007) and Middelberg et al. (2008b). The restoring beam of the LBA observations presented by Middelberg et al. (2008b) was 51.7 mas $\times$ 23.6 mas, i.e. 17 times larger compared to the median beam of 14.3 mas $\times$ 4.7 mas in our VLBA observations. Norris et al. (2007) did not image their (u, v) data because of the poor (u, v) coverage, but their angular

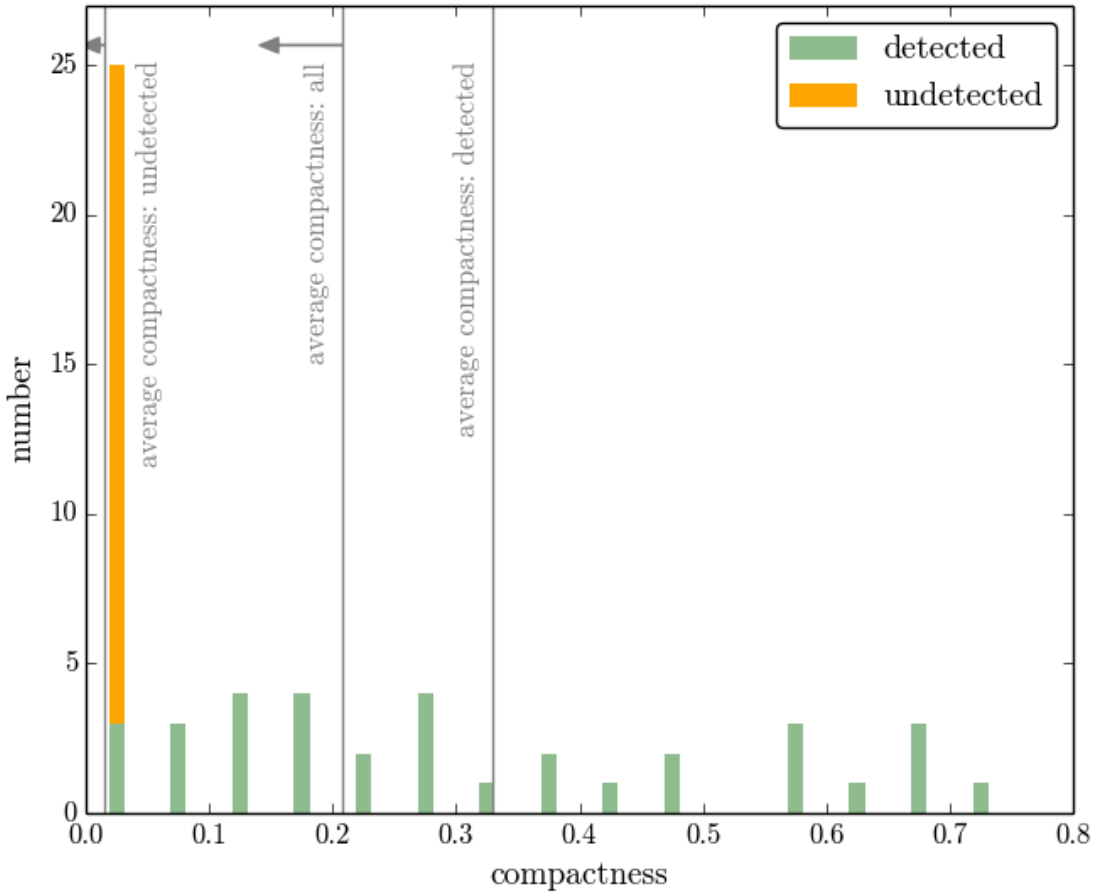

Figure 3.16: Histogram of the VLBA detections and non-detections, binned in the compactness at 1.4 GHz. Compactness is defined as the ratio of mas-scale flux density to arcsec-scale flux density. The vertical lines show the mean compactness—from left to right—of all VLBA-undetected IFRS, of all VLBA-observed IFRS, and of all VLBA-detected IFRS, respectively. The former two lines represent upper limits as indicated by the horizontal arrows.

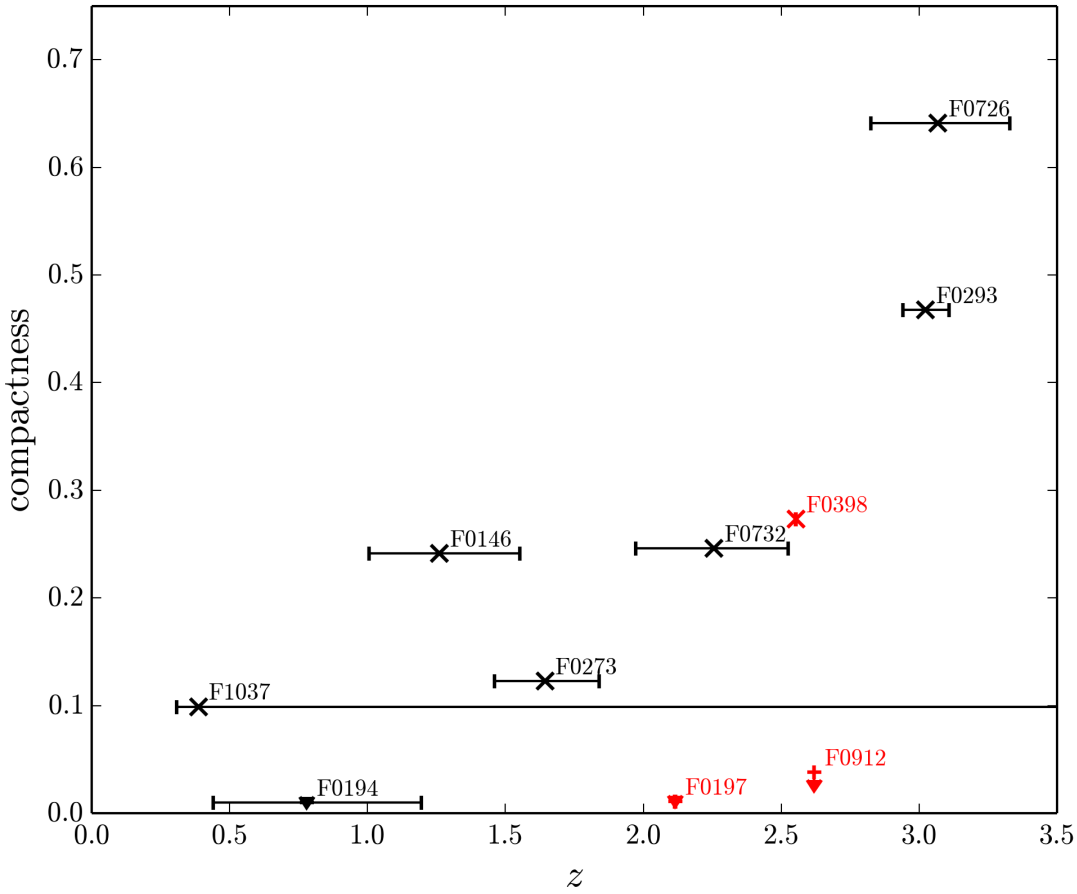

Figure 3.17: Compactness as a function of redshift for those IFRS with redshift information. VLBA-detected IFRS are shown by crosses and the 6.75σ upper limits on the compactness of VLBA-undetected IFRS are shown by arrows. Three spectroscopic (red markers) and seven photometric (black markers) redshifts were used in this analysis. Note that the errors on the compactness are around 20%.

resolution was similar to that of Middelberg et al. (2008b). Therefore, a lower fraction of detected flux in our VLBA observations could be expected.

Dependence of the compactness on the redshift:

In the following, we tested our data against a potential correlation between redshift and compactness. SDSS DR10 provides spectroscopic redshifts for three out of our 57 IFRS. Two ($z = 2.11$ and $z = 2.62$) of those are undetected and one ($z = 2.55$) is detected in the VLBA observations. However, IFRS F0912 at $z = 2.62$ was observed for only ~ 25 min with the VLBA, resulting in a reduced sensitivity compared to the other sources. Since the number of objects in this subsample is too low to test our data, we extended our subsample by including those IFRS with photometric redshifts presented in Sect. 3.4.2.2.

Figure 3.17 shows the compactness as a function of the redshift for all ten VLBA-observed IFRS with redshift information. The data do not provide compact objects at low redshifts, whereas compact objects were found at higher redshifts. The data suggest a possible correlation between compactness and redshift for IFRS. We tested the data using a *Spearman rank correlation test* (e.g. Wall and Jenkins, 2012) and found a correlation coefficient between 0.66

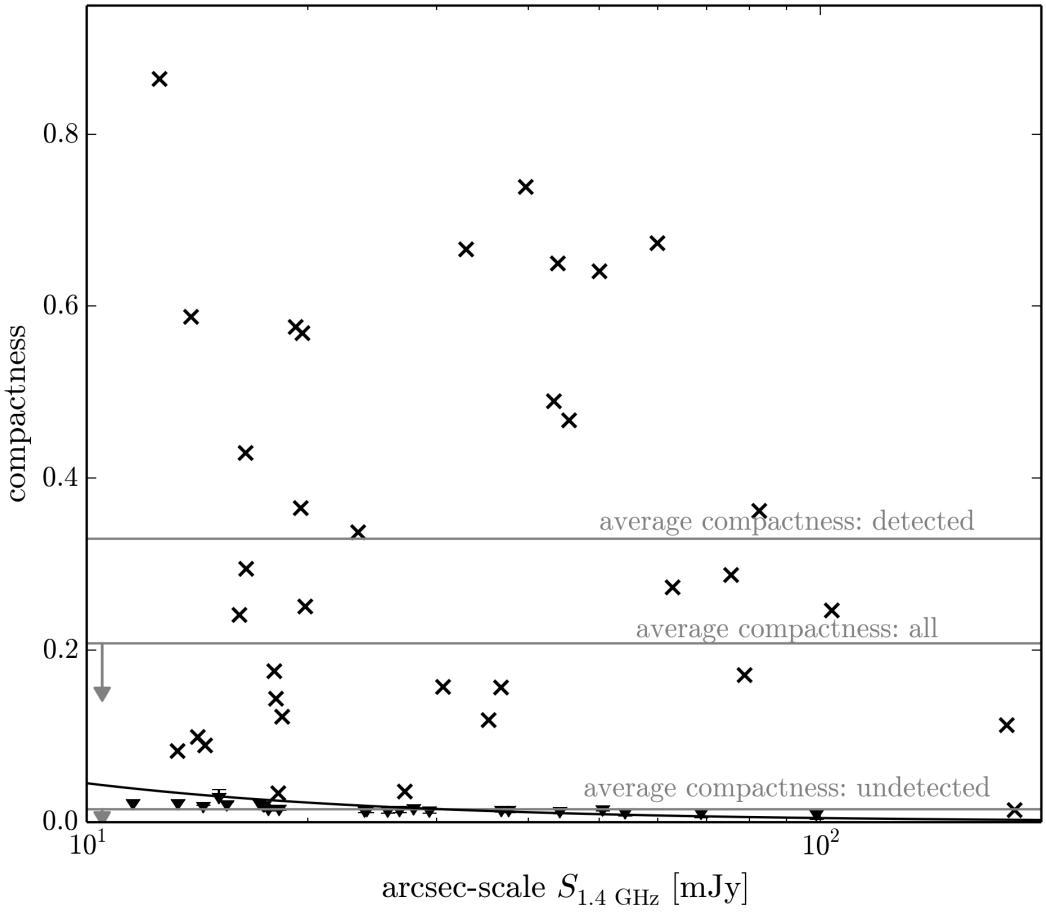

Figure 3.18: Compactness as a function of the arcsec-scale 1.4 GHz flux density. VLBA-detected IFRS are shown by crosses and the 6.75σ upper limits on the compactness of VLBA-undetected IFRS are shown by black arrows. The grey horizontal lines represent—from top to bottom—the mean compactness of all VLBA-detected IFRS, of all VLBA-observed IFRS, and all VLBA-undetected IFRS, respectively. The latter ones represent upper limits as indicated by grey arrows. The black line shows the minimal detectable compactness depending on the arcsec-scale flux density, based on an mean detection sensitivity of 450 μJy in our VLBA observations.

and 0.52, indicating a positive correlation between redshift and compactness. A correlation coefficient of $+1$ and -1 represents an ideal correlation and anticorrelation, respectively, whereas an uncorrelated data set is represented by a coefficient of 0. In our case, the probability that the two parameters are uncorrelated is between 0.019 and 0.063. The margin arises from the unknown compactnesses of the VLBA-undetected sources for which only upper limits are known. We determined this margin using a permutation test. Based on the strong positive correlation coefficients, we suggest a correlation between compactness and redshift for our sample of IFRS. When considering only the VLBA-detected sources, we found a correlation coefficient of 0.96 and a probability of 4.5×10^{-4} that the parameters are uncorrelated. We cautiously note that the putative positive correlation seems to be mainly based on the two highest-redshift IFRS in Fig. 3.17 which might be outliers. Therefore, we emphasise that this suggested correlation needs further testing.

Dependence of the compactness on the 1.4 GHz flux density:

Figure 3.18 shows the compactness as a function of the arcsec-scale 1.4 GHz flux density and in-

cludes detections and upper limits for the non-detections. We did not find compact radio-bright IFRS, whereas compact radio-faint IFRS are common in our sample. If we divide our sample at an arcsec-scale flux density of 60 mJy, we find twelve (25^{+7}_{-5}%) sources with compactnesses above 0.4 and 36 (75^{+5}_{-7}) sources with compactnesses below 0.4 in the fainter subsample. At arcsec-scale flux densities above 60 mJy, we find nine (100_{-17}%) sources with compactnesses below 0.4 and no (0^{+17}%) source with a compactness above 0.4. This is in agreement with results from Deller and Middelberg (2014), who found a statistically significant anti-correlation between compactness and arcsec-scale 1.4 GHz flux density in their sample of randomly selected radio sources. We used a *Spearman rank correlation test* (e.g. Wall and Jenkins, 2012) to test for putative correlations. However, because of the significant fraction of upper limits in this plot, we can only narrow down the correlation coefficient to a rather broad range. We found that the correlation coefficient is between 0.39 and −0.15. Based on this test, we cannot exclude either a positive or a negative correlation or a decorrelation.

3.4.3.3 Individual sources

In the following, we discuss three individual sources which are of particular interest.

F0398:

The only VLBA-detected IFRS with spectroscopic redshift is F0398 at $z = 2.55$, showing an arcsec-scale 1.4 GHz integrated flux density of 62.9 mJy. This corresponds to a K-corrected 1.4 GHz rest-frame luminosity of 2.3×10^{27} W Hz^{-1}, using the radio spectral index $\alpha = -0.72$ between 20 cm and 92 cm from Collier et al. (2014). In our VLBA observations, the source—shown in Fig. 3.12—is slightly resolved with a peak flux density of 13.7 mJy beam^{-1} and an integrated flux density of 17.2 mJy, corresponding to a luminosity of 6.3×10^{26} W Hz^{-1} on scales smaller than 146 pc × 43 pc. Based on this luminosity, F0398 can be classified as Fanaroff-Riley (FR; Fanaroff and Riley, 1974) type II. The source has a compactness of 0.283.

F0030:

A particularly interesting source is F0030 which has two spatially separated components in the VLBA map shown in Fig. 3.19. The first, brighter component shows a mas-scale flux density of 21.8 mJy (S/N = 55) and is spatially resolved with a complex morphology which is unique in our observations. The second component shows a flux density of 6.0 mJy (S/N = 46) and is separated by $442.1^{+0.3}_{-0.3}$ mas. The linear distance between both components is between 1.7 kpc and 3.8 kpc at any redshift in the range $0.5 \leq z \leq 12$.

In order to obtain a rough spectral index of the components, we separately imaged the four lower-frequency basebands and the four higher-frequency basebands centred at 1.380 GHz and 1.508 GHz, respectively. Fluxes were measured as described in Sect. 3.4.2.1. We obtained spectral indices of -1.2 ± 1.2 and -1.2 ± 0.6 for component 1 and 2, respectively.

F0257:

Source F0257—shown in Fig. 3.20—consists of two individual components. While the brighter component shows a flux density of 5.7 mJy (S/N = 77), the weaker component is $155.5^{+0.2}_{-0.2}$ mas distant and shows less than half of the other component's flux density (2.1 mJy beam^{-1}, S/N = 36). This angular distance corresponds to a linear distance between 0.6 kpc and 1.3 kpc. We

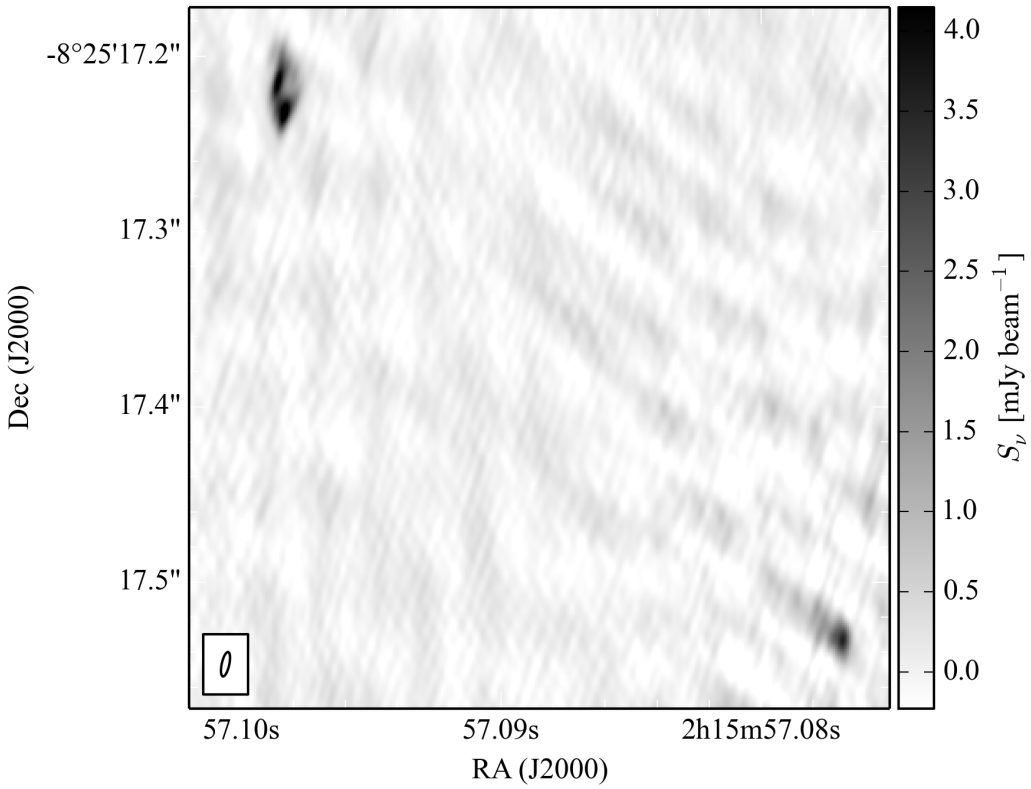

Figure 3.19: VLBA map of IFRS F0030. The brighter component (upper left) has a complex morphology and a flux density of 21.8 mJy. The second component (lower right) has a flux density of 6.0 mJy and is separated by $442.1^{+0.3}_{-0.3}$ mas, corresponding to a distance between 1.7 kpc and 3.8 kpc at any reasonable redshift.

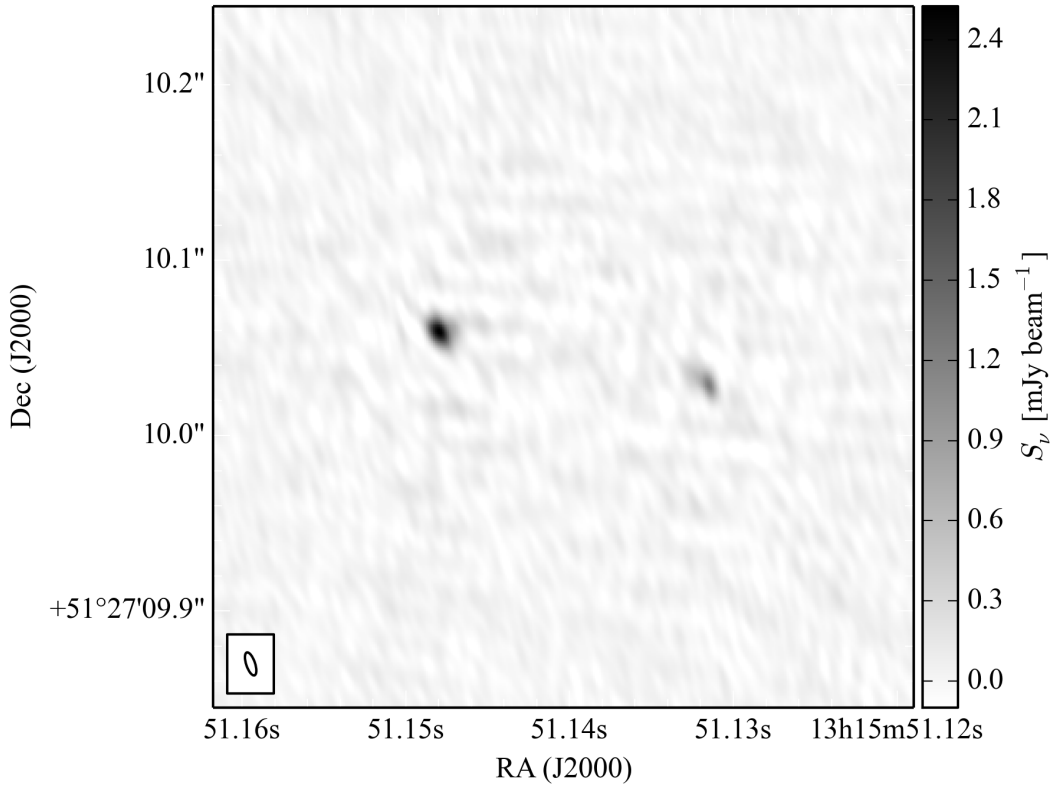

Figure 3.20: VLBA map of IFRS F0257. The brighter component (left) has a flux density of 5.7 mJy. The second component (right) has a flux density of 2.1 mJy and is separated by $155.5^{+0.2}_{-0.2}$ mas, corresponding to a distance between 0.6 kpc and 1.3 kpc at any reasonable redshift.

measured mas-scale radio spectral indices between 1.380 GHz and 1.508 GHz of -0.3 ± 0.4 and 0.2 ± 0.9, respectively, for component 1 and 2. Collier et al. (2014) measured an arcsec-scale radio spectral index of -0.6 between 6 cm, 20 cm, and 92 cm.

Could double component sources be a coincidence?:

Sources F0030 and F0257 have both two compact components separated by 445 mas and 155 mas, respectively. In the following, we estimate the probability that two close by components are unrelated background sources. NVSS found 1.8 million radio sources in an area of $3 \times 10^4\,\mathrm{deg}^2$, out of which less than 50% have compact cores detectable in VLBI observations (Deller and Middelberg, 2014). This corresponds to a sky density of $1.8 \times 10^{-6}\,\mathrm{arcsec}^{-2}$. The probability of finding an additional unrelated source at a given position in an area of $0.5'' \times 0.5''$ is therefore of the order of 5×10^{-7}. Thus, we can effectively rule out any chance that the two components found both in F0030 and F0257 are physically unrelated.

3.4.4 Discussion

Our observations increase the number of VLBI-detected IFRS from 2 to 37. Based on our detection fraction of $61^{+6}_{-7}\%$ and a reasonably large sample size, we find strong evidence that most—if not all—IFRS contain AGNs. This result confirms earlier studies by e.g. Garn and Alexander (2008), Middelberg et al. (2011b), and Herzog et al. (2014), who suggested compact cores in IFRS based on SED modelling, radio-to-IR flux density ratios, and emission lines in optical spectra. With higher sensitivity, we would have most likely detected more sources in our VLBA observations.

We also tested our data for different potential correlations in Sect. 3.4.3. Although not all of them are statistically significant, in the following, we explore the astrophysical consequences if these results are confirmed by subsequent observations and describe how these hypotheses can be tested.

In Sect. 3.4.3.2, we found a tendency that radio-brighter IFRS are less compact. Deller and Middelberg (2014) found the same behaviour when testing the general AGN population and argued that this anti-correlation might be explained by Doppler boosting effects as presented by Mullin et al. (2008). Mullin et al. (2008) studied a complete sample of narrow-line and broad-line radio galaxies and found an anti-correlation between radio luminosity and core prominence. They argued that higher-luminosity sources have higher boosting factors, associated with narrower boosting solid angles and a higher fraction of sources for which a Doppler suppressed core is seen. In contrast, lower-luminosity sources have lower boosting factors and wider solid angles, corresponding to a lower core supression fraction and a higher compactness.

We argue that another factor might contribute to the observed behaviour in our sample. It is known that AGNs evolve from very compact to extended objects via jet growth, associated with an increasing total luminosity. Namely, GPS sources are most compact and evolve into CSS sources and finally into the largest radio galaxies, FR type I or II (e.g. O'Dea, 1998; Snellen et al., 1999; Fanti, 2009a). Following this sequence, we would expect younger AGNs to be more compact than old AGNs.

We note that both effects might overlap since they both predict a lower compactness at higher luminosities. Based on the slightly higher VLBI detection fraction of IFRS—which is expected to be a result of higher compactnesses—compared to the general AGN population as found in Sections 3.4.3.1 and 3.4.3.1, we suggest that IFRS are on average younger than the

general AGN population. This would be in agreement with results by Middelberg et al. (2011b) and Collier et al. (2014) who found some IFRS to be GPS and CSS sources. The higher VLBI detection fraction for IFRS classified as GPS and CSS sources compared to non-classified IFRS reported in Sect. 3.4.3.1 also agrees with this reasoning.

We suggest that—at least some—IFRS are young AGNs. However, the sample presented by Collier et al. (2014) contains IFRS with different characteristics. IFRS, which are associated with more than one FIRST source, are clearly not GPS or CSS sources but extended radio galaxies. Those sources would be expected to be older and less compact than IFRS with exactly one FIRST counterpart. We found evidence for this expected behaviour in Sect. 3.4.3.1 based on a lower detection fraction for IFRS that are extended in arcsec-resolution images. We therefore suggest that these extended IFRS are on average older and more evolved than the VLBA-detected IFRS.

We found lower mean compactnesses of our VLBA-detected IFRS compared to the other two VLBI-detections of IFRS by Norris et al. (2007) and Middelberg et al. (2008b). In addition to the technical explanations given in Sect. 3.4.3.2, this discrepancy can also be explained by boosting effects. The IFRS from Norris et al. (2007) and Middelberg et al. (2008b) are radio-fainter than the IFRS analysed in our work. Following the reasoning by Deller and Middelberg (2014) that brighter objects are more likely to be Doppler suppressed, lower compactnesses for our IFRS compared to the fainter IFRS from Norris et al. (2007) and Middelberg et al. (2008b) could be expected.

In Sect. 3.4.3.2, we found a statistically significant correlation between redshift and compactness, with higher-redshift IFRS being more compact. Two arguments can explain this correlation. (a) Higher-redshift objects have a tendency to be younger than low-redshift versions of the same class of object. Combining the increasing luminosity of GPS and CSS sources with time and the boosting-related argument of decreasing compactness with luminosity, higher-redshift—and thus younger and fainter—IFRS would be expected to be more compact. (b) At higher redshifts, IFRS are more likely to be located in gas-rich environments as shown for high-redshift galaxies (Klamer et al., 2006). The higher gas density confines these objects and keeps them more compact.

These results are all in agreement with the scenario that IFRS are younger and therefore less luminous compared to the general AGN population, resulting in higher compactnesses and higher detection fractions. However, we stress that this putative connection between the age of IFRS and their VLBI properties is not statistically significant and needs further testing.

Alternatively, the slightly higher VLBI detection fraction of IFRS compared to the general AGN population could also be explained by a higher dust content of IFRS, making it harder for the jets to expand and resulting in a more compact object. However, no evidence has been found that IFRS are obscured by dust. On the contrary, Collier et al. (2014) and Herzog et al. (2014) argued that the IR faintness of IFRS is not caused by dust extinction. The SEDs resulting from our photometric redshift fitting presented in Sect. 3.4.2.2 also indicate that at least some IFRS are very blue and do not support the hypothesis that a significant fraction of IFRS is associated with dusty galaxies.

Future observations will help to test the hypotheses made in this work. In particular, additional VLBA observations—similar to the observations presented in this work—scheduled for semester 15A will increase the sample size of VLBI-observed IFRS, providing the basis for more robust tests.

We plan to match arcsec-resolution radio data at higher and lower frequencies, enabling the measurement of spectral indices and turnover frequencies of IFRS. This information will bring

out a putative overlap between IFRS and GPS/CSS sources and provide further insights into the evolutionary status of IFRS (Herzog et al., in prep.).

Radio observations—exposing the intermediate-resolution morphologies of IFRS—could discriminate between the two mechanisms which may be responsible for the lower compactness of brighter objects: beaming and age. If beaming is the predominant cause for this effect, the radio-fainter IFRS should mainly be one-sided objects (core-jet) since a beaming effect is more likely to be seen for fainter objects as discussed above. In contrast, radio-brighter IFRS would be expected to show a more symmetric structure. However, if the anti-correlation between compactness and arcsec-scale radio flux density is mainly driven by the age of the objects, no difference in the morphology would be expected, although radio-brighter objects should be larger.

Two IFRS stand out from our sample since they were found to be composed of two mas-scale components, separated by a few hundred mas. There are four different explanations for those sources which we now discuss.

(i) GPS/CSS double lobe sources: It is known that GPS and CSS double lobe sources can appear as separate components in VLBI observations (Snellen et al., 2003). In that case, the two components would be hot-spots in the two jets and steep spectral indices would be expected (e.g. Hovatta et al., 2014), while the VLBI-undetected core of the source would be between both components. GPS sources are usually smaller than 1 kpc (O'Dea, 1998), whereas CSS sources show extensions of a few to a few tens of kpc (Fanti, 2009a; Randall et al., 2011).

(ii) Compact core and jet of a GPS or CSS source: Related to the first scenario, the two components could be the compact core of the AGN and a hot-spot in one jet. In that case, the spectral indices of both components can be different. While the hot-spot should provide a steep spectrum as discussed above, the core component would most likely provide a flat spectrum. However, the core spectrum could also be steep (Hovatta et al., 2014).

(iii) Gravitational lensing: The appearence of two components can also be explained by gravitational lensing (e.g. Porcas, 1998). In that case, the emission seen as two components would originate from one distant source whose emission is deflected by the gravitation of a nearby object. Therefore, similar spectral indices for the two components are expected. In F0030 and F0257, the two components are too close to find a potential gravitational lensing effect in optical images.

(iv) Binary black hole: The two components could also be a binary black hole (e.g. Burke-Spolaor, 2011). In that case, the spectral indices of the components could be flat or steep or mixed as discussed in (ii) for the compact core.

Based on the available data, we are not able to exclude any of those four different explanations because of the large error bars on the spectral indices. F0030 is unlikely to be a GPS source because of the linear size of more than 1.7 kpc. Following the correlation between intrinsic peak frequency and linear size of compact AGNs presented by O'Dea and Baum (1997), F0030 would be expected to show a rest-frame turn-over frequency of less than a few hundred MHz. Particularly, F0030 has different characteristics than the high-redshift ($z = 5.774$) steep spectrum source J0836+0054 (Petric et al., 2003; Frey et al., 2005). This RL quasar shows arcsec-scale properties ($S_{1.4\,\mathrm{GHz}} = 1.75\,\mathrm{mJy}$, $\alpha = -0.8$) similar to those of IFRS. However, in contrast to F0030, J0836+0054 has a second arcsec-scale radio component which was undetected in VLBI observations and is most likely associated with a lower-redshift galaxy.

3.4.5 Conclusion

We observed 57 IFRS with the VLBA and detected compact emission in 35 of them. Based on these observations, we draw the following conclusions.

- We tested the hypothesis that IFRS contain AGNs. Our observations finally confirm the suggested compact cores in the majority of—if not all—IFRS, establishing IFRS as a new class of AGN. Our data increase the number of VLBI-detected IFRS from 2 to 37.
- Our data suggest that radio-brighter IFRS are on average less compact. This finding agrees with the evolutionary scenario that young AGNs evolve by expanding jets, becoming radio brighter and less compact with time. However, boosting effects may play a role, too.
- We found a marginal tendency for IFRS to show a higher VLBI detection fraction compared to randomly selected sources with mJy arcsec-scale flux densities, i.e. mainly AGNs. In our sample, the detection fraction is higher for IFRS with exactly one FIRST counterpart and for IFRS classified as GPS and CSS sources.
- A statistically significant correlation between redshift and compactness was found in our data for IFRS with higher-redshift sources to be more compact. This is in agreement with higher-redshift sources being located in denser environments and having a tendency to be younger.
- Two sources show two components each, separated by between 0.4 kpc and 3 kpc at any reasonable redshift. These components might be jet/jet or core/jet components of an AGN, a binary black hole, or arising from gravitational lensing.

All our findings are in agreement with the scenario that IFRS contain young AGNs which are in an early stage of their evolution. Their jets are not yet formed or expanded significantly, resulting in a very compact source. When evolving, the jets expand and the total radio fluxes of the sources increase, while the compactnesses decrease at the same time. We note that some IFRS already formed jets as known from arcsec-resolution maps.

Our analyses in this work were limited because of the low number of objects in relevant subsamples. Based on new data from VLBA observations of IFRS in semester 15A and planned lower-resolution observations, we are aiming at extending our study and further testing the hypotheses presented in this work.

3.5 Further work since Collier et al. (2014)

Since we published the all-sky IFRS sample (Collier et al., 2014, see section 3.1), further work has been undertaken toward understanding the nature of IFRSs. These studies have been particularly focussed on modelling the multi-wavelength SEDs or radio spectra of IFRSs. We summarise them below.

3.5.1 IFRSs amongst USS sources

Singh et al. (2014) searched for HzRGs in faint Ultra-Steep Spectrum (USS) sources and found a significant fraction of IFRSs amongst the sample. They found that selecting sources using a criterion similar to the second IFRS selection criterion from Zinn et al. (2011) (i.e. high radio-IR flux density ratio) was able to remove the majority of low-z SFGs from their sample, leaving only high-redshift ($z \geq 1$) AGN and a few very radio-loud AGN at low-z. This work suggests a similarity between USS sources, HzRGs and IFRSs.

3.5.2 Redshifts and SEDs of brighter IFRSs from ATLAS

Herzog et al. (2014) selected a sample of four IFRSs from the CDFS, which were similar to our all-sky sample in that they were IR- and optically-brighter than the *first generation* IFRSs. The sources satisfy the Zinn et al. (2011) criteria and were selected based on having optical counterparts to enable spectroscopic observations, which were between $22.0 < R_{\rm Vega} < 24.1$. Therefore these are also less extreme IFRSs, with radio-to-IR flux density ratios between $600 - 1000$, as opposed to the majority of more extreme IFRSs within the CDFS, with undetectable IR and optical counterparts and flux density ratios > 8000, which are clearly unsuitable for spectroscopy. As with the all-sky IFRSs, studying these less extreme IFRSs enabled conclusions to be made about the general class of IFRSs, including the most extreme versions.

The sample was observed with the Very Large Telescope at wavelengths between $330 - 1100$ nm and a slit width of $2''$. The total on-source times were between $44 - 128$ min, split into several shorter exposures to enable the correction of cosmic rays. The spectra of three sources contained two to three strong emission lines, with redshifts found in the range $1.84 < z < 2.76$. The fourth source suffered from low S/N, although Herzog et al. (2014) suggested a redshift of 3.1 based on a very faint emission feature at $\sim$4970 $\mathring{A}$ which contained a break toward lower wavelengths, which they interpreted as Lyα. These redshifts are consistent with our findings in table 3.4, which contain similar radio, optical and IR brightness and are also in the range $2 \lesssim z < 3$, which is the lower range of the expected redshift distributions for IFRSs. All spectra from Herzog et al. (2014) are also broad-line quasar spectra, consistent with the majority of spectra from table 3.4, and from the SED modelling of IFRSs (Garn and Alexander, 2008; Huynh et al., 2010; Maini et al., 2016). Herzog et al. (2014) showed that their sample was also consistent with the $S_{3.6\mu m} - z$ relation (see figure 1.17), giving further evidence that the *first generation* IFRSs are located at even higher redshift. Based on these findings, Herzog et al. (2014) concluded that most of the IFRSs in the ATLAS fields may have redshifts reaching up to 5 or 6.

Using assumed spectral indices of -1.4 based on the median spectral index found by Middelberg et al. (2011b), Herzog et al. (2014) calculated the rest-frame 1.4 GHz luminosities for their sources, assigning uncertainties based on the flattest (-0.7) and the steepest (-2.4) spectral indices from Middelberg et al. (2011b). The calculated luminosities were found within the range $3.2 \times 10^{26} - 7.6 \times 10^{27}$ W Hz^{-1}. Based on these luminosities, Herzog et al. (2014) classified their

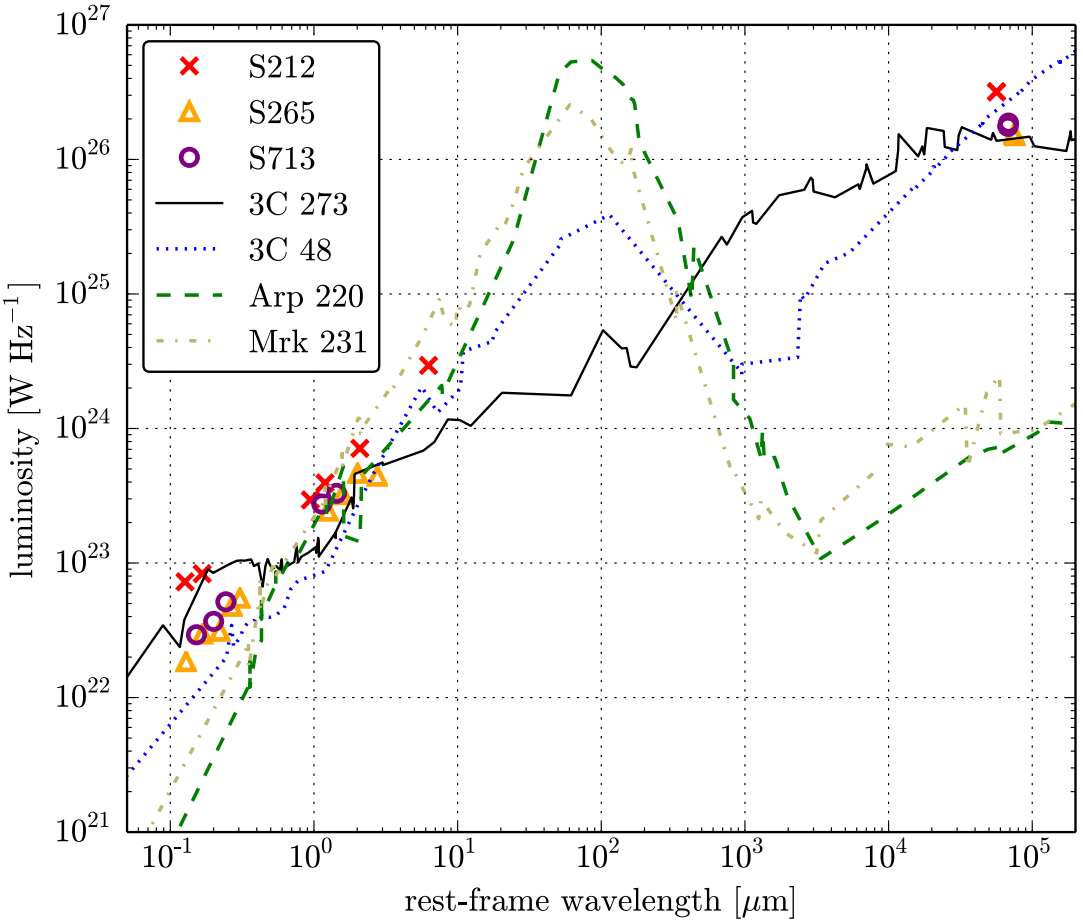

Figure 3.21: Rest-frame SED modelling from Herzog et al. (2014). The rest-frame photometric data points for the three IFRSs with detected redshifts are shown by the red crosses, yellow triangles and purple circles. The SED templates are shifted to rest-frame and scales in luminosity to match the photometric data and consist of SFG Arp220 (green dashed line), Seyfert galaxy Mrk231 (olive dashed-dotted line), radio-loud quasar 3C273 (black solid line) and CSS source 3C48 (blue dotted line). Only 3C273 and 3C48 are consistent with the data.

IFRSs as FR IIs and HzRGs, supporting the hypothesis that IFRSs and HzRGs are related.

Herzog et al. (2014) presented the first redshift-based SED modelling of IFRSs using SED templates of a starburst, RG, dwarf galaxy and quasar. They used the wealth of photometric data available in the CDFS for their SED modelling, including (but not limited to) flux densities from optical G and R bands, 3.6 and 4.5 μm IR bands, and most importantly, 1.4 GHz radio flux densities, which provided the strongest constraints. Assuming self-similarity between each IFRS, all photometric data was included together in the SED modelling, in order to constrain the class of object in general. To model the SEDs, the templates were shifted to rest-frame, scaled in luminosity to match the observed 3.6 μm flux density, and reduced in the rest-frame optical and near-IR due to extinction. The templates of 3C273 and 3C48 with no extinction added were consistent with the data after being scaled down in total luminosity by respective factors of 17 and 10 (see Fig. 3.21). None of the other templates were able to match the data, even with significant extinction added. This is consistent with the hypothesis that IFRSs are high-z radio-loud AGN and suggests that heavy dust extinction is not present in IFRSs.

3.5.3 Broadband SEDs of extreme IFRSs

Herzog et al. (2015b) studied the FIR properties of IFRSs using *Herschel* observations. The motivation for this study comes from the fact that HzRGs, which show significant similarities to IFRSs, are known to undergo vigorous SF, which dominates the IR emission along with the AGN. Their sample consisted of six ATLAS IFRSs from Zinn et al. (2011) (five in ELAIS-S1 and one from CDFS), which were selected based on comparatively bright radio emission, with $7 < S_{1.4\mathrm{GHz}} < 26$ mJy. No optical counterparts were known for these six IFRSs, while one IR counterpart was known at 3.6 μm based on a 3σ SERVS detection from Maini et al. (2016), found after the *Herschel* observations were carried out. These yielded radio-to-IR flux density ratios between $2300 - 8700$, and were therefore amongst the most extreme IFRSs.

The sample was observed with *Herschel* at 100 and 160 μm with total on-source times of 22.5 min and at 250, 350 and 500 μm with total on-source times of 12 min. The final maps from these five bands respectively reached resolutions of 6.69×6.89, 10.65×12.13, 17.6, 23.9 and 35.2 arcsec^2. At 100 and 160 μm, none of the six IFRSs were detected down to respective flux density uncertainties of $1.4 - 2.2$ and $2.4 - 6.1$ mJy (e.g. see Fig. 3.22). At 250, 350 and 500 μm, five were not detected, while one IFRS yielded 3σ detections at 350 and 500 μm. However, Herzog et al. (2015b) ruled out this detection as an unrelated source, since its position measured at 100 and 160 μm from *Herschel* and at 3.6 μm from SERVS was very close, while the radio position was $12''$ away. Therefore they concluded that none of their IFRSs were detected at 250, 350 and 500 μm down to respective flux density uncertainties of $4.2 - 5.0$, $3.8 - 5.7$ and $4.8 - 7.2$ mJy (e.g. see Fig. 3.22).

Since no detections were found, Herzog et al. (2015b) performed a median stacking analysis at the radio positions to search for faint emission below the detection limit. One source was excluded from this analysis due to having a higher noise. No detections were found in the stacked maps at 100, 160, 250, 350 and 500 μm down to respective flux density uncertainties of 0.76, 1.66, 2.68, 2.52 and 3.53 mJy (e.g. see Fig 3.23). In order to use more stringent limits when modelling the SEDs of their IFRSs, Herzog et al. (2015b) also performed a median stacking analysis at 3.6 and 24 μm, using SERVS data at 3.6 μm for four sources, and SWIRE data at 3.6 μm for the other two, and at 24 μm for all six. No sources were found in the stacked maps, which had uncertainties of $\sigma_{3.6\mu\mathrm{m}} = 0.397$ μJy and $\sigma_{24\mu\mathrm{m}} = 31.3$ μJy.

Herzog et al. (2015b) used these IR flux density upper limits between $3.6 - 500$ μm to represent the average upper limits of these extreme IFRSs and performed broad-band SED modelling based on these limits and the range of radio flux densities detected for their sample. Although there was evidence that these extreme IFRSs are at $z \gtrsim 3$, they considered the broad range of redshifts from $1 \leq z \leq 12$ in an attempt to rule out possible explanations for the nature of IFRSs.

During the modelling, Herzog et al. (2015b) used the median 1.4 GHz flux density of 15 mJy, but also discussed the outcomes of using the highest and lowest radio flux densities. In the IR, they used 3σ upper limits. They used SED templates of the HzRG called the spiderweb galaxy, the local radio galaxy Cygnus A, the CSS source 3C48, the radio-loud quasar 3C2734, the local ULIRG Arp220, the Seyfert galaxy Mrk231, the local starburst galaxy M82, a radio-loud Hyper-Luminous Infrared Galaxy (HyLIRG) IRAS F15307+3252, the ULIRG F00183-7111, and the quiescent elliptical brightest cluster galaxy NGC1316.

The SED modelling was performed in four different approaches using SED templates of known galaxies:

1. shifting the SED templates in the redshift range $1 \leq z \leq 12$;

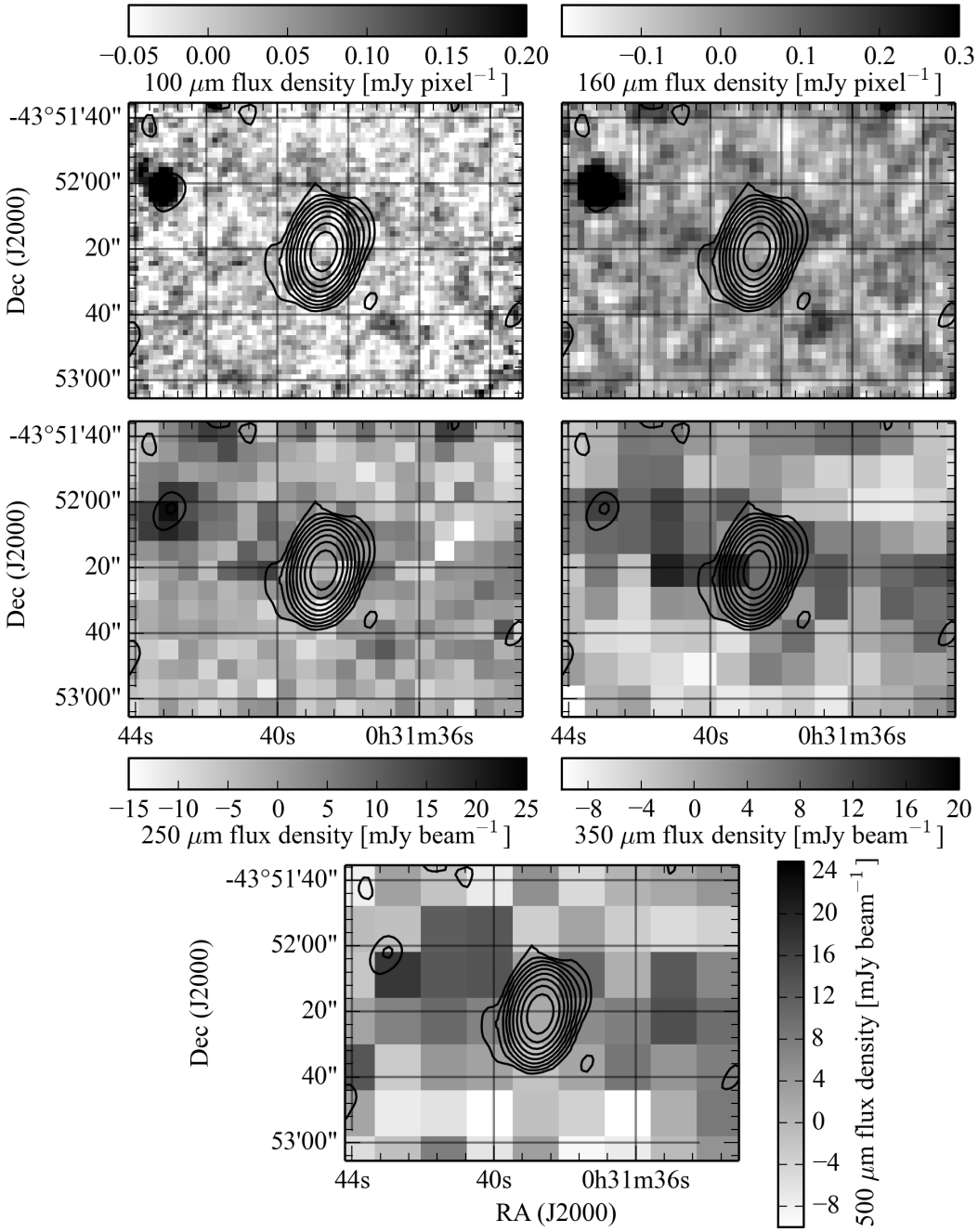

Figure 3.22: The final *Herschel* maps (greyscale) at 100, 160, 250, 350 and 500 μm and the 1.4 GHz radio contours of IFRS S509 from Herzog et al. (2015b). The contours are from ATLAS DR3 and represent levels of 2σ, 4σ, 8σ, etc.

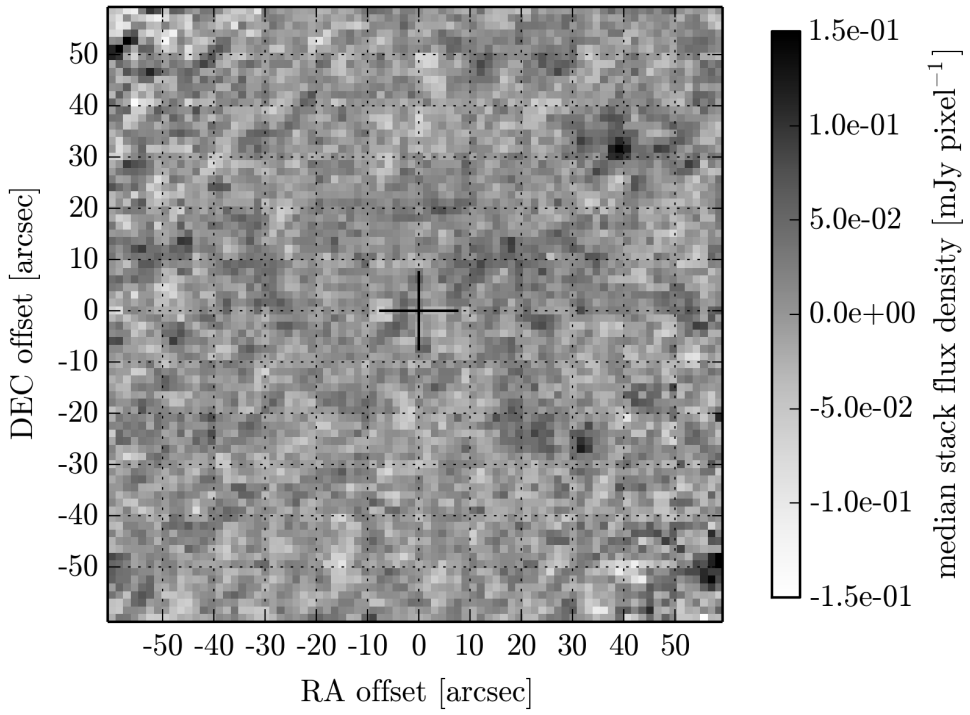

Figure 3.23: The stacked map at 100 μm resulting from the median stacking analysis performed using the individual maps for five IFRSs. No detection was found in this map.

2. shifting the templates and scaling them in luminosity;

3. shifting the templates and adding extinction;

4. shifting the templates, scaling them in luminosity and adding extinction.

The SED modelling from the first approach is shown in Fig. 3.24. At redshifts $z \lesssim 5$, none of the templates agree with the photometric data. Cygnus A in the range $5 \lesssim z \lesssim 8.5$ and the spiderweb galaxy at $z \gtrsim 10.5$ agreed with all photometric constraints. 3C48 at $6 \lesssim z \lesssim 9$ and 3C273 at $8 \lesssim z \lesssim 12$ agreed with all photometric constrains except the 3.6 μm upper limit. All other templates were found to be in strong disagreement with the photometric data at all redshifts between $1 - 12$, either falling short of the radio flux density range or exceeding the IR flux density upper limits by several orders of magnitude. Therefore, Herzog et al. (2015b) concluded that if IFRSs have the SED of a known galaxy, they must be a $z \gtrsim 5$, consistent with previous suggestions.

Herzog et al. (2015b) assigned a score for each SED template at each redshift. This score essentially measured how far the model deviated from the data (i.e. above upper limits of IR photometry, or outside range of radio flux densities), where a score of one denoted agreement between all photometric constrains, while a score less than one implied a deviation.[6] The score found during the first approach is shown in the upper left plot of Fig. 3.25.

Using the other three approaches (see Fig. 3.25), Herzog et al. (2015b) found that at $z \lesssim 5$, the IFRS SEDs can be modelled by low-luminosity versions of the spiderweb galaxy and Cygnus A or dust-obscured versions of 3C48 and 3C273. Based on these findings and the previous suggestions that IFRSs are HzRGs are related, Herzog et al. (2015b) suggested two different

[6]See Herzog et al. (2015b) for more details.

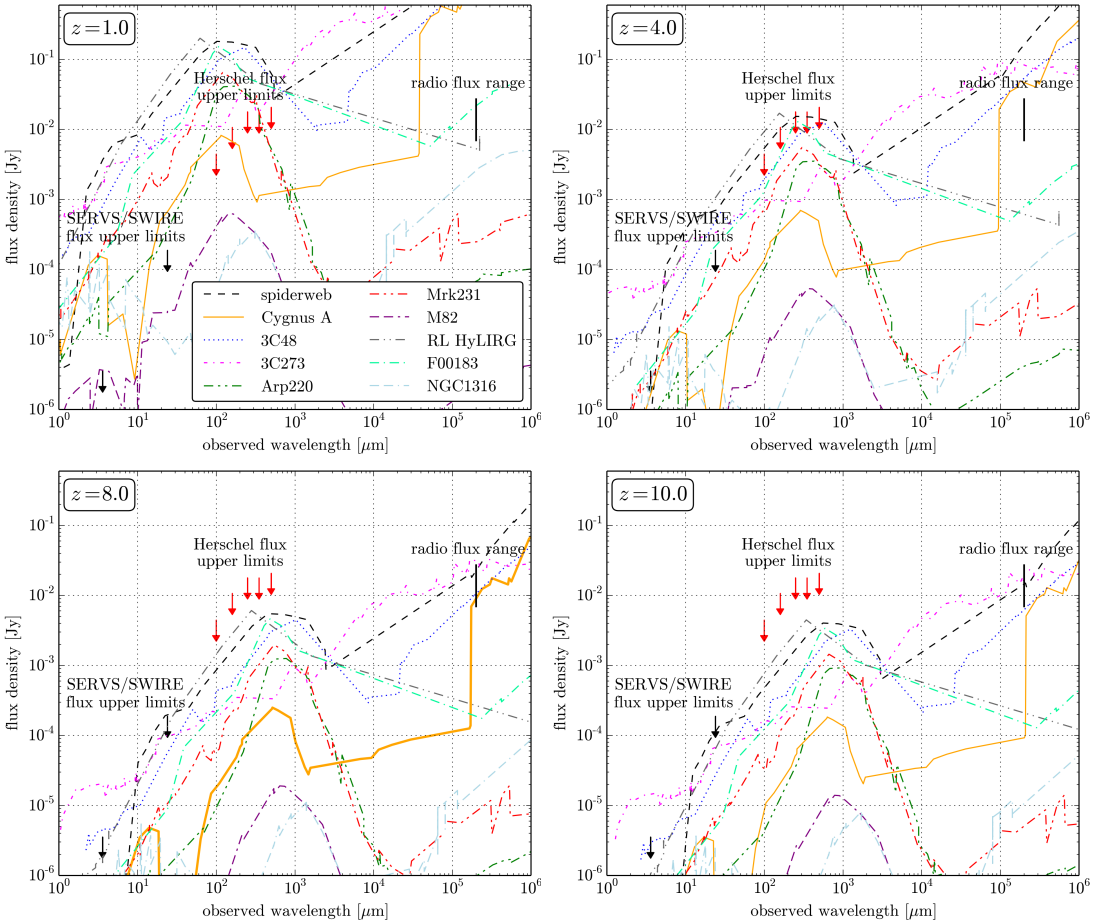

Figure 3.24: The broad-band SED modelling of IFRSs using IR flux density upper limits from stacked maps, and the range of detected radio flux densities, taken from Herzog et al. (2015b). The template SEDs shown in the legend in the upper left subplot were shifted between $1 < z < 12$. The results are shown at $z = 1$ (top left), $z = 4$ (top right), $z = 8$ (bottom left) and $z = 10$ (bottom right).

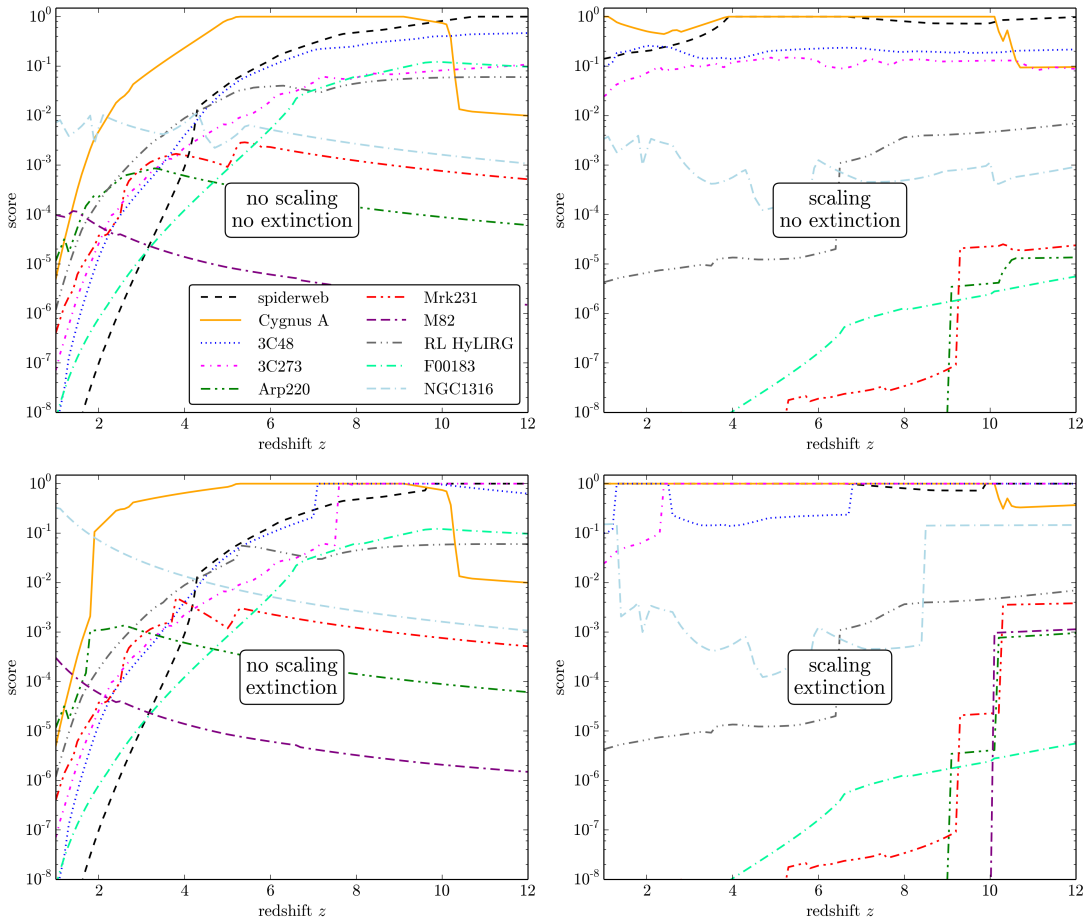

Figure 3.25: The scores denoting the goodness of fit for the different SED templates as a function of redshift, taken from Herzog et al. (2015b). A score of one indicates that the SED agrees with all photometric constraints, while a score less than this implies disagreement. Shown is the score resulting from the modelling with and without scaling in luminosity and additional extinction applied, as indicated by the labels in the centre of each plot.

options for the nature of IFRSs: 1) IFRSs are very similar to HzRGs, with similar luminosities, but at higher redshift ($z \gtrsim 5$); or 2) IFRSs are less-luminous versions of HzRGs at similar redshifts ($1 \leq z \lesssim 5$). Furthermore, Herzog et al. (2015b) suggest that if IFRSs have the same intrinsic properties as HzRGs (i.e. the same SED and luminosity), they are at $z \gtrsim 10.5$. Herzog et al. (2015b) were not able to rule out that IFRSs are lower-redshift galaxies similar to 3C48 or 3C273, but with significant dust extinctions. Several orders of magnitude of additional extinction was needed to account for the SEDs are these redshifts. In the case of the spiderweb galaxy, extinctions of up to 14 magnitudes was needed to account for the SED at $z \leq 2$. Given that all redshifts found for IFRSs were in the range $2 \lesssim z < 3$, Herzog et al. (2015b) suggested two explanations:

1. Their modelling is not physically realistic for galaxies at $z \sim 1$. All templates had to be scaled down in luminosity by factors up to 500. Herzog et al. (2015b) suggested the black hole mass must be scaled down by a similar factor, but that lower-mass black holes are very rare. Herzog et al. (2015b) discuss that scaling down the black hole mass would give a lower radio excess, which is in disagreement with the high radio-to-IR flux density ratios of IFRSs. They point out that such high amounts of extinctions are very rare at low redshifts, which decreases the possibility of finding IFRSs, which is in disagreement with the large sky density of IFRSs.

2. The IFRSs modelled by Herzog et al. (2015b) are intrinsically different to those with spectroscopic redshifts. For example, Cygnus A was the only template able to produce a good fit at $z \sim 1$ without additional dust obscuration, but this galaxy contains narrow emission lines, as opposed to the broad emission lines found for IFRSs with spectroscopy. If this SED model is accurate, then two populations of IFRSs exist with different redshift and emission line properties. Herzog et al. (2015b) point out, however, that no evidence exists for two sub-classes of IFRSs.

Herzog et al. (2015b) show that Cygnus A, 3C48 and 3C273 can be considered as HzRGs in their modelling at $z \geq 1$, fulfilling the selection criteria of $z > 1$ and $L_{3\mathrm{GHz}} > 10^{26}$ W Hz^{-1}, despite being scaled down in luminosity at low redshift. Therefore, Herzog et al. (2015b) conclude that only HzRGs can account for the SEDs of IFRSs.

Since HzRGs are known to be highly star forming, Herzog et al. (2015b) modelled the star forming contribution to the SED of their IFRSs by decomposing the IR emission into an AGN and SF component and independently scaling each of them in luminosity (see left plot of Fig 3.26). Herzog et al. (2015b) noted that almost any decomposition was possible, given that they were using upper limits. However, they were able to determine the maximum IR flux at each redshift from the composite SED model that was still in agreement with their upper limits. This in turn gave the maximum IR luminosity (from $8 - 1000$ μm) at each redshift of each component when assuming that only one component is contributing at one time, as well as the absolute maximum IR luminosity. Herzog et al. (2015b) presented these maximum luminosities at each redshift as the absolute upper limits on the total IR luminosities of extreme IFRSs (see right plot of Fig 3.26). Their IFRSs have $L_{8-1000\mu m} < 10^{12} L_{\odot}$ at $z \lesssim 1.5$, $L_{8-1000\mu m} < 10^{12-13} L_{\odot}$ at $z \lesssim 2.5$ and $L_{8-1000\mu m} < 10^{14} L_{\odot}$ at $z \lesssim 6$. At these redshifts, these luminosities would classify their IFRSs as ULIRGs or HyLIRGs. Herzog et al. (2015b) find that the maximum luminosities are unphysical at $z \leq 2.5$, since they predict a very low or absent AGN contribution and an IR luminosity mainly or even completely produced by SF. However, a purely star forming galaxy would follow the radio-FIR correlation, which

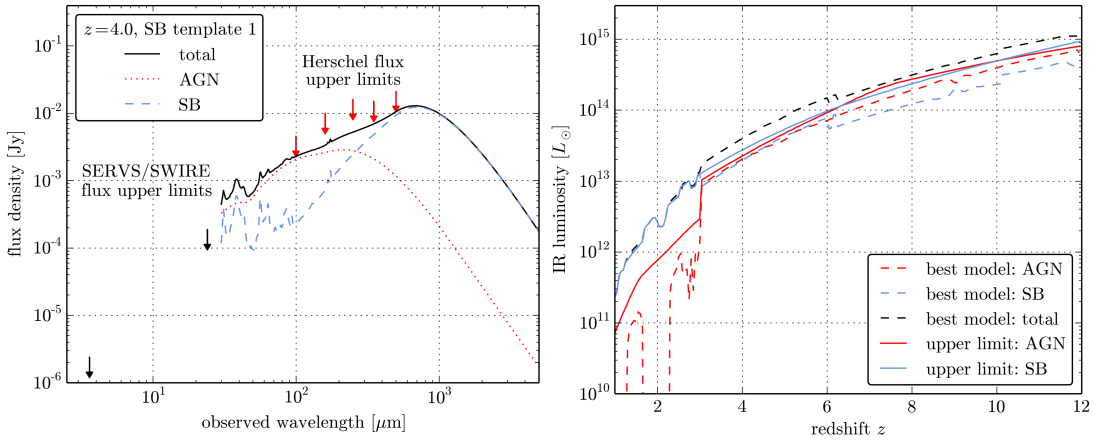

Figure 3.26: *Left:* The decomposed AGN/SF SED model of IFRSs at $z = 4$ using the IR upper limits, taken from Herzog et al. (2015b). The dotted red line and dashed blue line show the AGN and SF contributions, respectively. The solid line shows the maximum SED that is still in agreement with the upper limits. *Right:* The best fit (dashed line) and maximum possible (solid line) IR luminosity at each redshift of the AGN component (red), SF component (blue) and the total emission (black). The maximum luminosities are calculated assuming that only one component is contributing at one time and represent the absolute upper limits on the total IR luminosities of their IFRSs.

predicts a maximum radio luminosity two orders of magnitude lower than what is calculated from the 1.4 GHz detections. This showed that modelling the IR SED using only a SF template was unsuitable and that the existence of an AGN was necessary to account for the radio flux densities.

Following this finding, Herzog et al. (2015b) modelled the SEDs by decomposing the AGN and SF, but while also including the range of radio flux densities and using the radio-FIR correlation to calculate the radio luminosity based on the SF component. They did this using the same SF component as before and then added the SED template of the spiderweb galaxy, which covered the IR and radio. The fitting required that the SED matched the median 1.4 GHz flux density of 15 mJy. Given that significant SF is already present in the spiderweb galaxy, Herzog et al. (2015b) allowed their fitted SF component to be scaled by a negative factor, which represented less SF than what was already present. Based on this more appropriate fit, Herzog et al. (2015b) once again calculated the maximum possible IR luminosity at each redshift for the AGN and SF components, in which the AGN and SF contributions in the spiderweb galaxy were taken as 59% and 41%, as found by Seymour et al. (2012). The left plot of Fig 3.27 shows the contribution of each component from the fitted model that produced the maximum possible IR emission at $z = 4$. The right plot shows the maximum possible IR luminosities of the AGN and SF components and the maximum possible total IR luminosity at each redshift. At high redshift ($z \gtrsim 6$), these luminosities would classify IFRSs as HyLIRGs.

Herzog et al. (2015b) noted that the maximum possible luminosities when using and not using the radio fluxes were different by an order of magnitude, showing it is essential to consider the radio flux density in the SED modelling. However, Herzog et al. (2015b) pointed out that the second approach assumes that IFRSs are similar to HzRGs, which has compelling evidence, but has not been proven. Therefore Herzog et al. (2015b) conclude that the upper limits in Fig. 3.27 are more realistic, while those in Fig. 3.26 are absolute upper limits that cannot be exceeded, independent of the nature of IFRSs. Herzog et al. (2015b) also modelled the

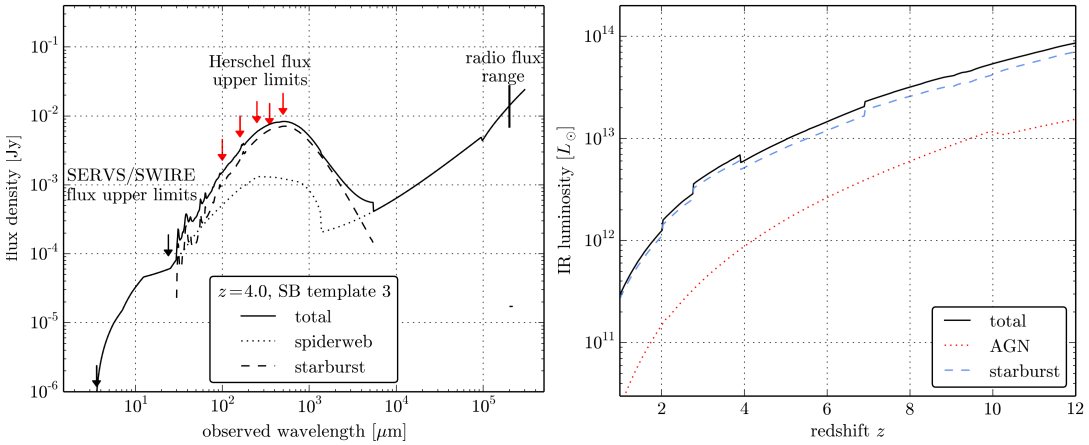

Figure 3.27: *Left:* The decomposed AGN/SF SED model of IFRSs at $z = 4$ using the IR upper limits as well as the range of radio flux densities, taken from Herzog et al. (2015b). The total SED (solid line) is composed of the spiderweb galaxy (dotted line) and the SF component (dashed line) and shows the maximum SED that is in agreement with the median radio flux density of 15 mJy and with the IR upper limits. *Right:* The maximum possible IR luminosity at each redshift of the AGN component (dotted red line), SF component (dashed blue line) and the total emission (solid black line), according to the fitted model.

decomposed AGN/SF SEDs of IFRSs using the templates of 3C237, 3C48 and Cygnus A, in addition to the SF component. Since no AGN to SF fractions are known for these, only the upper limits on the total IR luminosities were calculated. Herzog et al. (2015b) found that the results were very similar to those shown in Fig. 3.26, not differing by more than a factor of two. Therefore, Herzog et al. (2015b) concluded that the upper limits on the total IR luminosity from Fig. 3.27 hold for IFRSs in general, independent of their nature.

Based on these maximum IR luminosities, Herzog et al. (2015b) calculated upper limits on the star-formation rate and black hole accretion rate that could account for the SF and AGN components, respectively. They found upper limits on the star-formation rate of a few hundred $M_\odot$ yr^{-1} at $z \lesssim 4.5$, which increases with redshift and exceeds 10^4 $M_\odot$ yr^{-1} at $z \sim 11$. They found accretion rates of $< 1 M_\odot$ yr^{-1} at $z \lesssim 3$, $< 10 M_\odot$ yr^{-1} at $z \sim 6$ and less than a few tens of $M_\odot$ yr^{-1} at $z \geq 10$. These maximum IR luminosities, star-formation rates and black hole accretion rates were found to be consistent with previous findings for HzRGs. Based on all of these findings, Herzog et al. (2015b) conclude that they found no evidence ruling out the hypothesis that IFRSs are similar to HzRGs.

3.5.4 Radio spectra of extreme IFRSs

Given the evidence that a fraction of IFRSs consist of GPS and CSS sources, Herzog et al. (2016) studied the radio spectra of IFRSs. The majority of their sources come from those in the Zinn et al. (2011) catalogue that are located within the ATLAS fields, given the rich radio data available in these fields. One source (ID S11) was discarded since we found evidence in this thesis that it did not meet the criteria of an IFRS (see section 4.3.3). The rest of their sources are selected from those presented in Maini et al. (2016), based on the deeper SERVS data, which was able to uncover new IFRSs not catalogued by Zinn et al. (2011). While Maini et al. (2016) included sources which had lower radio-to-IR flux density ratios of > 200, Herzog et al. (2016) limited their sample to those with ratios of > 500, in order to study only the most extreme IFRSs. Their final sample from these two catalogues consisted of 34 IFRSs: 19 in the

CDFS and 15 in the ELAIS-S1.

Radio flux densities were drawn from the same observations as summarised for our ATLAS sample in section 2.2.2.1, although they made use of the 200 MHz deep GLEAM fluxes, and used narrow-band 4.8 and 8.6 GHz observations from Middelberg et al. (2011b) for the majority of sources, instead of broadband 5.5 and 9.0 GHz observations. Additionally, 844 MHz observations from ASKAP-BETA (Marvil et al. in prep.) were used in the CDFS. Careful attention was paid toward ensuring that the flux densities were not decreased by resolution effects. Ten measurements were discarded due to confusion effects, while the flux densities of four confused GLEAM sources were used as upper limits. Further upper limits were calculated for all non-detections, and used in the fitting where they were able to constrain the spectrum (i.e. when they predicted a lower flux than the spectral model that was fit without using these limits). Herzog et al. (2016) were not able to rule out variability effects, which may have affected a few tens of per cent of the spectra at $\gtrsim 5$ GHz at the level of $\sim$10%.

Herzog et al. (2016) built radio spectra for the IFRSs using a least-squares fitting routine. A power law was fit to the data and considered an appropriate fit if the cumulative deviation of the lowest and highest frequency data points constraining the spectrum were less than 1σ. If the spectra had the appearance of a turnover or deviated at the lowest frequency data point, they fit a single homogeneous SSA model according to equation 1.5. Spectra deviating at the highest frequency data point were not fitted with a different curve, but simply labelled as either upturning or steepening.

Herzog et al. (2016) also compiled a control sample of the general radio-loud galaxy population by randomly selecting 15 ELAIS-S1 and 19 CDFS sources which had similar 1.4 GHz flux densities to their IFRS sample. This was used for a comparison between the radio spectra of IFRSs and those of general radio-loud galaxies. Radio spectra for the control sample were built in the same way, and were found to be self-consistent, without spectral features that may arise from resolution effects. We refer to the sources from the control sample as RLGs (radio-loud galaxies) in the following statistics.

Herzog et al. (2016) found 24/34 IFRSs and 30/34 RLGs were well fit by a power law, but only 15 IFRSs and 22 RLGs had sufficient spectral coverage to enable a deviation to be ruled out a low and high frequencies. Five IFRSs (15^{+8}_{-4}%) and three RLGs (9^{+7}_{-3}%) showed a clear turnover in their spectra. Herzog et al. (2016) classified one IFRS and one RLG as a GPS source based on a turnover above 500 MHz, from which they estimated that 3^{+6}_{-1}% of IFRSs and RLGs are GPS sources. Since the spectra for nine IFRSs and eight RLGs were not detailed enough to rule out turnovers above 200 MHz, and since none of the spectra covered below 150 MHz, Herzog et al. (2016) suggested that $\geq 9^{+7}_{-3}$% of IFRSs and $\geq 6^{+7}_{-3}$% of RLGs consist of CSS sources. Based on these findings, they conclude that their sample presents no evidence that IFRSs consist of a higher fraction of GPS and CSS sources compared to general RLGs. However, they point out that the expected high redshifts of IFRSs may prevent the turnover from being observed in their data range. In fact, many sources are likely to be CSS sources based on their steep spectra and compact morphologies.

The spectral indices derived from the best fit radio spectra from Herzog et al. (2016) were in the range $-1.53 < \alpha < -0.52$ for their IFRSs and $-1.73 < \alpha < -0.09$ for the RLGs, with respective medians of -0.95 ± 0.05 and -0.79 ± 0.06. Herzog et al. (2016) find 29 IFRSs (85^{+4}_{-8}%) and 14 RLGs (41^{+9}_{-8}%) with steep spectra ($\alpha < -0.8$), four IFRSs (12^{+8}_{-4}%) and two RLGs (6^{+7}_{-2}%) which were USS ($\alpha < -1.3$), and twelve (35^{+9}_{-7}%) IFRSs and three (9^{+7}_{-3}%) RLGs which were USS candidates ($-1.3 \leq \alpha \leq -1.0$). Herzog et al. (2016) found three IFRSs (12^{+8}_{-4}%) and no RLGs (0^{+5}%) that showed a spectral steepening at high frequency. Based on

the distributions of spectral indices, Herzog et al. (2016) rejected the hypothesis that the IFRSs and RLGs are from the same parent population (probability $p < 0.001$).

Herzog et al. (2016) investigated the spectral index as a function of the 3.6 μm flux density, since higher-redshifts IFRSs are thought to have generally steeper radio spectra and fainter IR emission. Only 1/8 ($13^{+20}_{-4}\%$) of the IFRSs with $S_{3.6\mu m} < 15\mu$Jy had a spectral index steeper than the median, while 16/26 ($61^{+8}_{-10}\%$) with $S_{3.6\mu m} > 15\mu$Jy had a spectral index steeper than the median. They calculated a probability $0.0003 < p < 0.075$ that the two are uncorrelated.

Herzog et al. (2016) found one IFRS which had a morphology of an FR II galaxy and suggested it may differ from the majority of IFRSs, which are compact and possibly younger radio sources.

Two sources from Herzog et al. (2016) were also included in the SED modelling from Herzog et al. (2014). Herzog et al. (2016) showed that 3C273 provided an inadequate template in the radio regime since its spectral index was flat, as compared to the steep spectra of their sources. They show that 3C48 is a much more adequate template, with a spectral index of $\alpha \sim -0.8$. Furthermore, the sample from Herzog et al. (2016) includes all six sources from Herzog et al. (2015b), which have spectral indices between $-1.15 < \alpha < -0.98$. Herzog et al. (2016) show that even 3C48 does not provide a steep enough spectral index to account for these radio spectra. However, Cygnus A and the spiderweb galaxy are known to have ultra-steep spectral indices of $\alpha \sim -1.2$ and $\alpha \sim -1.3$, respectively. This provides further evidence that the SEDs of IFRSs are well represented by the spiderweb galaxy and Cygnus A.

To complement the cm-wave observations from ATLAS, Herzog et al. (2016) also studied the brightest IFRS in the Zinn et al. (2011) catalogue, xFLS478, located in the northern xFLS field. They observed this source at 105 GHz using the Plateau de Bure interferometer, which is the highest-frequency flux density measurement that has been made of an IFRS. Herzog et al. (2016) modelled xFLS478 with a power law and SSA model, since the lowest data point very slightly deviated from a power law. The power law with spectral index of $\alpha \sim -1.2$ was consistent with the 105 GHz measurement (rest frame $\sim$300 GHz at $z \sim 2$), implying the AGN dominates over SF emission even in the mm regime. Herzog et al. (2016) point out that similar behaviour has been observed in F00183-7111 (Norris et al., 2012) and some HzRGs (Emonts et al., 2011a,b).

Herzog et al. (2016) also presented a 4.5 μm detection of xFLS478 from *Spitzer* and FIR detections from *Herschel* observations at 250, 350 and 500 μm. Following the same procedure as in Herzog et al. (2015b), they modelled the broadband SED of this source in the range $0.5 \leq z \leq 12$. Interestingly, they could not find any SED template that could reproduce the SED of xFLS478, including the templates of HzRGs, which were found to be inconsistent with the FIR detections. This is surprising, since xFLS478 was only slightly radio-brighter than the IFRSs from Herzog et al. (2015b), and had FIR detections similar to the FIR flux density uncertainties from Herzog et al. (2015b). Therefore, given the similarities to F00183 mentioned above, Herzog et al. (2016) modelled xFLS478 using the radio SED of F00183 and the FIR SED template of a star forming galaxy composed of synchrotron, free-free and thermal dust emission. The best fit was found at $z = 1.1$ by scaling up the luminosity of F00183 by a factor of 3 and the FIR SED by a factor of 1.9, which gave a star-formation rate of 170 $M_\odot$ yr^{-1}. If this is accurate, xFLS478 is the lowest IFRS known, and has an SED significantly different from the majority of known galaxy SEDs.

3.6 Discussion

3.6.1 The link between IFRSs and HzRGs and its implications

It is now clear that a significant similarity exists between IFRSs and HzRGz. HzRGs are typically defined by $L_{3\mathrm{GHz}} > 10^{26}$ W Hz^{-1} and $z \geq 1$. They are amongst the most luminous and massive galaxies in the early universe and are expected to be the progenitors of the most massive galaxies in the local universe (Seymour et al., 2007). They are known to have high star-formation rates as well as host powerful AGN, which makes them key probes of the relationship between AGN and SF. However, only about $100 - 200$ HzRGs are known across the entire sky, depending on the definition. Miley and De Breuck (2008) find < 200 HzRGs with $z > 2$ and $L_{500\mu\mathrm{m(rest)}} > 10^{27}$ W Hz^{-1}. Comparatively, the sky density for the most extreme IFRSs of $\sim$7 per deg^{-2} suggests that a few hundred thousand IFRSs exists across the sub-mJy 1.4 GHz sky. As discussed by Herzog et al. (2014), this implies that IFRSs are cosmologically significant, representing an overlooked population of high-redshift AGN that could have considerably influenced the evolution of the universe. If this is true, then the number of AGN in the early universe is much higher, which presents much more significant problems to the cosmological model for the structure formation and the growth of SMBHs after the Big Bang (Herzog et al., 2014, and references therein.). As suggested by Zinn et al. (2011), IFRSs may make up the unresolved components of the Cosmic X-ray background.

Selecting IFRSs from existing co-spatial deep radio and IR surveys is very simple. We showed that this is a very effective technique in Collier et al. (2014) using *WISE*, NVSS and FIRST. Selecting more samples of IFRSs will enable important tests of galaxy evolution using large sample sizes. In particular, deeper samples will enable the relationship between the AGN and SF to be characterised across a vast range of cosmic time.

3.6.2 The link between IFRSs and USS sources and implications

USS sources are also closely related to HzRGs. USS sources are thought to be preferentially located at high redshift, and have been used effectively to find radio sources out to $z \sim 4$ (e.g. De Breuck et al., 2006; Norris et al., 2011b, and references therein.). However, it remains unclear why USS sources should be at high redshift (Miley and De Breuck, 2008). Callingham et al. (2015) have suggested that part of the USS population could be made up of dying GPS and CSS sources whose spectral breaks have shifted below a low frequency turnover. However, Klamer et al. (2006) find no evidence for high-frequency steepening in their sample of USS sources, and propose that USS sources reside within gas-rich clusters, which occur more commonly at high redshift.

Garn and Alexander (2008), Collier et al. (2014) and Herzog et al. (2016) found a significant fraction of USS sources in their samples of IFRSs. Herzog et al. (2016) showed that the more extreme IFRSs, which are thought to be at higher redshifts, have a larger fraction of USS sources. Furthermore, Singh et al. (2014) studied a sample of USS sources and found a significant fraction of IFRSs.

If USS sources are tracers of gas-rich clusters, which occur more commonly at high-redshift, then we expect them to be related to HzRGs, which host powerful AGN and rigorous SF, and therefore to also relate to IFRSs. Their connection implies that a significant fraction of IFRSs may be tracers of gas-rich galaxies or galaxy clusters.

3.6.3 The link between IFRSs and GPS/CSS sources and implications

We found in Collier et al. (2014) that 32 and 124 IFRSs in our sample consisted of GPS and CSS sources, respectively (see section 3.1.4). However, some of these had more than one FIRST counterpart within 30″ of the NVSS position, and therefore, may not be compact radio sources, but could be extended RGs. We found 31 GPS sources and 93 CSS sources with one FIRST counterpart. However, not all 1317 IFRSs had data sufficient to determine whether an IFRS was a GPS or CSS source, considering all the selection criteria and the measurements needed to define them. We found 145 IFRSs with data sufficient to determine whether they were GPS sources or not, 31 of which were GPS sources, which gives a fraction of 21%. We found 761 IFRSs with data sufficient to determine whether they were CSS sources or not, 93 of which were CSS sources, which gives a fraction of 12%. Since our criteria for selecting GPS and CSS sources was quite strict, and since we have only three flux density measurements, each from a different epoch and resolution, this fraction has a significant uncertainty associated with it. However, if these fractions are accurate, there are some interesting implications.

These fractions of 21% and 12% are generally within the range given by Orienti (2016) of $15 - 30\%$, which denotes the frequency-dependent fraction of GPS and CSS sources within the general cm-wavelength radio population. However, they are significantly different to the fraction of GPS and CSS sources amongst cm-wavelength radio sources given by O'Dea (1998) as ∼10% and ∼30%. This suggests that IFRSs are dominated by the most compact sources, with a higher fraction of GPS sources than compared to the general radio population. These are either in an early evolutionary stage, or are frustrated by a dense medium. As pointed out by Herzog et al. (2015a), both of these hypotheses can be accounted for at high redshift.

The GPS sources moderately suffer from small number statistics, and are much harder to detect in WENSS, so may be subject to selection effects. The CSS sources are not affected by these issues, so here we focus on the CSS sources. The lower fraction of CSS sources compared to O'Dea (1998) may suggest that we are observing radio spectra that have been more redshifted than typical CSS sources, with the turnover falling below our data range. These may even be made up of a large fraction of GPS (rather than CSS) sources with redshifted spectra. At $z = 2$, a GPS source with an intrinsic turnover of $\nu_m = 1$ GHz will have an observed turnover of $\nu_m = 333$ MHz, very close to the WENSS frequency of 325 MHz. Those 15 IFRSs we identified as curved CSS sources may represent this kind of behaviour.

Herzog et al. (2016) studied more extreme IFRSs and found that $3^{+6}_{-1}\%$ consisted of GPS sources, and $\geq 9^{+7}_{-3}\%$ consisted of CSS sources, both of which required observing a turnover to satisfy the classification as GPS or CSS. This fraction of CSS sources is significantly lower, and is closer to the fraction of GPS sources within the general cm-wavelength radio population of ∼10% suggested by O'Dea (1998). The evidence suggests that these more extreme IFRSs are at higher redshift, which would account for the lower fraction of CSS sources detected by Herzog et al. (2016), since their turnovers would have shifted below their lowest frequency of 150 MHz.

The same phenomenon has been found by Coppejans et al. (2015) and used to select high-redshift radio sources within the Boötes field. Coppejans et al. (2015) identified sources with turnovers in the MHz range, referred to as Megahertz Peaked Spectrum (MPS) sources. Because of the linear size − turnover relation (see equation 1.14), sources with low frequency turnovers are expected to be large in linear size. However, sources compact on mas scales and with low frequency turnovers are expected to be GPS sources at high redshifts ($z > 2$). Coppejans et al. (2015) used the deep optical, IR and UV data available in this field to fit photometric redshifts

and identified five sources at $z > 2$ from their sample of 33 MPS sources, which ranged from $0.1 < z < 3.2$. Coppejans et al. (2015) concluded that the four sources which were too faint to find photometric redshifts are likely at $z > 3$. These four may be similar to IFRSs since they are radio-loud sources located within the region with deep multi-wavelength coverage, which means they are likely to meet the Zinn et al. (2011) criteria. Coppejans et al. (in prep.)[7] followed up 11 of their MPS sources with VLBI observations. They found six sources unresolved at ∼14 mas and three double-lobed sources with $0.9 < l < 1.1$ kpc, giving encouraging evidence to this so called "MPS method".

Middelberg et al. (2011b), Collier et al. (2014) and Herzog et al. (2015b) found compact structures for a significant fraction of IFRSs. Furthermore, as summarised above, the fraction of observed turnover frequencies appears to decrease with decreasing near-IR flux density, which also appears to decrease with increasing redshift (see Fig 1.18). This may suggest that some IFRSs share the same phenomenon as those from Coppejans et al. (2015), and are GPS sources at high redshift, observed as MPS sources. Therefore, we can use the MPS method for IFRSs with low frequency turnovers to search for high-z AGN. For example, the ATLAS source S114 from the CDFS was fitted with a turnover of 300 MHz from Herzog et al. (2016). The source was observed with VLBI by Norris et al. (2007) and was found with a VLBI flux density of 5 mJy, compared to the peak and integrated flux densities from ATLAS of 5.7 mJy/beam and 7.2 mJy. Norris et al. (2007) suggested the source is resolved and consists of a 5 mJy core, surrounded by a 2 mJy low-brightness structure, which may be the lobes or jets. If so, then S114 is unlikely to be like an FR II, since they have weak cores and are very strongly lobe-dominated. This would mean that S114 is a FR I-like galaxy. Norris et al. (2007) show that if at $z = 1$, the lobes are 37 kpc and the luminosity is $S_{1.4\mathrm{GHz}} = 4 \times 10^{25}$ W Hz^{-1}, which would place it very close to the jet stability boundary in Fig. 1.12, although still above it. If this IFRSs is at $z > 2$ as the evidence suggests, it is well above this boundary and therefore cannot be FR-I-like, and therefore is unlikely to be core-dominated. Since the VLBI amplitude is most likely worse than 10%, if we can consider the source unresolved in ATLAS, most to all of its flux is recovered with VLBI. If so, then the physical size of the source is $< 0.03''$, corresponding to 260 pc or less at any redshift. Based on equation 1.14, this gives an intrinsic turnover of ∼1.4 GHz. If the observed turnover is 300 MHz, then S114 must be at $z \sim 4$.

3.6.4 The nature of IFRSs

There is substantial evidence that IFRSs are AGN, rather than SFGs. Therefore, their radio emission cannot be accounted for by SF. Furthermore, they are all extremely radio-loud, which means we expect that they are launching jets. Very few IFRSs have flat or upturned spectra. On the contrary, their spectra are extremely steep, and appear to steepen for the more extreme IFRSs. Furthermore, they are compact on arcsec scales (Middelberg et al., 2011b; Collier et al., 2014) and contain a high fraction of compact cores and a few that are most likely compact doubles (Herzog et al., 2015a), but no observed core-jet morphologies. These VLBI morphologies, the lack of flat or upturned radio spectra and the optical faintness rules out Blazars. The optical faintness and extreme radio-IR flux density ratios also rules out quasars (e.g. see Fig. 1.17) and suggests that the jets of IFRSs are oriented at large angles, although the brightest may consist of some quasars (e.g. Collier et al., 2014; Herzog et al., 2014). The low compactness (i.e. mas-to-arcsec flux ratios) found by Herzog et al. (2015a) and Middelberg et al. (2008b) may suggest that the jets are being resolved on intermediate scales between mas

[7] See `http://www.ira.inaf.it/meetings/cssgps2015/Presentations/Rocco_Coppejans.pdf`

and arcsec scales, with jets of a few kpc. If we can consider the general population of IFRS as being compact (many pc or a few kpc) in the radio, given that they are steep spectrum, then they ought to be GPS or CSS sources at high redshift.

Furthermore, the high VLBI detection fraction found by Herzog et al. (2015a) suggests that the majority of IFRSs contain very active AGN cores. Herzog et al. (2015a) found a correlation between the redshift and compactness and suggested that this may be accounted for by: 1) higher-redshift objects tending to be younger; 2) higher-redshift objects being located in more gas-rich environments which frustrate the jet growth (Klamer et al., 2006). If both of these work together then a significant fraction of IFRSs are very young AGN within dense and confining environments, which would fit within the "frustration scenario". If this is the case, this high density of gas may enable the AGN to be constantly active, as well as produce significant SF, accounting for the high VLBI detection fraction and the similarities to HzRGs.

Herzog et al. (2015b) found that the spiderweb galaxy and Cygnus A were the best fitting templates that account for the SEDs of IFRSs during each stage of their modelling (see Fig. 3.25), which included modelling the SEDs with and without scaling in luminosity and additional extinction. When the SEDs were not modified, these templates had to be at $z \geq 5$. Other templates could explain the SEDs only with significant modification to their luminosities or level of dust extinction. The simplest explanation is that IFRSs are at $z \geq 5$, since we know that galaxies with these inherent SEDs at these luminosities can exist at $z \geq 5$. Hypothesising that the SEDs of IFRSs represent a new kind of SED that is scaled down in luminosity or that has significant dust extinction requires proposing a new kind of object, which is equally as exciting.

Chapter 4

Gigahertz Peaked Spectrum and Compact Steep Spectrum Sources

As discussed in section 1.3.7, it is generally accepted that the majority of GPS and CSS sources are young and evolving, but good evidence exists in individual cases for frustrated, prematurely dying and restarted systems. As also discussed, it is still debated whether SSA or FFA accounts for the peaked spectra of GPS and CSS sources. Furthermore, the properties of faint GPS and CSS sources are generally unknown.

In this chapter, we present a study of the radio spectra and high-resolution morphologies of faint GPS and CSS sources from our SMC sample (section 4.1), our ATLAS VLBI sample (section 4.2), and our ATLAS ATCA sample (section 4.3). We use these results to determine plausible absorption mechanisms and the general nature and properties of faint GPS and CSS sources. Following this, we present the results from a case study of the spectral variability of 1718-649 (section 4.4). Finally, a general discussion about all samples is presented (section 4.5), followed by a summary and conclusion (section 4.6).

4.1 Mid-Strength Sample: SMC

4.1.1 Catalogue of faint sub-mJy GPS & CSS sources

The 5.5 and 9.0 GHz radio-continuum maps of all 72 SMC sources are shown in figure C.2 in Appendix C. The component and source catalogues are shown in Tables D.1 and E.1 in Appendix D and E.

4.1.2 Modelling the radio spectra

We use all 20 GLEAM sub-bands and all four ATCA sub-bands per frequency in the modelling. Based on the discussion in section 2.3.1.8, and since we want to use all available reliable flux densities, we use the following ATCA flux densities when modelling the radio spectra:

(1) pre-CABB beam-matched flux densities where available;

(2) pre-CABB non-beam-matched flux densities where these agree within 2σ to (3) and where (1) is unavailable;

(3) CABB flux densities where these agree within 2σ with whichever is used from (1) or (2).

If the fluxes don't agree to within 2σ, we use only the pre-CABB beam-matched fluxes. A handful of sources include pre-CABB beam-matched fluxes that also seem to be problematic (e.g. SMC_72 at 2.4 GHz). For such sources, we do not make conclusions about GPS and CSS sources in general.

When considering what models to fit to the radio spectra, we took into consideration the number of free parameters from each model, and the ranges of these parameters as compared to our data. Interestingly, despite being historically favoured, the single homogeneous SSA model was found to fit our data poorly, predicting too steep a spectral index in the optically-thick part of the spectrum, such as in the examples seen in Figures 4.1. The Bicknell et al. (1997) FFA model gave a much better fit in nearly all cases, and so we use the FFA model here. We also considered using a double SSA model, but this required two extra free parameters compared to the FFA model, and fitted no better than the FFA model, so was discarded following Occam's razor.

We also consider introducing a high-frequency break in the spectrum, either a Kardashev break or an exponential break (see section 1.3.1.3). We found that the fitted Kardashev model generally resulted in a break within the frequency range of our data, but that the exponential model resulted in a break beyond the frequency range of our data, sometimes so high that it was essentially reduced to a model without the break. However, for some sources, the exponential break was above but close to the highest frequency data points and had a small error, causing significant curvature in the model at high frequency (since it is a multiplicative term of $e^{-\nu/\nu_{br}}$), and therefore, we consider the exponential break in these models to be reasonable. These are presented during the analysis of individual sources (see section 4.1.5). However, during fitting all the spectra, we used a Kardashev break, since this model is generally used to represent the integrated flux of all components of the source.

In summary, we fit three models to the radio spectrum of each source and derived the reduced χ^2 values to estimate the goodness of fit:

1. a power law
2. the Bicknell et al. (1997) inhomogeneous FFA model (equation 1.10)[1]
3. model 2 with a Kardashev (1962) break (see section 1.3.1.3).

In general, the best fit model was chosen based on having the smallest reduced χ^2 value. We initially fitted spectra with a simple power law, which is the simplest model with only two free parameters. We then introduced two additional parameters to fit a FFA model, which in many cases gave a much better visual fit, with smaller reduced χ^2 values. In cases where the data indicated a high-frequency break which was not well-modelled by FFA, we then added a high-frequency Kardashev break to the model.

In most cases ($\sim 75\%$), it was found that the FFA models produced a much better fit than the simple power law fit. This is not surprising, since our data range from $\sim 0.07 - 10$ GHz, and we expect all radio galaxies to turn over at some point at low frequency, and therefore we begin to see curvature in the radio spectrum at low frequencies. However, in about half of these cases, the fitted model turns over at a frequency below ~76 MHz, and therefore the fitted parameters a and p were found to have extremely large uncertainties, which in many cases had $\delta a > a$ and $\delta p > |p| + 1$. Although this is the case, it could be seen that the power law fit

[1]From this point onwards, we simply refer to this model as the 'FFA model'.

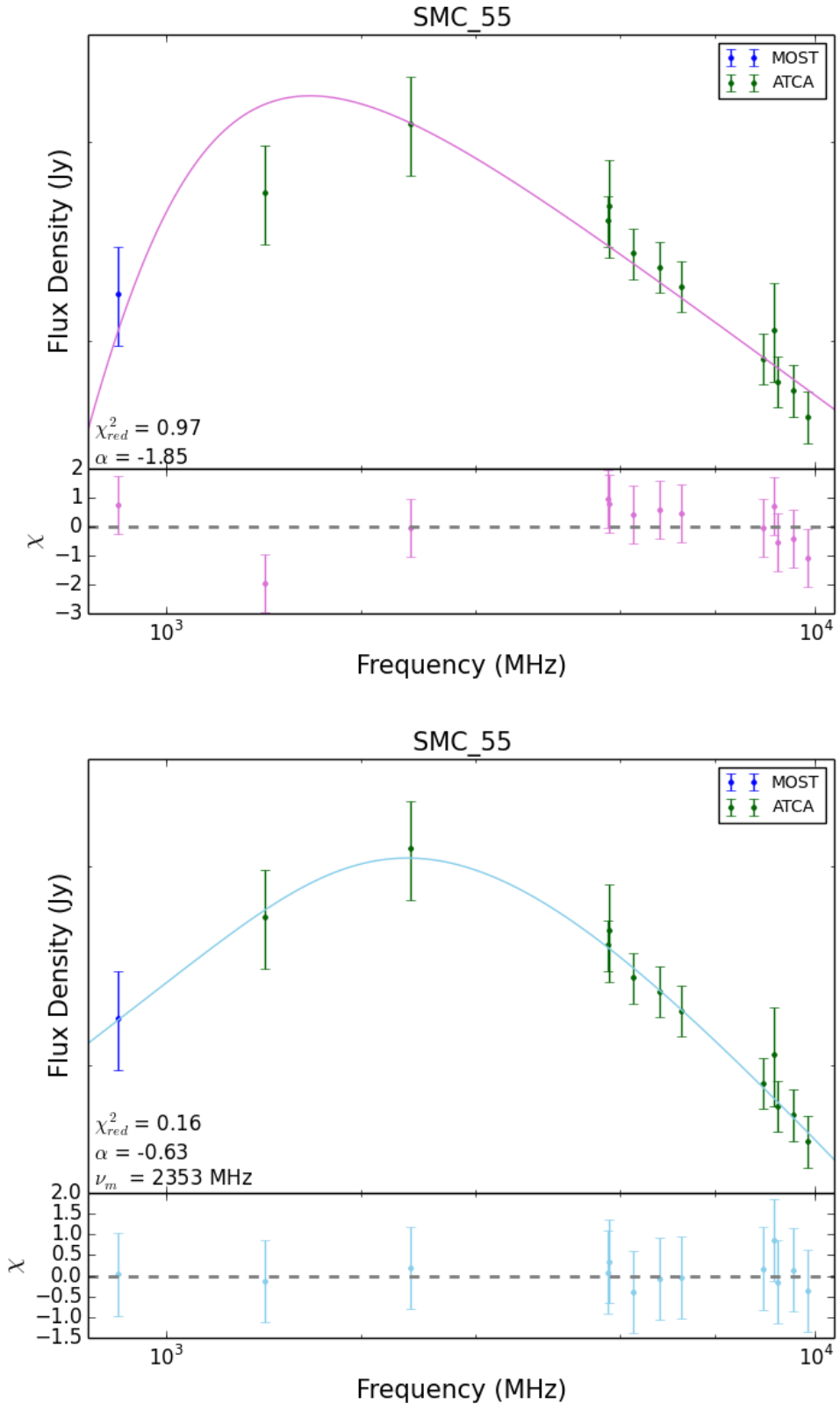

Figure 4.1: A SSA (top) and FFA model (bottom), fitted to source smc_55 (here) and smc_76 (next page). The homogeneous SSA model fits poorly when compared to the FFA model, predicting too steep a spectral index in the optically thick part of the spectrum. The peak of SMC_55 is ∼30 mJy.

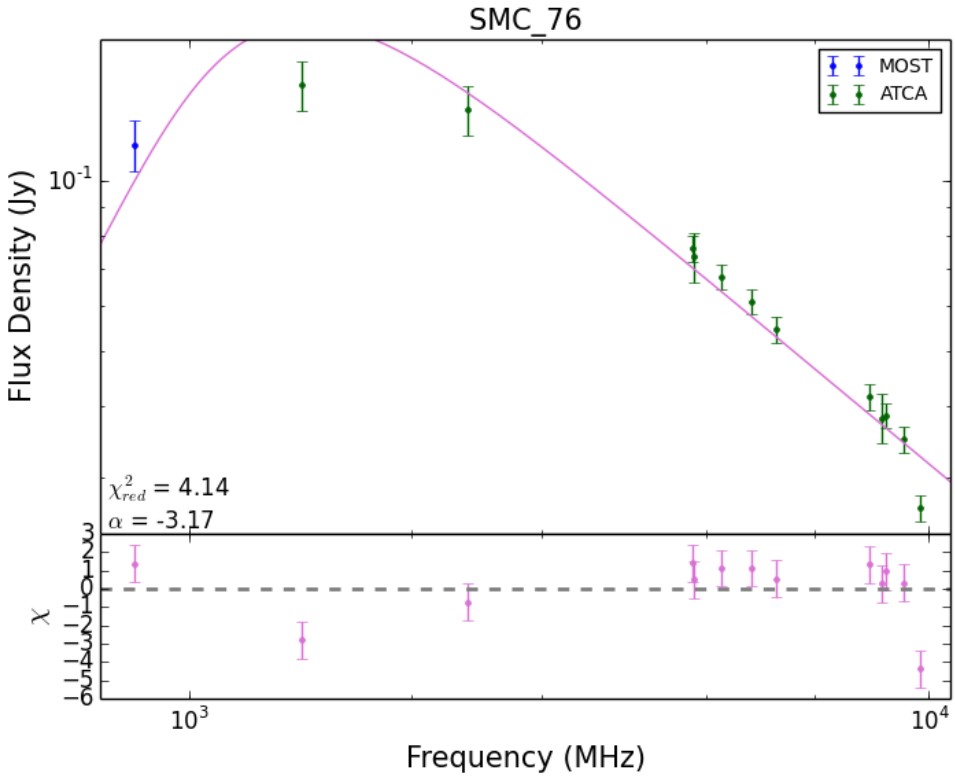

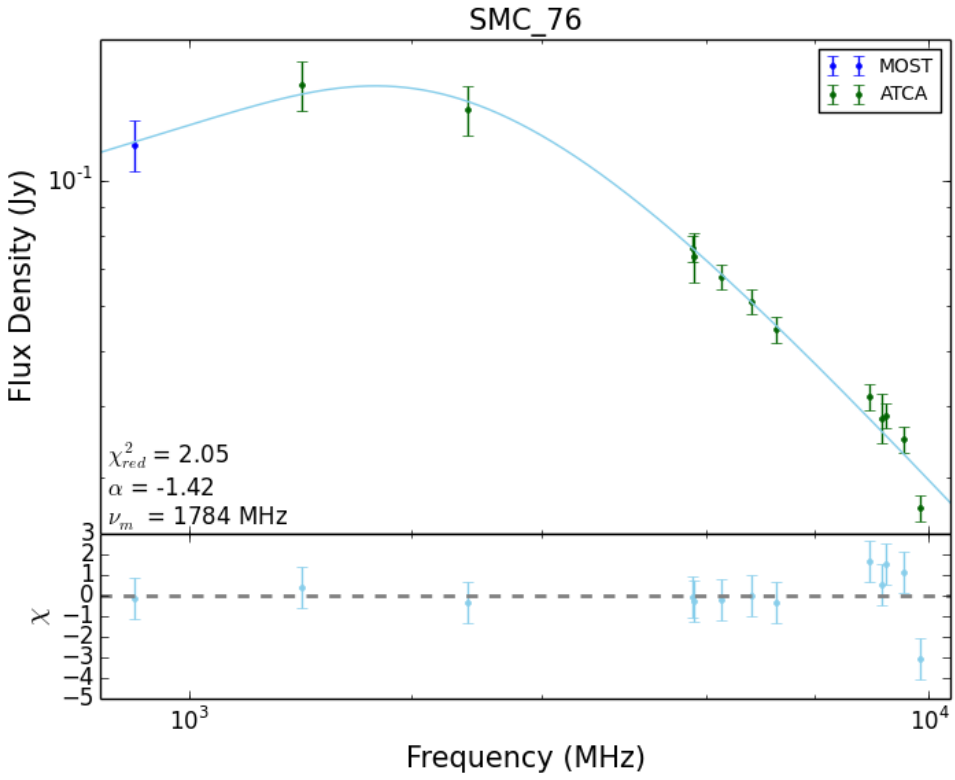

Fig. 4.1. (continued)

was inappropriate, even if a break was included (e.g. see Fig 4.2), and that the FFA models produced a much better fit, especially considering that we expect the sources to turn over at some point. Therefore we use the FFA models when they are found to produce a better fit.

The models we fit to the radio spectra of each source used the same procedure that we used in Tingay et al. (2015), which we now summarise. We fitted the models using a nonlinear least squares fitting routine that applied the Levenberg-Marquardt algorithm, which iteratively linearises the function during each iteration based on a new estimate of the function from the gradient of the previous iteration. This routine finds a minimum when the derivative of the sum of squares with respect to the new parameter estimates is zero. The fitting routine produces a covariance matrix that allows for the uncertainties to be estimated. This is formed by multiplying the Jacobian approximation to the Hessian of the least squares objective function by the residual variance. We take the uncertainties as the diagonal terms of this covariance matrix, which represent the 68.27% confidence interval (1σ). The uncertainties on the data points were assumed to be gaussian for this analysis.

4.1.3 Spectral Models

The measurements used to fit the spectral models for the SMC sources are shown in table 4.1. The models used to fit the radio spectra are summarised in table 4.2. The best fit models for all 70 SMC sources for which a successful fit was found are shown in figure 4.3. The models used in the fitting, and the values of each of the parameters are summarised in table 4.3.

The distributions of the turnover frequencies, break frequencies, spectral indices and p values are shown is figure 4.4, 4.5, 4.6 and 4.7, respectively. The statistics of each of these parameters are listed in table 4.4.

The majority of our sources have a turnover frequency $\nu_m < 500$ MHz, with only six sources having $\nu_m > 500$ MHz. Furthermore, only seven sources have $\nu_m > 200$ MHz. Based on the observed turnover frequency ν_m, we put the 70 sources for which we found a successful fit into three bins: 1) GPS sources with $\nu_m \geq 1$ GHz; 2) CSS sources with $0.08 < \nu_m < 1$ GHz; 3) general radio sources with upper limit $\nu_m < 0.08$ GHz (most likely extended radio galaxies or quasars, but could also be high-redshift GPS or CSS sources). Sources fitted with a power-law model are put in the third bin. According to the bins above, amongst our sample we find six GPS sources (9%), 15 CSS sources (21%), and 49 general radio sources (70%). Taking just the GPS and CSS sources from our sample, 29% are GPS and 71% are CSS. Comparatively, amongst the general cm-wavelength Jy-level radio population, ∼10% are GPS and ∼30% are CSS, and taking just the Jy-level GPS and CSS sources, ∼25% are GPS and ∼75% are CSS (O'Dea, 1998).

These fractions between our mJy-level sample and the O'Dea (1998) Jy-level sample are generally consistent and suggest that our sample is fairly representative of the general radio population and all stages of radio galaxy evolution, particularly compared to the GPS sources. If the two samples have the same redshift distribution, then we would expect a similar fraction of GPS and CSS sources, whereas a higher redshift distribution would result in a higher fraction of CSS sources (e.g. at $z = 1$, sources with a rest frame turnover of 1 GHz have an observed turnover of 500 MHz). This implies that mJy-level GPS and CSS sources have a very similar redshift distribution to the Jy-level GPS and CSS sources. If mJy-level and Jy-level GPS and CSS sources do have the same redshift distribution, which typically peaks at 0.5 for galaxy-type GPS and CSS sources (O'Dea, 1998), then mJy-level GPS and CSS sources have low luminosities, of the order of 10^{24} W Hz^{-1} and follow the lower track from Fig. 1.12. This is

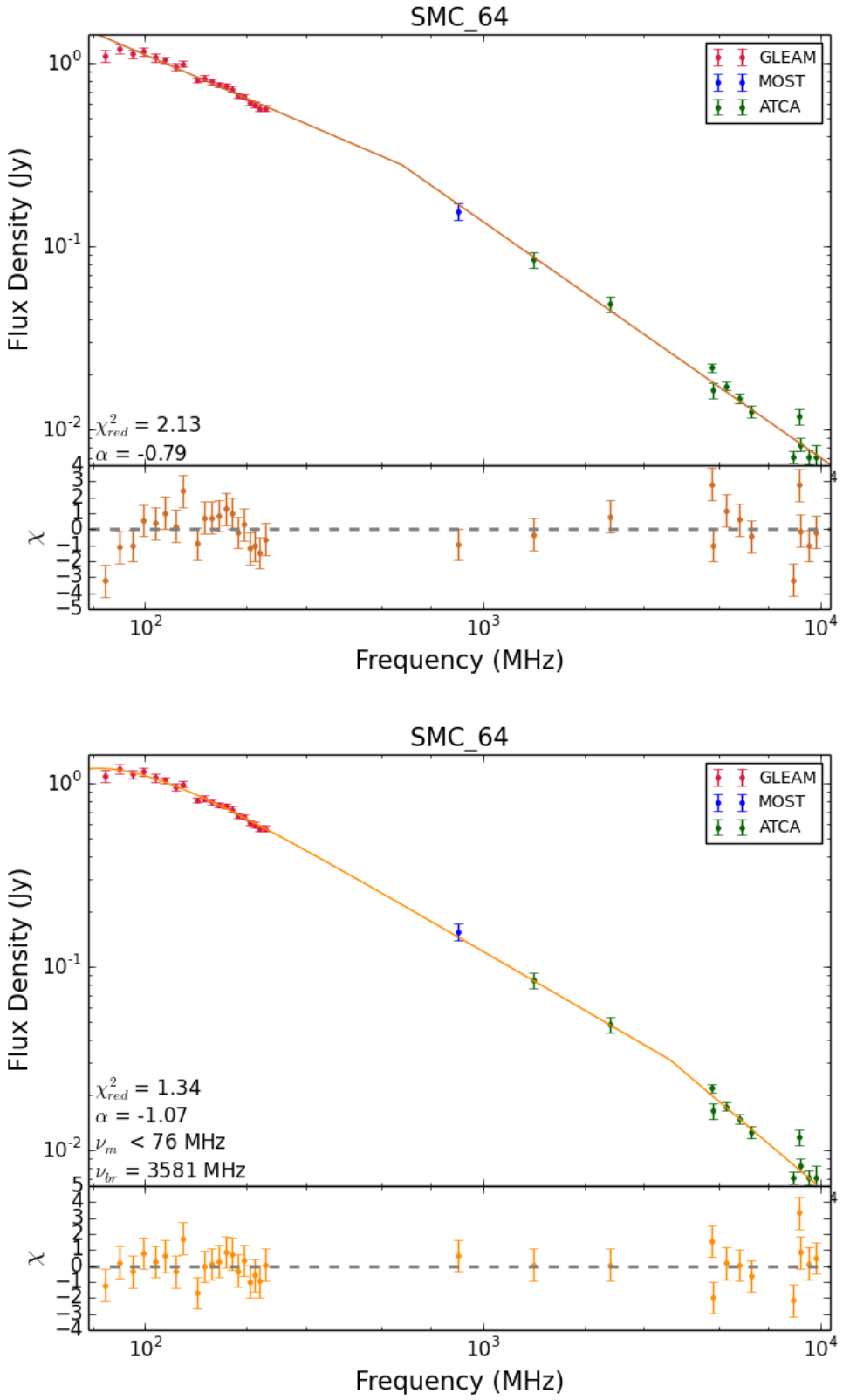

Figure 4.2: A simple power law model (top) and a FFA model (bottom) fitted to source smc_64, both with a high frequency break. It can be seen that the FFA model produces a better fit, despite not turning over within the frequency range of our data.

consistent with the redshifts and luminosities we estimate for a number of faint GPS and CSS sources in section 4.1.5.

The fraction of GPS sources amongst our sample is 9%, consistent with that of Jy-level GPS sources (10%). However, the fraction of CSS sources amongst our sample is 21%, lower than that of of Jy-level CSS sources (30%). The following explanations may account for this:

1. Since the spectra are faint, and because of the steep spectral indices either side of the turnover, only observations with frequencies close to the turnover will yield detections. Those with low turnovers will have less spectral coverage and be harder to identify. This is consistent with the small fraction of low luminosity CSS sources we estimate within our SMC sample (see section 4.1.5) and in current literature. Therefore, *faint GPS and CSS sources are preferentially detected with high turnover frequencies, resulting in fewer CSS sources*;

2. If our sample has the same redshift distribution as the Jy-level GPS sources, they represent the lower-luminosity tail of the known GPS population and are therefore more likely to be the compact counterparts of FR I galaxies (An and Baan, 2012; Tingay and Edwards, 2015). This implies they have low-power, unstable jets, implying that they are more likely to prematurely die and are unable to evolve into CSS sources. Therefore, *a lower fraction of mJy-level GPS sources evolve into CSS sources compared to the Jy-level GPS sources.*

The spectral index peaks and has a median at $\alpha \sim -0.8$, typical of the optically-thin spectral index of GPS and CSS sources. This is biased by our selection of $\alpha < -0.8$.

The majority of our SMC sources fit with the FFA model have typical values of $p < 0$, with a median of $p = -0.63$, implying the majority of absorbing clouds have low emission measure (Callingham et al., 2015). However, four sources have $p > 0$, implying the majority of absorbing clouds have high emission measure, suggesting they are within dense environments. These sources are discussed individually below.

Table 4.1: A summary of all the flux measurements made at all available frequencies. Listed is the instrument, the frequency, bandwidth, date and the number of sources which used a measurements at this frequency. Where the precise date is unknown, a range in years for that survey is listed. Where only the year is listed, this represents the average date of observation (e.g. when the image consists of multiple observations merged together). *Notes:* [1] These four were not used during the fitting, but are presented during the analysis of individual sources.

Instrument	Frequency (MHz)	Bandwidth (MHz)	Date	$N_{\rm used}$
MWA	76	8	2013-2014	62
MWA	84	8	2013-2014	62
MWA	92	8	2013-2014	62
MWA	99	8	2013-2014	62
MWA	107	8	2013-2014	62
MWA	115	8	2013-2014	62
MWA	122	8	2013-2014	62
MWA	130	8	2013-2014	62
MWA	143	8	2013-2014	62
MWA	151	8	2013-2014	62
MWA	158	8	2013-2014	62
MWA	166	8	2013-2014	62
MWA	174	8	2013-2014	62
MWA	181	8	2013-2014	62
MWA	189	8	2013-2014	62
MWA	197	8	2013-2014	62
MWA	204	8	2013-2014	62
MWA	212	8	2013-2014	62
MWA	220	8	2013-2014	62
MWA	227	8	2013-2014	62
MOST	408	2.5	1968-1974	5
MOST	843	3	2000	70
ATCA	1419	128	2004	53
ATCA	2379	8	6-14 Oct 1992	69
ATCA	4781	512	6 Feb 2013	57
ATCA	4802	128	2004	72
ATCA	5242	512	6 Feb 2013	57
ATCA	5744	512	6 Feb 2013	57
ATCA	6217	512	6 Feb 2013	56
ATCA	8297	512	6 Feb 2013	40
ATCA	8640	128	2005	53
ATCA	8743	512	6 Feb 2013	40
ATCA	9252	512	6 Feb 2013	40
ATCA	9716	512	6 Feb 2013	40
ATCA	19904	256	2005-2007	4[1]

Table 4.2: The models we fit to the data, the number of sources that use this fit, $N_{\rm sources}$, and the median reduced χ^2 from all of these models, $\widetilde{\chi}^2_{red}$.

Model	$N_{\rm sources}$	$\widetilde{\chi}^2_{red}$
Power law	18	2.40
FFA	11	1.04
FFA with break	41	1.05

Table 4.3: Radio spectrum model parameters for all 70 SMC sources for which a successful fit was found. Listed is the fitted model, the synchrotron normalisation parameter a, the spectral index α, the optical depth parameter p, the break frequency ν_{br}, the turnover frequency ν_m, the frequency ν_0 found during the fitting (i.e. the parameter from the Bicknell et al. (1997) model − see equation 1.10 and section 1.3.1.2), the reduced χ^2_{red} value, and the degrees of freedom (DOF). The uncertainties listed are the 1σ errors. Where $\delta a > a$ or $\delta p > |p| + 1$ (see section 4.1.2), we list '-'. Upper limits to the turnover frequencies are listed with '<', to signify where the model does not turnover within the range of our data points. The individual models are shown in Figure 4.3.

Source	Model	a (mJy)	α	p	ν_m (MHz)	ν_0 (MHz)	ν_{br} (MHz)	χ^2_{red}	DOF
SMC_0022-7428	FFA	1037.75 ± 463.94	−3.78 ± 0.92	0.52 ± 0.43	< 76	851.39 ± 163.66		0.19	17
SMC_0055-7211	FFA with break	-	−0.54 ± 0.04	-	< 76	-	1661.81 ± 475.95	1.29	27
SMC_10	FFA with break	-	−1.04 ± 0.11	-	< 76	-	2379.00 ± 1356.52	3.21	22
SMC_100	FFA with break	-	−0.81 ± 0.04	-	< 76	-	3706.67 ± 775.74	1.29	27
SMC_101	FFA with break	-	−0.76 ± 0.04	-	< 76	-	3063.31 ± 848.96	1.0	26
SMC_102	Power law	16.84 ± 5.61	0.07 ± 0.04					1.63	10
SMC_13	FFA with break	0.88 ± 0.68	−0.88 ± 0.04	−0.71 ± 0.22	< 76	138.02 ± 76.75	4078.89 ± 657.85	0.5	23
SMC_14	Power law	2105.99 ± 456.89	−0.63 ± 0.03					1.06	20
SMC_16	FFA with break	-	−1.04 ± 0.15	−0.57 ± 0.20	< 84	266.13 ± 151.62	4781.00 ± 1928.01	1.05	21
SMC_17	FFA	-	−1.18 ± 0.02	-	86	-		4.78	28
SMC_18	FFA with break	-	−0.84 ± 0.03	−1.00 ± 0.43	< 76	-	3025.03 ± 515.96	0.87	27
SMC_19	FFA with break	-	−0.47 ± 0.05	-	105	-	1673.19 ± 510.34	1.26	24
SMC_2	FFA with break	-	−0.88 ± 0.03	-	< 76	-	4989.33 ± 697.62	1.48	27
SMC_21	FFA with break	-	−0.85 ± 0.04	-	93	-	4356.85 ± 1047.79	0.59	18
SMC_23	FFA with break	-	−0.88 ± 0.04	−1.00 ± 1.40	< 76	-	2790.90 ± 586.97	1.04	22
SMC_25	FFA with break	-	−0.74 ± 0.06	-	< 76	-	3330.01 ± 942.94	0.9	18
SMC_26	Power law	107738.59 ± 10806.69	−1.10 ± 0.02					2.25	25
SMC_27	Power law	140228.73 ± 20765.72	−1.25 ± 0.02					1.45	25
SMC_29	Power law	9330.13 ± 1148.17	−0.79 ± 0.02					1.56	24

Continued on next page

Source	Model	a (mJy)	α	p	ν_m (MHz)	ν_0 (MHz)	ν_{br} (MHz)	χ^2_{red}	DOF
SMC_3	Power law	28419.24 ± 8094.31	−1.02 ± 0.04					7.2	30
SMC_30	FFA with break	-	−0.56 ± 0.05	-	132	-	3478.30 ± 721.92	0.86	26
SMC_31	FFA with break	-	−0.60 ± 0.07	-	90	-	219.00 ± 96.72	1.35	17
SMC_34	FFA with break	0.48 ± 0.34	−0.69 ± 0.05	−0.65 ± 0.28	105	187.76 ± 107.08	3768.04 ± 663.22	0.6	27
SMC_35	FFA with break	2.68 ± 1.79	−0.63 ± 0.05	−0.48 ± 0.41	144	153.79 ± 75.62	3806.27 ± 809.66	1.06	27
SMC_36	Power law	16130.44 ± 2656.99	−0.90 ± 0.02					2.4	25
SMC_38	Power law	19003.52 ± 3727.36	−0.93 ± 0.03					3.0	24
SMC_39	Power law	39915.80 ± 10770.40	−1.00 ± 0.04					8.22	30
SMC_4	FFA with break	-	−0.40 ± 0.04	-	179	-	3133.97 ± 551.14	0.73	25
SMC_41	FFA with break	0.46 ± 0.36	−0.92 ± 0.04	−0.63 ± 0.33	< 76	135.86 ± 77.04	3782.81 ± 644.30	0.65	27
SMC_44	FFA	-	−0.77 ± 0.04	-	124	-		1.53	28
SMC_45	FFA with break	-	−0.73 ± 0.03	-	< 76	-	3177.38 ± 441.75	0.51	27
SMC_46	FFA with break	-	−0.75 ± 0.03	-	< 76	-	3786.40 ± 645.66	0.77	27
SMC_47	FFA with break	-	−0.65 ± 0.06	−1.00 ± 1.63	< 76	-	180.35 ± 50.44	2.83	17
SMC_48	FFA with break	-	−0.85 ± 0.04	-	< 76	-	1159.37 ± 287.34	0.51	21
SMC_49	Power law	1466.65 ± 1149.45	−0.73 ± 0.10					3.2	4
SMC_5	FFA with break	-	−0.82 ± 0.06	-	< 76	-	4802.00 ± 1629.75	1.44	23
SMC_50	Power law	7639.90 ± 2027.87	−0.85 ± 0.04					1.1	20
SMC_52	FFA	238.44 ± 42.82	−1.69 ± 0.06	−0.12 ± 0.06	491	914.34 ± 133.91		1.04	28
SMC_54	FFA with break	39.70 ± 19.15	−0.55 ± 0.04	−0.10 ± 0.49	144	116.98 ± 26.97	2012.75 ± 509.26	1.24	28
SMC_55	FFA	40.89 ± 1.82	−0.63 ± 0.04	−0.49 ± 0.04	2353	2605.33 ± 316.13		0.16	8
SMC_56	FFA with break	-	−0.77 ± 0.04	-	< 76	-	4648.56 ± 1084.21	1.25	27
SMC_57	FFA with break	0.39 ± 0.38	−0.88 ± 0.05	−0.62 ± 0.43	< 76	132.17 ± 92.66	4288.15 ± 972.04	1.12	27

Continued on next page

Source	Model	a (mJy)	α	p	ν_m (MHz)	ν_0 (MHz)	ν_{br} (MHz)	χ^2_{red}	DOF
SMC_58	Power law	416.72 ± 61.99	−0.21 ± 0.02					2.49	30
SMC_59	FFA with break	1.37 ± 0.39	−1.07 ± 0.02	0.11 ± 0.06	192	210.88 ± 8.45	1756.42 ± 202.06	0.26	28
SMC_61	Power law	4207.72 ± 789.08	−0.68 ± 0.03					1.18	20
SMC_64	FFA with break	-	−1.07 ± 0.04	-	< 76	-	3580.64 ± 844.13	1.34	27
SMC_65	FFA with break	-	−0.57 ± 0.04	-	172	-	2645.59 ± 529.03	0.98	27
SMC_66	FFA with break	-	−0.89 ± 0.08	-	86	-	5242.00 ± 1527.44	5.67	27
SMC_68	FFA with break	-	−0.72 ± 0.06	−1.00 ± 0.68	< 76	-	1093.92 ± 390.55	1.17	22
SMC_7	FFA with break	-	−1.12 ± 0.07	−0.71 ± 0.03	< 76	433.24 ± 104.85	4802.00 ± 1587.01	1.13	20
SMC_70	Power law	20847.89 ± 2862.76	−0.87 ± 0.02					1.31	25
SMC_71	FFA	50.24 ± 10.23	−0.80 ± 0.07	0.24 ± 0.97	1660	1465.17 ± 521.64		0.79	8
SMC_72	Power law	-	−0.40 ± 0.14					10.86	19
SMC_74	FFA with break	-	−0.81 ± 0.10	-	< 76	-	1747.16 ± 800.46	1.39	21
SMC_75	FFA with break	0.34 ± 0.21	−0.98 ± 0.04	−0.80 ± 0.04	< 76	187.96 ± 56.69	3462.13 ± 618.46	0.76	27
SMC_76	FFA	196.11 ± 45.80	−1.42 ± 0.13	−0.13 ± 0.16	1784	2708.16 ± 664.69		2.05	8
SMC_77	FFA with break	-	−0.76 ± 0.10	−0.98 ± 0.71	< 76	-	2379.00 ± 820.27	0.74	17
SMC_8	FFA with break	2.05 ± 1.16	−0.82 ± 0.02	−0.65 ± 0.35	< 76	109.41 ± 60.01	2906.85 ± 286.16	0.25	27
SMC_80	FFA with break	-	−0.77 ± 0.13	-	< 76	-	1039.15 ± 660.90	2.22	21
SMC_83	FFA	-	−1.13 ± 0.04	-	88	-		1.49	22
SMC_84	Power law	6742.44 ± 811.48	−0.78 ± 0.01					1.27	30
SMC_86	FFA with break	-	−0.79 ± 0.02	-	< 76	-	5441.74 ± 575.71	0.95	23
SMC_9	FFA	24.40 ± 3.14	−0.22 ± 0.09	−0.50 ± 0.74	2344	1395.75 ± 1337.19		1.13	8
SMC_93	FFA with break	-	−1.01 ± 0.12	−0.77 ± 0.10	< 76	339.55 ± 193.87	4781.00 ± 1859.06	1.58	26
SMC_94	Power law	3640.32 ± 978.65	−0.73 ± 0.03					3.82	30

Continued on next page

Source	Model	a (mJy)	α	p	ν_m (MHz)	ν_0 (MHz)	ν_{br} (MHz)	χ^2_{red}	DOF
SMC_95	FFA	40.02 ± 5.30	−2.39 ± 0.11	0.34 ± 0.08	1989	3559.17 ± 312.43		0.66	8
SMC_97	FFA	-	−0.27 ± 0.07	-	3263	-		0.69	7
SMC_99	FFA with break	-	−1.05 ± 0.10	−0.71 ± 0.08	< 76	516.57 ± 234.99	4781.00 ± 1187.50	2.3	27
SMC_FRII	Power law	29024.26 ± 6739.93	−0.91 ± 0.03					5.46	26

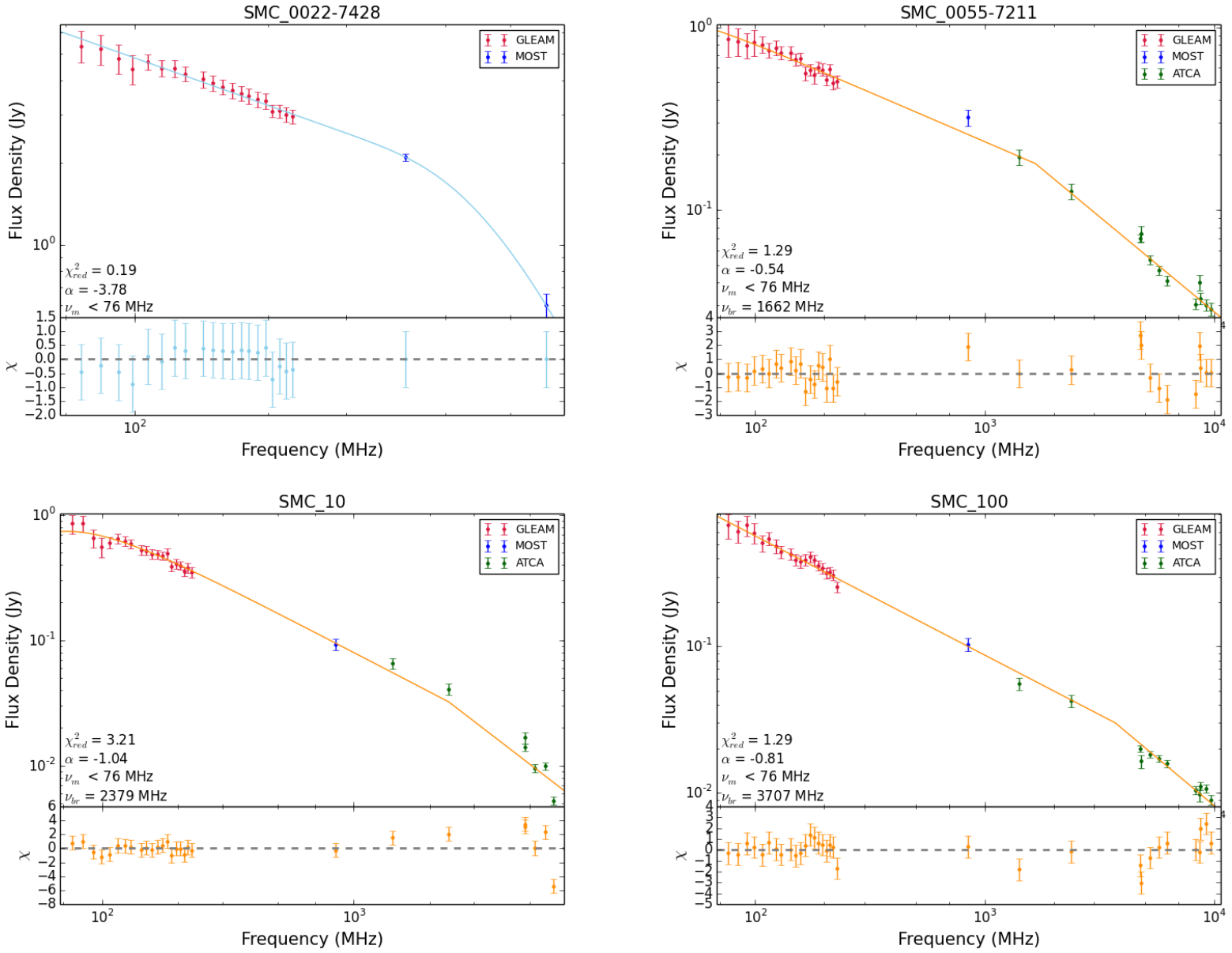

Figure 4.3: The models fit to the radio spectrum for all 70 SMC sources for which a successful fit was found, according to the models and their parameters listed in table 4.3.

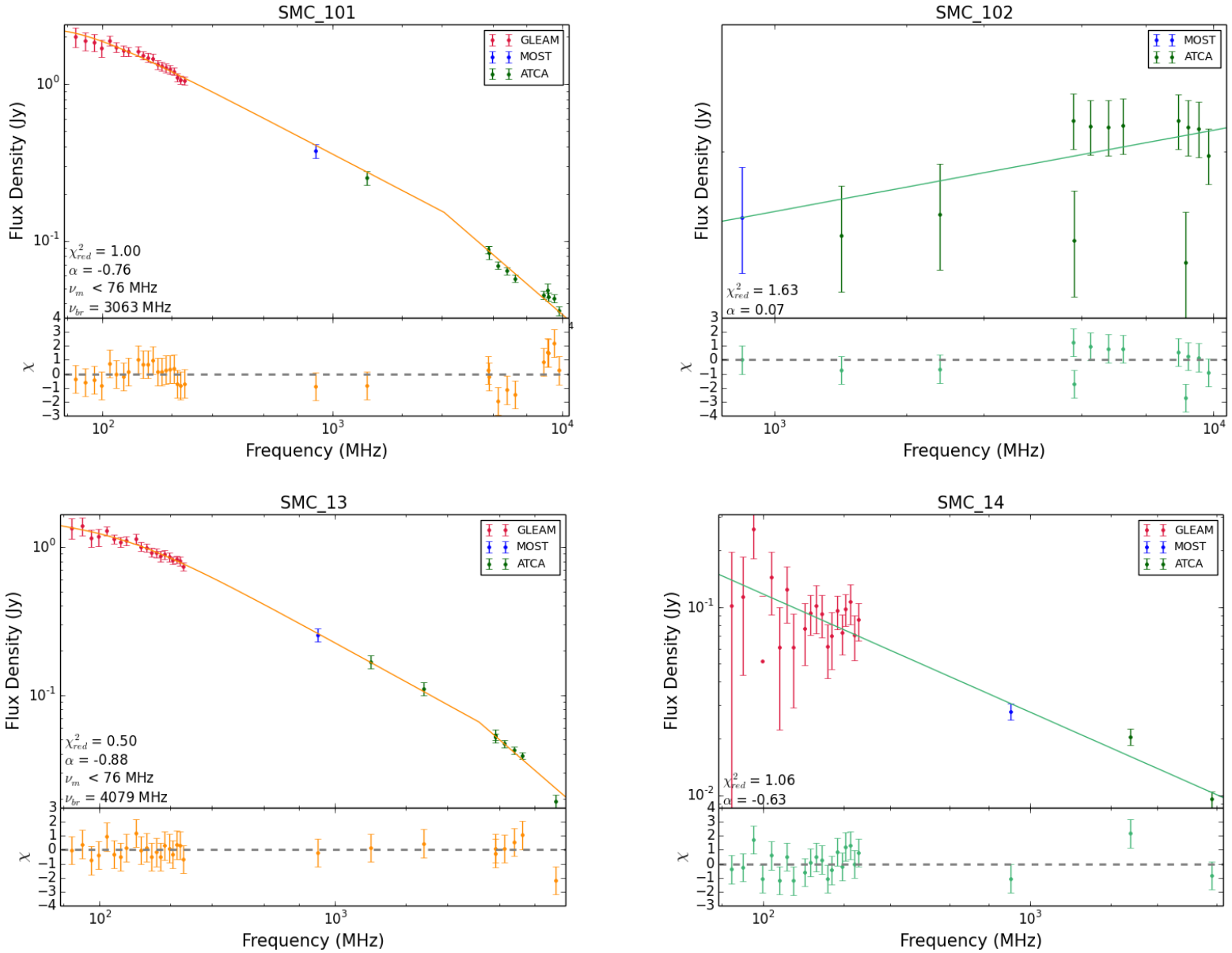

Fig. 4.3. (continued) – all measurements for SMC_101 are between 20-40 mJy.

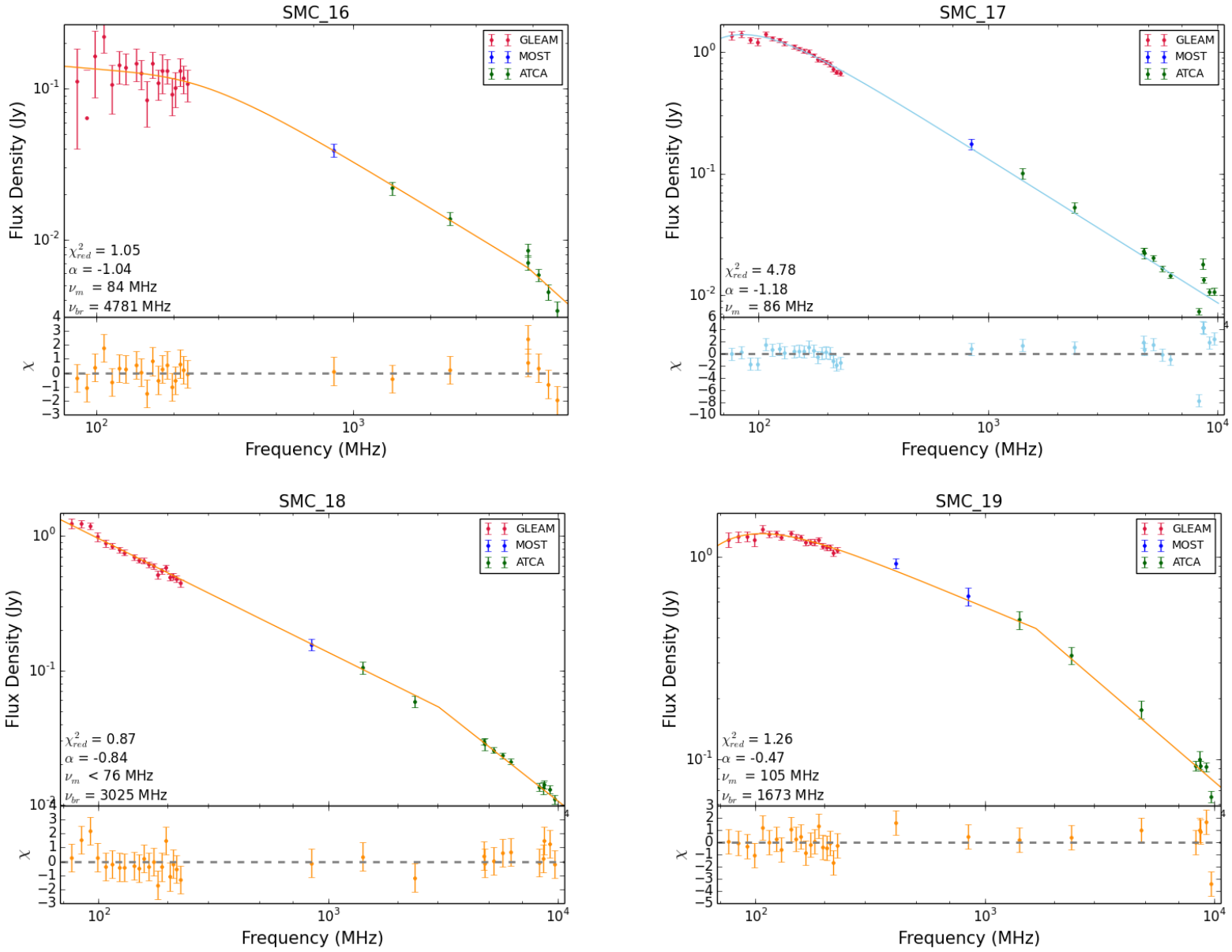

Fig. 4.3. (continued)

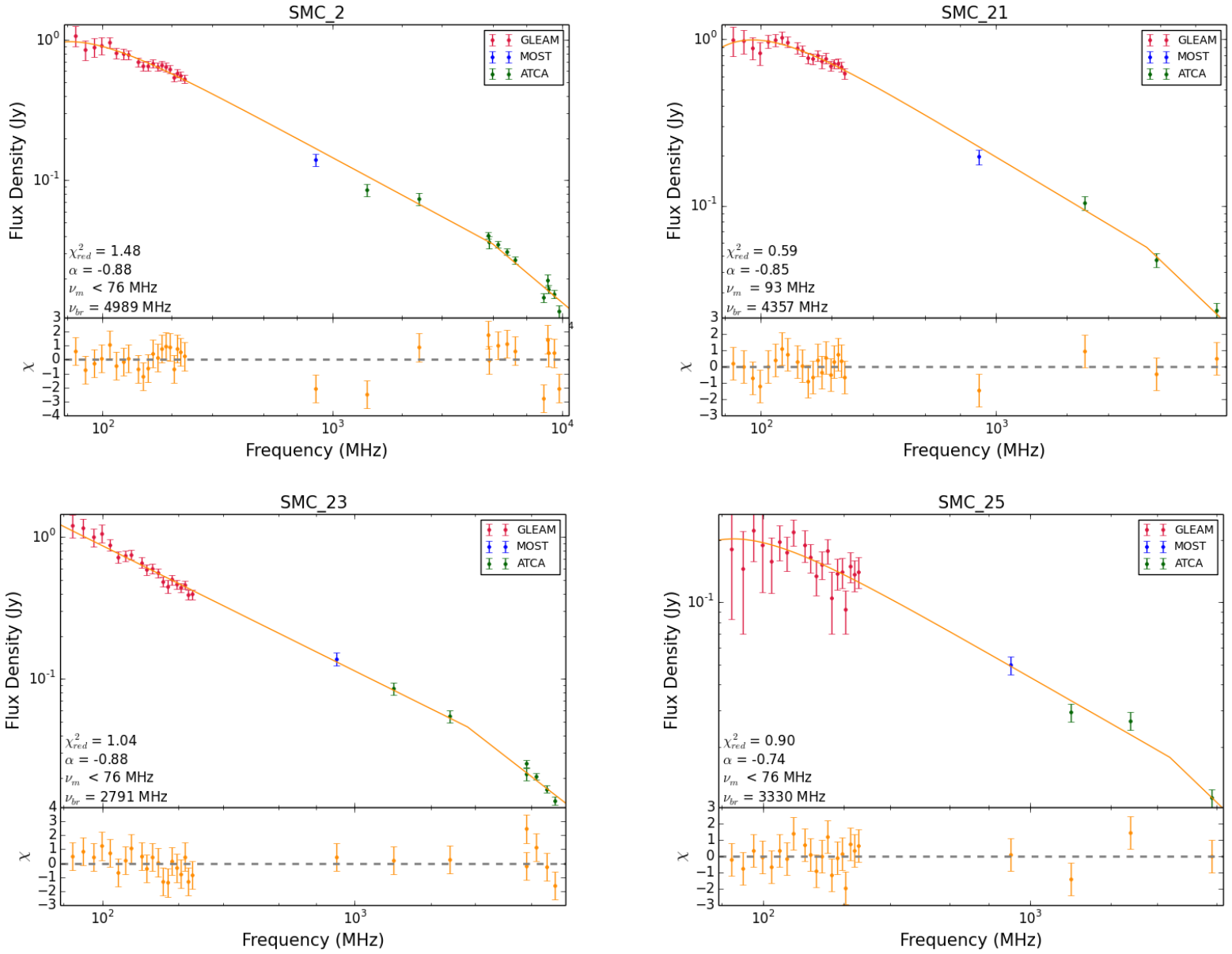

Fig. 4.3. (continued)

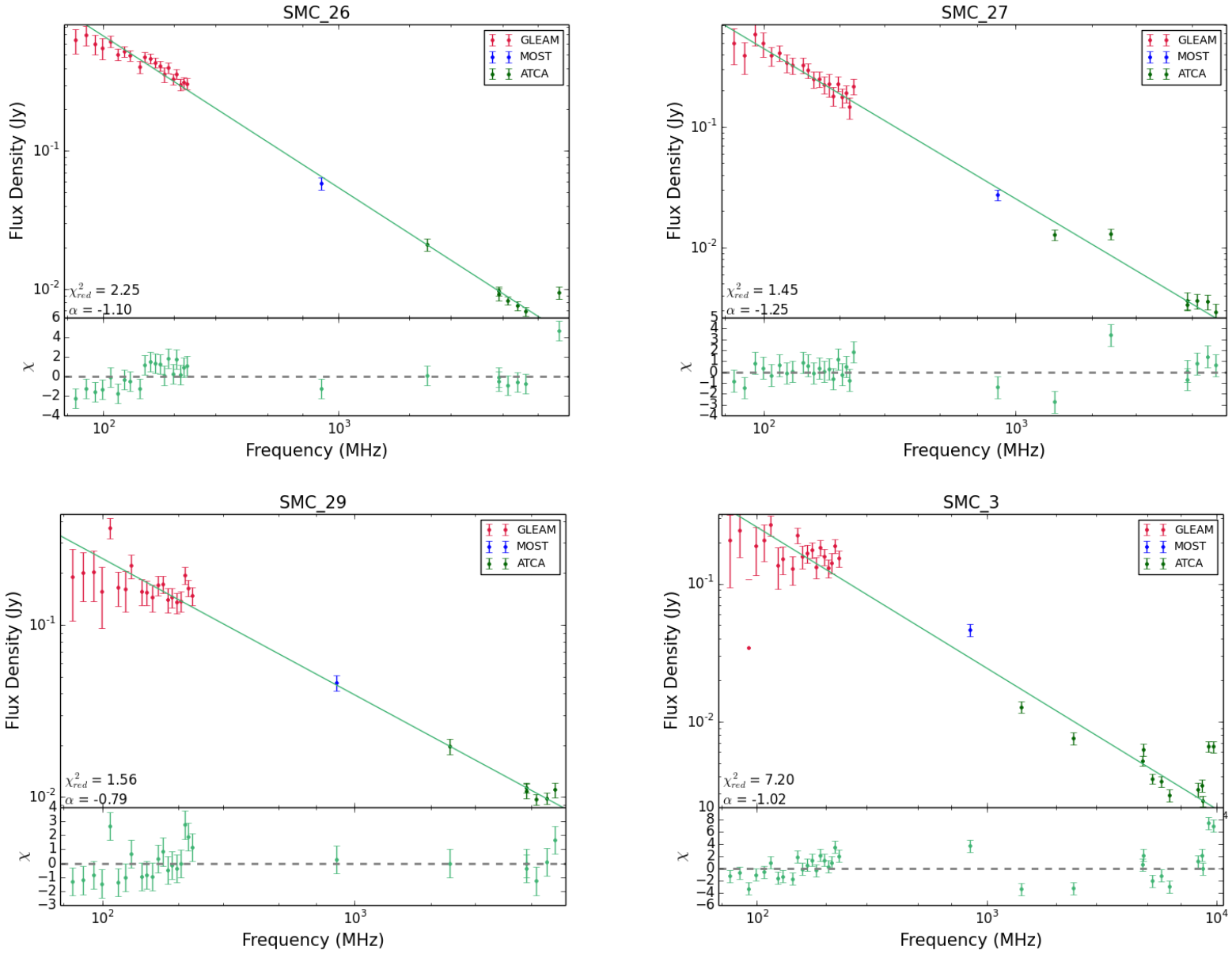

Fig. 4.3. (continued)

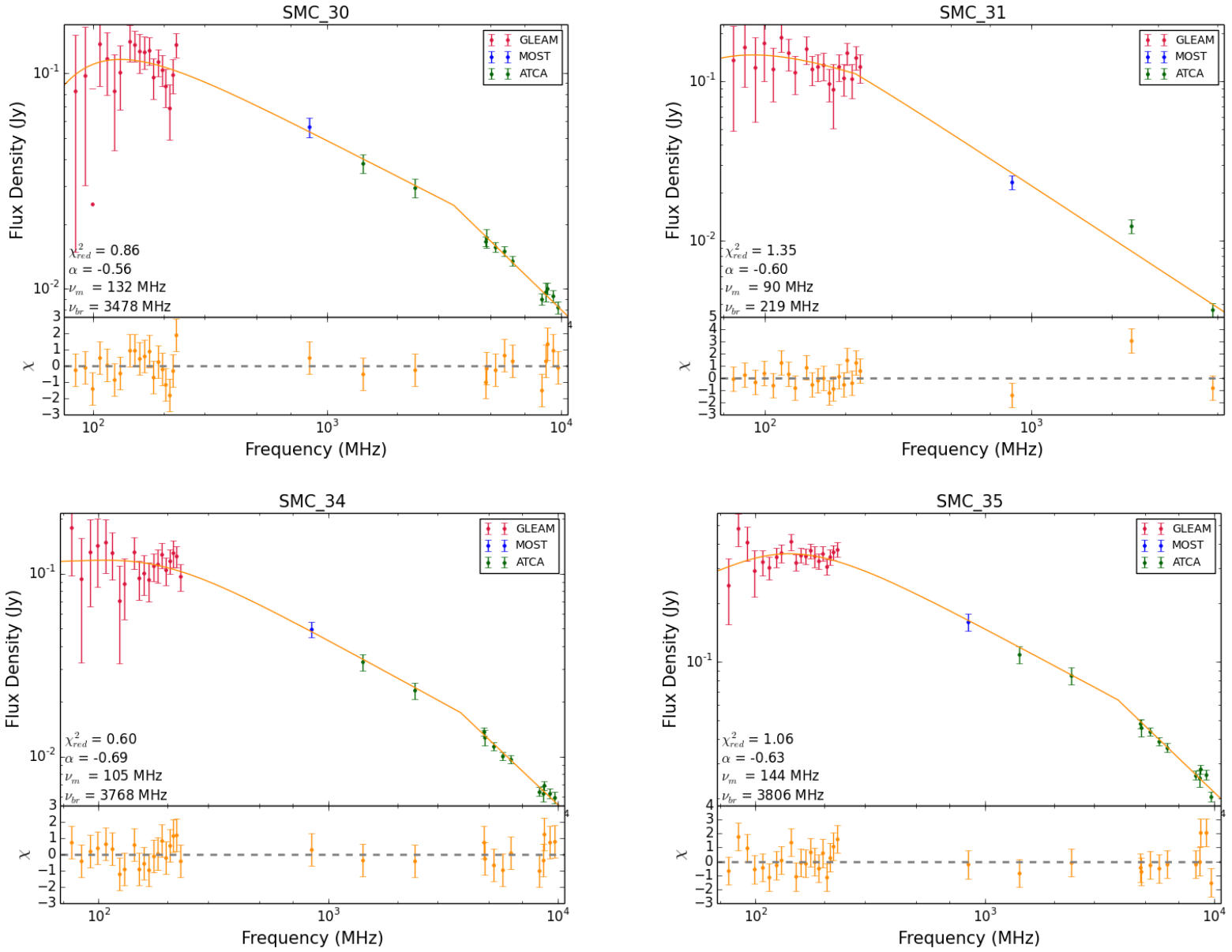

Fig. 4.3. (continued)

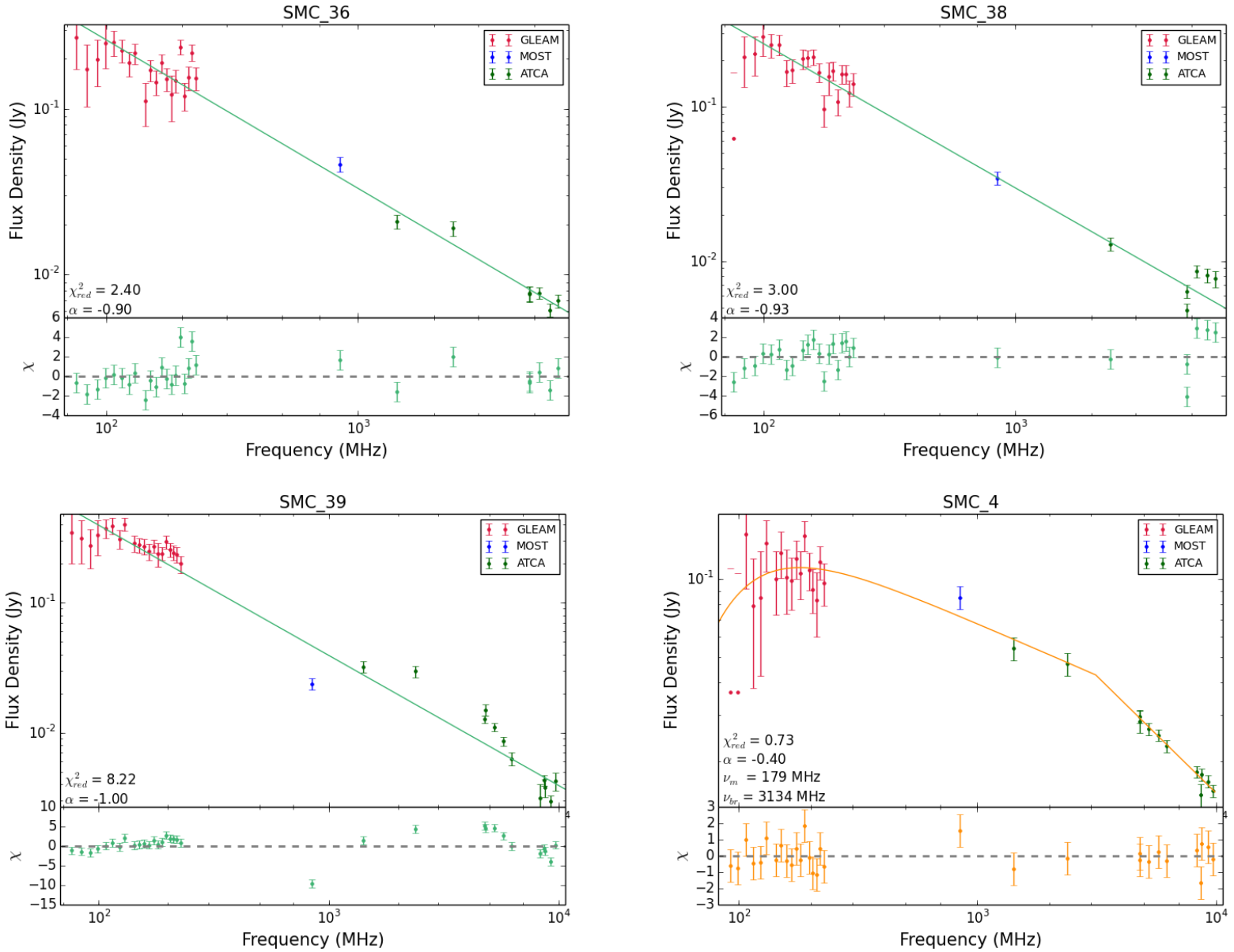

Fig. 4.3. (continued) – SMC_39 contains a blended counterpart within the GLEAM measurements, identified via the method discussed in section 2.3.1.8.

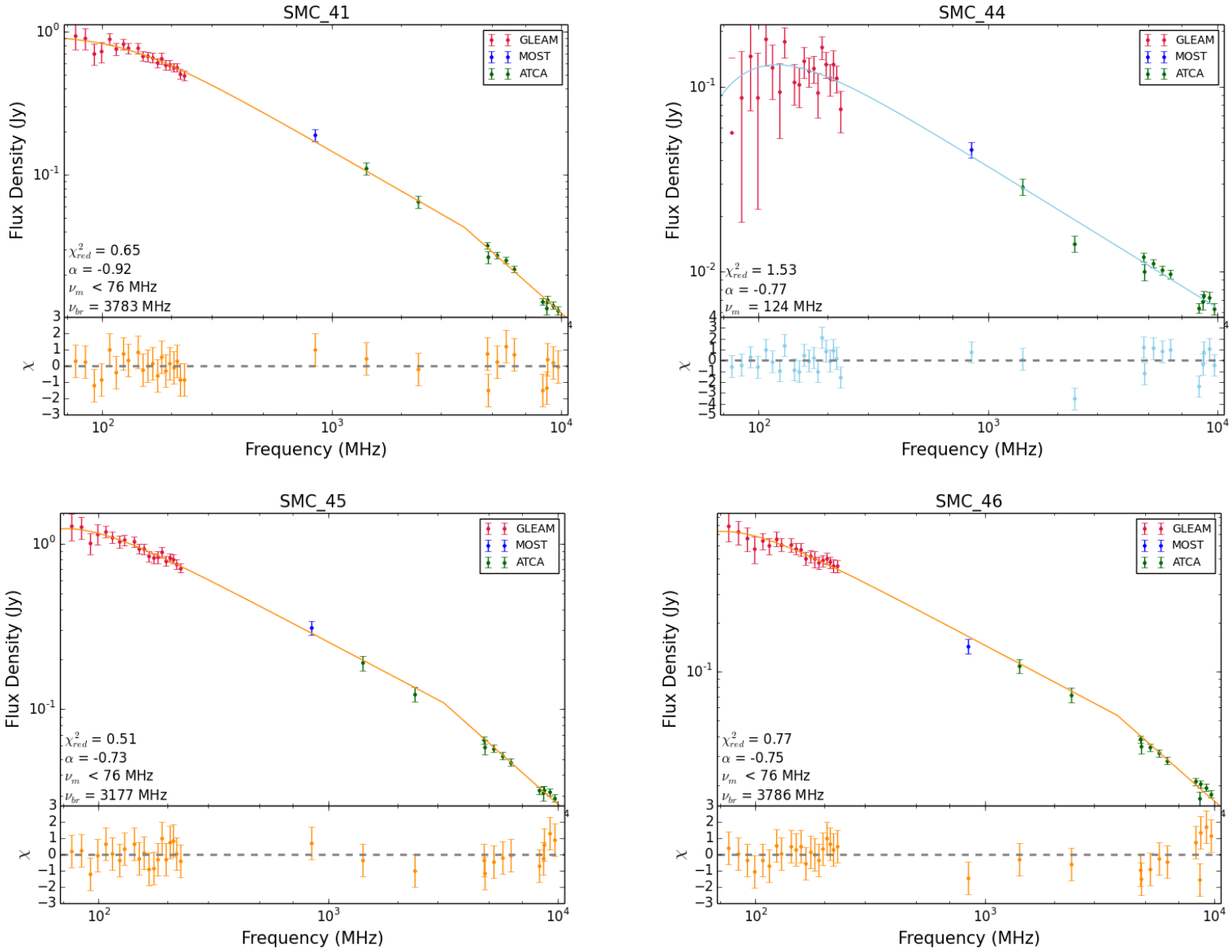

Fig. 4.3. (continued)

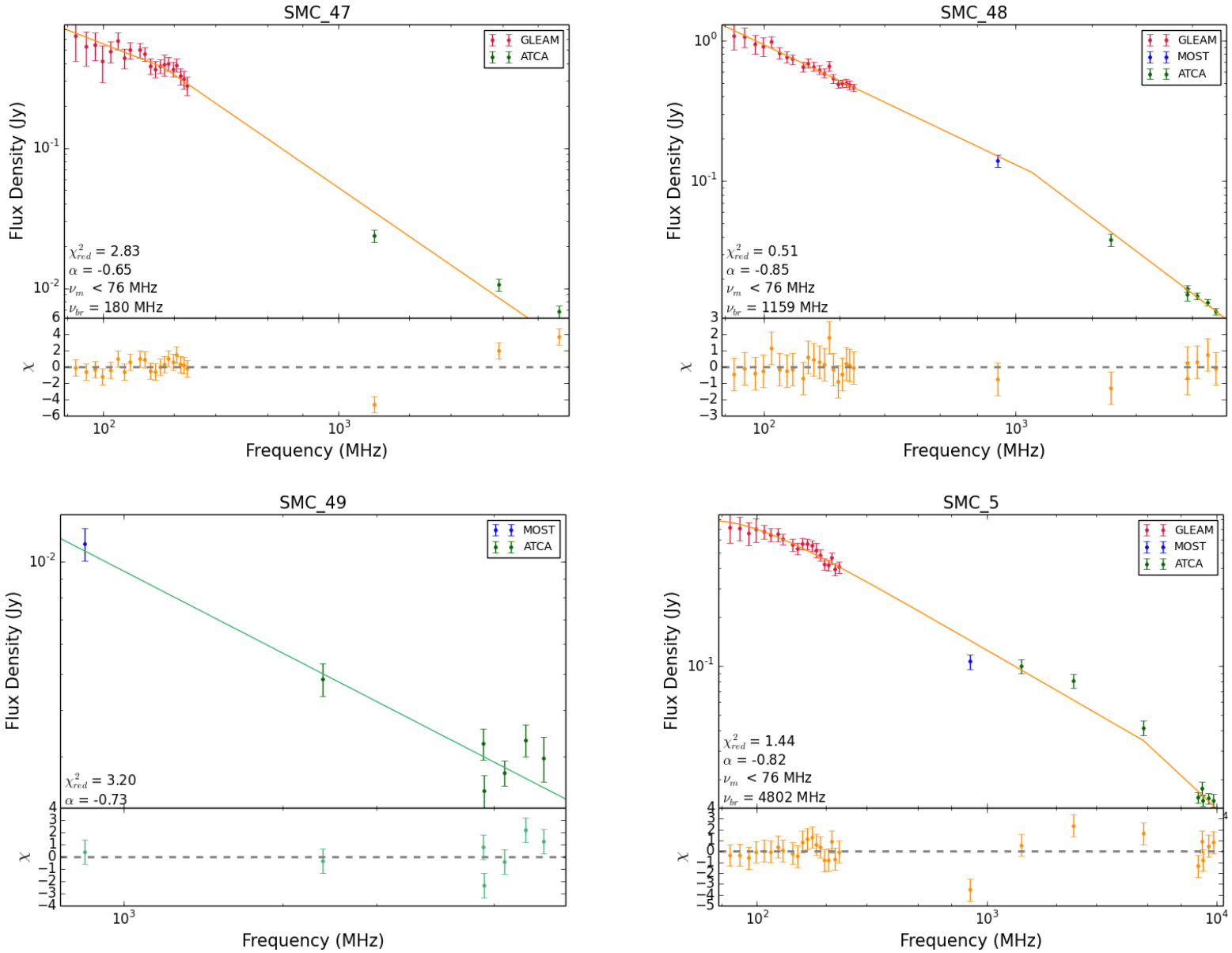

Fig. 4.3. (continued) – SMC_5 contains a blended component with extended emission, as shown in Appendix C.

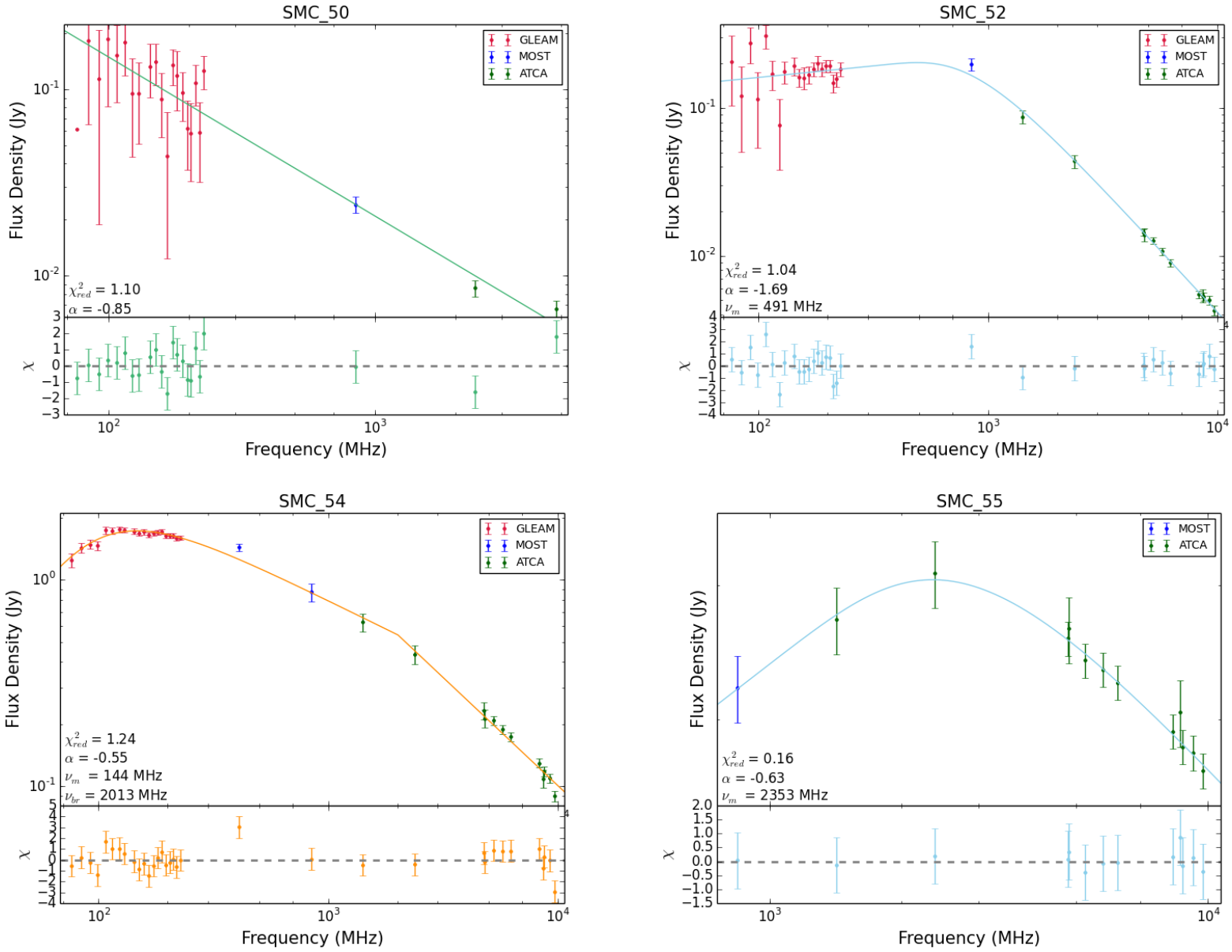

Fig. 4.3. (continued) – SMC_55 is $\sim$ 30 mJy at its peak.

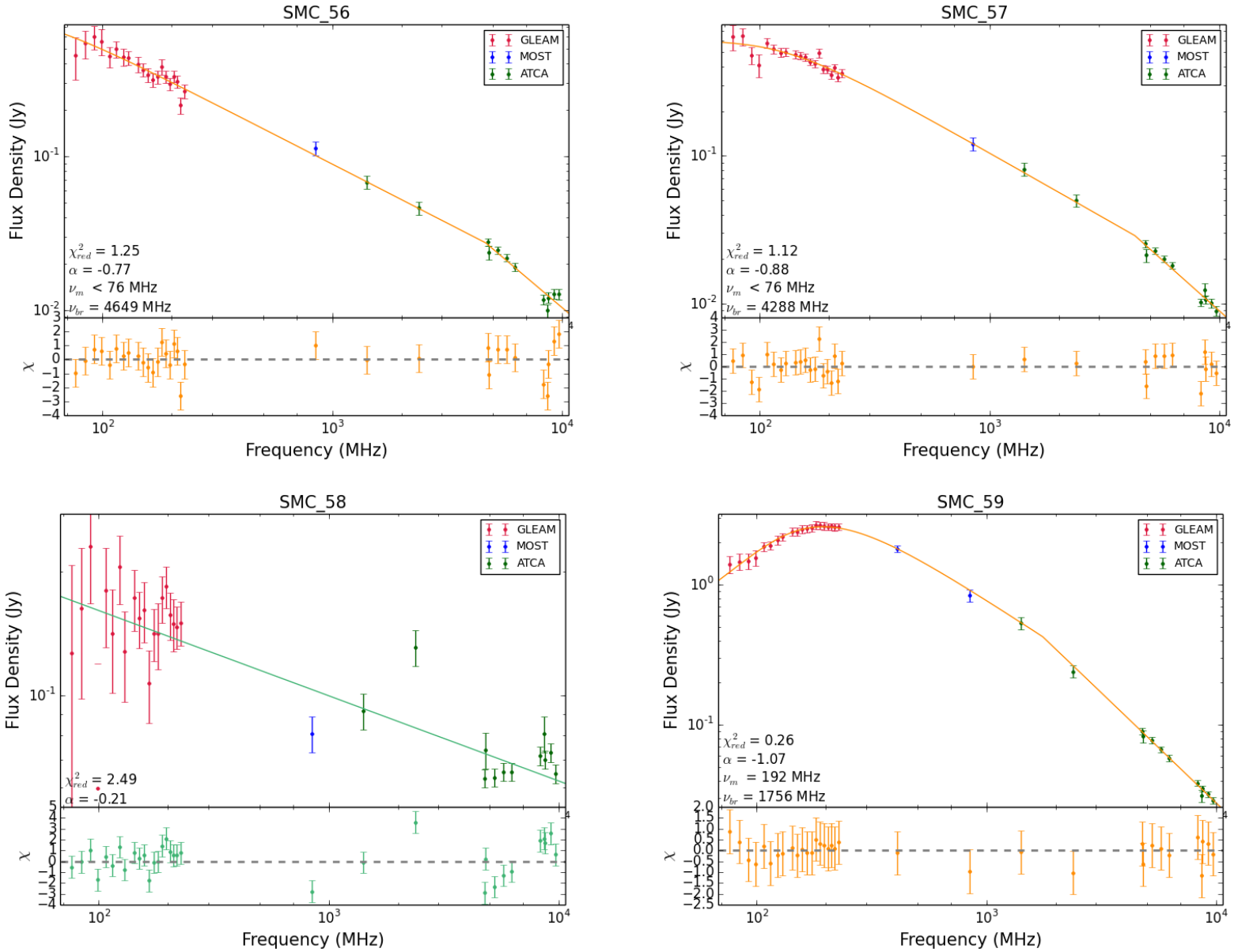

Fig. 4.3. (continued)

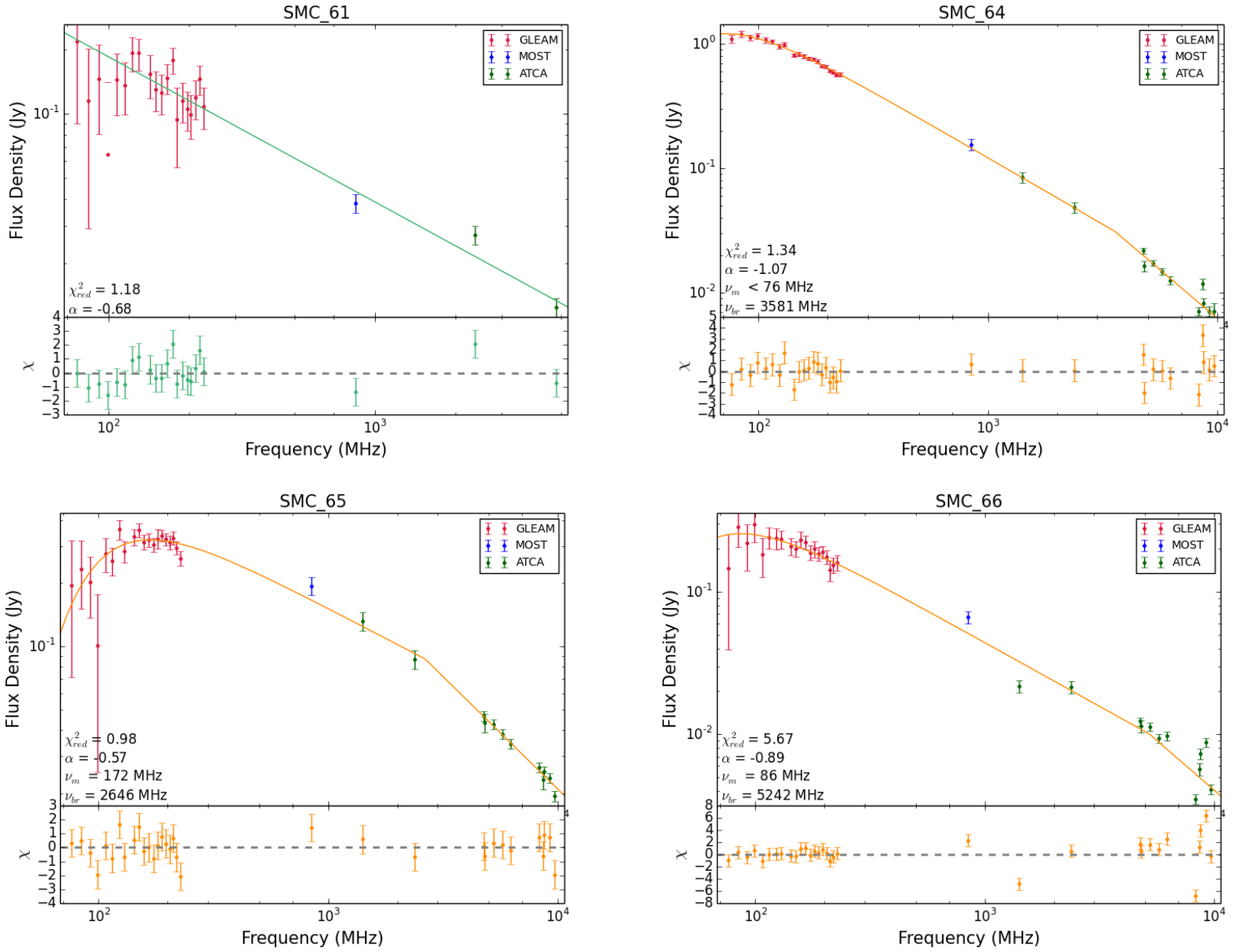

Fig. 4.3. (continued)

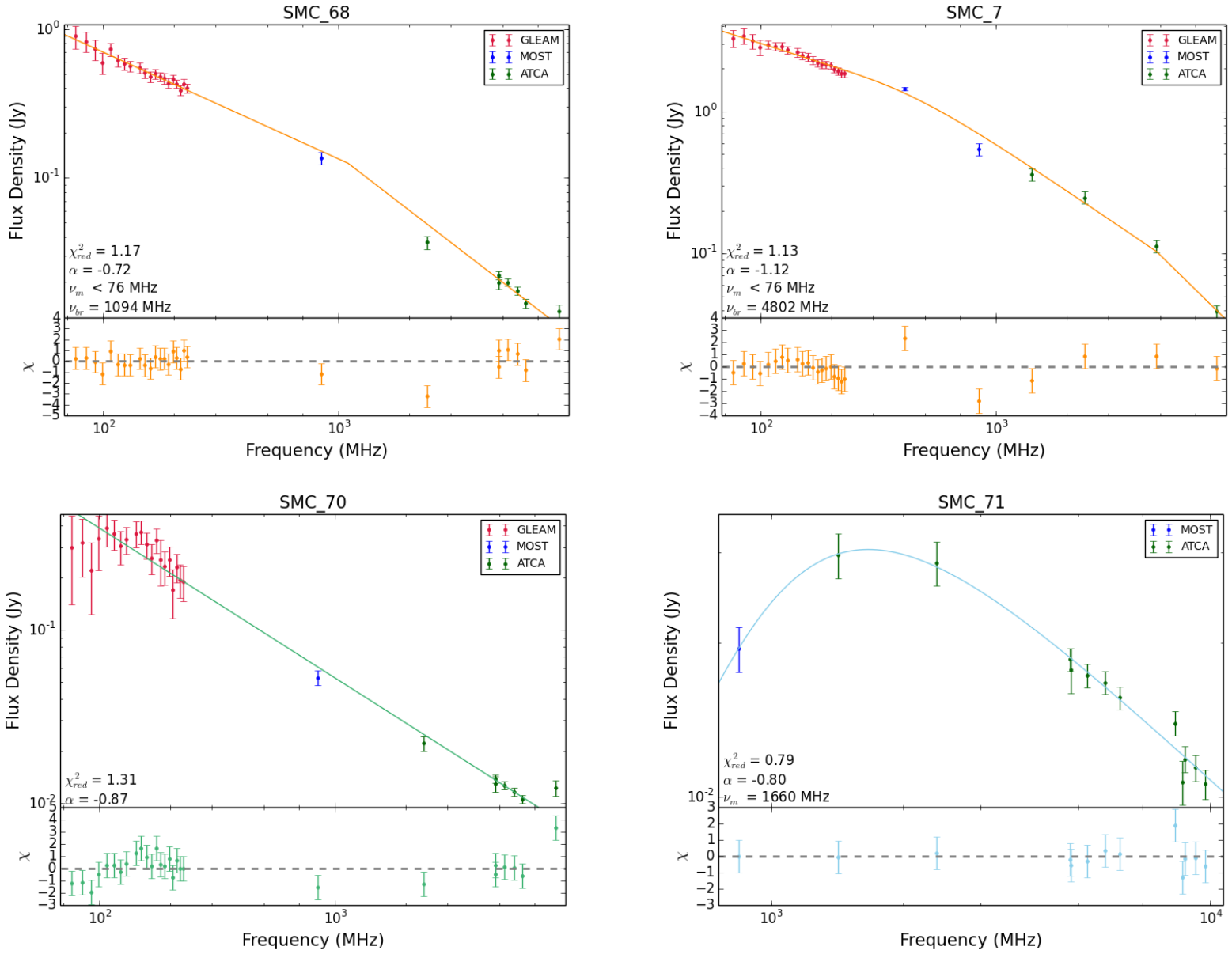

Fig. 4.3. (continued)

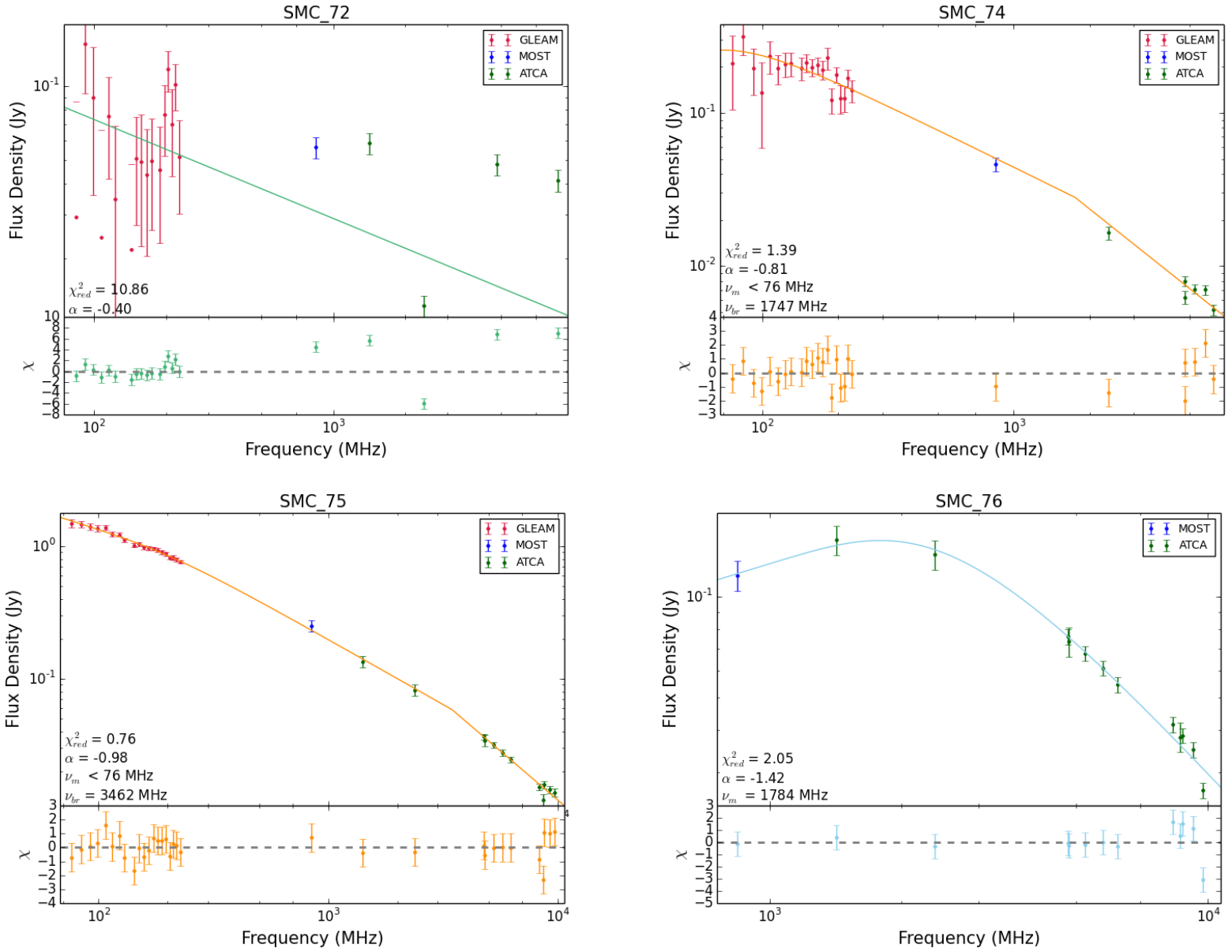

Fig. 4.3. (continued)

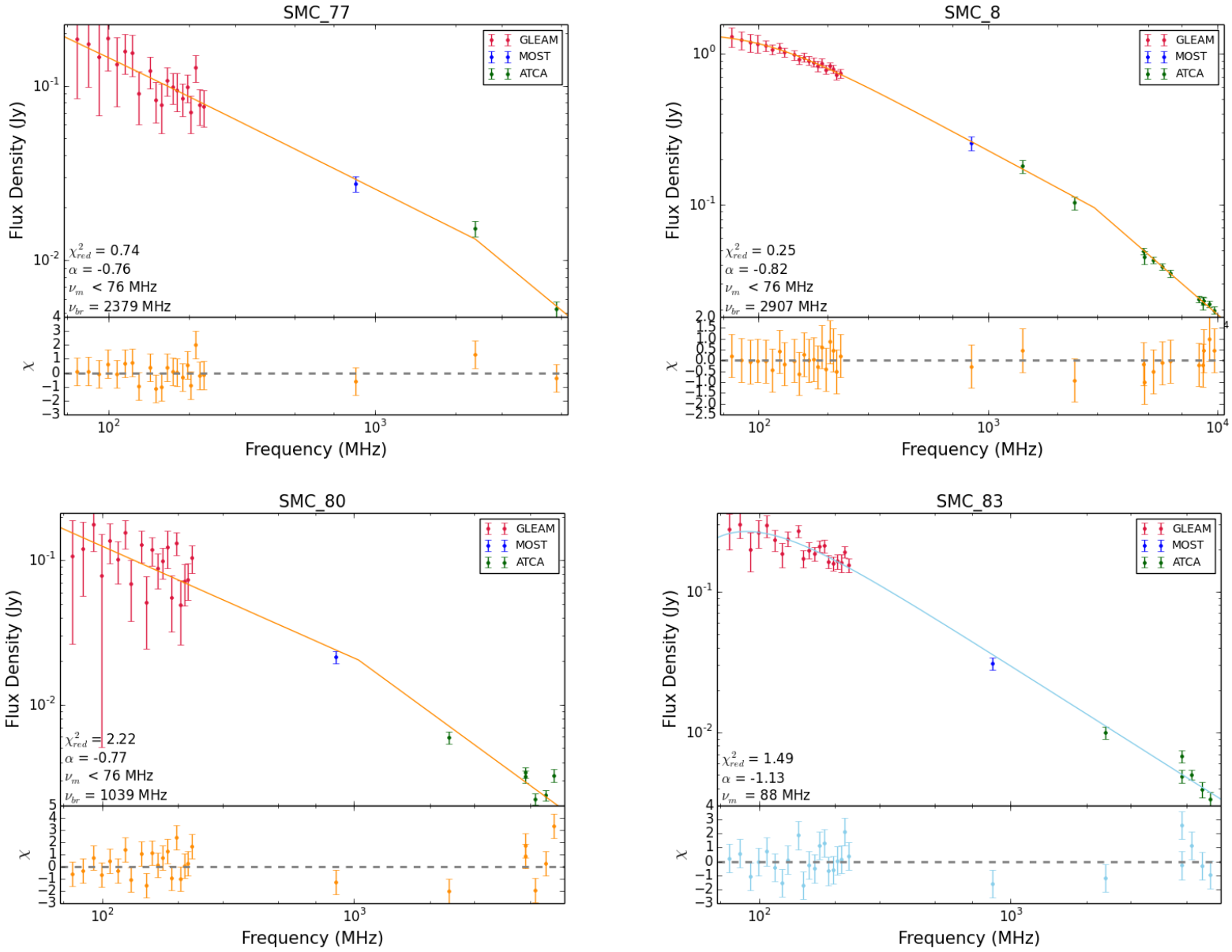

Fig. 4.3. (continued)

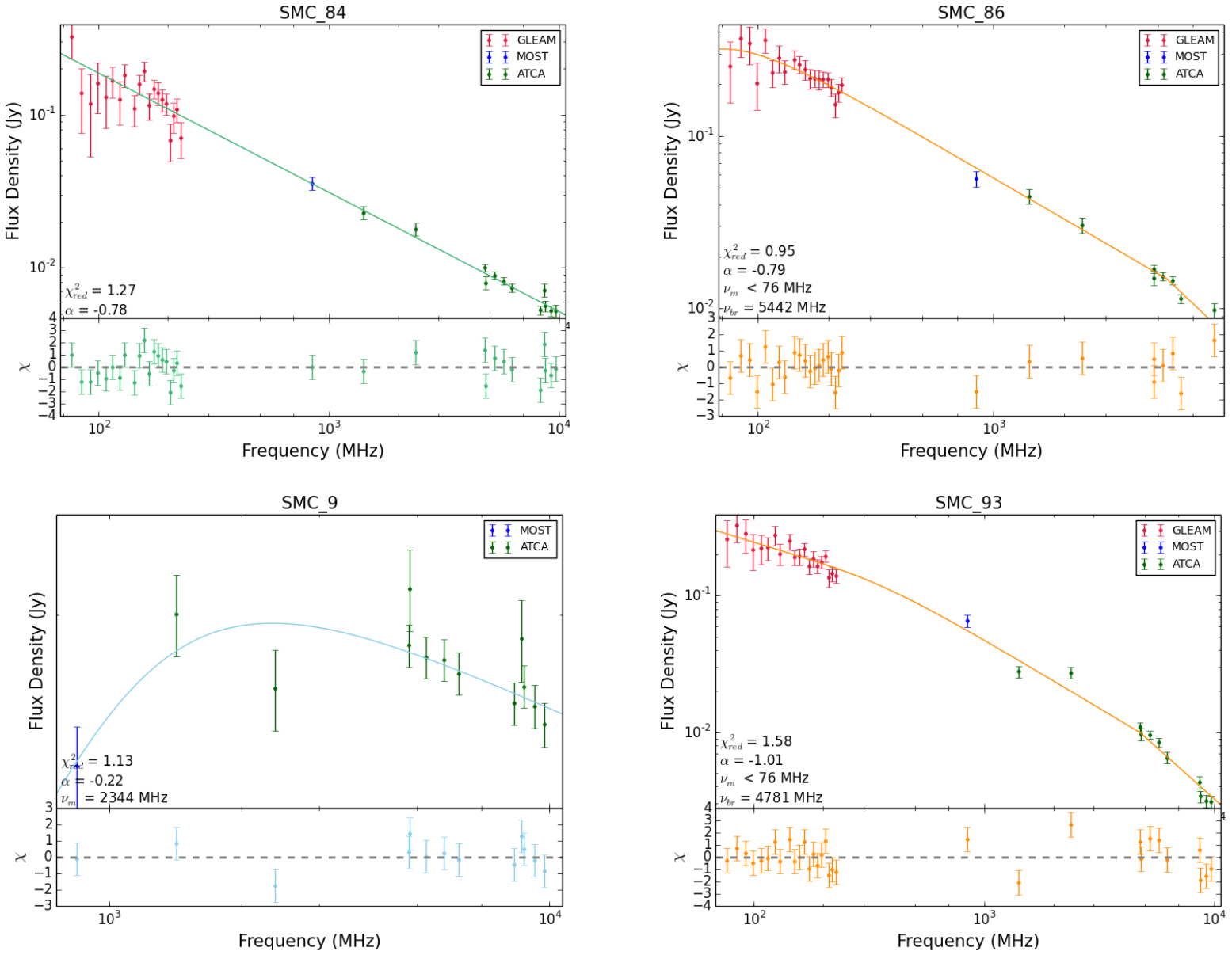

Fig. 4.3. (continued) – SMC_9 is $\sim$ 20 mJy at its peak.

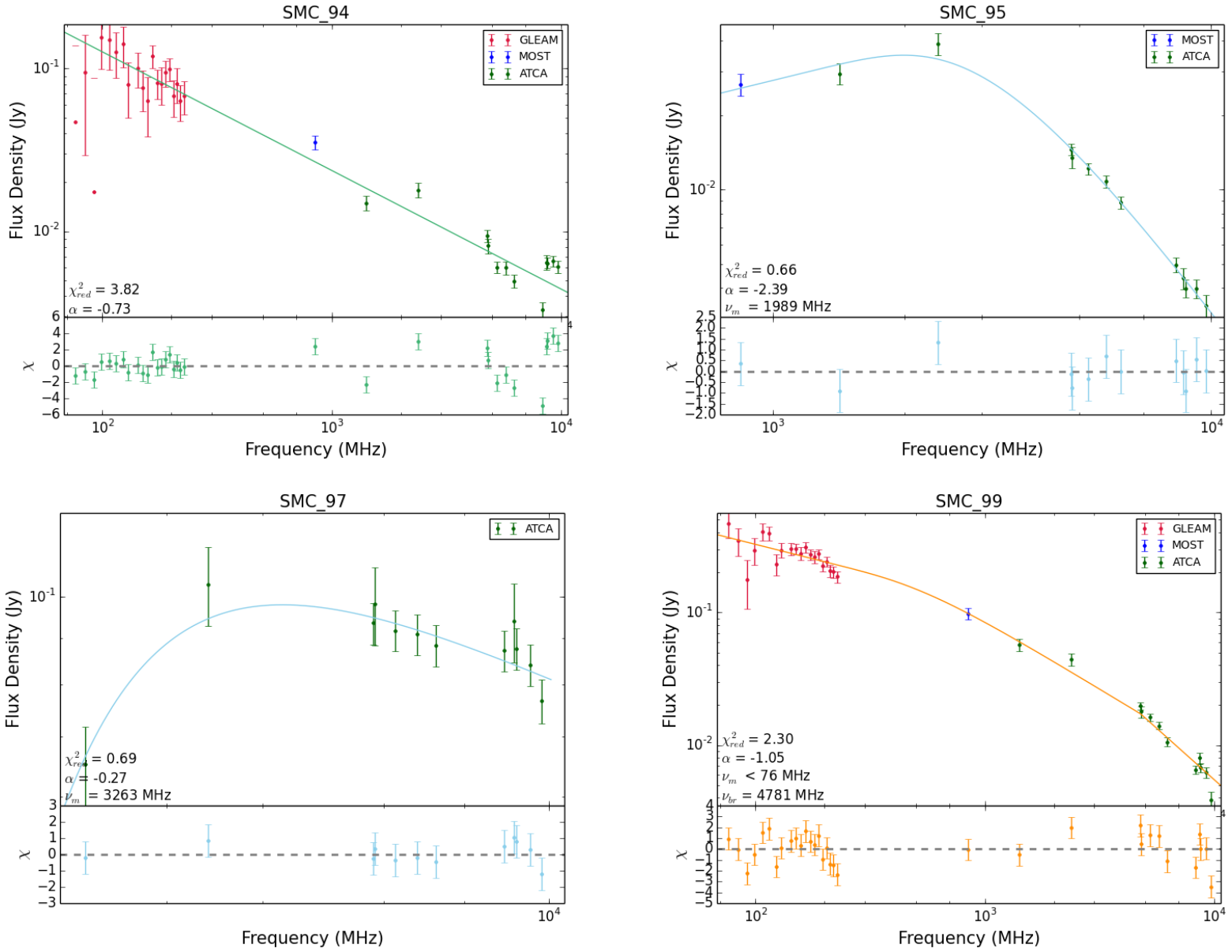

Fig. 4.3. (continued)

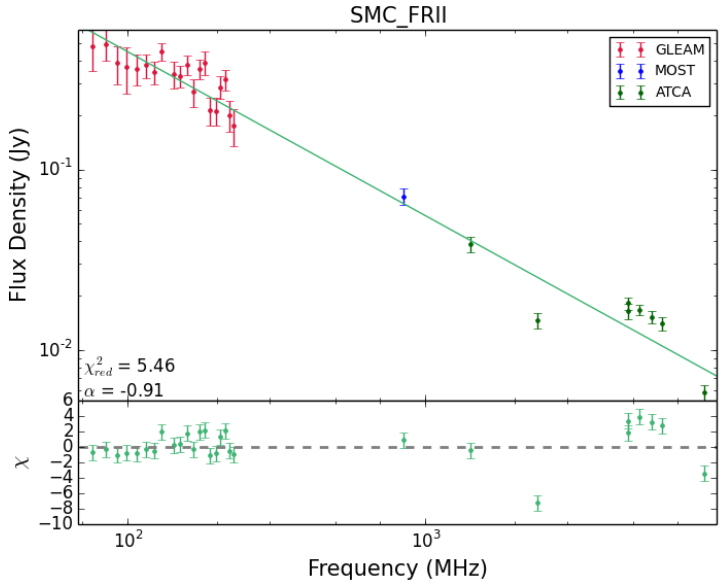

Fig. 4.3. (continued)

Table 4.4: The statistics of the values found for the parameters used in the spectral modelling. Shown is the parameter, the number of sources for which the parameter was fit, the mean and the median. Only 25 valid values of p are listed (i.e. when $\delta p < |p| + 1$).

Parameter	N	Mean	Median
ν_m	52	346 MHz	76 MHz
ν_{br}	41	3243 MHz	3462 MHz
α	70	-0.86	-0.81
p	25	-0.50	-0.63

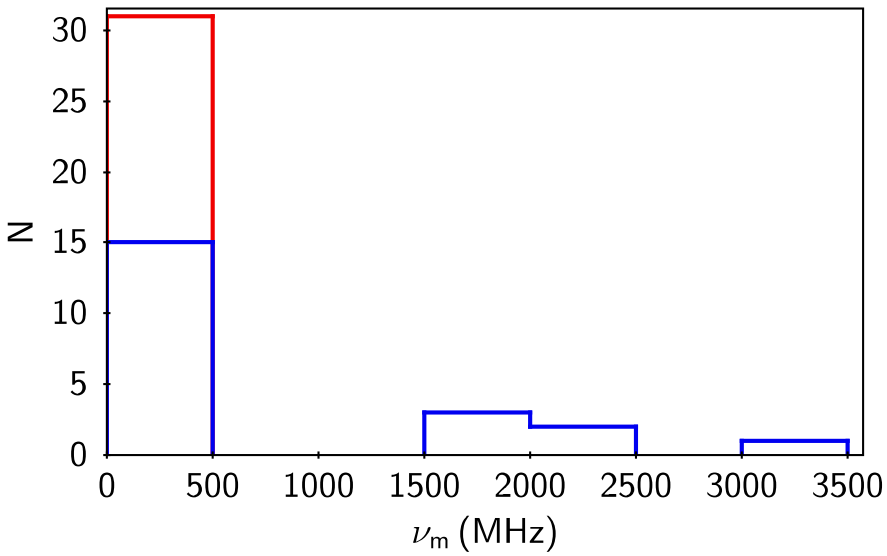

Figure 4.4: A histogram of the distribution of the turnover frequencies for all 52 sources fitted with a FFA model. Shown in red are the 31 sources with an upper limit on the turnover frequency of ∼76 MHz, and shown in blue are the 21 sources with a fitted turnover frequency.

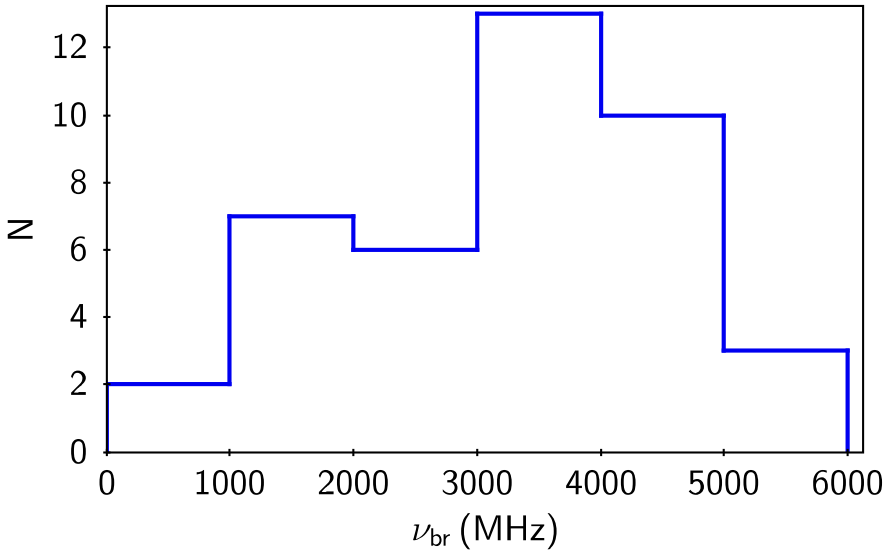

Figure 4.5: A histogram of the distribution of the break frequencies for all 41 sources fitted with a FFA model that includes a break in the spectrum.

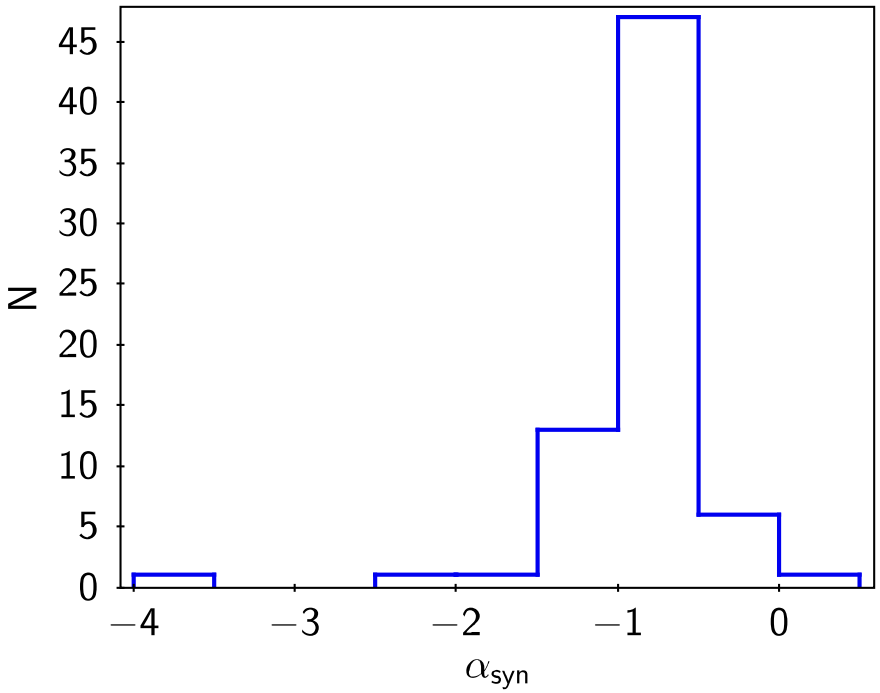

Figure 4.6: A histogram of the distribution of synchrotron spectral indices for all 70 SMC sources for which a successful fit was found. The source with $\alpha \sim -4$ is the source SMC_0022-7428, which suffers from significant resolutions effects due to its large size, causing the MOST 843 MHz data to resolve out much of its flux and predict an extremely steep slope.

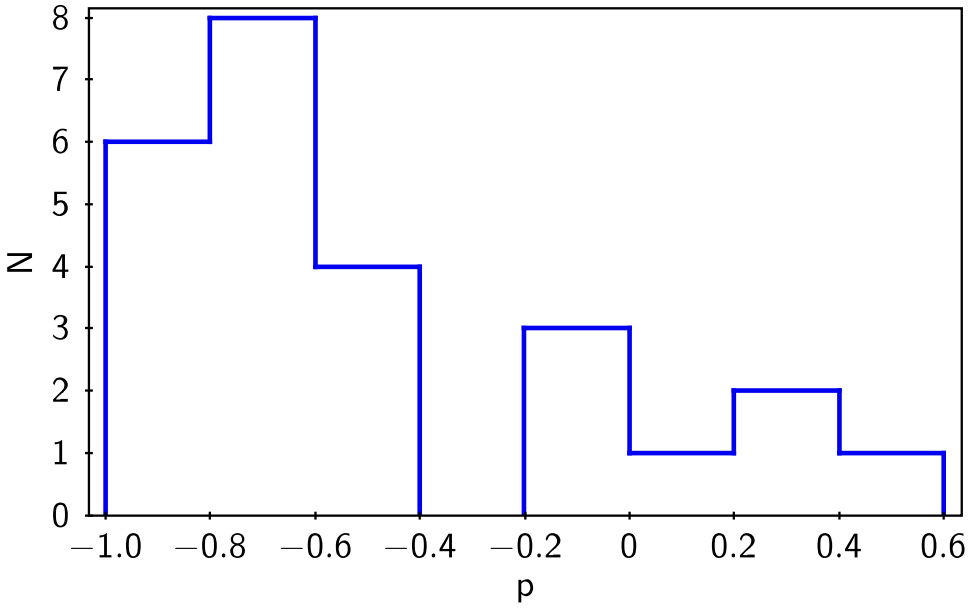

Figure 4.7: A histogram of the distribution of p values for all 25 SMC sources for which a valid p parameter was found (i.e. when $\delta p < |p| + 1$).

Table 4.5: The morphologies attributed to the 72 SMC sources during visual inspection.

Morphology	N_{total}	$N_{\text{FR I}-\text{like}}$	$N_{\text{FR II}-\text{like}}$
Unresolved	22		
Double-lobed	31	2	29
Uncertain / complex	19		
Core-dominance of double-lobed sources			
No core	20	0	20
Core-dominated	3	0	3
Lobe-dominated	8	2	6

4.1.4 Morphology

Table 4.5 summarises the morphologies that were found during visual inspection (see section 2.3.1.4). The majority of sources are resolved, and of these, most are double-lobed with no observable core, which suggests an FR-II-like morphology. Of those with an observable core, the majority were lobe-dominated, as expected from FR-II-like galaxies. This suggests the majority of our sources have high luminosities and follow the upper luminosity track from figure 1.12. We find no relic emission amongst our images, suggesting that no restarted radio galaxies exist amongst our sample.

4.1.5 Discussion of individual sources

Here we discuss the characteristics of individual sources. We derive estimates of the linear size based on an older derivation of equation 1.14, given by O'Dea (1998) as

$$\log \nu_m = -0.21(\pm 0.05) - 0.65(\pm 0.05) \log l, \tag{4.1}$$

where ν_m is the rest-frame turnover frequency in GHz, and l is the linear size in kpc. Using this, we estimate the angular scale of a source based on its angular size and estimated linear size. From this, we can estimate the redshift assuming typical ΛCDM cosmology, using $H_0 = 69.6$, $\Omega_M = 0.286$ and $\Omega_\lambda = 0.714$. However, since equation 4.1 uses the rest frame turnover frequency, we only use this technique when the redshift is estimated to be $z < 0.1$ (i.e. angular scale < 1.86 kpc/″), since above this, correcting the turnover to be in rest frame becomes significant. However, for some sources, we manually find a redshift which gives a self-consistent angular scale (e.g. smc_59 has a linear size of 0.274″ and a turnover at 192 MHz; at $z \sim 0.94$, the angular scale is ∼8.0 kpc/″, which gives a rest frame turnover of 373 MHz, and an estimated linear size of 2.2 kpc, from which we derive a self-consistent angular scale of 8.0 kpc/″). For sources where the redshift is estimated, we also estimate their 200 MHz luminosity, and compare this to the FR I/II break luminosity of $L_{178} = 2 \times 10^{25}$ W/Hz. We also refer to their images, which are shown in this section or can be found in Appendix C.2.

4.1.5.1 smc_2

smc_2 is a symmetric, double-lobed galaxy spanning 50″. The source's morphology resembles that of an FR II galaxy, with what appear to be strong hotspots (see Fig 4.8). The 4-10 GHz radio spectrum (from the CABB data) for each of the three components is shown in Fig. 4.9. The SE appears to be an unrelated source. Based on the flat spectrum of this component, it is a good candidate for the nucleus of the source. However, faint jets can be seen clearly at

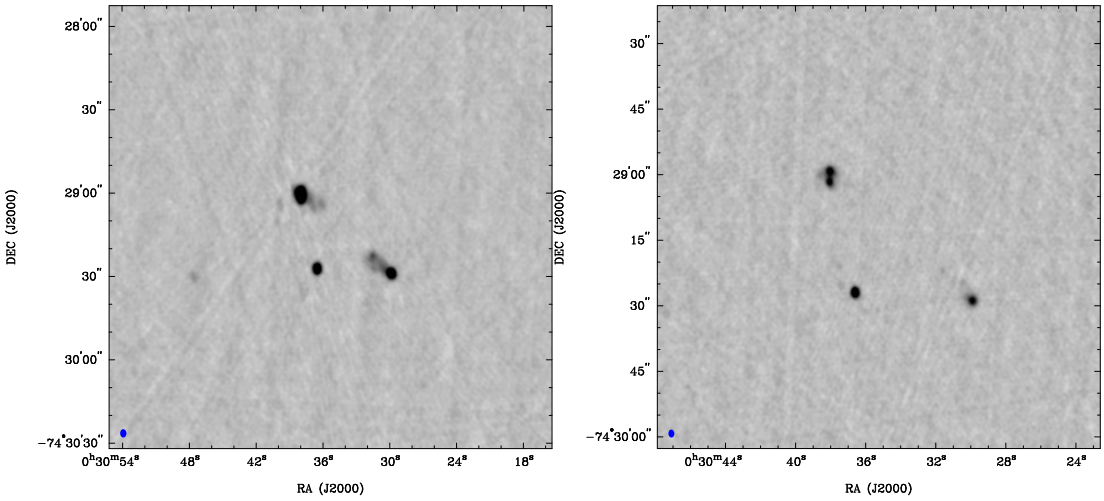

Figure 4.8: The 5.5 (left) and 9.0 (right) GHz image smc_2.

5.5 GHz, which are aligned along the axis of the hotspots, with the flat spectrum component far below this, meaning that this is unlikely to be the nucleus of this source. Therefore, we suggest no nucleus is observed and this source is strongly lobe-dominated. The SW component roughly follows a power-law spectrum, with very marginal evidence of curvature. The NE component, which itself is resolved into two components, contains an exponential spectral break at $\nu_{br} = 1101 \pm 170$ MHz. The spectral maps are shown in figure 4.10, which show a similar picture, with the southern source containing a relatively flat spectrum, and the jets, lobes and hotspots containing steep spectra. These components contain an emission ratio at 5.5 GHz of 1.5, suggesting a small asymmetry.

The integrated spectrum of the source (which includes the flat spectrum component, which is negligible at lower frequency) has a spectral index of -0.88 ± 0.03, typical of a CSS source, and contains a spectral break at $\nu_{br} = 4989 \pm 698$ MHz, above which the spectral index is ~ -1.4. The radio spectrum turns over below 76 MHz and has marginal evidence of curvature below 200 MHz.

Based on an upper limit on the turnover of 76 MHz, equation 4.1 gives an estimated lower limit on the linear size of 25 kpc. Based an angular size of 50 arcsec, this gives a lower limit on the scale of 0.5 kpc/arcsec, which gives $z \gtrsim 0.02$ and a 200 MHz luminosity $L_{200} \gtrsim 10^{24}$ W/Hz, just below the FR I/II break luminosity. Assuming this redshift, and assuming a typical magnetic field strength of $B = 5$ mG, we estimate the average spectral age across the source using equation 1.12 as $t_s < 1990$ yr, and a spectral age for the NE component of $t_{\rm off} < 4245$ yr.

The difference in spectral ages implies the integrated spectrum contains regions in which electrons were more recently injected or accelerated than the NE component. The hotspots are one of the primary regions of electron acceleration (Murgia, 2003), which implies that the NE component may not be a hotspot but part of the structure of the lobe. Alternatively, the source may have undergone a previous phase of injection which ceased accelerating electrons 4245 yr ago, and then restarted, without the fresher electrons having reached the NE component since the time of injection. Either way, we see strong evidence that the initial electron population has significantly aged. Furthermore, the lack of observed nucleus may imply that no new gas has been accreted in a significant amount of time.

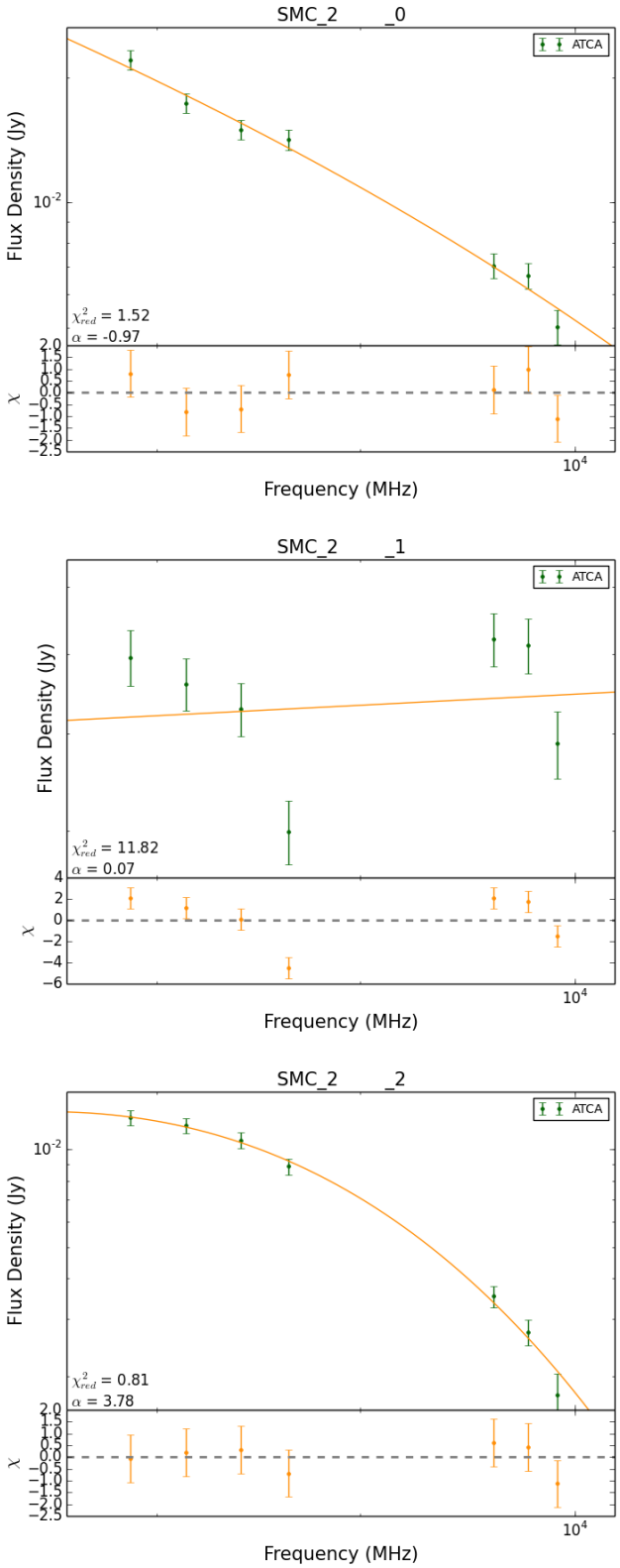

Figure 4.9: The 4-10 GHz radio spectra modelled by a power law with an exponential break of the SW (top), SE (middle) and NE (bottom) components of source smc_2.

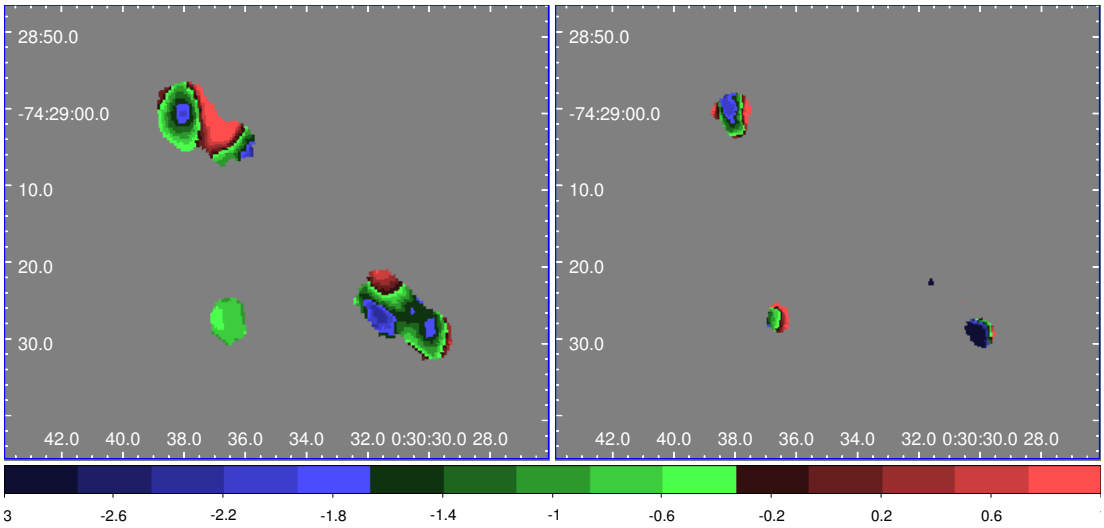

Figure 4.10: The spectral maps for source smc_2 derived from the alpha plane using MIRIAD task `mfspin` at 5.5 (left frame) and 9.0 GHz (right frame). The colourbar denotes the spectral index at each pixel. As also seen in figure 4.9, the SE component is mostly flat spectrum, while the jets, lobes and especially hotspots are steep.

4.1.5.2 smc_9

smc_9 is an unresolved source which has no extension measured by PYBDSM in the 9.0 GHz image with robust $= -2$ weighting, and therefore, we apply an upper limit of $0.14''$ to its angular size derived from equation 2.12. The integrated spectrum appears to turnover, but also appears to be variable, based on its 2379 MHz flux, which does not fit well with the peaked spectrum, and also based on the difference between the pre-CABB and CABB data fluxes, which are only just within 1σ uncertainties. The spectrum is fitted with a turnover at 2344 MHz and a spectral index of $\alpha = -0.22 \pm 0.09$. Although this source could plausibly be a quasar, based on its variability and compact nature, the turnover is well constrained by the 843 MHz flux in combination with the MWA non-detection, which gives an upper limit of $\sim$9 mJy at 200 MHz, which means the source cannot be flat spectrum. If this source is a genuine GPS source, its variability may be similar to that seen in the optically-thin part of the spectrum of PKS 1718-649 (Tingay et al., 2015).

The estimated linear size is 0.13 kpc, giving a scale of 0.94 kpc/arcsec, which gives $z \sim 0.05$ and $L_{200} \sim 5 \times 10^{22}$ W/Hz, well below the FR I/II break luminosity. If its spectrum and redshift can be considered accurate, this makes smc_9 one of the lowest luminosity GPS sources yet known.

4.1.5.3 smc_13

smc_13 is a symmetric, double-lobed galaxy with no observed core, spanning $40''$. The source's morphology resembles that of an FR II galaxy, with what appear to be strong hotspots (see Fig. 4.11). The radio spectrum for each component is shown in Fig. 4.12, which reveals the SE component has a spectral index of $\alpha = -0.70$, while the NW component has a much steeper spectral index of $\alpha = -1.40$, most likely due to containing significant emission from the NW jet and lobe, as is suggested from the image. Both components show little evidence of an exponential break and are well fit by a power law. This suggests that these components, which are likely to be dominated by hotspot emission, contain a spectral break at a higher frequency beyond 10 GHz. These components contain an emission ratio of 3.4, suggesting a significant

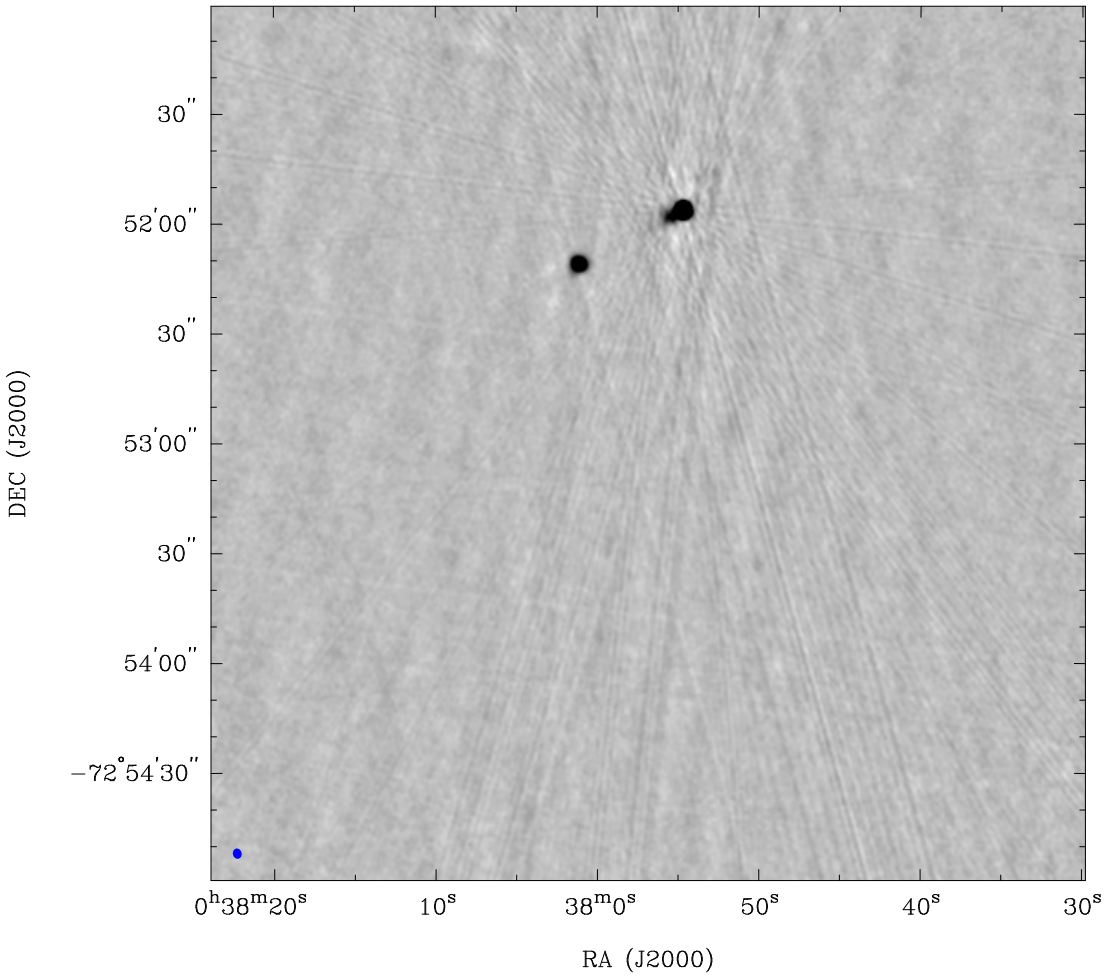

Figure 4.11: The 5.5 GHz image smc_13.

asymmetry, in which the NW component contains significantly more emission from the NW jet and lobe. The spectral maps are shown in figure 4.13, which show very steep spectral indices for the emission coming from the NW jet.

The integrated spectrum of the source has a spectral index of $\alpha = -0.88 \pm 0.04$, a spectral break at 4079 ± 658 MHz, and a turnover at < 76 MHz, with reasonable evidence of curvature below 200 MHz, given by a p value of -0.71 ± 0.22. The source is $\gtrsim 40\%$ variable at 9.0 GHz, but only ∼2% variable at 5.5 GHz, suggesting that the 9.0 GHz pre-CABB measurement may be inaccurate. Figure 4.14 shows the integrated spectrum of the source with the 9.0 GHz sub-bands included. Using these data, we find a spectral index of $\alpha = -0.82 \pm 0.03$ and a spectral break at 3380 ± 614 MHz.

The estimated linear size is > 25 kpc, giving a scale of > 0.63 kpc/arcsec, which gives $z \gtrsim 0.03$ and $L_{200} \gtrsim 10^{24}$ W/Hz, just below the FR I/II break luminosity. Assuming this redshift and a typical magnetic field strength of $B = 5$ mG, we estimate a spectral age of $t_s < 2411$ yr. If we take the spectral break of the individual components as > 10 GHz, we can estimate the spectral age of these components as $t_s \lesssim 1400$ yr.

4.1.5.4 smc_17

smc_17 is a resolved source with an uncertain morphology, spanning 4″. The source's morphology resembles that of a hotspot or lobe, with faint jet emission to the SE (see Fig. 4.15).

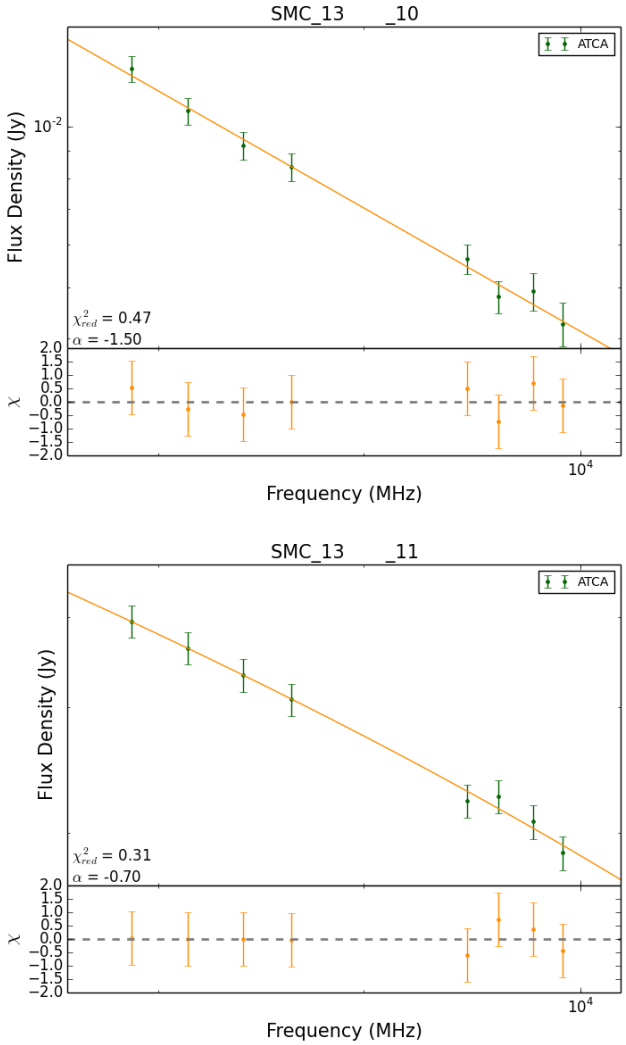

Figure 4.12: The 4-10 GHz radio spectra modelled by a power law with an exponential break of the NW (top), and SE (bottom) components of source smc_13.

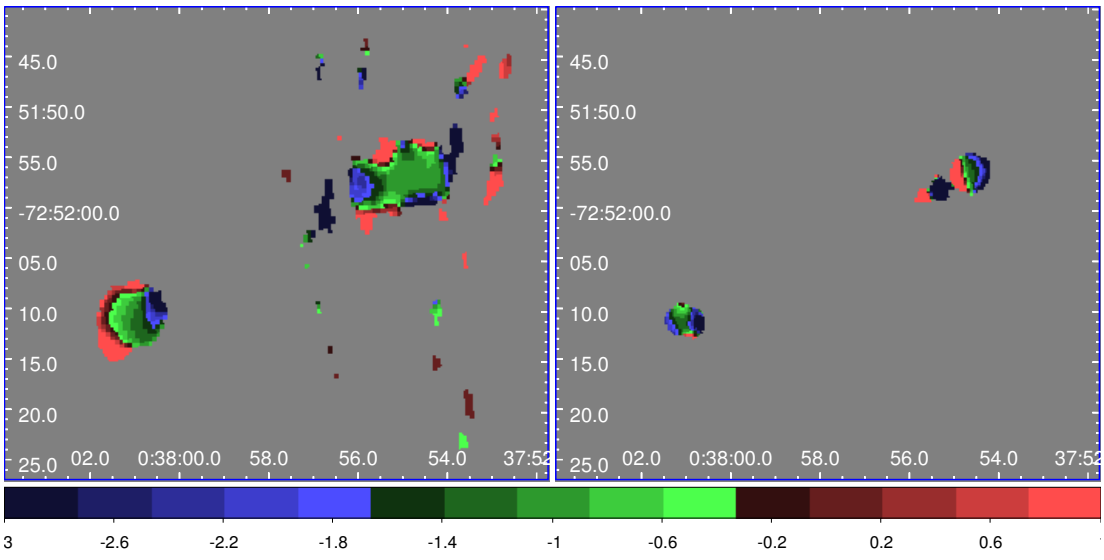

Figure 4.13: The spectral maps for source smc_13 at 5.5 (left frame) and 9.0 GHz (right frame). The colourbar denotes the spectral index at each pixel.

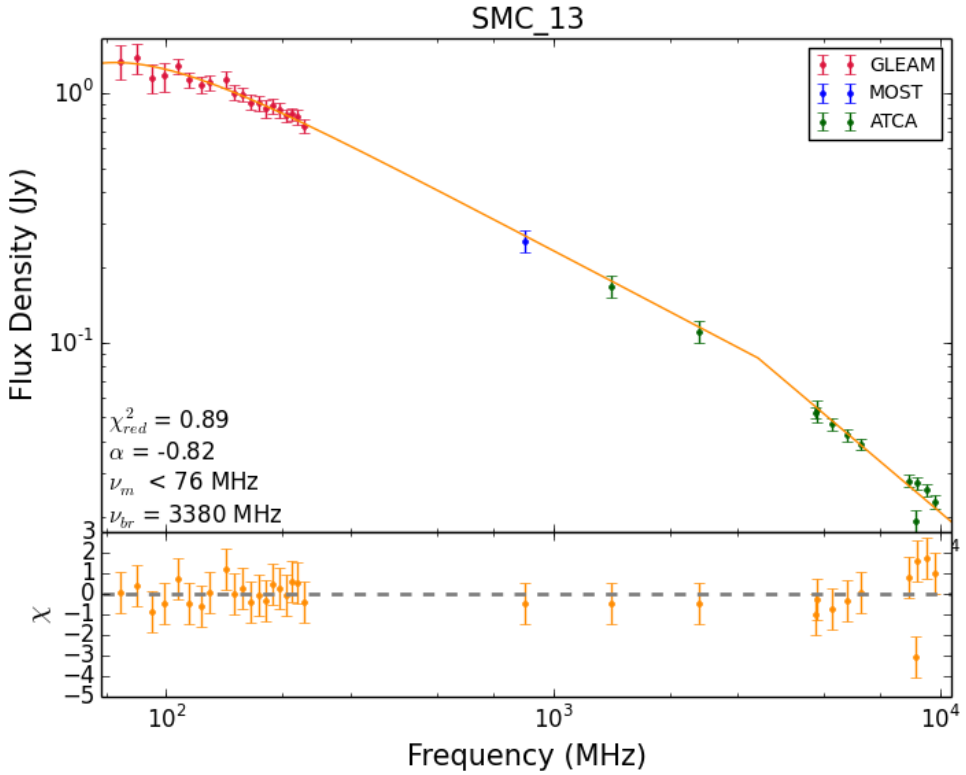

Figure 4.14: The integrated radio spectrum of smc_13, including the 9.0 GHz data that was previously excluded due to being inconsistent with the pre-CABB measurements beyond 2σ.

However, no nearby components that appear associated can be seen.

Alternatively, this source may have a core-jet morphology, as suggested by the lack of nearby components. Consistent with this interpretation are the spectral maps of smc_17 (Fig. 4.16), which reveal fairly flat and very steep components, consistent with that of a core and jet.

The integrated spectrum of the source has a spectral index of $\alpha = -1.18 \pm 0.02$ and marginal evidence of a turnover at 86 MHz. The source is $\gtrsim 26\%$ variable at 9.0 GHz, but only $\sim 4\%$ variable at 5.5 GHz, suggesting that all the 9.0 GHz measurements may be inaccurate.

4.1.5.5 smc_18

smc_18 is a symmetric, double-lobed galaxy with no observed core, spanning $6''$. The source's morphology resembles that of an FR II galaxy and the SE component is extended (see Fig. 4.17). The integrated spectrum of the source has a spectral index of $\alpha = -0.84 \pm 0.03$, a spectral break at 3025 ± 516 MHz, and a turnover much below 76 MHz, with no evidence of curvature below 200 MHz.

Based on the angular size and lack of evidence of a turnover, this source may well be a FR II galaxy. If true, this has very interesting connotations since its spectral break suggests a fairly young age. Alternatively, the source may be a CSO or MSO at low redshift.

4.1.5.6 smc_19

smc_19 is a resolved source with an uncertain morphology, spanning $2''$ (see Fig. 4.18). The integrated spectrum that includes AT20G data is shown in Fig. 4.19, which has a spectral index of $\alpha = -0.47 \pm 0.04$, a spectral break at 1788 ± 522 MHz, and reasonable evidence of a turnover

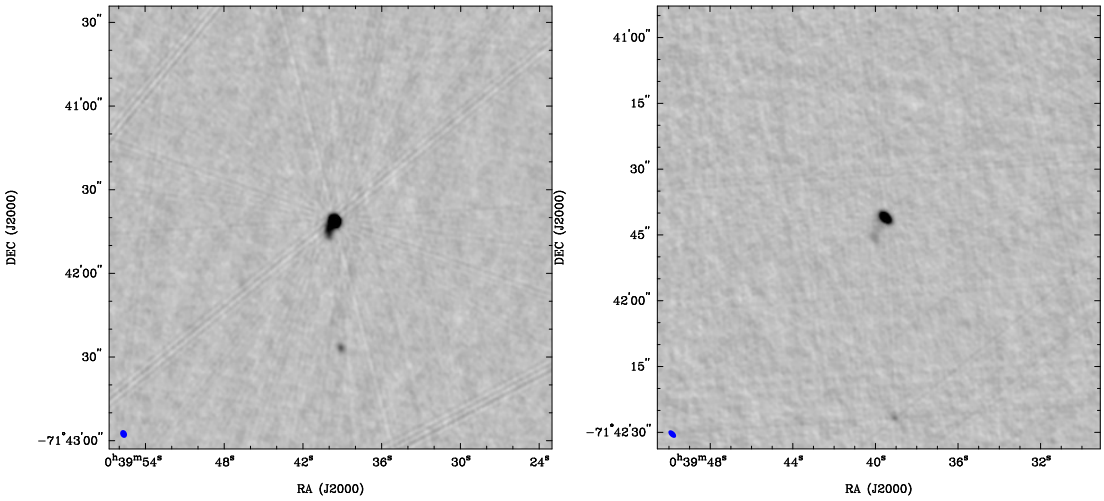

Figure 4.15: The 5.5 (left) and 9.0 (right) GHz image smc_17.

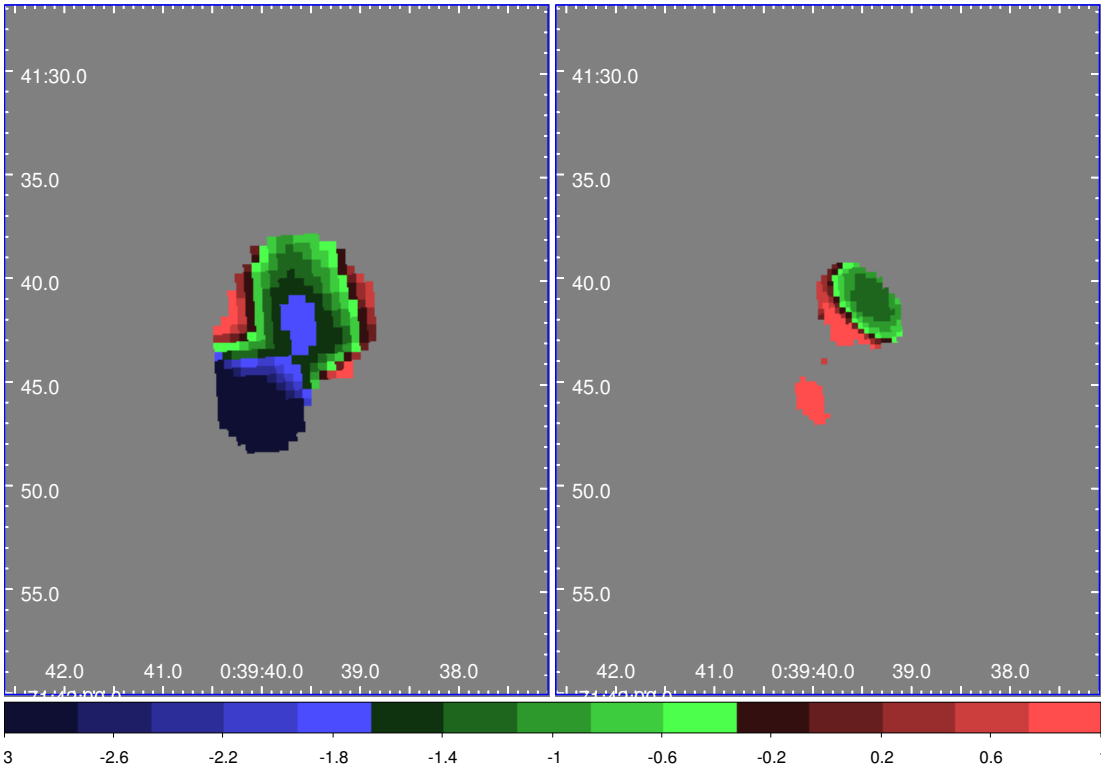

Figure 4.16: The spectral maps for source smc_17 at 5.5 (left frame) and 9.0 GHz (right frame). The colourbar denotes the spectral index at each pixel. It can be seen that the northern point source is close to flat spectrum, while the southern emission seen at 5.5 GHz is extremely steep, consistent with a core-jet morphology.

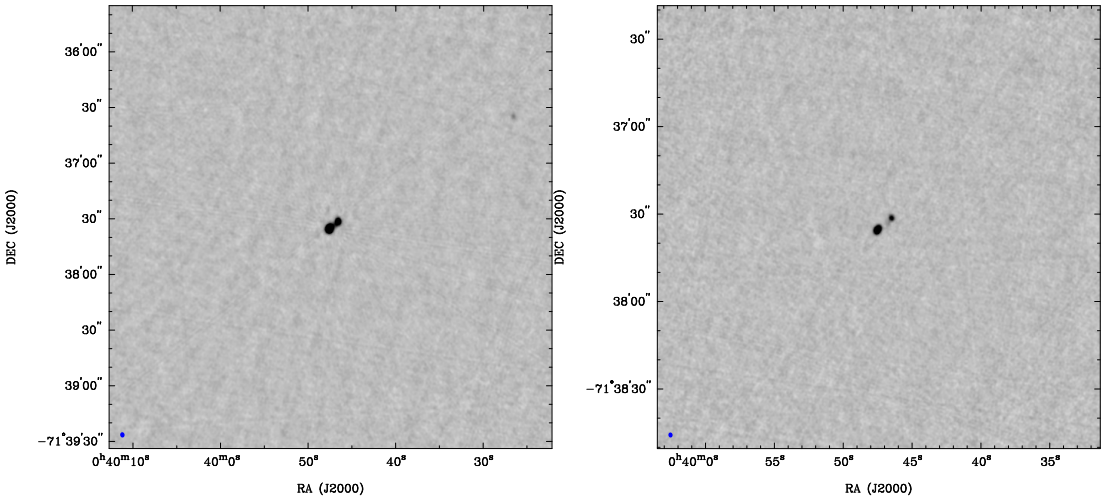

Figure 4.17: The 5.5 (left) and 9.0 (right) GHz image smc_18.

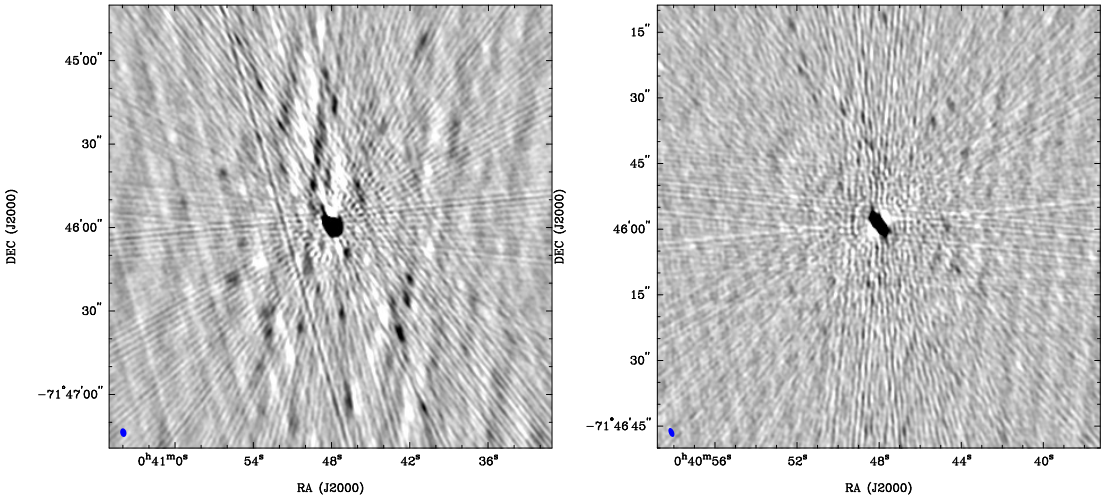

Figure 4.18: The 5.5 (left) and 9.0 (right) GHz image smc_19.

at 116 MHz. The consistency of the 408 MHz flux density with the rest of the spectrum suggests smc_19 has a very low level of variability, since the epoch of this measurement differs by $\gtrsim 20$ years compared to all other measurements.

We estimate a redshift of $z \sim 0.3$, which gives a scale of 4.5 kpc/arcsec. This redshift gives a rest frame turnover of 151 MHz, and an estimated linear size of 8.7 kpc, from which we derive a self-consistent scale of 4.5 kpc/arcsec. From this we derive $L_{200} \sim 3 \times 10^{26}$ W/Hz, above the FR I/II break luminosity. Assuming this redshift and a typical magnetic field strength of $B = 5$ mG, we estimate a spectral age of $t_s = 3050$ yr. Therefore we classify smc_19 as an FR-II-like MSO and CSS source.

4.1.5.7 smc_21

smc_21 is a wide-angle tail radio galaxy spanning $\sim 24''$, which is likely to reside within a cluster, in which the ICM is causing the jets to bend. This classifies it as an MType 7 according to An and Baan (2012). The 9.0 GHz image reveals two hotspots (see Fig 4.20). The western hotspot is close to the leading edge of the lobe, but the eastern is much closer to the core. This may be a projection effect, or perhaps the western jet is much a more powerful and efficient FR-II jet, while the eastern jet is significantly less powerful FR-I jet. A similar morphology is observed

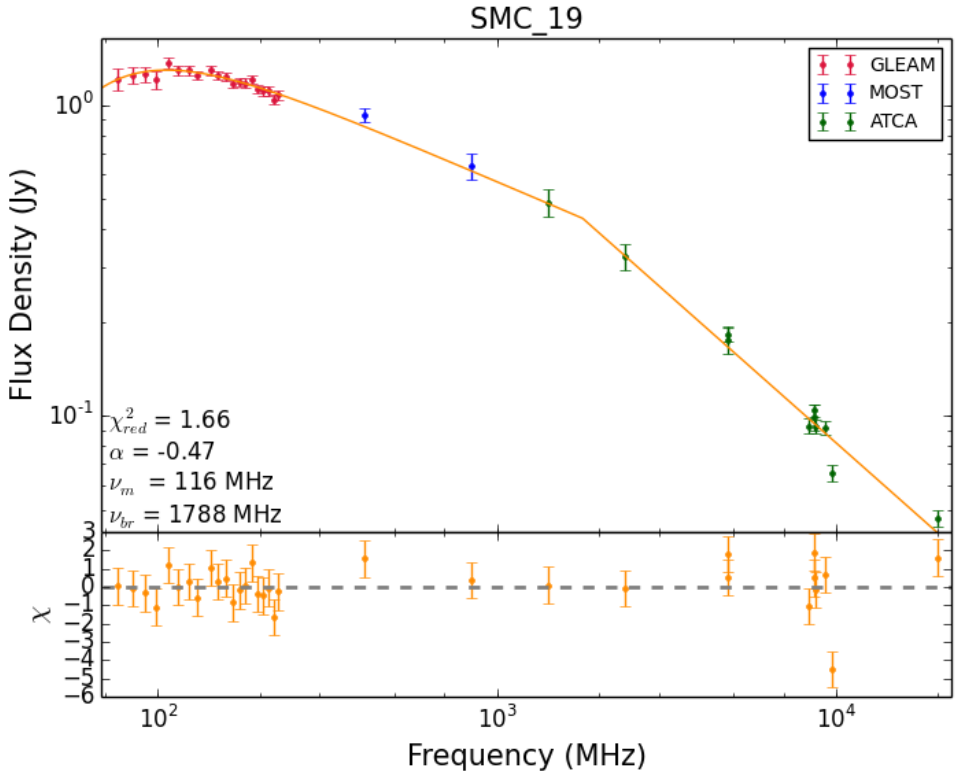

Figure 4.19: The integrated radio spectrum for source smc_19 that includes measurements from AT20G.

for the source smc_68 (see Fig 4.20), suggesting this may also be a wide-angle tail.

The spectrum of smc_21 contains a hint of a turnover at ∼100 MHz, but it may follow a power law. Its FFA model contains a poorly constrained spectral break, which is most likely due to the highest frequency flux density suffering from resolution effects due to its size.

4.1.5.8 smc_52

smc_52 is an unresolved source which has no extension measured by PYBDSM in the 9.0 GHz image with robust = −2 weighting, and therefore, we apply an upper limit of 0.13″ to its angular size derived from equation 2.12.

The spectrum is fitted with a turnover at $\nu_m = 491$ MHz and an extremely steep spectral index of $\alpha = -1.69 \pm 0.06$, classifying it as a USS. Its low frequency spectra is not well constrained, but suggests a very shallow optically-thick spectral index, which is the complete opposite of what is expected from homogeneous SSA. It is fitted with $p = -0.12 \pm 0.06$, which suggests that absorbing clouds of high emission measure are producing much of the absorption, implying a somewhat high density. Its USS may suggest it is hosted within a cluster environment (Klamer et al., 2006), which may account for its expected high density. Its compact nature and yet shallow optically-thick spectrum that is inconsistent with homogeneous SSA makes it an interesting GPS source.

4.1.5.9 smc_54

smc_54 is a point source with an extension of 0.36″ measured by PYBDSM in the 9.0 GHz image with robust = −2 weighting. The integrated spectrum that includes AT20G data is shown in

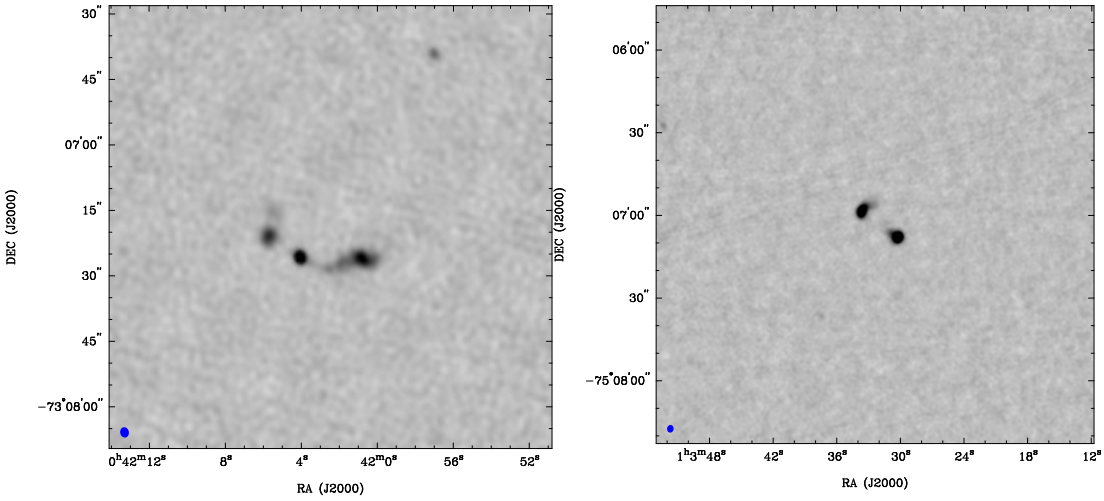

Figure 4.20: The 9.0 GHz image of smc_21 (left) and 5.5 GHz image of smc_68 (right).

Fig. 4.21, which has a spectral index of $\alpha = -0.61 \pm 0.03$, a spectral break at 2919 ± 541 MHz, $p = -0.32 \pm 0.18$, and a turnover at 155 MHz. Its 408 MHz flux density is inconsistent with all other measurements, which suggests variability related to its evolution (e.g. Tingay et al., 2015), given that the epoch of this measurement differs by $\gtrsim 20$ years compared to the other measurements.

We estimate a redshift of $z \sim 1.12$, which gives a scale of 8.3 kpc/″. This redshift gives a rest frame turnover of 329 MHz, and an estimated linear size of 3.0 kpc, from which we derive a self-consistent scale of 8.3 kpc/″. From this we derive an extremely high luminosity of $L_{200} \sim 1 \times 10^{28}$ W/Hz, well above the FR I/II break luminosity. Assuming this redshift and a typical magnetic field strength of $B = 5$ mG, we estimate a spectral age of $t_s = 2178$ yr. Therefore we classify smc_54 as an FR-II-like MSO and CSS source.

4.1.5.10 smc_55

smc_55 is a point source with an extension of 0.13″ measured by PYBDSM in the 9.0 GHz image with robust $= -2$ weighting. The integrated spectrum has a spectral index of $\alpha = -0.63 \pm 0.04$, $p = -0.49 \pm 0.04$, and a turnover at 2353 MHz. Its spectrum contains a small spectral width and a shallow optically-thick spectral index, which is poorly fit by a homogeneous SSA model (see Fig 4.1). The estimated linear size is 0.13 kpc, giving a scale of 1.0 kpc/arcsec, which gives $z \sim 0.05$ and a rest frame turnover of 2471 MHz. It is not detected in GLEAM, since it turns over at high frequency. However, based on its 5.5 GHz flux density, we derive $L_{5.5\ \mathrm{GHz}} \sim 1.5 \times 10^{23}$ W/Hz, making this one of the lowest-luminosity GPS sources yet known. The luminosity is so low that smc_55 may be a compact counterpart to an FR-I galaxy.

4.1.5.11 smc_0055-7211

smc_0055-7211 is a radio source spanning 124″, which appears to be a radio galaxy. Its morphology is very interesting and complex, with four main areas of emission (see Fig 4.22). Extended emission can be seen at the outward-most components, which are most likely to be lobes. Two strong point sources appear to the west, and to the east of this is another point source with an extended linear structure coming out of it. We may interpret each area of emission from left to right as the following: a lobe, a knot in the jet, the core, a hotspot within a lobe. If this is correct, the knot and hotspot may be indicative of the current cycle of radio activity, while the

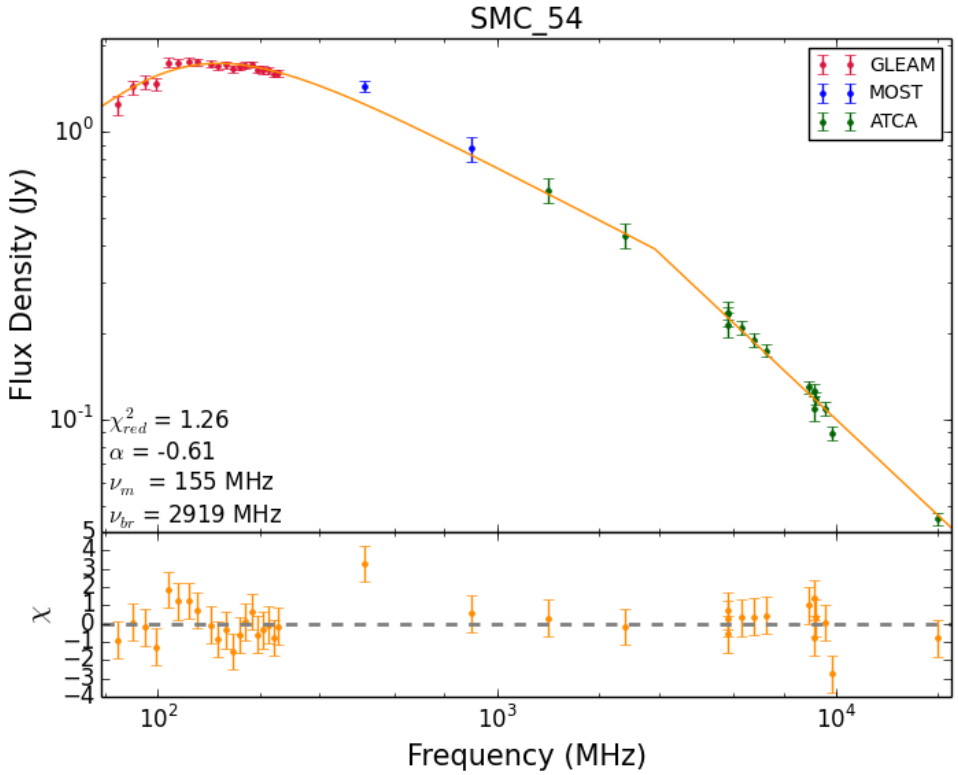

Figure 4.21: The integrated radio spectrum for source smc_54 that includes measurements from AT20G.

lobes are indicative of a previous cycle of radio activity, following the MType 4 classification for restarted sources from An and Baan (2012).

4.1.5.12 smc_56

smc_56 is a symmetric, double-lobed galaxy with no observed core, spanning 30″. The source's morphology resembles that of an FR II galaxy, with what appear to be strong hotspots (see Fig. 4.23). The radio spectrum for each component is shown in Fig. 4.24, which reveals the NW component has a spectral index of $\alpha = -0.92$, while the SE component has a much steeper spectral index of $\alpha \sim -1.74$, most likely due to containing significant contribution from the lobe, as suggested from the image. Both components show little to no evidence of an exponential break and are well fit by a power law. This suggests that these components, which are likely to be dominated by hotspot emission, contain a spectral break at a higher frequency beyond 10 GHz. These components contain an emission ratio of 1.3, suggesting minor asymmetry.

The integrated spectrum of the source has a spectral index of $\alpha = -0.77 \pm 0.04$, a spectral break at 4649 ± 1084 MHz, and a turnover at < 76 MHz, with no evidence of curvature below 200 MHz.

The estimated linear size is > 25 kpc, giving a scale of > 0.85 kpc/arcsec, which gives $z \gtrsim 0.04$ and $L_{200} \gtrsim 1 \times 10^{24}$ W/Hz, well below the FR I/II break luminosity. Assuming this redshift and a typical magnetic field strength of $B = 5$ mG, we estimate a spectral age of $t_s < 2043$ yr.

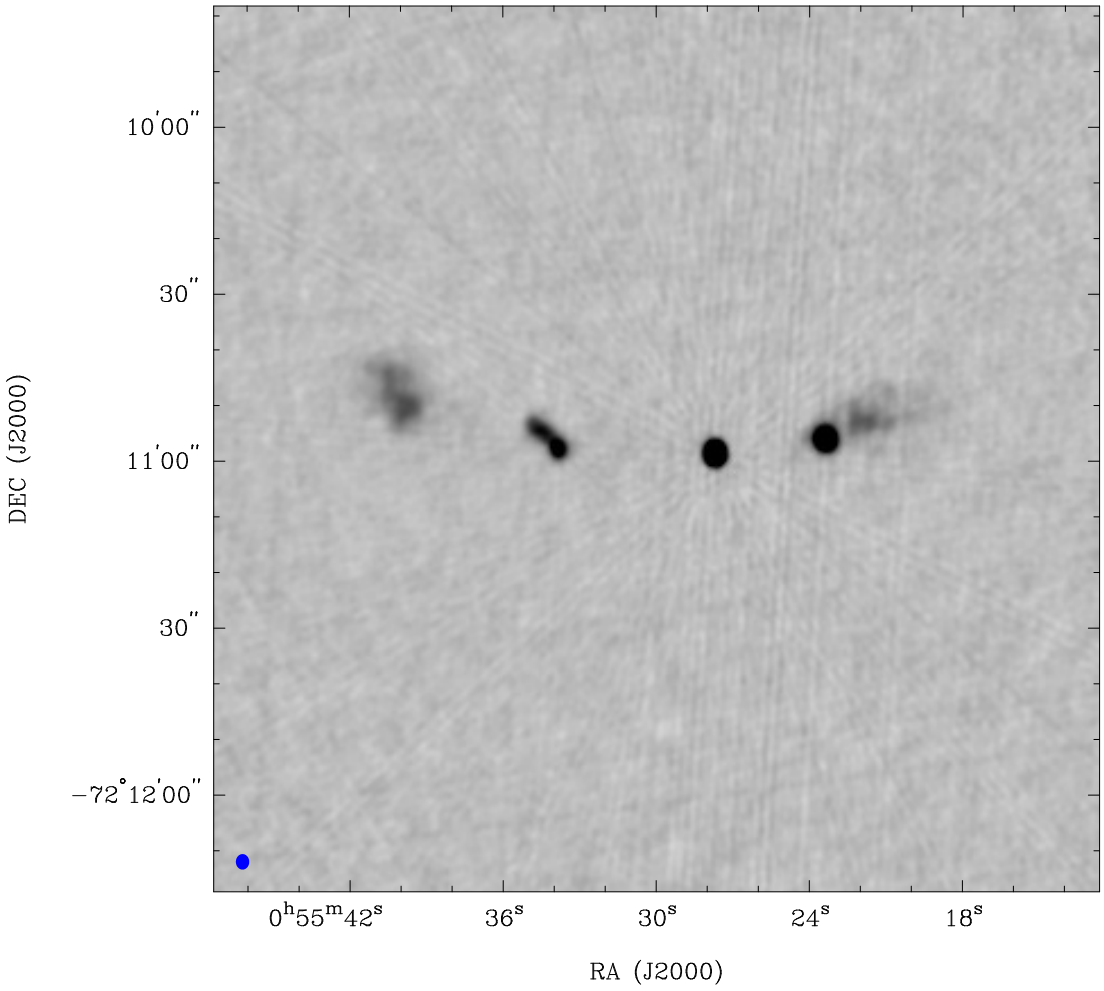

Figure 4.22: The 5.5 GHz image of smc_0055-7211.

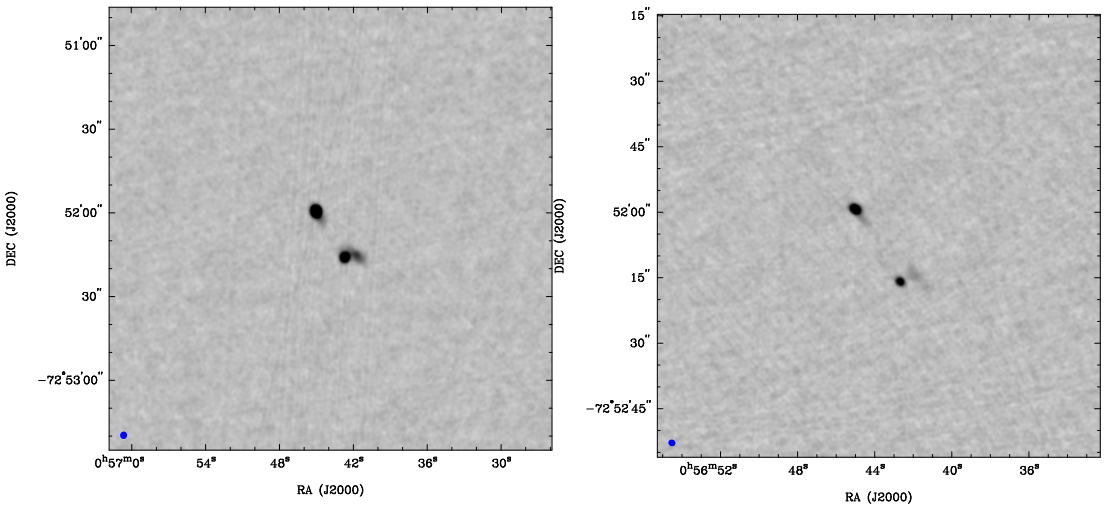

Figure 4.23: The 5.5 (left) and 9.0 (right) GHz image smc_56.

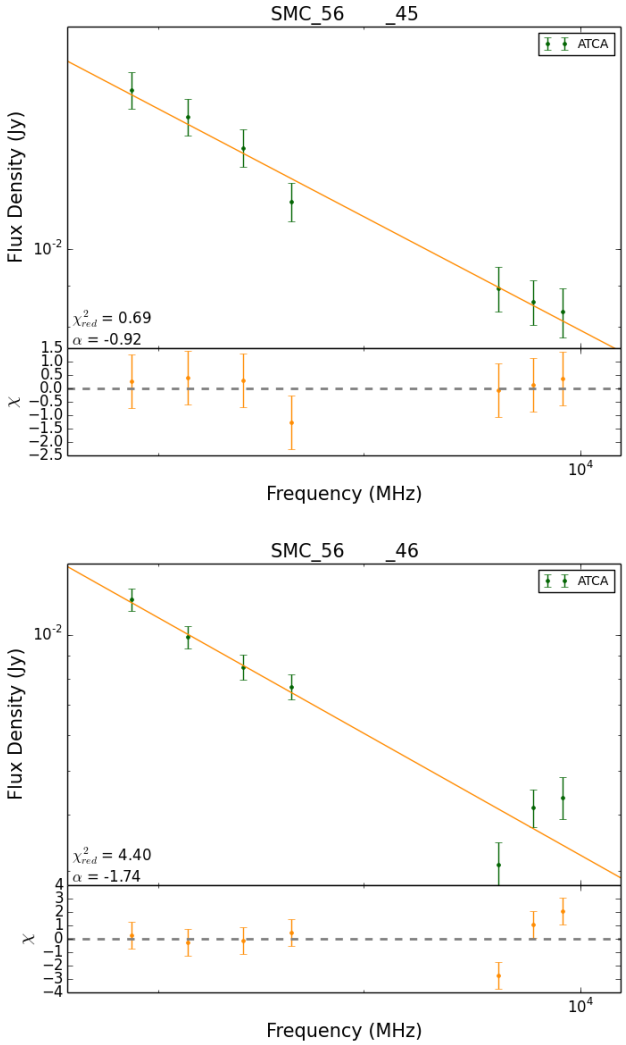

Figure 4.24: The 4-10 GHz radio spectra modelled by a power law with an exponential break of the NW (top), and SE (bottom) components of source smc_56.

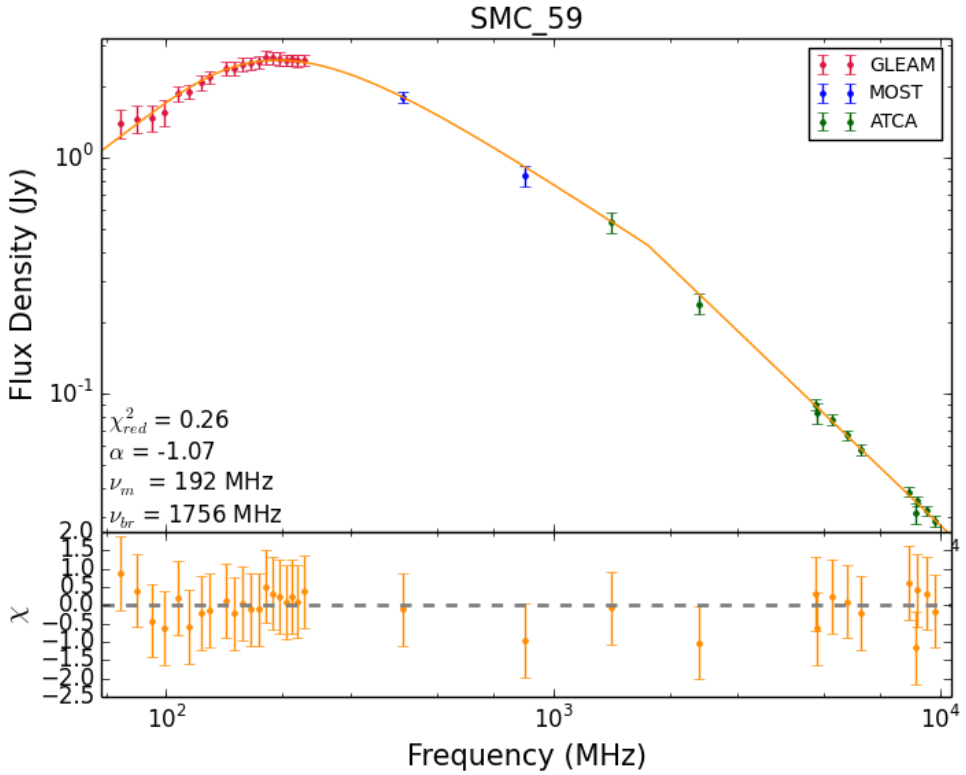

Figure 4.25: The integrated radio spectrum for source smc_59.

4.1.5.13 smc_59

smc_59 is a point source with an extension of 0.274″ measured by PYBDSM in the 9.0 GHz image with robust = −2 weighting. The integrated spectrum (see Fig 4.25) has a very steep spectral index of $\alpha = -1.07 \pm 0.02$, $p = -0.11 \pm 0.06$, and a turnover at 192 MHz. It is fit with a break frequency of 1756 ± 202 MHz, above which it becomes USS with $\alpha = -1.6$. The fitted value for p, which is close to 0, implies that many absorbing clouds with high emission measure exist within the environment of smc_59, which suggests a high density.

We estimate a redshift of $z \sim 0.94$, which gives a scale of ∼8.0 kpc/″. This redshift gives a rest frame turnover of 373 MHz, and an estimated linear size of 2.2 kpc, from which we derive a self-consistent scale of 8.0 kpc/″. From this we derive an extremely high luminosity of $L_{200} \sim 1 \times 10^{28}$ W/Hz, well above the FR I/II break luminosity. Assuming this redshift and a typical magnetic field strength of $B = 5$ mG, we estimate a spectral age of $t_s = 2437$ yr. Therefore we classify smc_59 as an FR-II-like MSO and CSS source.

4.1.5.14 smc_71

smc_71 is an unresolved source which has no extension measured by PYBDSM in the 9.0 GHz image with robust = −2 weighting, and therefore, we apply an upper limit of 0.13″ to its angular size derived from equation 2.12. The integrated spectrum has a spectral index of $\alpha = -0.80 \pm 0.07$, $p = 0.24 \pm 0.97$, and a turnover at 1660 MHz. The estimated linear size is 0.22 kpc, giving a scale of 1.6 kpc/arcsec, which gives $z \sim 0.09$ and a rest frame turnover of ∼1800 MHz. It is not detected in GLEAM, since it turns over at high frequency. However, based on its 5.5 GHz flux density, we derive $L_{5.5\ \mathrm{GHz}} \sim 3.1 \times 10^{23}$ W/Hz, making this one of

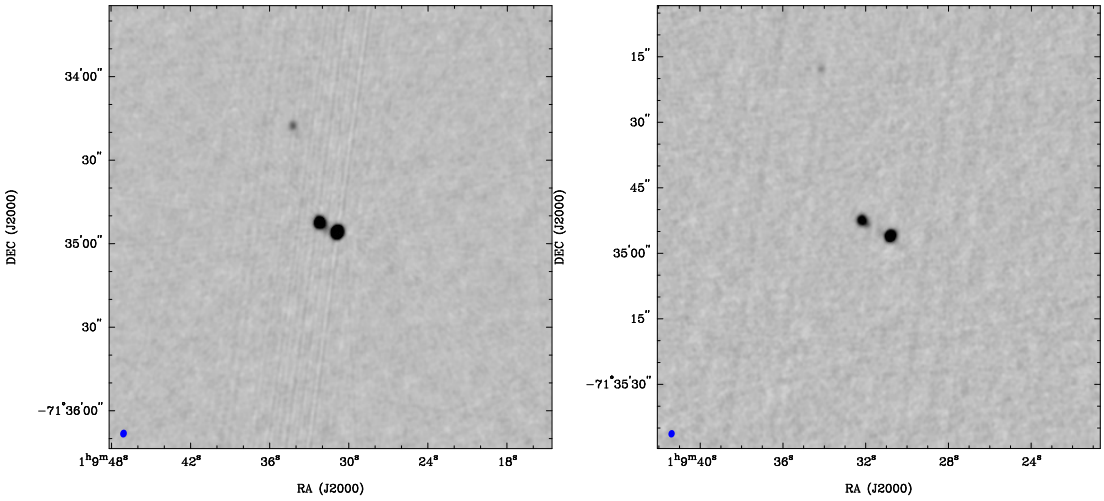

Figure 4.26: The 5.5 (left) and 9.0 (right) GHz image smc_75.

the lowest-luminosity GPS sources yet known. The luminosity is so low that smc_71 may also be a compact counterpart to an FR-I galaxy.

4.1.5.15 smc_75

smc_75 is a symmetric, double-lobed galaxy with no observed core, spanning 8.0″. The source's morphology resembles that of an FR II galaxy, with what appear to be strong hotspots (see Fig. 4.26). The radio spectrum for each component is shown in Fig. 4.27, which reveals the east component has a spectral index of $\alpha = -0.92$, while the west component has a much steeper spectral index of $\alpha = -1.31$. The east component shows marginal evidence of an exponential break, which was fit with $\nu_{br} = 9174 \pm 4734$ MHz, while the western component is well fit by a power law. These components contain an emission ratio of 2.2, suggesting a significant asymmetry.

The integrated spectrum of the source has a steep spectral index of $\alpha = -0.98 \pm 0.04$, $p = -0.80 \pm 0.04$, a spectral break at 3462 ± 618 MHz, and a turnover at < 76 MHz. Its very slight curvature that is well constrained by the p parameter is interesting and suggests smc_75 may have a very broad turnover, covering many tens of decades of frequency.

We estimate a redshift of $z > 0.15$, which gives a scale of >2.6 kpc/″. This redshift gives a rest frame turnover of < 87 MHz, and an estimated linear size of >20.8 kpc, from which we derive a self-consistent scale of >2.6 kpc/″. From this we derive a luminosity of $L_{200} > 5 \times 10^{25}$ W/Hz, just above the FR I/II break luminosity. Assuming this redshift and a typical magnetic field strength of $B = 5$ mG, we estimate a spectral age of $t_s = 2255$ yr.

4.1.5.16 smc_76

smc_76 is an unresolved source which has no extension measured by PYBDSM in the 9.0 GHz image with robust $= -2$ weighting, and therefore, we apply an upper limit of 0.16″ to its angular size derived from equation 2.12. The integrated spectrum has an extremely steep spectral index of $\alpha = -1.42 \pm 0.13$, $p = -0.13 \pm 0.16$, and a turnover at 1784 MHz. Its spectrum contains a large spectral width and a very shallow optically-thick spectral index, which is poorly fit by a homogeneous SSA model (see Fig 4.1). The estimated linear size is 0.20 kpc, giving a scale of 1.2 kpc/arcsec, which gives $z \sim 0.06$ and a rest frame turnover of 1891 MHz. It is not detected in GLEAM, since it turns over at high frequency. However, based on its 5.5 GHz flux density,

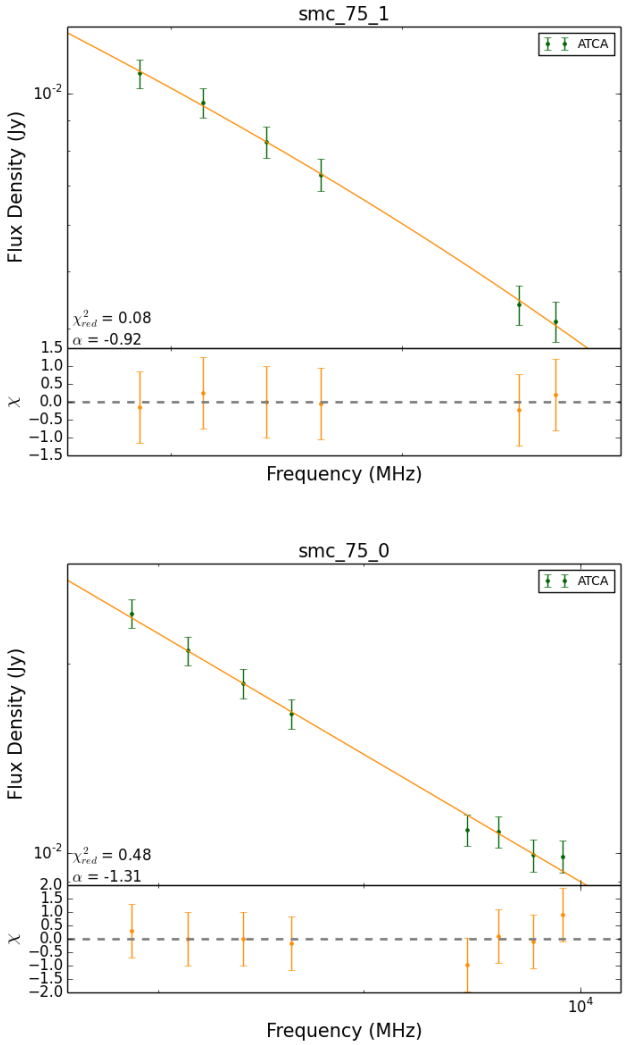

Figure 4.27: The 4-10 GHz radio spectra modelled by a power law with an exponential break of the east (top), and west (bottom) components of source smc_75.

we derive $L_{5.5\ \mathrm{GHz}} \sim 6.1 \times 10^{23}$ W/Hz, making this one of the lowest-luminosity GPS sources yet known. The luminosity is so low that smc_76 may be a compact counterpart to an FR-I galaxy.

4.1.5.17 smc_95

smc_95 is an unresolved source which has no extension measured by PYBDSM in the 9.0 GHz image with robust $= -2$ weighting, and therefore, we apply an upper limit of $0.14''$ to its angular size derived from equation 2.12. The integrated spectrum has a monumentally steep spectral index of $\alpha = -2.39 \pm 0.11$, $p = 0.34 \pm 0.08$, and a turnover at 1989 MHz. Its spectrum contains a large spectral width and a very shallow optically-thick spectral index, which is poorly fit by a homogeneous SSA model. The extremely steep spectral index is indicative of electron ageing and may suggest an exponential spectral break would fit better. If we take the FFA to be a good representation of its spectrum, the large, positive p value indicates that amongst the absorbing clouds, more with high emission measure exist compared to those with low emission measure. This suggests a significantly high density and gives favour to the frustrated hypothesis for smc_95.

The estimated linear size is 0.14 kpc, giving a scale of 1.16 kpc/arcsec, which gives $z \sim 0.06$ and a rest frame turnover of 2108 MHz. It is not detected in GLEAM, since it turns over at high frequency. However, based on its 5.5 GHz flux density, we derive $L_{5.5\ \mathrm{GHz}} \sim 1.0 \times 10^{22}$ W/Hz, making this possibly the lowest-luminosity GPS source yet known. The luminosity is so low that smc_95 may be a compact counterpart to an FR-I galaxy.

4.2 ATLAS VLBI sample

As discussed in section 2.2.4 and shown in table 2.4, we observed eight of the most compact GPS and CSS candidates from ATLAS with the Australian LBA, with the purpose of measuring their linear sizes and determining their small-scale morphologies. The data reduction is outlined in section 2.3.3.

The final models fit to the sources detected with the LBA are listed in Table 4.6, and the upper limits for the undetected sources are shown in Table 4.7.[2] The corresponding model images are shown in Figure 4.28. The Fourier transform of the visibility residuals for the six detected sources and the dirty maps of the two undetected sources are shown in Figure 4.29.

The large LBA-ATCA flux density ratios shown in Table 4.6 and 4.7 suggest a significant error may be present amongst the amplitude calibration, since a few have ratios significantly larger than one. This needs to be explored further. However, the VLBI flux densities are not used in the spectral modelling, but are used primarily to measure their linear sizes, which are not affected by the amplitude scale.

Source CI0008 is resolved into two components, and its Largest Linear Size (LLS) was measured using equation 2.9, but where θ_{psf} was simply taken as the major axis of the FWHM, since $\mathrm{PA_{gauss}} - \mathrm{PA_{sky}} < 1$ degree. For the other sources, the LLS was derived from the major axis of the fitted model.

[2]Throughout section 4.2, we use $H_0 = 69.6$, $\Omega_{\mathrm{M}} = 0.286$ and $\Omega_{\Lambda} = 0.714$.

Table 4.6: The ATLAS GPS and CSS candidates detected with the LBA. Shown is the ID, the fitted RA, Dec, LBA 1.67 GHz flux density, r.m.s. and S/N, the major and minor axes and PA from the LBA, the 1.71 GHz ATCA flux density from ATLAS DR3 (Franzen et al., 2015), the LBA-ATCA flux density ratio, the redshift and its reference, the Largest Linear Size (LLS), and the 1.71 GHz luminosity. All values are given to three significant figures. Source CI0008 was fitted with two components, which are listed separately. The LBA-ATCA flux density ratio listed for this source represents the sum of the flux density of both components as a fraction of the 1.71 GHz ATCA flux density. The LLS of this source corresponds to the distance between these components, measured from equation 2.9, but where $\theta_{\rm psf}$ was simply taken as the major axis of the FWHM, since $\mathrm{PA_{gauss}} - \mathrm{PA_{sky}} < 1$ degree. The LLS of all other sources is derived from the major axis of the FWHM. Sources with ID prefix 's' are from the ELAIS-S1 field, following the source IDs from Middelberg et al. (2008a). Sources with ID prefix 'C' are from the CDFS field, following an earlier version of the ATLAS DR3 catalogue. References for the redshifts are listed as the following: (1) = Rowan-Robinson et al. (2008) (photo$-z$); (2) = Mao et al. (2012); (3) = Coil et al. (2011); (4) = Mainieri et al. (2008).

ID	RA	Dec	$S_{\rm LBA}$	r.m.s.	S/N	$\Theta_{\rm maj} \times \Theta_{\rm min}$	PA	$S_{\rm ATCA}$	$\frac{S_{\rm LBA}}{S_{\rm ATCA}}$	z	Ref.	LLS	$L_{1.71\rm GHz}$
	(J2000)		(mJy)	(mJy/beam)		(mas × mas)	(deg)	(mJy)				(kpc)	W Hz^{-1}
s150	00:33:12.1954	−44:19:51.4418	29.6	0.195	152	29.3 × 0.0	−86.1	17.3	1.70				
s895	00:37:45.2726	−43:25:54.2412	6.50	0.0879	73.9	33.4 × 18.1	−58.9	6.44	1.01	1.14	(1)	0.279	4.77×10^{25}
s415	00:38:07.9339	−43:58:55.3721	1.95	0.0860	22.7	46.7 × 13.8	53.0	5.99	0.325	0.507	(2)	0.290	6.07×10^{24}
CI0008-1	03:35:53.3319	−27:27:40.2979	104	0.180	579	125 × 73.8	−83.7	98.9	2.36	0.256	(2)	1.79	2.01×10^{25}
CI0008-2	03:35:53.3486	−27:27:40.3363	129	0.180	716	154 × 98.8	70.9	98.9	2.36	0.256	(2)	1.79	2.01×10^{25}
CI0112	03:30:09.3647	−28:18:50.4100	1.87	0.0832	22.5	16.8 × 0.0	38.5	2.28	0.819	0.287	(3)	0.0730	6.05×10^{23}
CI0020	03:33:10.1976	−27:48:42.2056	48.0	0.104	463	112 × 75.0	−75.2	20.5	2.34	1.03	(4)	0.919	1.18×10^{26}

Table 4.7: The ATLAS GPS and CSS candidates not detected with the LBA. Shown is the ID, RA, Dec and 1.4 GHz ATCA flux density from ATLAS DR1 (Middelberg et al., 2008a), the r.m.s. and 1.67 GHz flux density upper limit from the LBA, the redshift and the 1.4 GHz luminosity. All values are given to three significant figures. Both sources are from the ELAIS-S1 field, and use the source IDs and 1.4 GHz flux densities from DR1, since one source is outside the field catalogued in DR3 by Franzen et al. (2015). We quote a 6.75σ flux density upper limit following the approach from Deller and Middelberg (2014). Both redshifts are photometric redshifts from Rowan-Robinson et al. (2008).

ID	RA	Dec	$S_{\rm ATCA}$	r.m.s.	$S_{\rm LBA}$	z	Ref.	$L_{1.4\rm GHz}$
	(J2000)		(mJy)	(mJy/beam)	(mJy/beam)			W Hz^{-1}
s798	00:39:07.934	−43:32:05.833	7.79	0.0807	< 0.545	0.400	(1)	4.47×10^{24}
s1218	00:35:08.380	−43:00:04.202	33.2	0.194	< 1.31	0.629	(1)	5.69×10^{25}

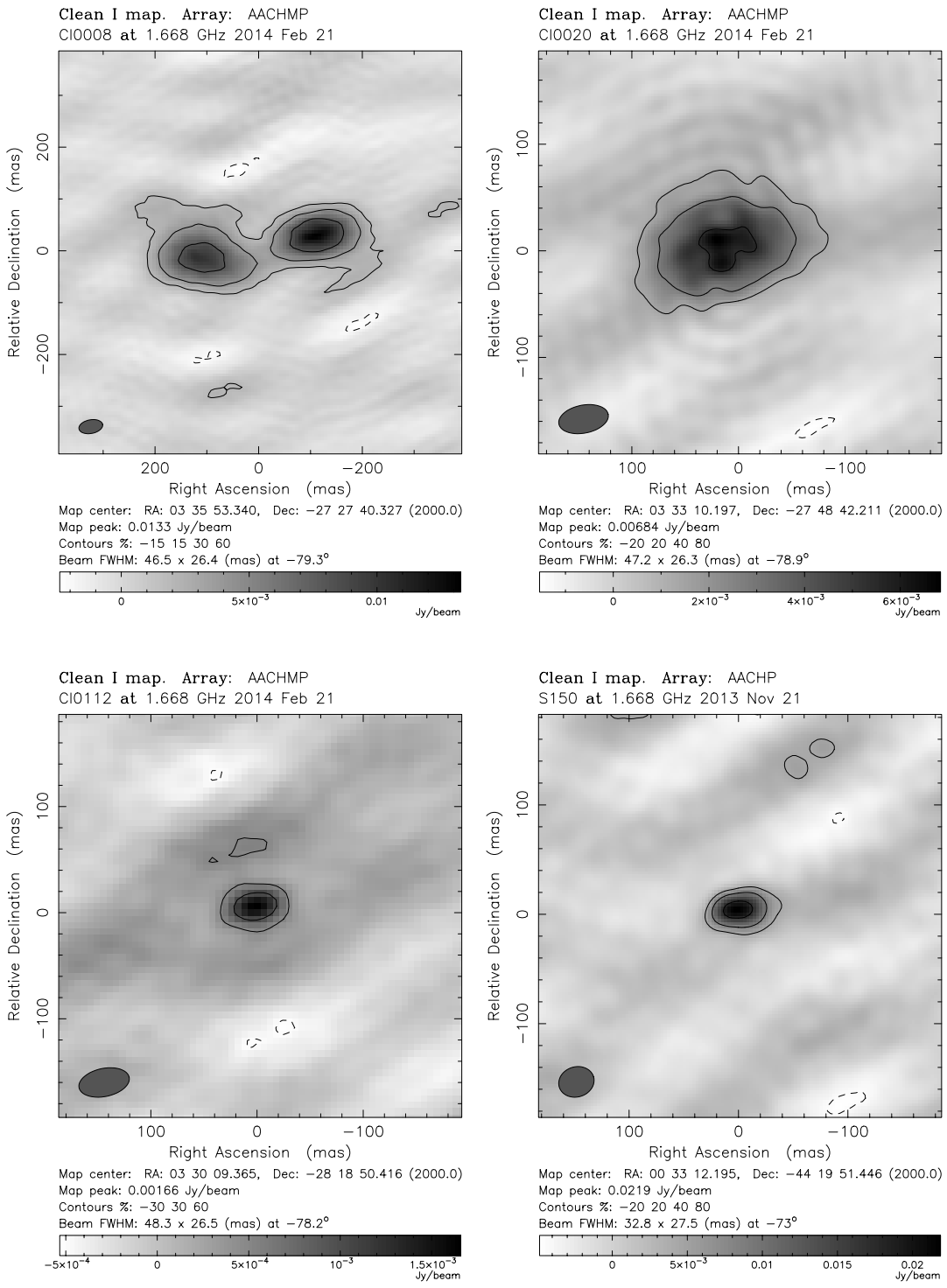

Figure 4.28: The LBA model images of the six detected GPS and CSS candidates. The contours represent the displayed percentages of the image peak, including a negative dashed contour, and are typically −30%, 30% and 60%. The synthesised beam is shown by the shaded ellipse in the bottom left hand corner, and its size is displayed in the information below the map.

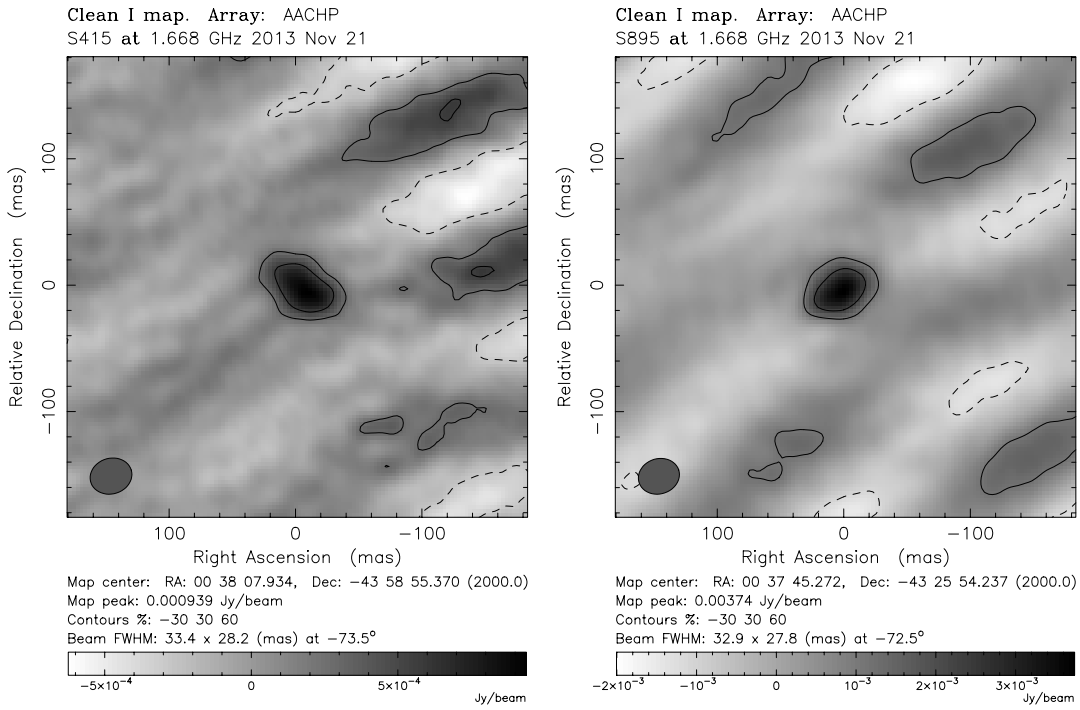

Figure 4.28 (continued)

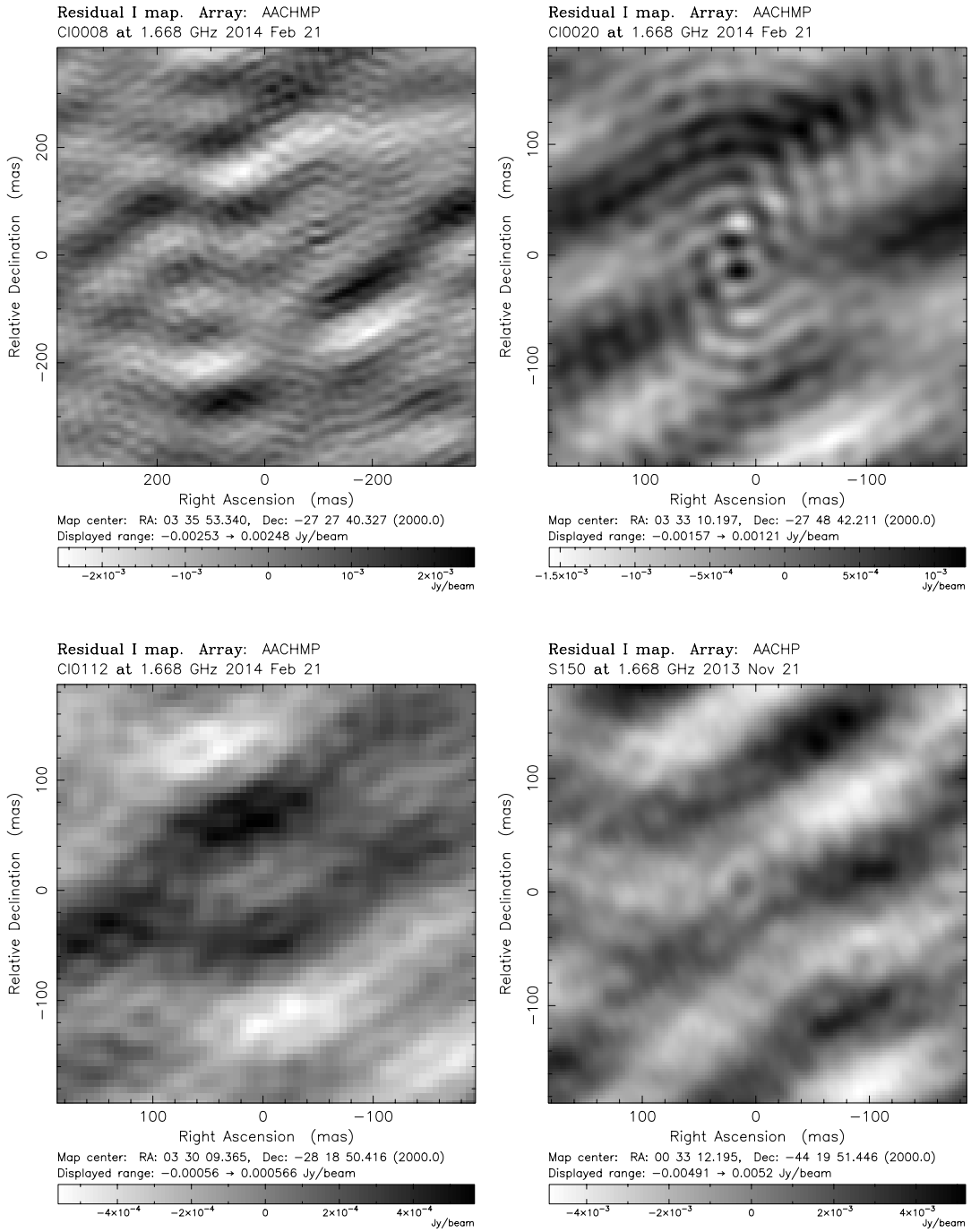

Figure 4.29: The LBA residual images for the six detected GPS and CSS candidates, after the model has been subtracted from the visibilities, and the dirty maps of the two undetected sources. The r.m.s. values are between $0.1 - 0.2$ mJy/beam.

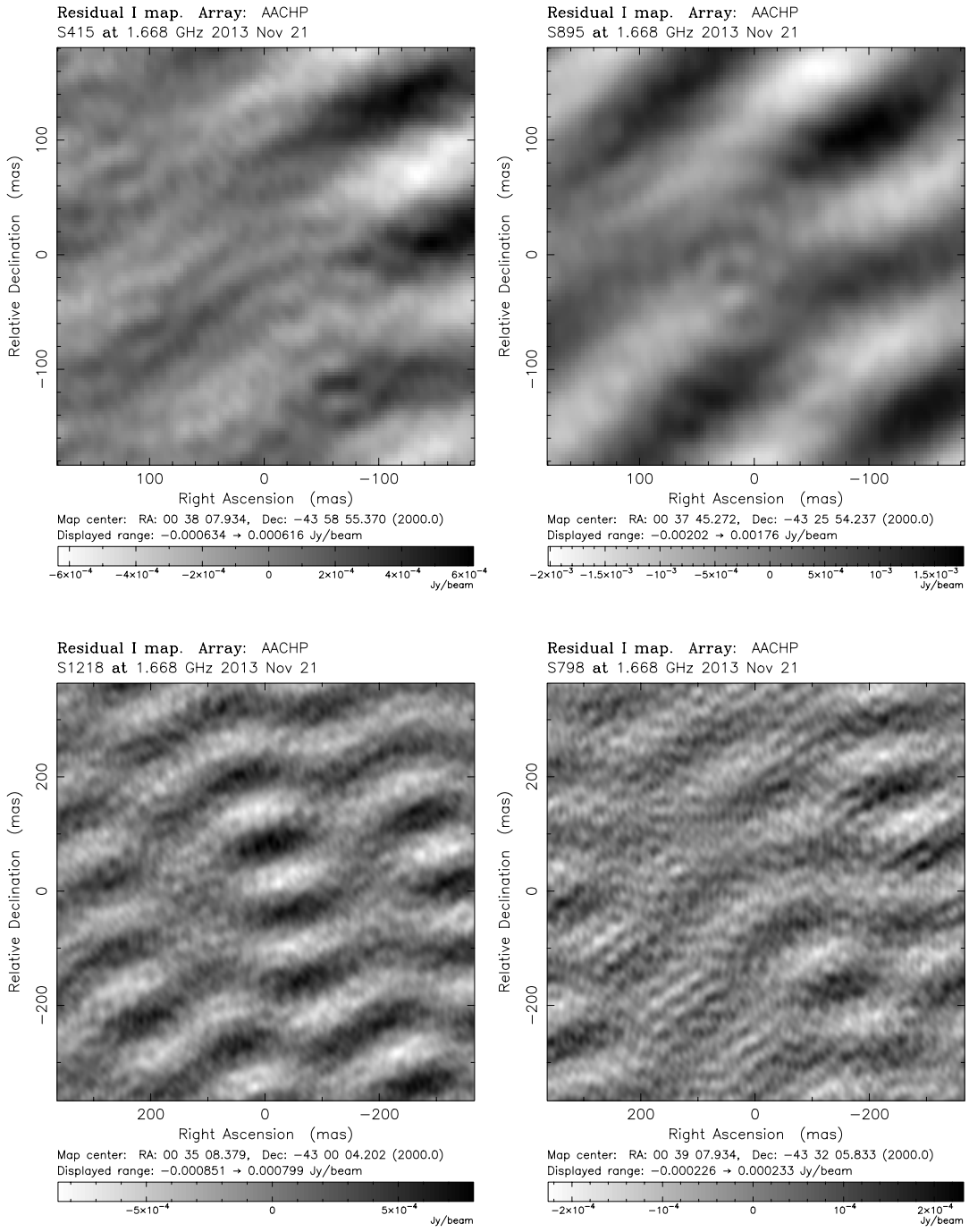

Figure 4.29 (continued)

4.2.1 Modelling the radio spectra

For source CI0008, since it is strongly detected at low frequency, we use the 20 GLEAM sub-bands in the modelling. For all other sources, we use GLEAM deep flux from 200 MHz, as well as the flux measurements we made from the other three deep bands using the priorised fitting feature of AEGEAN (see section 2.3.2.3). We also use all other flux density measurements that are available, up to 34 GHz. Since each source was selected to be unresolved in ATLAS (i.e. $\lesssim 10''$) and since they are detected at the mas scales of the LBA observations, we do not expect that any of the flux measurements suffer from resolution effects. Therefore, we used the peak flux density where available to model the spectrum and used all available flux density measurements. However, we discarded all measurements where the flux uncertainty was larger than the flux, which was the case for a few of the GLEAM deep band measurements. Where a source was undetected at low frequency, we assigned a flux density of $2 \pm 1\sigma$ as an upper limit.

4.2.2 Variability

Variability was investigated within ATLAS DR1, and it was concluded that only $\sim$10% of the radio sources were variable at 1.4 GHz at the level of $\sim$10% (Ray Norris, private communication). Furthermore, since our radio spectra span such a large range of frequencies over a large range of epochs, we expect variable sources will not maintain a typical GPS or CSS spectrum over these epochs (e.g. as we find for source CI0112). However, a low level of variability cannot be ruled out within the spectra, particularly at high frequency.

4.2.3 Spectral Models

The best fit models for all six sources are shown in figure 4.8. The models used in the fitting, and the values of each of the parameters are summarised in table 4.8.

Since we were fitting for only six sources, the best models were chosen on an individual basis. For source CI0008, we fit a FFA model, since this gave the lowest reduced χ^2 value and since the source appears to be just beginning to turn over below $\sim$200 MHz. For source CI0020, we fit a FFA model with an exponential break, since this agreed with the 34 GHz measurement and gave a low reduced χ^2 value, as compared to a Kardashev break, which did not agree with this measurement and gave a higher reduced χ^2 value. For source CI0112, we fit a FFA model based on having the lowest reduced χ^2 value. However, we interpret this source as a variable quasar, which is consistent with its highly compact VLBI emission, and which means the multi-epoch spectra we have measured does not represent its intrinsic spectrum. For source s150, we fit a FFA model. Although fitting a FFA model with a Kardashev break gave a slightly lower reduced χ^2 value, we did not see evidence that this was a better representation of the spectrum, particularly since we used upper limits to model the low frequency spectrum. For source s895, we fit a FFA model based on having the lowest reduced χ^2 value. For source s415, we fit a power law based on having the lowest reduced χ^2 value. The lowest frequency measurement at 119 MHz suggests that this source may be turning over at $\sim$150 MHz. However, in the subsequent analysis, we use an upper limit on the turnover frequency of 119 MHz.

Table 4.8: Radio spectrum model parameters for all ATLAS sources. Listed is the fitted model, the synchrotron normalisation parameter a, the spectral index α, the optical depth parameter p, the frequency ν_0 found during the fitting (i.e. the parameter from the Bicknell et al. (1997) model − see equation 1.10 and section 1.3.1.2), the break frequency ν_{br}, the turnover frequency ν_m, the peak flux density S_{ν_m}, the reduced χ^2 value, and the degrees of freedom (DOF). The uncertainties listed are the 1σ errors. Where the uncertainty is greater than the fitted value (see section 4.1.2), we list '-'. The individual models are shown in Figure 4.30.

Source	Model	a (mJy)	α	p	ν_0 (MHz)	ν_{br} (GHz)	ν_m (MHz)	S_{ν_m} (mJy)	χ^2_{red}	DOF
CI0008	FFA	547.13 ± 68.87	−0.91 ± 0.01	−0.81 ± 0.03	260.93 ± 43.23		< 76	> 940.75	1.08	42
CI0020	FFA with break	60.73 ± 11.72	−0.54 ± 0.03	−0.53 ± 0.31	260.57 ± 116.13	27.06 ± 3.73	254	54.98	0.69	16
CI0112	FFA	3.04 ± 1.13	−0.59 ± 0.20	−0.61 ± 0.30	1018.23 ± 1001.34		810	2.42	11.52	2
s150	FFA	26.74 ± 1.60	−0.95 ± 0.05	−0.21 ± 0.08	1521.89 ± 188.99		1302	18.27	0.76	10
s415	Power law	3352.00 ± 485.20	−0.86 ± 0.02						1.16	10
s895	FFA	-	−1.12 ± 0.05	-	-		277	28.12	1.33	5

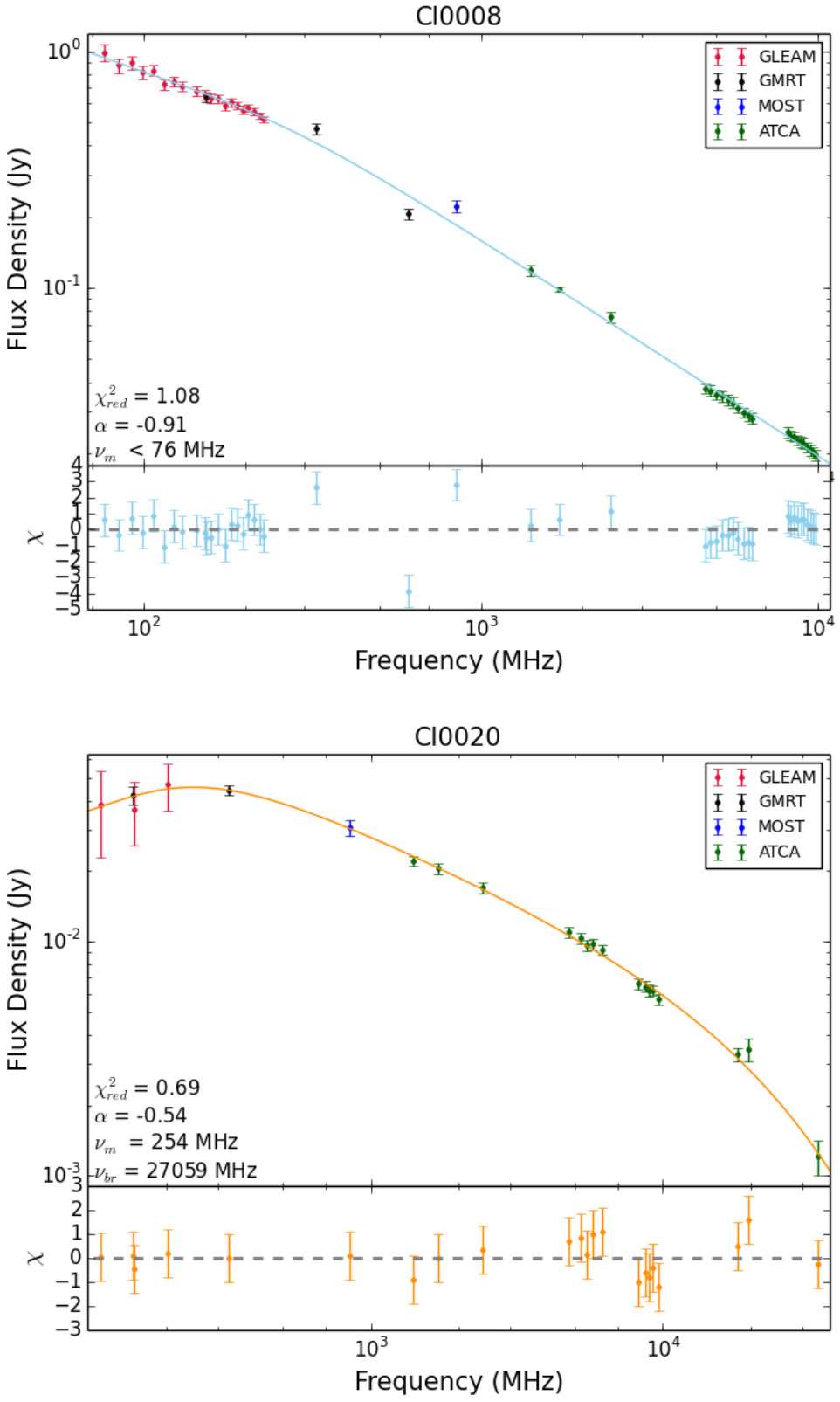

Figure 4.30: The models fit to the radio spectrum for all ATLAS sources, according to the models and their parameters listed in table 4.8. Upper limits measured between $1-3\sigma$ are shown by the downward arrows.

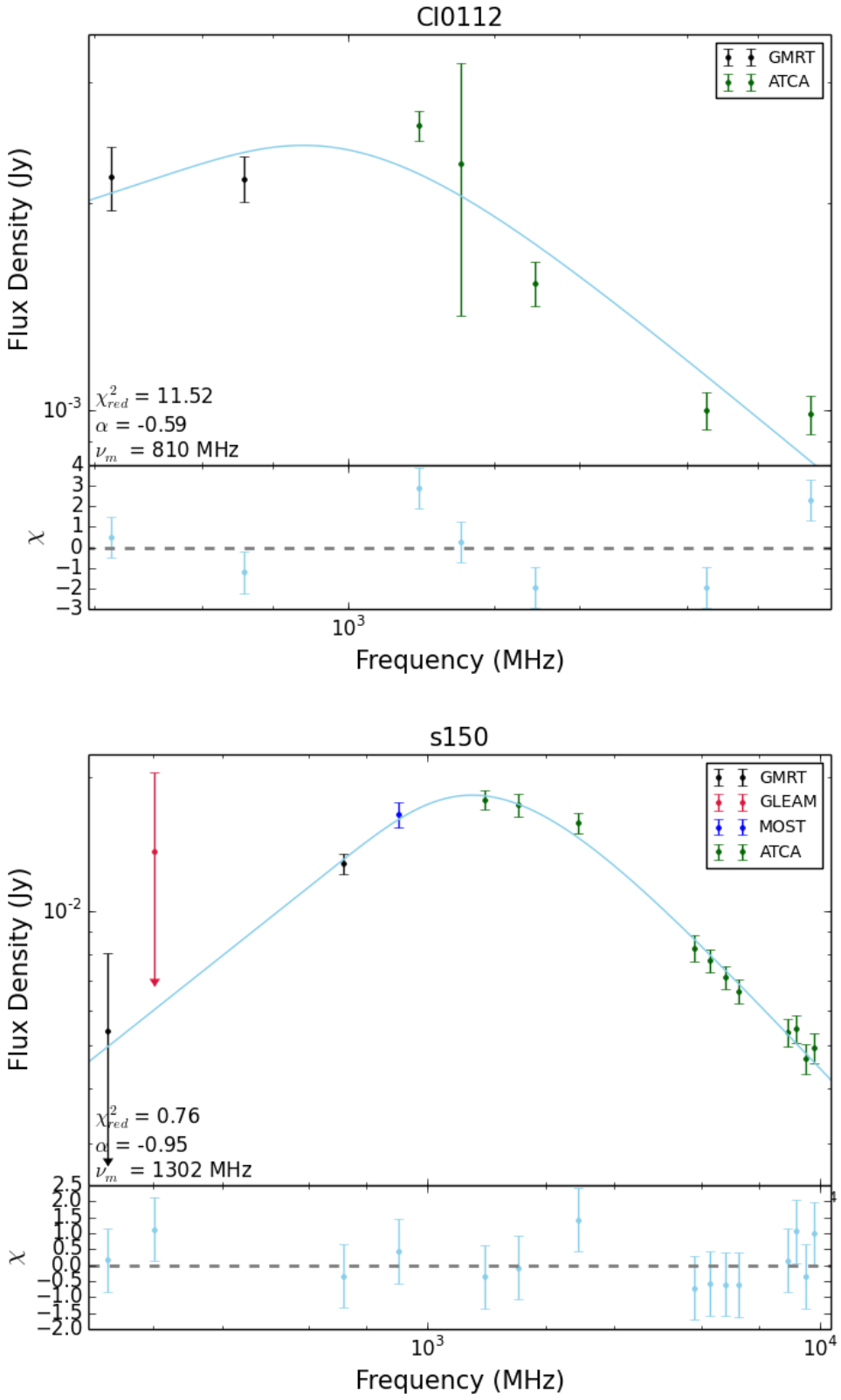

Fig. 4.30. (continued) – the uncertainty of the 1.7 GHz flux density for CI0112 is large due to the way it was derived (see section 2.2.2.1).

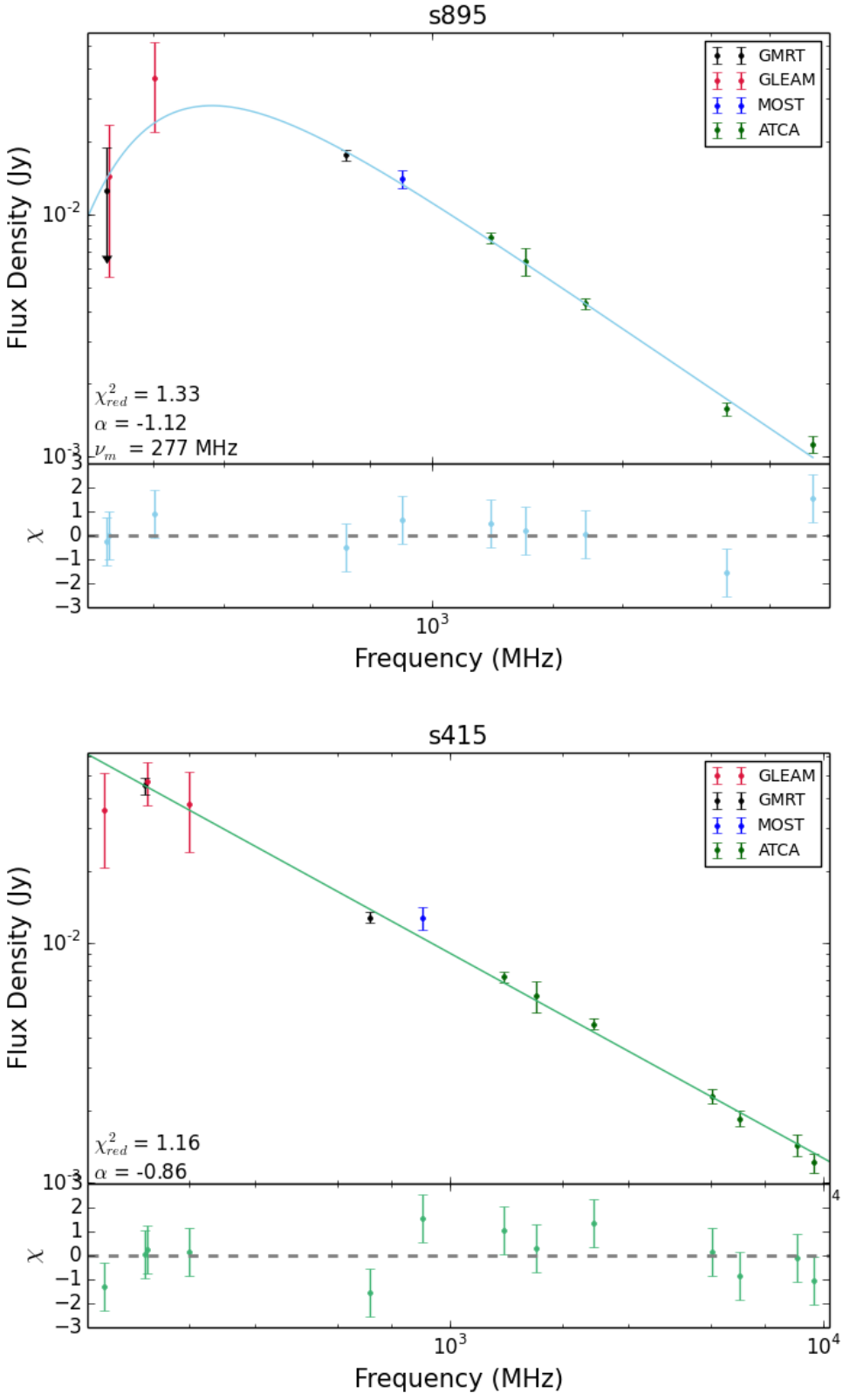

Fig. 4.30. (continued)

4.2.3.1 SSA models

Sources CI0020, s150 and s895 are also well modelled by SSA. In the case of CI0020, this again includes an exponential spectral break. In the case of s150, this can only be reasonably fit with SSA if a Kardashev break is included. In the case of s895, a simple SSA model fits well, since the low frequency spectra have large uncertainties.

The best fit SSA models for these three sources are shown in figure 4.9. The models used in the fitting, and the values of each of the parameters are summarised in table 4.9.

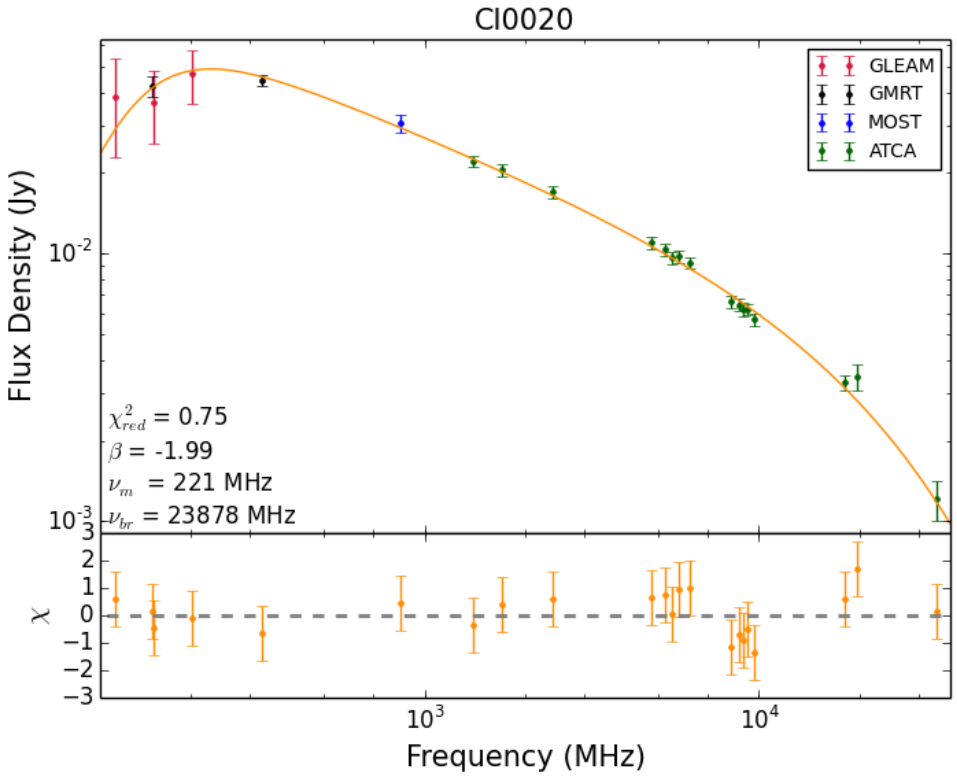

Figure 4.31: The SSA models fit to the radio spectrum. Upper limits measured between $1-3\sigma$ are shown by the downward arrows.

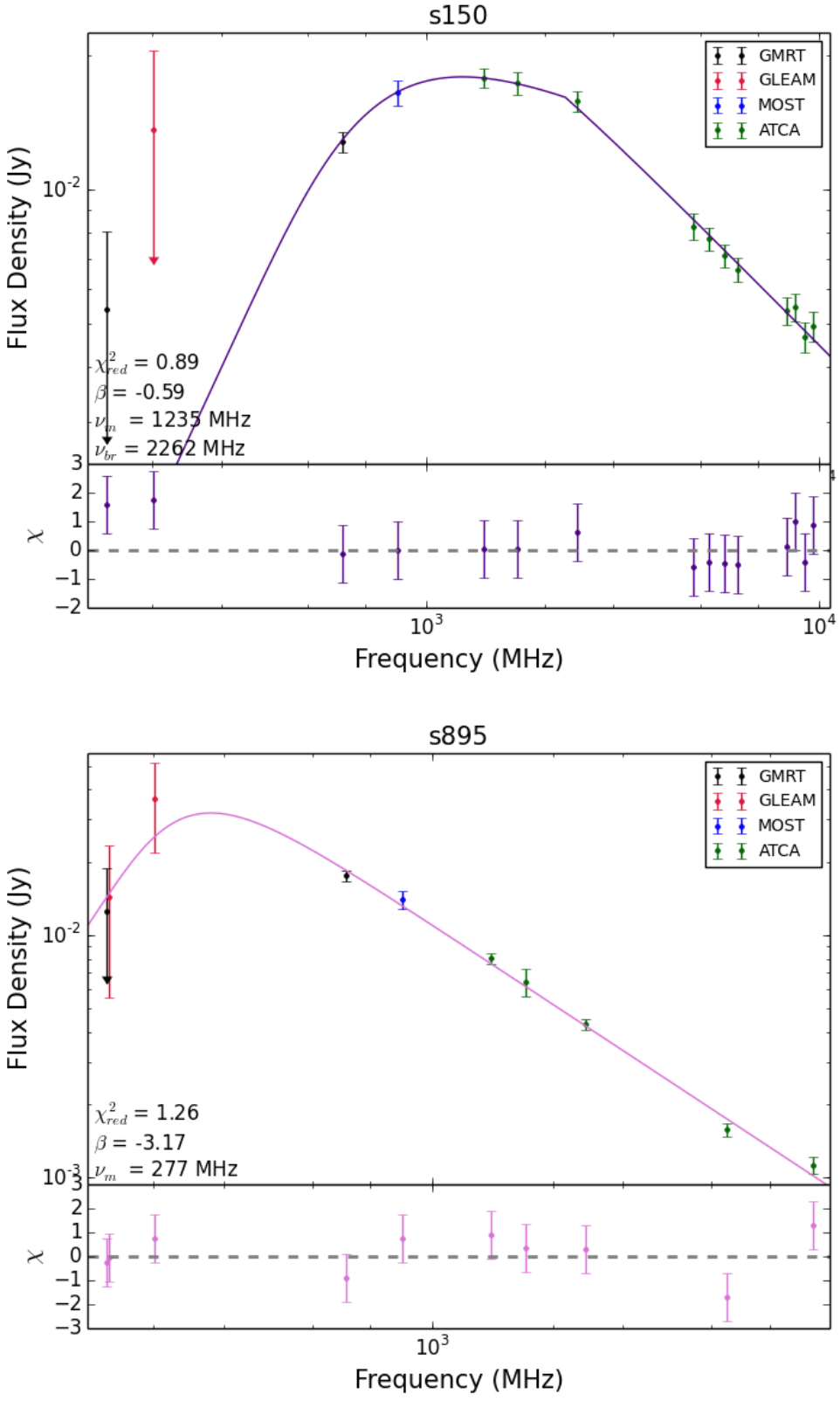

Fig. 4.31. (continued)

Table 4.9: Radio spectrum SSA model parameters for three ATLAS sources. Listed is the fitted model, the synchrotron normalisation parameter a, the electron energy distribution β, the frequency ν_0 found during the fitting, the break frequency ν_{br}, the turnover frequency ν_m, the peak flux density S_{ν_m}, the reduced χ^2_{red} value, and the degrees of freedom (DOF). The uncertainties listed are the 1σ errors. The individual models are shown in Figure 4.31.

Source	Model	a (mJy)	β	ν_0 (MHz)	ν_{br} (GHz)	ν_m (MHz)	S_{ν_m} (mJy)	χ^2_{red}	DOF
CI0020	SSA with exp. break	69.31 ± 2.57	1.99 ± 0.04	161.83 ± 10.44	23.75 ± 2.50	221	48.66	0.76	18
s150	SSA with Kard. break	13.65 ± 1.52	0.59 ± 0.03	794.06 ± 45.32	2.26 ± 0.31	1235	17.94	0.89	10
s895	SSA	49.48 ± 5.29	3.17 ± 0.06	250.79 ± 24.8		277	31.94	1.26	6
CI0008-1	SSA	1417.54 ± 6.33	3.13 ± 0.02	65.36 ± 4.46		< 76	914.33	0.45	40
CI0008-2	SSA	271.02 ± 6.33	2.64 ± 0.02	244.19 ± 4.46		292	179.80	0.45	40

4.2.4 Turnover−linear size relation

Figure 4.32 shows the turnover-linear size relation (see section 1.3.4.3) for the sources with reliable spectra and redshift information. Figure 4.33 shows the distribution of total luminosities for our VLBI sample compared to to those from Orienti and Dallacasa (2014). This figure shows that our VLBI sources are much less luminous in general than those from Orienti and Dallacasa (2014), which represent the typical luminosities of the known GPS and CSS population. Our sources are also much less luminous in general than those in Figure 1.12. Furthermore, the total luminosity as a function of the largest linear size (see Figure 4.34) shows that our sources are very under-represented amongst the GPS and CSS population, being low luminosity sources in the late CSO or early MSO stage. However, their core luminosities are fairly typical compared to those from Orienti and Dallacasa (2014) (see Figure 4.35). Comparing the two, their core vs. total luminosities are in a region unoccupied by those from Orienti and Dallacasa (2014) (see Figure 4.36), being low luminosity objects with high core luminosities, suggesting our sources are more compact in general.

Figures 4.32 and 4.33 show that low luminosity GPS and CSS sources also follow the turnover-linear size relation. s415 is somewhat of an outlier, which may suggest it does indeed turn over at ∼200 MHz, as suggested above.

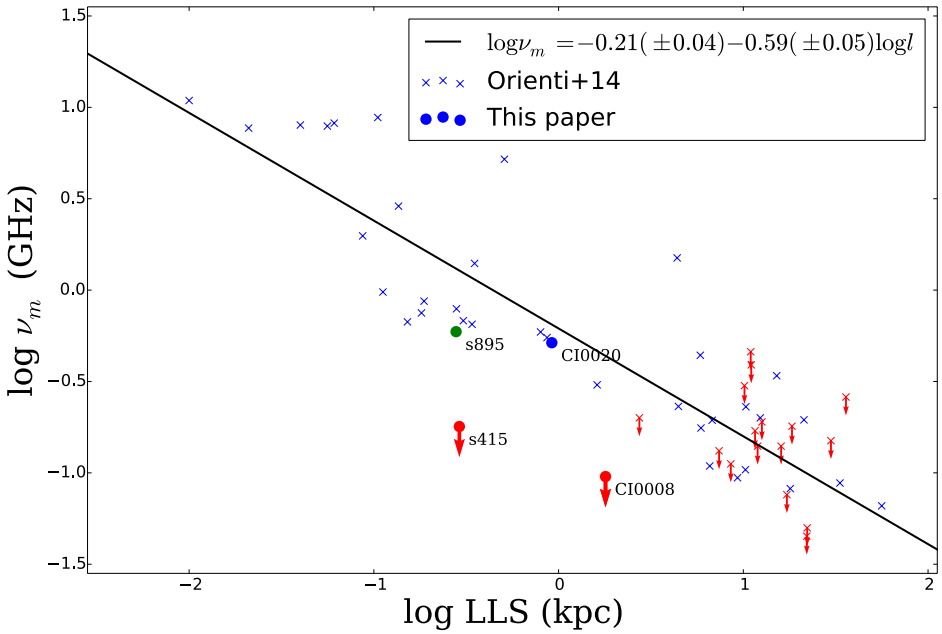

Figure 4.32: The turnover-linear size relation for our ATLAS VLBI sample (circles) compared to the sources from Orienti and Dallacasa (2014) (crosses). Shown are the four sources detected with VLBI with reliable spectra and redshift information. All turnover frequencies are shown in rest frame, taken from the FFA models. Sources with upper limits on the turnover frequency are shown in red and with downward arrows. The source in green (s895) has a photometric redshift. Source CI0112 would appear as an outlier, but was excluded since we interpret this as a variable quasar and not a GPS source. The solid line is given by equation 1.14.

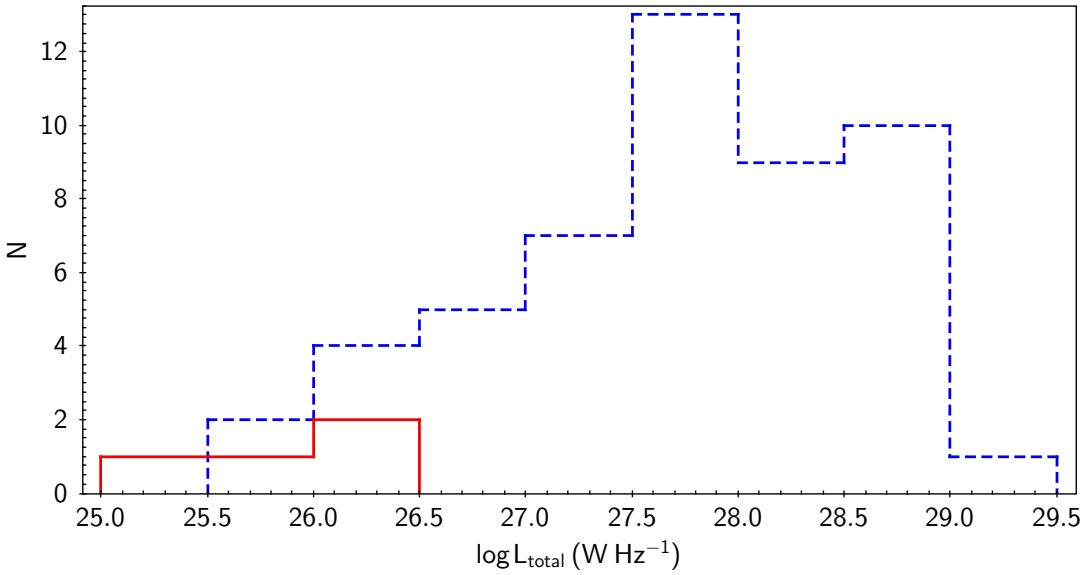

Figure 4.33: The distribution of 325 MHz total luminosities of our ATLAS VLBI sample (solid red line) compared to the 375 MHz total luminosities (dotted blue line) from Orienti and Dallacasa (2014). The ATLAS sources are much less luminous in general than those from Orienti and Dallacasa (2014).

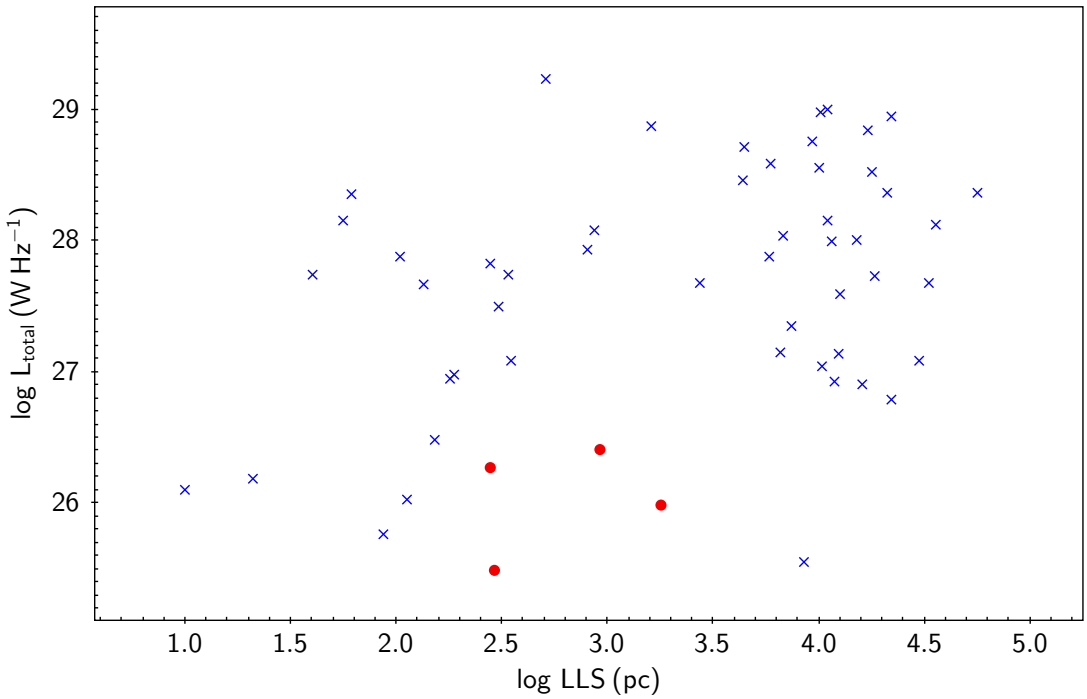

Figure 4.34: The total 325 MHz luminosities as a function of the largest linear size of our ATLAS VLBI sample (red circles) compared to the 375 MHz total luminosities (blue crosses) from Orienti and Dallacasa (2014).

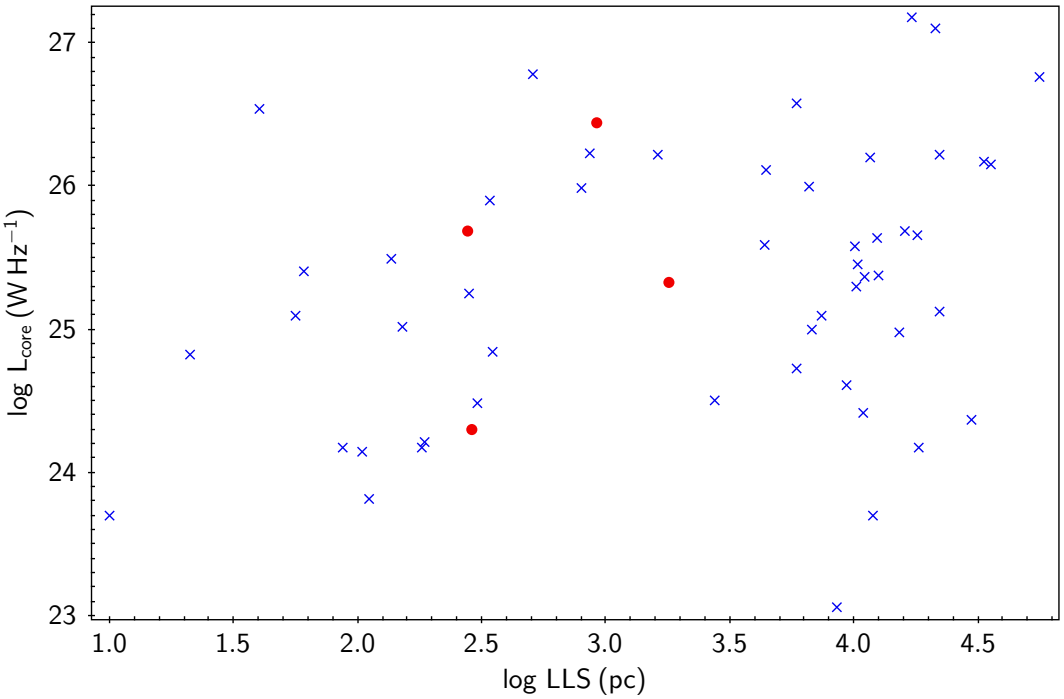

Figure 4.35: The 1.67 GHz core luminosities as a function of the largest linear size of our ATLAS VLBI sample (red circles) compared to the 5 GHz core luminosities (blue crosses) from Orienti and Dallacasa (2014).

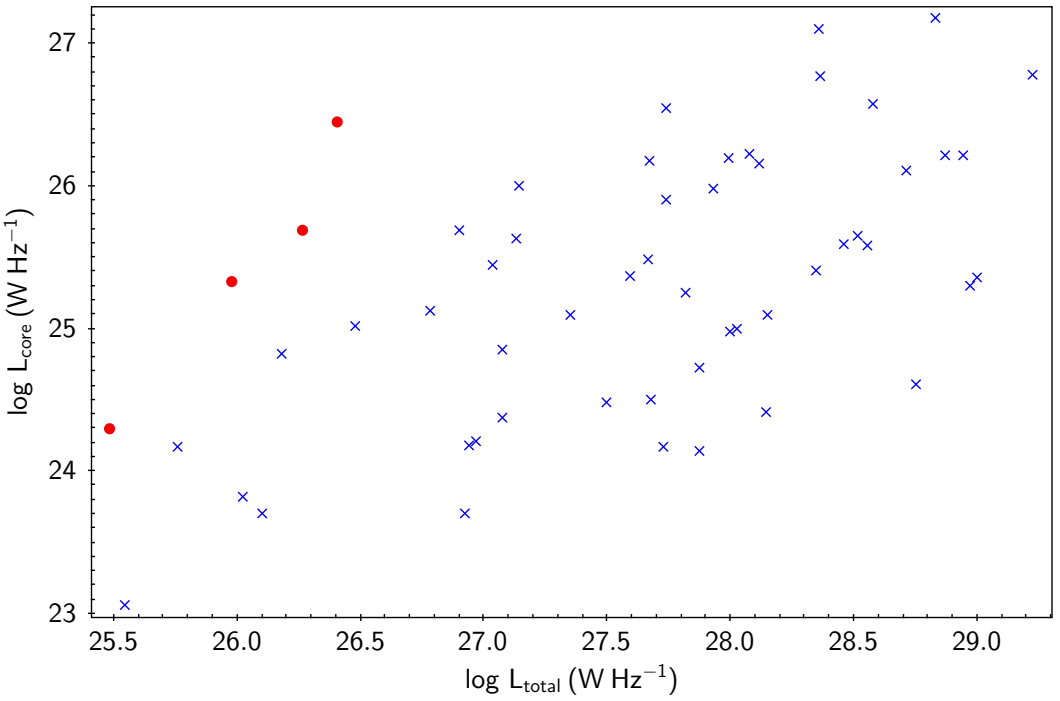

Figure 4.36: The 1.67 GHz core vs. 325 MHz total luminosities of our ATLAS VLBI sample (red circles) compared to the 5 GHz core vs. 375 MHz total luminosities (blue crosses) from Orienti and Dallacasa (2014).

4.2.5 Discussion on individual sources

4.2.5.1 CI0008

CI0008 is resolved into two components with VLBI and has the appearance of a classic double, with two mini-lobes spanning ∼448 mas. At a redshift of 0.256, it has a LLS of 1.79 kpc, classifying it as an MSO, and a radio luminosity of $L_{1.71\ \mathrm{GHz}} = 2.01 \times 10^{25}$ W Hz^{-1}. It is fit with an intrinsic turnover frequency of < 95 MHz, classifying it as a CSS source. It is very bright in the radio, with a peak flux density of > 941 mJy, and has a steep spectral index of $\alpha = -0.91 \pm 0.01$. The two components yield a hotspot emission ratio of 1.24, suggesting a slight asymmetry.

The FFA model produces a reasonable fit, with a reduced χ^2 value of 1.08. Some data points are in disagreement with a power law across the optically-thin spectra, which may be due to source variability, but is more likely due to calibration and measurement errors. Interestingly, a power law across the entire spectrum produces a poor fit, since there is a small amount of curvature < 250 MHz. This curvature is also poorly fit by a power law with a spectral break. The FFA model predicts a well constrained value of $p = -0.81 \pm 0.03$, implying that amongst the absorbing clouds, many more with low emission measure exist compared to those with high emission measure (see section 1.3.1.2). This suggests that CI0008 is in a very low density environment in which the absorption is relatively small, accounting for its small amount of curvature. This may suggest the jets of CI0008 have gone beyond the ISM-IGM boundary where the ambient medium is low in density.

Assuming the GLEAM sub-band measurements are accurate and the source variability is small, this may suggest that CI0008 has an extremely broad turnover, covering a FWHM of tens of decades of frequency, compared to typical spectral widths of ∼1.2 decades for GPS sources (O'Dea et al., 1991). This may be caused by many populations of electrons producing FFA at different frequencies, such as those seen in Clemens et al. (2010). The clear classification of CI0008 as an MSO with a classic double morphology makes this a very interesting CSS spectrum.

The small amount of curvature cannot be accounted for by homogeneous SSA, which predicts far too steep a slope in the optically-thick spectra. However, it could possibly be accounted for by inhomogeneous SSA, consisting of two homogeneous components, one for each lobe (equation 1.6). As seen in figure 4.28 and table 4.6, two mini-lobes are detected, with a hotspot emission ratio of 1.24 at 1.67 GHz. Although the absolute flux density of these components within our LBA observations does not seem to be accurate, the flux density ratio between these components should be accurate. Therefore, we can derive a_2, the normalisation flux density of the 2nd SSA component, as a function of a_1, the 1st SSA component at 1.67 GHz, given by

$$a_2 = \frac{a_1 \left(\frac{1.67\mathrm{GHz}}{\nu_m}\right)^{-(\beta-1)/2} \left(\frac{1-e^{-\tau}}{\tau}\right)}{1.24 \times \left(\frac{1.67\mathrm{GHz}}{\nu_m}\right)^{-(\beta-1)/2} \left(\frac{1-e^{-\tau}}{\tau}\right)} \tag{4.2}$$

The fit resulting from a double SSA model, in which a_2 is given as a function of a_1, is shown in figure 4.37, and the parameters of each individual SSA component are listed in table 4.9. According to this model, we derive a magnetic field strength of 18 mG for the one component and 895 G for the the other component (respectively CI0008-1 and CI0008-2 from table 4.6) using equation 1.7. This latter magnetic field strength differs by a few orders from the typical magnetic field strengths of GPS and CSS sources, which are a few mG down to 0.1 mG (Orienti and Dallacasa, 2008a; Orienti, 2016). This gives strong evidence that SSA cannot account for

the spectrum of this component of CI0008, unless its structure is highly inhomogeneous over scales of ∼100 mas, consisting of many knots of highly compact emission, atypical of the smooth emission we expect within a radio lobe.

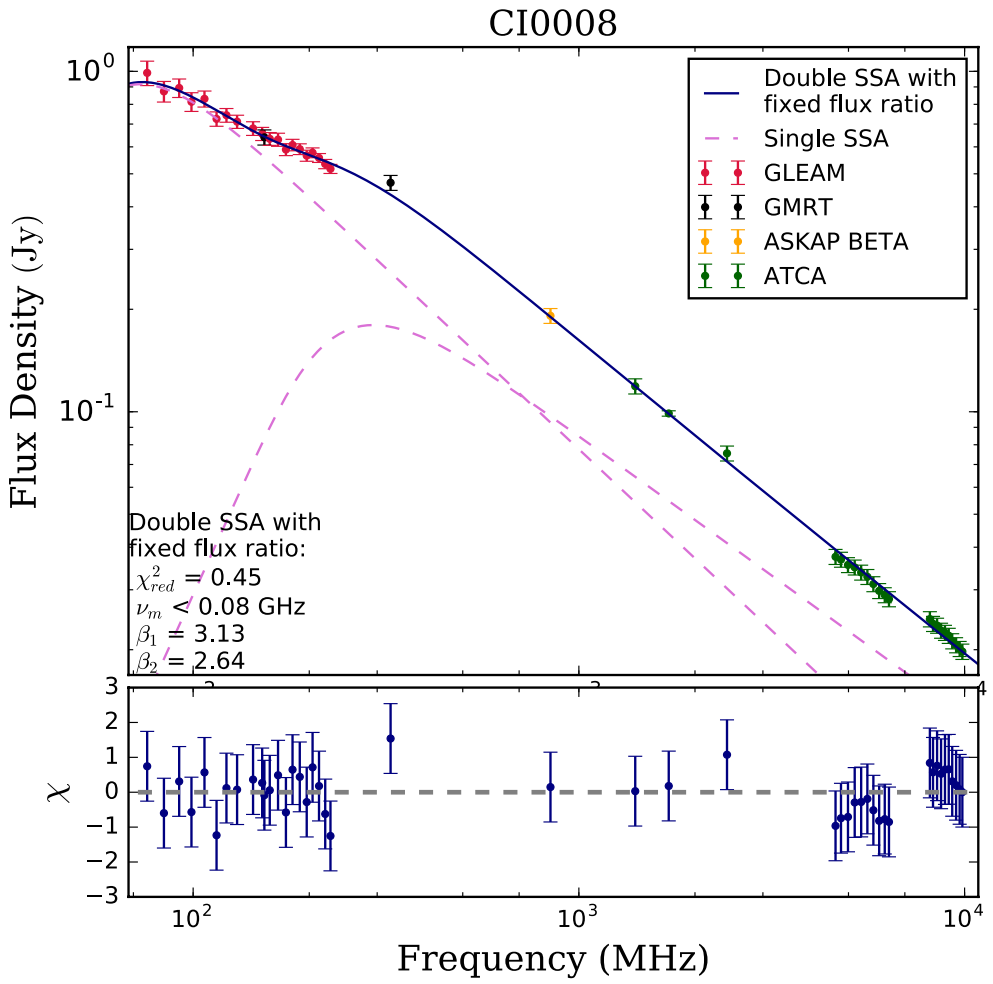

Figure 4.37: A double SSA model fit to the radio spectrum for CI0008, where a_2, the normalisation flux density of the 2nd SSA component, is given by equation 4.2. The solid blue line shows the superposition of the two individual SSA components, which are shown by the dashed pink lines.

4.2.5.2 CI0020

CI0020 is resolved with VLBI and at a redshift of 1.03, has a LLS of 0.92 kpc, classifying it as a CSO that is beginning to enter the MSO stage. It is fit with an intrinsic turnover frequency of ∼515 MHz, classifying it as a CSS source. It is faint in the radio, with a peak flux density of 55 mJy, and has a relatively shallow spectral index of $\alpha = -0.54 \pm 0.03$. However, being at high redshift, it is the most luminous source in the sample, with $L_{1.71\ \mathrm{GHz}} = 1.18 \times 10^{26}$ W Hz^{-1}. The FFA model produces a good fit, with a reduced χ^2 value of 0.69. This model predicts a negative value of $p = -0.53 \pm 0.31$, suggesting that CI0020 is in an environment with low density.

The homogeneous SSA model predicts $\nu_m = 221$ MHz, which gives $B \sim 535$ G according to equation 1.7. This magnetic field strength again differs by several orders from the typical magnetic field strengths of CSS sources. Therefore, if we assume a homogeneous structure over ∼1 kpc, SSA cannot be responsible for its spectra. If we were to assume this magnetic field strength, the SSA model predicts $\nu_{br} = 23.75 \pm 2.50$ GHz, and no Kardashev break is observed below 610 MHz, which gives $t_s > 1 \times 10^{-4}$ years and $t_{\rm off} > 2 \times 10^{-5}$ years, according to equations 1.12 and 1.13, both of which are several orders of magnitude lower than typical values. It is more reasonable, however, to assume this source has a typical CSO structure consisting of two mini-lobes, from which we would derive much small magnetic field strengths. Using a much more typical magnetic field strength of 5 mG and the break frequency predicted by the FFA model of $\nu_{br} = 27.06 \pm 3.73$ GHz, we derive $t_s > 4\,044$ years and $t_{\rm off} > 607$ years.

An and Baan (2012) found that the radiative ages of their sample of CSOs followed the trend $l \propto t_{\rm kin}^{3/2}$ years, which we can express as $l = c \cdot t_{\rm kin}^{3/2}$ years, where l is the linear size and $t_{\rm kin}$ is the kinematic age in the source rest frame, derived from the hotspot angular separation velocity μ. Performing a least-squares fitting routine using the kinematic ages and linear sizes from An and Baan (2012) gives $c = 0.0025 \pm 0.0004$. Therefore, assuming CI0020 follows the same trend, we derive $t_{\rm kin} = 5\,078^{+614}_{-471}$ years and a hotspot angular separation velocity of $\mu = 10.9^{+1.1}_{-1.2}$ μas yr^{-1}. This suggests the source age is $4\,600 \lesssim t \lesssim 5\,700$ years, implying that the magnetic field strength is $B < 4.6$ mG, which gives $t_s > 4\,580$ years. An even lower magnetic field strength is needed if $\nu_{br} \ll 610$ MHz.

4.2.5.3 CI0112

CI0112 is resolved with along one axis with VLBI and, at a redshift of 0.287, has a LLS of 73 pc. Its spectrum shows evidence of the source being variable and is very poorly fit even by the best-fitting FFA model, with a reduced χ^2 value of 11.52. The 5.5 and 9.0 GHz data were taken simultaneously and give a flat spectrum. A flat spectrum is also derived from the two low frequency GMRT measurements at 325 and 610 MHz, which are unlikely to significantly vary. Therefore, we interpret this source as a flat spectrum quasar, which may have undergone a flaring event during which it temporarily adopted a convex spectrum and was measured by ATLAS. This interpretation is consistent with its very compact size, typical of a quasar. The slight extension along one axis of the VLBI detection may suggest a core-jet morphology. If CI0112 were a GPS source, it would turn over at ∼2.6 GHz.

4.2.5.4 s150

s150 is resolved along one axis with VLBI, which gives a largest angular size of 29 mas. It is fit with an $\nu_m = 1302$ MHz, classifying it as a GPS source. It is very faint, with a peak flux density of 18 mJy and a steep spectral index of $\alpha = -0.95 \pm 0.05$. The FFA model produces a good fit, with a reduced χ^2 value of 0.76. The FFA model predicts a value of $p = -0.21 \pm 0.08$, implying a denser environment than CI0020.

The SSA model predicts $\nu_m = 1235$ MHz, which gives $B = 2 \times 10^5 (1+z)^{-1}$ G according to equation 1.7. The SSA model also predicts a Kardashev break at $\nu_{br} = 2.3 \pm 0.3$ GHz. Even assuming a redshift as high as $z = 1$, this gives $B = 1 \times 10^5$ G and $t_s = 2 \times 10^{-8}$ years. These values are also inconsistent with typical values by several orders of magnitude and show that the structure of s150 is also unlikely to be homogeneous. Using a much more typical magnetic field strength of 5 mG and assuming $z = 0.5$ and the same break frequency, we derive $t_s = 2\,442$ years.

4.2.5.5 s415

s415 is resolved with VLBI and appears to be composed of two components, suggesting a symmetric double morphology. At a redshift of 0.5066, it has a LLS of 0.29 kpc, classifying it as a CSO. The power law produces a reasonable fit, with a reduced χ^2 value of 1.16. Its spectrum contains a hint of a turnover at ∼150 MHz. However, assuming the power law model, it is fit with an intrinsic turnover frequency of < 119 MHz, classifying it as a CSS source. It is faint in the radio, with a peak flux density of > 60 mJy, and has a typical CSS spectral index of $\alpha = -0.86 \pm 0.02$. It has a relatively low luminosity of $L_{1.71\ \mathrm{GHz}} = 6.07 \times 10^{24}$ W Hz^{-1}.

Assuming s415 follows the same $l - t_{\mathrm{kin}}$ trend as the CSOs from An and Baan (2012), we derive $t_{\mathrm{kin}} = 2\,355^{+285}_{-219}$ years and $\mu = 13.2 \pm 1.4$ μas yr^{-1}. No Kardashev break is observed within the range of our data, and we don't expect it to be < 150 MHz, since this would give too shallow a injection spectral index of $\alpha_{\mathrm{inj}} = -0.36$. Therefore, if a spectral break exists, it must be at > 10 GHz. This suggests the magnetic field strength is $B > 3.0$ mG, which gives $t_s < 2\,500$ years.

4.2.5.6 s895

s895 is resolved with VLBI and, assuming its photometric redshift of 1.14 is correct, has a LLS of 0.28 kpc, classifying it as a CSO. It is fit with an intrinsic turnover frequency of ∼592 MHz, classifying it as a CSS source. It is faint in the radio, with a peak flux density of 28 mJy, and has a steep spectral index of $\alpha = -1.12 \pm 0.05$. However, being at high redshift, it is the second most luminous source in the sample, with $L_{1.71\ \mathrm{GHz}} = 4.77 \times 10^{25}$ W Hz^{-1}. The FFA model produces a reasonable fit, with a reduced χ^2 value of 1.13. However, the turnover and optically-thick region of the spectrum are poorly constrained.

The SSA model predicts $\nu_m = 277$ MHz, which gives $B \sim 28$ G according to equation 1.7. We expect a Kardashev break to exist at low frequency, giving a more typical injection spectral index of $\alpha_{\mathrm{inj}} = -0.62$. However, as in the case of CI0020, no spectral break is observed in s895 below 610 MHz, which gives $t_s > 0.01$ years according to equation 1.12. These values are once again inconsistent with typical values by several orders of magnitude and suggest that the structure of s895 is also inhomogeneous, although its turnover and optically-thick spectra are poorly constrained. Using a much more typical magnetic field strength of 5 mG, we derive $t_s > 3\,940$ years.

Assuming s895 follows the same $l - t_{\mathrm{kin}}$ trend as the CSOs from An and Baan (2012), we derive $t_{\mathrm{kin}} = 2\,292^{+277}_{-213}$ years and $\mu = 6.8 \pm 0.7$ μas yr^{-1}. This suggests the source age is $2\,080 < t < 2\,570$ years, implying that the magnetic field strength is $B < 7.7$ mG, which gives $t_s > 2\,060$ years. An even lower magnetic field strength is needed if $\nu_{br} \ll 610$ MHz.

4.2.6 Summary

Our LBA observations resolved all GPS and CSS candidates, one of which has a morphology of a classic double. Their redshifts range from $0.256 < z < 1.14$, giving $L_{1.7\ \mathrm{GHz}} = 10^{22-26}$ W Hz^{-1} and $0.07 < \mathrm{LLS} < 1.79$. Our observations confirm that s150 is a GPS sources turning over at ∼1.3 GHz, CI0112 is most likely a variable flat-spectrum quasar, while the other sources are CSS sources turning over between < 76 MHz and ∼280 MHz. These CSS sources are lower in luminosity compared to typical CSS sources, and follow the turnover-linear size relation, showing that low-luminosity CSS sources also co-evolve in size and spectrum.

We classify CI0020, s150 and s895 as CSOs, and derive kinematic ages in the range $2300 \lesssim$

$t_{\rm kin} \lesssim 5000$ years. Based on a typical magnetic field strength of $B = 5$ mG, we estimate spectral ages in the range $2500 \lesssim t_s \lesssim 4400$. Source CI0020 has an exponential spectral break, with a turnoff time of $t_{\rm off} \sim 600$ years, suggesting that this source is a prematurely dying radio galaxy. These ages confirm that our GPS and CSS sources are young and evolving, and give strong evidence that they are not within frustrated environments, which would cause a discrepancy between the spectral and kinematic ages, with the spectral age being larger.

The GPS and CSS sources were well fit by the inhomogeneous FFA model, but CI0020 and s150 were also well fit by SSA models with a spectral break. However, from these SSA models, and assuming a homogeneous structure over kpc scales, we derive magnetic field strengths orders of magnitude different from their expected values, as well as spectral ages orders of magnitude different to their kinematic ages based on their jet sizes. For source CI0008, we show that its structure consists of two mini-lobes. Attributing this to double SSA gives a magnetic field strength for one lobe a few orders of magnitude too high, giving strong evidence that SSA cannot account for its spectrum, unless the structure of the lobes is highly inhomogeneous, atypical of the smooth emission that comes from radio lobes.

4.3 Deep sample: ATLAS

4.3.1 Remaining sample

Amongst those GPS and CSS candidates that we observed with ATCA (see Table 2.4), 66 remain which have not yet been observed with VLBI. The most interesting sources are those which have low luminosities, since these have been proposed as the compact counterparts of FR-I galaxies, a hypothesis which remains unconfirmed and largely untested.

To inspect their luminosities, we found spectroscopic redshifts for half of the sample, which came from the OzDES Global Reference Catalogue (Uddin et al. in prep.; see section 2.2.2.1). Since this catalogue only included the highest quality spectra, we also manually added PRIMUS (Coil et al., 2011) spectroscopic redshifts marked with a quality flag of 2, denoting a possible redshift with $\delta z/(1+z) \sim 0.015$. Of those from the CDFS field, all sources were selected based on having a spectroscopic redshift. Of those from the ELAIS-S1 field, 12 have spectroscopic redshifts. Table 4.10 lists these sources, their redshifts, 1.4 GHz luminosities and spectral indices. Six sources have $L_{1.4\ \rm GHz} < 10^{23}$ W Hz^{-1} and therefore have luminosities at the level proposed by Tingay and Edwards (2015) for the FR-I precursors like PKS 2254-367. However, unlike PKS 2254-367, our sources are located at redshifts as high as 0.43, which means that if the hypothesis is correct, they will be the most distant FR-I precursors yet studied.

4.3.2 Preliminary spectral models

The reduction of the 5.5 and 9.0 GHz images of the remaining ATLAS GPS and CSS candidates not yet observed with VLBI remains ongoing. However, we performed a preliminary fitting of the spectral models in which the existing flux measurements were used. These models are shown in Figure 4.38. The majority of these spectra follow a power law distribution, although a few sources contain low frequency turnovers typical of CSS sources. This requires further investigation, which will be presented in Collier et al. (in prep.).

Table 4.10: The redshifts and radio luminosities of the remaining GPS and CSS candidates not yet observed with VLBI and with spectroscopic redshifts. Shown is the ID, the 1.4 GHz flux density from DR1 (Norris et al., 2006; Middelberg et al., 2008a) or DR3 (Franzen et al., 2015), the redshift and its associated quality flag (2,3,4 = possible, probably and certain redshift, respectively) and source, the 1.4 GHz luminosity and the spectral index derived between 1.4 and 1.71 GHz from DR3.

ID	$S_{1.4\ \mathrm{GHz}}$ (mJy)	z	flag	source	$L_{1.4\ \mathrm{GHz}}$ (W Hz^{-1})	α
CI0018	22.88	0.54	4	PRIMUS	2.75×10^{25}	−0.56
CI0036	14.99	0.98		NED	7.70×10^{25}	−0.68
CI0076	4.87	0.69	4	PRIMUS	1.03×10^{25}	−0.89
CI0085	4.36	0.94	-	ATLAS	1.99×10^{25}	−0.60
CI0088	4.97	1.02	2	PRIMUS	2.81×10^{25}	−0.92
CI0113	2.50	0.86	2	PRIMUS	9.32×10^{24}	−0.86
CI0128	2.90	0.60	4	PRIMUS	4.46×10^{24}	−0.43
CI0130	5.73	0.91	4	DES_AAOmega	2.43×10^{25}	−1.04
CI0145	1.99	1.12	2	PRIMUS	1.43×10^{25}	−0.52
CI0157	1.76	0.90		NED	7.34×10^{24}	−0.77
CI0158	1.83	1.11	2	ATLAS DR1	1.28×10^{25}	−0.98
CI0159	1.85	0.56		NED	2.34×10^{24}	−0.39
CI0170	1.73	0.10	5	2dFGRS	4.89×10^{22}	−0.32
CI0184	1.61	0.34	-	ATLAS	6.21×10^{23}	0.25
CI0200	1.33	0.43	4	DES_AAOmega	8.94×10^{23}	0.06
CI0207	1.75	1.08		ATLAS	1.15×10^{25}	−0.86
CI0213	1.68	0.07	4	NOAO_0522	2.03×10^{22}	−1.18
CI0242	1.52	0.69		ATLAS DR1	3.22×10^{24}	−0.25
CI0253	1.16	1.16	3	DES_AAOmega	9.05×10^{24}	−0.57
CI0265	0.87	0.15	-	ATLAS	5.00×10^{22}	−0.16
S1014	3.71	0.59	4	DES_AAOmega	5.50×10^{24}	
S220	5.78	0.56	3	DES_AAOmega	7.53×10^{24}	−1.39
S262	3.15	0.59	4	DES_AAOmega	4.60×10^{24}	−1.00
S29	5.25	0.41	-	ATLAS	3.30×10^{24}	
S346	2.43	0.68	4	DES_AAOmega	5.11×10^{24}	−1.09
S371	9.97	0.80	3	DES_AAOmega	3.07×10^{25}	
S703	11.61	1.30		NED	1.19×10^{26}	−0.81
S714	4.87	1.25		NED	4.54×10^{25}	0.19
S73	34.32	1.20	4	DES_AAOmega	2.90×10^{26}	−0.97
S769	13.09	2.30	3	DES_AAOmega	5.50×10^{26}	−0.74
S860	1.97	0.40	4	PRIMUS	1.13×10^{24}	−0.44
S896	1.45	0.05	4	6dF	9.78×10^{21}	−0.77

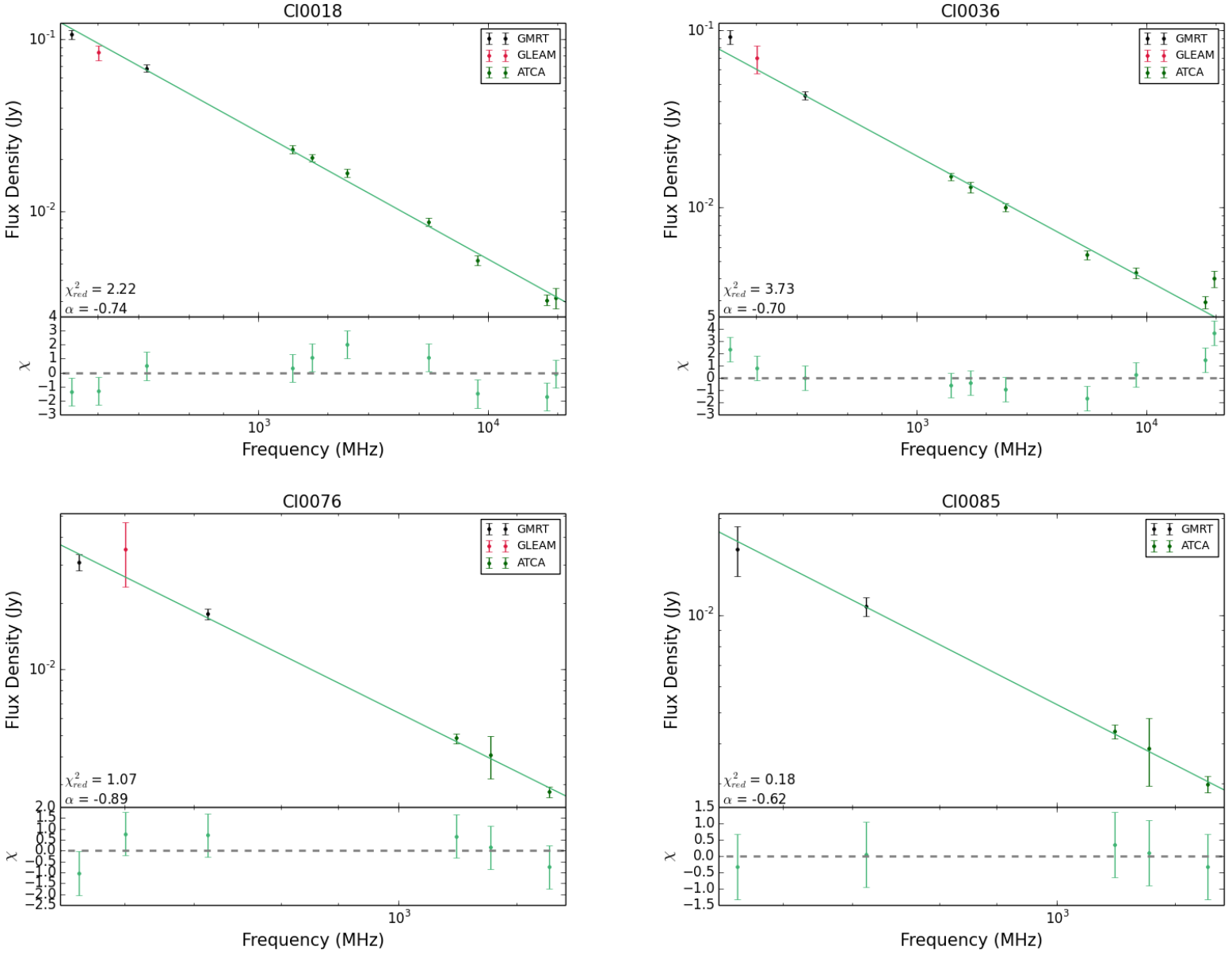

Figure 4.38: The preliminary models fit to the radio spectrum for all ATLAS sources for which a successful fit was found. The uncertainty of the 1.7 GHz flux density for some sources is large due to the way it was derived (see section 2.2.2.1)

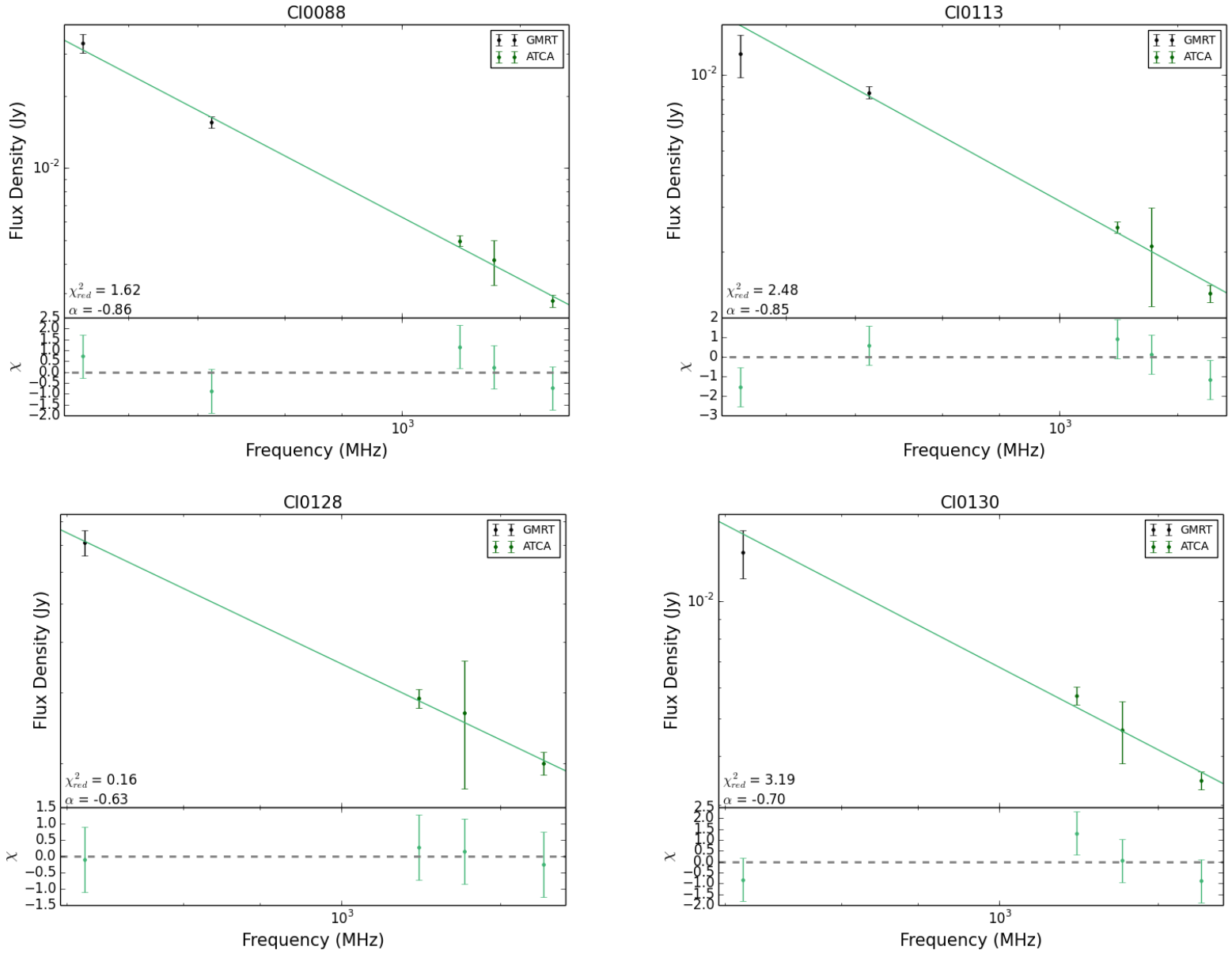

Fig. 4.38. (continued)

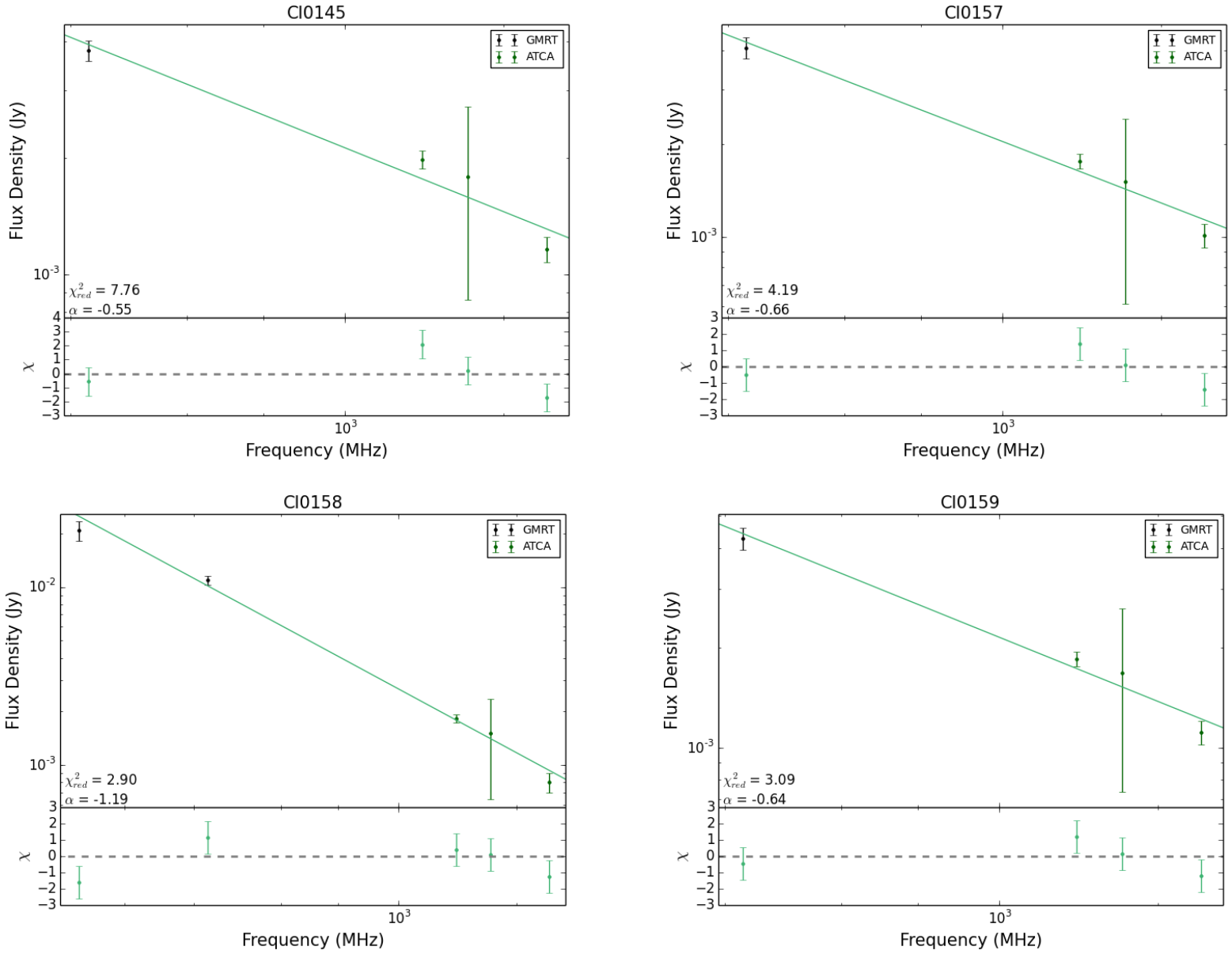

Fig. 4.38. (continued)

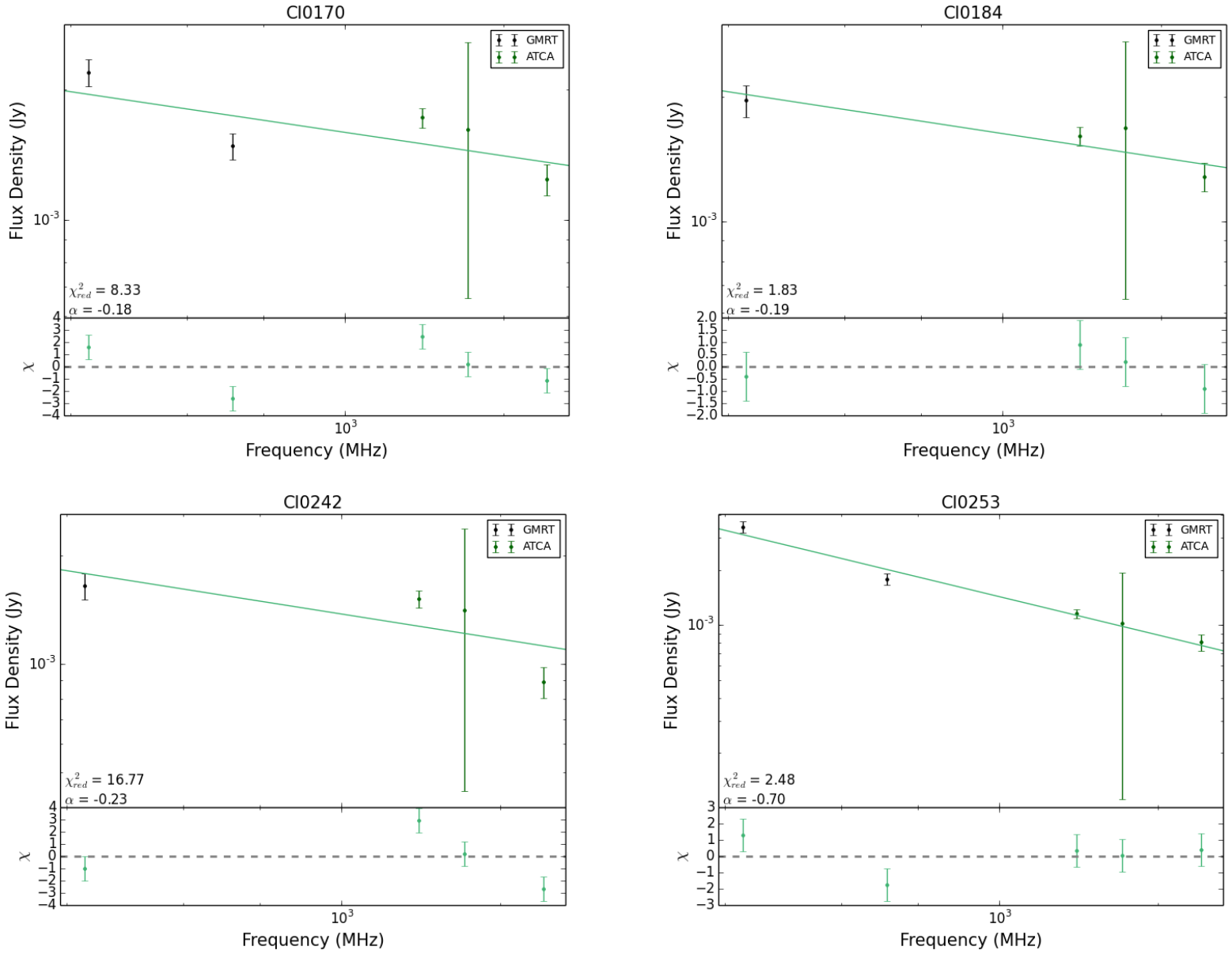

Fig. 4.38. (continued)

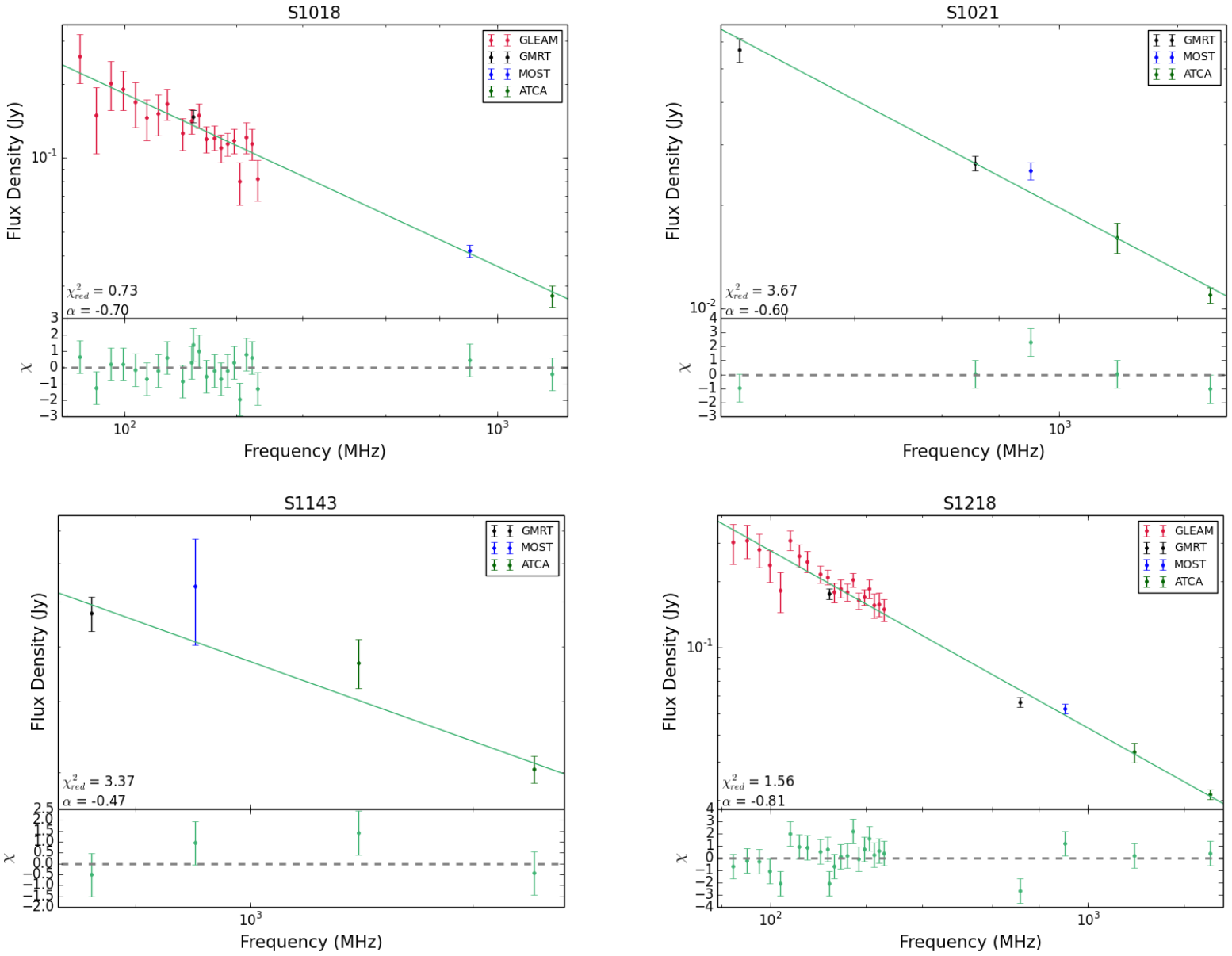

Fig. 4.38. (continued)

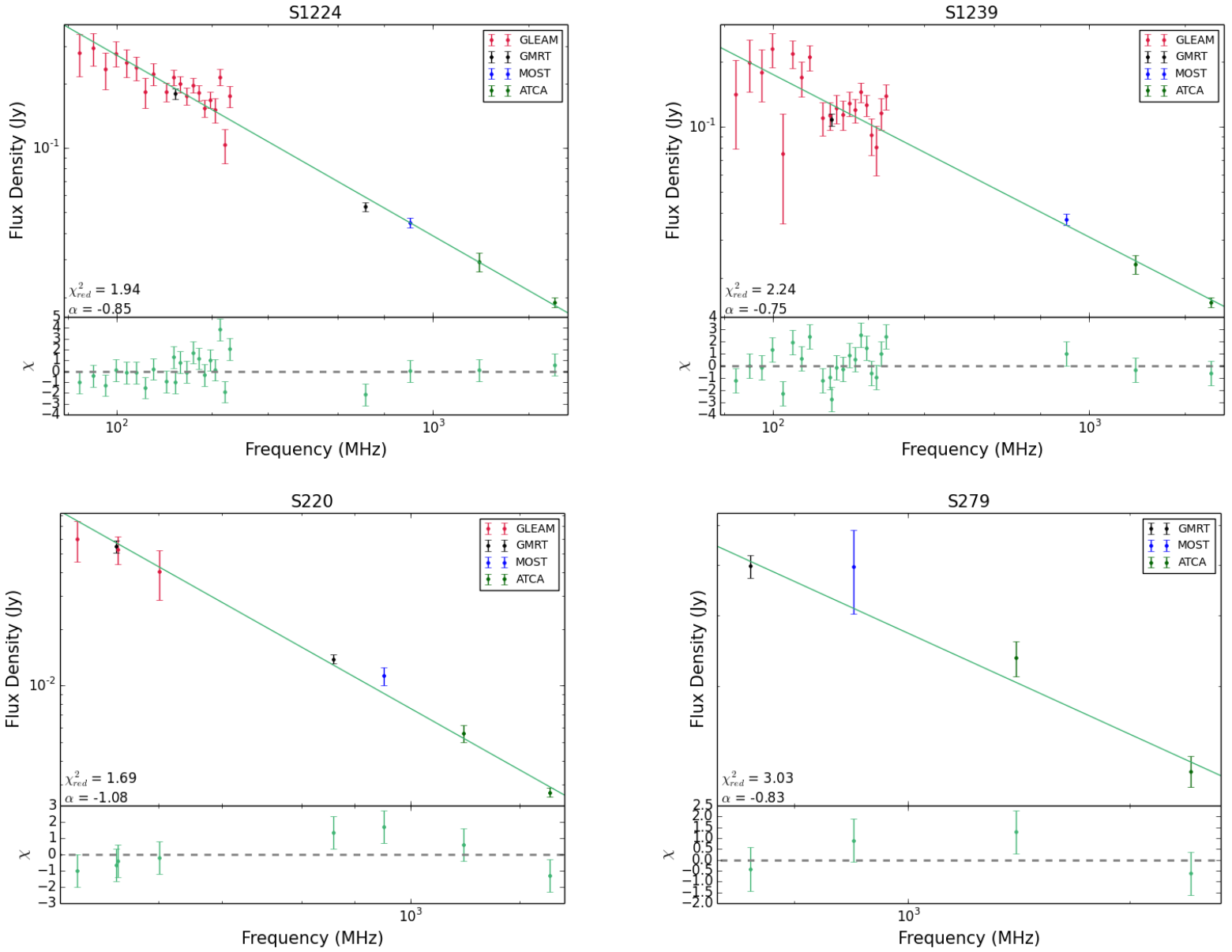

Fig. 4.38. (continued)

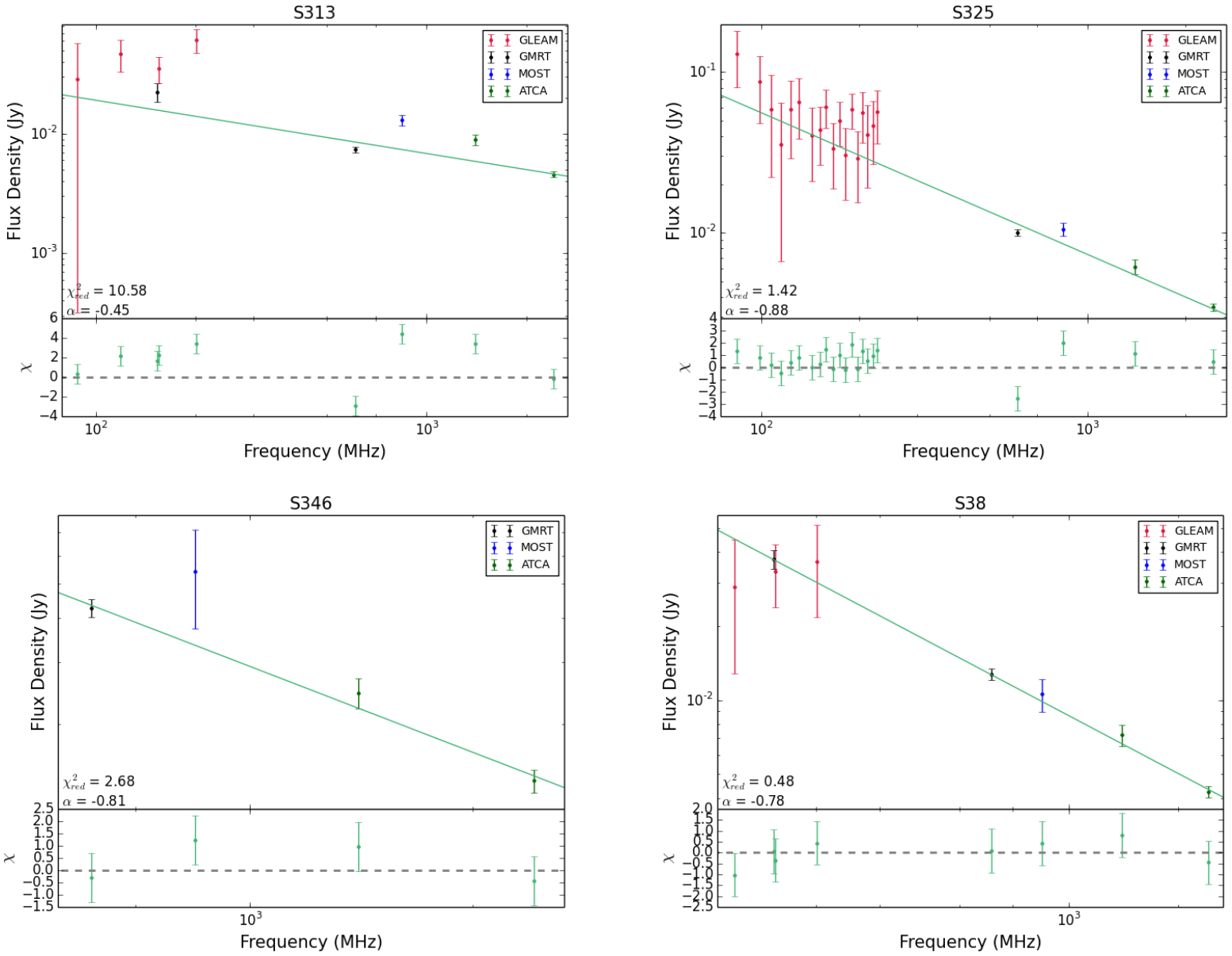

Fig. 4.38. (continued)

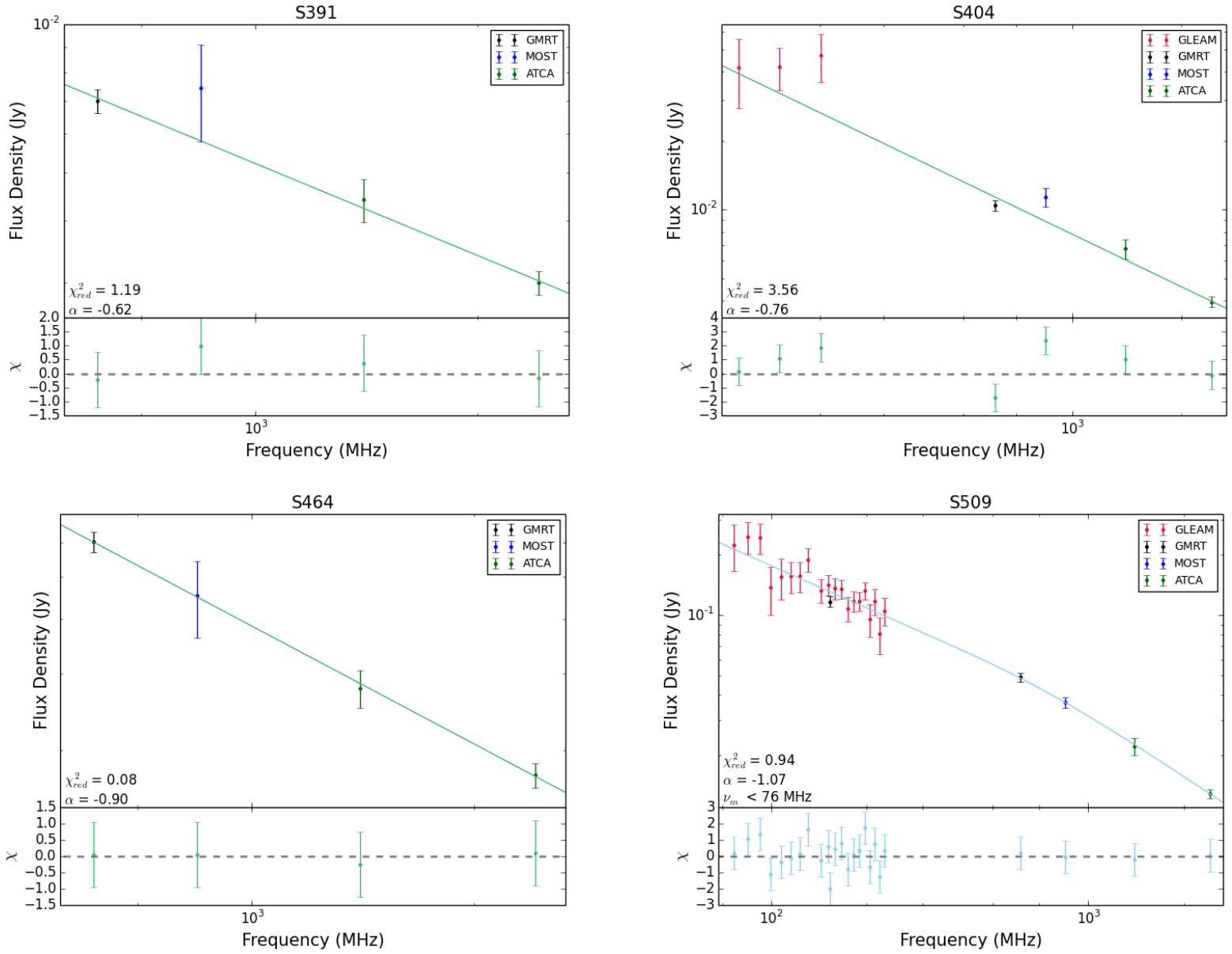

Fig. 4.38. (continued)

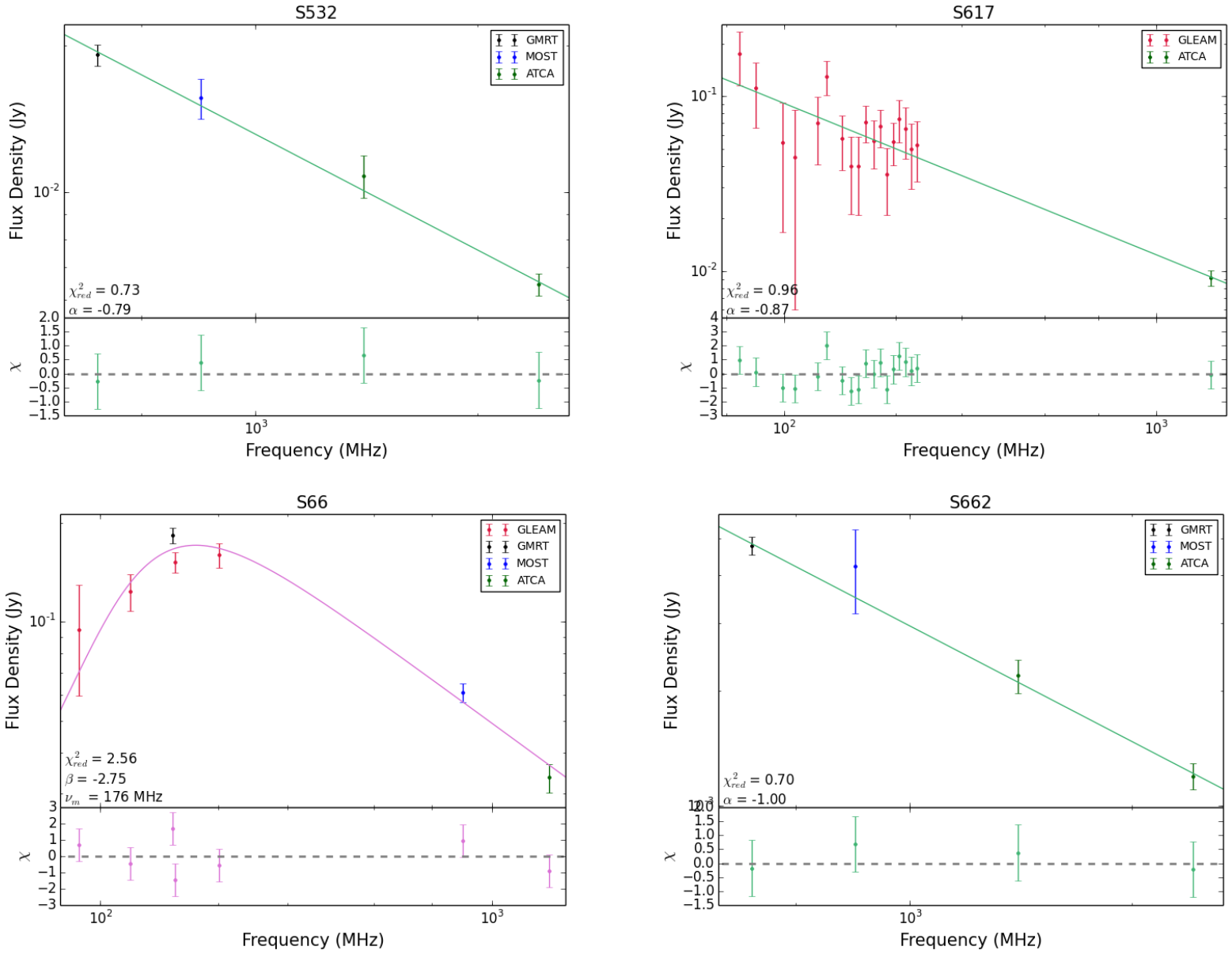

Fig. 4.38. (continued)

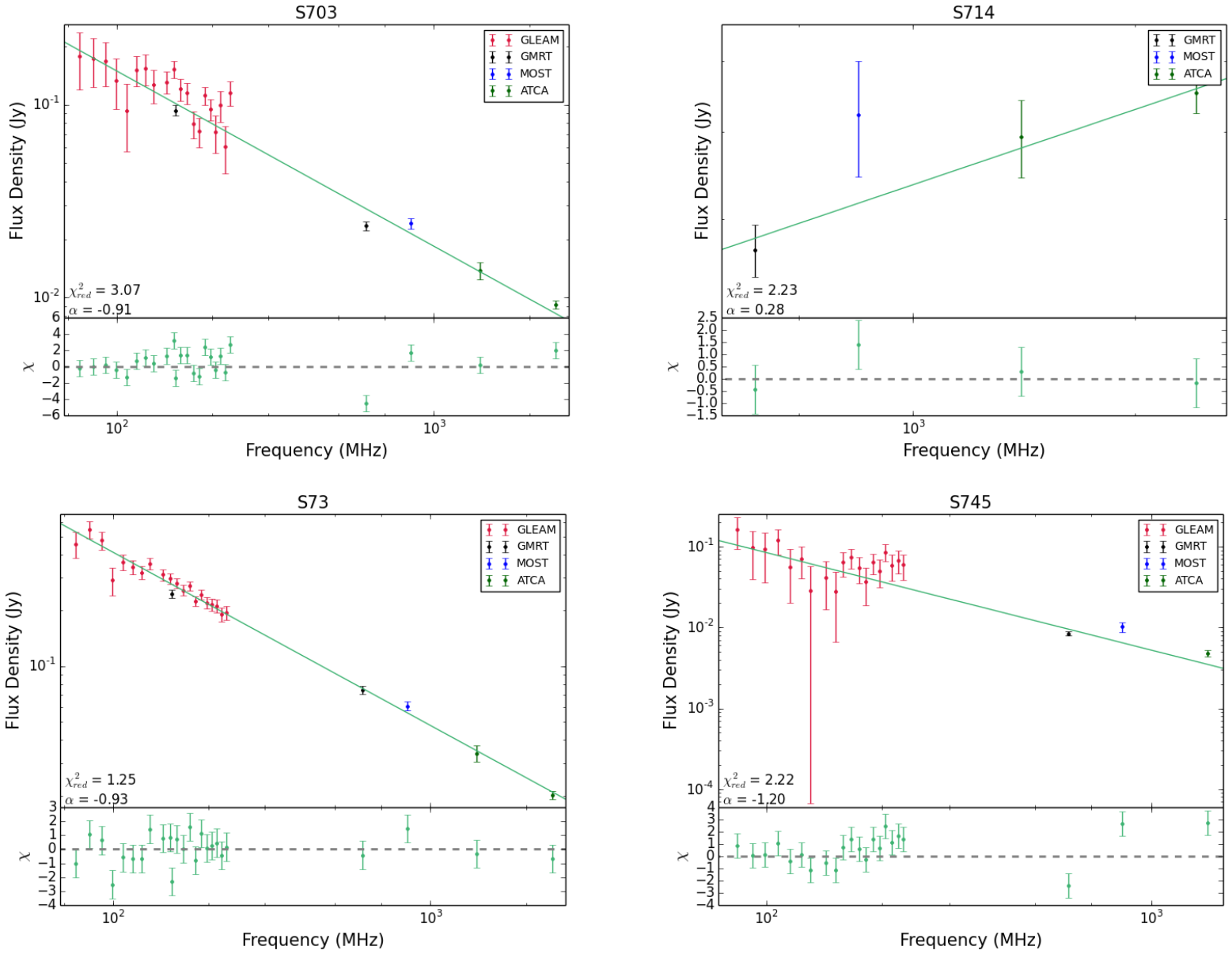

Fig. 4.38. (continued)

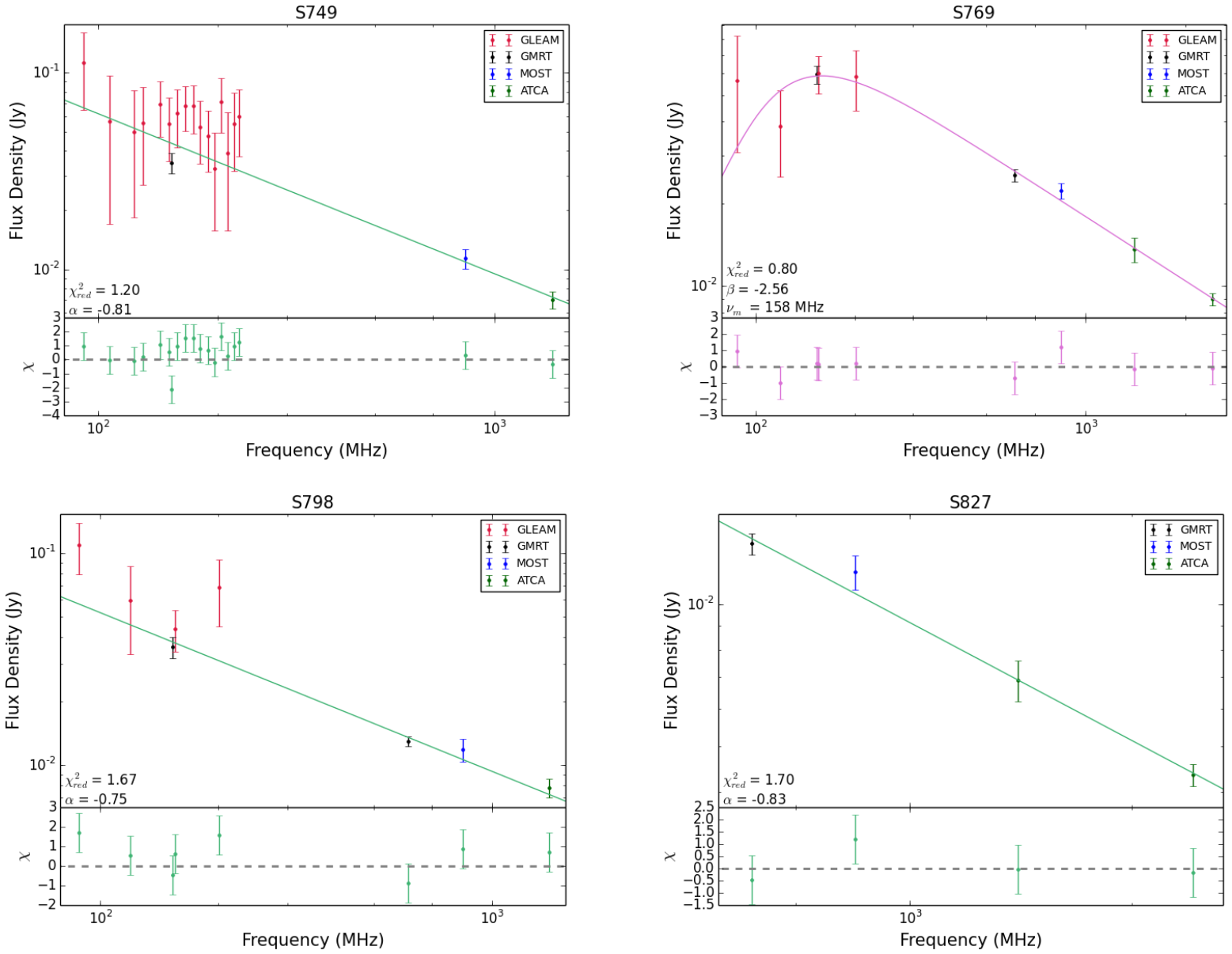

Fig. 4.38. (continued)

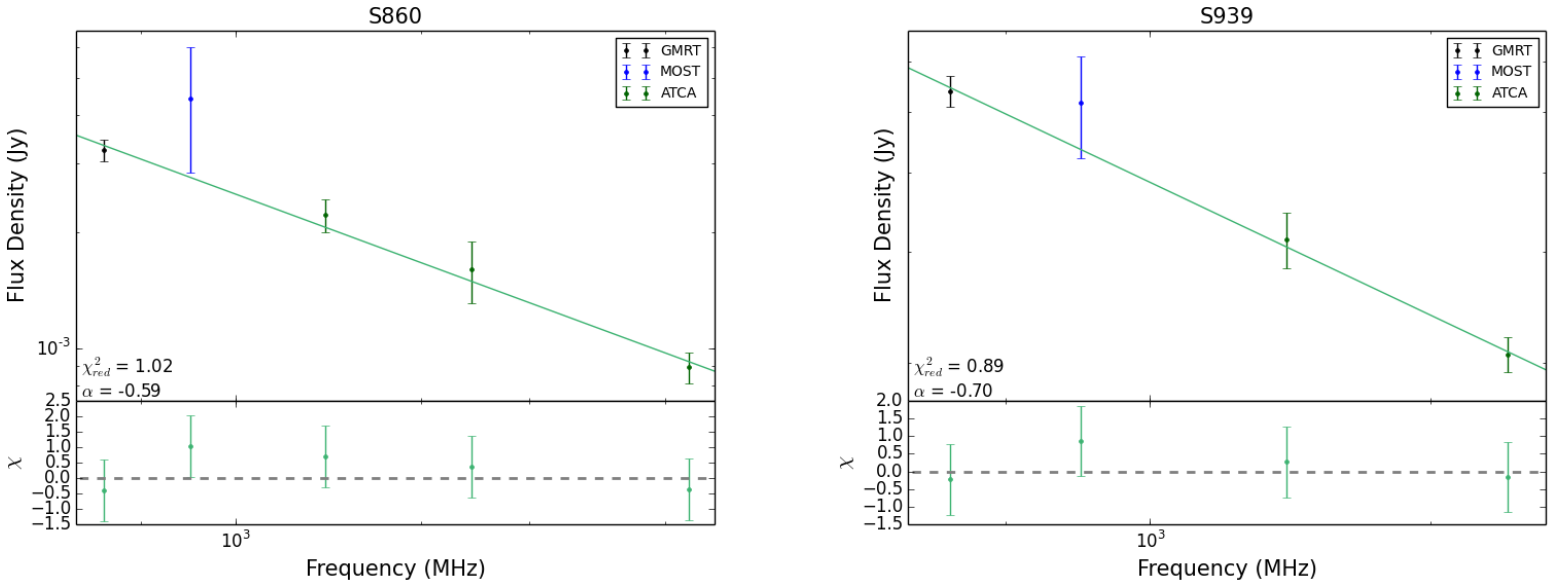

Fig. 4.38. (continued)

4.3.3 The mysterious case of S11

The source with ATLAS ID S11 was selected as a CSS candidate based on data from DR1. This source was close to the edge of the primary beam and appeared unresolved. The source was observed on day 1 of the C2730 observations of the ELAIS-S1. The initial images from our 5.5 and 9.0 GHz observations revealed no compact emission at the location of the source. However, we found compact emission nearby, which was associated with an IR source from SWIRE.

At a similar time, the much deeper DR3 images became available, and it became clear that this source was very extended, with the appearance of a radio lobe. A tentative 3σ contour connected the radio lobe with the nearby point source (see Fig. 4.39).

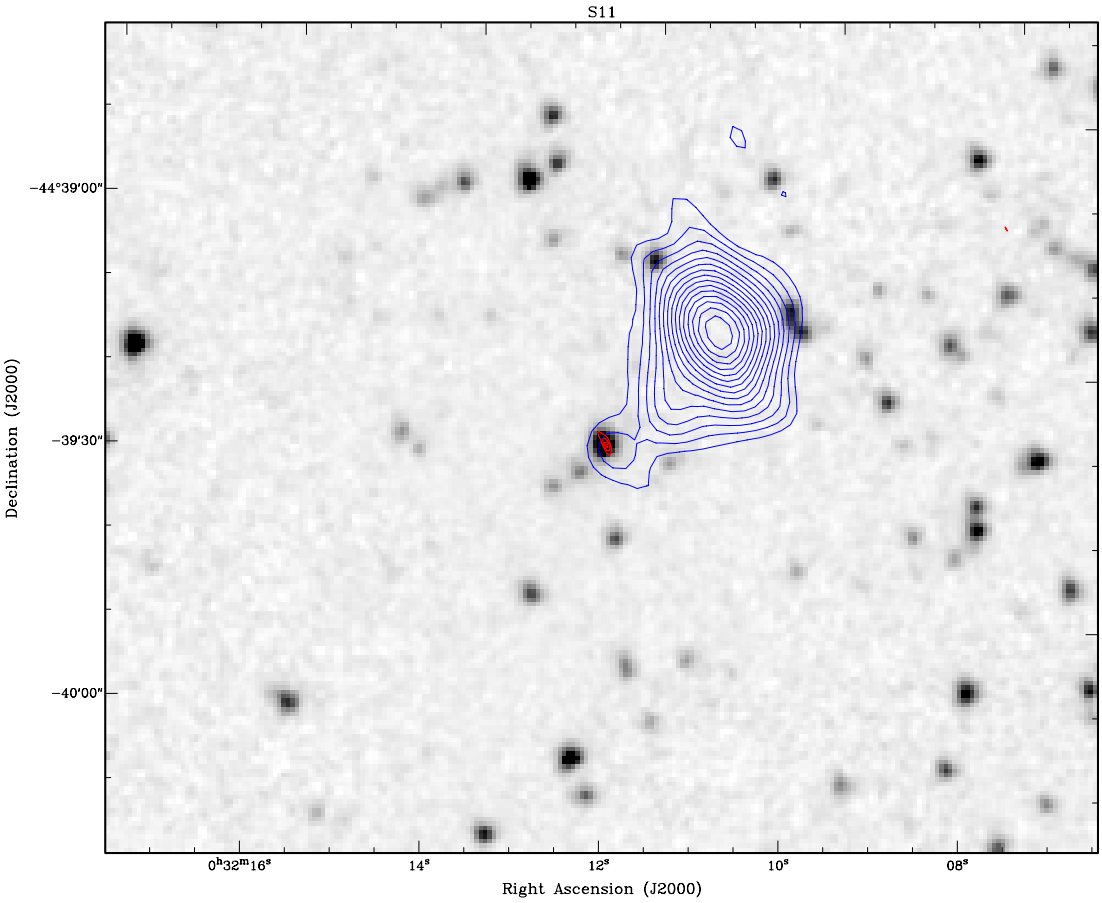

Figure 4.39: The background 3.6 μm SWIRE image of S11, overlaid with ATCA contours at 1.4 GHz (ATLAS DR3 - blue) and 9.0 GHz (this thesis - red). The DR3 contours are from 3σ, with 1σ intervals. The 9.0 GHz emission is coincident with an IR source, and tentatively associated with the 1.4 GHz emission.

This source requires further investigation, which will be presented in Collier et al. (in prep.). Below we present our preliminary analysis and discuss some implications.

We found that the extended 1.4 GHz source (S11 from this point onward) had a steep spectrum, while the compact 9.0 GHz source (J0032-4440 from this point onward) had an inverted spectrum, which was possibly turning over. Fig. 4.40 shows the radio spectra for each of these components. The components were confused at lower frequencies and therefore the spectra shown for component S11 represents the integrated spectrum of both components at low frequency. We take this as an approximation of the spectrum of S11 since the low frequency emission appears to be dominated by the extended emission of S11. The 5.5 and 9.0 GHz flux

densities of S11 were taken from low resolution images in which we had tapered the visibilities, although the 9 GHz flux appears to be underpredicted due to resolution effects.

A flat or inverted spectrum is expected for an AGN core, while a spectrum that is turning over is expected for compact HFPs, both of which would be expected to be coincident with a host galaxy. A steep spectrum is consistent with an extended lobe.

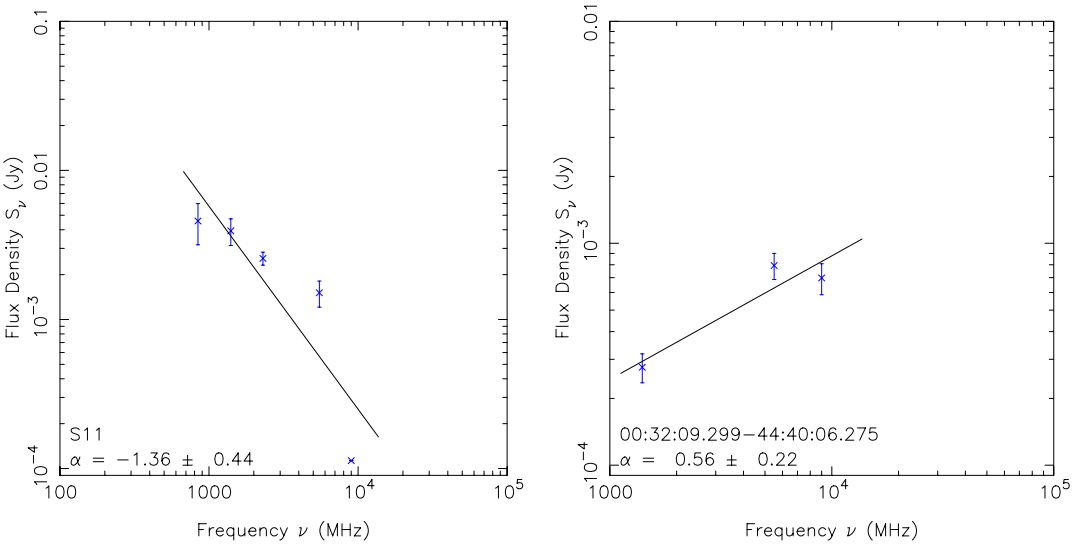

Figure 4.40: The radio spectra of S11 (left) and the nearby compact source, J0032-4440 (right). The 9 GHz flux of S11 appears to be underpredicted due to resolution effects.

Based on these results, we interpreted S11 as either:

1. A one-sided radio galaxy, hosted by the IR source coincident with J0032-4440;
2. A cluster halo, unassociated with the IR source and J0032-4440.

4.3.3.1 A one-sided radio galaxy?

S11 and J0032-4400 may represent a one-sided (i.e. one-lobed) radio galaxy. Radio galaxies with one observable jet (i.e. core-jet objects) are common, since the relativistic boosting amplifies the jet oriented toward us, while the counter-jet remains undetectable. However, radio lobes do not undergo relativistic speeds and therefore do not experience such effects. One-sided radio galaxies are extremely rare, but not unheard of, with two existing candidates in the literature to the best of my knowledge, CGCG 049–033 (Bagchi et al., 2007, 2009) and 26W20 (Harris et al., 1984; Silverman et al., 1998; Harris et al., 1999).

We postulate the following scenarios that may account for one-sided radio galaxies:

1. The jet is only emanating out of one side of the accretion disc. This would differ from all other radio galaxies and may require a new theoretical model to explain why the jet is not launched from both sides;
2. The host galaxy has a significantly different environment on either side of the accretion disc, with one significantly denser than the other and confining the jet growth (i.e. 'the frustration scenario'). One side would essentially act like an unaged CSO, while the other would act like a FR I or FR II.

3. Both jets experienced similar growth, but only one lobe has faded from detection. In this case, a denser environment may surround the lobe that is still visible, which is prevented from adiabatically expanding;

4. There is a geometric delay along the line of sight from the far lobe compared to the near lobe, which would cause the lobe to vary with time.

In this scenario, if the compact source is indeed a HFP, then it would be a restarted radio galaxy with a previous cycle of radio activity.

As a preliminary test, I looked for a connection between the compact and diffuse sources S11 and J0032-4400 at 5.5 GHz. We collected further observations at 5.5 GHz using ATCA during unallocated "green time". However, we could neither confirm nor reject a connection between these components (see Fig. 4.41).

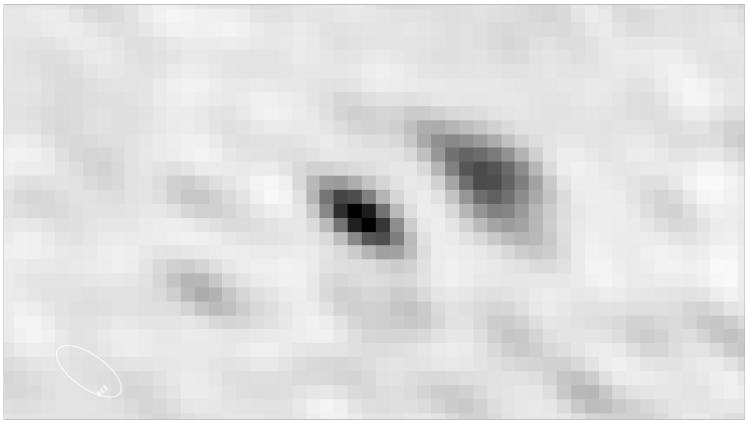

Figure 4.41: A preliminary 5.5 GHz image of (right component) S11 and J0032-4400 (left component). The image has a low resolution since we tapered the visibilities in order to detect S11. A connection between these components could neither be confirmed nor rejected.

This scenario requires further investigation, including an analysis of the environment surrounding both sources, VLBI observations of possible jet(s), and deeper 2.1 or 5.5 GHz ATCA observations using combinations of different array configurations, giving an image that is sensitive to the different spatial scales of radio emission.

4.3.3.2 A cluster halo?

Alternatively, the extended emission may be coming from a diffuse cluster halo. In this case, J0032-4400 would most likely be unassociated. However, if they were connected, the IR source could be accreting halo material and confining the radio source to small scales.

I tested this scenario by investigating the redshift distribution of surrounding sources from the OzDES Global Reference Catalogue (Uddin et al. in prep.; see section 2.2.2.1), and looking for those with similar redshifts.

S11 fell in an area sparsely covered by OzDES, but contained a few redshifts at ∼0.178. Fig. 4.42 shows the distribution of measured redshifts surrounding S11. Between $0.17591 < z < 0.178021$, the difference in comoving radial distance is ∼8.4 Mpc.

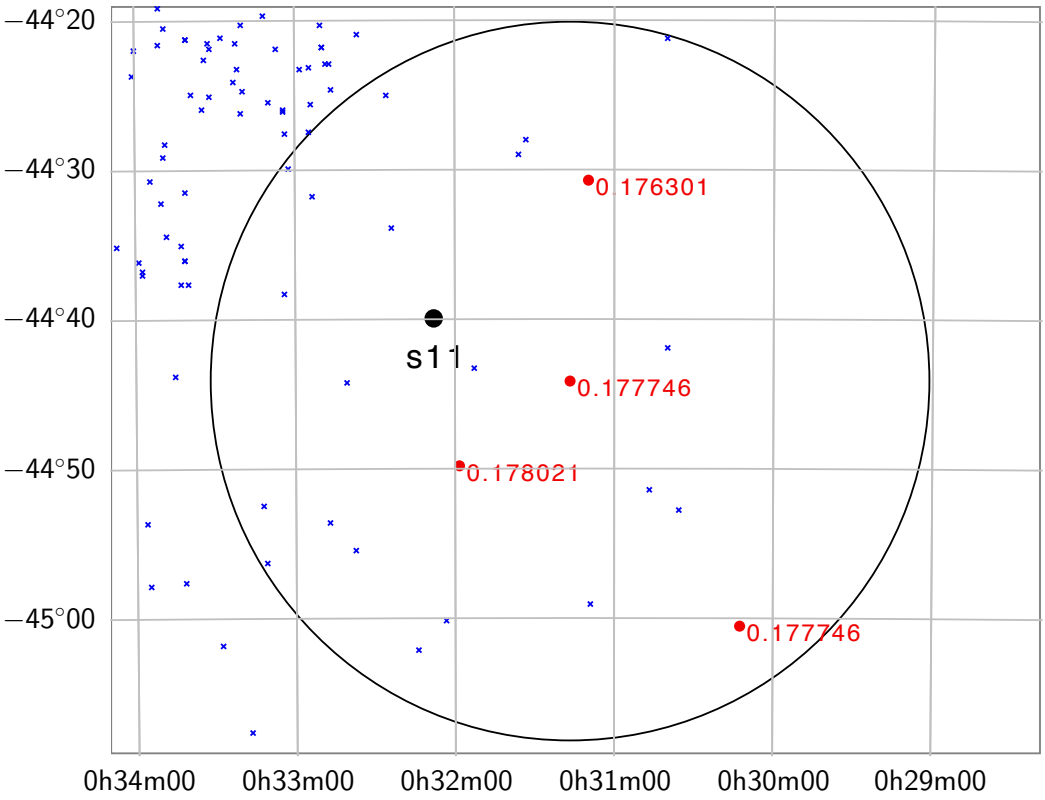

Figure 4.42: The spectroscopic redshifts surrounding source S11. Sources in the range $0.17591 < z < 0.178021$ are plotted in red, while sources outside this range are plotted in blue. The source in the middle is very bright in the optical and IR and a good candidate for the Brightest Cluster Galaxy, and has a circle drawn around it with a radius of $\sim$5 Mpc.

Since the coverage is quite sparse, it seems unlikely that so many objects within this region would have redshifts in such a narrow range by chance. Similar to the large Wide-Angle Tail in this same ATLAS field (Mao et al., 2010), there are a few sources with diffuse emission near S11.

This scenario requires further investigation, but may suggest that S11 resides within a cluster. If so, the most likely scenario is that S11 represents a cluster halo, although some explanations that account for a one-sided radio galaxy cannot be ruled out.

Each of these scenarios will be investigated and presented in Collier et al. (in prep.).

Section 4.4 is taken from Tingay et al. (2015), to which I contributed ∼30%, which included performing all observations and data reduction, as well as giving comments on the paper. The text remains the same except for formatting and minor editorial changes.

4.4 A case study of 1718-649

4.4.1 Introduction

PKS 1718−649 (NGC 6328: $z = 0.014428 \pm 0.000023$ from (Meyer et al., 2004)) is a well-studied gigahertz-peaked spectrum (GPS) radio galaxy, displaying all the classic attributes of this class of object, as presented in previous studies (Tingay et al., 1997, 2003): a compact double radio morphology on parsec scales; low radio variability; low radio polarisation; a persistently peaked radio spectrum; and a kinematically complicated, high gas density host galaxy environment. Recently the GPS classification has been supplemented by the Compact Symmetric Object (CSO) classification, where CSOs are suggested to be young radio galaxies and possess the characteristics that PKS 1718−649 displays (Wilkinson et al., 1994). The CSO classification guards against the selection of radio AGN that occasionally possess peaked radio spectra (Tremblay, 2011).

The origin of the peaked radio spectrum in this class of object is still a matter for debate, with a number of absorption models previously proposed to explain the inverted low frequency radio spectrum. Tingay et al. (2003) reviewed the various models and tested many of them against radio data obtained for PKS 1718−649 from the Australia Telescope Compact Array (ATCA), consisting of 30 - 40 flux density measurements over the frequency range 1 - 9 GHz over four epochs of observation spanning 14 months. The goal of these observations was to characterise the radio spectrum of PKS 1718−649 and attempt to use the radio spectrum and its spectral variability (spectral variability in this paper is defined as the variability of the spectral shape as a function of time) to constrain the different absorption models. Tingay et al. (2003) concluded that the leading contenders, free-free absorption and synchrotron self-absorption, produced similar quality parameterisations of the measured spectra, and that the spectral variability observed was marginal and difficult to interpret given the measurement errors. Although an excellent fit to the data was obtained with the free-free absorption model proposed by Bicknell et al. (1997), the spectral coverage of the measurements at low frequencies did not allow a compelling test of the model. Taking all of the evidence into account, including VLBI measurements of the sizes of the compact radio emitting regions, the conclusion of Tingay et al. (2003) was that synchrotron self-absorption was the most likely contributor to the peaked radio spectrum in PKS 1718−649.

While the Tingay et al. (2003) study represented a very detailed investigation of absorption models for PKS 1718−649, the measurements were sub-optimal in some respects. The spectral coverage of the ATCA at the time of the observations was good at frequencies within the 6 cm and 3 cm bands but sparse at frequencies in the 21 cm and 13 cm bands. At 21 cm and 13 cm, due to the presence of Radio Frequency Interference (RFI) and the limitation of the 128 MHz instantaneous bandwidth of the ATCA, it was difficult to obtain good frequency coverage below the spectral peak for PKS 1718−649 (at approximately 3 GHz, between the 13 cm and 6 cm bands). The paucity of the low frequency coverage, where absorption processes have the largest effect, somewhat hindered the investigation.

Due to the installation of the new Compact Array Broadband Backend (CABB) (Wilson

Table 4.11: Summary of the ATCA observations.

Project ID	Date	Frequency (GHz)	Duration (hours)	Array Configuration
C1034	2012 Feb 29	2.1, 5.5, 9.0	0.9	750D
C1034	2012 Sep 27	2.1, 5.5, 9.0	2.6	H214
C2768	2013 Feb 17	2.1, 5.5, 9.0	2.5	6A
C2768	2013 Dec 16	2.1, 5.5, 9.0	1.1	750B

et al., 2011), a far better instantaneous frequency coverage is now available in all bands of the ATCA, meaning that monitoring observations focused on spectral coverage are far easier and more robust than a decade ago. An example of the quality and utility of results possible with the CABB system can be seen in Macquart et al. (2013), where broadband measurements aided the study of microarcsecond-scale structure in AGN via intersteller scintillation. The new CABB system has motivated us to revisit PKS 1718−649, in order to better characterise its spectrum and spectral variability. The new CABB data allow a better measurement of the spectrum and also reveal other possible issues with the previous study by Tingay et al. (2003).

In addition, the new low frequency radio telescope, the Murchison Widefield Array (MWA) (Tingay et al., 2013), is starting to produce very large surveys of the southern sky in continuum radio emission between the frequencies of 80 and 300 MHz, substantially lower than the lowest frequency available at the ATCA. We use the MWA, as well as the Parkes radio telescope, to help characterise the PKS 1718−649 spectrum well below the peak frequency, which assists in distinguishing between absorption models.

4.4.2 Observations and data analysis

4.4.2.1 Australia Telescope Compact Array observations

In 2012-2013, a series of four snapshot observations of PKS 1718−649 were made using the ATCA during unallocated "green time". The CABB system gives an instantaneous 2 GHz bandwidth for both linear polarisations. The observations are summarised in Table 4.11. Frequency switching was used between the 16 cm (2.1 GHz) and 4 cm (5.5 and 9.0 GHz) bands, which required adjusting the subreflector focus for some antennas. The frequency ranges for each of these bands were 1075 − 3123 MHz, 4477 − 6525 MHz, and 7977 − 10025 MHz, respectively. Observations for all bands used 2048×1 MHz channels and a 10 second correlator integration time. For each observation, PKS 1934−638 was used for bandpass, flux density, and phase calibration, since it is only ∼15 degrees away from PKS 1718-649. Each observation repeated through a cycle of 10 minute scans of PKS 1718−649 bracketed by 5 minute scans of PKS 1934−638, before switching frequencies and repeating the process.

The MIRIAD software package (Sault et al., 1995) was used to analyse the data. Each set of observations was analysed using the same process, as follows.

The data were loaded using `atlod`. The 40 channels at either end of the band were flagged using `uvflag`. The data were split into single observing band datasets using `uvsplit`. We iteratively flagged and calibrated PKS 1934−649, checking flagging with `uvspec` and calibration with `uvplt`. Data were flagged for RFI using `pgflag` and `blflag`. Calibration consisted of estimating the bandpass solution using `mfcal` and then estimating the gain (amplitude and phase) and leakage solutions over four frequency bins and a solution interval of 10 seconds using `gpcal`. This flagging and calibration process was repeated until good calibration solutions were

found. The calibration solutions were transferred to PKS 1718−649 using `gpcopy`. The PKS 1718−649 data were then flagged and calibrated, also solving for the source polarisation in `gpcal`. The flux density scale was set to that defined by PKS 1934−638 by using `gpboot`.

During the analysis, the 2012 September 27 data were found to have had a number of instrumental problems during the observations, such that no stable calibration solutions could be found. These data were therefore discarded and further observations were obtained on 2013 February 17.

The excellent frequency coverage provided by CABB allows a closer examination of the spectrum of PKS 1718−649 than was possible by Tingay et al. (2003), especially at low frequencies. This is illustrated in Figure 4.43, which shows the calibrated Stokes I measurements from 2013 December 16 on a single baseline (antennas 3 - 4; 415 m length baseline) as a function of frequency. Clearly apparent in Figure 4.43 is significant beating in the visibility amplitude, indicating the presence of a confusing source $\sim 40'$from PKS 1718−649 on the sky (identified as 1722−64: RA=17:26:57.813; DEC=−64:27:52.79; J2000. Approximately 4 Jy at 16 cm and 1 Jy at 6 cm[3]). Such confusing structure was not apparent in the data of Tingay et al. (2003), due to limited spectral coverage. The effect of the confusing source changes with frequency (both due to the response of the interferometer and the response of the individual antenna elements), baseline length, and orientation.

The confusing object needs to be identified, modelled, and its effects removed from the data in the (u, v) plane before the spectrum of PKS 1718−649 can be isolated and measured. To model the confusing object, we used the `uvsfit` task in MIRIAD. `uvsfit` fits model components to visibility data, taking into account the frequency dependence of the model component flux densities. `uvsfit` was run at each epoch by simultaneously fitting all available data at all frequencies, using two point source model components (PKS 1718−649 and 1722−64 are both unresolved at the frequencies used here with the ATCA), and allowing `uvsfit` full freedom to utilise the frequency dependence of the flux density for both components. `uvsfit` produces visibility datasets representing the fitted model, visibility datasets containing the residuals on the fits, and reports the parameters of the models with errors on those parameters. Figure 4.43 shows the model fit to the data from the December 2013 observation.

The model parameters generated for each epoch of observation are given in Table 4.12. The reader is referred to the documentation for `uvsfit`[4] for an explanation of the model parameters (and the caption to Table 4.12). For all of the model fits performed, a reference frequency of 3.0 GHz was chosen in `uvsfit`. The RMS residuals resulting from the fits in February 2012, February 2013 and December 2013 were 98 mJy, 69 mJy, and 64 mJy, respectively. The component representing PKS 1718−649 in the model fits was held constant at the interferometer phase centre. The 1722−64 position was not held constant, to allow for any phase errors due to the differential ionosphere and/or atmosphere to be accounted for in the fit. The expected angular separation between PKS 1718−649 and 1722−64 is 0.6476° and the measured angular distance from Table 4.12 is 0.6470°.

Errors on the spectral model for PKS 1718−649, for each spectral channel, for each observation, are determined as follows. The RMS residuals between the measured visibility amplitudes and the model visibility amplitudes, for each spectral channel, over each observation duration, are taken as the one sigma errors on the individual spectral channels. Some variation of these errors over the fitted frequency change is apparent, with larger errors assigned to parts of the frequency range that are not as well fit by the model as other frequency ranges. Also, a rela-

[3]http://www.narrabri.atnf.csiro.au/calibrators (1722-64 does not appear in the Parkes catalog)
[4]http://www.atnf.csiro.au/computing/software/miriad/doc/uvsfit.html

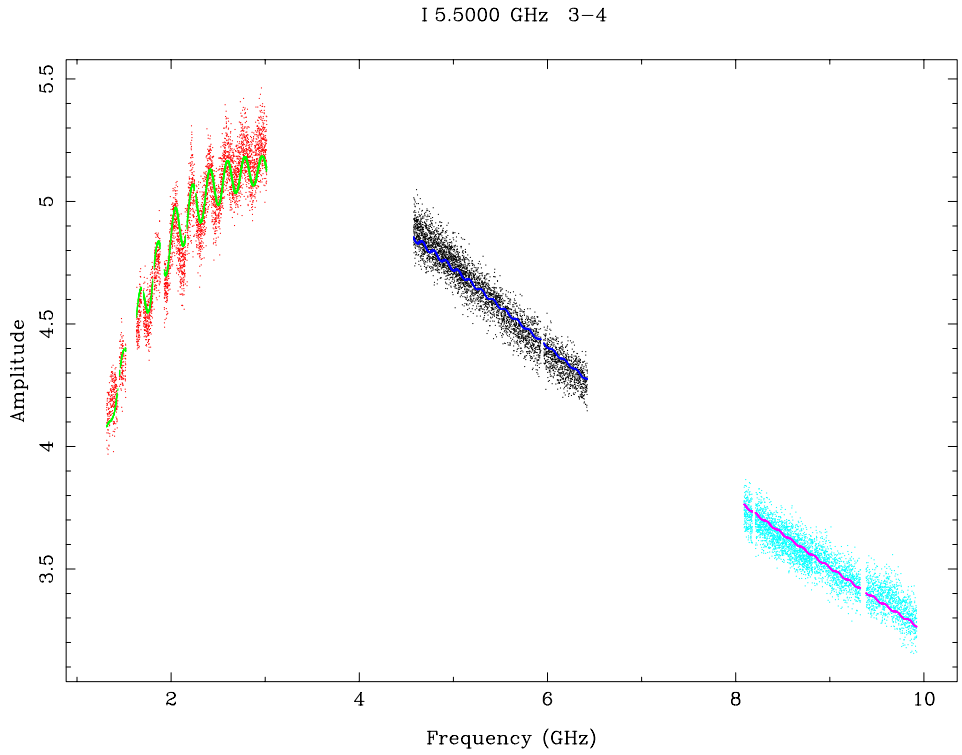

Figure 4.43: Measured spectrum for PKS 1718−649 from the December 2013 data on a single 415 m baseline, shown with a model fit derived via MIRIAD task `uvsfit`, as described in the text. Red is the 16 cm (2.1 GHz) band data, with green as model. Black is the 4 cm (5.5 GHz) band data, with dark blue as model. Light blue is the 4 cm (9.0 GHz) band data, with red as model. The data, particularly in the 16 cm band show the beating of the visibility amplitude, indicating a confusing source.

tively conservative RFI flagging has been applied, causing a small number of spectral channels to have larger than typical errors due to residual RFI. Figure 4.44 shows the model spectra for PKS 1718−649 for the three observations, from Table 4.12, along with the errors on the flux densities per spectral channel.

The model parameters for 1722−64 are difficult to interpret, as they represent the true spectrum of the radio source as well as the frequency dependent response of the antennas beyond the half power points.

We note that we do not explore the polarisation properties of PKS 1718−649 in this paper, as our sensitivity to polarised emission is lower than the deep polarisation observations of Tingay et al. (2003). Spectro-polarimetry of PKS 1718−649 could provide several interesting tests of the absorption mechanisms under consideration here (Mutoh et al., 2002) but would require deep CABB observations that are properly configured for accurate polarisation calibration. This will be the subject of a future investigation.

In Tingay et al. (2003), the error analysis took into account the errors on the absolute flux density scale in the Southern Hemisphere, strictly rendering the errors on the flux density measurements comparable to the flux density variations observed. In order to utilise the current data for variability analyses, here we assume that the error on the flux density scale in the Southern Hemisphere remains constant over the course of the observations. Explicit in this

Date	Source	Flux density (Jy)	Offset position RA/DEC (″)	α_0	α_1	α_2
Feb 2012	A	5.194±0.002	0/0	0.0881±0.0001	−0.3812±0.0001	0.0210±0.0001
Feb 2012	B	0.036±0.003	1272.12±0.11/ 1950.99±0.16	−2.313±0.002	−1.630±0.002	2.311±0.003
Feb 2013	A	5.222±0.001	0/0	0.0143±0.0001	−0.3580±0.0001	0.0211±0.0001
Feb 2013	B	0.038±0.001	1276.14±0.05/ 1954.71±0.08	−2.124±0.007	−1.339±0.006	2.029±0.011
Dec 2013	A	5.130±0.002	0/0	0.0068±0.0001	−0.3318±0.0002	0.0093±0.0002
Dec 2013	B	0.054±0.001	1256.16±0.20/ 1887.24±0.20	−2.87±0.03	−2.10±0.02	2.40±0.04

Table 4.12: The models produced from `uvsfit` for each of the three datasets. Source A is PKS 1718−649. Source B is 1722−64. α_0, α_1, and α_2 are defined in $\alpha(\nu) = \alpha_0 + l_{fr}(\alpha_1 + l_{fr}\alpha_2)$, where $\alpha(\nu)$ is the spectral index as a function of frequency. $l_{fr} = ln(\nu/\nu_0)$, where ν_0 is the reference frequency. The flux density in the table is at the reference frequency (3.0 GHz for these models).

assumption is that the spectrum of the ATCA primary flux density calibrator, PKS 1934−638, does not change over the course of the observations. This assumption is supported by the results of multi-frequency, multi-epoch monitoring of a sample of stable, compact radio sources by Tingay and de Kool (2003), showing that epoch-to-epoch variations of PKS 1934−638 over sixteen epochs spanning three and a half years were limited to less than 2%. The variations in the PKS 1718−649 flux densities shown in Figure 4.44 significantly exceed 2%. We therefore ascribe these variations to PKS 1718–649 itself, rather than any variability in PKS 1934–638.

For example, above the peak frequency of ∼3 GHz, the flux density has dropped by approximately 0.3 Jy over the course of the observations. Conversely, below the peak frequency, the flux density has risen by approximately 0.5 Jy at 1.2 GHz. These variations are at the ∼10% level and are in opposite senses either side of the peak frequency. The flux density at the peak frequency itself is less variable, rising by approximately 0.1 Jy over the course of the observations. The spectral shape of PKS 1718−649 therefore evolves significantly with time. These results support previous observations by Gaensler and Hunstead (2000) that show that PKS 1718−649 is more variable than PKS 1934−638 over decade timescales.

Thus, the ATCA results presented in Figure 4.44 represent the best observations to date of the spectral variability (time variability of the shape of the radio spectrum) of PKS 1718−649 or indeed any member of the GPS/CSO classes of radio source. With these measurements in hand, we can seek to interpret the spectral variability in terms of different models for absorption and emission processes in these objects. This will be the primary subject of sections 3 and 4.

In addition to the ATCA results, we have further information on the PKS 1718−649 spectrum at lower frequencies, discussed in the remainder of section 2. This additional information is also discussed in sections 3 and 4.

4.4.2.2 Murchison Widefield Array observations and data analysis

The MWA is a new low frequency interferometric radio telescope operating in the 80 - 300 MHz frequency range (Lonsdale et al., 2009; Tingay et al., 2013). We have used the MWA to measure the flux density of PKS 1718−649 at a centre frequency of 199 MHz, using a 30 MHz bandwidth at each of the two linear polarisations. A "snapshot" observation of 2 minutes duration was made on 2014 March 21 using all 128 antenna tiles of the array. A calibration scan of Hercules A was also undertaken, immediately prior to the PKS 1718−649 observations.

The data were analysed in MIRIAD, as follows. The auto-correlation spectra for the tiles were

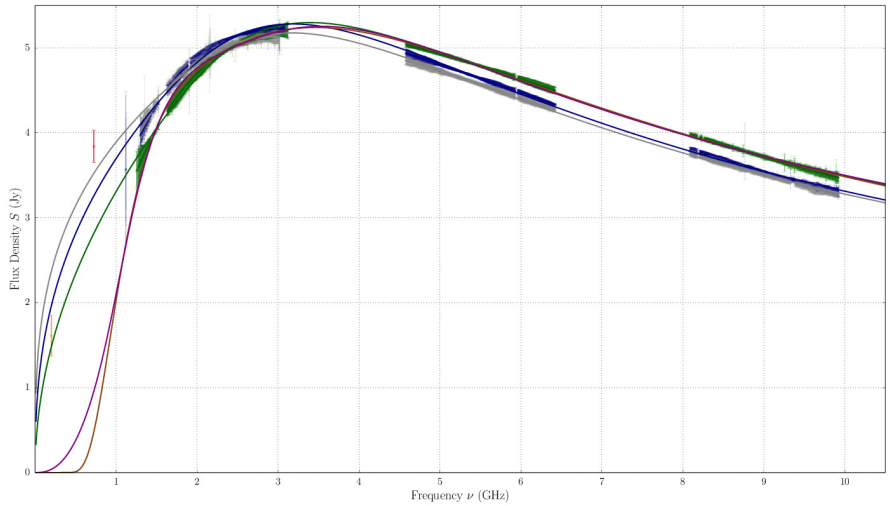

Figure 4.44: Measured radio spectra for PKS 1718−649 as described in the text, for the three epochs of observation. Also shown are a variety of model fits to the spectra, as described in the text. The ATCA data for 2012 February are shown in green. The ATCA data for 2013 February are shown in blue. The ATCA data for 2013 December are shown in grey. The fits of the Bicknell et al. (1997) model to these data are shown as solid lines in the same colours. Also shown are example homogenous free-free and synchrotron self-absorption model fits to the 2012 February data: purple solid line for a homogenous synchrotron self-absorption model with two components; brown solid line for a homogenous free-free absorption model with two components. Finally, data from Parkes at 725.75 MHz and the MWA at 199 MHz are shown, but not used in the fitting, as described in the text.

examined and three tiles were found to have anomolously high power levels, due to instrumental reasons. The data for these tiles (numbered 56, 99, and 106 in the array) were flagged. The task `mfcal` was run on the remaining 125 tiles, on the Hercules A data, to derive bandpass corrections and an initial estimate of the tile-based gains, for each linear polaristaion independently. These calibration parameters were copied to the PKS 1718−649 field data using `gpcopy` and the data were imaged using `invert` (4096×4096 pixel images; 32.2″pixel sizes; robust=0.5 weighting; and multi-frequency treatment of the channelised visibilities). The resulting images are dominated by a bright radio galaxy, far away from PKS 1718−649, PKS 1610−607, which is several hundred Jy at 200 MHz (see McKinley et al., in preparation, for a detailed study of PKS 1610−607 with the MWA), generating complex sidelobes across the field. Initially only PKS 1610−607 was cleaned (task `clean`), with subsequent self-calibration (task `selfcal`) of phase and amplitude (only a single amplitude gain per antenna tile for the duration of the 2 minute observation) based on that model. These actions substantially improved subsequent inversions of the incrementally calibrated visibilities, allowing images of good quality to be made at each linear polarisation, with PKS 1718−649 and many other known objects clearly detected. After a full-field clean of 10000 iterations, the residual images were dominated by residual sidelobe confusion from PKS 1610−607 and imperfect modelling of the nearby Galactic Plane. The images at each linear polarisation were independently corrected for the MWA primary beam response, which is different for each polarisation, and summed in the image plane to form a Stokes I image. The RMS in the final image was approximately 170 mJy.

In order to examine the flux density scale in the vicinity of PKS 1718−649, a number of

known radio sources within approximately 2° of PKS 1718−649 were inspected. These objects are unresolved at MWA angular resolution. The flux densities for these sources were measured from the MWA image by measuring the peak brightness and assuming a point source brightness distribution. The measured flux densities were compared to cataloged data at 4.85 GHz from the Parkes-MIT-NRAO (PMN) survey (Griffith and Wright, 1993) and at 843 MHz from the Sydney University Molonglo Sky Survey (SUMSS) survey (Bock et al., 1999; Mauch et al., 2003). The spectral indices calculated from the 843 MHz and 4.85 GHz data, assuming a power law spectrum of the form $S \propto \nu^{\alpha}$, were extrapolated to 199 MHz to calculate an expected flux density, to be compared to the measurements from the MWA data. Further, we take into account the errors on the published flux densities at 843 and 4850 MHz, to calculate errors on the spectral indices and hence errors on the predicted flux densities at 199 MHz. The errors on the MWA measurements are taken as the combination in quadrature of the image RMS and an estimated error on the primary beam correction of approximately 10% (Sutinjo et al., 2015).

Table 4.13 contains the results of this analysis. Of the 11 objects inspected, we find that 8/11 have measured 199 MHz flux densities that agree with the predicted 199 MHz flux densities to within the observational errors. One object, PMN J1724−6443 has a measured flux density significantly higher than predicted, which may plausibly be the result of temporal variation of the flux density, given its relatively flat spectral index. Two objects, PKS 1726−656 and PMN J1734−6421 have measured flux densities significantly lower than predicted, perhaps due to a flattening of the spectrum at low frequencies due to absorption processes. Overall, 6/11 objects have flux densities higher than predicted (but generally within the errors) and 5/11 have flux densities lower than predicted (but again generally within the errors). Thus, within the observational errors, there is no evidence to suggest a significant overall offset in the flux density scale in this image.

The measured 199 MHz flux density for PKS 1718−649 is 1610 mJy. Using the approach described above, the error on this measurement is approximately 240 mJy.

Source	S_{843} (mJy)	α_{843}^{4850}	$S_{e,199}$ (mJy)	$S_{m,199}$ (mJy)
PMN J1705−6516	261.6 ± 10.4	-0.81 ± 0.12	$840\pm^{200}_{160}$	940 ± 190
PMN J1706−6453	212.3 ± 6.5	-1.08 ± 0.21	$1010\pm^{400}_{290}$	1230 ± 210
PKS 1708−648	568.8 ± 17.1	-1.09 ± 0.09	$2740\pm^{470}_{410}$	3150 ± 360
PMN J1715−6524	368.5 ± 11.1	-1.06 ± 0.12	$1700\pm^{380}_{310}$	1540 ± 230
PMN J1720−6358	263.3 ± 7.2	-0.94 ± 0.14	$1020\pm^{260}_{210}$	630 ± 180
PMN J1720−6452	196.8 ± 7.7	-0.86 ± 0.16	$680\pm^{210}_{160}$	800 ± 190
PMN J1724−6443	103 ± 3.7	-0.49 ± 0.16	$210\pm^{60}_{50}$	740 ± 190
PKS 1726−656	998.1 ± 30	-0.86 ± 0.05	$3450\pm^{370}_{340}$	2610 ± 310
PMN J1728−6432	186.1 ± 8.8	-1.04 ± 0.23	$840\pm^{380}_{260}$	730 ± 190
PMN J1734−6407	337 ± 10.2	-0.8 ± 0.09	$1070\pm^{190}_{160}$	1290 ± 210
PMN J1734−6421	950.9 ± 28.6	-0.95 ± 0.06	$3750\pm^{460}_{410}$	1670 ± 240

Table 4.13: Data for 11 radio sources in the vicinity of PKS 1718−649. S_{843} is the flux density at 843 MHz from the SUMSS catalog, in mJy. α_{843}^{4850} is the spectral index between 843 MHz and 4850 MHz from the SUMSS and PMN catalogs. $S_{e,199}$ is the expected flux density at 199 MHz, extrapolated from 843 and 4850 MHz, in mJy. $S_{m,199}$ is the 199 MHz flux density measured from the MWA image, in mJy.

While this flux density estimate is approximate, for the reasons given above, it nevertheless suits our purposes well. As can be seen in section 3, different absorption models give very different predictions for the flux density in the MWA frequency range, with one family of models predicting mJy flux densities and another family of models predicting Jy flux densities.

Thus, even an approximate estimate of the flux density from the MWA data is very useful, as it clearly supports one family of models over another on a qualitative basis. Since the MWA data are not simultaneous with the ATCA data, we do not use the MWA data explicitly in the spectral modelling for PKS 1718−649.

4.4.2.3 Parkes observations and data analysis

Observations of PKS 1718−649 were made with the Parkes radio telescope on 2014 April 9, at a centre frequency of 732 MHz and with a bandwidth of 64 MHz. During the observation, local Digital TV transmitters were active, with the result that much of the band was lost to interference. After flagging affected data, a 6.5 MHz usable bandwidth remained, centred on 725.75 MHz. The flux density of PKS 1718−649 was measured in this band, calibrated by observations of PKS 1934−638 (same calibrator as for the ATCA observations described above), yielding a flux density of 3.84±0.19 Jy. With the large beam of the Parkes radio telescope at this frequency (∼30 arcminutes), it is possible that this measurement is affected by diffuse galactic synchrotron variations in this region of the sky. However, we expect any error due to this effect to be small compared with the approximate 5% error on the flux density scale that dominates the quoted error on the measurement. The Parkes data are included in the plotted spectra in Figure 4.44.

As above for the MWA data, the Parkes data have not been used explicitly in the spectral modelling, as the Parkes data are not simultaneous with the ATCA data. However, along with the MWA data, the Parkes data are useful in qualitatively assessing the plausibility of different families of absorption models.

4.4.3 Discussion

4.4.3.1 Application of absorption models to the PKS 1718−649 spectrum

Tingay et al. (2003) explored a wide range of models involving free-free absorption and synchrotron self-absorption as explanations for the peaked radio spectrum of PKS 1718−649. The most successful model in terms of its fit to the data was that adopted from Bicknell et al. (1997). We have adopted a similar approach here, attempting fits of the same models to these improved data.

The absorption model fits to the spectra of PKS 1718-649 were performed using a non-linear least squares routine that applied the Levenberg-Marquardt algorithm, an iterative procedure that linearises the function at each step based on a new estimate of the function from the gradient of the previous step. The minimum of the function is found when the derivative of the sum of squares with respect to new parameter estimates is zero. To ensure that the fitting routine finds the global minimum, and not a local minimum, different initial parameters were used to ensure the fitting routine converged to the same parameter values.

The covariance matrix produced by the fitting routine was formed by multiplying the Jacobian approximation to the Hessian of the least squares objective function by the residual variance. The reported uncertainties on the parameters to the fits were taken from the diagonal terms of this covariance matrix and represent the 68.27% confidence interval (one-sigma). The uncertainties on the data points were assumed to be gaussian for this analysis.

The fitting has only been undertaken using the ATCA data, as neither the MWA nor Parkes data were obtained simultaneous with the ATCA observations. The MWA and Parkes data are plotted along with the ATCA data, but have not been used in the fits.

Figure 4.44 shows the results of the various fits. As can be seen, Figure 4.44 reproduces many aspects of the Tingay et al. (2003) results in that all of the homogeneous free-free and synchrotron self-absorption models drop too quickly at low frequencies, with a large discrepancy at the lowest frequencies covered by Parkes and the MWA. Additionally, Figure 4.44 reproduces another result of Tingay et al. (2003), that the most successful model is the inhomogeneous free-free absorption model of Bicknell et al. (1997). The results of the application of the Bicknell et al. (1997) model to the ATCA data are listed in Table 4.14. The Parkes and MWA data broadly agree with the form of the low frequency power law spectrum predicted by this model.

Date	S (Jy)	α	p	ν_0 (GHz)	Reduced χ^2
Feb 12	7.274±0.002	0.716±0.005	−0.421±0.004	3.840±0.004	0.45
Feb 13	7.077±0.002	0.747±0.004	−0.457±0.004	3.855±0.003	1.04
Dec 13	6.758±0.007	0.746±0.001	−0.498±0.001	4.052±0.010	0.72

Table 4.14: The parameters of the Bicknell et al. (1997) model as fitted to the PKS 1718−649 data.

The Bicknell et al. (1997) model continues to provide an excellent description of the PKS 1718−649 radio spectrum, even with the addition of measurements below the ATCA frequency range and a greatly improved frequency coverage (particularly below the peak frequency). In the next section we examine the spectral variability of PKS 1718−649 in terms of both free-free and synchrotron self-absorption explanations.

One of the main constraints from the data on the absorption mechanisms under consideration in the next section is the value of the peak frequency. From a Markov Chain Monte Carlo analysis of the Bicknell et al. (1997) model fits to the data, using the model parameter errors in Table 4.14, the peak frequency and one sigma error on the peak frequency at each epoch were estimated: $\nu_{\rm p}$=3.399±0.001 GHz for February 2012; $\nu_{\rm p}$=3.175±0.001 GHz for February 2013; and $\nu_{\rm p}$=3.163$\pm^{0.001}_{0.002}$ for December 2013. These results are model-dependant and slightly different results may be obtained if models other than the Bicknell et al. (1997) model are used. However, given the quality of the fits indicated by the reduced χ^2 values listed in Table 4.14, the model appears to adequately characterise the data such that the estimates of peak frequency can be trusted.

4.4.3.2 Interpretation of spectral variability

The spectral variability observed in PKS 1718−649 is most likely intrinsic. Several arguments suggest that the contribution of interstellar scintillation is negligible. Specifically, interstellar scintillation at centimetre wavelengths is only present if the source exhibits structure on scales of less than tens of microarceseconds. However, 22 GHz VLBI imaging (Tingay et al., 2003) reveals that at most 10 mJy of the emission is unresolved, and most of the emission occurs on scales of 5 mas, which is too large to be subject to the effects of interstellar scintillation. The structure is likely even more extended at frequencies < 10 GHz, since it has a steep spectrum. Moreover, inspection of Figure 4.44 shows that the variations between epochs does not resemble the frequency dependence characteristic of interstellar scintillation (Narayan, 1992). For a source observed off the Galactic plane, the amplitude of scintillations peaks in the range $\sim 3-6$ GHz and is typically less than 50% of this value at 1.4 GHz and 10 GHz (Kedziora-Chudczer et al., 1997; Walker, 1998). Given this conclusion, the remainder of this discussion examines the spectral variability of PKS 1718−649 in terms of mechanisms intrinsic to the AGN.

Based on the relatively compact nature of PKS 1718−649 revealed by the VLBI data pre-

sented in Tingay et al. (2003) and given that they were unable to ascertain the precise origin of the spectral variability, Tingay et al. (2003) concluded that synchrotron self-absorption was the most likely explanation for the peaked spectrum of PKS 1718−649, given the turnover frequency. However, with better data available, and solid evidence for spectral variability in PKS 1718−649, we can revisit the question of the cause of the peaked spectrum in this object.

If the turnover were due to synchrotron emission, then the changes in the turnover frequency (i.e. between approximately $\nu_{\rm p} = 3.163\,{\rm GHz}$ and $\nu_{\rm p} = 3.399\,{\rm GHz}$) would be accompanied by changes in the peak flux density that are considerably larger than the 0.12 Jy observed. The peak flux density, $S_{\nu,t}$ at the peak of the turnover, $\nu_{\rm p}$, in a simple synchrotron model is derived by equating $k_B T_B$, where T_B is the rest-frame brightness temperature of the emission, to the energy of the emitting particles:

$$k_B T_B \approx m_e c^2 \left(\frac{2\pi m_e \nu_{\rm p}}{0.47 e B \sin\theta} \right)^{1/2}, \tag{4.3}$$

where θ is the angle that the magnetic field of strength B makes to the line of sight and k_B, e and m_e are the Boltzmann constant, electron charge, and electron mass respectively. For a source of angular diameter θ_S, one therefore has,

$$S_{\nu,t} = \left(\frac{\pi^3 m_e^3 \nu_{\rm p}^5 \theta_S^4}{0.94 e B \sin\theta} \right)^{1/2}, \tag{4.4}$$

and the measured variation in $\nu_{\rm p}$ would imply an approximate 20% (i.e. $\sim$1.1 Jy) variation in the peak flux density in the context of this model. Since such variations of this order are not observed (only $\sim$10% of this level is observed), it is difficult to straightforwardly attribute the observed changes in the spectral turnover frequency to changes in the synchrotron optical depth. We note that a change in $\nu_{\rm p}$ could instead be caused by changes in $B\sin\theta$ or θ_S, however $\nu_{\rm p}$ is relatively insensitive to changes in B: the observed change in ν_p would require a 30% increase in $B\sin\theta$ for fixed $S_{\nu,t}$. If the change in ν_p were instead ascribed to source size changes, it would require a 7% *contraction* of the source diameter, which appears implausible.

In the context of the free-free absorption models, other comments on the spectrum deserve mention. The $\sim$ 0.5 Jy flux density variations observed below the spectral turnover (e.g. at 1 GHz) could be due to variations in the free-free opacity, caused by the passage of individual clouds (in an inhomogeneous medium) across the line-of-sight to a compact component of the source. The free-free opacity scales as $\nu^{-2.1}$ (Altenhoff et al., 1960; Lang, 1980), so such inhomogeneity could explain at most 0.01 Jy of the $\sim$ 0.3 Jy flux density changes observed at $\nu = 4.5\,{\rm GHz}$ and only 3 mJy of the similar variation at 9 GHz. It therefore seems that a model beyond the context of free-free models is required to explain the variability above the peak frequency.

We can place limits on the free-free opacity variation. The flux density difference, ΔS, for an opacity that changes from $\tau_{\rm ff}$ to $\tau_{\rm ff} + \Delta\tau_{\rm ff}$ is $\Delta S = S_0 e^{-\tau_{\rm ff}}(1 - e^{-\Delta\tau_{\rm ff}})$, where S_0 is the flux density of the compact component covered by the absorbing material. Hence,

$$\Delta\tau = -\ln\left[1 - \frac{\Delta S}{S_0 e^{-\tau_{\rm ff}}}\right]. \tag{4.5}$$

Assuming that $\tau_{\rm ff} > 0$ (i.e. absorption only), the observed 0.5 Jy flux density variation at 1 GHz constrains the opacity change to be $\Delta\tau > 0.13$ for $S_0 = 4.0$ Jy.

This opacity change would imply the existence of large density gradients in the absorbing

medium. Taking a fiducial speed for the absorbing clouds of $v = 200 v_{200}\,\mathrm{km\,s^{-1}}$, a variation on a timescale of T years traces structure on a scale of $2 \times 10^{-4}\,T\,v_{200}$ pc, and the implied gradient is $\Delta\tau_{\rm ff}/\Delta L = 4.9 \times 10^{3} \Delta\tau\, T^{-1} v_{200}^{-1}\,\mathrm{pc^{-1}}$. Using the approximation for the free-free opacity used in Bicknell et al. (1997) and derived in Altenhoff et al. (1960), this in turn implies an emission measure gradient of

$$\left(\frac{\Delta \mathrm{EM}}{\Delta L}\right) = 1.5 \times 10^{10} \Delta\tau\, T^{-1} v_{200}^{-1} \left(\frac{T_{\rm gas}}{10^4\,\mathrm{K}}\right)^{1.35} \left(\frac{\nu}{1\,\mathrm{GHz}}\right)^{2.1} \mathrm{cm^{-6}\,pc\,pc^{-1}}. \quad (4.6)$$

The idea of a rapidly variable column of ionised material providing a highly variable free-free opacity is qualitatively supported by the observations of ubiquitous variability in the X-ray absorbing columns of neutral hydrogen in Seyfert 2 galaxies by Risaliti et al. (2002). These authors studied 25 X-ray defined Seyfert 2 galaxies and found that variations in the neutral hydrogen X-ray absorbing column were present in 22/25 of the galaxies at the 20% to 80% level. The timescales for variability were less than one year. Risaliti et al. (2002) suggest that these results rule out a homogenous obscuring torus and support the presence of a clumpy circumnuclear medium with structure scales well below 1 pc. If variations of this nature are seen in neutral hydrogen, we suppose it is reasonable that similar variations will be present in the ionised component of the circumnuclear environment, especially if the environment is fragmented into an ensemble of sub-pc scale clouds.

For example, a uniform electron/ion density of 3×10^4 cm^{-3} over a path length of 10 pc gives an EM of $\sim 10^{10}$ cm^{-6}pc. A 10% variation in this EM over a length scale of $\Delta L = 0.1$ pc gives an EM gradient of the same order of magnitude as equation 4. For these parameters, assuming only hydrogen atoms and an ionisation fraction of 10%, the implied neutral hydrogen column density is 10^{25} cm^{-2}. This column density is within an order of magnitude of the highest column densities considered by Risaliti et al. (2002). Given the level of uncertainty in most of the parameters in equation 4, and the assumptions above, this represents reasonable consistency. In addition, the results of Risaliti et al. (2002) show that the timescales of variability in the column density are in the range of months to years, consistent with the variability timescales seen below the peak frequency in the radio. The results of monitoring PKS 1718−649 at 843 GHz by Gaensler and Hunstead (2000) show time variations consistent with the ATCA data in the current study and the proposed time-scale of neutral hydrogen column density variations.

Within the context of the Bicknell et al. (1997) model for free-free absorption, the discussion above would relate to changes in the number and size/density distributions of absorbing clouds along the line of sight to the radio source. A requirement of the Bicknell et al. (1997) model is that whatever variations in the absorbing clouds take place, the distribution must remain in the form of a power law.

In principle, some of the evolution observed in the PKS 1718−649 spectra could be attributed to various cooling mechanisms. The effect of three forms of cooling on the spectral evolution of the emission from the hotspot of a compact source was considered by Manolakou and Kirk (2002). The principal mechanisms are: adiabatic expansion and cooling; synchrotron cooling; and Inverse Compton cooling. While these three mechanisms do not adequately explain the variability across the entirety of the PKS 1718−649 spectrum, they may explain some facets of its variability, particularly in the optically thin region of the spectrum. However, the synchrotron and Inverse Compton cooling models fail in detail because there is no evidence in the data for a break in the optically thin part of the spectrum. Both synchrotron and Inverse Compton cooling insert a break in the spectrum that changes the slope (e.g. from $\alpha \rightarrow \alpha + 1/2$) but there is no evidence for a break in the optically thin part of the spectrum observed for PKS

1718−649. A break may exist at frequencies higher than our 10 GHz upper frequency.

It is possible that adiabatic expansion plays some role in the time evolution of the spectrum, however it cannot explain the observed changes in spectral shape with time. For a source expanding isotropically, the electron energy scales as the linear dimension (L) of the source. For a particle with energy ϵ, we have $\epsilon \propto L^{-1}$ and for a source expanding at a constant speed $\epsilon = \epsilon_0(t_0/t)$, the power law distribution of electron energies at some time t after t_0 is (Shklovskii 1960):

$$N(\epsilon, t) = K_0 \left(\frac{t}{t_0}\right)^{-(2\alpha+3)} \epsilon^{-(2\alpha+1)}. \tag{4.7}$$

This then implies that the spectrum of the source retains its initial shape but its flux density scales with time as $S_\nu \propto t^{-2(2\alpha+1)}$. The upper and lower cutoffs in the energy distribution similarly decrease. In summary, it is therefore possible in principle to attribute changes in the amplitude of the optically thin emission of the spectrum of PKS 1718−649 to adiabatic losses, but it is not possible to explain the evolution of the entire spectrum using this mechanism.

A combination of adiabatic losses in the optically thin part of the PKS 1718−649 spectrum and variability of the Emission Measure causing the spectral turnover and variability of the low frequency spectrum, appears to be a plausible explanation for the shape and variation of the PKS 1718−649 spectrum.

A possible route to model both the synchrotron spectrum above the spectral peak and the apparently free-free absorbed synchrotron spectrum below the spectral peak may be via numerical simulations of hotspots, where jets impinge upon an ensemble of clouds, such as in the dense and kinematically confused AGN environment (Sutherland and Bicknell, 2007). Saxton et al. (2002) present a simulation of time-variability in AGN hotspots. The variability evident in their simulations appears to be due to the surging of the jet near the hot-spot caused by alternate compression and decompression of the jet by turbulence in the backflow in the cocoon. The dynamical timescale depends on the ratio of the jet diameter to the internal sound speed.

However, the simulations are of limited applicability to the present problem because there is no straightforward means of deducing the synchrotron spectrum on the basis of the underlying density field. The model is purely hydrodynamical, and the absence of magnetic field information impedes detailed investigation of the emissivity of the jet. In the simulation the emissivity is deduced by equating the magnetic pressure to the particle pressure, assuming a specific magnetic field geometry and assuming that the emission is optically thick. The absence of opacity effects in their simulation precludes its application to PKS 1718−649.

4.4.4 Summary

We have presented new measurements of the radio spectrum of PKS 1718−649 between the frequencies of 1 and 10 GHz, using the Compact Array Broadband Backend of the Australia Telescope Compact Array at three epochs spread over approximately 21 months. These measurements improve on previous attempts to measure the radio spectrum of this object by Tingay et al. (2003). The new data show that significant spectral variability is present for this object, which is interesting when considering the absorption mechanisms that could produce the spectral turnover observed. The free-free absorption model of Bicknell et al. (1997) provides the best fit of the spectral data at each epoch of observation, as was the case for Tingay et al. (2003), and remains the best model when flux density measurements below the ATCA frequency range

are considered, obtained at 726 MHz from Parkes and at 199 MHz from the Murchison Widefield Array. When considering the spectral variability of PKS 1718−649, neither synchrotron self-absorption nor free-free absorption can explain all aspects of the variability. A model in which adiabatic losses in a synchrotron spectrum account for the variability in the optically thin part of the spectrum above the peak frequency, and variations in the free-free opacity cause variations at frequencies below the peak, appears to be plausible. This is supported by observations of large variations in the neutral hydrogen column density toward a number of AGN from X-ray observations. As a typical example of a Compact Symmetric Object, this analysis may hold important conclusions for the CSO class as a whole. Similar monitoring observations of spectral variability in a large sample of similar objects would therefore be interesting as future work.

4.5 Discussion

Amongst our SMC sources and ATLAS GPS and CSS candidates, we found a number of interesting sources, which we discuss here.

4.5.1 Large scale radio galaxies with spectral breaks

We found a number of sources which we classified as large scale radio galaxies with strong hotspots and spectral breaks, estimated to be between the CSS stage and FR-II stage (e.g. smc_2, smc_8, smc_13, smc_18, smc_56). The spectral breaks show that the initial electron populations in these sources have significantly aged. If the emission comes mainly from hotspots, which are one of the primary regions of electron acceleration (Murgia, 2003), then this implies the injection has not been continuous, but has experienced cycles of accretion and jet growth, during which the electrons have aged. This suggests an inhomogeneous and clumpy circumstellar environment, which is in agreement with the FFA model, in which the environment is modelled by a power law distribution of absorbing clouds. This is also consistent with the hypothesis that most radio galaxies are triggered by major mergers, which causes an unsettled and inhomogeneous distribution of gas. If we assume that these conditions exist throughout the evolution of the large-scale radio galaxies, then it is likely that gas is not always available, but that there are phases during which the jets are switched on and off. This is analogous to what is suggested to be experienced by GPS and CSS sources (Orienti, 2016). If true, then a difference in accretion may account for the fact that evolutionary models predict that a large number of GPS and CSS sources experience termination and are unable to grow to large sizes (An and Baan, 2012; Orienti, 2016, and references therein.). Other modes of accretion that may account for this include minor mergers, secular processes, or the infalling of hot halo gas (Alexander and Hickox, 2012, see section 1.1).

4.5.2 Low-luminosity GPS sources

We found a number of compact GPS sources for which we estimated luminosities of $L_{5.5\ \mathrm{GHz}} \sim 10^{22-23}$ (e.g. smc_9, smc_55, smc_71, smc_76 and smc_95). These have tentative luminosities as low as the GPS sources from Tingay and Edwards (2015) which have been proposed as the compact counterparts to FR-I galaxies. Furthermore, a number of GPS and CSS candidates exist amongst our deep ATLAS sample with confirmed luminosities at this level, based on spectroscopic redshifts (see table 4.10). Tingay and Edwards (2015) propose that a luminosity-morphology break exists amongst GPS and CSS sources, analogous to the FR-I/II luminosity-morphology break. This hypothesis remains untested beyond a few tens of Mpc, but now we have candidates which can be followed up with VLBI and spectroscopy that enable this hypothesis to be tested out even more significant distances. As a comparison, we propose to test this against CI0008, CI0020, smc_54 and smc_59, which are good candidates for the compact counterparts of FR-II sources.

4.5.3 GPS sources inconsistent with SSA

We found a number of compact GPS and CSS sources whose radio spectra, magnetic field strengths and spectral ages were inconsistent with SSA theory. Sources smc_52, smc_55, smc_76, smc_95, CI0020 and s150 were poorly fit by a single homogeneous SSA model, but were well fit by the inhomogeneous FFA model, some of which have very shallow optically-thick spectral indices, in comparison to the steep spectral index predicted by SSA. This gives strong evidence

that simple SSA models are no longer adequate. However, some of these may be reasonably fit by more complex SSA models, such as a double SSA model, or a SSA model with a spectral break, such as in the cases of CI0008, CI0020, s150 and s895. However, for source CI0008, we derive a magnetic field strength for one component within the double SSA model that is orders of magnitude different from its expected value.

Furthermore, the case study of PKS 1718-649 gives strong evidence that its spectrum is due to FFA rather than SSA. FFA is the best fit model, particularly with respect to the low frequency spectra, and is able to explain the spectral variability, accounted for as changes in the free-free opacity of the low frequency spectra and adiabatic losses in the high frequency spectra. However, even a double SSA model underestimates the low frequency flux densities and cannot adequately account for the spectral variability.

4.5.4 Young GPS and CSS sources

Based on the spectral and kinematic ages of a number of sources, we find evidence that the GPS and CSS sources within our sample are indeed young and evolving objects. In particular, for the sources observed with VLBI, their kinematic ages based on their jet sizes are generally consistent with the spectral ages we estimate, which supports the hypothesis that their compact nature is due to their young age, rather than due to frustration. We find evidence for a significantly dense medium in a number of the most compact GPS sources, which are fit by an FFA model with the parameter $p \gtrsim 0$. However, the majority of sources are fit by an FFA model with $p < 0$. Based on this and the similarity between the kinematic and spectral ages, we suggest that in general, this dense medium is unable to permanently confine the jets of typical GPS and CSS sources.

We find that CI0020 is well modelled by the Jaffe and Perola (1973) model of an exponential spectral break. From this we derive $t_{\rm off} > 607$, suggesting that CI0020 is a prematurely dying radio source. However, we cannot rule out that CI0020 will undergo another cycle of radio emission, which would classify it as a recurrent radio galaxy.

If we assume FFA is responsible for the absorption of the majority of sources, then we expect that the ambient medium is inhomogeneous and clumpy. This suggests that while the majority of our sources may be young and evolving, they may also undergo recurrent activity as various clumps of gas accrete onto the SMBH at different stages. However, we find no evidence for restarted radio galaxies amongst all of our high resolution images. Therefore, we suggest that the timescales of the recurrent activity are not long enough to produce significant numbers of restarted radio galaxies.

4.5.5 Faint GPS and CSS sources

Our SMC sample general consists of GPS and CSS sources at mJy levels, as compared to the majority of samples such as O'Dea (1998) which are at Jy levels. We find tentative evidence that the fraction of CSS sources is smaller than the fraction estimated for Jy-level sources. This may be accounted for as a selection effect or if a smaller fraction of mJy-level GPS sources evolve into CSS sources as compared to the Jy-level GPS sources. Furthermore, we found that the mJy-level sources within the ATLAS VLBI sample follow the turnover−linear size relation in the same way as the Jy-level, showing that mJy-level GPS and CSS sources also co-evolve in size and spectrum.

4.6 Summary and Conclusion

We studied the radio spectra and high-resolution morphologies of faint GPS and CSS sources. We used these observations to determine plausible absorption mechanisms and the general nature and properties of faint GPS and CSS sources. Amongst our SMC sample (section 4.1), we find that the radio spectra are well modelled by FFA. We find tentative evidence that at mJy-levels, the fraction of CSS sources is smaller than the fraction estimated for Jy-level sources. This may be accounted for as a selection effect or if a smaller fraction of mJy-level GPS sources evolve into CSS sources as compared to the Jy-level GPS sources. Amongst our ATLAS VLBI sample (section 4.2), we find that FFA provides a more straight forward explanation of the radio spectra, and provide strong evidence again SSA for source CI0008. We derive kinematic and spectral ages consistent with the hypothesis that GPS and CSS sources are young and evolving. Amongst our ATLAS ATCA sample (see section 4.3), we found a number of low-luminosity sources, which we propose to follow up with VLBI to test whether they are the compact counterparts of FR I galaxies. Lastly, for PKS 1718-649 (section 4.4), we found that the low-frequency spectra and spectral variability is best explained by FFA.

We conclude that, despite being historically favoured, single homogeneous SSA is not the dominant form of absorption amongst a large fraction of GPS and CSS sources. We conclude that the inhomogeneous FFA model from Bicknell et al. (1997) provides a good model for the majority of the spectra with observable turnovers, suggesting an inhomogeneous and clumpy ambient medium. We conclude that a double SSA model, consisting of one homogeneous SSA component for each lobe, can also provide a good model for the spectra of GPS and CSS source, but can give inconsistent properties, as in the case of source CI0008. While even more complex SSA models could provide a good fit, in which there are more than two homogeneous SSA components, it is not necessary to add the level of complexity and increase of the number of free parameters within the corresponding models to account for the spectra of GPS and CSS sources. Therefore, inhomogeneous FFA provides a simple and satisfactory explanation for the spectra of GPS and CSS sources that is consistent with their expected properties, including the inhomogeneous ambient medium, and spectral variability. We conclude that the majority of our GPS and CSS sources are young and evolving and may undergo recurrent activity over small time scales. We conclude that a very small fraction of faint GPS and CSS sources consists of frustrated, dying or restarted radio galaxies.

Chapter 5

Future Work, Summary and Conclusion

5.1 Future Work

Here I list some suggestions for future work based on the results of this thesis. These are broken up into ideas for the various objects and samples.

5.1.1 IFRSs

Given the large sky density of IFRSs of several per square degree, and the prediction that their existence at high redshifts causes further problems for the growth of SMBHs in the early Universe, the primary goal is to confirm the redshift range of IFRSs. Since IFRSs are so faint at optical and IR wavelengths, the observations to confirm their redshifts would need to be close to the radio frequencies at which they are strong. Therefore, the primary goal for the future study of IFRSs is to use ALMA to observe CO in the most extreme ATLAS IFRSs with no IR counterparts, to measure their redshifts and test whether they indeed represent a large population of high$-z$ radio-loud AGN at $z \sim 7$.

Further future work includes SED modelling of the Collier et al. (2014) all-sky IFRSs in deep fields, particularly the four with spectroscopic redshifts, and comparing these to the SED modelling of ATLAS IFRSs with no IR counterparts, to see whether they have similar SEDs, how they relate to one another and whether both populations of IFRSs represent a continuous population spanning a large redshift range. Furthermore, collecting wideband ATCA or ASKAP data for the GPS and CSS candidates from the all-sky IFRSs would enable detailed spectral modelling, further uncovering their nature and determining what fraction consist of GPS and CSS sources.

Lastly, a useful further study of IFRSs would be to use the same technique as in Collier et al. (2014) to compile a new sample of all-sky IFRSs using new deeper WISE data and adjusting the selection criteria (like we did for the supplementary sample) to find more sources with spectroscopic redshifts using SDSS DR12.

5.1.2 SMC GPS/CSS candidates

The study of our SMC GPS/CSS samples was limited to radio observations, and therefore the primary goal for future studies is to perform a multi-wavelength analysis of the colours,

SEDs and optical spectra, comparing the host properties to radio properties, to see if they self-consistently evolve and to test against the general accepted model of AGN evolution. This would primarily make use of the deep *Spitzer, Chandra and XMM* data available in the SMC field. Secondary to this is observe the sources with estimated luminosities of $L_{5.5\ \mathrm{GHz}} \sim 10^{22-23}$ (smc_9, smc_55, smc_71, smc_76 and smc_95) to confirm their redshifts and luminosities. If confirmed, VLBI observations using the LBA would enable us to determine their morphology and test whether they are the compact counterparts to FR-I galaxies, as hypothesised by Tingay and Edwards (2015).

5.1.3 ATLAS VLBI sources

In the same way, since the study of our ATLAS VLBI sources was limited to radio observations, the primary goal for future studies is to perform a multi-wavelength study (see section 5.1.2). This would make use of the deep observations that exist at virtually every wavelength within the ATLAS fields, particularly within the CDFS. Secondary to this would be to obtain higher-resolution VLBI observations using the LBA or VLBA to estimate the hotspot expansion velocity and kinematic ages of each source. These observations would also uncover their morphologies, enabling more accurate estimations of the magnetic field strengths derived for each component within the SSA models, which would provide a much more rigorous test of SSA. In the same way, observing CI0008 at lower frequency to determine its spectral behaviour below the turnover would enable us to test the viability of the more complex SSA models. Furthermore, radio polarimetry measurements using the ATCA data would enable more accurate estimates of the magnetic field strength to be made based on equipartition assumptions, and therefore, more accurate estimates of their spectral ages. If these age estimates were accurate enough, we may be able to observe small discrepancies between their kinematic and spectral ages, telling us whether any minor frustration has occurred during their jet growth.

5.1.4 ATLAS GPS/CSS candidates

Since only a preliminary study of the ATLAS GPS and CSS sample was performed in this thesis, the primary goal of future studies is the reduction of the 5.5 and 9.0 GHz ATCA data for the ∼70 remaining candidates that weren't observed with VLBI. Following this, we would perform the same detailed spectral modelling and analysis as we did with the ATLAS VLBI sample. Further future work include ongoing VLBI observations of those with confirmed GPS and CSS spectra that are unresolved with ATCA at $\sim$ 1 arcsec resolution. Particular focus should be on those with low luminosities, to test whether they are the compact counterparts to FR-I galaxies, as hypothesised by Tingay and Edwards (2015). This sample would also benefit from a multi-wavelength study (see section 5.1.2), making use of the deep data existing at almost every wavelength within the ATLAS fields.

5.1.5 s11

The nature of source s11 remains unconfirmed. Therefore, the primary goal of future studies is to further test our two hypotheses. Firstly, to analyse the redshift distribution of nearby sources (particularly as more redshifts are measured during the ongoing OzDES program) to test the hypothesis that s11 is a cluster halo. And secondly, to combine of the four days of ATCA observations of s11 to see if there is a connection to the nearby compact source, testing the hypothesis that s11 is a one-sided RG.

5.2 Summary and Conclusion

We studied two classes of object to gain a better understanding of the evolution of AGN: IFRSs and GPS / CSS sources. We present individual conclusions in sections 3.3, 3.4.5, 4.2.6, 4.4.4 and 4.6, which we summarise here.

We discovered a population of 1317 brighter IFRSs which were, for the first time, reliably detected in the IR and optical. We found the first spectroscopic redshifts of IFRSs and showed that the brightest IFRSs are at $z > 2$. Furthermore, we ruled out that IFRSs are SFGs, hotspots, lobes or misidentifications. We found the first X-ray counterparts of IFRSs, and increased the number of known polarised IFRSs by five-fold. We presented an analysis of their radio spectra and showed that IFRSs consist of GPS, CSS and USS sources. We followed up 57 of these using VLBI observations, and confirmed the AGN status of IFRSs. We conclude that IFRSs represent a new population of high-redshift radio galaxies, which, for the faintest IFRSs, may have redshifts as high as $z = 7$ and consist of a few hundred thousand objects across the μJy sky.

We have observed the faintest population of GPS and CSS sources to date, consisting of $\sim$150 sources, many of which are low-luminosity. We followed up eight of the most compact sources with VLBI and detected six of them. We modelled their radio spectra and concluded that single inhomogeneous SSA is not the dominant form of absorption amongst a large fraction of GPS and CSS sources. We find that FFA provides a good model for the majority of the spectra with observable turnovers, suggesting an inhomogeneous and clumpy ambient medium. Furthermore, we conclude that the majority of our GPS and CSS sources are young and evolving and may undergo recurrent activity over small time scales. We conclude that a very small fraction of GPS and CSS sources consists of frustrated, dying or restarted radio galaxies.

For both of these classes of AGN, the Evolutionary Map of the Universe (EMU; Norris et al., 2011b) and other ASKAP, MWA and MeerKAT surveys and observations will revolutionise our understanding. Early science for ASKAP will give continuous radio coverage from $\sim 700 - 1800$ MHz, enabling GPS and CSS samples to be selected from within one set of observations. MWA observations will enable the turnovers and optically-thick spectra to be thoroughly measured, enabling the different spectral models be tested over large samples. EMU will detect several million GPS and CSS sources, and uncover the low-luminosity population. Furthermore, existing and future co-spatial deep radio and IR fields will uncover larger and deeper samples of IFRSs, which will uncover significantly larger numbers of galaxies within the high-redshift universe. Studying these samples of AGN will enable their evolution to be characterised across a vast range of cosmic time and evolutionary ages, enabling us to build a picture of the history and evolution of young and distant radio sources in the Universe.

References

Abazajian, K., Adelman-McCarthy, J. K., Agüeros, M. A., et al. (2004). The Second Data Release of the Sloan Digital Sky Survey. *AJ*, 128:502–512.

Abazajian, K., Adelman-McCarthy, J. K., Agüeros, M. A., et al. (2005). The Third Data Release of the Sloan Digital Sky Survey. *AJ*, 129:1755–1759.

Abazajian, K. N., Adelman-McCarthy, J. K., Agüeros, M. A., et al. (2009). The Seventh Data Release of the Sloan Digital Sky Survey. *ApJS*, 182:543–558.

Adelman-McCarthy, J. K., Agüeros, M. A., Allam, S. S., et al. (2008). The Sixth Data Release of the Sloan Digital Sky Survey. *ApJS*, 175:297–313.

Adelman-McCarthy, J. K., Agüeros, M. A., Allam, S. S., et al. (2006). The Fourth Data Release of the Sloan Digital Sky Survey. *ApJS*, 162:38–48.

Ahn, C. P., Alexandroff, R., Allende Prieto, C., et al. (2014). The Tenth Data Release of the Sloan Digital Sky Survey: First Spectroscopic Data from the SDSS-III Apache Point Observatory Galactic Evolution Experiment. *ApJS*, 211:17.

Ahn, C. P., Alexandroff, R., Allende Prieto, C., et al. (2012). The Ninth Data Release of the Sloan Digital Sky Survey: First Spectroscopic Data from the SDSS-III Baryon Oscillation Spectroscopic Survey. *ApJS*, 203:21.

Alexander, D. M. and Hickox, R. C. (2012). What drives the growth of black holes? *New A Rev.*, 56:93–121.

Alexander, P. (2000). Evolutionary models for radio sources from compact sources to classical doubles. *MNRAS*, 319:8–16.

Allison, J. R., Sadler, E. M., Moss, V. A., et al. (2015). Discovery of H I gas in a young radio galaxy at z = 0.44 using the Australian Square Kilometre Array Pathfinder. *MNRAS*, 453:1249–1267.

Altenhoff, W., Mezger, P. G., Strassl, H., Wendker, H., and Westerhout, G. (1960). Die Durchmusterung der Milchstraße und die Quellendurchmusterung bei 2.7 GHz. *Veröff Sternwarte Bonn*, 59:48–86.

An, T. and Baan, W. A. (2012). The Dynamic Evolution of Young Extragalactic Radio Sources. *ApJ*, 760:77.

Antonucci, R. (1993). Unified models for active galactic nuclei and quasars. *ARA&A*, 31:473–521.

Antonuccio-Delogu, V. and Silk, J. (2008). Active galactic nuclei jet-induced feedback in galaxies - I. Suppression of star formation. *MNRAS*, 389:1750–1762.

Appleton, P. N., Fadda, D. T., Marleau, F. R., et al. (2004). The Far- and Mid-Infrared/Radio Correlations in the Spitzer Extragalactic First Look Survey. *ApJS*, 154:147–150.

Aravena, M., Spilker, J. S., Bethermin, M., et al. (2016). A survey of the cold molecular gas in gravitationally lensed star-forming galaxies at $z > 2$. *MNRAS*, 457:4406–4420.

Ashby, M. L. N., Stern, D., Brodwin, M., et al. (2009). The Spitzer Deep, Wide-field Survey. *ApJ*, 701:428–453.

Assef, R. J., Stern, D., Kochanek, C. S., et al. (2013). Mid-infrared Selection of Active Galactic Nuclei with the Wide-field Infrared Survey Explorer. II. Properties of WISE-selected Active Galactic Nuclei in the NDWFS Boötes Field. *ApJ*, 772:26.

Bagchi, J., Gopal-Krishna, Krause, M., and Joshi, S. (2007). A Giant Radio Jet Ejected by an Ultramassive Black Hole in a Single-lobed Radio Galaxy. *ApJ*, 670:L85–L88.

Bagchi, J., Gopal-Krishna, Krause, M., Konar, C., and Joshi, S. (2009). A Giant Radio Jet of Very Unusual Polarization in a Single-Lobed Radio Galaxy. In Saikia, D. J., Green, D. A., Gupta, Y., and Venturi, T., editors, *The Low-Frequency Radio Universe*, volume 407 of *Astronomical Society of the Pacific Conference Series*, page 200.

Banfield, J. K., George, S. J., Taylor, A. R., et al. (2011). Polarized Radio Sources: A Study of Luminosity, Redshift, and Infrared Colors. *ApJ*, 733:69.

Barthel, P. D. (1989). Is every quasar beamed? *ApJ*, 336:606–611.

Baum, S. A., O'Dea, C. P., Murphy, D. W., and de Bruyn, A. G. (1990). 0108 + 388 - A compact double source with surprising properties. *A&A*, 232:19–26.

Becker, R. H., White, R. L., and Helfand, D. J. (1995). The FIRST Survey: Faint Images of the Radio Sky at Twenty Centimeters. *ApJ*, 450:559.

Best, P. N. and Heckman, T. M. (2012). On the fundamental dichotomy in the local radio-AGN population: accretion, evolution and host galaxy properties. *MNRAS*, 421:1569–1582.

Best, P. N., Kaiser, C. R., Heckman, T. M., and Kauffmann, G. (2006). AGN-controlled cooling in elliptical galaxies. *MNRAS*, 368:L67–L71.

Bicknell, G. V., Dopita, M. A., and O'Dea, C. P. O. (1997). Unification of the Radio and Optical Properties of Gigahertz Peak Spectrum and Compact Steep-Spectrum Radio Sources. *ApJ*, 485:112–124.

Bock, D. C.-J., Large, M. I., and Sadler, E. M. (1999). SUMSS: A Wide-Field Radio Imaging Survey of the Southern Sky. I. Science Goals, Survey Design, and Instrumentation. *AJ*, 117:1578–1593.

Brammer, G. B., van Dokkum, P. G., and Coppi, P. (2008). EAZY: A Fast, Public Photometric Redshift Code. *ApJ*, 686:1503–1513.

Brocksopp, C., Kaiser, C. R., Schoenmakers, A. P., and de Bruyn, A. G. (2007). Three episodes of jet activity in the Fanaroff-Riley type II radio galaxy B0925+420. *MNRAS*, 382:1019–1028.

Burke-Spolaor, S. (2011). A radio Census of binary supermassive black holes. *MNRAS*, 410:2113–2122.

Callingham, J. R., Gaensler, B. M., Ekers, R. D., et al. (2015). Broadband Spectral Modeling of the Extreme Gigahertz-peaked Spectrum Radio Source PKS B0008-421. *ApJ*, 809:168.

Cameron, A. D., Keith, M., Hobbs, G., et al. (2011). Are the infrared-faint radio sources pulsars? *MNRAS*, 415:845–848.

Cameron, E. (2011). On the Estimation of Confidence Intervals for Binomial Population Proportions in Astronomy: The Simplicity and Superiority of the Bayesian Approach. *PASA*, 28:128–139.

Cassaro, P., Dallacasa, D., and Stanghellini, C. (2009). A complete sample of low polarization CSO/MSO. *Astronomische Nachrichten*, 330:203.

Chhetri, R., Ekers, R. D., Jones, P. A., and Ricci, R. (2013). The AT20G high-angular-resolution catalogue. *MNRAS*, 434:956–965.

Chiaberge, M., Gilli, R., Lotz, J. M., and Norman, C. (2015). Radio Loud AGNs Are Mergers. *ApJ*, 806:147.

Clemens, M. S., Scaife, A., Vega, O., and Bressan, A. (2010). Starburst evolution: free-free absorption in the radio spectra of luminous IRAS galaxies. *MNRAS*, 405:887–897.

Coil, A. L., Blanton, M. R., Burles, S. M., et al. (2011). The PRIsm MUlti-object Survey (PRIMUS). I. Survey Overview and Characteristics. *ApJ*, 741:8.

Collier, J. D., Banfield, J. K., Norris, R. P., et al. (2014). Infrared-faint radio sources: a new population of high-redshift radio galaxies. *MNRAS*, 439:545–565.

Collier, J. D., Norris, R. P., Filipović, M. D., and Tothill, N. F. H. (2016). An evolutionary sequence of young radio galaxies. *Astronomische Nachrichten*, 337:36.

Condon, J. J. (1997). Errors in Elliptical Gaussian FITS. *PASP*, 109:166–172.

Condon, J. J., Cotton, W. D., Fomalont, E. B., et al. (2012). Resolving the Radio Source Background: Deeper Understanding through Confusion. *ApJ*, 758:23.

Condon, J. J., Cotton, W. D., Greisen, E. W., et al. (1998). The NRAO VLA Sky Survey. *AJ*, 115:1693–1716.

Condon, J. J., Cotton, W. D., Yin, Q. F., et al. (2003). The SIRTF First-Look Survey. I. VLA Image and Source Catalog. *AJ*, 125:2411–2426.

Condon, J. J., Huang, Z.-P., Yin, Q. F., and Thuan, T. X. (1991). Compact starbursts in ultraluminous infrared galaxies. *ApJ*, 378:65–76.

Coppejans, R., Cseh, D., Williams, W. L., van Velzen, S., and Falcke, H. (2015). Megahertz peaked-spectrum sources in the Boötes field I - a route towards finding high-redshift AGN. *MNRAS*, 450:1477–1485.

Crawford, E. J., Filipovic, M. D., De Horta, A. Y., et al. (2011). New 6 and 3-cm Radio-Continuum Maps of the Small Magellanic Cloud. Part I - The Maps. *Serbian Astronomical Journal*, 183:95–102.

Croton, D. J., Springel, V., White, S. D. M., et al. (2006). The many lives of active galactic nuclei: cooling flows, black holes and the luminosities and colours of galaxies. *MNRAS*, 365:11–28.

Cutri, R. M., Wright, E. L., Conrow, T., et al. (2011). Explanatory Supplement to the WISE Preliminary Data Release Products. Technical report.

Dallacasa, D., Stanghellini, C., Centonza, M., and Fanti, R. (2000). High frequency peakers. I. The bright sample. *A&A*, 363:887–900.

Davis, M., Guhathakurta, P., Konidaris, N. P., et al. (2007). The All-Wavelength Extended Groth Strip International Survey (AEGIS) Data Sets. *ApJ*, 660:L1–L6.

De Breuck, C., Klamer, I., Johnston, H., et al. (2006). A search for distant radio galaxies from SUMSS and NVSS - II. Optical spectroscopy[1*]. *MNRAS*, 366:58–72.

De Horta, A. Y., Collier, J. D., Filipović, M. D., et al. (2013). Radio confirmation of Galactic supernova remnant G308.3-1.4. *MNRAS*, 428:1980–1985.

De Horta, A. Y., Filipović, M. D., Bozzetto, L. M., et al. (2012). Multi-frequency study of supernova remnants in the Large Magellanic Cloud. The case of LMC SNR J0530-7007. *A&A*, 540:A25.

De Horta, A. Y., Filipovic, M. D., Crawford, E. J., et al. (2014a). Radio-Continuum Emission from the Young Galactic Supernova Remnant G1.9+0.3. *Serbian Astronomical Journal*, 189:41–51.

De Horta, A. Y., Sommer, E. R., Filipović, M. D., et al. (2014b). Multi-frequency Observations of a Superbubble in the LMC: The Case of LHA 120-N 70. *AJ*, 147:162.

de Vries, N., Snellen, I. A. G., Schilizzi, R. T., Mack, K.-H., and Kaiser, C. R. (2009). VLBI observations of the CORALZ sample: young radio sources at low redshift. *A&A*, 498:641–659.

de Vries, W. H., Barthel, P. D., and O'Dea, C. P. (1997). Radio spectra of Gigahertz Peaked Spectrum radio sources. *A&A*, 321:105–110.

Deller, A. T., Brisken, W. F., Phillips, C. J., et al. (2011). DiFX-2: A More Flexible, Efficient, Robust, and Powerful Software Correlator. *PASP*, 123:275–287.

Deller, A. T. and Middelberg, E. (2014). mJIVE-20: A Survey for Compact mJy Radio Objects with the Very Long Baseline Array. *AJ*, 147:14.

Deller, A. T., Tingay, S. J., Bailes, M., and West, C. (2007). DiFX: A Software Correlator for Very Long Baseline Interferometry Using Multiprocessor Computing Environments. *PASP*, 119:318–336.

Dickel, J. R., Gruendl, R. A., McIntyre, V. J., and Amy, S. W. (2010). A 4.8 and 8.6 GHz Survey of the Small Magellanic Cloud: The Images. *AJ*, 140:1511–1518.

El Bouchefry, K. (2009). X-ray identifications of FIRST radio sources in the XBoötes field. *MNRAS*, 396:2011–2037.

Elvis, M. (1994). Extreme quasars: observations and constraints. In Courvoisier, T. and Blecha, A., editors, *Multi-Wavelength Continuum Emission of AGN*, volume 159 of *IAU Symposium*, pages 25–28.

Emonts, B. H. C., Feain, I., Mao, M. Y., et al. (2011a). Molecular CO(1-0) Gas in the z ˜ 2 Radio Galaxy MRC 0152-209. *ApJ*, 734:L25.

Emonts, B. H. C., Norris, R. P., Feain, I., et al. (2011b). CO observations of high-z radio galaxies MRC 2104-242 and MRC 0943-242: spectral-line performance of the Compact Array Broadband Backend. *MNRAS*, 415:655–664.

Fanaroff, B. L. and Riley, J. M. (1974). The morphology of extragalactic radio sources of high and low luminosity. *MNRAS*, 167:31P–36P.

Fanti, C. (2009a). Radio properties of CSSs and GPSs. *Astronomische Nachrichten*, 330:120–127.

Fanti, C., Fanti, R., Dallacasa, D., et al. (1995). Are compact steep-spectrum sources young? *A&A*, 302:317.

Fanti, C., Pozzi, F., Dallacasa, D., et al. (2001). Multi-frequency VLA observations of a new sample of CSS/GPS radio sources. *A&A*, 369:380–420.

Fanti, C., Pozzi, F., Fanti, R., et al. (2000). ISO observations of a sample of Compact Steep Spectrum and GHz Peaked Spectrum radio galaxies. *A&A*, 358:499–513.

Fanti, R. (2009b). CSS and GPS research: A status report. *Astronomische Nachrichten*, 330:303.

Fanti, R., Fanti, C., Schilizzi, R. T., et al. (1990). On the nature of compact steep spectrum radio sources. *A&A*, 231:333–346.

Fazio, G. G., Hora, J. L., Allen, L. E., et al. (2004). The Infrared Array Camera (IRAC) for the Spitzer Space Telescope. *ApJS*, 154:10–17.

Filipović, M. D., Bohlsen, T., Reid, W., et al. (2002). An ATCA radio-continuum study of the Small Magellanic Cloud - I. Source catalogues at 1.42, 2.37, 4.80 and 8.64 GHz. *MNRAS*, 335:1085–1090.

Filipovic, M. D., Cajko, K. O., Collier, J. D., and Tothill, N. F. H. (2013). Radio-Continuum Observations of a Giant Radio Source QSO J0443.8-6141. *Serbian Astronomical Journal*, 187:1–10.

Filipovic, M. D., Jones, P. A., White, G. L., et al. (1997). A radio continuum study of the Magellanic Clouds V. Catalogues of radio sources in the Small Magellanic Cloud at 1.42, 2.45, 4.75, 4.85 and 8.55 GHz. *A&AS*, 121:321–326.

Franzen, T. M. O., Banfield, J. K., Hales, C. A., et al. (2015). ATLAS - I. Third release of 1.4 GHz mosaics and component catalogues. *MNRAS*, 453:4020–4036.

Franzen, T. M. O., Sadler, E. M., Chhetri, R., et al. (2014). Deep 20-GHz survey of the Chandra Deep Field South and SDSS Stripe 82: source catalogue and spectral properties. *MNRAS*, 439:1212–1230.

Frey, S., Paragi, Z., Mosoni, L., and Gurvits, L. I. (2005). High-resolution radio imaging of the most distant radio quasar SDSS J0836+0054. *A&A*, 436:L13–L16.

Gaensler, B. M. and Hunstead, R. W. (2000). Long-term Monitoring of Molonglo Calibrators. *PASA*, 17:72–82.

Garn, T. and Alexander, P. (2008). Deep 610-MHz Giant Metrewave Radio Telescope observations of the Spitzer extragalactic First Look Survey field - III. The radio properties of infrared-faint radio sources. *MNRAS*, 391:1000–1008.

Garrington, S. T., Garrett, M. A., and Polatidis, A. (1999). A VLBI and MERLIN Survey of faint, compact radio sources. *New A Rev.*, 43:629–632.

Gelderman, R. and Whittle, M. (1994). An optical study of compact steep-spectrum radio sources. 1: The spectroscopic data. *ApJS*, 91:491–505.

Giavalisco, M., Ferguson, H. C., Koekemoer, A. M., et al. (2004). The Great Observatories Origins Deep Survey: Initial Results from Optical and Near-Infrared Imaging. *ApJ*, 600:L93–L98.

Giroletti, M. and Polatidis, A. (2009). Samples and statistics of CSS and GPS sources. *Astronomische Nachrichten*, 330:193.

Grant, J. K., Taylor, A. R., Stil, J. M., et al. (2010). The DRAO Planck Deep Fields: The Polarization Properties of Radio Galaxies at 1.4 GHz. *ApJ*, 714:1689–1701.

Gregory, P. C., Scott, W. K., Douglas, K., and Condon, J. J. (1996). The GB6 Catalog of Radio Sources. *ApJS*, 103:427.

Griffith, M. R. and Wright, A. E. (1993). The Parkes-MIT-NRAO (PMN) surveys. I - The 4850 MHz surveys and data reduction. *AJ*, 105:1666–1679.

Griffith, M. R., Wright, A. E., Burke, B. F., and Ekers, R. D. (1995). The Parkes-MIT-NRAO (PMN) surveys. 6: Source catalog for the equatorial survey (-9.5 deg less than delta less than +10.0 deg). *ApJS*, 97:347–453.

Gugliucci, N. E., Taylor, G. B., Peck, A. B., and Giroletti, M. (2005). Dating COINS: Kinematic Ages for Compact Symmetric Objects. *ApJ*, 622:136–148.

Gupta, N., Salter, C. J., Saikia, D. J., Ghosh, T., and Jeyakumar, S. (2006). Probing radio source environments via HI and OH absorption. *MNRAS*, 373:972–992.

Hales, C. A., Murphy, T., Curran, J. R., et al. (2012). BLOBCAT: software to catalogue flood-filled blobs in radio images of total intensity and linear polarization. *MNRAS*, 425:979–996.

Hancock, P. J. (2009). High frequency GPS sources in the AT20G survey. *Astronomische Nachrichten*, 330:180.

Hancock, P. J., Murphy, T., Gaensler, B. M., Hopkins, A., and Curran, J. R. (2012). Compact continuum source finding for next generation radio surveys. *MNRAS*, 422:1812–1824.

Hancock, P. J., Sadler, E. M., Mahony, E. K., and Ricci, R. (2010). Observations and properties of candidate high-frequency GPS radio sources in the AT20G survey. *MNRAS*, 408:1187–1206.

Hancock, P. J., Tingay, S. J., Sadler, E. M., Phillips, C., and Deller, A. T. (2009). e-VLBI observations of GHz-peaked spectrum radio sources in nearby galaxies from the AT20G survey. *MNRAS*, 397:2030–2036.

Hardcastle, M. J., Evans, D. A., and Croston, J. H. (2007). Hot and cold gas accretion and feedback in radio-loud active galaxies. *MNRAS*, 376:1849–1856.

Harris, D. E., Costain, C. H., and Dewdney, P. E. (1984). The X-ray features of a single-lobed radio galaxy in Abell 754. *ApJ*, 280:532–541.

Harris, D. E., Junor, W., and Silverman, J. D. (1999). 26W20: an Apparently One-Sided Radio Galaxy. In *American Astronomical Society Meeting Abstracts #194*, volume 31 of *Bulletin of the American Astronomical Society*, page 899.

Herzog, A., Middelberg, E., Norris, R. P., et al. (2014). Infrared-faint radio sources are at high redshifts. Spectroscopic redshift determination of infrared-faint radio sources using the Very Large Telescope. *A&A*, 567:A104.

Herzog, A., Middelberg, E., Norris, R. P., et al. (2015a). Active galactic nuclei cores in infrared-faint radio sources. Very long baseline interferometry observations using the Very Long Baseline Array. *A&A*, 578:A67.

Herzog, A., Norris, R. P., Middelberg, E., et al. (2016). The radio spectral energy distribution of infrared-faint radio sources. *ArXiv e-prints*, arXiv:1607.02707.

Herzog, A., Norris, R. P., Middelberg, E., et al. (2015b). Infrared-faint radio sources remain undetected at far-infrared wavelengths. Deep photometric observations using the Herschel Space Observatory. *A&A*, 580:A7.

Higdon, J. L., Higdon, S. J. U., Weedman, D. W., et al. (2005). Spitzer Observations of Optically "Invisible" Radio and X-Ray Sources: High-Redshift Active Galactic Nuclei. *ApJ*, 626:58–69.

Higdon, J. L., Higdon, S. J. U., Willner, S. P., et al. (2008). Radio and Infrared Selected Optically Invisible Sources in the Boötes NDWFS. *ApJ*, 688:885–904.

Holt, J. (2009). The host galaxies of Compact Steep Spectrum and Gigahertz-Peaked Spectrum radio sources. *Astronomische Nachrichten*, 330:226.

Hopkins, P. F., Hernquist, L., Cox, T. J., and Kereš, D. (2008). A Cosmological Framework for the Co-Evolution of Quasars, Supermassive Black Holes, and Elliptical Galaxies. I. Galaxy Mergers and Quasar Activity. *ApJS*, 175:356–389.

Hovatta, T., Aller, M. F., Aller, H. D., et al. (2014). MOJAVE: Monitoring of Jets in Active Galactic Nuclei with VLBA Experiments. XI. Spectral Distributions. *AJ*, 147:143.

Hsieh, B. C., Yee, H. K. C., Lin, H., and Gladders, M. D. (2005). A Photometric Redshift Galaxy Catalog from the Red-Sequence Cluster Survey. *ApJS*, 158:161–177.

Huang, Z. P., Thuan, T. X., Chevalier, R. A., Condon, J. J., and Yin, Q. F. (1994). Compact radio sources in the starburst galaxy M82 and the Sigma-D relation for supernova remnants. *ApJ*, 424:114–125.

Huynh, M. T., Bell, M. E., Hopkins, A. M., Norris, R. P., and Seymour, N. (2015). The ATLAS 5.5 GHz survey of the extended Chandra Deep Field South: the second data release. *MNRAS*, 454:952–972.

Huynh, M. T., Hopkins, A. M., Lenc, E., et al. (2012). The ATLAS 5.5 GHz survey of the extended Chandra Deep Field South: catalogue, source counts and spectral indices. *MNRAS*, 426:2342–2358.

Huynh, M. T., Norris, R. P., Siana, B., and Middelberg, E. (2010). Evidence for Infrared-faint Radio Sources as z > 1 Radio-loud Active Galactic Nuclei. *ApJ*, 710:698–705.

Intema, H. T., Jagannathan, P., Mooley, K. P., and Frail, D. A. (2016). The GMRT 150 MHz All-sky Radio Survey: First Alternative Data Release TGSS ADR1. *ArXiv e-prints*, arXiv:1603.04368.

Jaffe, W. J. and Perola, G. C. (1973). Dynamical Models of Tailed Radio Sources in Clusters of Galaxies. *A&A*, 26:423.

Jarrett, T. H., Cohen, M., Masci, F., et al. (2011). The Spitzer-WISE Survey of the Ecliptic Poles. *ApJ*, 735:112.

Jarvis, M. J., Teimourian, H., Simpson, C., et al. (2009). The discovery of a typical radio galaxy at z = 4.88. *MNRAS*, 398:L83–L87.

Kaiser, C. R. and Best, P. N. (2007). Luminosity function, sizes and FR dichotomy of radio-loud AGN. *MNRAS*, 381:1548–1560.

Kameno, S., Horiuchi, S., Shen, Z.-Q., et al. (2000). Asymmetric Free-Free Absorption towards a Double Lobe of OQ 208. *PASJ*, 52:209.

Kardashev, N. S. (1962). Nonstationarity of Spectra of Young Sources of Nonthermal Radio Emission. *Soviet Ast.*, 6:317.

Kedziora-Chudczer, L., Jauncey, D. L., Wieringa, M. H., et al. (1997). PKS 0405-385: The Smallest Radio Quasar? *ApJ*, 490:L9–L12.

Kellermann, K. I. and Pauliny-Toth, I. I. K. (1981). Compact radio sources. *ARA&A*, 19:373–410.

Kettenis, M., van Langevelde, H. J., Reynolds, C., and Cotton, B. (2006). ParselTongue: AIPS Talking Python. In Gabriel, C., Arviset, C., Ponz, D., and Enrique, S., editors, *Astronomical Data Analysis Software and Systems XV*, volume 351 of *Astronomical Society of the Pacific Conference Series*, page 497.

Kewley, L. J., Heisler, C. A., Dopita, M. A., et al. (2000). Compact Radio Emission from Warm Infrared Galaxies. *ApJ*, 530:704–718.

Kimball, A. and Ivezic, Z. (2014). An Updated Version of the Unified Radio Catalog: A Multi-Wavelength Radio and Optical Catalog of Quasars and Radio Galaxies. *ArXiv e-prints*, arXiv:1401.1535.

Kimball, A. E. and Ivezić, Ž. (2008). A Unified Catalog of Radio Objects Detected by NVSS, First, WENSS, GB6, and SDSS. *AJ*, 136:684–712.

Klamer, I. J., Ekers, R. D., Bryant, J. J., et al. (2006). A search for distant radio galaxies from SUMSS and NVSS - III. Radio spectral energy distributions and the z-α correlation. *MNRAS*, 371:852–866.

Kunert, M., Marecki, A., Spencer, R. E., Kus, A. J., and Niezgoda, J. (2002). FIRST-based survey of Compact Steep Spectrum sources. I. MERLIN images of arc-second scale objects. *A&A*, 391:47–54.

Kunert-Bajraszewska, M. (2016). Dichotomy in the population of young AGN: Optical, radio, and X-ray properties. *Astronomische Nachrichten*, 337:27.

Kunert-Bajraszewska, M., Gawroński, M. P., Labiano, A., and Siemiginowska, A. (2010). A survey of low-luminosity compact sources and its implication for the evolution of radio-loud active galactic nuclei - I. Radio data. *MNRAS*, 408:2261–2278.

Kunert-Bajraszewska, M., Marecki, A., and Thomasson, P. (2006). FIRST-based survey of compact steep spectrum sources. IV. Multifrequency VLBA observations of very compact objects. *A&A*, 450:945–958.

Kunert-Bajraszewska, M., Marecki, A., Thomasson, P., and Spencer, R. E. (2005). FIRST-based survey of Compact Steep Spectrum sources. II. MERLIN and VLA observations of medium-sized symmetric objects. *A&A*, 440:93–105.

Labiano, A., Barthel, P. D., O'Dea, C. P., et al. (2007). GPS radio sources: new optical observations and an updated master list. *A&A*, 463:97–104.

Labiano, A., O'Dea, C. P., Barthel, P. D., de Vries, W. H., and Baum, S. A. (2008). Star formation in the hosts of GHz peaked spectrum and compact steep spectrum radio galaxies. *A&A*, 477:491–501.

Lane, W. M., Cohen, A. S., Cotton, W. D., et al. (2008). The VLA Low-Frequency Sky Survey (VLSS). In Bridle, A. H., Condon, J. J., and Hunt, G. C., editors, *Frontiers of Astrophysics: A Celebration of NRAO's 50th Anniversary*, volume 395 of *Astronomical Society of the Pacific Conference Series*, page 370.

Lang, K. R. (1980). *Astrophysical Formulae. A Compendium for the Physicist and Astrophysicist.*

Large, M. I., Mills, B. Y., Little, A. G., Crawford, D. F., and Sutton, J. M. (1981). The Molonglo Reference Catalogue of Radio Sources. *MNRAS*, 194:693.

Leverenz, H., Filipović, M. D., Bojičić, I. S., et al. (2016). Radio planetary nebulae in the Small Magellanic Cloud. *Ap&SS*, 361:108.

Lonsdale, C. J., Cappallo, R. J., Morales, M. F., et al. (2009). The Murchison Widefield Array: Design Overview. *IEEE Proceedings*, 97:1497–1506.

Lonsdale, C. J., Smith, H. E., Rowan-Robinson, M., et al. (2003). SWIRE: The SIRTF Wide-Area Infrared Extragalactic Survey. *PASP*, 115:897–927.

Macquart, J.-P., Godfrey, L. E. H., Bignall, H. E., and Hodgson, J. A. (2013). The Microarcsecond Structure of an Active Galactic Nucleus Jet via Interstellar Scintillation. *ApJ*, 765:142.

Magnelli, B., Ivison, R. J., Lutz, D., et al. (2015). The far-infrared/radio correlation and radio spectral index of galaxies in the SFR-M plane up to z˜2. *A&A*, 573:A45.

Maini, A., Prandoni, I., Norris, R. P., et al. (2016). Infrared-Faint Radio Sources in the SERVS deep fields: Pinpointing AGNs at high redshift. *ArXiv e-prints*, arXiv:1609.02278.

Mainieri, V., Kellermann, K. I., Fomalont, E. B., et al. (2008). The VLA Survey of the Chandra Deep Field-South. II. Identification and Host Galaxy Properties of Submillijansky Sources. *ApJS*, 179:95–113.

Malbon, R. K., Baugh, C. M., Frenk, C. S., and Lacey, C. G. (2007). Black hole growth in hierarchical galaxy formation. *MNRAS*, 382:1394–1414.

Manolakou, K. and Kirk, J. G. (2002). Modelling the spectral evolution of classical double radio sources. *A&A*, 391:127–138.

Mao, M. Y., Sharp, R., Norris, R. P., et al. (2012). The Australia Telescope Large Area Survey: spectroscopic catalogue and radio luminosity functions. *MNRAS*, 426:3334–3348.

Mao, M. Y., Sharp, R., Saikia, D. J., et al. (2010). Wide-angle tail galaxies in ATLAS. *MNRAS*, 406:2578–2590.

Mao, S. A., Gaensler, B. M., Stanimirović, S., et al. (2008). A Radio and Optical Polarization Study of the Magnetic Field in the Small Magellanic Cloud. *ApJ*, 688:1029–1049.

Marr, J., Snell, R., and Kurtz, S. (2015). *Fundamentals of Radio Astronomy: Observational Methods*. Series in Astronomy and Astrophysics. CRC Press.

Marr, J. M., Perry, T. M., Read, J., Taylor, G. B., and Morris, A. O. (2014). Multi-frequency Optical-depth Maps and the Case for Free-Free Absorption in Two Compact Symmetric Radio Sources: The CSO Candidate J1324 + 4048 and the CSO J0029 + 3457. *ApJ*, 780:178.

Marr, J. M., Taylor, G. B., and Crawford, III, F. (2001). Nonuniform Free-Free Absorption in the GPS Radio Galaxy 0108+388. *ApJ*, 550:160–171.

Mauch, T., Murphy, T., Buttery, H. J., et al. (2003). SUMSS: a wide-field radio imaging survey of the southern sky - II. The source catalogue. *MNRAS*, 342:1117–1130.

Mauduit, J.-C., Lacy, M., Farrah, D., et al. (2012). The Spitzer Extragalactic Representative Volume Survey (SERVS): Survey Definition and Goals. *PASP*, 124:714–736.

Meyer, M. J., Zwaan, M. A., Webster, R. L., et al. (2004). The HIPASS catalogue - I. Data presentation. *MNRAS*, 350:1195–1209.

Middelberg, E. (2006). Automated Editing of Radio Interferometer Data with pieflag. *PASA*, 23:64–68.

Middelberg, E., Deller, A., Morgan, J., et al. (2011a). Wide-field VLBA observations of the Chandra deep field South. *A&A*, 526:A74.

Middelberg, E., Deller, A. T., Norris, R. P., et al. (2013). Mosaiced wide-field VLBI observations of the Lockman Hole/XMM. *A&A*, 551:A97.

Middelberg, E., Norris, R. P., Cornwell, T. J., et al. (2008a). Deep Australia Telescope Large Area Survey Radio Observations of the European Large Area ISO Survey S1/Spitzer Wide-Area Infrared Extragalactic Field. *AJ*, 135:1276–1290.

Middelberg, E., Norris, R. P., Hales, C. A., et al. (2011b). The radio properties of infrared-faint radio sources. *A&A*, 526:A8.

Middelberg, E., Norris, R. P., Tingay, S., et al. (2008b). The first VLBI image of an infrared-faint radio source. *A&A*, 491:435–439.

Miley, G. and De Breuck, C. (2008). Distant radio galaxies and their environments. *A&A Rev.*, 15:67–144.

Miller, N. A., Bonzini, M., Fomalont, E. B., et al. (2013). The Very Large Array 1.4 GHz Survey of the Extended Chandra Deep Field South: Second Data Release. *ApJS*, 205:13.

Mohan, N. and Rafferty, D. (2015). PyBDSM: Python Blob Detection and Source Measurement. Astrophysics Source Code Library.

Morganti, B., Emonts, R., Holt, J., et al. (2009). Gas and stars in compact (young) radio sources. *Astronomische Nachrichten*, 330:233.

Morganti, R., Greenhill, L. J., Peck, A. B., Jones, D. L., and Henkel, C. (2004). Disks, tori, and cocoons: emission and absorption diagnostics of AGN environments. *New A Rev.*, 48:1195–1209.

Mullin, L. M., Riley, J. M., and Hardcastle, M. J. (2008). Observed properties of FRII quasars and radio galaxies at $z < 1.0$. *MNRAS*, 390:595–621.

Murgia, M. (2003). Spectral Ages of CSOs and CSS Sources. *PASA*, 20:19–24.

Murgia, M., Fanti, C., Fanti, R., et al. (1999). Synchrotron spectra and ages of compact steep spectrum radio sources. *A&A*, 345:769–777.

Murphy, T., Sadler, E. M., Ekers, R. D., et al. (2010). The Australia Telescope 20 GHz Survey: the source catalogue. *MNRAS*, 402:2403–2423.

Murray, S. S., Kenter, A., Forman, W. R., et al. (2005). XBootes: An X-Ray Survey of the NDWFS Bootes Field. I. Overview and Initial Results. *ApJS*, 161:1–8.

Mutoh, M., Inoue, M., Kameno, S., et al. (2002). A New Test for the Absorption Mechanism of GPS Radio Sources Using Polarization Properties. *PASJ*, 54:131–138.

Narayan, R. (1992). The Physics of Pulsar Scintillation. *Philosophical Transactions of the Royal Society of London Series A*, 341:151–165.

Norris, R. P. (1992). Active galaxies - unity or diversity? *Australian Journal of Astronomy*, 4:117–124.

Norris, R. P., Afonso, J., Appleton, P. N., et al. (2006). Deep ATLAS Radio Observations of the Chandra Deep Field-South/Spitzer Wide-Area Infrared Extragalactic Field. *AJ*, 132:2409–2423.

Norris, R. P., Afonso, J., Bacon, D., et al. (2013). Radio Continuum Surveys with Square Kilometre Array Pathfinders. *PASA*, 30:20.

Norris, R. P., Afonso, J., Cava, A., et al. (2011a). Deep Spitzer Observations of Infrared-faint Radio Sources: High-redshift Radio-loud Active Galactic Nuclei? *ApJ*, 736:55.

Norris, R. P., Hopkins, A. M., Afonso, J., et al. (2011b). EMU: Evolutionary Map of the Universe. *PASA*, 28:215–248.

Norris, R. P., Lenc, E., Roy, A. L., and Spoon, H. (2012). The radio core of the ultraluminous infrared galaxy F00183-7111: watching the birth of a quasar. *MNRAS*, 422:1453–1459.

Norris, R. P., Tingay, S., Phillips, C., et al. (2007). Very long baseline interferometry detection of an Infrared-Faint Radio Source. *MNRAS*, 378:1434–1438.

O'Brien, A. N., Filipović, M. D., Crawford, E. J., et al. (2013). Radio-continuum study of the nearby Sculptor group Galaxies. Part 2: NGC 55 at λ=20, 13, 6 and 3 cm. *Ap&SS*, 347:159–168.

O'Dea, C. P. (1998). The Compact Steep-Spectrum and Gigahertz Peaked-Spectrum Radio Sources. *PASP*, 110:493–532.

O'Dea, C. P. and Baum, S. A. (1997). Constraints on Radio Source Evolution from the Compact Steep Spectrum and GHz Peaked Spectrum Radio Sources. *AJ*, 113:148–161.

O'Dea, C. P., Baum, S. A., and Stanghellini, C. (1991). What are the gigahertz peaked-spectrum radio sources? *ApJ*, 380:66–77.

Oliver, S., Rowan-Robinson, M., Alexander, D. M., et al. (2000). The European Large Area ISO Survey - I. Goals, definition and observations. *MNRAS*, 316:749–767.

Orienti, M. (2016). Radio properties of Compact Steep Spectrum and GHz-Peaked Spectrum radio sources. *Astronomische Nachrichten*, 337:9.

Orienti, M. and Dallacasa, D. (2008a). Are young radio sources in equipartition? *A&A*, 487:885–894.

Orienti, M. and Dallacasa, D. (2008b). On the Nature of High Frequency Peakers: Young Radio Sources or Flaring Blazars? In Rector, T. A. and De Young, D. S., editors, *Extragalactic Jets: Theory and Observation from Radio to Gamma Ray*, volume 386 of *Astronomical Society of the Pacific Conference Series*, page 196.

Orienti, M. and Dallacasa, D. (2014). Physical properties of young radio sources: VLBA observations of high-frequency peaking radio sources. *MNRAS*, 438:463–475.

Orienti, M., Dallacasa, D., Fanti, C., et al. (2004). The B3-VLA CSS sample. V. VLBA images at 6 and 3.6 cm. *A&A*, 426:463–470.

Orienti, M., Dallacasa, D., and Stanghellini, C. (2007). Constraining the nature of high frequency peakers. The spectral variability. *A&A*, 475:813–820.

Orienti, M., Dallacasa, D., and Stanghellini, C. (2010a). Spectral variability in faint high-frequency peakers. *MNRAS*, 408:1075–1088.

Orienti, M., Dallacasa, D., Tinti, S., and Stanghellini, C. (2006). VLBA images of high frequency peakers. *A&A*, 450:959–970.

Orienti, M., Murgia, M., and Dallacasa, D. (2010b). The last breath of the young gigahertz-peaked spectrum radio source PKS1518+047. *MNRAS*, 402:1892–1898.

Parma, P., Murgia, M., de Ruiter, H. R., et al. (2007). In search of dying radio sources in the local universe. *A&A*, 470:875–888.

Peck, A. B. and Taylor, G. B. (2000). The COINS Sample: VLBA Identifications of Compact Symmetric Objects. *ApJ*, 534:90–103.

Peck, A. B., Taylor, G. B., and Conway, J. E. (1999). Obscuration of the Parsec-Scale Jets in the Compact Symmetric Object 1946+708. *ApJ*, 521:103–111.

Petric, A. O., Carilli, C. L., Bertoldi, F., et al. (2003). Sensitive Observations at 1.4 and 250 GHz of $z > 5$ QSOs. *AJ*, 126:15–23.

Pihlström, Y. M., Conway, J. E., and Vermeulen, R. C. (2003). The presence and distribution of H I absorbing gas in sub-galactic sized radio sources. *A&A*, 404:871–881.

Polatidis, A. G. (2009). Expansion velocities and kinematic ages of Compact Symmetric Objects. *Astronomische Nachrichten*, 330:149.

Polatidis, A. G. and Conway, J. E. (2003). Proper Motions in Compact Symmetric Objects. *PASA*, 20:69–74.

Porcas, R. W. (1998). VLBI Observations of Gravitational Lenses. In Zensus, J. A., Taylor, G. B., and Wrobel, J. M., editors, *IAU Colloq. 164: Radio Emission from Galactic and Extragalactic Compact Sources*, volume 144 of *Astronomical Society of the Pacific Conference Series*, page 303.

Randall, K. E., Hopkins, A. M., Norris, R. P., and Edwards, P. G. (2011). An unbiased sample of bright southern compact steep spectrum and gigahertz peaked spectrum sources. *MNRAS*, 416:1135–1151.

Randall, K. E., Hopkins, A. M., Norris, R. P., et al. (2012). Spectral index properties of milliJansky radio sources. *MNRAS*, 421:1644–1660.

Readhead, A. C. S. (1994). Equipartition brightness temperature and the inverse Compton catastrophe. *ApJ*, 426:51–59.

Readhead, A. C. S., Taylor, G. B., Pearson, T. J., and Wilkinson, P. N. (1996). Compact Symmetric Objects and the Evolution of Powerful Extragalactic Radio Sources. *ApJ*, 460:634.

Rengelink, R. B., Tang, Y., de Bruyn, A. G., et al. (1997). The Westerbork Northern Sky Survey (WENSS), I. A 570 square degree Mini-Survey around the North Ecliptic Pole. *A&AS*, 124:259–280.

Richards, G. T., Nichol, R. C., Gray, A. G., et al. (2004). Efficient Photometric Selection of Quasars from the Sloan Digital Sky Survey: 100,000 $z < 3$ Quasars from Data Release One. *ApJS*, 155:257–269.

Rieke, G. H., Alonso-Herrero, A., Weiner, B. J., et al. (2009). Determining Star Formation Rates for Infrared Galaxies. *ApJ*, 692:556–573.

Rieke, G. H., Young, E. T., Engelbracht, C. W., et al. (2004). The Multiband Imaging Photometer for Spitzer (MIPS). *ApJS*, 154:25–29.

Risaliti, G., Elvis, M., and Nicastro, F. (2002). Ubiquitous Variability of X-Ray-absorbing Column Densities in Seyfert 2 Galaxies. *ApJ*, 571:234–246.

Rosati, P., Tozzi, P., Giacconi, R., et al. (2002). The Chandra Deep Field-South: The 1 Million Second Exposure. *ApJ*, 566:667–674.

Rossetti, A., Fanti, C., Fanti, R., Dallacasa, D., and Stanghellini, C. (2006). The B3-VLA CSS sample. VI. VLA images at 2 cm. *A&A*, 449:49–60.

Rossetti, A., Mantovani, F., Dallacasa, D., Fanti, C., and Fanti, R. (2005). Multi-frequency VLBA observations of compact sources from the Peacock and Wall catalogue. *A&A*, 434:449–458.

Rowan-Robinson, M., Babbedge, T., Oliver, S., et al. (2008). Photometric redshifts in the SWIRE Survey. *MNRAS*, 386:697–714.

Sadler, E. M. (2016). GPS/CSS radio sources and their relation to other AGN. *Astronomische Nachrichten*, 337:105.

Saikia, D. J., Jeyakumar, S., Mantovani, F., et al. (2003). Symmetry Parameters of CSS Sources: Evidence of Fuelling? *PASA*, 20:50–56.

Sault, B. and Killeen, N. (2011). *Miriad Users Guide*. Australia Telescope National Facility.

Sault, R. J., Teuben, P. J., and Wright, M. C. H. (1995). A Retrospective View of MIRIAD. In Shaw, R. A., Payne, H. E., and Hayes, J. J. E., editors, *Astronomical Data Analysis Software and Systems IV*, volume 77 of *Astronomical Society of the Pacific Conference Series*, page 433.

Saxton, C. J., Sutherland, R. S., Bicknell, G. V., Blanchet, G. F., and Wagner, S. J. (2002). Complex shock structure in the western hot-spot of Pictor A. *A&A*, 393:765–792.

Schawinski, K., Koss, M., Berney, S., and Sartori, L. F. (2015). Active galactic nuclei flicker: an observational estimate of the duration of black hole growth phases of $\sim 10^5$ yr. *MNRAS*, 451:2517–2523.

Schmidt, S. J., Connolly, A. J., and Hopkins, A. M. (2006). The DRaGONS Survey: A Search for High-Redshift Radio Galaxies and Heavily Obscured Active Galactic Nuclei. *ApJ*, 649:63–78.

Schnitzeler, D. H. F. M. (2010). The latitude dependence of the rotation measures of NVSS sources. *MNRAS*, 409:L99–L103.

Scott, M. A. and Readhead, A. C. S. (1977). The low-frequency structure of powerful radio sources and limits to departures from equipartition. *MNRAS*, 180:539–550.

Seymour, N., Altieri, B., De Breuck, C., et al. (2012). Rapid Coeval Black Hole and Host Galaxy Growth in MRC 1138-262: The Hungry Spider. *ApJ*, 755:146.

Seymour, N., Stern, D., and De Breuck, C. (2007). Spitzer Observations of High Redshift Radio Galaxies. In Afonso, J., Ferguson, H. C., Mobasher, B., and Norris, R., editors, *Deepest Astronomical Surveys*, volume 380 of *Astronomical Society of the Pacific Conference Series*, page 393.

Shabala, S. S., Ting, Y.-S., Kaviraj, S., et al. (2012). Galaxy Zoo: dust lane early-type galaxies are tracers of recent, gas-rich minor mergers. *MNRAS*, 423:59–67.

Shulevski, A., Morganti, R., Oosterloo, T., and Struve, C. (2012). Recurrent radio emission and gas supply: the radio galaxy B2 0258+35. *A&A*, 545:A91.

Siemiginowska, A., Cheung, C. C., LaMassa, S., et al. (2005). X-Ray Cluster Associated with the z = 1.063 CSS Quasar 3C 186: The Jet is Not Frustrated. *ApJ*, 632:110–121.

Silverman, J. D., Harris, D. E., and Junor, W. (1998). Multiwavelength observations of 26W20, a radio galaxy which displays BL Lacertae characteristics. *A&A*, 335:443–448.

Singh, V., Beelen, A., Wadadekar, Y., et al. (2014). Multiwavelength characterization of faint ultra steep spectrum radio sources: A search for high-redshift radio galaxies. *A&A*, 569:A52.

Sirothia, S. K., Dennefeld, M., Saikia, D. J., et al. (2009). 325-MHz observations of the ELAIS-N1 field using the Giant Metrewave Radio Telescope. *MNRAS*, 395:269–281.

Smith, H. E., Lonsdale, C. J., Lonsdale, C. J., and Diamond, P. J. (1998). A Starburst Revealed—Luminous Radio Supernovae in the Nuclei of ARP 220. *ApJ*, 493:L17–L21.

Snellen, I. A. G., Mack, K.-H., Schilizzi, R. T., and Tschager, W. (2003). Constraining the Evolution of Young Radio-Loud AGN. *PASA*, 20:38–41.

Snellen, I. A. G., Mack, K.-H., Schilizzi, R. T., and Tschager, W. (2004). The CORALZ sample - I. Young radio-loud active galactic nuclei at low redshift. *MNRAS*, 348:227–234.

Snellen, I. A. G., Schilizzi, R. T., de Bruyn, A. G., et al. (1998). A new sample of faint Gigahertz Peaked Spectrum radio sources. *A&AS*, 131:435–449.

Snellen, I. A. G., Schilizzi, R. T., Miley, G. K., et al. (1999). Faint Gigahertz Peaked Spectrum sources and the evolution of young radio sources. *New A Rev.*, 43:675–679.

Snellen, I. A. G., Schilizzi, R. T., Miley, G. K., et al. (2000). On the evolution of young radio-loud AGN. *MNRAS*, 319:445–456.

Spencer, R. E., McDowell, J. C., Charlesworth, M., et al. (1989). MERLIN and VLA observations of compact steep-spectrum radio sources. *MNRAS*, 240:657–687.

Spilker, J. S., Aravena, M., Marrone, D. P., et al. (2015). Sub-kiloparsec Imaging of Cool Molecular Gas in Two Strongly Lensed Dusty, Star-forming Galaxies. *ApJ*, 811:124.

Stanghellini, C. (2003). Radio Properties of GPS and CSS Sources: Galaxies versus Quasars. *PASA*, 20:118–122.

Stanghellini, C., O'Dea, C. P., Baum, S. A., et al. (1997). A VLBI study of GHz-peaked-spectrum radio sources. I. VLBI images at 6cm. *A&A*, 325:943–953.

Stanghellini, C., O'Dea, C. P., Dallacasa, D., et al. (1998). A complete sample of GHz-peaked-spectrum radio sources and its radio properties. *A&AS*, 131:303–315.

Sturm, R., Drašković, D., Filipović, M. D., et al. (2013). Active galactic nuclei behind the SMC selected from radio and X-ray surveys. *A&A*, 558:A101.

Sutherland, R. S. and Bicknell, G. V. (2007). Interaction of jets with the ISM of radio galaxies. *Ap&SS*, 311:293–303.

Sutinjo, A., O'Sullivan, J., Lenc, E., et al. (2015). Understanding instrumental Stokes leakage in Murchison Widefield Array polarimetry. *Radio Science*, 50:52–65.

Taylor, A. R., Stil, J. M., and Sunstrum, C. (2009). A Rotation Measure Image of the Sky. *ApJ*, 702:1230–1236.

Tingay, S. J. and de Kool, M. (2003). An Investigation of Synchrotron Self-absorption and Free-Free Absorption Models in Explanation of the Gigahertz-peaked Spectrum of PKS 1718-649. *AJ*, 126:723–733.

Tingay, S. J. and Edwards, P. G. (2015). The multifrequency parsec-scale structure of PKS 2254-367 (IC 1459): a luminosity-dependent break in morphology for the precursors of radio galaxies? *MNRAS*, 448:252–257.

Tingay, S. J., Goeke, R., Bowman, J. D., et al. (2013). The Murchison Widefield Array: The Square Kilometre Array Precursor at Low Radio Frequencies. *PASA*, 30:e007.

Tingay, S. J., Jauncey, D. L., King, E. A., et al. (2003). ATCA Monitoring Observations of 202 Compact Radio Sources in Support of the VSOP AGN Survey. *PASJ*, 55:351–384.

Tingay, S. J., Jauncey, D. L., Reynolds, J. E., et al. (1997). The Nearest GHz Peaked-Spectrum Radio Galaxy, PKS 1718-649. *AJ*, 113:2025–2030.

Tingay, S. J., Macquart, J.-P., Collier, J. D., et al. (2015). The Spectral Variability of the GHz-Peaked Spectrum Radio Source PKS 1718-649 and a Comparison of Absorption Models. *AJ*, 149:74.

Tinti, S., Dallacasa, D., de Zotti, G., Celotti, A., and Stanghellini, C. (2005). High Frequency Peakers: Young radio sources or flaring blazars? *A&A*, 432:31–43.

Tinti, S. and de Zotti, G. (2006). Constraints on evolutionary properties of GHz Peaked Spectrum galaxies. *A&A*, 445:889–899.

Torniainen, I., Tornikoski, M., Lähteenmäki, A., et al. (2007). Radio continuum spectra of gigahertz-peaked spectrum galaxies. *A&A*, 469:451–457.

Torniainen, I., Tornikoski, M., Teräsranta, H., Aller, M. F., and Aller, H. D. (2005). Long term variability of gigahertz-peaked spectrum sources and candidates. *A&A*, 435:839–856.

Tremblay, S. E. (2011). *Early Stages of Radio Galaxy Evolution*. PhD thesis, The University of New Mexico.

Tremblay, S. E., Taylor, G. B., Helmboldt, J. F., Fassnacht, C. D., and Pearson, T. J. (2008). A Shrinking Compact Symmetric Object: J11584+2450? *ApJ*, 684:153–159.

Tremblay, S. E., Taylor, G. B., Helmboldt, J. F., Fassnacht, C. D., and Romani, R. W. (2009). Identifying Compact Symmetric Objects from the VLBA Imaging and Polarization Survey. *Astronomische Nachrichten*, 330:206.

Turtle, A. J., Ye, T., Amy, S. W., and Nicholls, J. (1998). A radio survey of the SMC at 843 MHz with the MOST: I. The survey. *PASA*, 15:280–298.

Tzioumis, T. (2010). VLBI progress down under - First VLBI with ASKAP and NZ. In *10th European VLBI Network Symposium and EVN Users Meeting: VLBI and the New Generation of Radio Arrays*, page 20.

van Breugel, W., Miley, G., and Heckman, T. (1984). Studies of kiloparsec-scale, steep-spectrum radio cores. I VLA maps. *AJ*, 89:5–22.

van Haarlem, M. P., Wise, M. W., Gunst, A. W., et al. (2013). LOFAR: The LOw-Frequency ARray. *A&A*, 556:A2.

Verkhodanov, O. V., Kopylov, A. I., Pariiskii, Y. N., et al. (2002). Color Redshifts and the Age of the Stellar Population of Distant RC Radio Galaxies. *Astronomy Reports*, 46:531–542.

Vermeulen, R. C., Pihlström, Y. M., Tschager, W., et al. (2003). Observations of H I absorbing gas in compact radio sources at cosmological redshifts. *A&A*, 404:861–870.

Voges, W., Aschenbach, B., Boller, T., et al. (1999). ROSAT All-Sky Bright Source Catalogue (1RXS) (Voges+ 1999). *VizieR Online Data Catalog*, 9010:0.

Voges, W., Aschenbach, B., Boller, T., et al. (2000). ROSAT All-Sky Survey Faint Source Catalog (Voges+ 2000). *VizieR Online Data Catalog*, 9029:0.

Walker, M. A. (1998). Interstellar scintillation of compact extragalactic radio sources. *MNRAS*, 294:307.

Wall, J. V. and Jenkins, C. R. (2012). *Practical Statistics for Astronomers*.

Wayth, R. B., Lenc, E., Bell, M. E., et al. (2015). GLEAM: The GaLactic and Extragalactic All-Sky MWA Survey. *PASA*, 32:e025.

Werner, M. W., Murphy, D. W., Livingston, J. H., et al. (2012). Spitzer Observations of Hotspots in Radio Lobes. *ApJ*, 759:86.

Wilkinson, P. N., Polatidis, A. G., Readhead, A. C. S., Xu, W., and Pearson, T. J. (1994). Two-sided ejection in powerful radio sources: The compact symmetric objects. *ApJ*, 432:L87–L90.

Williams, W. L., Intema, H. T., and Röttgering, H. J. A. (2013). T-RaMiSu: the Two-meter Radio Mini Survey. I. The Boötes Field. *A&A*, 549:A55.

Willott, C. J., Rawlings, S., Jarvis, M. J., and Blundell, K. M. (2003). Near-infrared imaging and the K-z relation for radio galaxies in the 7C Redshift Survey. *MNRAS*, 339:173–188.

Wilson, W. E., Ferris, R. H., Axtens, P., et al. (2011). The Australia Telescope Compact Array Broad-band Backend: description and first results. *MNRAS*, 416:832–856.

Wong, G. F., Crawford, E. J., Filipovic, M. D., et al. (2012). New 6 and 3-cm Radio-Continuum Maps of the Small Magellanic Cloud: Part II - Point Source Catalogue. *Serbian Astronomical Journal*, 184:93–95.

Wong, G. F., Filipovic, M. D., Crawford, E. J., et al. (2011a). New 20-cm Radio-Continuum Study of the Small Magellanic Cloud: Part I - Images. *Serbian Astronomical Journal*, 182:43–52.

Wong, G. F., Filipovic, M. D., Crawford, E. J., et al. (2011b). New 20-cm Radio-Continuum Study of the Small Magellanic Cloud: Part II - Point Sources. *Serbian Astronomical Journal*, 183:103–106.

Wright, E. L. (2006). A Cosmology Calculator for the World Wide Web. *PASP*, 118:1711–1715.

Wright, E. L., Eisenhardt, P. R. M., Mainzer, A. K., et al. (2010). The Wide-field Infrared Survey Explorer (WISE): Mission Description and Initial On-orbit Performance. *AJ*, 140:1868–1881.

Wright, E. L. and WISE Team (2009). WISE - the Wide-field Infrared Survey Explorer. In *American Astronomical Society Meeting Abstracts #214*, volume 214 of *American Astronomical Society Meeting Abstracts*, page 217.01.

Yan, L., Donoso, E., Tsai, C.-W., et al. (2013). Characterizing the Mid-infrared Extragalactic Sky with WISE and SDSS. *AJ*, 145:55.

Yuan, F., Lidman, C., Davis, T. M., et al. (2015). OzDES multifibre spectroscopy for the Dark Energy Survey: first-year operation and results. *MNRAS*, 452:3047–3063.

Zinn, P.-C., Middelberg, E., and Ibar, E. (2011). Infrared-faint radio sources: a cosmological view. AGN number counts, the cosmic X-ray background and SMBH formation. *A&A*, 531:A14.

Zinn, P.-C., Middelberg, E., Norris, R. P., et al. (2012). The Australia Telescope Large Area Survey: 2.3 GHz observations of ELAIS-S1 and CDF-S. Spectral index properties of the faint radio sky. *A&A*, 544:A38.

Appendix A

Papers published during PhD

The following list constitutes the papers that I published during the course of my PhD. Where I was not first author, the estimated percentage of work that I contributed toward the paper has been listed at the end of the reference in bold.

Aravena, M., Spilker, J. S., Bethermin, M., et al. (2016). A survey of the cold molecular gas in gravitationally lensed star-forming galaxies at $z > 2$. *MNRAS*, 457:4406–4420

Citations: 8 $<$ 10%

Collier, J. D., Banfield, J. K., Norris, R. P., et al. (2014). Infrared-faint radio sources: a new population of high-redshift radio galaxies. *MNRAS*, 439:545–565

Citations: 9

Collier, J. D., Norris, R. P., Filipović, M. D., and Tothill, N. F. H. (2016). An evolutionary sequence of young radio galaxies. *Astronomische Nachrichten*, 337:36

Citations: 1

De Horta, A. Y., Collier, J. D., Filipović, M. D., et al. (2013). Radio confirmation of Galactic supernova remnant G308.3-1.4. *MNRAS*, 428:1980–1985

Citations: 6 50%

De Horta, A. Y., Filipović, M. D., Bozzetto, L. M., et al. (2012). Multi-frequency study of supernova remnants in the Large Magellanic Cloud. The case of LMC SNR J0530-7007. *A&A*, 540:A25

Citations: 16 $<$ 10%

De Horta, A. Y., Filipovic, M. D., Crawford, E. J., et al. (2014a). Radio-Continuum Emission from the Young Galactic Supernova Remnant G1.9+0.3. *Serbian Astronomical Journal*, 189:41–51

Citations: 4 $<$ 10%

De Horta, A. Y., Sommer, E. R., Filipović, M. D., et al. (2014b). Multi-frequency Observations of a Superbubble in the LMC: The Case of LHA 120-N 70. *AJ*, 147:162

Citations: 3 $<$ 10%

Filipovic, M. D., Cajko, K. O., Collier, J. D., and Tothill, N. F. H. (2013). Radio-Continuum Observations of a Giant Radio Source QSO J0443.8-6141. *Serbian Astronomical Journal*, 187:1–10 **30%**

Herzog, A., Middelberg, E., Norris, R. P., et al. (2015a). Active galactic nuclei cores in infrared-faint radio sources. Very long baseline interferometry observations using the Very Long Baseline Array. *A&A*, 578:A67

Citations: 4 10%

Leverenz, H., Filipović, M. D., Bojičić, I. S., et al. (2016). Radio planetary nebulae in the Small Magellanic Cloud. *Ap&SS*, 361:108 **< 10%**

O'Brien, A. N., Filipović, M. D., Crawford, E. J., et al. (2013). Radio-continuum study of the nearby Sculptor group Galaxies. Part 2: NGC 55 at λ=20, 13, 6 and 3 cm. *Ap&SS*, 347:159–168

Citations: 2 < 10%

Spilker, J. S., Aravena, M., Marrone, D. P., et al. (2015). Sub-kiloparsec Imaging of Cool Molecular Gas in Two Strongly Lensed Dusty, Star-forming Galaxies. *ApJ*, 811:124

Citations: 9 < 10%

Sturm, R., Drašković, D., Filipović, M. D., et al. (2013). Active galactic nuclei behind the SMC selected from radio and X-ray surveys. *A&A*, 558:A101

Citations: 3 < 10%

Tingay, S. J., Macquart, J.-P., Collier, J. D., et al. (2015). The Spectral Variability of the GHz-Peaked Spectrum Radio Source PKS 1718-649 and a Comparison of Absorption Models. *AJ*, 149:74

Citations: 11 30%

Wong, G. F., Crawford, E. J., Filipovic, M. D., et al. (2012). New 6 and 3-cm Radio-Continuum Maps of the Small Magellanic Cloud: Part II - Point Source Catalogue. *Serbian Astronomical Journal*, 184:93–95

Citations: 6 < 10%

Appendix B

The work completed by myself and others used in this thesis

The work presented in this thesis has been completed within various collaborations, within which I did most of the work, but some of which was done by co-investigators. Here I present a detailed outline of the major components from this thesis completed by me and by others. For clarity, I've printed in italics the work done by others. Sections 3.4 and 4.4 have been excluded, since individual statements about the work completed by me have been listed there. Any other work not listed here (e.g. s11 - section 4.3.3) was entirely my own work.

B.0.1 IFRS sample from Collier et al. (2014)

- *Co-authors Julie Banfield, Amy Kimball and Dominic Schnitzeler gave me a copy of the radio data within the URC*
- I updated the fluxes and positions according to the URC version 2.0
- I cross-matched to *WISE* and converted the magnitudes to flux densities
- I cross-matched to all ancillary data and listed the survey fields within which the IFRSs fall
- I selected the candidate IFRS sample of 1471 before visual inspection
- *Co-author Julie Banfield created postage stamps between FIRST and WISE, visually inspected the sources and discarded some of them*
- I performed the misidentification analysis between FIRST and WISE
- *Co-author Julie Banfield selected the subsample of 41 polarised IFRSs*
- I performed the statistical analysis of radio and IR fluxes, radio morphology and spectra, optical photometry and spectroscopy
- *Co-author Julie Banfield created the FIRST/WISE/SDSS postage stamps from Fig. 3.11*
- I wrote the paper and all the sections of the thesis concerning these data

B.0.2 ATLAS VLBI sample

- I selected the ATLAS VLBI sample
- I scheduled the observations and observed the VLBI sample with the LBA
- *Co-investigator Steve Tingay performed the data reduction, including calibration, imaging and source extraction*
- *Co-investigator Joe Callingham wrote the majority of the code to perform the spectral modelling*
- I modified the code to include additional models, output the model parameters, and create the modify the output images
- I performed the spectral modelling
- I performed all the analyses
- *Co-investigator Steve Tingay wrote some of section 2.3.3, which I edited and added to*
- I wrote all other sections of the thesis concerning these data

B.0.3 SMC sample

- I cross-matched the 3, 6, 13 20 and 36 cm radio data and created the pre-CABB spectral index catalogue
- *Co-investigator Evan Crawford created the beam-matched images*
- I ran IMSAD on these images and added the beam-matched fluxes to the catalogue
- I selected the SMC sample
- I scheduled the observations and observed the SMC sample with ATCA
- I performed the data reduction, including calibration, imaging and source extraction
- I performed the visual inspection, measured the angular sizes and created the component and source catalogues
- I performed the cross-matching and catalogue preparation for modelling the radio spectra
- *Co-investigator Nathan Kayani performed the misidentification analysis between GLEAM and ATCA*
- *Co-investigator Joe Callingham wrote the majority of the code to perform the spectral modelling*
- I modified the code to include additional models, output the model parameters, and create the modify the output images
- I performed the spectral modelling
- I performed all the analyses and wrote all the sections of the thesis concerning these data

B.0.4 ATLAS sample

- I selected the ATLAS sample
- I scheduled the observations and observed the ATLAS sample with ATCA
- I performed the data reduction, including calibration, imaging and source extraction
- *Co-investigator Joe Callingham wrote the majority of the code to perform the spectral modelling*
- I modified the code to include additional models, output the model parameters, and create the modify the output images
- I performed the spectral modelling
- I performed all the analyses and wrote all the sections of the thesis concerning these data

Appendix C

SMC ATCA and MWA images

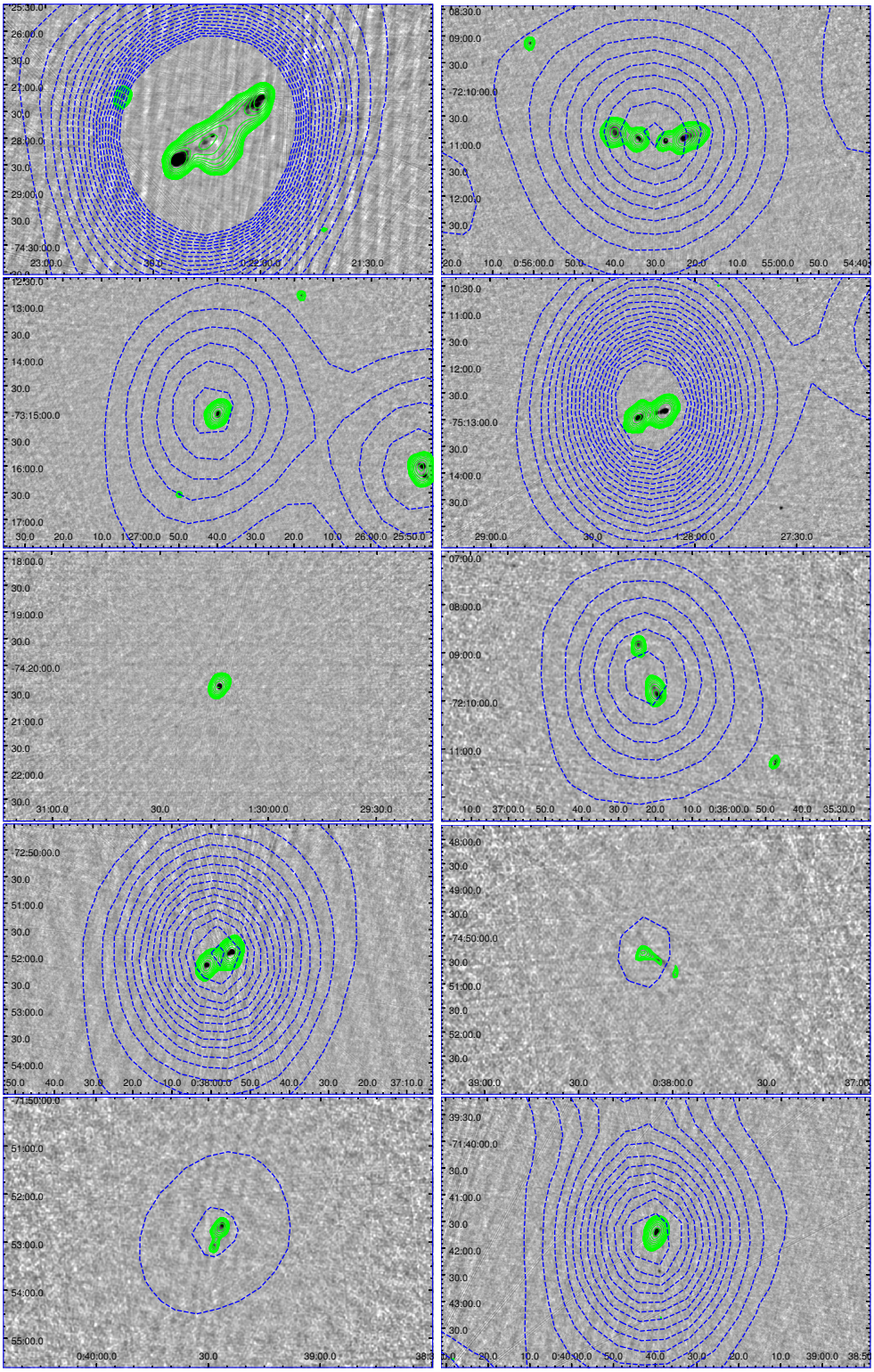

Figure C.1: The 72 SMC sources, with the background greyscale showing our final ATCA CABB images at 5.5 GHz, the solid green contours showing the Wong et al. (2011a) 1.4 GHz image and the dashed blue contours showing the "deep" 200 MHz GLEAM image. All contours are from $5 - 100\sigma$, in 5σ intervals, where σ was taken as 0.7 mJy at 1.4 GHz and 9 mJy at 200 MHz. Shown here are smc_0022-7428, smc_0055-7211, smc_100, smc_101, smc_102, smc_10, smc_13, smc_14, smc_16 and smc_17.

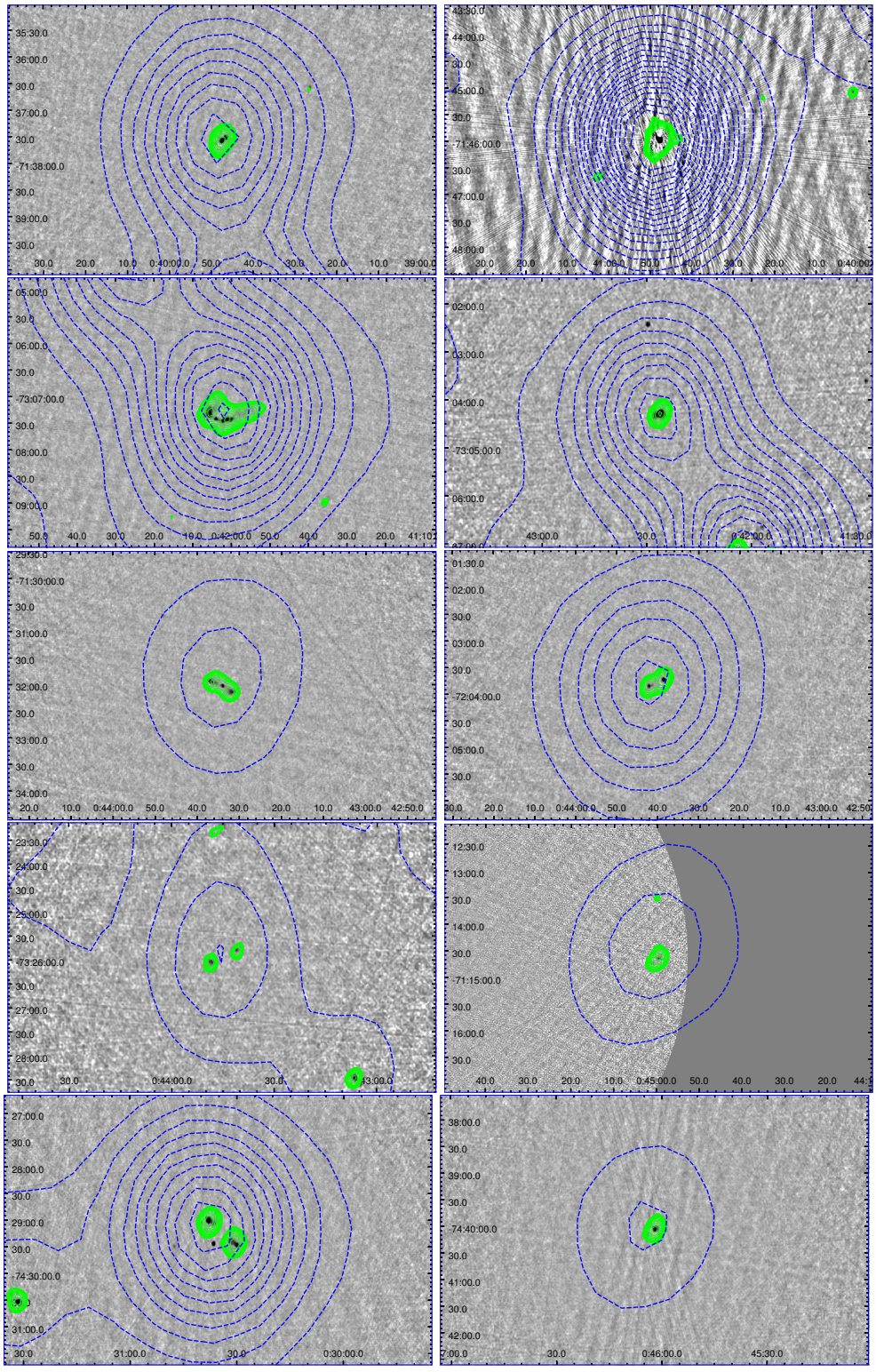

Fig. C.1. (continued) for smc_18, smc_19, smc_21, smc_23, smc_25, smc_26, smc_27, smc_29, smc_2 and smc_30.

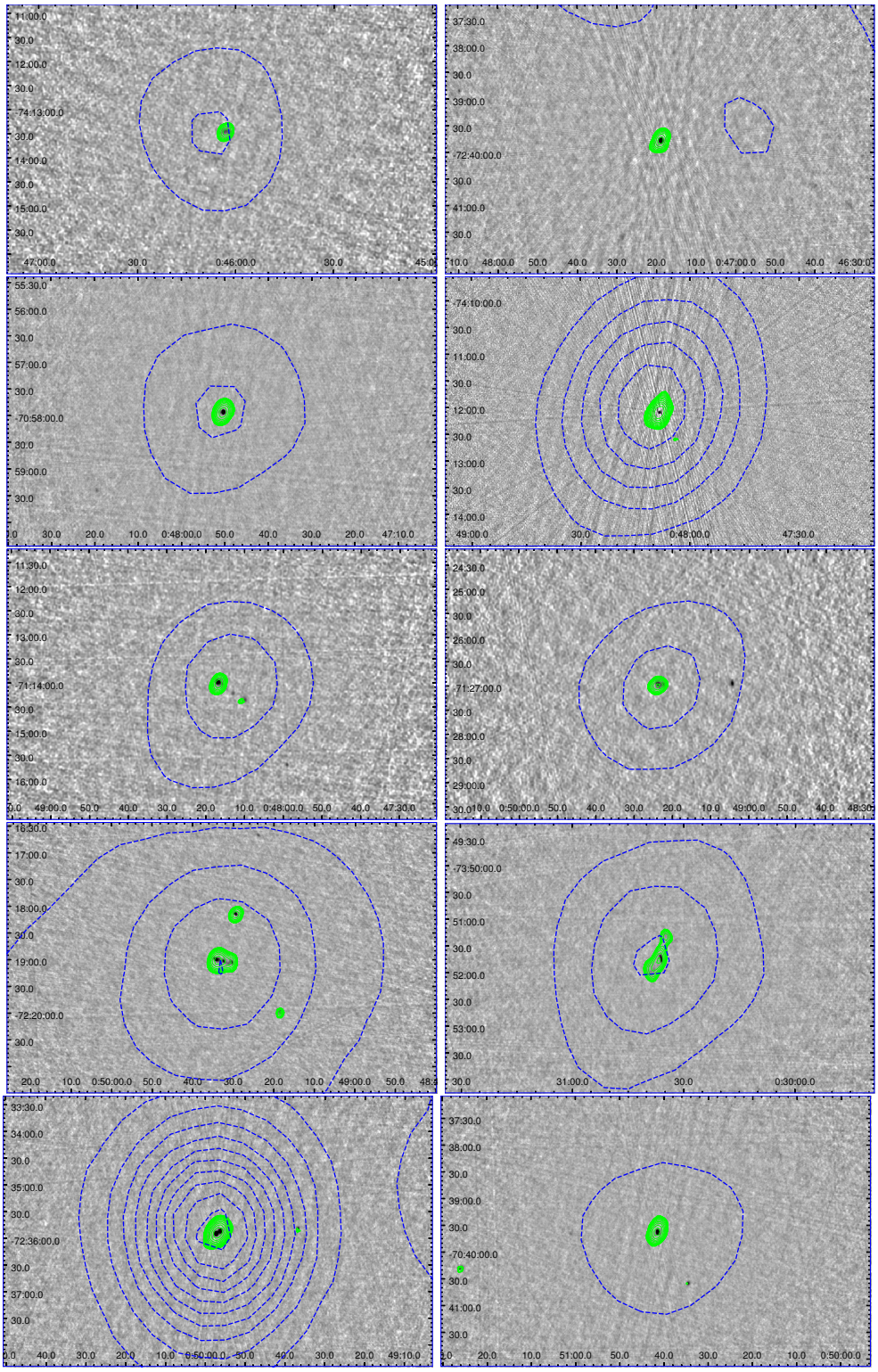

Fig. C.1. (continued) for smc_31, smc_32, smc_34, smc_35, smc_36, smc_38, smc_39, smc_3, smc_41 and smc_44.

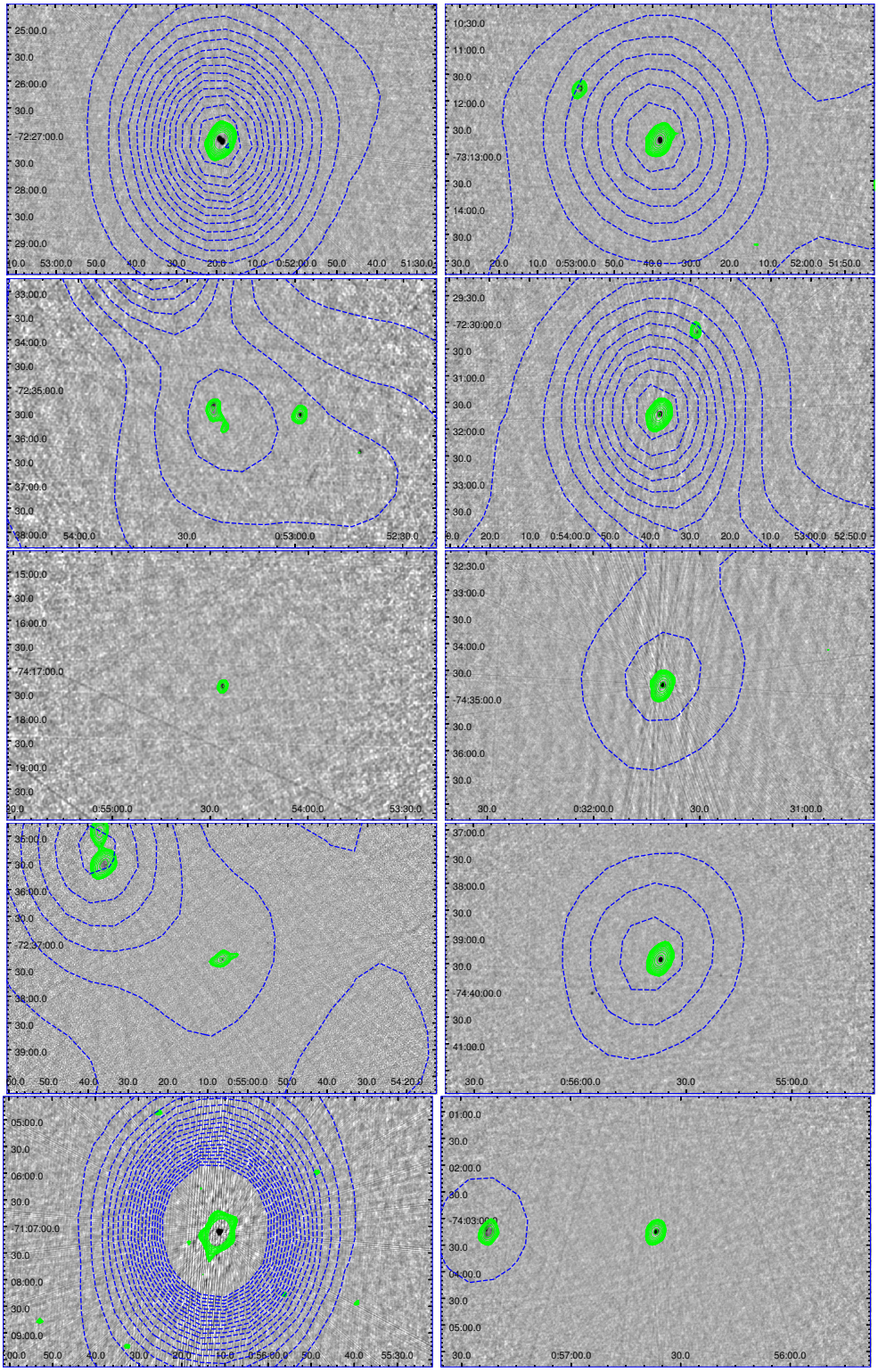

Fig. C.1. (continued) for smc_45, smc_46, smc_47, smc_48, smc_49, smc_4, smc_50, smc_52, smc_54 and smc_55.

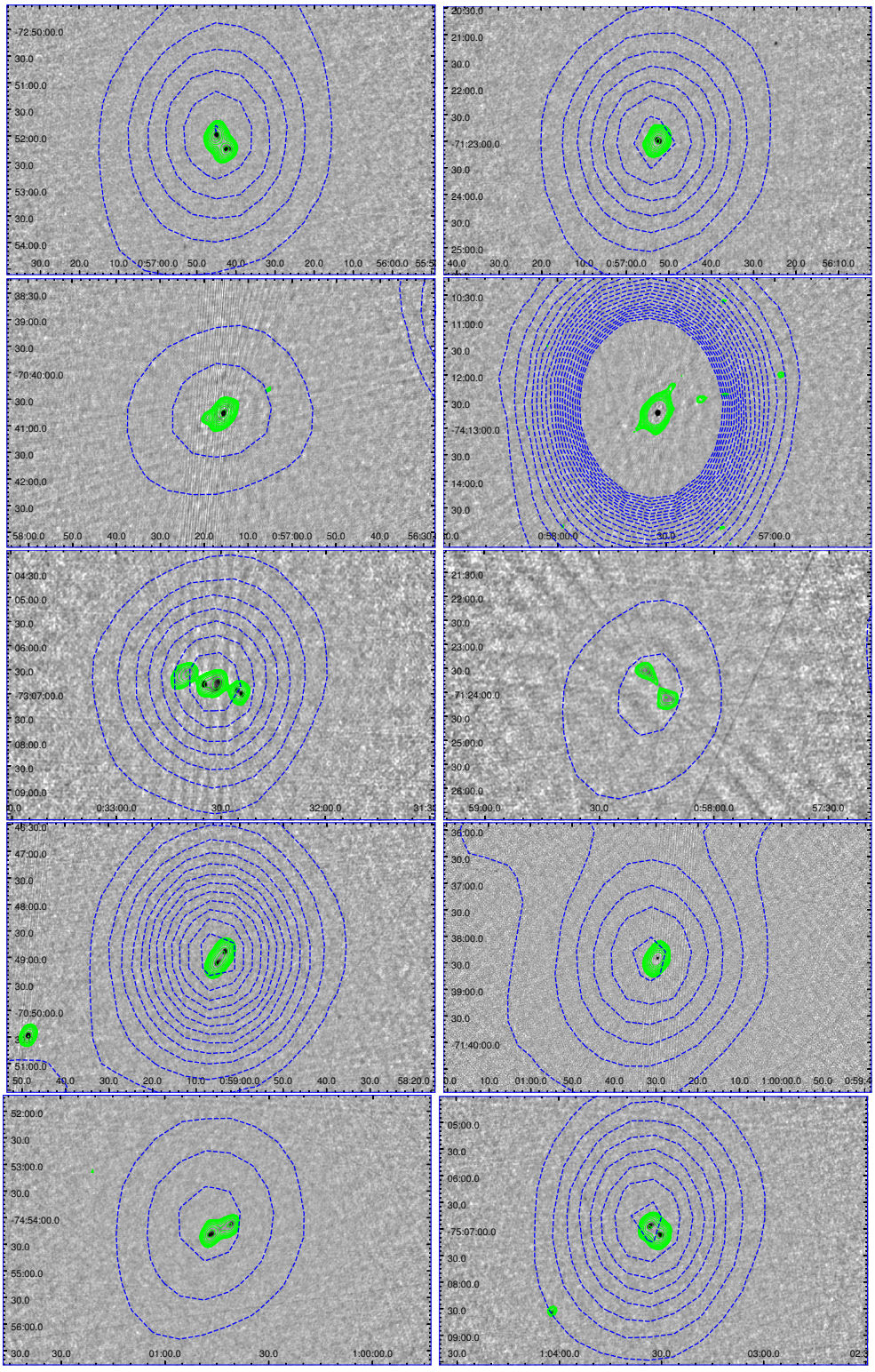

Fig. C.1. (continued) for smc_56, smc_57, smc_58, smc_59, smc_5, smc_61, smc_64, smc_65, smc_66 and smc_68.

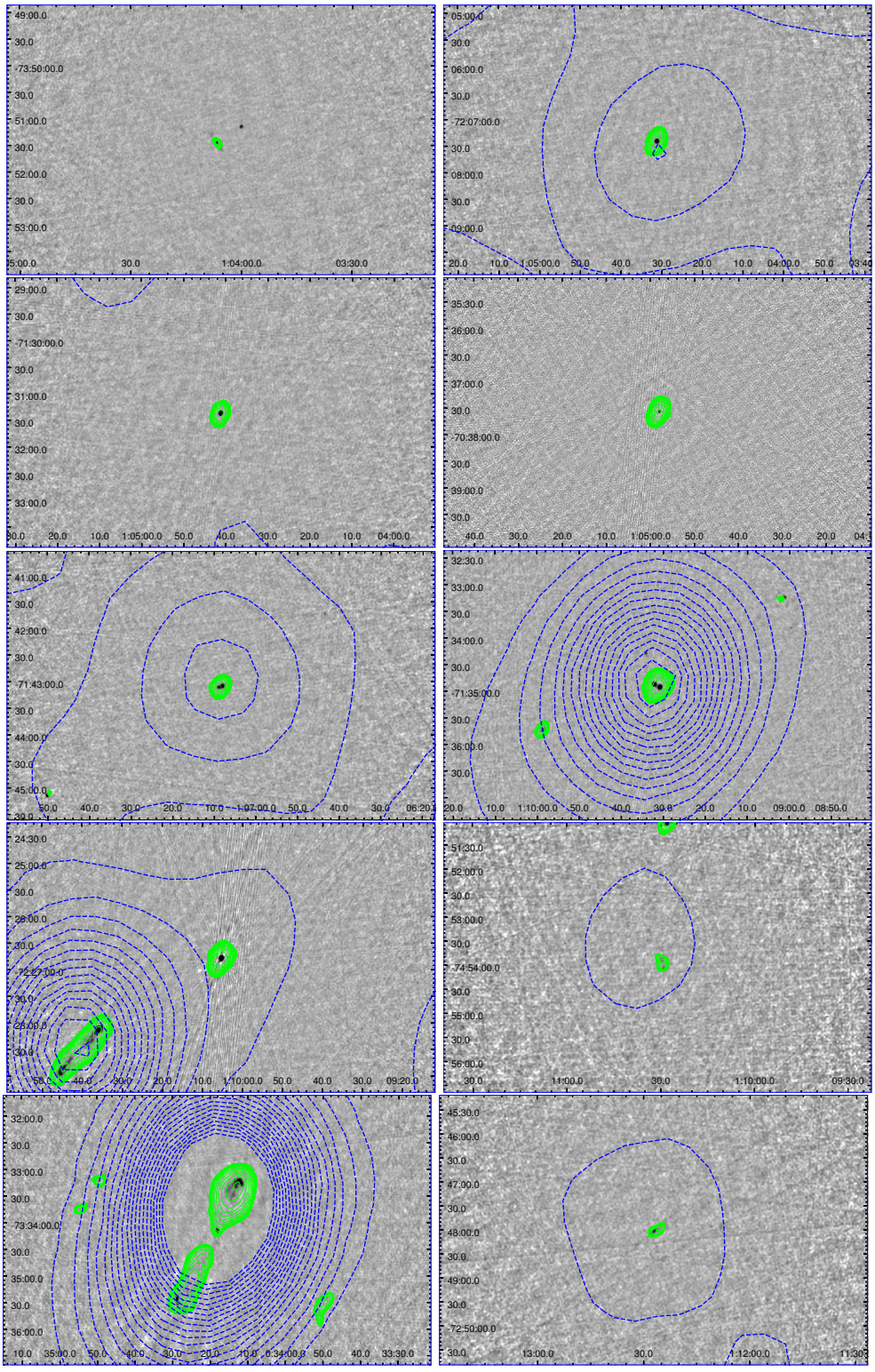

Fig. C.1. (continued) for smc_69, smc_70, smc_71, smc_72, smc_74, smc_75, smc_76, smc_77, smc_7 and smc_80.

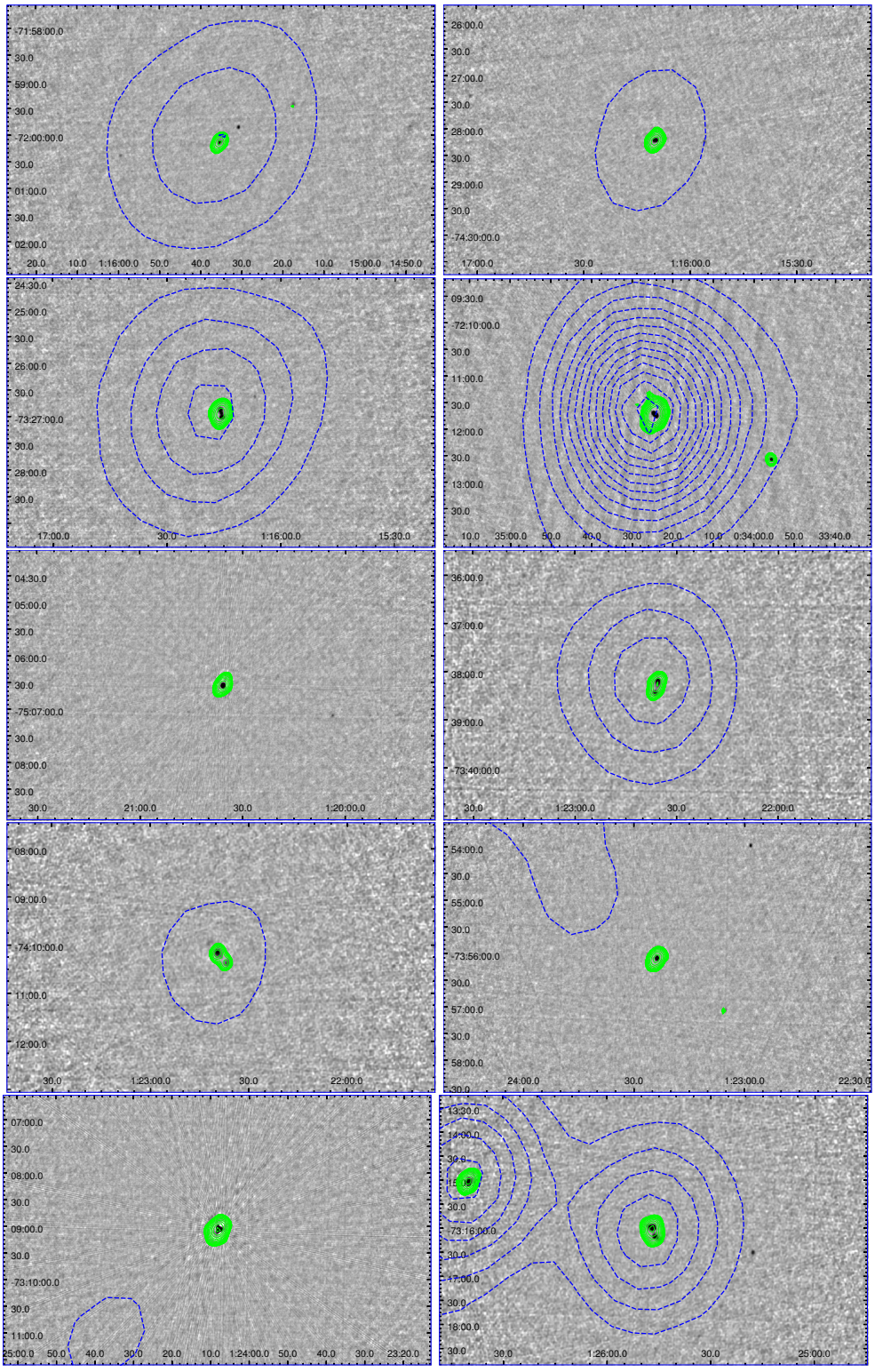

Fig. C.1. (continued) for smc_83, smc_84, smc_86, smc_8, smc_90, smc_93, smc_94, smc_95, smc_97 and smc_99.

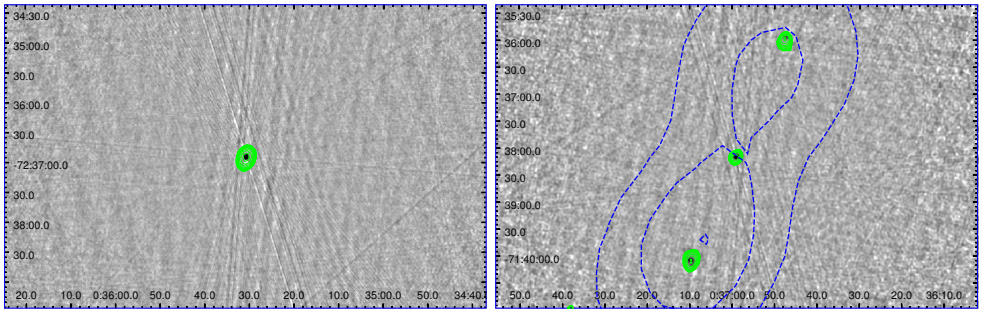

Fig. C.1. (continued) for smc_9 and smc_frii.

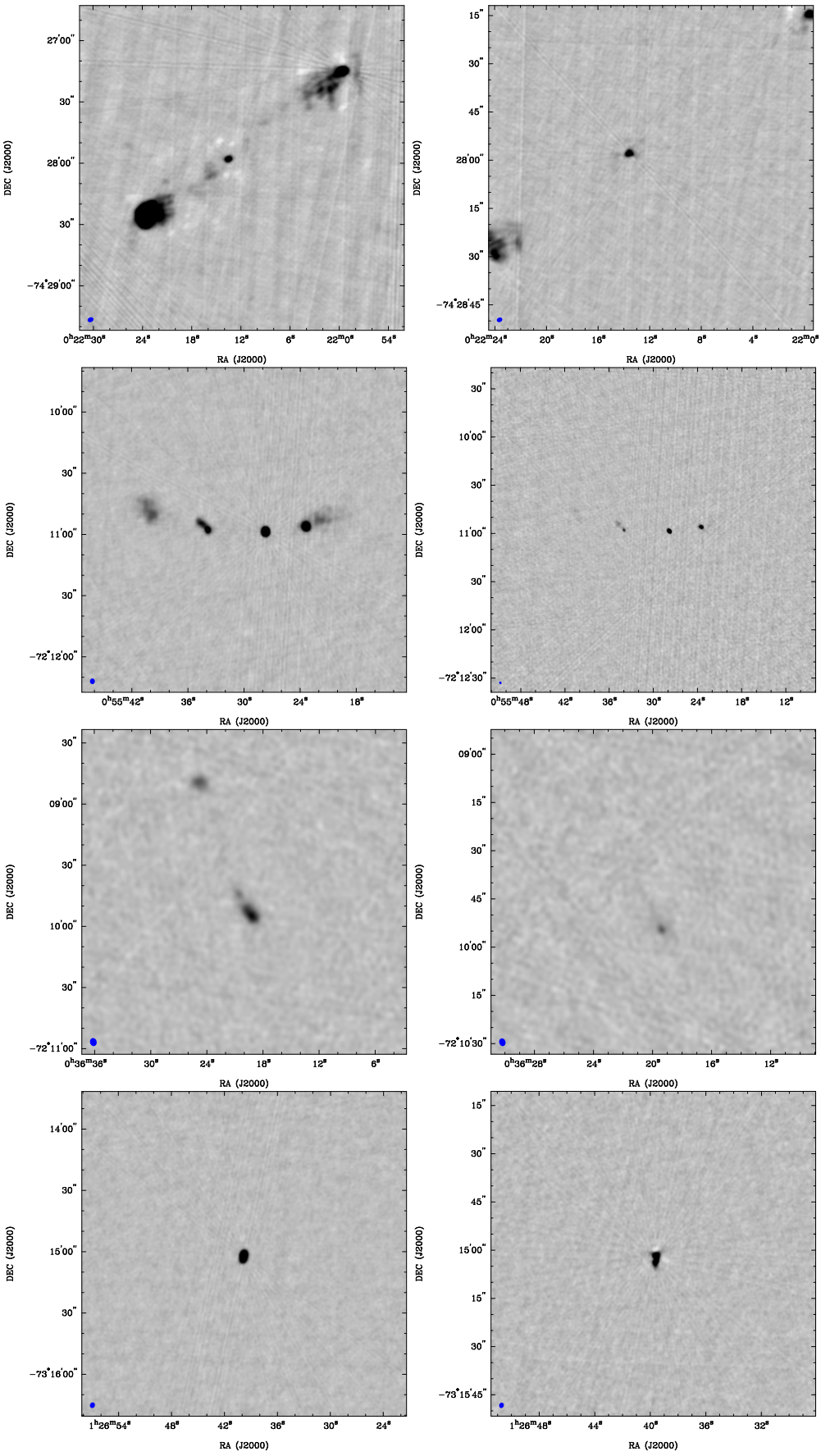

Figure C.2: The 5.5 (left) and 9.0 GHz (right) radio-continuum maps of all 72 SMC sources, imaged with the weighting shown in table D.1. The blue ellipse in the bottom-left-hand corner signifies the FWHM of the synthesised beam, typically $\sim 0.41''$ and $\sim 0.26''$ for robust weighting = 2, respectively at 5.5 and 9.0 GHz. Shown here are smc_0022-7428, smc_0055-7211, smc_10 and smc_100.

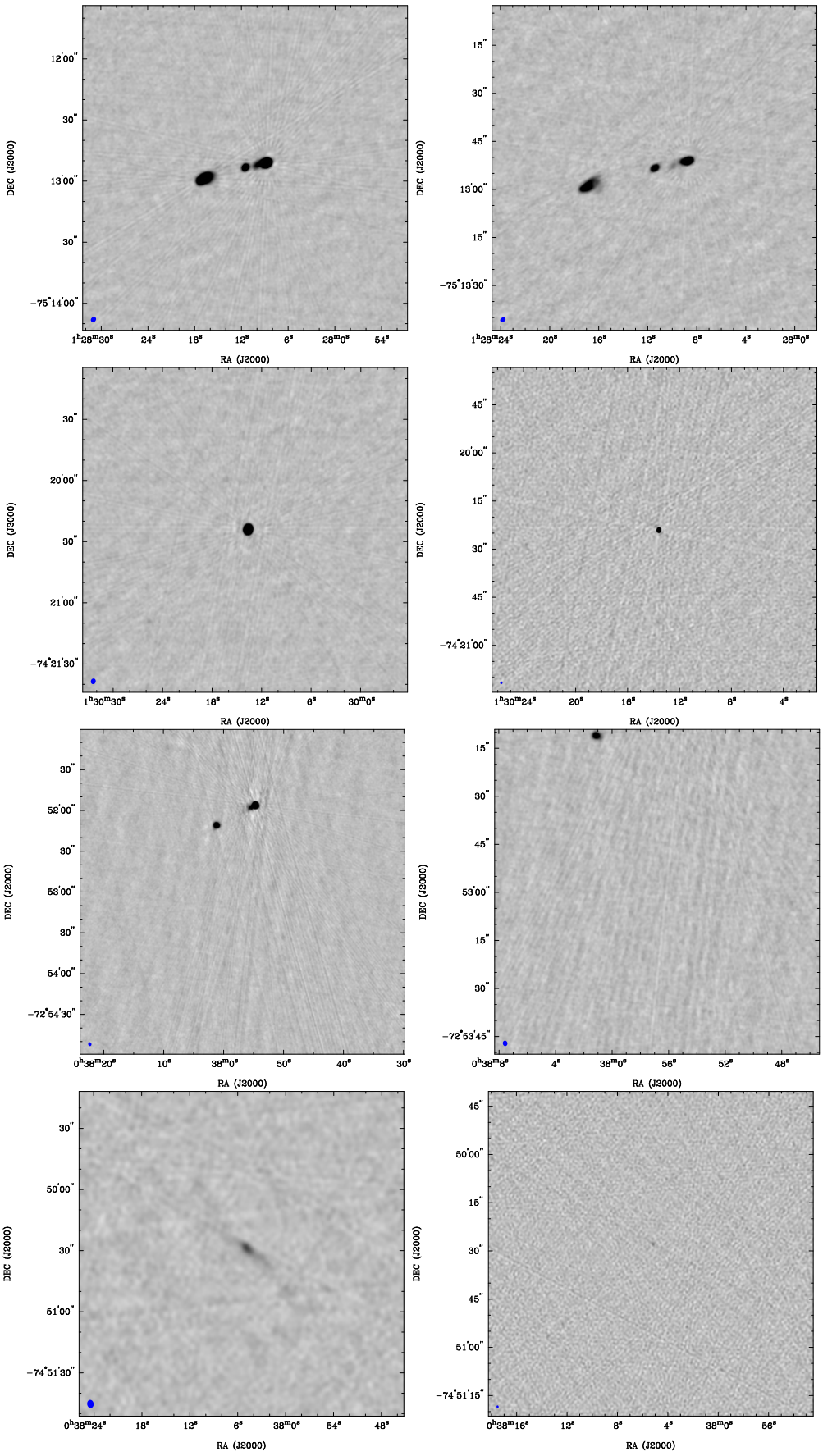

Fig. C.2. (continued) for smc_101, smc_102, smc_13 and smc_14.

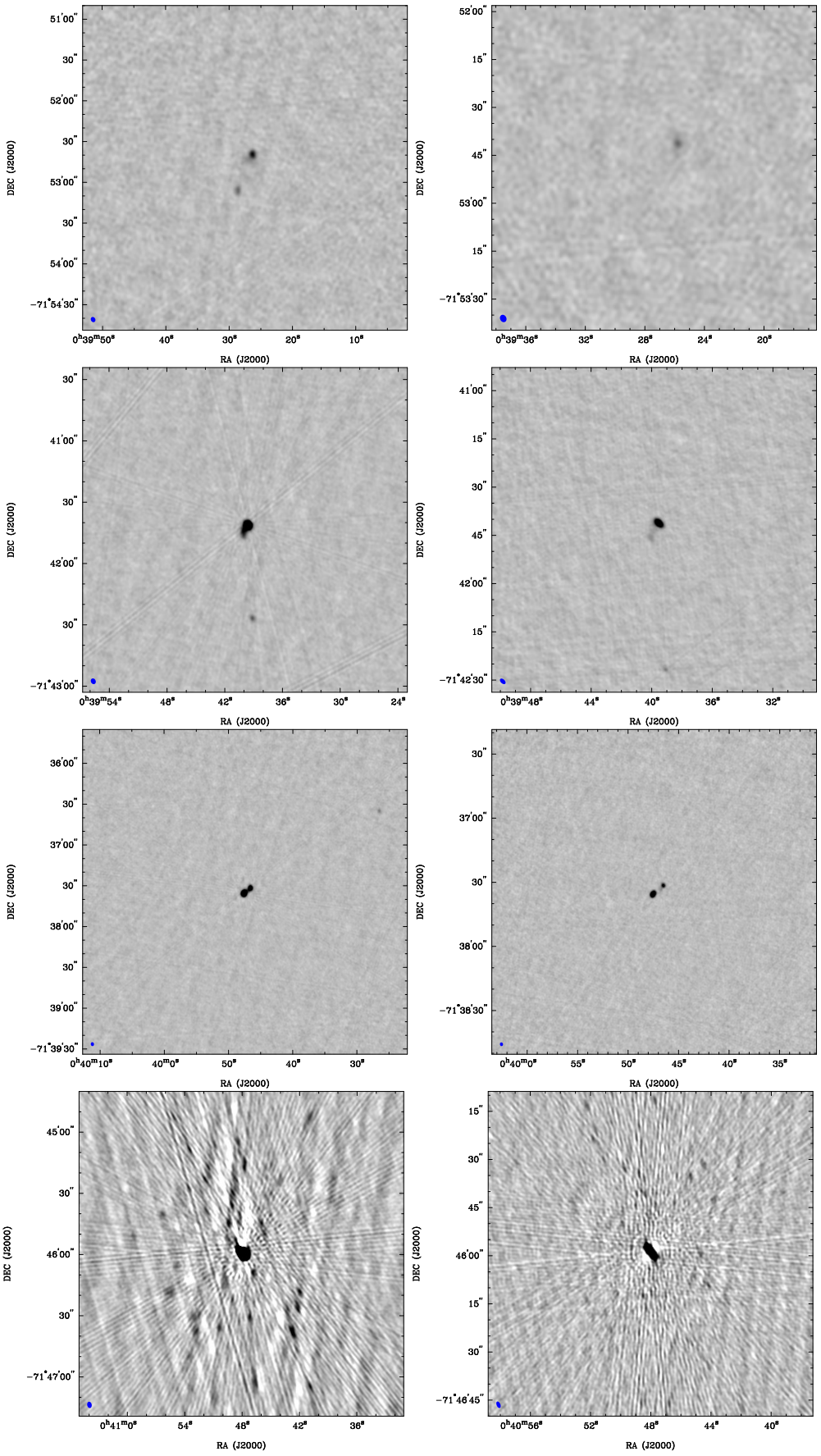

Fig. C.2. (continued) for smc_16, smc_17, smc_18 and smc_19.

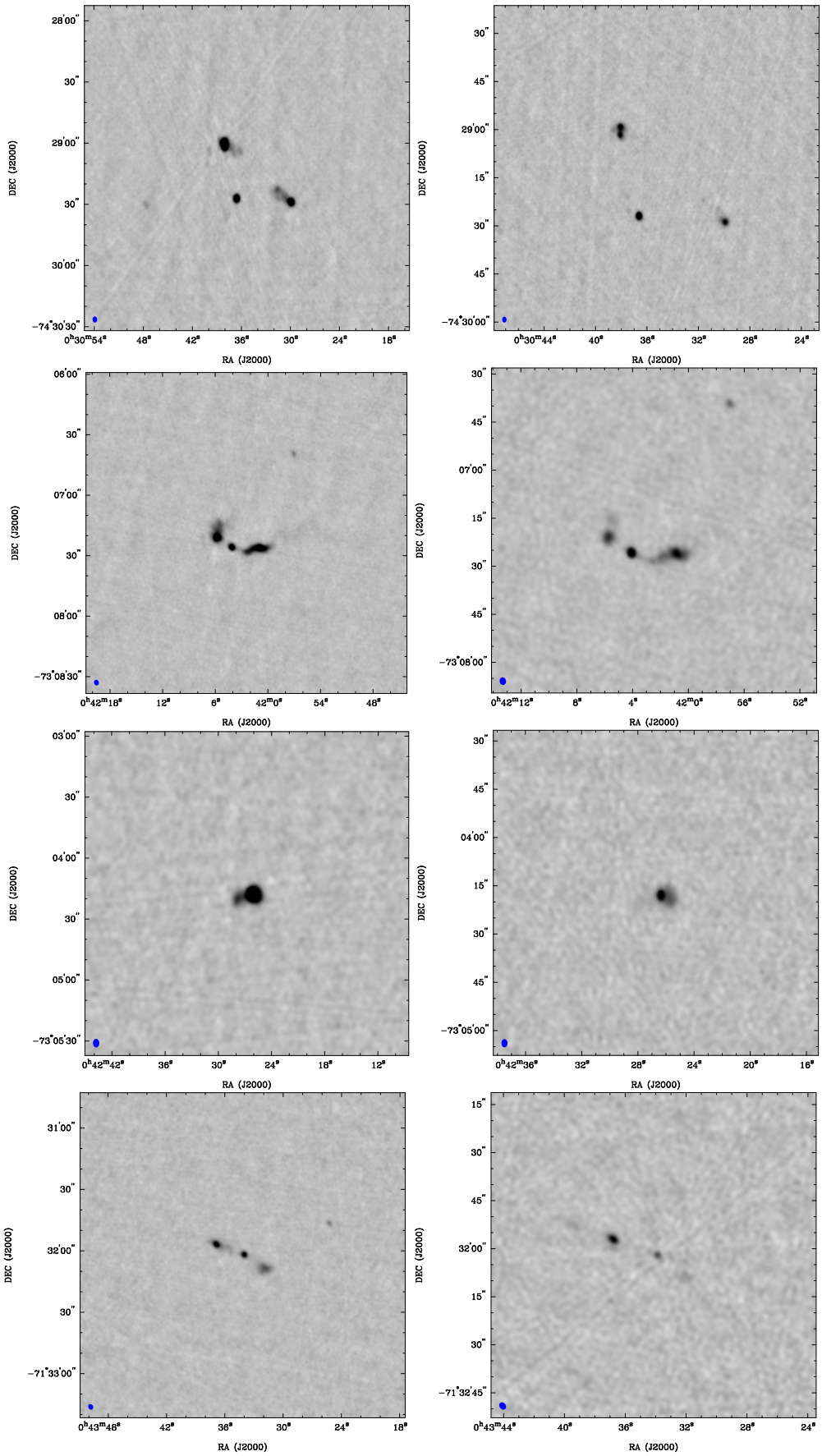

Fig. C.2. (continued) for smc_2, smc_21, smc_23 and smc_25.

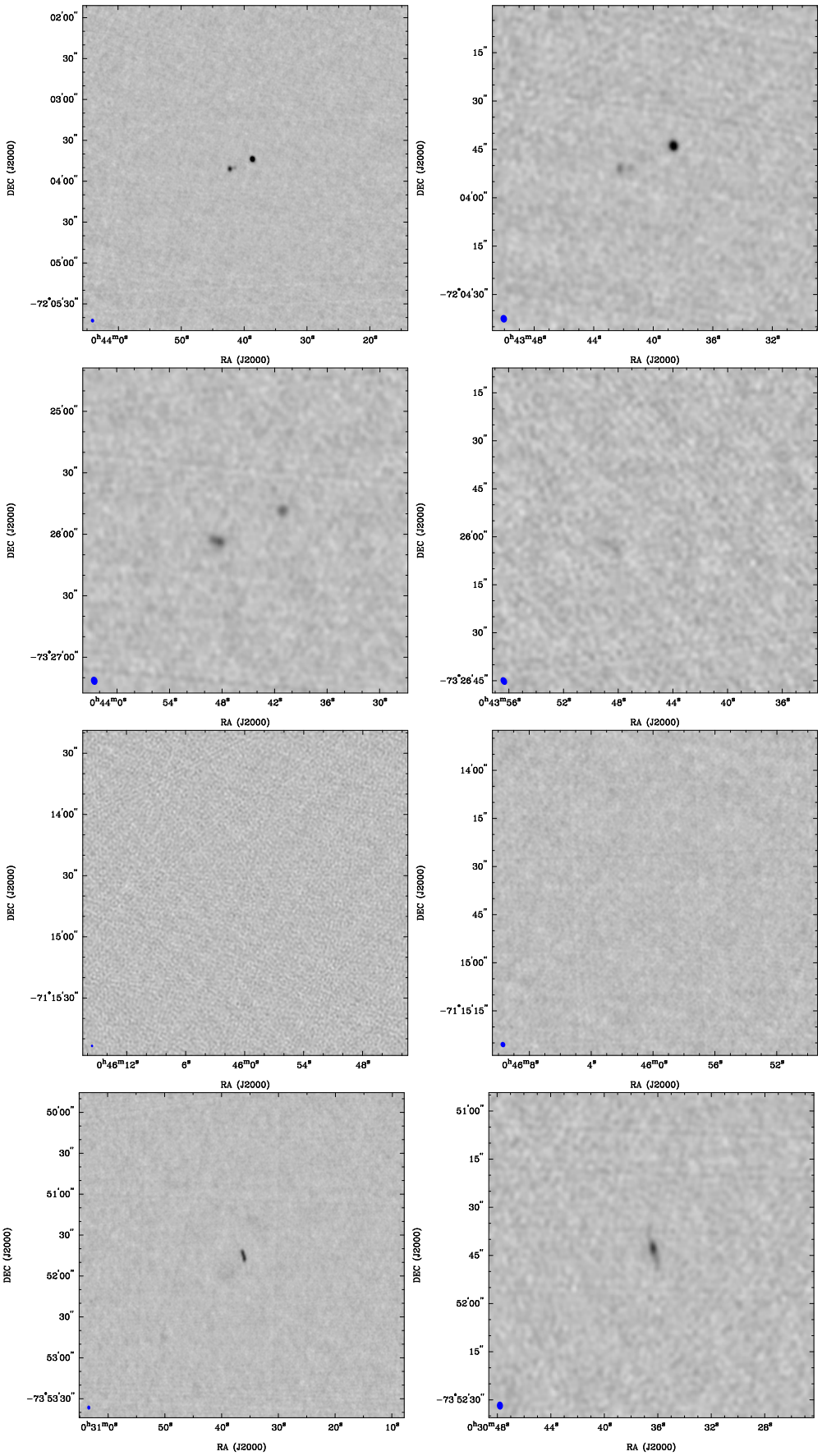

Fig. C.2. (continued) for smc_26, smc_27, smc_29 and smc_3.

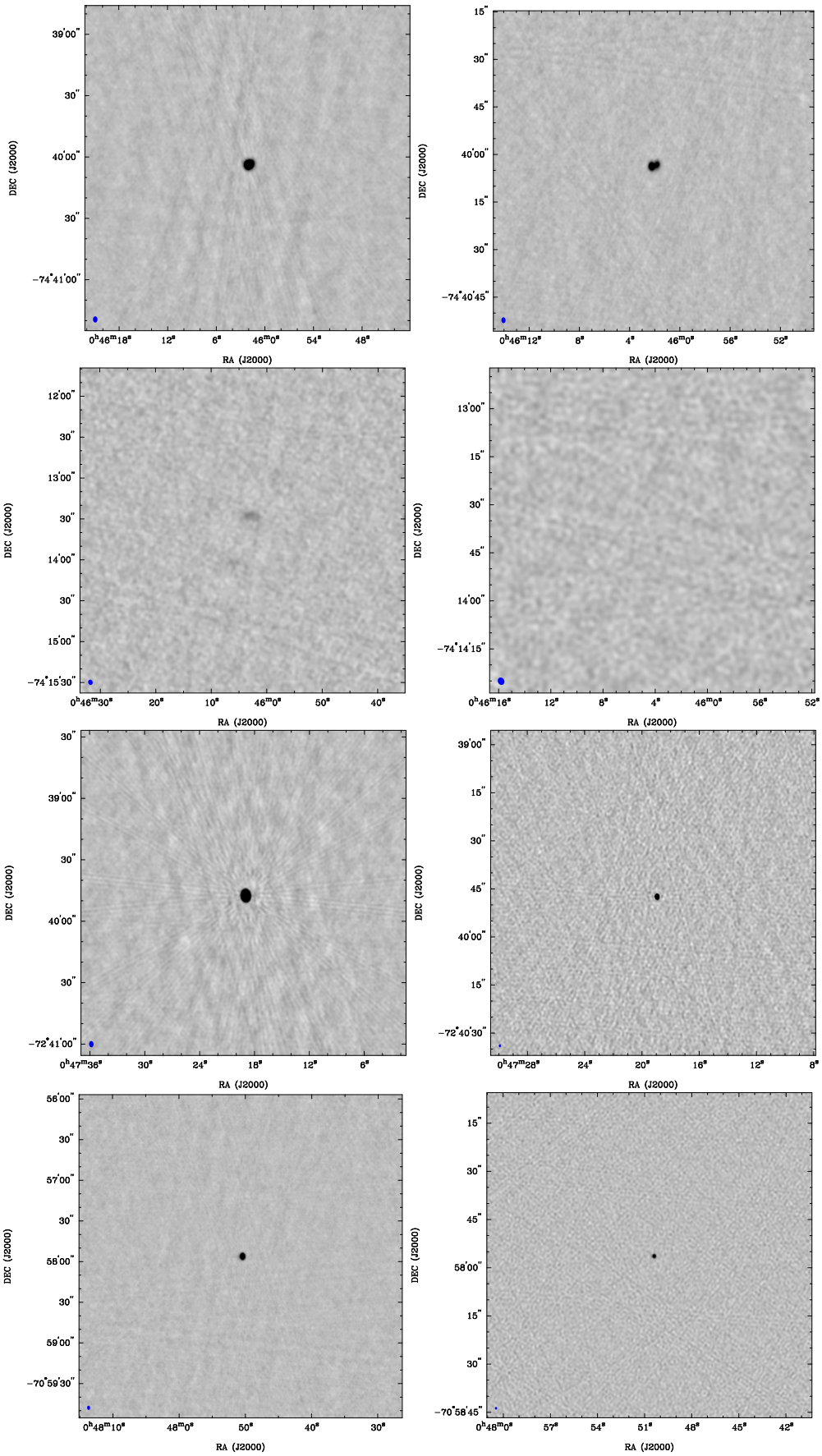

Fig. C.2. (continued) for smc_30, smc_31, smc_32 and smc_34.

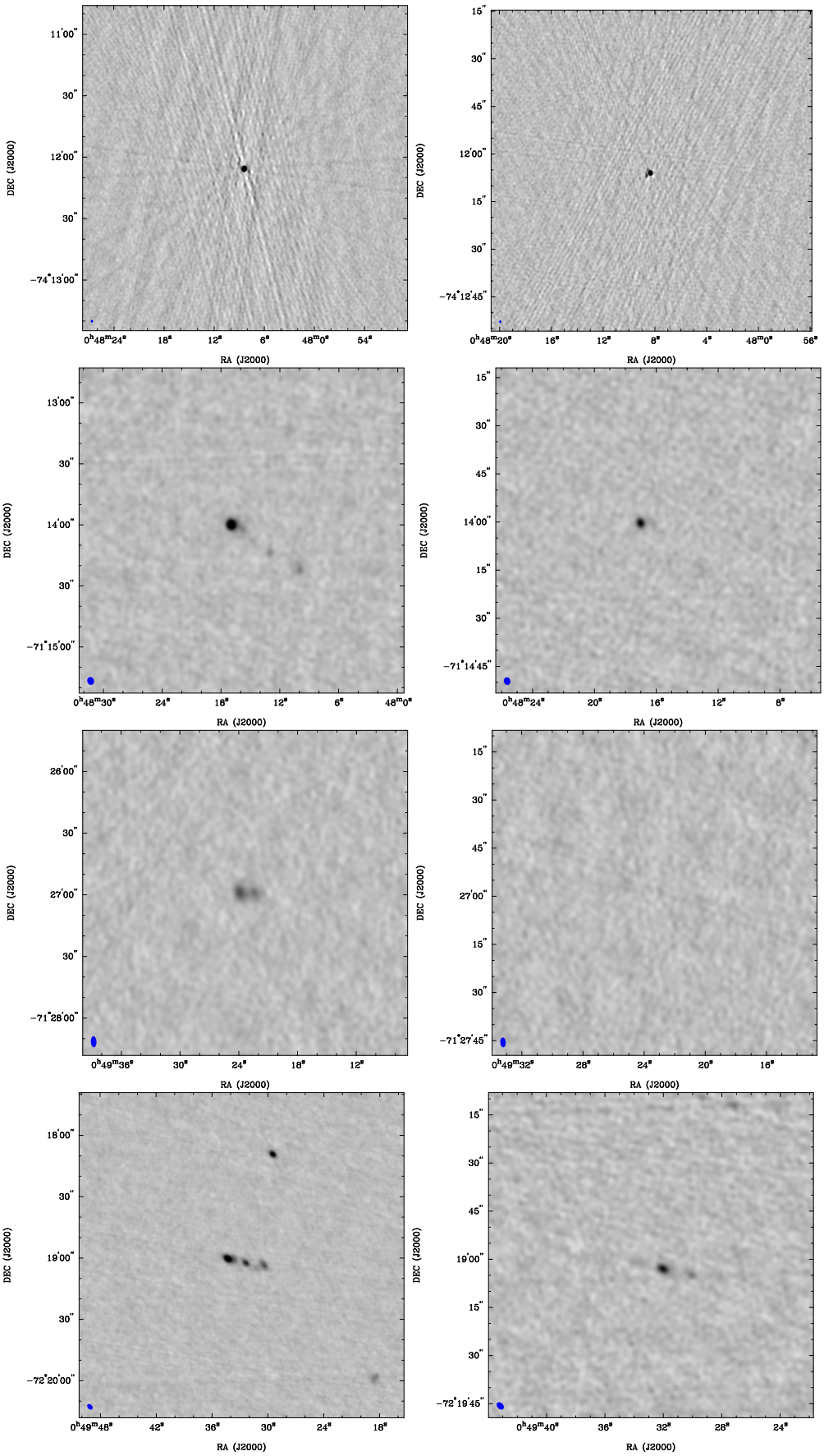

Fig. C.2. (continued) for smc_35, smc_36, smc_38 and smc_39.

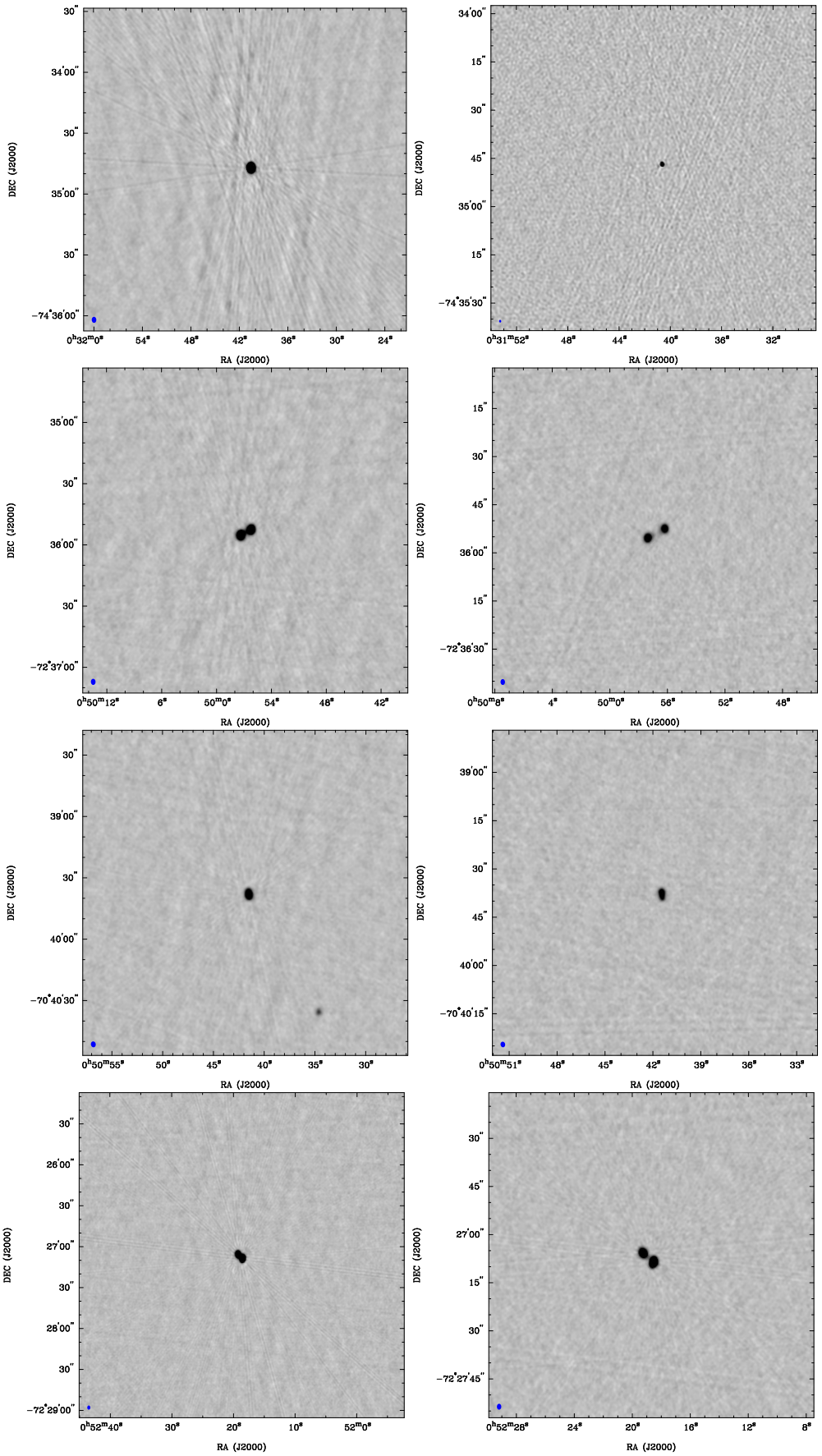

Fig. C.2. (continued) for smc_4, smc_41, smc_44 and smc_45.

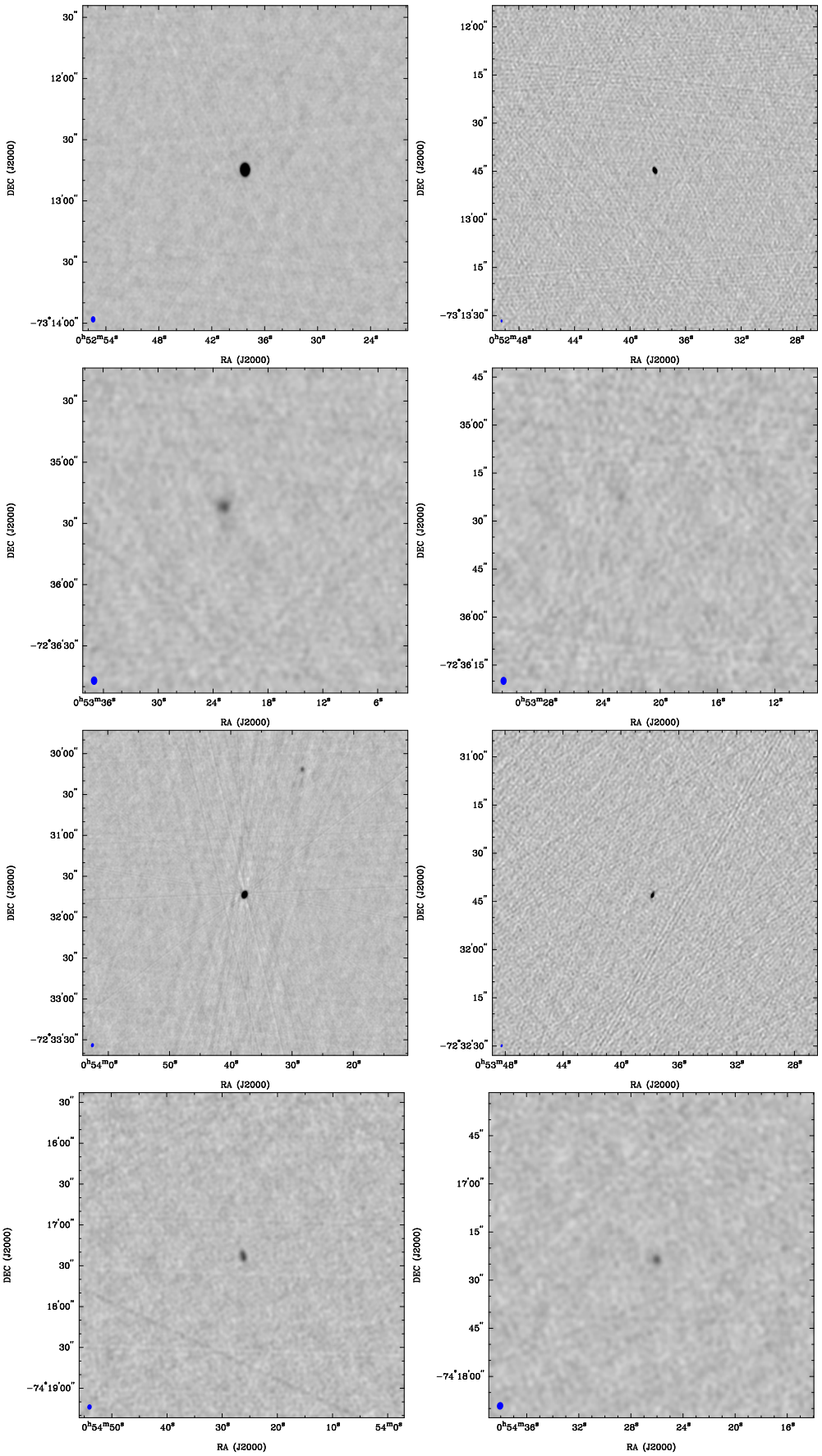

Fig. C.2. (continued) for smc_46, smc_47, smc_48 and smc_49.

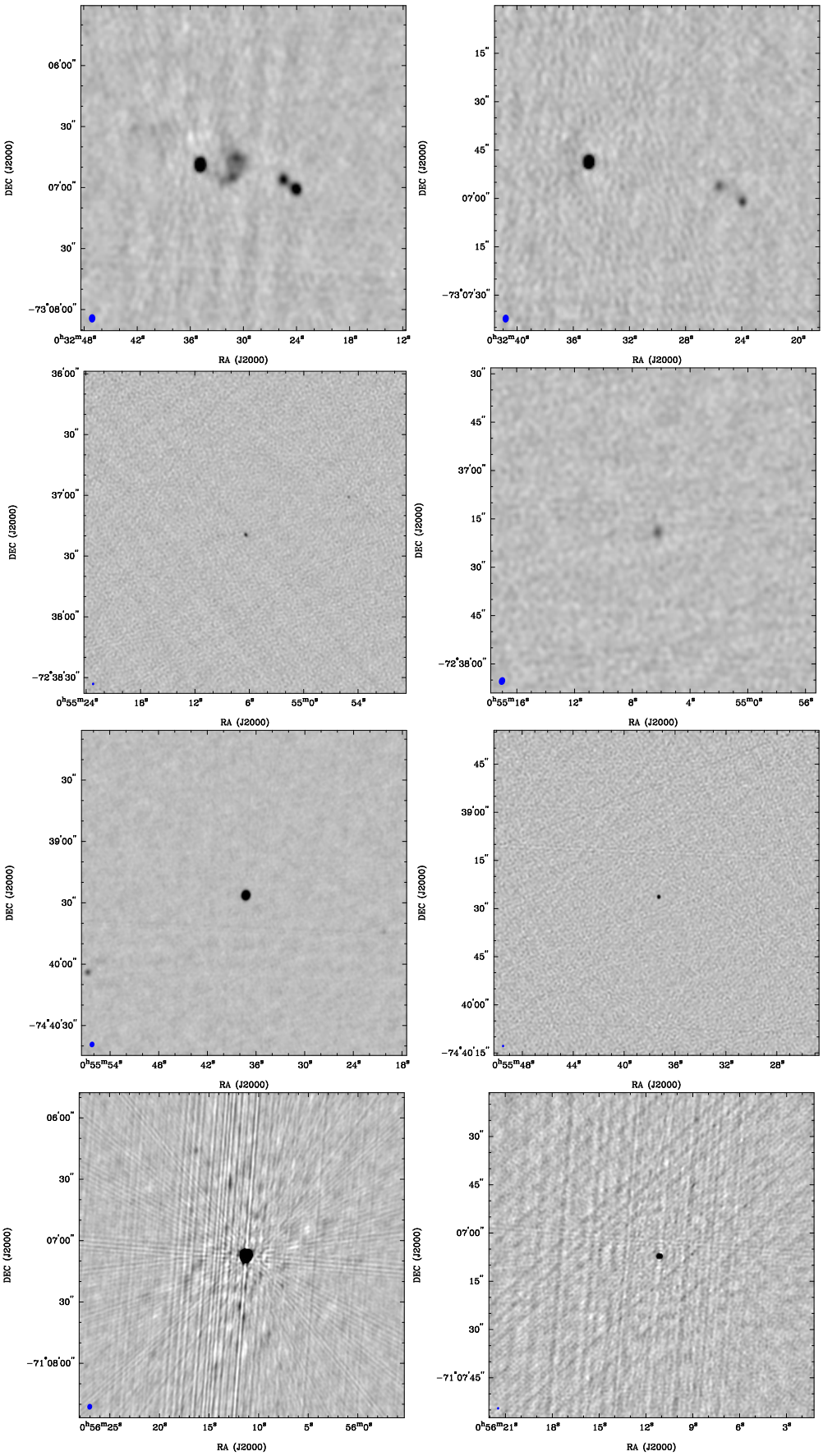

Fig. C.2. (continued) for smc_5, smc_50, smc_52 and smc_54.

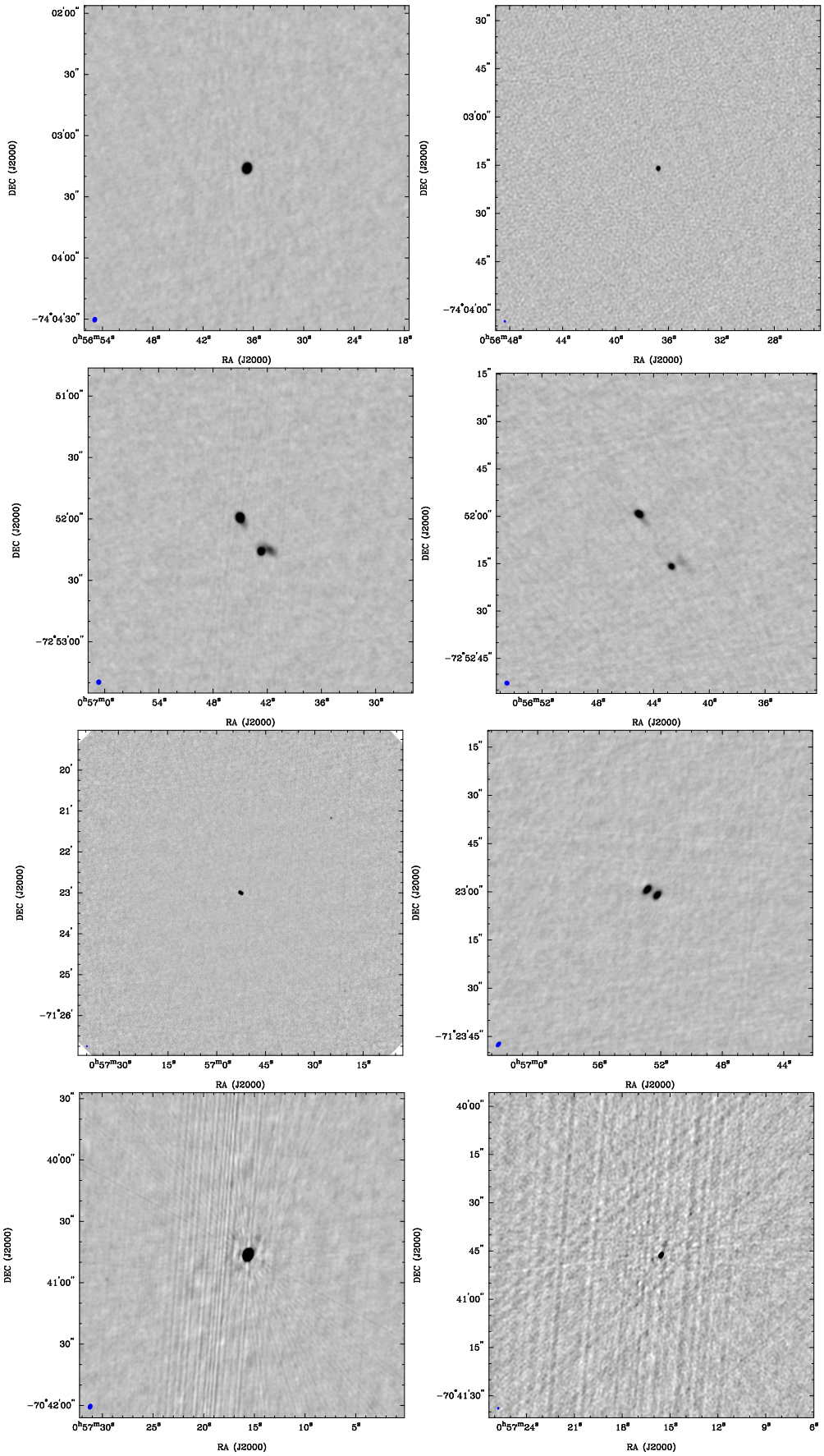

Fig. C.2. (continued) for smc_55, smc_56, smc_57 and smc_58.

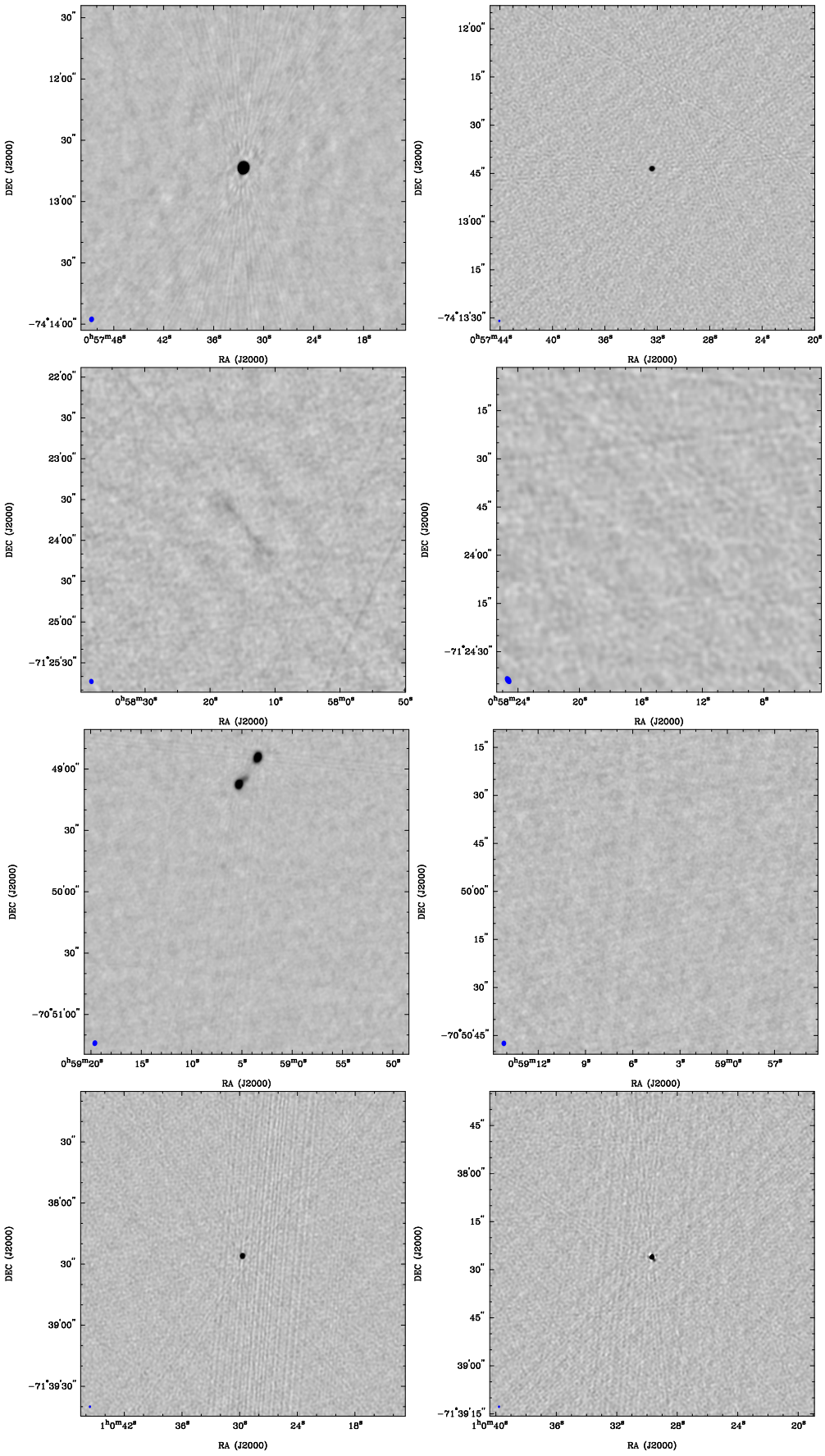

Fig. C.2. (continued) for smc_59, smc_61, smc_64 and smc_65.

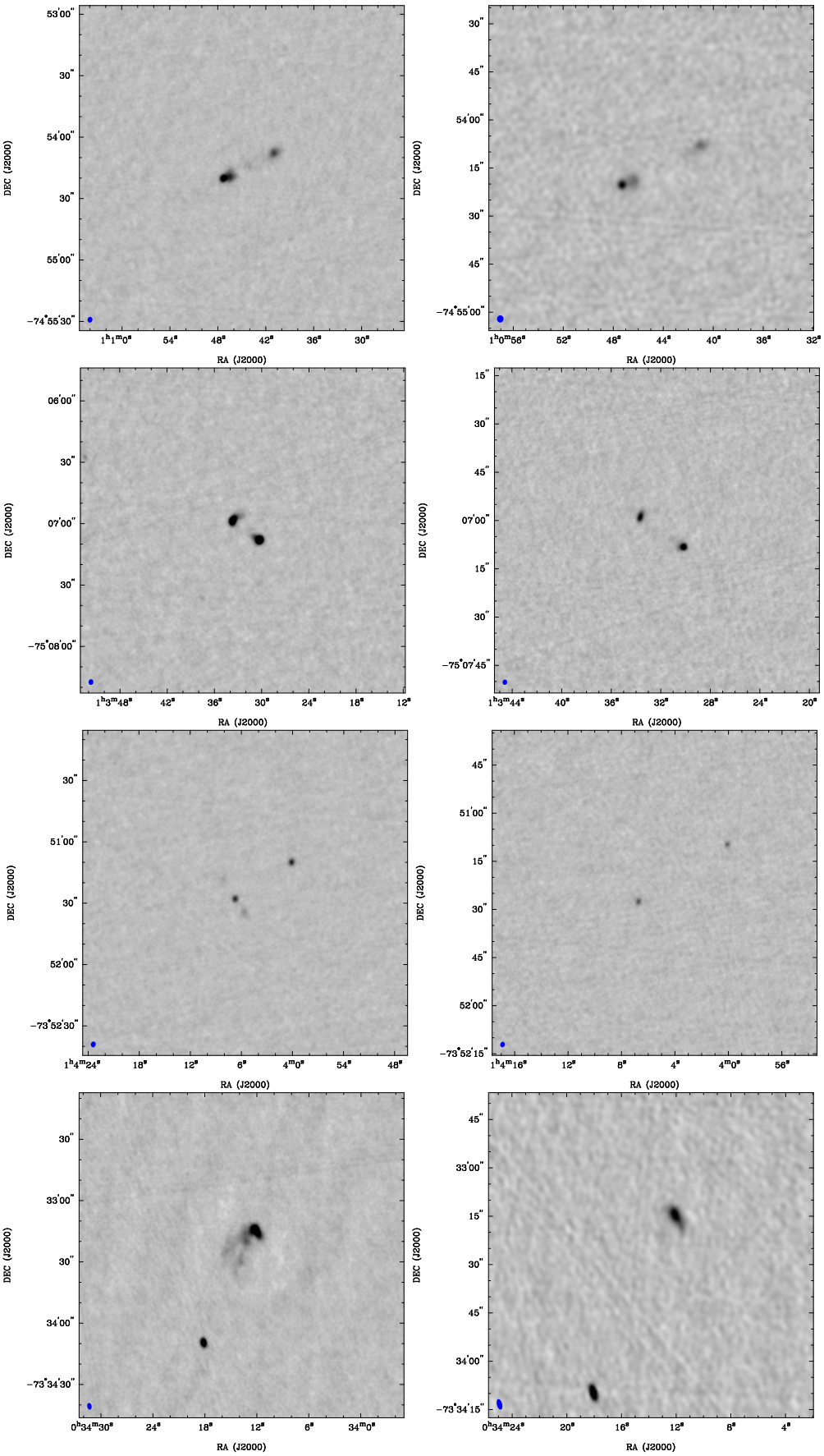

Fig. C.2. (continued) for smc_66, smc_68, smc_69 and smc_7.

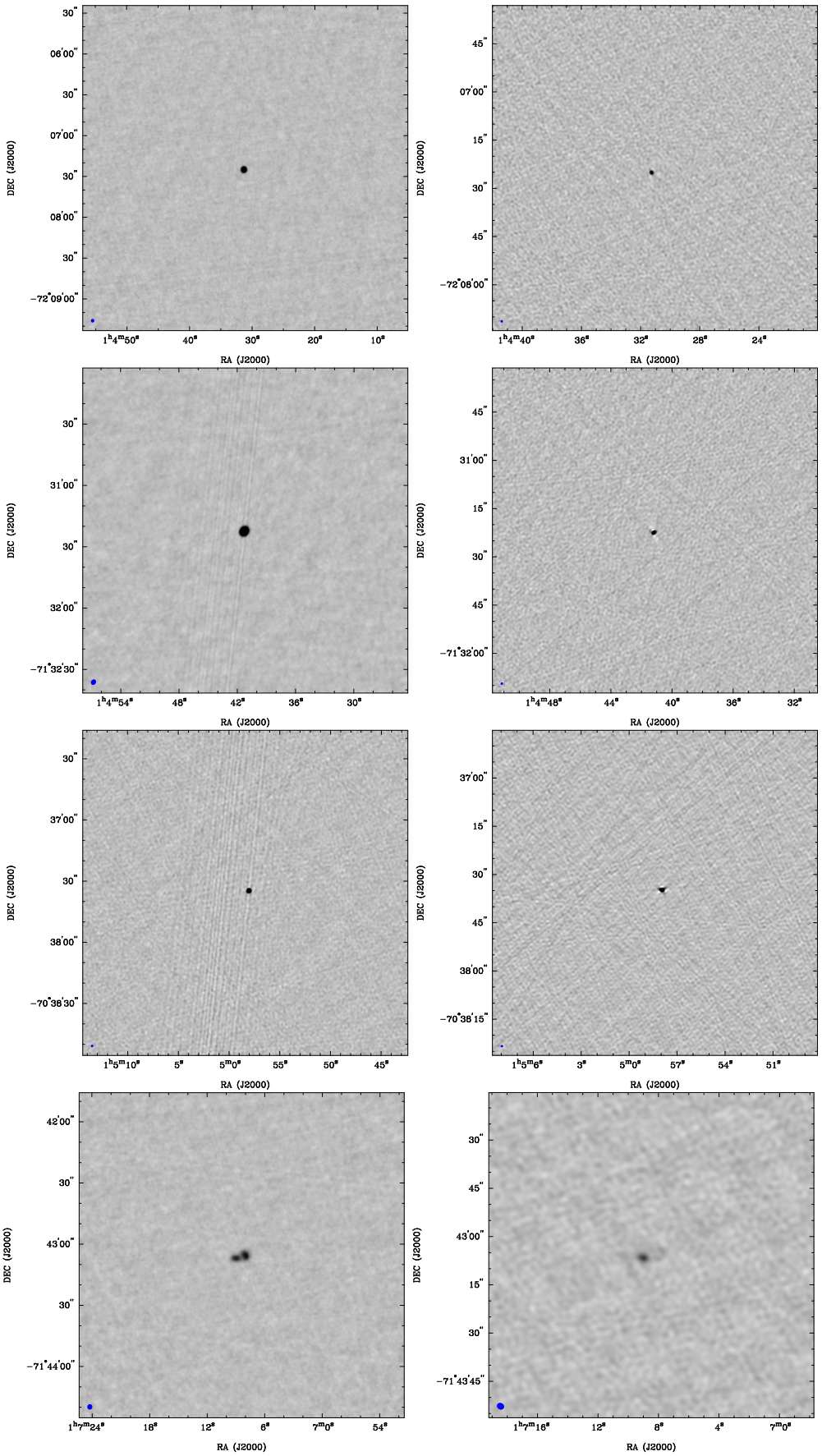

Fig. C.2. (continued) for smc_70, smc_71, smc_72 and smc_74.

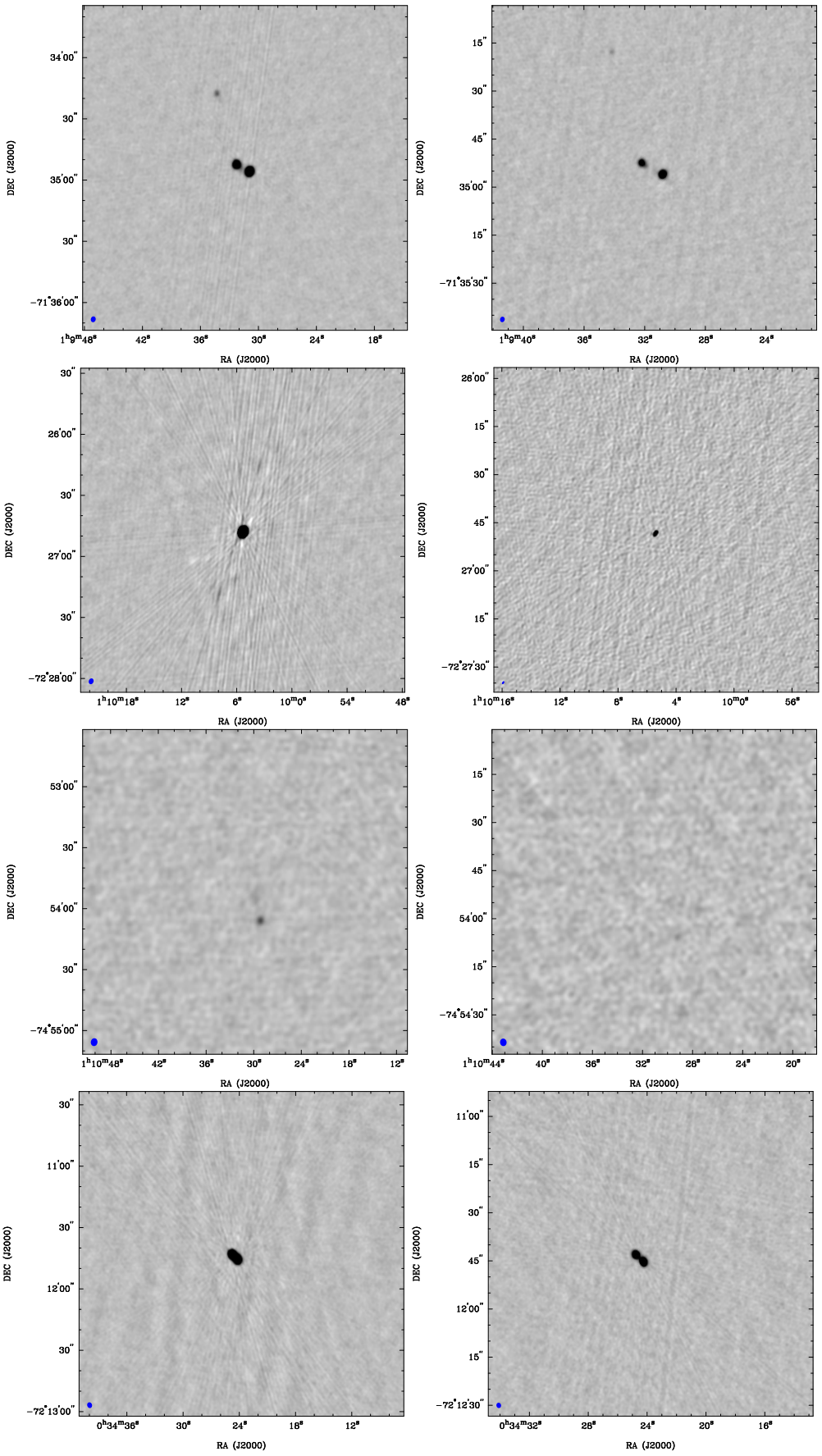

Fig. C.2. (continued) for smc_75, smc_76, smc_77 and smc_8.

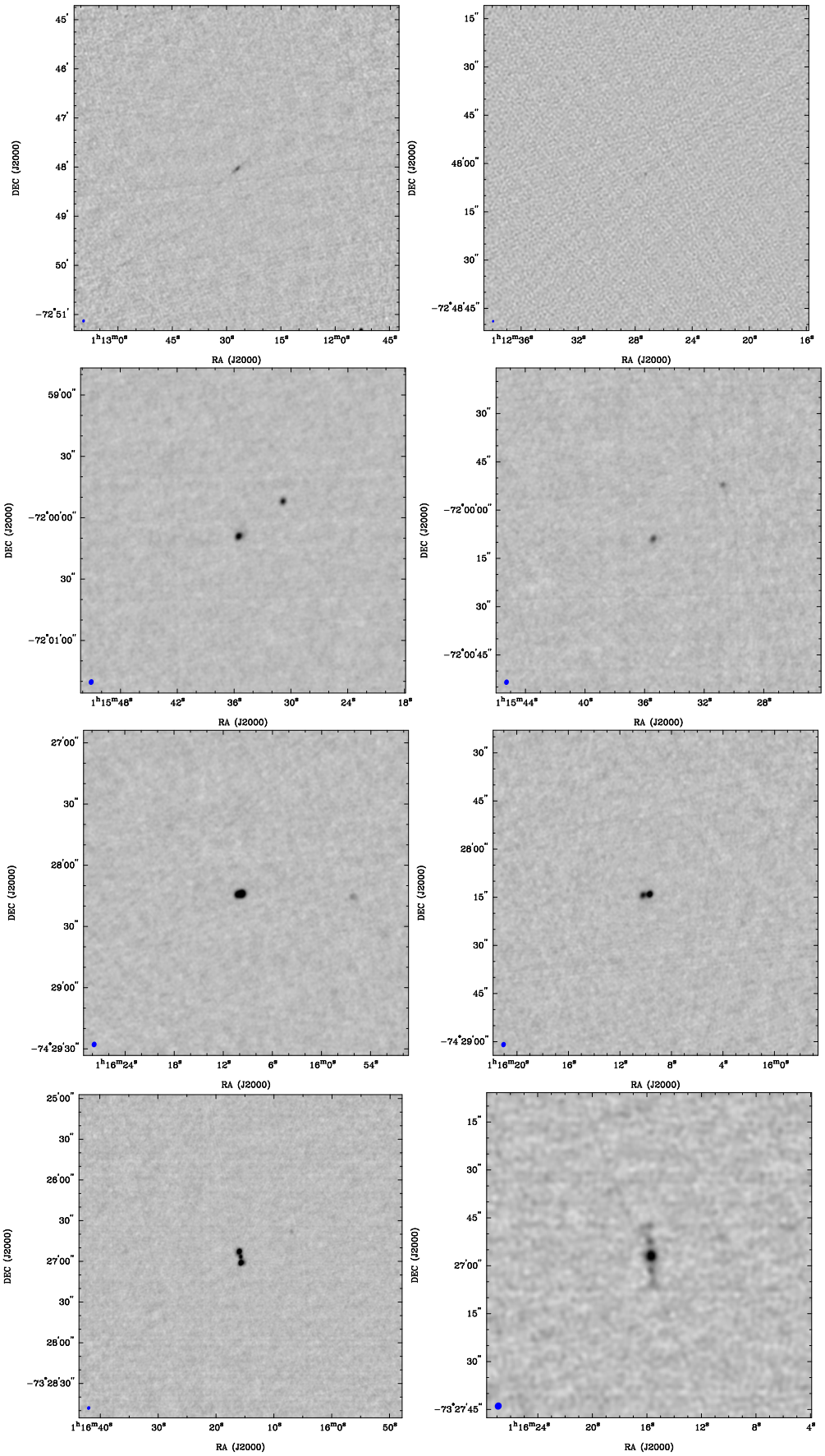

Fig. C.2. (continued) for smc_80, smc_83, smc_84 and smc_86.

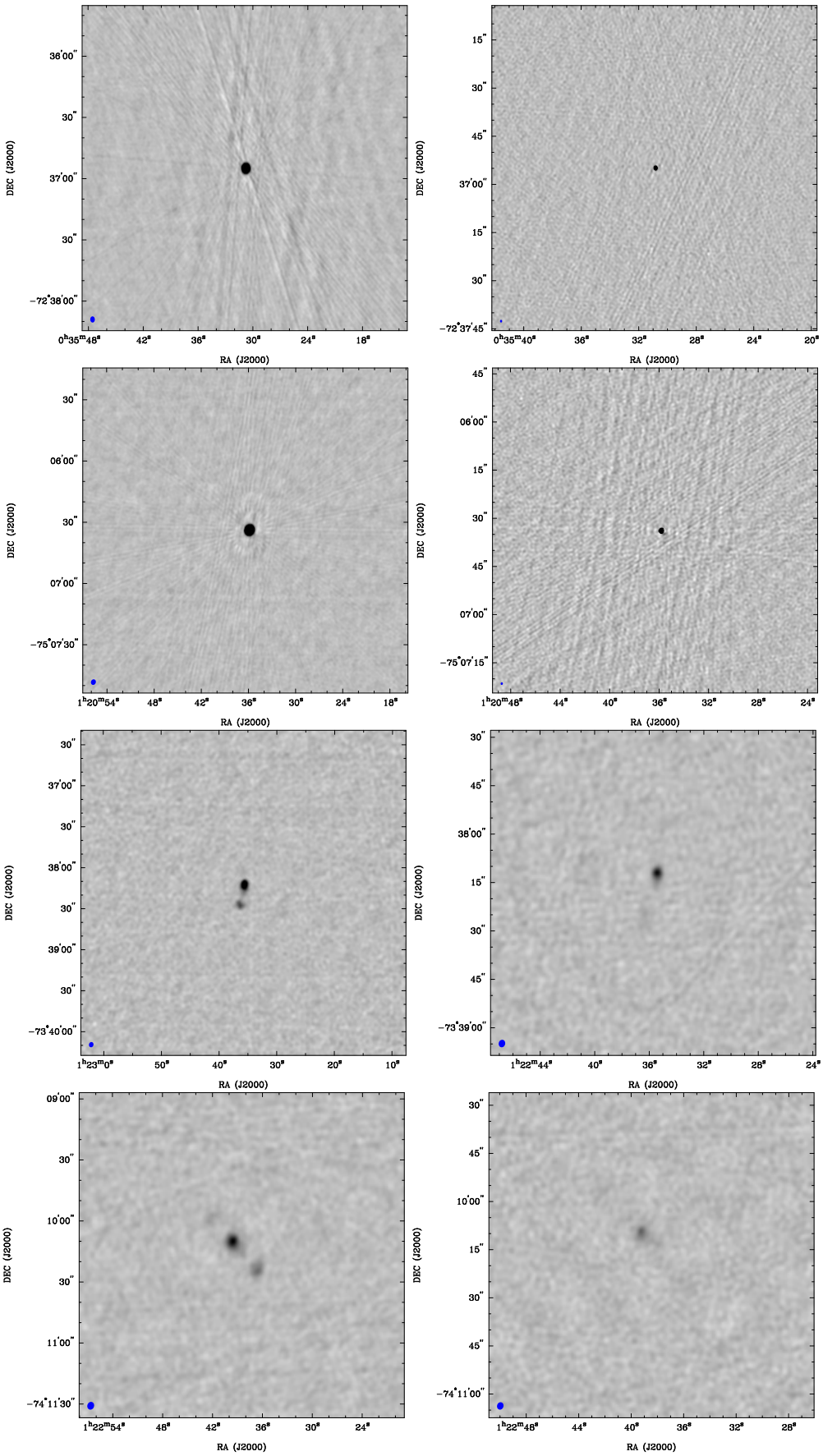

Fig. C.2. (continued) for smc_9, smc_90, smc_93 and smc_94.

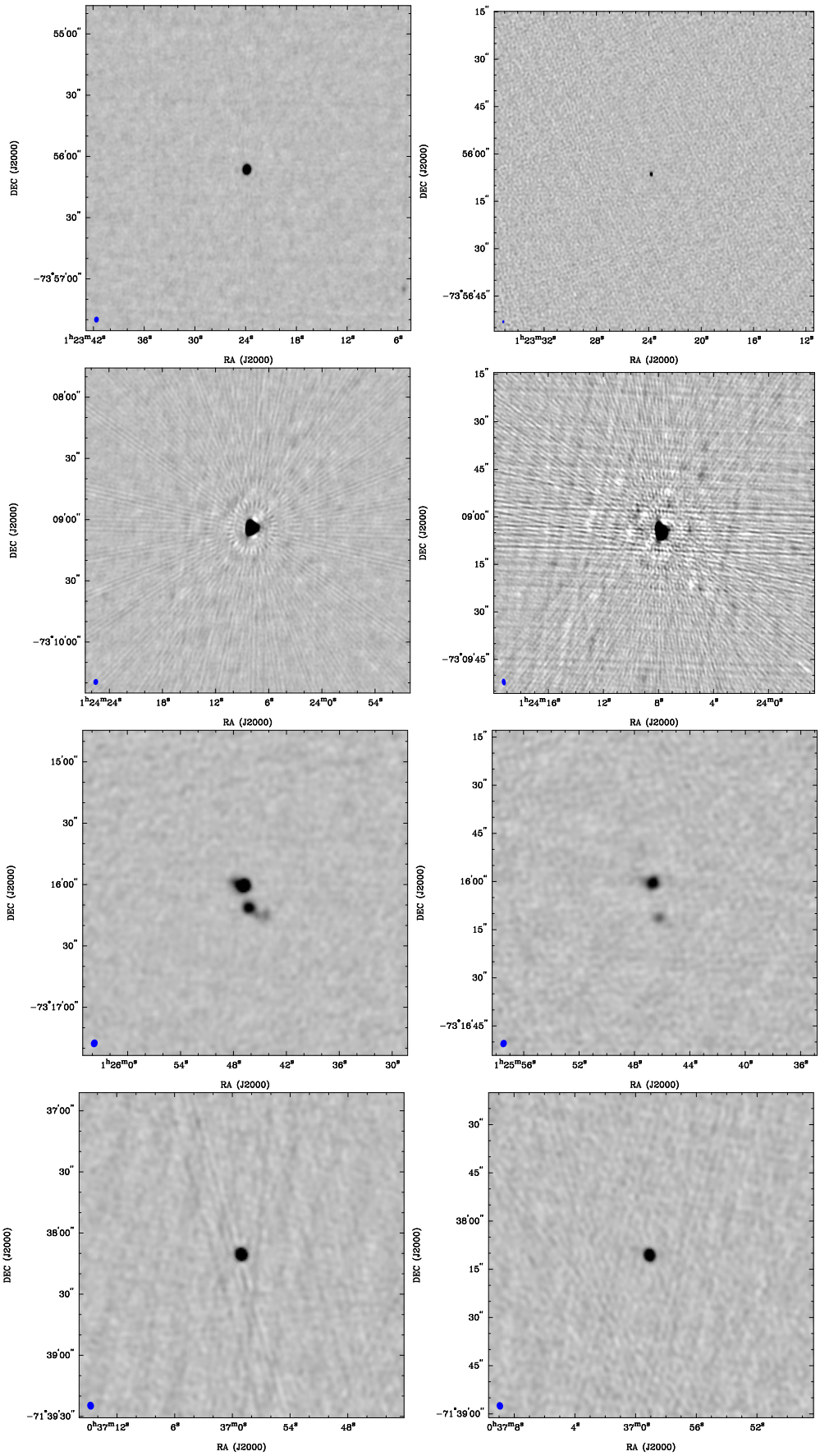

Fig. C.2. (continued) for smc_95, smc_97, smc_99 and smc_frii.

Appendix D

SMC component catalogue

Table D.1: The SMC 5.5 and 9.0 GHz component catalogue. Shown is the source name, the robust weighting (RW), the frequency ν, the RA and Dec, the integrated (S_{int}) and peak (S_p) flux densities, the FWHM of the deconvolved major ($\theta_{\rm maj}$) and minor ($\theta_{\rm min}$) axes, the local r.m.s. (σ_L), and the integrated flux density from sub-band channels 1-4 (e.g. $S_{\rm ch1}$). All fluxes and axes are listed to three significant figures.

Name	RW	ν	RA	Dec	S_{int}	S_p	$\theta_{\rm maj}$	$\theta_{\rm min}$	σ_L	$S_{\rm ch1}$	$S_{\rm ch2}$	$S_{\rm ch3}$	$S_{\rm ch4}$
		(GHz)	(J2000)		(mJy)	(mJy)	(arcsec)	(arcsec)	(μJy)	(mJy)	(mJy)	(mJy)	(mJy)
SMC_0022-7428	2	5.466	00:22:13.52	−74:27:58.1	4.89	4.94	0.	0.	69.6				
SMC_0022-7428	2	5.466	00:22:15.68	−74:28:05.9	6.65	0.798	7.59	6.50	88.2				
SMC_0022-7428	2	5.466	00:22:23.05	−74:28:25.1	94.5	6.73	11.5	7.64	100				
SMC_0022-7428	2	5.466	00:22:00.85	−74:27:19.3	63.7	14.1	16.2	5.52	143				
SMC_0055-7211	2	5.466	00:55:27.69	−72:10:58.7	16.5	16.0	0.586	0.368	91.8				
SMC_0055-7211	2	5.466	00:55:34.15	−72:10:56.2	8.86	3.00	5.87	1.05	57.9				
SMC_0055-7211	2	5.466	00:55:40.08	−72:10:48.2	13.3	1.22	8.53	5.43	57.2				
SMC_0055-7211	2	5.466	00:55:22.70	−72:10:54.6	35.6	9.53	12.6	3.37	41.3				
SMC_10	2	5.466	00:36:24.71	−72:08:49.7	3.57	1.09	6.25	4.59	55.3				
SMC_10	2	5.466	00:36:19.52	−72:09:52.1	8.37	1.94	11.4	3.38	49.8				
SMC_100	2	5.466	01:26:39.80	−73:15:02.3	18.0	12.4	2.42	0.451	50.6				
SMC_101	2	5.466	01:28:09.26	−75:12:51.6	47.3	30.4	8.63	0.323	87.4				
SMC_101	2	5.466	01:28:16.73	−75:12:59.0	32.2	13.2	4.43	2.03	85.3				
SMC_102	2	5.466	01:30:13.60	−74:20:24.1	31.9	31.7	0.	0.	71.5				
SMC_13	2	5.466	00:38:01.14	−72:52:11.0	12.3	8.75	1.86	0.833	109				
SMC_13	2	5.466	00:37:54.77	−72:51:56.5	36.4	29.5	3.08	0.	160				
SMC_14	2	5.466	00:38:04.25	−74:50:30.8	2.85	1.17	11.3	0.	62.8				
SMC_16	2	5.466	00:39:28.58	−71:53:06.1	1.70	0.911	5.05	1.61	30.4				
SMC_16	2	5.466	00:39:26.48	−71:52:41.4	5.97	1.90	6.52	3.97	41.8				
SMC_17	2	5.466	00:39:39.65	−71:41:41.9	19.3	13.0	3.92	0.977	81.3				
SMC_18	2	5.466	00:39:47.30	−71:37:34.5	26.2	15.5	6.19	0.183	71.9				

Continued on next page

Name	RW	ν	RA	Dec	S_{int}	S_p	$\theta_{\rm maj}$	$\theta_{\rm min}$	σ_L	$S_{\rm ch1}$	$S_{\rm ch2}$	$S_{\rm ch3}$	$S_{\rm ch4}$
		(GHz)	(J2000)		(mJy)	(mJy)	(arcsec)	(arcsec)	(μJy)	(mJy)	(mJy)	(mJy)	(mJy)
SMC_19	2	5.466	00:40:47.93	−71:45:59.5	165	128	1.93	0.	1020				
SMC_2	2	5.466	00:30:36.56	−74:29:27.2	6.13	6.09	0.	0.	41.7				
SMC_2	2	5.466	00:30:37.83	−74:29:01.1	18.7	7.29	5.75	2.49	67.8				
SMC_2	2	5.466	00:30:30.52	−74:29:27.2	12.5	4.85	8.51	1.94	51.3				
SMC_21	2	5.466	00:42:03.40	−73:07:23.4	34.0	3.79	24.0	5.93	65.0				
SMC_23	2	5.466	00:42:26.30	−73:04:18.4	21.6	7.61	7.66	3.73	80.4				
SMC_25	2	5.466	00:43:34.50	−71:32:02.0	14.8	2.51	25.9	2.68	45.5				
SMC_26	2	5.466	00:43:42.10	−72:03:51.0	2.75	1.79	2.99	0.	28.4				
SMC_26	2	5.466	00:43:38.64	−72:03:44.0	5.42	5.40	0.	0.	75.7				
SMC_27	2	5.466	00:43:48.46	−73:26:03.5	2.52	1.02	4.44	1.26	43.2				
SMC_27	2	5.466	00:43:41.07	−73:25:48.6	1.48	0.907	3.27	2.24	26.6				
SMC_29	-2	5.466	00:44:59.65	−71:14:38.2	9.59	5.28	0.	0.	77.3				
SMC_3	2	5.466	00:30:36.17	−73:51:45.3	4.28	1.57	5.21	0.	27.8				
SMC_30	2	5.466	00:46:01.98	−74:40:03.9	15.2	10.1	2.19	0.	52.7				
SMC_31	2	5.469	00:46:03.14	−74:13:27.8	3.26	0.613	10.6	4.77	96.4				
SMC_31	2	5.469	00:46:06.10	−74:14:02.5	1.63	0.231	10.8	6.96	71.2				
SMC_32	2	5.466	00:47:18.95	−72:39:47.4	51.6	51.4	0.	0.	84.3				
SMC_34	2	5.466	00:47:50.43	−70:57:56.5	11.4	10.3	0.	0.	36.6				
SMC_35	-2	5.466	00:48:08.38	−74:12:05.8	39.4	36.9	0.	0.	172				
SMC_36	2	5.466	00:48:13.02	−71:14:13.9	0.511	0.568	0.	0.	14.8				
SMC_36	2	5.466	00:48:16.74	−71:14:00.4	6.64	3.61	5.15	2.32	46.8				
SMC_36	2	5.466	00:48:10.05	−71:14:21.9	1.31	0.566	5.09	3.28	57.5				
SMC_38	2	5.474	00:49:23.23	−71:26:59.0	4.67	1.08	8.68	1.34	53.5				

Continued on next page

Name	RW	ν	RA	Dec	S_{int}	S_p	$\theta_{\rm maj}$	$\theta_{\rm min}$	σ_L	$S_{\rm ch1}$	$S_{\rm ch2}$	$S_{\rm ch3}$	$S_{\rm ch4}$
		(GHz)	(J2000)		(mJy)	(mJy)	(arcsec)	(arcsec)	(μJy)	(mJy)	(mJy)	(mJy)	(mJy)
SMC_39	2	5.465	00:49:32.91	−72:19:01.8	10.3	2.92	16.7	1.59	66.1				
SMC_4	2	5.466	00:31:40.51	−74:34:47.3	24.9	24.7	0.	0.	176				
SMC_41	2	5.466	00:49:56.78	−72:35:54.0	27.4	11.0	6.72	0.563	74.3				
SMC_44	2	5.466	00:50:41.49	−70:39:38.0	10.8	8.34	1.59	0.768	76.2				
SMC_45	2	5.466	00:52:18.83	−72:27:07.6	58.1	30.4	4.93	0.778	131				
SMC_46	2	5.466	00:52:38.20	−73:12:44.9	33.5	32.2	0.716	0.194	60.9				
SMC_47	2	5.466	00:53:22.70	−72:35:24.2	4.32	0.998	9.01	3.15	84.7				
SMC_48	2	5.466	00:53:37.72	−72:31:43.5	13.9	12.9	0.	0.	120				
SMC_49	2	5.466	00:54:26.21	−74:17:23.1	2.87	1.33	6.02	1.86	53.9				
SMC_5	2	5.466	00:32:24.64	−73:06:59.1	7.52	3.33	8.73	0.	25.4				
SMC_5	2	5.466	00:32:34.87	−73:06:48.9	12.5	12.4	0.496	0.201	89.7				
SMC_5	2	5.466	00:32:31.04	−73:06:49.3	13.0	0.873	18.4	9.64	194				
SMC_50	-2	5.466	00:55:06.39	−72:37:19.4	2.68	1.67	1.30	0.506	38.9				
SMC_52	2	5.466	00:55:37.29	−74:39:26.3	11.9	11.9	0.	0.	29.1				
SMC_54	2	5.466	00:56:11.27	−71:07:07.5	205	201	0.	0.	552				
SMC_55	2	5.466	00:56:36.76	−74:03:16.1	24.2	24.1	0.	0.	38.7				
SMC_56	2	5.466	00:56:44.99	−72:51:59.6	14.7	11.8	2.69	0.	49.0				
SMC_56	2	5.466	00:56:42.36	−72:52:15.5	11.1	5.83	5.42	2.08	71.1				
SMC_57	2	5.466	00:56:52.61	−71:23:00.1	22.2	8.76	4.06	0.256	67.9				
SMC_58	2	5.466	00:57:15.59	−70:40:46.3	64.7	63.7	0.	0.	157				
SMC_59	2	5.466	00:57:32.40	−74:12:43.6	74.4	73.8	0.	0.	154				
SMC_61	2	5.466	00:58:12.46	−71:24:04.5	7.93	0.405	16.8	6.18	30.8				
SMC_61	2	5.466	00:58:16.67	−71:23:37.8	1.35	0.369	9.93	0.	72.3				

Continued on next page

Name	RW	ν	RA	Dec	S_{int}	S_p	$\theta_{\rm maj}$	$\theta_{\rm min}$	σ_L	$S_{\rm ch1}$	$S_{\rm ch2}$	$S_{\rm ch3}$	$S_{\rm ch4}$
		(GHz)	(J2000)		(mJy)	(mJy)	(arcsec)	(arcsec)	(μJy)	(mJy)	(mJy)	(mJy)	(mJy)
SMC_64	2	5.466	00:59:05.19	−70:49:07.2	9.14	6.29	3.41	0.739	59.2				
SMC_64	2	5.466	00:59:03.42	−70:48:54.5	8.91	6.75	1.77	0.496	60.3				
SMC_65	-2	5.466	01:00:29.71	−71:38:26.1	41.4	39.5	0.353	0.0190	207				
SMC_66	2	5.466	01:00:41.57	−74:54:09.2	6.14	1.35	12.3	3.27	46.6				
SMC_66	2	5.466	01:00:46.80	−74:54:19.6	8.85	3.18	4.86	2.63	38.6				
SMC_68	2	5.466	01:03:30.32	−75:07:07.9	10.6	6.80	2.75	1.17	53.9				
SMC_68	2	5.466	01:03:33.46	−75:06:58.2	9.90	5.21	4.13	1.19	49.4				
SMC_69	2	5.466	01:04:06.35	−73:51:30.0	2.79	1.63	8.92	0.	32.7				
SMC_69	2	5.466	01:04:08.10	−73:51:18.2	0.780	0.245	4.83	2.94	23.2				
SMC_69	2	5.466	01:04:00.10	−73:51:10.0	1.58	1.68	0.	0.	28.6				
SMC_7	2	5.466	00:34:18.14	−73:34:09.5	5.26	4.70	0.	0.	33.9				
SMC_7	2	5.466	00:34:13.03	−73:33:18.6	28.3	4.58	16.1	6.63	106				
SMC_7	2	5.466	00:34:28.88	−73:35:27.0	7.38	3.19	5.83	1.10	49.8				
SMC_70	2	5.466	01:04:31.28	−72:07:25.3	12.3	11.9	0.	0.	32.8				
SMC_71	2	5.466	01:04:41.26	−71:31:22.5	16.8	16.9	0.	0.	74.5				
SMC_72	-2	5.466	01:04:58.03	−70:37:34.7	28.1	26.9	0.301	0.210	168				
SMC_74	2	5.466	01:07:08.44	−71:43:06.2	7.09	1.93	5.89	1.86	40.0				
SMC_75	2	5.466	01:09:31.35	−71:34:54.8	31.9	19.2	7.96	0.191	109				
SMC_76	2	5.466	01:10:05.33	−72:26:48.2	66.3	66.2	0.	0.	256				
SMC_77	2	5.466	01:10:29.14	−74:54:05.8	1.27	1.24	0.	0.	42.5				
SMC_77	2	5.466	01:10:29.68	−74:53:53.9	1.16	0.289	8.86	4.11	45.0				
SMC_8	2	5.466	00:34:24.47	−72:11:44.4	42.4	20.5	3.80	0.186	104				
SMC_80	2	5.466	01:12:27.08	−72:48:02.5	5.94	1.16	10.7	0.	31.7				

Continued on next page

Name	RW	ν	RA	Dec	S_{int}	S_p	$\theta_{\rm maj}$	$\theta_{\rm min}$	σ_L	$S_{\rm ch1}$	$S_{\rm ch2}$	$S_{\rm ch3}$	$S_{\rm ch4}$
		(GHz)	(J2000)		(mJy)	(mJy)	(arcsec)	(arcsec)	(μJy)	(mJy)	(mJy)	(mJy)	(mJy)
SMC_83	2	5.466	01:15:35.51	−72:00:09.1	2.81	2.26	1.55	0.0392	54.8				
SMC_83	2	5.466	01:15:30.88	−71:59:52.0	1.89	1.86	0.388	0.232	18.2				
SMC_84	2	5.466	01:16:09.87	−74:28:14.1	8.65	5.55	0.	0.	29.9				
SMC_86	2	5.466	01:16:15.77	−73:26:57.4	16.0	4.44	9.09	2.07	45.7				
SMC_9	2	5.466	00:35:30.77	−72:36:55.1	17.3	17.2	0.	0.	104				
SMC_90	2	5.466	01:20:35.84	−75:06:33.9	35.5	35.2	0.	0.	99.0				
SMC_93	2	5.466	01:22:35.81	−73:38:16.8	11.0	4.31	14.9	2.57	35.7				
SMC_94	2	5.466	01:22:39.42	−74:10:10.9	6.82	1.97	6.14	4.08	43.8				
SMC_94	2	5.466	01:22:36.66	−74:10:24.0	2.64	0.815	6.50	4.36	48.8				
SMC_94	2	5.466	01:22:42.11	−74:09:58.7	1.27	0.293	8.92	4.55	37.3				
SMC_95	2	5.466	01:23:23.83	−73:56:06.6	11.7	11.8	0.	0.	60.6				
SMC_97	2	5.466	01:24:07.91	−73:09:04.1	99.0	75.0	1.58	1.52	169				
SMC_99	2	5.466	01:25:46.97	−73:16:00.2	12.5	6.84	4.67	1.34	52.6				
SMC_99	2	5.466	01:25:45.81	−73:16:12.3	7.02	2.95	8.49	0.	69.5				
SMC_E0102	2	5.466	01:04:01.45	−72:01:46.9	42.6	2.49	34.8	20.6	121				
SMC_FRII	2	5.466	00:36:59.08	−71:38:10.6	10.5	10.3	0.	0.	74.6				
SMC_FRII	2	5.466	00:37:09.74	−71:40:06.5	5.30	1.93	5.42	3.40	91.9				
SMC_FRII	2	5.466	00:36:47.38	−71:35:58.0	1.82	0.784	5.27	2.83	30.2				
SMC_0022-7428	2	9.002	00:22:13.60	−74:27:58.0	8.99	4.65	3.06	0.926	63.0				
SMC_0022-7428	2	9.002	00:22:12.59	−74:27:54.1	0.717	0.328	2.25	1.21	23.8				
SMC_0022-7428	2	9.002	00:22:23.58	−74:28:26.3	41.4	2.52	7.55	6.14	82.8				
SMC_0022-7428	2	9.002	00:21:59.61	−74:27:15.4	16.9	5.77	3.57	2.76	63.4				
SMC_0055-7211	2	9.002	00:55:34.34	−72:10:56.0	5.04	1.79	6.15	0.941	58.6				

Continued on next page

Name	RW	ν	RA	Dec	S_{int}	S_p	$\theta_{\rm maj}$	$\theta_{\rm min}$	σ_L	$S_{\rm ch1}$	$S_{\rm ch2}$	$S_{\rm ch3}$	$S_{\rm ch4}$
		(GHz)	(J2000)		(mJy)	(mJy)	(arcsec)	(arcsec)	(μJy)	(mJy)	(mJy)	(mJy)	(mJy)
SMC_0055-7211	2	9.002	00:55:27.82	−72:10:58.6	17.8	17.7	0.	0.	50.8				
SMC_0055-7211	2	9.002	00:55:23.50	−72:10:56.1	8.14	4.94	1.74	0.862	46.4				
SMC_0055-7211	2	9.002	00:55:40.43	−72:10:46.0	1.01	0.332	0.	0.	23.1				
SMC_10	2	9.002	00:36:19.42	−72:09:53.5	4.49	0.955	6.18	2.96	49.0				
SMC_100	2	9.002	01:26:39.59	−73:15:02.6	11.7	4.79	2.63	0.861	105				
SMC_101	2	9.000	01:28:16.71	−75:12:58.9	19.2	4.43	4.31	2.17	51.3				
SMC_101	2	9.000	01:28:11.42	−75:12:53.4	6.85	6.67	0.580	0.	108				
SMC_101	2	9.000	01:28:08.83	−75:12:51.3	19.7	12.3	2.78	0.266	57.8				
SMC_102	-2	9.002	01:30:13.59	−74:20:24.1	32.1	31.1	0.221	0.	180				
SMC_13	2	9.002	00:38:01.05	−72:52:11.2	5.94	3.68	1.48	0.122	61.2				
SMC_13	2	9.002	00:37:54.67	−72:51:56.5	22.4	18.4	2.52	0.	105				
SMC_14	-2	9.002	00:38:05.19	−74:50:27.9	1.28	0.774	0.791	0.422	19.4				
SMC_16	2	9.002	00:39:25.79	−71:52:41.2	1.77	0.803	3.19	1.66	87.9				
SMC_17	2	9.002	00:39:39.56	−71:41:41.5	9.75	6.33	3.06	0.434	81.3				
SMC_18	2	9.002	00:39:47.52	−71:37:35.5	11.3	7.70	1.32	0.	41.8				
SMC_18	2	9.002	00:39:46.54	−71:37:31.7	3.58	2.44	1.59	0.	38.1				
SMC_19	2	9.009	00:40:48.03	−71:45:58.7	97.2	64.0	1.97	0.	671				
SMC_2	2	9.002	00:30:38.06	−74:29:00.4	8.88	2.40	2.70	1.91	39.6				
SMC_2	2	9.002	00:30:36.61	−74:29:27.0	5.55	5.24	0.455	0.163	77.4				
SMC_2	2	9.002	00:30:31.63	−74:29:22.0	0.254	0.363	0.	0.	7.93				
SMC_2	2	9.002	00:30:30.00	−74:29:28.6	4.58	2.15	1.73	0.898	38.8				
SMC_2	2	9.002	00:30:30.48	−74:29:24.8	0.516	0.328	1.58	0.741	25.8				
SMC_21	2	9.002	00:42:05.65	−73:07:19.8	5.49	1.61	5.76	2.02	37.9				

Continued on next page

Name	RW	ν	RA	Dec	S_{int}	S_p	$\theta_{\rm maj}$	$\theta_{\rm min}$	σ_L	$S_{\rm ch1}$	$S_{\rm ch2}$	$S_{\rm ch3}$	$S_{\rm ch4}$
		(GHz)	(J2000)		(mJy)	(mJy)	(arcsec)	(arcsec)	(μJy)	(mJy)	(mJy)	(mJy)	(mJy)
SMC_21	2	9.002	00:42:02.03	−73:07:26.3	16.0	3.98	15.3	2.59	39.1				
SMC_23	2	9.002	00:42:26.14	−73:04:18.4	11.0	2.77	5.17	3.22	48.1				
SMC_25	2	9.001	00:43:36.80	−71:31:57.1	3.25	2.26	2.12	0.716	114				
SMC_25	2	9.001	00:43:33.89	−71:32:02.1	1.41	1.22	0.	0.	12.3				
SMC_25	2	9.001	00:43:32.06	−71:32:08.8	1.32	0.336	4.39	3.09	46.7				
SMC_26	2	9.002	00:43:42.01	−72:03:51.0	1.26	0.691	0.	0.	14.6				
SMC_26	2	9.002	00:43:38.64	−72:03:44.0	3.19	3.07	0.469	0.392	35.5				
SMC_3	2	9.002	00:30:36.36	−73:51:43.2	4.02	1.36	5.63	0.290	56.0				
SMC_30	2	9.002	00:46:02.09	−74:40:03.5	9.61	4.69	2.06	0.543	36.2				
SMC_32	-2	8.988	00:47:18.94	−72:39:47.4	40.8	39.1	0.193	0.114	306				
SMC_34	-2	9.002	00:47:50.37	−70:57:56.4	6.34	5.13	0.437	0.199	96.4				
SMC_35	-2	9.002	00:48:08.34	−74:12:05.9	26.3	23.6	0.276	0.220	424				
SMC_36	2	9.001	00:48:16.93	−71:14:00.4	3.69	2.15	2.79	1.07	61.1				
SMC_39	2	9.001	00:49:32.06	−72:19:03.0	2.61	1.90	1.81	0.723	94.5				
SMC_39	2	9.001	00:49:30.11	−72:19:04.9	1.03	0.712	2.11	0.871	42.8				
SMC_4	-2	9.002	00:31:40.62	−74:34:46.9	16.6	15.3	0.296	0.	130				
SMC_41	2	9.001	00:49:56.81	−72:35:54.1	15.9	5.47	6.81	0.756	41.2				
SMC_44	2	9.002	00:50:41.43	−70:39:37.8	6.93	4.24	1.71	0.456	64.1				
SMC_45	2	9.002	00:52:18.82	−72:27:07.5	34.4	16.6	4.93	0.825	73.1				
SMC_46	-2	9.002	00:52:38.21	−73:12:44.9	20.4	13.6	0.817	0.0790	143				
SMC_47	2	9.003	00:53:22.67	−72:35:22.5	0.282	0.337	0.	0.	36.6				
SMC_48	-2	8.995	00:53:37.81	−72:31:43.0	7.27	4.80	0.829	0.	48.8				
SMC_49	2	9.002	00:54:26.03	−74:17:23.6	0.982	0.916	1.07	0.	48.6				

Continued on next page

Name	RW	ν	RA	Dec	S_{int}	S_p	$\theta_{\rm maj}$	$\theta_{\rm min}$	σ_L	$S_{\rm ch1}$	$S_{\rm ch2}$	$S_{\rm ch3}$	$S_{\rm ch4}$
		(GHz)	(J2000)		(mJy)	(mJy)	(arcsec)	(arcsec)	(μJy)	(mJy)	(mJy)	(mJy)	(mJy)
SMC_5	2	9.002	00:32:34.88	−73:06:48.8	13.5	13.5	0.	0.	79.0				
SMC_5	2	9.002	00:32:25.55	−73:06:56.3	2.02	1.00	0.	0.	23.4				
SMC_5	2	9.002	00:32:24.00	−73:07:00.6	2.45	1.42	1.72	0.	23.6				
SMC_50	2	9.002	00:55:06.25	−72:37:19.3	1.69	0.980	2.34	1.39	32.3				
SMC_52	-2	9.003	00:55:37.30	−74:39:26.3	5.12	5.18	0.	0.	30.8				
SMC_54	-2	9.003	00:56:11.15	−71:07:07.2	116	103	0.357	0.0786	597				
SMC_55	-2	9.002	00:56:36.75	−74:03:16.1	18.6	18.4	0.127	0.	96.4				
SMC_56	2	9.001	00:56:44.97	−72:51:59.5	8.93	6.07	2.36	0.	57.8				
SMC_56	2	9.001	00:56:42.37	−72:52:15.5	6.07	3.07	4.72	2.20	58.4				
SMC_57	2	9.001	00:56:52.60	−71:23:00.1	11.7	4.71	4.04	0.861	60.5				
SMC_58	-2	8.995	00:57:15.56	−70:40:46.3	73.1	70.2	0.245	0.0760	405				
SMC_59	-2	9.002	00:57:32.40	−74:12:43.6	33.8	30.9	0.274	0.151	205				
SMC_64	2	8.988	00:59:05.27	−70:49:07.6	4.74	2.41	1.46	0.593	36.7				
SMC_64	2	8.988	00:59:03.38	−70:48:54.6	4.31	2.26	1.65	0.545	42.6				
SMC_65	-2	9.002	01:00:29.69	−71:38:26.1	25.3	23.0	0.286	0.160	572				
SMC_66	2	9.003	01:00:46.86	−74:54:19.8	5.57	2.01	4.26	1.97	47.7				
SMC_66	2	9.003	01:00:41.20	−74:54:08.7	3.25	0.841	4.87	0.498	39.6				
SMC_68	2	9.002	01:03:33.61	−75:06:58.8	4.74	2.19	2.11	0.971	48.6				
SMC_68	2	9.002	01:03:30.24	−75:07:08.2	4.88	3.14	1.48	0.616	88.3				
SMC_69	2	9.003	01:04:06.72	−73:51:27.5	1.34	1.11	0.912	0.473	45.4				
SMC_69	2	9.003	01:04:00.09	−73:51:09.8	0.960	0.955	0.	0.	46.3				
SMC_7	2	8.999	00:34:12.06	−73:33:15.2	7.73	2.29	4.61	1.92	34.0				
SMC_7	2	8.999	00:34:28.80	−73:35:27.0	6.07	1.79	5.60	1.19	138				

Continued on next page

Name	RW	ν	RA	Dec	S_{int}	S_p	$\theta_{\rm maj}$	$\theta_{\rm min}$	σ_L	$S_{\rm ch1}$	$S_{\rm ch2}$	$S_{\rm ch3}$	$S_{\rm ch4}$
		(GHz)	(J2000)		(mJy)	(mJy)	(arcsec)	(arcsec)	(μJy)	(mJy)	(mJy)	(mJy)	(mJy)
SMC_7	2	8.999	00:34:18.07	−73:34:09.7	5.46	5.03	1.36	0.0759	65.6				
SMC_70	-2	9.001	01:04:31.24	−72:07:25.2	6.55	5.91	0.365	0.0873	77.5				
SMC_71	-2	9.001	01:04:41.19	−71:31:22.5	11.5	10.8	0.	0.	151				
SMC_72	-2	9.002	01:04:57.94	−70:37:34.8	20.6	18.7	0.327	0.146	445				
SMC_74	2	9.000	01:07:08.90	−71:43:06.4	2.43	1.40	4.62	0.791	82.0				
SMC_75	2	9.003	01:09:32.16	−71:34:52.6	5.57	3.89	1.32	0.	38.9				
SMC_75	2	9.003	01:09:30.80	−71:34:56.0	10.4	9.00	0.	0.	113				
SMC_76	-2	9.002	01:10:05.42	−72:26:48.4	37.4	36.5	0.	0.	206				
SMC_8	2	9.002	00:34:24.50	−72:11:44.2	23.9	10.0	3.86	0.355	52.2				
SMC_80	-2	9.001	01:12:27.27	−72:48:03.4	0.861	0.631	0.566	0.332	8.87				
SMC_83	2	9.003	01:15:35.39	−72:00:09.0	1.79	1.23	0.	0.	49.7				
SMC_83	2	9.003	01:15:30.77	−71:59:52.1	0.918	0.790	0.	0.	82.3				
SMC_84	2	9.001	01:16:09.88	−74:28:14.1	5.74	2.93	2.42	0.	58.4				
SMC_86	2	8.985	01:16:15.69	−73:26:56.9	9.90	3.05	10.8	0.792	81.9				
SMC_9	-2	9.002	00:35:30.81	−72:36:55.0	16.1	15.2	0.	0.	99.6				
SMC_90	-2	9.002	01:20:35.81	−75:06:33.9	77.9	76.8	0.	0.	360				
SMC_93	2	9.003	01:22:35.43	−73:38:12.5	3.89	1.90	2.99	0.657	29.9				
SMC_94	2	9.002	01:22:39.02	−74:10:10.4	4.23	0.884	4.98	2.59	52.1				
SMC_95	-2	9.001	01:23:23.82	−73:56:06.5	4.35	4.20	0.	0.	72.3				
SMC_97	2	9.003	01:24:07.81	−73:09:04.7	94.6	52.2	1.45	1.28	353				
SMC_99	2	9.002	01:25:46.75	−73:16:00.3	6.94	2.93	3.28	1.40	59.6				
SMC_99	2	9.002	01:25:46.13	−73:16:11.5	2.18	1.01	2.95	0.	19.0				
SMC_E0102	2	9.003	01:04:00.34	−72:01:43.6	25.2	0.848	11.9	4.68	80.2				

Continued on next page

Name	RW	ν	RA	Dec	S_{int}	S_p	$\theta_{\rm maj}$	$\theta_{\rm min}$	σ_L	$S_{\rm ch1}$	$S_{\rm ch2}$	$S_{\rm ch3}$	$S_{\rm ch4}$
		(GHz)	(J2000)		(mJy)	(mJy)	(arcsec)	(arcsec)	(μJy)	(mJy)	(mJy)	(mJy)	(mJy)
SMC_FRII	2	9.002	00:36:59.10	−71:38:10.6	9.20	9.06	0.	0.	37.0				
SMC_FRII	2	9.002	00:37:10.02	−71:40:05.1	0.717	0.872	0.	0.	9.33				
SMC_0022-7428	2	5.496	00:22:15.42	−74:28:06.0	1.16	0.446	5.76	2.18	22.6				
SMC_0022-7428	2	5.496	00:22:13.52	−74:27:58.1	3.98	3.99	0.	0.	39.4	4.76	4.27	4.60	2.31
SMC_0022-7428	2	5.496	00:22:23.24	−74:28:25.0	61.8	7.39	10.6	7.28	60.3	99.7	63.9	51.4	33.4
SMC_0022-7428	2	5.496	00:22:00.81	−74:27:18.9	42.4	14.1	17.1	6.35	48.8	77.8	41.7	30.6	19.6
SMC_0055-7211	2	5.496	00:55:34.15	−72:10:56.3	6.54	2.78	5.58	0.574	30.7	9.04	6.47	5.36	5.27
SMC_0055-7211	2	5.496	00:55:27.68	−72:10:58.6	15.7	15.4	0.513	0.319	45.9	15.9	15.5	15.4	16.3
SMC_0055-7211	2	5.496	00:55:40.09	−72:10:48.4	8.88	1.28	8.74	4.62	48.4	13.9	9.32	6.93	5.34
SMC_0055-7211	2	5.496	00:55:23.38	−72:10:56.1	13.0	10.0	1.58	1.14	35.8	16.2	13.8	12.0	9.86
SMC_0055-7211	2	5.496	00:55:21.18	−72:10:53.0	7.31	0.913	10.6	7.32	56.1	15.0	8.26	6.89	4.14
SMC_10	2	5.496	00:36:19.40	−72:09:53.3	6.97	2.49	9.54	3.74	57.2	12.0	8.36	8.26	5.24
SMC_10	2	5.496	00:36:24.74	−72:08:49.4	1.28	0.389	8.20	4.31	17.3	1.90	1.20	1.61	
SMC_100	2	5.496	01:26:39.80	−73:15:02.8	17.9	13.2	2.48	0.609	33.0	20.0	18.4	17.2	15.8
SMC_101	2	5.496	01:28:16.80	−75:12:59.0	27.6	14.7	3.86	1.63	42.2	35.3	27.0	24.8	23.5
SMC_101	2	5.496	01:28:09.19	−75:12:51.5	42.3	30.6	7.67	0.456	72.5	52.7	42.7	39.8	34.1
SMC_102	2	5.496	01:30:13.63	−74:20:24.0	31.5	31.3	0.	0.	38.3	31.8	31.4	31.4	31.5
SMC_13	2	5.496	00:38:01.18	−72:52:10.9	10.3	8.80	1.41	0.914	73.2	12.9	10.7	9.22	8.42
SMC_13	2	5.496	00:37:54.81	−72:51:56.4	34.9	29.9	2.69	0.279	50.0	39.5	36.2	33.2	30.7
SMC_14	2	5.496	00:38:04.18	−74:50:31.8	6.70	1.39	13.5	0.	44.0	5.76	6.87	8.89	7.06
SMC_16	2	5.496	00:39:28.56	−71:53:06.2	1.00	0.523	5.48	2.39	11.8	1.38	1.44	0.604	0.596
SMC_16	2	5.496	00:39:26.48	−71:52:40.8	4.23	2.17	5.47	2.43	22.6	5.73	4.44	3.92	2.83
SMC_17	2	5.496	00:39:39.64	−71:41:42.0	18.6	13.3	3.84	0.971	37.5	23.1	20.3	16.6	14.5

Continued on next page

Name	RW	ν	RA	Dec	S_{int}	S_p	$\theta_{\rm maj}$	$\theta_{\rm min}$	σ_L	$S_{\rm ch1}$	$S_{\rm ch2}$	$S_{\rm ch3}$	$S_{\rm ch4}$
		(GHz)	(J2000)		(mJy)	(mJy)	(arcsec)	(arcsec)	(μJy)	(mJy)	(mJy)	(mJy)	(mJy)
SMC_18	2	5.496	00:39:47.31	−71:37:34.5	24.9	15.7	6.00	0.	39.1	29.6	25.6	23.4	21.1
SMC_19	2	5.734	00:40:47.93	−71:45:59.4	140	123	1.58	0.	775	166	137	118	
SMC_2	2	5.496	00:30:37.92	−74:29:00.8	16.8	8.64	5.43	2.68	64.0	22.1	17.4	15.0	14.2
SMC_2	2	5.496	00:30:36.60	−74:29:27.0	5.21	5.19	0.	0.	33.1	5.96	5.60	5.29	3.99
SMC_2	2	5.496	00:30:30.33	−74:29:27.6	11.0	5.00	7.50	0.	78.5	12.5	11.8	10.7	8.85
SMC_21	2	5.496	00:42:05.74	−73:07:19.2	10.4	3.64	6.10	2.54	57.1	13.8	12.4	9.61	5.80
SMC_21	2	5.496	00:42:01.79	−73:07:26.4	14.9	3.63	14.0	1.09	56.7	20.1	13.8	13.6	12.1
SMC_23	2	5.496	00:42:26.11	−73:04:18.4	19.0	8.31	6.86	3.08	185	25.3	20.6	16.7	13.8
SMC_25	2	5.496	00:43:36.64	−71:31:57.0	5.61	2.64	6.07	1.32	33.5	8.10	4.23	5.75	4.42
SMC_25	2	5.496	00:43:33.97	−71:32:01.9	2.54	2.09	1.61	1.10	38.5	3.53	4.30	0.919	1.42
SMC_25	2	5.496	00:43:32.04	−71:32:08.4	2.67	0.618	5.28	2.21	30.4	5.54	2.22	1.36	1.53
SMC_26	2	5.496	00:43:42.13	−72:03:51.2	2.39	1.69	2.31	0.	18.1	2.84	2.42	2.34	1.93
SMC_26	2	5.496	00:43:38.65	−72:03:44.1	5.72	5.45	0.771	0.492	26.5	6.83	5.84	5.26	4.96
SMC_27	2	5.496	00:43:48.39	−73:26:03.6	2.29	1.03	5.60	3.33	54.3	2.43	2.68	2.38	1.68
SMC_27	2	5.496	00:43:41.06	−73:25:48.5	1.13	0.877	2.74	1.07	57.7	1.22	0.912	1.16	1.22
SMC_29	2	5.496	00:44:59.63	−71:14:38.1	10.5	7.33	2.17	1.61	189	11.4	9.69	9.88	11.1
SMC_3	2	5.496	00:30:36.19	−73:51:45.3	3.93	1.66	5.10	0.239	12.2	5.22	3.86	3.71	2.94
SMC_30	2	5.496	00:46:01.90	−74:40:03.8	15.2	11.3	1.99	0.613	45.3	16.6	15.7	14.9	13.5
SMC_31	2	5.495	00:46:02.93	−74:13:28.2	6.79	0.985	13.8	6.82	66.7	5.81	8.78	5.82	6.59
SMC_32	2	5.496	00:47:18.93	−72:39:47.5	51.3	51.2	0.	0.	53.9	54.2	52.1	50.7	48.2
SMC_34	2	5.496	00:47:50.41	−70:57:56.5	11.2	10.3	0.	0.	21.3	13.7	11.4	10.1	9.65
SMC_35	2	5.496	00:48:08.43	−74:12:05.7	41.7	40.8	0.479	0.283	78.4	48.1	43.8	39.0	36.3
SMC_36	2	5.496	00:48:16.68	−71:14:00.5	6.05	3.77	4.25	1.99	21.2	6.51	6.19	5.19	6.30

Continued on next page

Name	RW	ν	RA	Dec	S_{int}	S_p	$\theta_{\rm maj}$	$\theta_{\rm min}$	σ_L	$S_{\rm ch1}$	$S_{\rm ch2}$	$S_{\rm ch3}$	$S_{\rm ch4}$
		(GHz)	(J2000)		(mJy)	(mJy)	(arcsec)	(arcsec)	(μJy)	(mJy)	(mJy)	(mJy)	(mJy)
SMC_36	2	5.496	00:48:09.99	−71:14:21.7	1.06	0.446	5.67	4.03	29.3	1.10	1.55	0.932	0.659
SMC_38	2	5.496	00:49:23.32	−71:26:58.5	7.24	1.33	6.81	0.859	47.6	4.79	8.61	8.10	7.68
SMC_39	2	5.496	00:49:33.15	−72:19:01.4	9.63	3.29	14.7	1.03	35.6	12.6	11.1	8.57	6.31
SMC_4	2	5.496	00:31:40.54	−74:34:47.2	26.0	25.2	0.608	0.370	51.7	29.6	26.6	25.2	22.9
SMC_41	2	5.496	00:49:56.78	−72:35:54.1	26.6	11.4	6.64	0.739	35.0	31.9	27.3	25.2	21.9
SMC_44	2	5.496	00:50:41.51	−70:39:38.2	10.7	9.03	1.95	0.527	43.5	12.0	11.1	10.2	9.68
SMC_45	2	5.496	00:52:18.83	−72:27:07.6	55.3	28.5	4.86	0.814	63.4	65.1	57.8	52.2	47.7
SMC_46	2	5.496	00:52:38.19	−73:12:44.9	33.0	31.9	0.511	0.244	27.1	38.3	34.2	31.5	28.2
SMC_47	2	5.496	00:53:22.76	−72:35:23.0	3.00	1.07	7.95	2.02	42.2	2.20	3.09	2.43	4.26
SMC_48	2	5.496	00:53:37.73	−72:31:43.4	14.4	13.5	1.08	0.495	30.5	17.1	15.1	13.7	11.8
SMC_49	2	5.496	00:54:26.22	−74:17:23.3	3.05	1.55	5.83	2.30	62.0	3.25	2.71	3.33	2.98
SMC_5	2	5.496	00:32:34.77	−73:06:49.0	12.3	12.2	0.	0.	43.4	12.7	12.2	11.7	12.4
SMC_5	2	5.496	00:32:30.99	−73:06:49.2	5.47	1.18	10.0	3.41	38.9	7.04	7.35	4.49	3.04
SMC_5	2	5.496	00:32:24.43	−73:06:59.5	5.21	2.88	8.21	0.	30.3	6.68	5.79	4.52	3.88
SMC_50	2	5.496	00:55:06.39	−72:37:19.4	2.85	2.33	1.56	1.12	38.7	3.17	2.77	3.14	2.32
SMC_52	2	5.496	00:55:37.30	−74:39:26.3	11.7	11.6	0.439	0.139	31.2	14.4	12.6	10.7	8.97
SMC_54	2	5.496	00:56:11.27	−71:07:07.4	201	197	0.	0.	696	233	208	188	173
SMC_55	2	5.496	00:56:36.76	−74:03:16.2	23.8	23.6	0.333	0.118	30.4	25.6	23.9	23.3	22.4
SMC_56	2	5.496	00:56:44.97	−72:51:59.6	13.8	11.8	1.99	0.	17.3	15.8	14.7	13.4	11.5
SMC_56	2	5.496	00:56:42.38	−72:52:15.6	9.51	5.63	4.93	1.73	58.5	12.0	9.89	8.49	7.68
SMC_57	2	5.496	00:56:52.60	−71:23:00.1	21.7	9.94	4.01	0.	32.1	25.4	22.9	20.2	18.2
SMC_58	2	5.496	00:57:15.60	−70:40:46.3	64.3	63.4	0.	0.	59.4	63.0	63.4	65.3	65.4
SMC_59	2	5.496	00:57:32.41	−74:12:43.7	73.1	72.1	0.	0.	61.9	90.1	77.6	66.8	58.0

Continued on next page

Name	RW	ν	RA	Dec	S_{int}	S_p	$\theta_{\rm maj}$	$\theta_{\rm min}$	σ_L	$S_{\rm ch1}$	$S_{\rm ch2}$	$S_{\rm ch3}$	$S_{\rm ch4}$
		(GHz)	(J2000)		(mJy)	(mJy)	(arcsec)	(arcsec)	(μJy)	(mJy)	(mJy)	(mJy)	(mJy)
SMC_64	2	5.496	00:59:05.17	−70:49:07.2	8.28	6.19	3.18	0.757	19.5	11.1	8.65	7.22	6.11
SMC_64	2	5.496	00:59:03.40	−70:48:54.4	8.32	6.80	1.59	0.774	27.5	10.6	8.65	7.64	6.42
SMC_65	2	5.496	01:00:29.74	−71:38:26.0	40.5	39.9	0.	0.	70.6	46.5	42.7	38.4	34.5
SMC_66	2	5.496	01:00:46.62	−74:54:19.5	8.37	3.29	4.66	2.04	46.2	9.25	8.89	7.52	7.80
SMC_66	2	5.496	01:00:40.69	−74:54:07.7	2.30	1.15	3.42	2.37	67.6	3.08	2.38	1.89	1.97
SMC_68	2	5.496	01:03:33.50	−75:06:58.1	8.77	5.57	3.62	1.14	28.0	10.3	9.82	8.26	6.67
SMC_68	2	5.496	01:03:30.32	−75:07:07.8	9.75	7.01	2.38	0.989	35.0	11.9	10.1	9.25	7.74
SMC_69	2	5.496	01:04:06.67	−73:51:27.9	1.30	0.992	1.74	1.49	24.2	2.92	1.38	0.499	
SMC_69	2	5.496	01:04:00.10	−73:51:09.7	1.43	1.56	0.	0.	24.0	0.637	2.11	1.82	1.93
SMC_7	2	5.496	00:34:12.80	−73:33:18.2	24.3	5.74	15.6	7.11	83.0	50.0	28.6	18.9	13.5
SMC_7	2	5.496	00:34:28.91	−73:35:27.1	5.78	3.06	5.63	0.737	33.4	8.31	6.30	4.61	3.92
SMC_7	2	5.496	00:34:18.17	−73:34:09.7	4.92	4.49	0.	0.	20.1	5.28	4.87	4.95	4.60
SMC_70	2	5.496	01:04:31.29	−72:07:25.2	12.1	11.8	0.605	0.417	41.7	13.8	12.7	11.6	10.5
SMC_71	2	5.496	01:04:41.23	−71:31:22.4	17.0	16.7	0.502	0.301	46.8	18.5	17.3	16.7	15.6
SMC_72	2	5.496	01:04:58.00	−70:37:34.7	27.8	27.2	0.532	0.309	51.8	30.1	28.6	27.0	25.5
SMC_74	2	5.496	01:07:08.42	−71:43:06.2	6.81	2.16	5.87	1.71	15.3	7.98	7.09	7.01	5.18
SMC_75	2	5.496	01:09:31.31	−71:34:54.9	30.1	19.2	7.82	0.379	21.9	36.5	31.6	27.6	24.6
SMC_76	2	5.496	01:10:05.33	−72:26:48.2	64.8	64.4	0.263	0.179	117	75.8	67.6	61.2	54.5
SMC_77	2	5.496	01:10:29.07	−74:54:06.0	1.13	0.830	2.81	1.84	38.5	1.39	1.35	1.09	
SMC_8	2	5.496	00:34:24.49	−72:11:44.4	41.5	23.0	3.75	0.149	48.5	49.2	42.8	38.7	35.0
SMC_80	2	5.496	01:12:27.18	−72:48:02.8	2.82	1.12	8.82	1.53	46.9	3.40	2.23	2.37	3.26
SMC_83	2	5.496	01:15:35.51	−72:00:09.2	3.05	2.60	1.34	1.07	64.7	3.46	3.37	2.95	2.75
SMC_83	2	5.496	01:15:30.85	−71:59:52.1	1.15	1.02	0.	0.	21.3	1.42	1.62	0.975	0.587

Continued on next page

Name	RW	ν	RA	Dec	S_{int}	S_p	$\theta_{\rm maj}$	$\theta_{\rm min}$	σ_L	$S_{\rm ch1}$	$S_{\rm ch2}$	$S_{\rm ch3}$	$S_{\rm ch4}$
		(GHz)	(J2000)		(mJy)	(mJy)	(arcsec)	(arcsec)	(μJy)	(mJy)	(mJy)	(mJy)	(mJy)
SMC_84	2	5.496	01:16:09.97	−74:28:14.0	8.62	5.96	2.85	0.405	62.3	9.98	8.91	8.19	7.41
SMC_86	2	5.496	01:16:15.76	−73:26:57.4	14.6	4.62	9.02	1.78	36.9	17.0	15.4	14.6	11.4
SMC_9	2	5.496	00:35:30.79	−72:36:55.1	18.0	17.6	0.	0.	28.5	18.6	18.0	17.9	17.3
SMC_90	2	5.496	01:20:35.85	−75:06:33.9	35.2	34.7	0.409	0.278	71.6	29.0	32.2	37.9	42.4
SMC_93	2	5.496	01:22:36.37	−73:38:28.1	1.98	0.978	4.48	3.72	40.5	3.07	2.19	1.75	0.921
SMC_93	2	5.496	01:22:35.64	−73:38:13.8	6.91	4.55	3.42	1.11	24.6	7.90	7.45	6.65	5.63
SMC_94	2	5.496	01:22:39.45	−74:10:10.8	4.78	2.09	4.88	3.16	21.5	6.06	4.72	4.40	3.90
SMC_94	2	5.496	01:22:36.67	−74:10:24.0	1.82	0.809	5.76	3.47	32.4	3.33	1.29	1.58	1.06
SMC_95	2	5.496	01:23:23.84	−73:56:06.5	11.6	11.5	0.385	0.192	38.1	14.6	12.2	10.8	8.86
SMC_97	2	5.496	01:24:07.90	−73:09:04.1	91.1	79.5	1.12	0.695	218	93.5	91.7	90.9	88.3
SMC_99	2	5.496	01:25:46.97	−73:16:00.4	10.6	7.06	3.81	0.721	33.8	13.1	11.4	9.80	8.22
SMC_99	2	5.496	01:25:45.99	−73:16:12.0	4.52	2.82	6.66	0.	26.7	6.71	4.82	4.22	2.34
SMC_E0102	2	5.496	01:04:01.63	−72:01:44.3	19.7	2.02	31.9	18.7	115	26.0	18.6	19.6	16.7
SMC_FRII	2	5.496	00:36:59.10	−71:38:10.2	10.6	10.5	0.	0.	51.4	11.1	10.6	10.5	9.98
SMC_FRII	2	5.496	00:37:09.76	−71:40:06.0	4.07	1.85	4.99	2.19	30.0	5.55	4.39	3.17	3.18
SMC_FRII	2	5.496	00:36:47.26	−71:35:57.9	1.42	0.863	3.95	2.38	35.3	1.54	1.67	1.60	0.866
SMC_0022-7428	2	9.002	00:22:13.55	−74:27:58.0	4.94	4.28	0.497	0.265	83.8	4.45	5.30	5.26	4.96
SMC_0022-7428	2	9.002	00:22:23.91	−74:28:26.8	18.1	1.81	6.22	3.23	87.1	12.3	27.1	21.2	12.7
SMC_0022-7428	2	9.002	00:21:59.60	−74:27:14.7	7.10	5.39	1.28	0.558	124	6.80	8.89	7.79	6.93
SMC_0055-7211	2	9.002	00:55:34.30	−72:10:55.9	4.70	1.29	5.85	0.683	36.6	4.03	6.08	4.39	4.27
SMC_0055-7211	2	9.002	00:55:27.77	−72:10:58.6	17.9	16.7	0.571	0.280	60.0	17.7	18.5	18.2	17.3
SMC_0055-7211	2	9.002	00:55:23.46	−72:10:56.0	7.93	5.12	1.25	0.836	30.3	8.80	8.24	7.52	7.15
SMC_10	2	9.002	00:36:19.37	−72:09:54.4	2.54	1.27	2.72	2.00	11.9	1.70	2.18	2.95	3.31

Continued on next page

Name	RW	ν	RA	Dec	S_{int}	S_p	$\theta_{\rm maj}$	$\theta_{\rm min}$	σ_L	$S_{\rm ch1}$	$S_{\rm ch2}$	$S_{\rm ch3}$	$S_{\rm ch4}$
		(GHz)	(J2000)		(mJy)	(mJy)	(arcsec)	(arcsec)	(μJy)	(mJy)	(mJy)	(mJy)	(mJy)
SMC_100	2	9.002	01:26:39.58	−73:15:02.7	10.3	5.03	2.52	0.684	50.0	10.5	11.1	10.7	8.97
SMC_101	2	9.002	01:28:16.71	−75:12:58.9	17.7	4.70	4.27	2.09	67.2	19.1	19.5	18.0	14.2
SMC_101	2	9.002	01:28:11.42	−75:12:53.4	5.84	5.81	0.	0.	95.3	6.18	6.33	6.25	6.35
SMC_101	2	9.002	01:28:08.85	−75:12:51.3	18.3	12.3	2.86	0.351	38.5	20.1	18.4	19.1	15.4
SMC_102	2	9.002	01:30:13.59	−74:20:24.1	31.0	30.5	0.373	0.	90.2	31.8	31.4	31.3	29.7
SMC_13	2	9.002	00:38:01.04	−72:52:11.1	4.90	3.64	0.	0.	18.4	5.65	4.80	4.91	4.26
SMC_13	2	9.002	00:37:54.63	−72:51:56.5	21.0	18.6	2.01	0.187	34.9	22.2	22.5	20.7	18.8
SMC_14	2	9.002	00:38:05.15	−74:50:28.1	2.70	1.09	4.10	1.61	78.4	1.67	2.90	3.37	2.91
SMC_16	2	9.002	00:39:25.80	−71:52:41.3	2.64	0.890	4.34	2.40	55.3	3.68	3.15	3.35	
SMC_17	2	9.002	00:39:39.59	−71:41:41.4	10.6	6.40	2.54	0.736	35.2	7.36	13.4	10.7	10.7
SMC_18	2	9.002	00:39:47.55	−71:37:35.3	10.8	7.80	1.38	0.614	41.7	11.3	11.6	10.7	9.60
SMC_18	2	9.002	00:39:46.51	−71:37:31.2	2.02	1.85	0.652	0.257	97.1	2.37	2.71	2.39	1.39
SMC_19	2	9.002	00:40:48.04	−71:45:58.7	85.6	62.3	1.79	0.	404	92.9	92.7	91.7	65.5
SMC_2	2	9.002	00:30:38.01	−74:29:00.6	6.10	2.34	2.56	0.722	88.7	5.67	7.05	6.66	5.03
SMC_2	2	9.002	00:30:36.56	−74:29:27.2	5.89	5.21	0.649	0.537	36.1	6.33	6.21	6.12	4.89
SMC_2	2	9.002	00:30:29.89	−74:29:28.9	2.66	1.85	1.36	0.901	37.2	2.62	3.53	2.74	1.75
SMC_21	2	9.002	00:42:05.61	−73:07:21.4	1.43	0.791	2.36	1.87	16.1	1.62	1.42	1.29	1.40
SMC_21	2	9.002	00:42:03.95	−73:07:26.2	4.61	4.11	1.15	0.228	49.4	4.77	4.49	4.67	4.52
SMC_21	2	9.002	00:42:00.76	−73:07:26.5	2.67	1.06	4.28	1.51	48.4	3.33	2.07	2.91	2.39
SMC_23	2	9.002	00:42:26.15	−73:04:18.4	6.53	2.98	3.08	1.66	159	5.47	8.21	5.33	6.63
SMC_25	2	9.002	00:43:36.80	−71:31:57.1	2.79	2.11	1.74	0.970	57.6	2.55	2.95	3.00	2.67
SMC_25	2	9.002	00:43:33.86	−71:32:02.1	0.754	0.794	0.	0.	12.9	0.733	0.877		
SMC_26	2	9.002	00:43:38.66	−72:03:44.0	3.06	2.91	0.	0.	22.5	3.19	3.16	3.00	2.91

Continued on next page

Name	RW	ν	RA	Dec	S_{int}	S_p	$\theta_{\rm maj}$	$\theta_{\rm min}$	σ_L	$S_{\rm ch1}$	$S_{\rm ch2}$	$S_{\rm ch3}$	$S_{\rm ch4}$
		(GHz)	(J2000)		(mJy)	(mJy)	(arcsec)	(arcsec)	(μJy)	(mJy)	(mJy)	(mJy)	(mJy)
SMC_26	2	9.002	00:43:42.13	−72:03:51.5	0.884	0.297	4.53	2.06	36.9	0.969	0.703	1.00	1.34
SMC_3	2	9.002	00:30:36.30	−73:51:44.0	4.80	1.45	4.51	0.935	29.7	3.22	2.66	6.63	6.59
SMC_30	2	9.002	00:46:01.98	−74:40:03.8	9.13	5.03	1.88	0.618	46.9	9.00	10.0	9.28	8.23
SMC_32	2	9.000	00:47:18.94	−72:39:47.4	39.7	38.8	0.269	0.209	70.4	42.1	40.8	39.3	36.4
SMC_34	2	9.002	00:47:50.36	−70:57:56.5	6.41	6.00	0.489	0.313	43.3	6.44	6.92	6.30	5.99
SMC_35	2	9.002	00:48:08.37	−74:12:05.9	25.2	24.0	0.	0.	96.5	26.2	28.1	26.4	20.3
SMC_36	2	9.002	00:48:17.01	−71:14:00.3	2.75	2.07	1.42	1.27	88.8	2.55	2.79	2.62	3.14
SMC_39	2	9.002	00:49:32.02	−72:19:03.0	2.59	1.83	1.99	0.965	64.9	1.91	2.61	2.97	2.85
SMC_39	2	9.002	00:49:30.14	−72:19:04.8	0.879	0.406	3.09	2.11	36.8	1.24	1.15	1.36	
SMC_4	2	9.002	00:31:40.56	−74:34:47.2	17.0	16.3	0.	0.	34.4	18.2	17.8	16.7	15.4
SMC_41	2	9.002	00:49:56.84	−72:35:54.1	11.8	5.48	7.11	0.228	69.5	12.9	13.3	12.2	11.2
SMC_44	2	9.002	00:50:41.44	−70:39:37.9	6.82	4.30	1.62	0.605	29.3	6.35	7.40	7.24	6.30
SMC_45	2	9.002	00:52:18.81	−72:27:07.6	31.3	17.0	4.85	0.745	52.7	32.4	32.5	31.5	29.0
SMC_46	2	9.002	00:52:38.20	−73:12:44.8	19.6	18.2	0.635	0.229	41.1	21.0	20.3	19.3	17.6
SMC_48	2	9.001	00:53:37.82	−72:31:43.0	7.37	5.34	1.37	0.811	48.9	6.98	8.11	8.13	6.26
SMC_49	2	9.002	00:54:26.09	−74:17:23.6	2.58	1.03	3.13	2.60	41.8	1.45	3.09	2.91	2.87
SMC_5	2	9.002	00:32:34.86	−73:06:48.8	12.9	12.7	0.	0.	53.8	13.3	12.9	12.9	12.7
SMC_5	2	9.002	00:32:25.55	−73:06:56.2	1.05	0.599	2.63	1.10	22.5	0.774	1.05	1.36	1.02
SMC_5	2	9.002	00:32:23.99	−73:07:01.0	1.08	0.925	1.41	0.	30.2	1.37	0.864	0.975	1.11
SMC_50	2	9.002	00:55:06.26	−72:37:19.2	2.20	1.08	2.60	2.21	32.4	2.09	2.16	2.63	1.89
SMC_52	2	9.002	00:55:37.28	−74:39:26.2	5.02	4.96	0.214	0.106	18.3	5.48	5.29	5.02	4.28
SMC_54	2	9.002	00:56:11.15	−71:07:07.2	112	110	0.	0.	146	130	118	109	89.5
SMC_55	2	9.002	00:56:36.76	−74:03:16.1	18.2	18.2	0.176	0.	29.6	19.3	18.4	18.1	17.1

Continued on next page

Name	RW	ν	RA	Dec	S_{int}	S_p	$\theta_{\rm maj}$	$\theta_{\rm min}$	σ_L	$S_{\rm ch1}$	$S_{\rm ch2}$	$S_{\rm ch3}$	$S_{\rm ch4}$
		(GHz)	(J2000)		(mJy)	(mJy)	(arcsec)	(arcsec)	(μJy)	(mJy)	(mJy)	(mJy)	(mJy)
SMC_56	2	9.002	00:56:44.97	−72:51:59.4	8.53	6.39	1.78	0.0940	34.7	8.70	8.94	8.59	8.36
SMC_56	2	9.002	00:56:42.51	−72:52:15.5	3.66	2.41	3.49	0.209	21.6	3.02	3.11	4.15	4.37
SMC_57	2	9.002	00:56:52.58	−71:23:00.1	9.26	4.49	4.09	0.	118	10.2	10.7	10.1	8.97
SMC_58	2	9.001	00:57:15.56	−70:40:46.3	69.6	67.6	0.367	0.212	133	71.5	70.0	72.8	64.6
SMC_59	2	9.002	00:57:32.40	−74:12:43.6	33.5	32.6	0.326	0.225	44.6	38.4	35.0	31.9	28.8
SMC_64	2	9.000	00:59:05.27	−70:49:07.8	3.12	2.32	1.10	0.890	61.3	2.86	3.37	3.08	3.20
SMC_64	2	9.000	00:59:03.38	−70:48:54.6	4.25	2.23	2.20	1.04	47.0	4.22	4.88	4.02	3.86
SMC_65	2	9.002	01:00:29.68	−71:38:26.1	23.8	23.1	0.	0.	45.6	26.7	25.5	23.8	19.4
SMC_66	2	9.002	01:00:46.93	−74:54:19.8	5.06	2.12	3.66	1.14	33.6	3.52	5.95	6.63	4.14
SMC_66	2	9.002	01:00:40.92	−74:54:08.2	1.10	0.408	3.45	2.61	15.0	1.36	2.14		
SMC_68	2	9.002	01:03:33.62	−75:06:58.9	2.07	1.18	1.78	1.15	49.8	2.11	2.35	2.24	1.57
SMC_68	2	9.002	01:03:30.19	−75:07:08.2	4.71	3.55	1.11	0.753	57.0	5.27	5.08	4.50	4.00
SMC_69	2	9.002	01:04:06.72	−73:51:27.4	2.39	1.06	2.01	1.75	69.7	1.72	2.23	2.97	2.59
SMC_69	2	9.002	01:04:00.07	−73:51:09.9	1.69	0.866	2.05	1.25	60.0	1.31	1.94	1.50	1.99
SMC_7	2	9.002	00:34:12.09	−73:33:14.7	4.60	2.46	3.48	1.45	104	4.24	5.10	4.60	4.47
SMC_7	2	9.002	00:34:28.78	−73:35:26.7	4.34	1.42	6.00	1.91	102	2.96	4.00	3.36	7.05
SMC_7	2	9.002	00:34:18.07	−73:34:09.7	5.07	4.18	1.52	0.814	72.1	4.60	5.07	5.18	5.47
SMC_70	2	9.002	01:04:31.26	−72:07:25.1	6.68	6.57	0.	0.	43.6	6.86	6.95	6.86	6.10
SMC_71	2	9.002	01:04:41.19	−71:31:22.4	11.9	10.9	0.	0.	48.5	13.9	11.9	11.4	10.6
SMC_72	2	9.002	01:04:57.93	−70:37:34.7	20.3	19.8	0.338	0.166	53.7	21.2	20.9	20.1	18.9
SMC_74	2	9.002	01:07:09.02	−71:43:06.7	1.64	1.46	1.24	0.	54.4	1.87	2.74	3.09	2.27
SMC_75	2	9.002	01:09:32.14	−71:34:52.5	4.47	3.49	0.	0.	14.2	4.36	5.01	4.61	3.90
SMC_75	2	9.002	01:09:30.79	−71:34:56.0	10.4	8.72	0.907	0.438	34.9	10.9	10.8	9.92	9.88

Continued on next page

Name	RW	ν	RA	Dec	S_{int}	S_p	$\theta_{\rm maj}$	$\theta_{\rm min}$	σ_L	$S_{\rm ch1}$	$S_{\rm ch2}$	$S_{\rm ch3}$	$S_{\rm ch4}$
		(GHz)	(J2000)		(mJy)	(mJy)	(arcsec)	(arcsec)	(μJy)	(mJy)	(mJy)	(mJy)	(mJy)
SMC_76	2	9.002	01:10:05.42	−72:26:48.4	35.4	34.9	0.284	0.111	79.8	41.6	38.5	35.0	26.5
SMC_8	2	9.002	00:34:24.50	−72:11:44.3	22.2	9.67	3.79	0.308	16.2	23.7	22.9	22.0	20.0
SMC_80	2	9.002	01:12:27.23	−72:48:03.3	2.80	0.914	5.14	1.88	73.2	2.92	2.81	2.88	2.52
SMC_83	2	9.002	01:15:35.42	−72:00:09.0	2.08	1.20	1.66	1.25	34.5	2.23	2.21	2.10	1.79
SMC_83	2	9.002	01:15:30.76	−71:59:52.3	1.29	0.736	1.67	1.22	24.5	0.748	1.07	1.66	1.69
SMC_84	2	9.002	01:16:09.88	−74:28:14.1	5.33	2.94	0.	0.	38.2	5.28	5.62	5.21	5.23
SMC_86	2	9.001	01:16:15.69	−73:26:56.9	5.40	2.70	4.67	0.	30.7	5.22	6.57	4.70	5.13
SMC_9	2	9.002	00:35:30.83	−72:36:55.0	16.0	15.4	0.	0.	27.7	16.1	16.8	16.0	15.3
SMC_90	2	8.809	01:20:35.81	−75:06:34.0	73.5	73.1	0.	0.	243	68.2	73.7	79.8	78.8
SMC_93	2	9.002	01:22:35.31	−73:38:12.2	2.53	1.53	2.48	1.27	64.4	3.39	3.14	3.08	
SMC_94	2	9.002	01:22:39.15	−74:10:10.0	5.65	1.08	5.54	4.07	95.6	3.30	6.38	6.57	6.05
SMC_95	2	9.002	01:23:23.83	−73:56:06.4	4.08	3.74	0.727	0.300	42.1	4.97	4.00	3.98	3.39
SMC_97	2	9.002	01:24:07.81	−73:09:04.7	83.8	58.9	1.17	0.818	427	87.2	87.6	84.0	76.7
SMC_99	2	9.002	01:25:46.72	−73:16:00.2	4.76	2.48	3.08	1.18	45.9	5.62	5.10	5.28	3.07
SMC_99	2	9.002	01:25:46.18	−73:16:10.9	0.961	0.304	5.16	1.81	23.3	0.887	1.68	0.948	0.818
SMC_E0102	2	9.002	01:04:00.24	−72:01:44.4	5.55	0.746	6.67	1.70	38.9	3.55	6.30	6.56	6.03
SMC_FRII	2	9.002	00:36:59.20	−71:38:10.4	9.18	8.38	0.790	0.624	23.8	9.39	9.40	9.14	8.80
SMC_FRII	2	9.002	00:37:10.13	−71:40:04.8	0.711	0.616	0.	0.	16.0	0.832	1.03		

Appendix E

SMC source catalogue

Table E.1: The SMC source catalogue. Shown is the source name, RA and Dec, the source flux density at 5.5 ($S_{5.5,\mathrm{src}}$) and 9.0 GHz ($S_{9.0,\mathrm{src}}$), the total source angular size (θ_{src}), the estimated linear size (l_{est}) and redshift (z_{est}), the number of components at 5.5 GHz (N_{comp}), the morphology, the variability at 5.5 ($\mathrm{Var}_{5.5}$) and 9.0 GHz ($\mathrm{Var}_{9.0}$), the MWA 200 MHz deep flux ($S_{0.2}$), and the MWA and ATCA blends. As outlined in section 2.3.1.6, the RA and Dec are taken from the component identified during visual inspection as closest to the nucleus, and the source flux density represents the total integrated flux density of all source components. The source angular sizes were measured as outlined in section 2.3.1.7. The estimated linear size and redshift were estimated as discussed in section 4.1.5. The morphology is represented by $1-3$ digits, with the following meaning: first digit: 0 = unresolved; 1 = double-lobed; 2 = resolved with uncertain / complex morphology; second digit: 0 = no core; 1 = core-dominated; 2 = lobe-dominated; third digit: 1 = FR-I-like; 2 = FR-II-like. The variability is measured between the pre-CABB flux density ($S_{\mathrm{pre-CABB}}$) and CABB flux density (S_{CABB}), and is taken as $|1 - S_{\mathrm{CABB}}/S_{\mathrm{pre-CABB}}|$. This value is also sensitive to flux being resolved out in the high-resolution CABB images, and therefore doesn't strictly represent the variability, but is used in determining whether or not to use the CABB flux densities to model the radio spectrum. The MWA and ATCA blend columns list 'b' when there is a blended source contributing to the pre-CABB or MWA flux measurements (see section 2.3.1.8).

Name	RA	Dec	$S_{5.5,\mathrm{src}}$	$S_{9.0,\mathrm{src}}$	θ_{src}	l_{est}	z_{est}	N_{comp}	morph	$\mathrm{Var}_{5.5}$	$\mathrm{Var}_{9.0}$	$S_{0.2}$	MWA	ATCA
	(J2000)		(mJy)	(mJy)	(arcsec)	(kpc)						(Jy)	blend	blend
SMC_0022-7428	00:22:13.52	−74:27:58.1	170	68.0	138	> 25	> 0.01	4	122			3.23		
SMC_0055-7211	00:55:27.69	−72:10:58.7	74.4	32.0	124	> 25	> 0.01	4	2	0.059	0.18	0.548		
SMC_10	00:36:24.71	−72:08:49.7	11.9	4.49	78.9	> 25	> 0.02	2	102	0.16		0.400		
SMC_100	01:26:39.80	−73:15:02.3	18.0	11.7	2.42			1	2	0.22	0.14	0.346		
SMC_101	01:28:09.26	−75:12:51.6	79.5	45.8	36.7	> 25	> 0.03	2	122	0.040	0.086	1.24		
SMC_102	01:30:13.60	−74:20:24.1	31.9	32.1	0.221			1	0	0.26				
SMC_13	00:38:01.14	−72:52:11.0	48.8	28.3	40.1	> 25	> 0.03	2	102	0.017	0.42	0.812		
SMC_14	00:38:04.25	−74:50:30.8	2.85	1.28	66.0			1	2	0.39		0.0816		
SMC_16	00:39:28.58	−71:53:06.1	7.67	1.77	36.0	> 21	> 0.03	2	102			0.118		
SMC_17	00:39:39.65	−71:41:41.9	19.3	9.75	3.92			1	2	0.041		0.790		
SMC_18	00:39:47.30	−71:37:34.5	26.2	14.9	6.19			1	102	0.040	0.068	0.514		
SMC_19	00:40:47.93	−71:45:59.5	165	97.2	1.93			1	2		0.068	1.12		
SMC_2	00:30:36.56	−74:29:27.2	37.4	19.8	49.9	> 25	> 0.02	3	102	0.12	0.13	0.582		b

Continued on next page

Name	RA	Dec	$S_{5.5,\mathrm{src}}$	$S_{9.0,\mathrm{src}}$	θ_{src}	l_{est}	z_{est}	N_{comp}	morph	$\mathrm{Var}_{5.5}$	$\mathrm{Var}_{9.0}$	$S_{0.2}$	MWA	ATCA
	(J2000)		(mJy)	(mJy)	(arcsec)	(kpc)						(Jy)	blend	blend
SMC_21	00:42:03.40	−73:07:23.4	34.0	21.5	24.0	18.36	0.04	1	121	0.28	0.66	0.714		
SMC_23	00:42:26.30	−73:04:18.4	21.6	11.0	7.66			1	2	0.19		0.450		
SMC_25	00:43:34.50	−71:32:02.0	14.8	5.97	25.9	> 25	> 0.05	1	112	0.52		0.135		
SMC_26	00:43:42.10	−72:03:51.0	8.17	4.46	20.7			2	102		0.59	0.347		
SMC_27	00:43:48.46	−73:26:03.5	4.00		43.9			2	102	0.089		0.215		
SMC_29	00:44:59.65	−71:14:38.2	9.59		0.274			1	2	0.042		0.153	b	
SMC_3	00:30:36.17	−73:51:45.3	4.28	4.02	61.0			1	2	0.17		0.150		
SMC_30	00:46:01.98	−74:40:03.9	15.2	9.61	2.19			1	2	0.033	0.038	0.104		
SMC_31	00:46:03.14	−74:13:27.8	4.89		48.4	19.31	0.02	2	2	0.58		0.113		
SMC_32	00:47:18.95	−72:39:47.4	51.6	40.8	0.193			1	0	0.34	0.34			
SMC_34	00:47:50.43	−70:57:56.5	11.4	6.34	0.437			1	0			0.116		
SMC_35	00:48:08.38	−74:12:05.8	39.4	26.3	0.276			1	0	0.051	0.11	0.334		
SMC_36	00:48:13.02	−71:14:13.9	8.46	3.69	49.4			3	122			0.165		
SMC_38	00:49:23.23	−71:26:59.0	4.67		8.68			1	2	0.25		0.141		
SMC_39	00:49:32.91	−72:19:01.8	10.3	3.64	16.7			1	122	0.15		0.254		
SMC_4	00:31:40.51	−74:34:47.3	24.9	16.6	0.296			1	0	0.038	0.20	0.105		
SMC_41	00:49:56.78	−72:35:54.0	27.4	15.9	6.72			1	102	0.20	0.14	0.560		
SMC_44	00:50:41.49	−70:39:38.0	10.8	6.93	1.59			1	2	0.20	0.079	0.117	b	
SMC_45	00:52:18.83	−72:27:07.6	58.1	34.4	4.93			1	102	0.10	0.043	0.790		
SMC_46	00:52:38.20	−73:12:44.9	33.5	20.4	0.716			1	0	0.10	0.23	0.474		
SMC_47	00:53:22.70	−72:35:24.2	4.32	0.282	45.0	> 25	> 0.03	1	2	0.79		0.378		
SMC_48	00:53:37.72	−72:31:43.5	13.9	7.27	0.829			1	2	0.091		0.517		
SMC_49	00:54:26.21	−74:17:23.1	2.87	0.982	6.02			1	0					

Continued on next page

Name	RA	Dec	$S_{5.5,\mathrm{src}}$	$S_{9.0,\mathrm{src}}$	θ_{src}	l_{est}	z_{est}	N_{comp}	morph	$\mathrm{Var}_{5.5}$	$\mathrm{Var}_{9.0}$	$S_{0.2}$	MWA	ATCA
	(J2000)		(mJy)	(mJy)	(arcsec)	(kpc)						(Jy)	blend	blend
SMC_5	00:32:24.64	−73:06:59.1	33.0	18.0	52.3	> 25	> 0.02	3	2	0.37	0.16	0.442		
SMC_50	00:55:06.39	−72:37:19.4	2.68	1.69	1.30			1	0	0.53		0.104		
SMC_52	00:55:37.29	−74:39:26.3	11.9	5.12	0.126			1	0	0.034		0.183		
SMC_54	00:56:11.27	−71:07:07.5	205	116	0.357			1	0	0.092	0.082	1.64		
SMC_55	00:56:36.76	−74:03:16.1	24.2	18.6	0.127	0.13	0.05	1	0	0.029	0.100			
SMC_56	00:56:44.99	−72:51:59.6	25.8	15.0	29.5	> 25	> 0.04	2	102	0.17	0.21	0.301		
SMC_57	00:56:52.61	−71:23:00.1	22.2	11.7	4.06			1	102	0.19	0.15	0.382		
SMC_58	00:57:15.59	−70:40:46.3	64.7	73.1	0.245			1	0	0.15	0.14	0.154		
SMC_59	00:57:32.40	−74:12:43.6	74.4	33.8	0.274			1	0	0.088	0.12	2.50		
SMC_61	00:58:12.46	−71:24:04.5	9.27		78.0			2	0			0.123		
SMC_64	00:59:05.19	−70:49:07.2	18.1	9.05	19.7	> 25	> 0.07	2	102	0.33		0.632		
SMC_65	01:00:29.71	−71:38:26.1	41.4	25.3	0.353			1	0	0.072	0.098	0.307		
SMC_66	01:00:41.57	−74:54:09.2	15.0	8.83	36.0	20.71	0.03	2	122	0.077	0.28	0.175		
SMC_68	01:03:30.32	−75:07:07.9	20.5	9.62	20.1	> 25	> 0.06	2	102	0.13	0.42	0.442		
SMC_69	01:04:06.35	−73:51:30.0	5.15	2.30	38.2			3	2	0.091				
SMC_7	00:34:18.14	−73:34:09.5	41.0	19.2	167	> 25	> 0.01	3	121	0.44	0.64	1.97		
SMC_70	01:04:31.28	−72:07:25.3	12.3	6.55	0.365			1	0	0.069	0.43	0.307	b	
SMC_71	01:04:41.26	−71:31:22.5	16.8	11.5	0.134	0.22	0.09	1	0	0.046				
SMC_72	01:04:58.03	−70:37:34.7	28.1	20.6	0.301			1	0	0.37	0.49	0.0651		
SMC_74	01:07:08.44	−71:43:06.2	7.09	2.43	5.89			1	102	0.27		0.163		
SMC_75	01:09:31.35	−71:34:54.8	31.9	16.0	7.96			1	102	0.067	0.29	0.864	b	
SMC_76	01:10:05.33	−72:26:48.2	66.3	37.4	0.163	0.20	0.06	1	0	0.029	0.0100			
SMC_77	01:10:29.14	−74:54:05.8	2.43		21.5	> 25	> 0.06	2	2	0.74		0.0940		

Continued on next page

Name	RA	Dec	$S_{5.5,\mathrm{src}}$	$S_{9.0,\mathrm{src}}$	θ_{src}	l_{est}	z_{est}	N_{comp}	morph	$\mathrm{Var}_{5.5}$	$\mathrm{Var}_{9.0}$	$S_{0.2}$	MWA	ATCA
	(J2000)		(mJy)	(mJy)	(arcsec)	(kpc)						(Jy)	blend	blend
SMC_8	00:34:24.47	−72:11:44.4	42.4	23.9	3.80			1	102		0.032	0.790		
SMC_80	01:12:27.08	−72:48:02.5	5.94	0.861	10.7			1	2	0.065		0.0897		
SMC_83	01:15:35.51	−72:00:09.1	4.70	2.71	30.7	19.99	0.03	2	102	0.28		0.177	b	
SMC_84	01:16:09.87	−74:28:14.1	8.65	5.74	2.42			1	102	0.25		0.114	b	
SMC_86	01:16:15.77	−73:26:57.4	16.0	9.90	9.09			1	122	0.12	0.33	0.213		
SMC_9	00:35:30.77	−72:36:55.1	17.3	16.1	0.136	0.13	0.05	1	0	0.13	0.11			
SMC_90	01:20:35.84	−75:06:33.9	35.5	77.9	0.128			1	0	1.5	3.6			
SMC_93	01:22:35.81	−73:38:16.8	11.0	3.89	14.9	> 25	> 0.09	1	102	0.13		0.175		
SMC_94	01:22:39.42	−74:10:10.9	10.7	4.23	42.0			3	112	0.15		0.0849		
SMC_95	01:23:23.83	−73:56:06.6	11.7	4.35	0.142	0.17	0.06	1	0	0.078				
SMC_97	01:24:07.91	−73:09:04.1	99.0	94.6	1.58	0.08	0.00	1	2	0.046	0.068			
SMC_99	01:25:46.97	−73:16:00.2	19.5	9.12	28.5	> 25	> 0.04	2	102	0.11		0.253		
SMC_E0102	01:04:01.45	−72:01:46.9	42.6	25.2	34.8	> 25	> 0.04	1	0	0.83	0.93	0.928		
SMC_FRII	00:36:59.08	−71:38:10.6	17.6	9.92	282			3	112	0.11	0.78	0.323		

Appendix F

SMC pre-CABB spectral index catalogue

Table F.1: The SMC *pre-CABB* spectral index component catalogue (see section 2.2.1.2.) Listed is the RA and DEC, in this order of preference: 20, 3, 6, 13, and 36 cm. Also listed are the λ = 36, 20, 13, 6 and 3 cm (ν = 0.84, 1.35, 2.37, 4.80 and 8.64 GHz) flux densities in mJy, for those with default resolutions, as well for those whose beams were matched to the 36 cm image. The spectral index α is taken from the beam-matched flux densities. The blend flag lists 'b' to indicate when a single-component source from one frequency is resolved into multiple components at another frequency. Since the non-beam-matched 20 cm image is much larger and deeper, many sources are detected only at 20 cm.

RA (J2000)	DEC (J2000)	S_{36cm} (mJy)	S_{20cm} (mJy)	S_{13cm} (mJy)	S_{6cm} (mJy)	S_{3cm} (mJy)	Blend Flag	$S_{20cm,matched}$ (mJy)	$S_{13cm,matched}$ (mJy)	$S_{6cm,matched}$ (mJy)	$S_{3cm,matched}$ (mJy)	α
00:10:08.55	−73:21:11.8		19.75									
00:10:13.39	−73:21:20.6		26.97									
00:10:14.54	−75:35:30.8		35.13									
00:10:55.62	−72:44:28.8		12.14									
00:11:06.34	−73:11:55.8		15.00									
00:11:16.21	−74:57:23.1		14.11									
00:11:57.38	−73:49:55.4		107.45									
00:12:24.45	−75:27:07.8		8.25									
00:12:43.70	−74:16:43.5		49.10									
00:12:46.62	−73:12:50.7		7.65									
00:12:50.81	−73:42:56.7		10.00									
00:12:58.79	−73:27:28.3		8.17									
00:13:07.74	−72:25:00.8		37.36									
00:13:20.40	−72:29:34.5		22.99									
00:13:20.50	−74:17:09.5		12.37									
00:13:26.63	−72:48:33.6		98.33									
00:13:56.79	−73:36:35.6		13.95									
00:14:00.52	−74:10:01.3		11.16									
00:14:24.29	−73:39:08.7		296.22									

Continued on next page

RA (J2000)	DEC	S_{36cm} (mJy)	S_{20cm} (mJy)	S_{13cm} (mJy)	S_{6cm} (mJy)	S_{3cm} (mJy)	Blend Flag	$S_{20cm,matched}$ (mJy)	$S_{13cm,matched}$ (mJy)	$S_{6cm,matched}$ (mJy)	$S_{3cm,matched}$ (mJy)	α
00:14:37.41	−73:46:09.6		18.59									
00:14:59.36	−75:01:28.5	14.38	10.27									
00:15:03.61	−72:47:37.4		25.47									
00:15:09.98	−73:24:08.6		6.68									
00:15:10.15	−72:48:02.5		4.37									
00:15:14.72	−73:31:02.1		7.67									
00:15:21.64	−75:31:36.2		44.01									
00:15:26.39	−74:42:46.7	12.61	8.25									
00:15:44.37	−74:49:02.9	3.75										
00:15:45.53	−72:42:00.7		5.89									
00:15:56.88	−74:45:59.9	10.23	5.60									
00:16:02.57	−74:16:58.5	6.92	5.96									
00:16:08.59	−74:15:41.1	4.14										
00:16:12.06	−75:19:46.7		8.36									
00:16:12.81	−73:13:54.0		6.37									
00:16:13.97	−74:14:46.5	3.28										
00:16:18.56	−72:35:45.1		6.58									
00:16:22.00	−74:45:24.7	8.38										
00:16:22.30	−75:28:15.1		7.78									
00:16:25.89	−72:36:29.7		17.87									
00:16:26.02	−74:25:01.3	11.70	10.11									
00:16:38.89	−74:35:23.1	3.65										
00:16:38.95	−74:33:54.2	5.21	4.38									

Continued on next page

RA (J2000)	DEC	S_{36cm} (mJy)	S_{20cm} (mJy)	S_{13cm} (mJy)	S_{6cm} (mJy)	S_{3cm} (mJy)	Blend Flag	$S_{20cm,matched}$ (mJy)	$S_{13cm,matched}$ (mJy)	$S_{6cm,matched}$ (mJy)	$S_{3cm,matched}$ (mJy)	α
00:16:48.43	−73:04:40.5		7.06									
00:16:59.70	−73:38:46.7		4.92									
00:17:07.58	−75:14:18.1		75.51									
00:17:18.24	−72:43:04.5		4.24									
00:17:19.67	−72:34:07.7		4.79									
00:17:20.59	−73:05:54.4		109.12									
00:17:26.04	−73:50:28.1	5.79										
00:17:48.92	−74:51:48.5	4.05										
00:17:55.49	−73:27:58.4	4.16										
00:17:58.78	−73:29:40.8	6.41										
00:18:07.91	−72:39:22.7		11.97									
00:18:16.84	−74:15:17.5	38.75	25.04									
00:18:18.53	−73:25:18.6	15.34	8.94									
00:18:19.69	−73:09:09.1	18.34	7.40									
00:18:20.51	−73:41:45.7	3.41										
00:18:41.05	−72:54:46.2		4.01									
00:18:41.55	−75:28:09.4		9.66									
00:18:45.98	−74:11:59.7	3.14										
00:18:51.73	−73:42:17.8		15.58									
00:18:52.12	−72:37:05.5		4.30									
00:18:57.76	−73:42:22.8	98.31	28.57									
00:18:58.43	−73:24:48.8	52.32	25.98									
00:18:59.95	−73:22:54.8	3.77										

Continued on next page

RA (J2000)	DEC	S_{36cm} (mJy)	S_{20cm} (mJy)	S_{13cm} (mJy)	S_{6cm} (mJy)	S_{3cm} (mJy)	Blend Flag	$S_{20cm,matched}$ (mJy)	$S_{13cm,matched}$ (mJy)	$S_{6cm,matched}$ (mJy)	$S_{3cm,matched}$ (mJy)	α
00:19:02.60	−73:41:27.7	28.70										
00:19:03.29	−73:41:16.4		6.43									
00:19:07.81	−75:18:43.5		13.56									
00:19:09.31	−74:40:28.8	25.15	14.33									
00:19:15.41	−74:29:11.1	3.28	4.90									
00:19:20.01	−75:14:30.6		4.04									
00:19:32.15	−72:31:32.5		12.96									
00:19:33.88	−73:33:05.9	10.79	5.43									
00:19:35.63	−73:49:22.3	12.73										
00:19:35.98	−74:44:30.9	5.27	5.39									
00:19:38.36	−72:31:23.0		19.98									
00:19:38.61	−74:58:03.3	2.91										
00:19:39.61	−74:46:43.0	5.83	5.42									
00:20:01.04	−72:44:39.4	3.82										
00:20:05.73	−72:32:38.3	7.78										
00:20:07.00	−75:12:27.7	43.17	27.34									
00:20:07.33	−73:27:49.4	18.88	6.50									
00:20:10.85	−74:46:28.6	4.18										
00:20:17.10	−73:21:21.1		12.33									
00:20:19.76	−73:18:50.0	14.92	8.07									
00:20:19.90	−73:21:19.7	86.90										
00:20:24.50	−72:57:22.0	3.93										
00:20:24.58	−74:57:57.0	13.63										

Continued on next page

RA (J2000)	DEC	S_{36cm} (mJy)	S_{20cm} (mJy)	S_{13cm} (mJy)	S_{6cm} (mJy)	S_{3cm} (mJy)	Blend Flag	$S_{20cm,matched}$ (mJy)	$S_{13cm,matched}$ (mJy)	$S_{6cm,matched}$ (mJy)	$S_{3cm,matched}$ (mJy)	α
00:20:31.42	−72:41:58.3	15.85	7.34									
00:20:33.50	−73:50:42.1	3.05										
00:20:33.83	−73:39:28.5	3.29										
00:20:34.26	−74:31:45.3	7.67	4.73									
00:20:43.45	−74:43:09.7	75.39	44.92									
00:20:43.90	−73:21:28.0		8.37									
00:20:47.61	−73:21:33.5	52.41										
00:20:49.82	−73:53:19.4		5.77									
00:20:50.78	−75:13:59.2	3.37										
00:20:51.37	−73:21:37.8		14.41									
00:20:51.81	−73:53:26.8	11.17										
00:20:54.93	−73:46:43.3	7.09	4.13									
00:21:01.67	−74:36:14.6	4.40										
00:21:13.04	−72:23:07.8	5.74										
00:21:20.32	−72:55:31.3	21.93	7.72									
00:21:20.47	−72:58:26.8	3.21										
00:21:25.30	−73:22:17.5	31.70										
00:21:26.56	−74:51:24.2	6.19										
00:21:27.89	−73:22:22.1		8.54									
00:21:29.38	−74:49:45.7	5.21										
00:21:29.95	−73:48:28.1	5.38										
00:21:32.11	−75:01:25.0	30.85	31.98									
00:21:42.37	−74:29:42.6		4.35									

Continued on next page

RA (J2000)	DEC	S_{36cm} (mJy)	S_{20cm} (mJy)	S_{13cm} (mJy)	S_{6cm} (mJy)	S_{3cm} (mJy)	Blend Flag	$S_{20cm,matched}$ (mJy)	$S_{13cm,matched}$ (mJy)	$S_{6cm,matched}$ (mJy)	$S_{3cm,matched}$ (mJy)	α
00:21:43.82	−74:14:59.5	166.40	116.50									
00:21:45.06	−72:35:48.6	11.47	4.90									
00:21:45.93	−74:52:53.4	6.65										
00:21:52.27	−74:31:22.5	41.16	42.94									
00:21:54.53	−72:38:10.3	3.17										
00:21:56.14	−72:25:54.4	6.76										
00:21:59.76	−74:27:16.3		104.10									
00:22:02.64	−73:45:57.9	6.39	6.31									
00:22:07.01	−74:09:41.2	34.62	22.55									
00:22:09.00	−75:13:54.9	12.23	8.75									
00:22:11.83	−74:28:02.2											
00:22:15.30	−73:08:33.4	13.67	8.37									
00:22:15.39	−73:26:01.5	3.39										
00:22:15.45	−74:28:04.8		55.50									
00:22:17.42	−73:14:58.6	3.15										
00:22:17.47	−74:28:13.3	603.10										
00:22:20.28	−72:21:05.6	7.75										
00:22:23.01	−74:28:25.1		145.10									
00:22:26.47	−71:50:29.3	10.84	8.20									
00:22:26.87	−71:37:22.4	25.04	11.65									
00:22:27.55	−73:41:34.5	11.10	4.73									
00:22:28.67	−72:44:55.7	4.05										
00:22:30.54	−74:38:34.0	5.82	4.24									

Continued on next page

RA (J2000)	DEC	S_{36cm} (mJy)	S_{20cm} (mJy)	S_{13cm} (mJy)	S_{6cm} (mJy)	S_{3cm} (mJy)	Blend Flag	$S_{20cm,matched}$ (mJy)	$S_{13cm,matched}$ (mJy)	$S_{6cm,matched}$ (mJy)	$S_{3cm,matched}$ (mJy)	α
00:22:30.83	−71:58:59.9	3.48										
00:22:37.28	−72:46:38.3	10.61	6.68									
00:22:38.43	−74:27:14.6	27.30	14.55									
00:22:39.33	−74:43:39.8	3.96										
00:22:46.91	−71:06:54.3		28.92									
00:22:48.02	−73:40:08.1	81.93	48.26									
00:22:48.80	−71:44:18.7	5.45										
00:22:51.73	−74:29:14.0	3.64										
00:22:53.50	−74:11:35.5	7.95	7.11									
00:22:54.39	−74:10:14.2	6.98	2.76									
00:22:54.49	−74:48:54.8	3.32										
00:22:55.75	−74:08:51.5	7.50	3.04									
00:22:56.15	−72:33:05.5	114.10	58.39									
00:23:00.47	−72:27:39.5	10.59	4.48									
00:23:03.83	−72:17:22.8	3.82										
00:23:06.01	−73:48:42.7	3.78										
00:23:07.21	−74:22:19.2	3.79										
00:23:09.25	−71:59:20.2	4.50										
00:23:09.75	−75:25:29.5		6.84									
00:23:14.03	−69:52:12.6		16.66									
00:23:15.47	−74:46:56.0	6.33	3.74									
00:23:18.50	−72:00:32.4	3.80										
00:23:20.41	−72:23:17.5		3.89									

Continued on next page

RA (J2000)	DEC	S_{36cm} (mJy)	S_{20cm} (mJy)	S_{13cm} (mJy)	S_{6cm} (mJy)	S_{3cm} (mJy)	Blend Flag	$S_{20cm,matched}$ (mJy)	$S_{13cm,matched}$ (mJy)	$S_{6cm,matched}$ (mJy)	$S_{3cm,matched}$ (mJy)	α
00:23:25.77	−73:55:13.7		5.63									
00:23:27.54	−72:24:11.5	15.76	10.90									
00:23:31.09	−72:29:44.4	6.31										
00:23:32.63	−73:27:32.9	7.23	3.20									
00:23:35.75	−70:08:27.2		6.03									
00:23:36.22	−73:55:28.1	434.60	201.90									
00:23:39.62	−73:13:10.9		4.28									
00:23:43.31	−75:02:40.8	9.21										
00:23:50.12	−73:17:03.2	32.05	23.12									
00:23:57.93	−72:47:46.6	3.32										
00:23:59.71	−72:32:53.4	6.32	4.52									
00:24:00.69	−72:59:05.3	33.40	15.69									
00:24:04.43	−71:17:58.5	3.06										
00:24:04.81	−69:48:59.6		15.81									
00:24:08.78	−73:14:45.7	3.23										
00:24:09.19	−72:58:04.9	71.49	29.53									
00:24:09.62	−71:15:05.1	7.95										
00:24:10.68	−71:42:54.4	5.85	6.73									
00:24:11.46	−73:57:16.8	328.70	149.60									
00:24:11.92	−73:28:47.1	3.28										
00:24:15.56	−73:21:27.2	3.85										
00:24:17.10	−75:18:23.6	8.47	7.17									
00:24:21.15	−74:03:38.0	7.19										

Continued on next page

RA (J2000)	DEC	S_{36cm} (mJy)	S_{20cm} (mJy)	S_{13cm} (mJy)	S_{6cm} (mJy)	S_{3cm} (mJy)	Blend Flag	$S_{20cm,matched}$ (mJy)	$S_{13cm,matched}$ (mJy)	$S_{6cm,matched}$ (mJy)	$S_{3cm,matched}$ (mJy)	α
00:24:22.12	−71:49:08.6	16.89	9.33									
00:24:28.27	−70:35:50.0	8.75										
00:24:28.33	−70:09:25.9		82.75									
00:24:30.34	−72:12:25.2	21.26	14.69									
00:24:32.99	−70:08:29.2		6.80									
00:24:37.53	−72:25:33.3	7.63										
00:24:39.71	−73:05:01.5	4.69										
00:24:39.98	−73:45:40.6	63.10	33.03									
00:24:42.52	−74:14:19.2	8.14	4.27									
00:24:43.16	−74:56:00.6	27.52	18.40									
00:24:44.60	−72:15:25.2	3.51										
00:24:45.89	−72:42:05.9	4.55										
00:24:46.03	−73:46:14.4		3.90									
00:24:47.14	−71:59:15.1	79.28	33.54									
00:24:48.37	−70:55:44.2	132.60	100.02									
00:24:50.63	−70:48:55.0	4.36										
00:24:51.32	−70:30:13.5	3.95										
00:24:59.26	−73:24:16.1	2.77										
00:25:04.22	−72:02:38.5	14.63	5.46									
00:25:05.20	−74:26:44.4	3.35										
00:25:06.40	−71:40:24.0	3.79										
00:25:07.19	−72:02:38.1		4.41									
00:25:11.05	−72:11:54.6	8.71										

Continued on next page

RA (J2000)	DEC	S_{36cm} (mJy)	S_{20cm} (mJy)	S_{13cm} (mJy)	S_{6cm} (mJy)	S_{3cm} (mJy)	Blend Flag	$S_{20cm,matched}$ (mJy)	$S_{13cm,matched}$ (mJy)	$S_{6cm,matched}$ (mJy)	$S_{3cm,matched}$ (mJy)	α
00:25:18.11	−73:50:21.9	9.20	4.70									
00:25:21.57	−75:00:49.7	4.42										
00:25:22.65	−73:56:54.0	15.59	6.28									
00:25:29.41	−75:24:16.3		8.38									
00:25:35.69	−72:36:06.1	11.73	2.98									
00:25:37.69	−74:57:30.9	4.48										
00:25:41.32	−69:37:52.6		5.79									
00:25:42.99	−74:07:18.4	12.72	4.67									
00:25:44.60	−74:31:33.9	33.90										
00:25:47.93	−73:21:50.2	10.30	5.84									
00:25:48.06	−70:14:40.2	7.21										
00:25:51.21	−71:00:24.8	4.77										
00:25:52.98	−74:54:57.4	15.11	4.99									
00:25:54.72	−72:23:53.8	3.45										
00:25:54.81	−73:20:58.2	8.80	5.77									
00:25:57.80	−73:13:12.9	2.80										
00:25:58.14	−72:19:36.3	4.23	4.33									
00:26:04.70	−73:21:53.7	40.30	18.25									
00:26:05.16	−71:25:42.5	8.29	4.02									
00:26:05.53	−72:49:40.0	22.54	7.54									
00:26:05.60	−72:04:00.9	4.96										
00:26:06.29	−72:50:07.2		4.74									
00:26:06.88	−73:23:07.7	114.00	34.27									

Continued on next page

RA (J2000)	DEC	S_{36cm} (mJy)	S_{20cm} (mJy)	S_{13cm} (mJy)	S_{6cm} (mJy)	S_{3cm} (mJy)	Blend Flag	$S_{20cm,matched}$ (mJy)	$S_{13cm,matched}$ (mJy)	$S_{6cm,matched}$ (mJy)	$S_{3cm,matched}$ (mJy)	α
00:26:07.42	−74:21:29.8	12.48	8.08									
00:26:08.68	−72:59:33.0	3.15										
00:26:10.97	−73:23:50.9		9.81									
00:26:11.15	−75:18:29.9		5.18									
00:26:12.76	−71:35:28.0	4.51										
00:26:13.13	−75:26:00.3		5.72									
00:26:13.65	−74:44:49.2	10.84	7.05									
00:26:14.15	−70:51:35.1	10.17										
00:26:20.95	−74:37:39.8	18.82	11.29									
00:26:22.08	−74:22:59.6	9.11	7.11									
00:26:24.59	−70:49:22.4	6.62										
00:26:27.66	−69:36:42.7		25.34									
00:26:28.00	−74:00:19.6	13.71	13.84		36.44					29.19		0.43
00:26:29.65	−72:32:24.0	6.83	3.10									
00:26:31.53	−74:13:14.5	47.85	21.60									
00:26:31.64	−75:18:57.4		10.00									
00:26:31.75	−72:41:33.8	9.07										
00:26:34.38	−75:19:02.7		11.20							6.90		
00:26:37.97	−72:50:00.6	34.96	16.99									
00:26:40.84	−71:15:23.3	3.44										
00:26:45.27	−74:41:37.2	51.30	27.30									
00:26:45.71	−71:00:08.1	47.53	25.50									
00:26:46.74	−73:27:34.7	21.32	12.68									

Continued on next page

RA (J2000)	DEC	S_{36cm} (mJy)	S_{20cm} (mJy)	S_{13cm} (mJy)	S_{6cm} (mJy)	S_{3cm} (mJy)	Blend Flag	$S_{20cm,matched}$ (mJy)	$S_{13cm,matched}$ (mJy)	$S_{6cm,matched}$ (mJy)	$S_{3cm,matched}$ (mJy)	α
00:26:47.14	−70:40:44.8	90.64	118.40									
00:26:47.30	−73:10:13.4	2.70										
00:26:55.92	−74:02:55.2	5.28										
00:26:57.36	−74:10:32.5	65.36	29.30									
00:26:58.72	−72:02:42.4	15.12	8.88									
00:27:02.37	−73:44:58.5	9.96	10.50									
00:27:02.73	−69:28:50.5		9.09									
00:27:03.41	−72:03:48.2	3.66										
00:27:05.70	−74:10:28.3		7.32									
00:27:06.70	−74:25:32.3	2.90										
00:27:07.05	−69:42:20.6		6.16									
00:27:24.16	−70:31:56.1	32.77	20.20									
00:27:24.46	−73:36:51.5	22.11	12.35									
00:27:26.94	−71:08:07.0	5.40										
00:27:29.22	−72:02:31.8	6.83										
00:27:29.31	−71:13:36.2		4.48									
00:27:37.43	−73:11:14.6	3.92										
00:27:37.66	−73:31:36.7	34.01	15.37									
00:27:38.65	−74:45:30.1	3.16										
00:27:42.63	−75:12:52.6	6.50										
00:27:44.22	−70:01:04.7		4.24									
00:27:45.75	−72:20:12.4	4.32										
00:27:49.85	−75:31:12.6		6.13									

Continued on next page

RA (J2000)	DEC	S_{36cm} (mJy)	S_{20cm} (mJy)	S_{13cm} (mJy)	S_{6cm} (mJy)	S_{3cm} (mJy)	Blend Flag	$S_{20cm,matched}$ (mJy)	$S_{13cm,matched}$ (mJy)	$S_{6cm,matched}$ (mJy)	$S_{3cm,matched}$ (mJy)	α
00:27:50.56	−75:31:46.1		6.73									
00:27:53.15	−69:58:17.6		11.38									
00:28:00.69	−70:29:41.0	4.01										
00:28:03.92	−69:48:04.1		8.58									
00:28:04.40	−71:19:40.2	3.22										
00:28:04.69	−72:45:06.9	6.26										
00:28:08.17	−70:34:33.4	6.05										
00:28:14.72	−73:11:35.3	22.68	16.19									
00:28:16.17	−74:18:31.6	21.44	15.07		8.20	3.79						
00:28:16.37	−71:14:21.9	2.95										
00:28:17.73	−74:12:16.1	3.09										
00:28:18.55	−69:42:30.4		68.36									
00:28:20.23	−72:31:56.9	10.15	6.74									
00:28:20.33	−70:53:44.3	3.97										
00:28:20.96	−73:33:21.5	9.00	6.84									
00:28:21.78	−73:50:39.6	7.00	6.41		1.89							
00:28:22.96	−70:34:19.1		21.43									
00:28:23.75	−72:43:11.8	46.55	21.92									
00:28:25.01	−70:08:23.8		10.67									
00:28:26.37	−74:46:25.4					5.69						
00:28:26.45	−70:35:01.0	78.54	44.49									
00:28:33.45	−70:56:08.4	13.54	8.64									
00:28:35.32	−69:33:40.8		45.90									

Continued on next page

RA (J2000)	DEC	S_{36cm} (mJy)	S_{20cm} (mJy)	S_{13cm} (mJy)	S_{6cm} (mJy)	S_{3cm} (mJy)	Blend Flag	$S_{20cm,matched}$ (mJy)	$S_{13cm,matched}$ (mJy)	$S_{6cm,matched}$ (mJy)	$S_{3cm,matched}$ (mJy)	α
00:28:37.90	−70:36:29.2	4.29										
00:28:40.56	−74:20:12.6	3.11										
00:28:41.63	−70:45:16.0	91.87	98.36					130.80				0.74
00:28:43.33	−73:13:26.9	4.76										
00:28:43.78	−73:45:54.9		4.10									
00:28:50.44	−75:11:15.9				4.27							
00:28:53.20	−70:44:40.2		6.98									
00:28:56.09	−73:13:52.8	3.65										
00:28:57.15	−71:35:38.0	3.59										
00:28:57.40	−73:23:46.1	10.22	5.02									
00:29:00.01	−69:45:55.8		14.47									
00:29:02.38	−75:18:03.2		11.51		5.71							
00:29:03.35	−71:27:31.2	18.01	8.42									
00:29:03.36	−69:56:13.9		5.55									
00:29:07.01	−73:53:48.7	132.60	83.23	6.00	33.62	20.10				34.90		−0.77
00:29:08.10	−71:16:26.5	3.52										
00:29:09.74	−74:11:31.2				9.27	7.58				9.60	5.02	−1.10
00:29:10.77	−74:09:07.0	13.98	6.54		2.65					4.46		−0.66
00:29:17.05	−72:37:07.0	3.20										
00:29:18.95	−72:28:11.3	149.70	105.00		31.04					38.82		−0.77
00:29:19.21	−75:40:19.1		255.29									
00:29:21.90	−74:45:08.0				2.88							
00:29:22.54	−71:15:13.9	3.14										

Continued on next page

RA (J2000)	DEC	S_{36cm} (mJy)	S_{20cm} (mJy)	S_{13cm} (mJy)	S_{6cm} (mJy)	S_{3cm} (mJy)	Blend Flag	$S_{20cm,matched}$ (mJy)	$S_{13cm,matched}$ (mJy)	$S_{6cm,matched}$ (mJy)	$S_{3cm,matched}$ (mJy)	α
00:29:23.19	−74:44:55.9	13.26	6.24									
00:29:25.33	−72:00:27.4	5.28										
00:29:26.45	−73:23:42.0	6.91	11.16		10.30							
00:29:26.83	−69:34:41.8		291.10									
00:29:29.53	−70:32:17.6	32.03	14.44									
00:29:29.61	−74:59:26.2		3.71									
00:29:29.93	−73:16:16.5	16.81	4.15									
00:29:36.77	−72:19:20.0	6.11										
00:29:37.19	−72:23:26.0	3.29										
00:29:37.61	−73:45:43.3	6.55			3.69							
00:29:38.77	−71:29:56.7	13.70	7.97									
00:29:44.81	−71:26:36.2	10.09	4.11									
00:29:45.22	−73:04:19.3	42.79	15.94									
00:29:49.66	−73:04:18.9				5.75							
00:29:50.94	−72:07:31.6	41.04	20.72									
00:29:51.34	−72:00:02.1	3.90										
00:29:53.90	−73:02:54.3	2.70										
00:29:55.58	−75:35:37.5		7.54									
00:29:56.77	−71:46:37.8	38.23	20.56									
00:29:57.42	−73:59:38.1		7.20		7.31	3.84	b					
00:29:57.90	−73:37:14.3	2.90										
00:29:58.07	−74:06:09.3	3.43										
00:30:01.84	−73:59:40.8		7.90				b					

Continued on next page

RA (J2000)	DEC	S_{36cm} (mJy)	S_{20cm} (mJy)	S_{13cm} (mJy)	S_{6cm} (mJy)	S_{3cm} (mJy)	Blend Flag	$S_{20cm,matched}$ (mJy)	$S_{13cm,matched}$ (mJy)	$S_{6cm,matched}$ (mJy)	$S_{3cm,matched}$ (mJy)	α
00:30:05.75	−70:00:18.1		11.57									
00:30:06.48	−72:41:54.4	4.37										
00:30:07.14	−74:00:15.2	76.24	30.88	17.70	20.78	18.20			32.00	30.60	14.42	−0.65
00:30:07.82	−74:48:59.8					4.01						
00:30:12.85	−74:49:32.0	6.95			3.54							
00:30:13.99	−70:03:05.9		30.80									
00:30:21.55	−73:56:47.9	7.26	4.50									
00:30:22.38	−70:03:19.7		53.90									
00:30:22.40	−72:19:23.2	2.80										
00:30:22.80	−73:36:29.3	2.40										
00:30:25.77	−73:18:10.6	63.90	34.42	1.60	15.58	8.91			11.30	14.15		−0.93
00:30:25.96	−70:23:31.7	7.26	4.52									
00:30:30.65	−74:29:26.7		36.91			3.07						
00:30:30.91	−73:18:56.8		5.00									
00:30:31.14	−75:01:05.5		4.57									
00:30:35.22	−74:29:11.9								74.26	36.33	19.29	−1.04
00:30:37.22	−73:51:49.2	46.41	12.80	1.60	8.25	3.46			7.63	6.30		−1.19
00:30:37.71	−74:29:01.7	140.10	48.82	51.40	38.38	7.47						
00:30:38.77	−72:57:17.9	16.13	8.51									
00:30:42.58	−74:59:33.6	7.18										
00:30:47.03	−71:54:51.5	10.40	3.79									
00:30:48.29	−69:44:49.7		81.55									
00:30:52.57	−71:34:40.5	10.44	7.33									

Continued on next page

RA (J2000)	DEC	S_{36cm} (mJy)	S_{20cm} (mJy)	S_{13cm} (mJy)	S_{6cm} (mJy)	S_{3cm} (mJy)	Blend Flag	$S_{20cm,matched}$ (mJy)	$S_{13cm,matched}$ (mJy)	$S_{6cm,matched}$ (mJy)	$S_{3cm,matched}$ (mJy)	α
00:30:52.70	−71:37:38.7	2.90										
00:30:53.84	−74:34:07.1		3.72									
00:30:57.81	−72:24:35.6	3.83										
00:31:01.08	−70:58:38.0	32.54	16.22									
00:31:01.59	−72:37:32.0	3.67										
00:31:02.95	−71:55:13.2	11.42	5.77									
00:31:06.66	−71:01:11.5	92.90	54.71					72.75				−0.52
00:31:06.79	−72:48:27.7				2.99							
00:31:07.67	−71:06:57.9	39.50	25.83									
00:31:07.96	−71:51:03.8	4.97										
00:31:08.07	−72:48:13.5	9.05	5.73									
00:31:13.44	−71:42:32.8	3.53										
00:31:15.93	−71:49:48.4	12.26	4.23									
00:31:20.36	−70:36:48.5	188.60	131.20									
00:31:20.81	−73:23:03.2	16.77	10.04									
00:31:23.50	−73:23:01.7				3.68							
00:31:25.06	−70:19:51.1	9.79	4.84									
00:31:27.82	−74:05:44.3	3.27										
00:31:29.03	−70:41:09.4	10.21	4.21									
00:31:31.69	−74:30:30.7	45.61	22.37	18.70	8.86	6.14			19.85			−0.80
00:31:31.85	−72:10:18.7	3.67										
00:31:36.31	−70:33:13.0	73.69	53.28									
00:31:37.00	−71:50:24.6	4.14										

Continued on next page

RA (J2000)	DEC	S_{36cm} (mJy)	S_{20cm} (mJy)	S_{13cm} (mJy)	S_{6cm} (mJy)	S_{3cm} (mJy)	Blend Flag	$S_{20cm,matched}$ (mJy)	$S_{13cm,matched}$ (mJy)	$S_{6cm,matched}$ (mJy)	$S_{3cm,matched}$ (mJy)	α
00:31:40.56	−74:34:47.2	85.05	54.25	42.20	28.21	16.90			47.17	28.48	14.83	−0.73
00:31:40.76	−73:55:14.1	4.12										
00:31:40.79	−73:47:55.0	4.35			3.72	6.61						
00:31:42.74	−71:12:26.2	5.00	3.51									
00:31:48.76	−72:13:28.6					4.23						
00:31:50.27	−74:17:43.2		3.50									
00:31:52.33	−72:31:41.5	6.89										
00:31:52.50	−72:13:03.0	3.00										
00:31:52.57	−73:56:13.4					4.89						
00:31:55.76	−72:48:35.0	4.33			3.92							
00:31:58.85	−70:35:14.8	79.37	50.37									
00:32:04.70	−70:18:21.5	14.80	7.95									
00:32:08.76	−73:50:38.2	43.78	24.69	8.80	7.81							
00:32:11.13	−70:38:14.4	10.34	4.10									
00:32:14.51	−72:31:22.7	3.65										
00:32:15.07	−70:48:04.8	4.73										
00:32:15.64	−71:35:51.2	13.24	8.67		4.37				1.84			−1.90
00:32:15.82	−69:37:52.0		4.48									
00:32:17.46	−70:39:46.2	23.32	12.67									
00:32:24.83	−73:06:57.5		23.40									
00:32:25.40	−70:51:26.7	7.24										
00:32:30.13	−71:04:18.8	9.16	6.34		3.77							
00:32:30.78	−69:24:24.7		154.57									

Continued on next page

RA (J2000)	DEC	S_{36cm} (mJy)	S_{20cm} (mJy)	S_{13cm} (mJy)	S_{6cm} (mJy)	S_{3cm} (mJy)	Blend Flag	$S_{20cm,matched}$ (mJy)	$S_{13cm,matched}$ (mJy)	$S_{6cm,matched}$ (mJy)	$S_{3cm,matched}$ (mJy)	α
00:32:31.12	−73:06:46.4	106.60	22.50	46.70	24.82	33.40		99.94	80.97	41.62	17.59	−0.77
00:32:31.75	−70:31:18.8	19.29	7.06									
00:32:34.29	−73:41:38.7	7.98	5.13	6.60	9.29	8.74			10.50		9.50	0.07
00:32:34.52	−73:46:33.1		4.02									
00:32:37.03	−70:49:14.6	14.64	16.87		9.35					7.73		−0.37
00:32:37.04	−73:44:49.1	4.72										
00:32:39.10	−73:06:36.1		10.50									
00:32:41.72	−71:16:32.6	7.64	3.04									
00:32:42.36	−73:31:52.7	80.76	44.92	20.20	12.83	6.91			27.24			−1.05
00:32:47.50	−73:37:42.0	2.90										
00:32:49.66	−74:18:56.9	75.42	39.59	27.60	15.91	6.68		413.30	30.33	15.61		−1.33
00:32:50.36	−73:57:40.6	6.82							2.75			−0.87
00:32:52.52	−72:29:33.6	55.69	67.14	36.80	79.10	55.80			65.70	78.82		0.20
00:32:54.54	−70:18:59.8	11.67	6.10									
00:32:55.13	−71:45:45.6	109.80	52.40	9.10	19.88	12.00		72.84	16.62	20.47	10.42	−0.99
00:33:01.27	−71:53:17.1	8.83	5.54		2.79							
00:33:03.14	−69:42:41.3		6.97									
00:33:03.89	−70:44:40.2	3.18										
00:33:04.72	−71:56:17.6	3.91			2.22							
00:33:05.19	−74:21:27.8	16.05	9.66	4.50	2.01							
00:33:05.55	−73:27:19.9	3.59										
00:33:07.20	−75:37:40.9		6.72									
00:33:10.56	−74:55:18.4	37.12	17.46	11.50	7.27				10.30			−1.24

Continued on next page

RA (J2000)	DEC	S_{36cm} (mJy)	S_{20cm} (mJy)	S_{13cm} (mJy)	S_{6cm} (mJy)	S_{3cm} (mJy)	Blend Flag	$S_{20cm,matched}$ (mJy)	$S_{13cm,matched}$ (mJy)	$S_{6cm,matched}$ (mJy)	$S_{3cm,matched}$ (mJy)	α
00:33:11.55	−74:03:42.5	19.22	14.46	11.80	6.75	2.21			12.01			−0.45
00:33:11.76	−70:31:25.7	61.71	32.21									
00:33:12.72	−70:48:47.1	3.86	3.71									
00:33:13.52	−70:55:24.9		22.50									
00:33:14.85	−74:39:07.4					5.36						
00:33:15.59	−74:18:38.6	7.22	5.36									
00:33:15.62	−70:56:03.9	124.20	39.90	3.50	40.52	34.00						
00:33:17.98	−70:32:18.3	15.70	9.74									
00:33:20.38	−69:15:11.6		11.38									
00:33:22.02	−73:10:32.6	3.25										
00:33:26.21	−72:37:12.1	24.28	11.85		1.68							
00:33:26.25	−72:23:48.4	8.63	4.95	1.40	1.98				6.07			−0.34
00:33:26.45	−74:18:37.2					5.75						
00:33:27.81	−72:37:19.1			2.30					10.49			
00:33:31.64	−70:13:31.4	5.66										
00:33:32.04	−73:32:00.4					8.01						
00:33:33.56	−69:34:44.3		22.20									
00:33:41.34	−74:30:55.9	17.54	10.31	8.40	4.90	3.05			10.39	5.26		−0.68
00:33:42.72	−70:41:18.6	21.48	9.28		3.77							
00:33:43.07	−69:59:30.1		6.71									
00:33:43.90	−69:28:07.4		3.85									
00:33:45.35	−73:21:13.0	7.35										
00:33:46.11	−72:02:03.1	11.52	4.76									

Continued on next page

RA (J2000)	DEC	S_{36cm} (mJy)	S_{20cm} (mJy)	S_{13cm} (mJy)	S_{6cm} (mJy)	S_{3cm} (mJy)	Blend Flag	$S_{20cm,matched}$ (mJy)	$S_{13cm,matched}$ (mJy)	$S_{6cm,matched}$ (mJy)	$S_{3cm,matched}$ (mJy)	α
00:33:48.05	−73:14:40.4	8.79	6.31	1.30					4.43			−0.66
00:33:48.60	−74:31:24.2		3.87									
00:33:49.78	−73:14:26.5				1.79							
00:33:49.87	−73:35:32.4		8.03									
00:33:52.18	−70:30:53.3	90.75	43.13									
00:33:52.80	−72:10:52.9	6.84										
00:33:53.35	−70:19:20.1	9.45	4.96									
00:33:53.44	−72:59:59.6	3.55										
00:33:55.73	−72:12:34.5	9.52	7.16		4.13							
00:33:56.91	−72:28:39.8	36.56	15.30	12.00	9.81	4.79			17.07	10.55		−0.71
00:33:57.61	−74:23:22.9	43.59	21.90	18.60	10.08	12.50			19.96	9.46		−0.87
00:33:57.97	−70:08:23.9	5.88										
00:33:58.54	−70:39:47.8	16.32	6.12		3.95							
00:34:00.98	−70:26:27.0	138.50	65.00									
00:34:01.55	−70:35:22.2	3.15										
00:34:02.44	−71:10:17.6	5.48	4.41									
00:34:02.73	−73:22:49.0					4.65						
00:34:03.93	−71:45:55.8	14.55	8.82		2.40							
00:34:05.47	−70:25:52.3		25.80					288.30				
00:34:09.87	−72:02:39.6	4.08										
00:34:09.88	−70:25:21.2	185.20	62.00									
00:34:13.34	−73:33:21.2	433.60	111.50	212.70	83.76	54.30		359.50	248.00	113.10	39.27	−1.02
00:34:14.09	−72:26:55.5			2.51								

Continued on next page

RA (J2000)	DEC	S_{36cm} (mJy)	S_{20cm} (mJy)	S_{13cm} (mJy)	S_{6cm} (mJy)	S_{3cm} (mJy)	Blend Flag	$S_{20cm,matched}$ (mJy)	$S_{13cm,matched}$ (mJy)	$S_{6cm,matched}$ (mJy)	$S_{3cm,matched}$ (mJy)	α
00:34:15.12	−70:45:47.0					4.25						
00:34:15.28	−73:18:28.2					5.94						
00:34:15.52	−73:34:50.3					7.75						
00:34:17.27	−73:34:07.5					6.92						
00:34:20.56	−75:19:57.2		4.56									
00:34:23.50	−73:14:16.6	2.80										
00:34:24.50	−72:11:44.4	255.40	149.50	74.80	44.85	24.10		180.10	103.20		22.24	−1.07
00:34:25.14	−73:35:09.0	110.40	24.71	87.00	18.46							
00:34:25.74	−69:19:25.6		8.92									
00:34:26.52	−71:54:54.2	8.92	6.29	2.20	3.66							
00:34:27.66	−73:35:23.3					5.32						
00:34:31.69	−71:33:12.9	4.98	3.30			4.05						
00:34:33.81	−69:25:16.2		8.42									
00:34:36.03	−72:27:50.9	10.14	4.74	3.50								
00:34:36.06	−74:42:42.8					5.74						
00:34:38.38	−72:27:51.7				2.16							
00:34:40.09	−72:41:41.2	12.63	7.74		2.59							
00:34:42.44	−74:30:08.1					5.15						
00:34:46.05	−73:33:21.0			2.77					3.51			
00:34:46.63	−70:39:52.1	6.27			3.86							
00:34:47.72	−70:51:32.7	3.89										
00:34:49.52	−73:33:13.1		5.57									
00:34:49.98	−74:29:41.6	3.76										

Continued on next page

RA (J2000)	DEC	S_{36cm} (mJy)	S_{20cm} (mJy)	S_{13cm} (mJy)	S_{6cm} (mJy)	S_{3cm} (mJy)	Blend Flag	$S_{20cm,matched}$ (mJy)	$S_{13cm,matched}$ (mJy)	$S_{6cm,matched}$ (mJy)	$S_{3cm,matched}$ (mJy)	α
00:34:50.66	−70:44:51.2	3.26										
00:34:52.08	−72:46:10.0	3.65										
00:34:53.43	−70:52:30.6	9.04	6.59									
00:34:54.25	−73:33:44.0		5.48									
00:34:54.73	−70:38:01.1	3.54										
00:34:55.18	−72:46:54.8					5.05						
00:34:55.52	−71:35:58.3	9.32	3.04	2.30	2.87				5.33			−0.54
00:35:04.11	−73:06:53.4	7.54	4.39									
00:35:06.35	−70:22:00.1	6.94										
00:35:09.91	−69:22:53.3		5.09									
00:35:11.17	−71:09:56.0	104.10	52.40	18.70	10.87				28.69			−1.24
00:35:11.98	−75:27:32.9		3.65									
00:35:12.83	−70:10:30.0	4.43										
00:35:13.46	−70:47:29.6					4.37						
00:35:17.82	−70:08:40.1		10.91									
00:35:18.59	−73:34:52.9					5.33						
00:35:24.27	−73:22:22.3	40.14	24.91	17.60	10.39				19.21			−0.71
00:35:25.07	−71:37:49.7	4.33										
00:35:28.53	−72:06:55.1	3.22										
00:35:30.72	−72:36:55.4	13.81	20.06	16.70	21.45	19.90				21.35	18.86	0.16
00:35:31.91	−69:41:19.3		13.67									
00:35:36.85	−71:46:03.8	26.22	14.09	7.50	4.29				9.40	3.57		−1.13
00:35:44.73	−73:52:08.8	19.34	11.86	7.80	4.18				8.00			−0.85

Continued on next page

RA (J2000)	DEC	S_{36cm} (mJy)	S_{20cm} (mJy)	S_{13cm} (mJy)	S_{6cm} (mJy)	S_{3cm} (mJy)	Blend Flag	$S_{20cm,matched}$ (mJy)	$S_{13cm,matched}$ (mJy)	$S_{6cm,matched}$ (mJy)	$S_{3cm,matched}$ (mJy)	α
00:35:47.48	−72:11:17.5	11.19	6.80	3.40	3.25							
00:35:50.38	−69:35:10.9		3.85									
00:35:52.23	−69:31:29.9		29.86									
00:35:52.31	−72:53:01.8	42.08	18.96	19.50	12.97	8.82				10.99	6.13	−0.81
00:35:53.21	−69:39:35.4		3.82									
00:36:07.48	−75:12:16.1	9.10										
00:36:08.60	−74:29:24.8	7.59	6.43	1.60	1.06				3.34			−0.79
00:36:08.83	−75:44:36.7		8.82									
00:36:09.61	−74:04:54.5		3.93	2.79					4.25			
00:36:10.24	−72:54:01.8	13.10	6.13	31.20	0.88							
00:36:17.68	−73:59:55.8	4.06										
00:36:19.24	−72:58:57.3	5.90										
00:36:19.92	−72:09:50.3	61.13	24.89	19.00	10.02			65.39	40.77	16.67		−0.78
00:36:24.51	−72:08:52.0	31.50	12.83	4.90	4.15	4.73						
00:36:24.59	−72:53:42.6	15.13	19.44	26.30	19.48	17.70					18.87	0.09
00:36:26.62	−70:15:14.3	5.51										
00:36:28.25	−71:46:33.8	21.89	10.49	2.60	1.01				5.10			−1.41
00:36:28.78	−72:03:22.2					5.70						
00:36:35.60	−75:25:46.9		5.14									
00:36:36.20	−71:51:32.5	8.68	5.30	2.60	1.15							
00:36:42.31	−73:54:23.1	5.40										
00:36:42.76	−71:36:01.7					4.93						
00:36:43.09	−75:45:09.5		57.01									

Continued on next page

RA (J2000)	DEC	S_{36cm} (mJy)	S_{20cm} (mJy)	S_{13cm} (mJy)	S_{6cm} (mJy)	S_{3cm} (mJy)	Blend Flag	$S_{20cm,matched}$ (mJy)	$S_{13cm,matched}$ (mJy)	$S_{6cm,matched}$ (mJy)	$S_{3cm,matched}$ (mJy)	α
00:36:45.27	−72:34:37.3	3.39										
00:36:46.30	−70:53:12.6	7.47		1.30								
00:36:47.54	−71:36:01.4	26.03	7.90	12.50	6.11			13.76	14.65			−0.53
00:36:50.59	−73:06:50.8	4.79										
00:36:50.63	−70:39:34.0	10.07	7.35		1.86							
00:36:55.02	−74:13:51.9	5.96										
00:36:55.64	−74:44:28.9	8.56	4.39	2.10	3.47				3.88			−0.76
00:36:59.13	−71:38:10.7	10.37	7.95	9.30	11.91	8.60				10.71	5.85	−0.19
00:36:59.84	−72:02:09.8	3.23							1.20			−0.95
00:37:01.63	−71:49:06.3	12.61	7.97	4.20	5.54	4.83			8.24			−0.41
00:37:01.71	−74:30:49.1	3.02										
00:37:03.59	−70:47:26.3	24.05	11.61	9.90	8.59	10.30		16.91	10.88	7.61		−0.67
00:37:05.13	−75:27:59.0		3.89									
00:37:05.91	−73:07:53.1	3.32										
00:37:08.28	−69:47:16.1		6.31									
00:37:09.31	−71:21:11.4			2.10								
00:37:09.35	−71:20:54.7	13.34	6.38		4.56				8.09			−0.48
00:37:09.67	−71:40:05.8	34.72	11.48	15.00	7.00	4.21		24.95		5.69		−1.06
00:37:12.08	−75:14:17.8		10.80									
00:37:13.02	−70:56:16.0		4.11									
00:37:16.06	−69:22:04.0		7.96									
00:37:16.12	−75:14:12.2	48.42	15.80	1.90	19.76	13.90			12.84	17.88	13.07	−0.51
00:37:16.78	−70:56:45.5	12.01	9.95	10.10	8.70	7.44			13.22	9.53		−0.12

Continued on next page

RA (J2000)	DEC	S_{36cm} (mJy)	S_{20cm} (mJy)	S_{13cm} (mJy)	S_{6cm} (mJy)	S_{3cm} (mJy)	Blend Flag	$S_{20cm,matched}$ (mJy)	$S_{13cm,matched}$ (mJy)	$S_{6cm,matched}$ (mJy)	$S_{3cm,matched}$ (mJy)	α
00:37:25.75	−69:30:03.0		3.96									
00:37:26.39	−69:52:46.2		6.98									
00:37:26.50	−74:18:25.3		4.57									
00:37:32.03	−70:48:56.2	3.14										
00:37:32.69	−75:13:05.9	4.76										
00:37:38.55	−71:41:02.4	6.18	4.77	1.30	1.93	4.33						
00:37:43.45	−71:07:36.6	83.19	43.29	35.80	23.13	10.20		58.45	37.04	20.59		−0.80
00:37:49.84	−73:51:28.2	14.70	12.73	13.30	3.89							
00:37:51.95	−71:05:02.5					4.96						
00:37:53.43	−69:47:53.9		5.40									
00:37:55.02	−70:43:12.8	9.01	4.60									
00:37:55.20	−72:51:57.7	255.86	103.70	99.00	50.97	19.80		168.40	110.70	53.25	19.28	−1.07
00:37:56.09	−72:06:02.8			3.30					6.52			
00:37:56.83	−69:48:03.4		10.60									
00:37:57.22	−72:05:51.4	5.55										
00:37:58.88	−74:50:45.9		4.58									
00:38:00.77	−72:52:11.5		46.70									
00:38:01.94	−73:04:34.1	8.08	6.98	5.20								
00:38:05.32	−74:50:30.8								20.47	9.52		−1.08
00:38:08.70	−74:50:23.2	27.82	8.77	17.10	7.38							
00:38:09.15	−73:50:23.9	208.50	132.10	101.30	59.98	36.30		149.50	110.20	61.86	36.61	−0.74
00:38:09.61	−71:07:21.9	7.46	4.80									
00:38:11.68	−74:50:17.9					6.88						

Continued on next page

RA (J2000)	DEC	S_{36cm} (mJy)	S_{20cm} (mJy)	S_{13cm} (mJy)	S_{6cm} (mJy)	S_{3cm} (mJy)	Blend Flag	$S_{20cm,matched}$ (mJy)	$S_{13cm,matched}$ (mJy)	$S_{6cm,matched}$ (mJy)	$S_{3cm,matched}$ (mJy)	α
00:38:14.71	−70:14:43.3	4.85	3.99									
00:38:17.87	−71:31:45.9	4.25	4.05						1.89			−0.78
00:38:18.30	−69:24:15.5		4.25									
00:38:19.01	−72:34:20.9	21.10	4.96	6.30	4.27				8.34			−0.89
00:38:20.83	−72:34:00.9		5.42									
00:38:21.24	−74:30:36.6	3.77										
00:38:22.30	−72:32:44.2	5.40										
00:38:24.41	−74:22:11.9	436.40	255.70	159.90	76.80	37.90			178.60	77.67	36.75	−1.06
00:38:28.29	−74:04:51.1	5.50										
00:38:29.21	−72:47:03.0	4.84							4.06			−0.17
00:38:36.27	−69:53:25.2		16.24									
00:38:46.90	−70:56:07.1	5.68										
00:38:50.07	−70:42:10.3	5.96							3.29			−0.57
00:38:50.14	−72:08:48.3	10.67	5.96	5.50	3.88				6.05			−0.55
00:38:50.26	−72:00:15.5	5.62	4.43		2.39							
00:38:50.79	−73:10:52.8	13.84	13.23	14.80	21.91	32.70			14.44	22.29	32.85	0.37
00:38:51.68	−73:29:51.8	7.23	4.87	2.57					4.33			−0.49
00:38:53.69	−70:20:53.8	4.23	3.88									
00:38:54.80	−70:49:32.0	6.24	3.15	1.50								
00:38:55.58	−72:08:42.1					4.18						
00:38:57.26	−70:59:23.3	8.17										
00:38:57.81	−72:48:50.8	5.70	3.93	1.90	3.37	5.35			5.49			−0.04
00:38:58.66	−70:20:00.1	3.55										

Continued on next page

RA (J2000)	DEC	S_{36cm} (mJy)	S_{20cm} (mJy)	S_{13cm} (mJy)	S_{6cm} (mJy)	S_{3cm} (mJy)	Blend Flag	$S_{20cm,matched}$ (mJy)	$S_{13cm,matched}$ (mJy)	$S_{6cm,matched}$ (mJy)	$S_{3cm,matched}$ (mJy)	α
00:39:01.02	−72:57:26.4	12.48	4.19	5.00					4.74			−0.93
00:39:02.24	−75:26:20.0		6.20									
00:39:03.58	−73:51:48.8			2.48								
00:39:04.68	−72:43:37.3	16.42	6.69	5.80	2.58				8.16			−0.67
00:39:06.59	−73:46:27.5		5.30									
00:39:06.79	−73:51:57.9	4.26										
00:39:17.14	−73:18:42.9					6.55						
00:39:17.35	−69:48:42.7		72.98									
00:39:17.53	−72:03:45.2		3.89									
00:39:20.74	−72:04:05.7	23.07	9.36	7.60	4.70			12.20	9.32	3.99		−0.96
00:39:21.93	−72:43:13.7	8.00		1.40								
00:39:24.12	−72:03:38.2					4.51						
00:39:24.79	−69:55:52.2		4.23									
00:39:26.61	−71:52:42.7	39.31	13.37	16.70	8.57			22.07	13.82			−1.00
00:39:26.62	−71:36:37.1	6.57	3.60									
00:39:28.71	−70:12:50.8	3.87										
00:39:31.20	−72:13:46.6	3.81										
00:39:33.96	−73:48:27.3	4.18										
00:39:36.44	−74:20:17.3	30.88	20.50	13.80	8.34				14.68	7.57		−0.80
00:39:37.90	−71:43:15.9	13.50										
00:39:39.02	−73:56:11.8				2.19							
00:39:39.76	−71:41:42.4	174.00	84.50	49.70	23.12	18.10		101.10	52.83	22.24		−1.18
00:39:40.81	−74:34:53.4					5.24						

Continued on next page

RA (J2000)	DEC	S_{36cm} (mJy)	S_{20cm} (mJy)	S_{13cm} (mJy)	S_{6cm} (mJy)	S_{3cm} (mJy)	Blend Flag	$S_{20cm,matched}$ (mJy)	$S_{13cm,matched}$ (mJy)	$S_{6cm,matched}$ (mJy)	$S_{3cm,matched}$ (mJy)	α
00:39:41.23	−71:42:28.9				3.53							
00:39:42.37	−73:56:22.3	12.76	7.34	4.20								
00:39:43.48	−69:47:18.0		4.39									
00:39:44.06	−70:52:48.8	49.23	30.33	20.60	11.25	7.31			23.20			−0.73
00:39:45.30	−69:58:48.5		18.58									
00:39:45.48	−72:55:50.6	3.93										
00:39:47.41	−71:37:34.8	156.00	83.84	55.10	27.83	14.00		105.30	58.81	28.45	13.37	−1.05
00:39:48.63	−73:34:14.8					5.06						
00:39:50.61	−70:55:05.2	25.12	12.30	3.00		4.32						
00:39:51.59	−72:29:15.8					6.22						
00:39:54.50	−72:22:43.7	2.10										
00:39:59.91	−72:26:11.1					7.52						
00:40:01.47	−71:45:04.9	10.76	5.90									
00:40:06.44	−71:41:42.9	3.82										
00:40:09.20	−70:58:11.5	7.81	4.11						3.27			−0.84
00:40:13.10	−71:43:29.1					5.05						
00:40:14.08	−72:27:17.3					5.93						
00:40:18.75	−71:38:21.8	3.92										
00:40:21.04	−72:38:02.4					8.92						
00:40:21.14	−73:52:11.3			2.22								
00:40:21.70	−72:26:45.4	2.50										
00:40:22.52	−71:45:11.8		3.98									
00:40:23.32	−72:38:08.6	15.26		8.50					6.57			−0.81

Continued on next page

RA (J2000)	DEC	S_{36cm} (mJy)	S_{20cm} (mJy)	S_{13cm} (mJy)	S_{6cm} (mJy)	S_{3cm} (mJy)	Blend Flag	$S_{20cm,matched}$ (mJy)	$S_{13cm,matched}$ (mJy)	$S_{6cm,matched}$ (mJy)	$S_{3cm,matched}$ (mJy)	α
00:40:23.95	−73:52:02.8	5.19										
00:40:23.96	−74:22:00.8	4.44										
00:40:25.30	−72:37:57.4				4.13							
00:40:27.40	−74:39:23.3	3.61										
00:40:28.74	−71:44:05.7		3.34									
00:40:28.76	−70:35:15.8	48.08	24.64	1.70	4.09			31.18				−0.91
00:40:33.51	−69:51:26.0		6.18									
00:40:33.69	−75:14:57.3	11.23	7.01		2.37	2.46						
00:40:37.55	−71:43:37.8		3.43									
00:40:40.24	−75:03:58.1	8.24	5.59									
00:40:44.14	−74:12:21.7	5.39							2.95			−0.58
00:40:45.83	−70:23:56.5	33.30	15.28									
00:40:46.30	−73:52:11.7	5.21										
00:40:47.02	−71:22:06.2					5.64						
00:40:47.76	−73:48:18.1					5.06						
00:40:47.94	−71:45:59.7	637.80	409.70	295.10	175.50	99.90		487.30	325.90	175.80	99.42	−0.80
00:40:47.96	−73:37:01.4		35.58	84.10	48.13	36.30		136.70	126.90	77.87	34.60	−0.74
00:40:52.34	−71:21:54.4	9.30	5.88	2.30	1.89				5.38			−0.53
00:40:56.46	−73:43:21.7					4.49						
00:40:58.23	−74:13:19.0	7.29										
00:40:59.27	−73:36:49.6			45.50		11.00						
00:41:02.69	−71:46:40.4		4.93									
00:41:05.22	−70:14:13.8	7.43										

Continued on next page

RA (J2000)	DEC	S_{36cm} (mJy)	S_{20cm} (mJy)	S_{13cm} (mJy)	S_{6cm} (mJy)	S_{3cm} (mJy)	Blend Flag	$S_{20cm,matched}$ (mJy)	$S_{13cm,matched}$ (mJy)	$S_{6cm,matched}$ (mJy)	$S_{3cm,matched}$ (mJy)	α
00:41:12.18	−71:58:59.8	11.22	7.65	5.60	4.87	6.01						
00:41:23.45	−72:39:23.2	5.44										
00:41:24.66	−73:47:06.2	8.03	4.39	2.10	4.42							
00:41:25.04	−74:07:06.8	11.30	4.15	2.90					3.75			−1.06
00:41:25.38	−70:57:44.0	73.55	87.31	67.60	59.18	49.50			76.21	60.10	48.27	−0.18
00:41:26.36	−70:04:00.3	7.10	4.31									
00:41:27.65	−74:07:19.4				2.05							
00:41:27.95	−71:40:09.7	3.88										
00:41:28.93	−72:06:25.6	3.80										
00:41:30.75	−75:04:56.8	6.04										
00:41:31.08	−72:06:35.9					4.70						
00:41:33.54	−71:11:03.6	12.21	6.12	1.50					4.13			−1.05
00:41:34.65	−72:26:48.4					5.84						
00:41:35.76	−73:08:59.3	3.00	4.55									
00:41:41.16	−73:39:25.6	5.72										
00:41:43.72	−72:18:29.0	5.21	3.14	1.40	2.71	4.21						
00:41:44.14	−73:33:42.5	7.56										
00:41:45.05	−71:44:47.4	11.72			3.57							
00:41:50.87	−72:07:22.1	4.96										
00:41:52.10	−74:33:39.2	6.53	3.89	3.00								
00:41:54.54	−72:22:44.6	4.60										
00:41:54.58	−71:46:18.7	6.00							2.65			−0.79
00:41:59.21	−72:05:09.3		7.18	17.90	9.62	3.62			20.03	8.65		−1.19

Continued on next page

RA (J2000)	DEC	S_{36cm} (mJy)	S_{20cm} (mJy)	S_{13cm} (mJy)	S_{6cm} (mJy)	S_{3cm} (mJy)	Blend Flag	$S_{20cm,matched}$ (mJy)	$S_{13cm,matched}$ (mJy)	$S_{6cm,matched}$ (mJy)	$S_{3cm,matched}$ (mJy)	α
00:42:00.78	−70:04:41.3	14.45	7.40									
00:42:01.44	−73:07:27.1	197.40	37.60	92.00	37.55				104.00	47.21	23.58	−0.91
00:42:04.76	−71:17:24.0	29.60	16.25	12.90	7.92	5.26			13.09			−0.79
00:42:05.03	−73:07:17.5		39.00									
00:42:06.60	−73:35:37.1	2.50										
00:42:07.80	−72:34:16.5					4.79						
00:42:09.55	−72:38:41.4	5.66										
00:42:09.96	−72:14:45.4	17.81	9.71	7.00	3.59				7.62			−0.82
00:42:11.85	−72:25:09.2	5.03	5.10	2.60	1.75							
00:42:13.57	−74:08:35.0	6.63	4.18									
00:42:13.61	−74:03:25.7	8.29		2.60								
00:42:13.76	−69:52:20.9		19.37									
00:42:15.20	−73:09:16.9		3.79									
00:42:15.54	−71:47:08.9	7.68	5.11									
00:42:16.56	−71:52:00.9	3.23										
00:42:16.79	−72:59:10.5			2.60								
00:42:18.39	−73:10:59.1		4.06									
00:42:19.33	−73:10:47.3			11.70								
00:42:21.48	−73:10:51.1	11.48							13.66			0.17
00:42:24.32	−70:31:13.0	10.76	8.87									
00:42:24.78	−70:02:44.3	182.00	59.90									
00:42:26.12	−74:46:36.9					8.14						
00:42:26.25	−73:04:18.0	138.90	77.55	50.00	19.95			85.53	54.49	21.31		−1.06

Continued on next page

RA (J2000)	DEC	S_{36cm} (mJy)	S_{20cm} (mJy)	S_{13cm} (mJy)	S_{6cm} (mJy)	S_{3cm} (mJy)	Blend Flag	$S_{20cm,matched}$ (mJy)	$S_{13cm,matched}$ (mJy)	$S_{6cm,matched}$ (mJy)	$S_{3cm,matched}$ (mJy)	α
00:42:27.42	−75:13:55.5	53.36	18.55	7.00	14.82	18.00			16.57	17.00	11.79	−0.61
00:42:28.21	−70:02:57.2		41.60									
00:42:29.81	−69:39:17.6		19.83									
00:42:29.95	−74:28:47.6	13.34	7.43	5.30	2.38	2.04			5.84			−0.80
00:42:30.62	−74:54:50.7	6.91	6.34	5.40	4.72							
00:42:33.53	−71:37:37.6	5.38										
00:42:35.74	−70:36:51.7	6.36										
00:42:37.00	−70:06:22.2	9.01	5.48									
00:42:39.21	−70:01:33.8	93.45	42.10									
00:42:40.03	−72:33:25.1	12.31	10.44	9.50	5.50				10.45			−0.16
00:42:41.60	−70:33:28.1	5.37	6.63									
00:42:49.42	−74:24:27.1	5.65										
00:42:52.54	−72:56:12.4					6.01						
00:43:00.28	−71:59:43.2	4.60										
00:43:01.32	−74:25:21.0	7.84	3.80						1.69			−1.48
00:43:02.97	−73:39:50.1	3.19										
00:43:04.77	−75:23:37.4		7.24									
00:43:06.56	−73:28:27.9	29.20	19.67	14.40	5.46				13.33			−0.76
00:43:07.57	−71:13:28.9	3.12										
00:43:08.59	−74:28:41.1	5.31							3.27			−0.47
00:43:10.68	−72:36:23.5	5.49										
00:43:11.68	−71:04:25.6	49.32	21.44	28.30	14.10	11.10		31.11	29.02	12.03		−0.75
00:43:12.11	−74:34:24.4	3.51										

Continued on next page

RA (J2000)	DEC	S_{36cm} (mJy)	S_{20cm} (mJy)	S_{13cm} (mJy)	S_{6cm} (mJy)	S_{3cm} (mJy)	Blend Flag	$S_{20cm,matched}$ (mJy)	$S_{13cm,matched}$ (mJy)	$S_{6cm,matched}$ (mJy)	$S_{3cm,matched}$ (mJy)	α
00:43:15.83	−70:05:36.4		4.28									
00:43:18.30	−71:40:58.5	41.28	23.62	15.20	8.80	6.38			16.59		7.12	−0.75
00:43:19.20	−72:48:34.8	2.10										
00:43:19.30	−73:55:15.9	10.20	4.39	1.30								
00:43:20.30	−71:27:17.3				6.21							
00:43:20.71	−73:48:10.1					4.43						
00:43:25.55	−70:34:16.3				6.32							
00:43:27.91	−70:41:38.8	875.30	318.20	223.00	182.90	130.00		542.40	348.40	183.90	100.90	−0.91
00:43:31.10	−72:10:24.5	24.55	18.50	13.10	8.44				13.47	7.61		−0.66
00:43:34.59	−70:55:13.6	44.83	17.85	13.00	6.58				14.01	5.61		−1.19
00:43:35.23	−71:31:59.3	49.75	17.96	21.10	12.97	13.40		29.32	26.75	11.33		−0.79
00:43:36.66	−73:02:25.0	6.25	5.24	5.90	6.00	5.64			11.62			0.60
00:43:37.72	−70:41:01.1					4.09						
00:43:39.36	−72:03:46.8	58.37	26.70	19.20	9.20	9.02			21.15		9.47	−0.77
00:43:40.27	−70:38:19.6	3.43	3.92									
00:43:40.74	−73:25:50.1		8.80									
00:43:41.55	−71:15:27.1	13.36	6.54	1.70					4.06			−1.15
00:43:41.74	−71:16:50.2					4.57						
00:43:41.85	−71:22:30.9		4.47	5.10	3.99							
00:43:42.38	−73:29:23.8	6.50	5.39						3.30			−0.65
00:43:43.14	−73:02:20.9					6.51						
00:43:43.91	−73:29:41.6			2.00								
00:43:44.20	−74:04:59.6	3.63										

Continued on next page

RA (J2000)	DEC	S_{36cm} (mJy)	S_{20cm} (mJy)	S_{13cm} (mJy)	S_{6cm} (mJy)	S_{3cm} (mJy)	Blend Flag	$S_{20cm,matched}$ (mJy)	$S_{13cm,matched}$ (mJy)	$S_{6cm,matched}$ (mJy)	$S_{3cm,matched}$ (mJy)	α
00:43:46.36	−70:38:08.3				6.73					2.83		
00:43:46.41	−73:25:54.7	27.46		2.40					13.02	3.35		−1.17
00:43:47.12	−73:23:19.3	16.91	5.34	7.30	4.55				5.78			−1.04
00:43:48.57	−73:26:03.9		10.74					12.82				
00:43:48.60	−73:03:28.0	8.15										
00:43:48.70	−72:46:13.5	2.00										
00:43:48.72	−70:41:59.1					6.73						
00:43:51.22	−70:42:50.4			3.21								
00:43:52.33	−70:57:44.2	6.02							3.28			−0.59
00:43:55.40	−71:04:46.7	6.54										
00:44:01.58	−69:52:06.3		4.10									
00:44:08.48	−73:50:14.3					4.84						
00:44:13.69	−72:43:01.3	30.68	18.80	17.60	8.42	2.46			19.30	7.73		−0.76
00:44:14.59	−73:33:11.9	8.41	4.65	4.30	2.41				4.09			−0.70
00:44:15.29	−71:09:49.1					7.48						
00:44:16.89	−70:27:46.7	6.33	5.43									
00:44:17.19	−70:22:50.6	5.55										
00:44:17.55	−75:02:15.6	18.41	9.94	13.00	13.88	8.34			13.09	12.66		−0.22
00:44:19.82	−70:32:59.1	9.04	4.82									
00:44:21.12	−74:43:16.0	37.62	24.06	14.30	8.93	5.77			15.91			−0.83
00:44:24.75	−69:37:23.6		5.90									
00:44:26.19	−74:54:23.0					5.54						
00:44:26.69	−73:49:00.0					4.39						

Continued on next page

RA (J2000)	DEC	S_{36cm} (mJy)	S_{20cm} (mJy)	S_{13cm} (mJy)	S_{6cm} (mJy)	S_{3cm} (mJy)	Blend Flag	$S_{20cm,matched}$ (mJy)	$S_{13cm,matched}$ (mJy)	$S_{6cm,matched}$ (mJy)	$S_{3cm,matched}$ (mJy)	α
00:44:31.90	−69:27:07.0		4.51									
00:44:32.83	−71:38:03.1					5.33						
00:44:37.10	−74:39:17.0	4.47										
00:44:37.65	−74:23:20.9					6.45						
00:44:38.73	−73:37:10.9	12.20	12.52	9.10	4.84				9.47			−0.24
00:44:39.87	−74:23:41.9	4.30										
00:44:41.91	−75:03:00.7					5.07						
00:44:43.47	−70:09:06.8	39.47	21.37									
00:44:44.12	−71:00:08.4					4.31						
00:44:45.25	−73:35:29.6	4.21		2.66								
00:44:45.42	−75:04:03.4				4.63							
00:44:46.58	−74:25:14.4	7.11	4.41		2.45							
00:44:47.68	−75:13:05.3					3.59						
00:44:48.02	−72:12:23.7	3.57										
00:44:50.62	−75:13:23.9	8.24										
00:44:52.05	−69:16:41.0		48.12									
00:44:52.08	−72:32:05.2	4.77										
00:44:52.19	−73:45:37.8	33.90	18.13	16.10	7.78	6.43			14.38	7.27		−0.88
00:44:52.41	−73:18:51.6		3.80									
00:44:53.43	−70:48:43.4	31.45	18.72	10.80	6.63	6.48			13.05			−0.85
00:44:57.46	−73:10:10.9	5.80		11.70							6.65	0.06
00:44:59.68	−71:14:38.8	46.19	25.98	18.10	11.36	6.49			19.74	10.90		−0.83
00:44:59.90	−71:13:30.6	8.00	4.19									

Continued on next page

RA (J2000)	DEC	S_{36cm} (mJy)	S_{20cm} (mJy)	S_{13cm} (mJy)	S_{6cm} (mJy)	S_{3cm} (mJy)	Blend Flag	$S_{20cm,matched}$ (mJy)	$S_{13cm,matched}$ (mJy)	$S_{6cm,matched}$ (mJy)	$S_{3cm,matched}$ (mJy)	α
00:45:01.20	−71:02:57.6	4.35		2.70					3.66			−0.17
00:45:02.19	−71:55:56.6					3.38						
00:45:02.93	−73:16:38.7	6.56	6.38	12.20						5.41	4.96	−0.12
00:45:04.45	−71:56:13.6	18.07	11.33	7.40	4.80				8.01			−0.78
00:45:05.99	−73:33:57.9			2.52								
00:45:08.15	−73:51:45.9				3.77	6.14						
00:45:11.97	−73:56:20.9	3.75										
00:45:14.22	−70:43:06.7		4.31						4.35			
00:45:15.23	−70:42:46.7	11.88										
00:45:17.23	−72:35:14.3					5.26						
00:45:18.48	−73:15:28.6	4.21										
00:45:19.94	−69:55:19.7		15.40									
00:45:20.43	−70:44:42.7		3.68									
00:45:20.93	−74:08:30.8	4.94							1.37			−1.24
00:45:22.33	−73:15:20.2			30.10								
00:45:22.95	−69:55:09.6		6.60									
00:45:25.68	−73:22:59.1	44.30	16.07	625.50	30.03	56.00		50.02	57.84	45.06	43.14	−0.03
00:45:26.90	−74:53:50.4	2.90										
00:45:27.34	−69:32:50.4		5.06									
00:45:29.20	−75:01:35.4	6.98	6.33	1.80	2.86				3.59			−0.64
00:45:30.11	−74:50:56.2	12.28	9.89	7.40	4.55							
00:45:30.78	−73:04:53.6			87.40				57.49		68.66	45.03	−0.09
00:45:32.96	−72:04:02.2	12.99	5.85	2.00	2.47				4.05			−1.12

Continued on next page

RA (J2000)	DEC	S_{36cm} (mJy)	S_{20cm} (mJy)	S_{13cm} (mJy)	S_{6cm} (mJy)	S_{3cm} (mJy)	Blend Flag	$S_{20cm,matched}$ (mJy)	$S_{13cm,matched}$ (mJy)	$S_{6cm,matched}$ (mJy)	$S_{3cm,matched}$ (mJy)	α
00:45:37.20	−71:23:16.8	41.31	22.35	13.20	7.63				14.55			−1.01
00:45:40.35	−75:00:34.4					5.71						
00:45:45.51	−72:41:42.5	8.91	6.31						2.71			−1.15
00:45:46.30	−75:29:06.4		7.29									
00:45:48.15	−72:41:07.1					5.29						
00:45:48.54	−72:41:38.1			1.30								
00:45:48.67	−71:49:32.2	9.28	7.64	6.10	5.14	4.58						
00:45:52.33	−73:13:39.1			7.80								
00:45:53.71	−70:47:00.7					4.40						
00:45:54.57	−73:06:45.9			16.50								
00:45:55.45	−70:46:46.6	28.92	16.33	9.00	6.40				9.89			−1.03
00:45:56.18	−71:20:54.2	3.18										
00:45:57.65	−73:13:31.6	6.35	4.59						1.31			−1.52
00:45:59.81	−72:32:01.8					9.08						
00:46:00.35	−70:34:33.0	3.83										
00:46:01.96	−74:40:04.1	56.34	38.22	27.10	17.19	11.70			29.54	17.19	9.67	−0.75
00:46:03.03	−74:13:28.8	23.44	10.81	10.20	5.26				12.41	3.69		−1.03
00:46:04.17	−74:13:37.8											
00:46:04.50	−71:31:51.3			2.48					3.80			
00:46:05.58	−74:47:52.7				4.42							
00:46:07.10	−74:31:03.8	2.70										
00:46:07.76	−70:56:08.0					17.90						
00:46:08.33	−72:01:56.7	65.63	24.43	21.90	9.65	4.63						

Continued on next page

RA (J2000)	DEC	S_{36cm} (mJy)	S_{20cm} (mJy)	S_{13cm} (mJy)	S_{6cm} (mJy)	S_{3cm} (mJy)	Blend Flag	$S_{20cm,matched}$ (mJy)	$S_{13cm,matched}$ (mJy)	$S_{6cm,matched}$ (mJy)	$S_{3cm,matched}$ (mJy)	α
00:46:09.20	−73:12:35.3	3.85										
00:46:11.09	−74:17:59.9	8.93	4.93	5.40	4.44							
00:46:11.93	−73:00:43.3	3.94		3.00								
00:46:16.75	−71:16:11.7	13.19	5.51	3.30								
00:46:19.32	−73:23:24.8	8.42		39.20								
00:46:20.44	−72:45:14.2	4.46		1.30								
00:46:21.51	−72:01:54.0	49.05	19.25	13.90	2.05							
00:46:21.83	−74:00:57.7	3.14							1.16			−0.96
00:46:23.35	−71:00:41.6	15.92	7.01	5.90								
00:46:23.45	−72:27:24.6	15.40	10.88	7.30	4.43				7.22			−0.73
00:46:24.97	−72:23:50.8	3.58										
00:46:26.10	−71:00:39.8				3.61							
00:46:27.72	−74:26:20.9	3.50										
00:46:28.60	−74:24:32.7					3.68						
00:46:28.72	−73:15:08.4		4.38									
00:46:29.00	−74:25:06.8				3.86							
00:46:29.48	−73:14:49.0		3.98									
00:46:30.94	−72:22:50.5	4.88	3.43						2.19			−0.77
00:46:30.95	−72:04:19.0	4.02	3.49									
00:46:32.35	−74:25:07.0	11.06	7.36	1.60					11.15			0.01
00:46:32.41	−70:58:56.8	55.66	47.17	32.30	29.50	23.40			35.90	29.43	24.55	−0.35
00:46:33.00	−73:01:48.1	2.20										
00:46:33.48	−73:06:04.7			117.60						49.65	31.50	−0.77

Continued on next page

RA (J2000)	DEC	S_{36cm} (mJy)	S_{20cm} (mJy)	S_{13cm} (mJy)	S_{6cm} (mJy)	S_{3cm} (mJy)	Blend Flag	$S_{20cm,matched}$ (mJy)	$S_{13cm,matched}$ (mJy)	$S_{6cm,matched}$ (mJy)	$S_{3cm,matched}$ (mJy)	α
00:46:35.17	−73:53:44.9			4.20								
00:46:35.21	−73:05:57.9					45.20						
00:46:36.07	−73:53:32.9	7.91	5.10						5.17			−0.41
00:46:37.30	−72:36:24.3	2.40										
00:46:37.64	−73:08:23.2			21.10								
00:46:37.95	−73:53:58.2				3.68							
00:46:39.09	−69:57:12.3		69.70									
00:46:39.58	−73:22:04.3			38.10								
00:46:39.62	−69:31:28.8		41.02									
00:46:40.12	−73:21:49.4	8.30										
00:46:40.59	−73:31:50.9			45.40								
00:46:44.15	−69:57:10.3		52.80									
00:46:44.92	−74:32:40.8	3.33										
00:46:45.56	−73:27:04.6			30.70								
00:46:46.12	−74:34:05.5	14.44	8.84	5.50	2.55				5.95			−0.86
00:46:47.69	−69:57:15.4		33.40									
00:46:48.77	−70:46:42.9	5.98										
00:46:49.11	−73:13:55.9					6.04						
00:46:50.12	−71:39:25.3			4.30	14.54	13.20			7.99	15.27		0.92
00:46:52.25	−73:43:23.0					5.51						
00:46:52.93	−73:17:31.2			5.30								
00:46:59.39	−73:45:27.0	5.07		3.60								
00:46:59.87	−71:12:17.5	3.84										

Continued on next page

RA (J2000)	DEC	S_{36cm} (mJy)	S_{20cm} (mJy)	S_{13cm} (mJy)	S_{6cm} (mJy)	S_{3cm} (mJy)	Blend Flag	$S_{20cm,matched}$ (mJy)	$S_{13cm,matched}$ (mJy)	$S_{6cm,matched}$ (mJy)	$S_{3cm,matched}$ (mJy)	α
00:47:00.36	−71:18:59.0	5.49										
00:47:00.63	−70:03:47.0	12.14	7.11									
00:47:01.35	−73:05:21.3			17.70								
00:47:01.74	−70:14:38.0	15.82	9.96									
00:47:02.05	−71:01:43.1	2.90	4.55		3.58				2.82			−0.03
00:47:03.89	−71:49:57.5	42.48	23.07	16.70	8.99	6.75			18.05	9.01		−0.88
00:47:05.09	−75:02:33.0	17.70	6.60	9.80	4.41							
00:47:06.41	−74:30:03.6	5.36										
00:47:09.37	−74:30:11.6		3.24									
00:47:11.68	−74:59:29.7	24.12	9.80	11.10	5.11				10.80			−0.77
00:47:13.10	−73:40:51.1					6.24						
00:47:13.40	−74:56:58.0	6.05										
00:47:14.23	−75:02:55.3				4.27							
00:47:16.61	−73:08:11.5			341.00								
00:47:18.99	−72:39:47.5	6.96	20.74	22.20	38.72	29.90			21.48	40.48	30.45	0.70
00:47:24.36	−73:21:59.3			21.70								
00:47:24.96	−73:22:14.8	9.93							21.66			0.75
00:47:25.53	−71:27:28.1	7.96	11.69	1.60	24.02	24.90				22.73	22.02	0.47
00:47:28.58	−73:06:01.5			28.40								
00:47:28.70	−75:03:32.1	4.50										
00:47:29.34	−73:22:10.8					4.09						
00:47:31.19	−71:11:01.2	8.05	4.06						1.76			−1.47
00:47:31.99	−75:00:57.6	23.64	9.19	9.30	5.12	4.38			6.95	3.60		−1.09

Continued on next page

RA (J2000)	DEC	S_{36cm} (mJy)	S_{20cm} (mJy)	S_{13cm} (mJy)	S_{6cm} (mJy)	S_{3cm} (mJy)	Blend Flag	$S_{20cm,matched}$ (mJy)	$S_{13cm,matched}$ (mJy)	$S_{6cm,matched}$ (mJy)	$S_{3cm,matched}$ (mJy)	α
00:47:36.94	−69:43:27.3		17.50									
00:47:40.85	−75:30:11.1		339.60									
00:47:40.90	−73:34:34.2					6.57						
00:47:48.96	−73:17:25.4			26.60		5.65						
00:47:50.48	−70:57:56.7	49.63	32.88	20.80	12.72	6.28			22.92			−0.74
00:47:52.28	−70:39:46.1	7.31	3.09									
00:47:56.82	−73:17:52.5			64.90								
00:47:58.96	−71:15:44.5	6.98							1.17			−1.72
00:48:01.23	−70:18:20.7	8.34	3.84									
00:48:02.79	−73:16:53.4			100.90								
00:48:03.59	−70:49:11.4	6.39	3.87									
00:48:03.94	−74:12:34.5		3.05									
00:48:05.66	−75:23:45.0		8.72									
00:48:06.06	−73:08:42.7			104.70								
00:48:06.73	−74:19:59.5	6.23	5.19	2.10								
00:48:07.33	−74:19:46.9				2.00							
00:48:08.41	−74:12:05.7	159.60	109.10	76.10	45.82	29.10			84.93	45.80	25.26	−0.79
00:48:08.42	−73:14:54.2		17.24					32.86				
00:48:08.87	−74:33:03.6		3.71									
00:48:09.22	−73:14:42.6			56.20							31.64	
00:48:10.82	−71:14:22.9		4.33									
00:48:15.17	−70:36:45.7	7.54	4.08									
00:48:16.72	−71:14:01.6	39.44	17.72	14.50	7.70	6.00		20.92	17.88			−0.75

Continued on next page

RA (J2000)	DEC	S_{36cm} (mJy)	S_{20cm} (mJy)	S_{13cm} (mJy)	S_{6cm} (mJy)	S_{3cm} (mJy)	Blend Flag	$S_{20cm,matched}$ (mJy)	$S_{13cm,matched}$ (mJy)	$S_{6cm,matched}$ (mJy)	$S_{3cm,matched}$ (mJy)	α
00:48:16.92	−74:11:58.9					4.83						
00:48:19.16	−73:10:32.3			8.70								
00:48:21.24	−73:19:31.6			112.00								
00:48:23.68	−73:05:57.2			34.20						10.50	8.91	−0.28
00:48:25.63	−72:00:34.0	6.24	3.76	1.60	1.92							
00:48:27.00	−74:27:53.9	2.70										
00:48:28.18	−73:15:56.9			22.80								
00:48:30.85	−71:03:15.6		7.19		5.86	4.28						
00:48:32.37	−74:33:10.1	8.48	4.80	4.10	2.37							
00:48:32.52	−72:04:36.2	3.37										
00:48:34.04	−73:15:09.8			20.50								
00:48:34.76	−70:12:16.2	8.76										
00:48:35.30	−71:03:22.5	27.10		18.50				34.96				0.54
00:48:35.65	−73:44:33.5	8.89	5.38	4.30					2.94			−1.07
00:48:36.62	−73:30:55.5	13.92	8.80	10.70	4.70				8.23			−0.51
00:48:37.17	−71:28:39.1	7.55		1.40					3.65			−0.70
00:48:37.50	−70:12:23.4		4.36									
00:48:39.80	−75:31:48.2		4.83									
00:48:41.33	−73:56:56.2	4.86										
00:48:42.06	−73:42:11.3					5.54						
00:48:44.09	−74:07:29.1	19.61	13.91	7.80	4.09				7.71			−0.90
00:48:49.97	−72:51:23.4	14.86	6.38	10.30	5.62	4.24				4.99		−0.63
00:48:51.21	−71:05:13.0	23.70	9.85	11.40	7.18	5.97						

Continued on next page

RA (J2000)	DEC	S_{36cm} (mJy)	S_{20cm} (mJy)	S_{13cm} (mJy)	S_{6cm} (mJy)	S_{3cm} (mJy)	Blend Flag	$S_{20cm,matched}$ (mJy)	$S_{13cm,matched}$ (mJy)	$S_{6cm,matched}$ (mJy)	$S_{3cm,matched}$ (mJy)	α
00:48:56.00	−70:41:16.7		3.65									
00:48:56.30	−73:07:48.8			127.10				72.46			33.35	−0.42
00:48:58.20	−75:29:44.0		26.18									
00:48:58.27	−70:09:06.0	10.32	6.61									
00:49:01.60	−73:44:55.3	12.28	11.64	8.60	5.08							
00:49:05.42	−71:26:54.0	4.30		1.30								
00:49:07.75	−73:14:02.0			19.30								
00:49:08.00	−71:03:46.4	57.94	13.99	24.10	10.52			45.24		8.38		−1.15
00:49:08.78	−74:46:21.3	23.36	12.41	10.50	2.17				7.29			−1.12
00:49:10.06	−72:22:11.8					5.64						
00:49:12.41	−70:20:30.1	8.20	3.83									
00:49:12.48	−72:09:21.4	5.64							3.20			−0.55
00:49:12.92	−70:08:15.0		12.20									
00:49:15.34	−72:09:22.7			3.10								
00:49:16.22	−72:04:13.6	3.50										
00:49:17.10	−74:47:07.0	4.30										
00:49:17.29	−73:20:44.4	22.33	14.01	15.10	4.97	4.72						
00:49:18.21	−70:07:54.0		22.80									
00:49:18.25	−73:15:51.0			11.40								
00:49:18.37	−72:34:08.2					5.27						
00:49:18.64	−72:20:00.0	8.30	5.33	11.70	3.56							
00:49:18.85	−74:56:59.0	126.60	62.21	49.30	27.13	16.10			41.71	25.85	15.76	−0.88
00:49:18.85	−73:43:17.2					3.44						

Continued on next page

RA (J2000)	DEC	S_{36cm} (mJy)	S_{20cm} (mJy)	S_{13cm} (mJy)	S_{6cm} (mJy)	S_{3cm} (mJy)	Blend Flag	$S_{20cm,matched}$ (mJy)	$S_{13cm,matched}$ (mJy)	$S_{6cm,matched}$ (mJy)	$S_{3cm,matched}$ (mJy)	α
00:49:20.55	−74:47:12.9			3.30								
00:49:23.80	−71:26:59.8	34.54	15.39	12.40	8.03	4.05			12.92	6.37		−0.97
00:49:24.94	−71:05:18.8	45.51	15.04	17.40	6.52							
00:49:25.01	−71:05:52.1		12.47									
00:49:25.80	−73:09:40.5			6.60								
00:49:27.11	−69:50:19.1		11.18									
00:49:28.60	−74:01:25.9	5.04										
00:49:28.64	−73:34:00.4					6.57						
00:49:29.00	−73:26:33.5	11.07	6.45	13.60		9.02				8.81		−0.13
00:49:29.36	−72:18:09.7		9.38		5.36							
00:49:33.34	−72:19:01.6	23.77	25.38	26.70	7.03	4.29		32.21	29.64	14.90		−0.29
00:49:35.65	−74:15:43.8	55.25	18.07	24.80	11.10	9.38					15.18	−0.55
00:49:35.87	−72:46:35.7	33.41	17.51	19.60	7.30	4.17			11.38			−1.04
00:49:36.96	−72:35:52.4	6.60	3.77	9.40								
00:49:37.16	−70:52:12.3	14.14	21.58	13.70	46.95	62.70			16.64	46.19	59.44	0.67
00:49:37.66	−70:01:32.8		73.42									
00:49:38.51	−74:16:06.1		11.66									
00:49:42.06	−72:48:44.5	6.87	4.90	22.20					4.40			−0.43
00:49:42.41	−74:19:08.7	3.40	4.27									
00:49:44.88	−73:10:30.4			22.80						7.14		
00:49:45.05	−69:26:24.5		7.33									
00:49:48.88	−72:22:12.8	6.15	3.04									
00:49:54.00	−71:51:51.4	24.06	19.79	18.30	8.96	3.99			20.71			−0.14

Continued on next page

RA (J2000)	DEC	S_{36cm} (mJy)	S_{20cm} (mJy)	S_{13cm} (mJy)	S_{6cm} (mJy)	S_{3cm} (mJy)	Blend Flag	$S_{20cm,matched}$ (mJy)	$S_{13cm,matched}$ (mJy)	$S_{6cm,matched}$ (mJy)	$S_{3cm,matched}$ (mJy)	α
00:49:56.85	−72:35:54.3	188.60	98.90	72.90	27.65	12.80		110.70	64.53	26.59	11.69	−1.18
00:49:58.05	−69:33:26.5		7.90									
00:49:58.48	−72:05:37.1	11.38		3.90	3.76				5.31			−0.74
00:50:01.60	−72:22:31.5	3.80										
00:50:04.41	−71:41:54.5	3.68										
00:50:05.76	−69:47:26.7		8.72									
00:50:07.81	−73:41:34.3	12.53	7.38	6.10	2.59				5.83			−0.74
00:50:13.94	−73:21:28.6	5.67	3.79									
00:50:15.02	−73:03:25.2	48.30	20.14	31.20		5.72		42.39	13.75	10.40		−0.98
00:50:15.40	−72:32:32.1	4.47		10.90	5.25				6.37	5.71		0.16
00:50:21.58	−74:41:51.0	9.25	6.17		3.46	2.81			3.96			−0.82
00:50:22.29	−74:56:09.5	3.23										
00:50:22.35	−71:21:28.3		4.48	2.73	5.53	3.60			3.94	4.52		0.19
00:50:22.50	−73:03:06.8		9.63									
00:50:24.36	−73:59:43.2					5.12						
00:50:24.58	−70:52:58.7	7.43		3.80	4.71				6.84			−0.08
00:50:27.57	−69:58:32.3		7.17									
00:50:28.11	−72:53:11.5			154.10								
00:50:31.46	−71:19:22.9					5.14						
00:50:32.73	−73:07:11.3			8.00								
00:50:34.80	−70:40:36.2		3.72							2.31		
00:50:34.87	−69:15:34.9		13.33									
00:50:35.77	−73:20:12.6	3.81										

Continued on next page

RA (J2000)	DEC	S_{36cm} (mJy)	S_{20cm} (mJy)	S_{13cm} (mJy)	S_{6cm} (mJy)	S_{3cm} (mJy)	Blend Flag	$S_{20cm,matched}$ (mJy)	$S_{13cm,matched}$ (mJy)	$S_{6cm,matched}$ (mJy)	$S_{3cm,matched}$ (mJy)	α
00:50:38.28	−69:15:43.4		4.46									
00:50:40.47	−73:20:22.5			19.30						6.95		
00:50:41.57	−70:39:37.6	45.71	28.73	3.90	12.71	6.17			14.13	9.96	6.86	−0.80
00:50:42.11	−71:58:28.4	10.80	6.92	1.30	4.35	4.66			5.23	2.58		−0.81
00:50:42.26	−70:09:12.7		5.32									
00:50:45.82	−74:10:36.7	3.13										
00:50:49.66	−72:48:19.4			205.10								
00:50:52.64	−72:01:07.9	3.77										
00:50:53.36	−73:17:07.6	4.27	3.94	9.20								
00:50:56.62	−70:09:21.9		35.58									
00:50:57.27	−73:12:47.8		3.86	12.70	3.57	2.47				4.90		
00:51:01.50	−75:32:48.5		5.68									
00:51:10.24	−73:22:12.5			78.80								
00:51:11.70	−71:20:30.6				3.81	4.60						
00:51:15.82	−71:30:58.0	26.35	17.08	9.00	6.47	3.41						
00:51:17.07	−73:39:59.8	86.00	48.62	54.30	29.83	25.10		63.35	50.59	32.54	19.01	−0.62
00:51:17.64	−70:56:08.8	6.18	4.41		6.57	5.08			3.27			−0.61
00:51:17.68	−74:51:42.3	4.38										
00:51:25.21	−71:21:13.8	3.37							1.92			−0.54
00:51:25.73	−75:38:36.5		11.20									
00:51:26.05	−70:40:19.1		4.10									
00:51:26.57	−71:21:36.9					3.73						
00:51:26.63	−72:24:39.2	3.89	3.30									

Continued on next page

RA (J2000)	DEC	S_{36cm} (mJy)	S_{20cm} (mJy)	S_{13cm} (mJy)	S_{6cm} (mJy)	S_{3cm} (mJy)	Blend Flag	$S_{20cm,matched}$ (mJy)	$S_{13cm,matched}$ (mJy)	$S_{6cm,matched}$ (mJy)	$S_{3cm,matched}$ (mJy)	α
00:51:26.80	−74:46:06.4	2.90										
00:51:28.27	−74:28:22.0		6.11	1.96								
00:51:30.24	−71:36:18.7	5.65										
00:51:30.92	−73:44:18.9	7.21										
00:51:34.56	−72:32:36.2					6.50						
00:51:35.05	−73:44:20.5		3.76									
00:51:35.66	−69:46:32.4		7.34									
00:51:39.67	−72:38:13.7	6.19										
00:51:40.53	−73:13:34.4	13.96	9.22	19.50	10.00	11.10				9.91		−0.20
00:51:41.43	−72:55:55.8	71.88	33.41	42.60	21.29	7.26			34.93	18.90		−0.76
00:51:47.58	−73:04:52.7	20.24	11.03	6.20	2.10							
00:51:48.04	−72:50:46.7	9.63	7.21	10.30								
00:51:51.24	−72:55:37.8					4.87						
00:51:53.18	−73:45:22.6	5.90	3.66									
00:51:53.36	−72:16:50.9			3.40								
00:51:53.85	−74:35:32.4		3.94									
00:51:55.47	−73:26:50.9			44.50								
00:51:56.43	−72:16:51.2					5.67						
00:52:01.09	−71:19:26.7	4.30										
00:52:01.29	−73:32:35.0	10.51	5.75	7.10								
00:52:01.55	−72:17:08.0				3.90							
00:52:01.99	−74:57:04.5	3.51										
00:52:04.25	−72:16:07.7				4.12							

Continued on next page

RA (J2000)	DEC	S_{36cm} (mJy)	S_{20cm} (mJy)	S_{13cm} (mJy)	S_{6cm} (mJy)	S_{3cm} (mJy)	Blend Flag	$S_{20cm,matched}$ (mJy)	$S_{13cm,matched}$ (mJy)	$S_{6cm,matched}$ (mJy)	$S_{3cm,matched}$ (mJy)	α
00:52:06.20	−71:44:14.5	4.54							1.86			−0.86
00:52:06.60	−72:16:15.7			11.40								
00:52:06.68	−73:37:22.1	13.85	6.08	8.50	3.61				7.27			−0.62
00:52:12.58	−73:08:50.2	10.37	7.46	8.30	1.97							
00:52:13.36	−73:14:41.8		4.15									
00:52:17.57	−73:01:56.5	39.57	24.56	16.30	6.76	1.87						
00:52:18.54	−73:11:06.4	3.57										
00:52:18.83	−72:27:07.8	310.30	179.60	117.60	60.57	31.80		190.30	123.20	59.00	31.17	−0.97
00:52:22.56	−75:25:43.8		85.58		20.41							
00:52:24.70	−71:32:09.0	3.55										
00:52:26.03	−72:36:30.2				4.03							
00:52:26.20	−71:29:24.1					6.97						
00:52:26.69	−71:13:44.5	3.86										
00:52:27.46	−72:36:19.5			60.70								
00:52:28.87	−73:59:43.6	3.42	5.50		4.74							
00:52:30.23	−74:37:48.2	9.95	6.65	2.20	2.21				2.89			−1.19
00:52:31.92	−69:30:01.1		7.01									
00:52:34.58	−70:28:16.8		32.31									
00:52:35.72	−73:26:10.9			10.60					7.33			
00:52:38.19	−73:26:13.4	4.47										
00:52:38.26	−73:12:44.7	143.94	98.30	74.50	33.25	15.80		108.50	71.91	34.74	16.59	−0.93
00:52:39.50	−72:38:18.0			109.60	3.72					9.36		
00:52:39.77	−73:53:43.0	5.92										

Continued on next page

RA (J2000)	DEC	S_{36cm} (mJy)	S_{20cm} (mJy)	S_{13cm} (mJy)	S_{6cm} (mJy)	S_{3cm} (mJy)	Blend Flag	$S_{20cm,matched}$ (mJy)	$S_{13cm,matched}$ (mJy)	$S_{6cm,matched}$ (mJy)	$S_{3cm,matched}$ (mJy)	α
00:52:40.12	−71:19:09.5	7.34		1.40					4.45			−0.48
00:52:41.40	−70:26:35.3		5.58									
00:52:49.82	−74:11:33.7	6.74		2.00								
00:52:53.55	−71:15:24.3	3.75										
00:52:54.17	−72:01:32.8	13.44	13.27	14.10	7.10	7.73			11.12	8.76		−0.24
00:52:54.71	−71:45:40.1	2.74										
00:52:55.10	−71:45:50.8		4.24									
00:52:56.34	−71:14:20.3	3.14	3.83									
00:52:57.13	−73:29:56.8	4.66										
00:52:58.62	−72:35:34.7		12.27									
00:52:59.04	−73:11:47.2	15.80	8.96	11.70	3.63							
00:52:59.68	−72:35:20.9			39.10								
00:53:00.34	−72:12:38.5			38.20								
00:53:00.90	−71:01:15.1	3.75										
00:53:05.11	−69:22:43.8		23.90									
00:53:06.80	−70:29:20.3		10.47									
00:53:07.97	−74:39:04.9	2.40	13.77	20.70	2.96	2.44			25.29			2.27
00:53:09.67	−70:16:33.9		4.18									
00:53:09.80	−74:13:48.5	2.40										
00:53:14.20	−72:18:37.8					5.08						
00:53:15.61	−74:42:37.4	5.54										
00:53:17.42	−71:06:56.3		3.86									
00:53:18.29	−72:08:57.0	19.10	14.71	10.90	4.63				9.23			−0.70

Continued on next page

RA (J2000)	DEC	S_{36cm} (mJy)	S_{20cm} (mJy)	S_{13cm} (mJy)	S_{6cm} (mJy)	S_{3cm} (mJy)	Blend Flag	$S_{20cm,matched}$ (mJy)	$S_{13cm,matched}$ (mJy)	$S_{6cm,matched}$ (mJy)	$S_{3cm,matched}$ (mJy)	α
00:53:20.18	−72:35:11.1					11.00						
00:53:20.30	−72:35:32.7							23.84		10.57	6.82	−0.67
00:53:22.53	−72:35:28.3		10.46	36.10	7.72							
00:53:23.43	−71:21:24.5	3.56							3.21			−0.10
00:53:25.10	−74:55:56.7	10.53	5.10	4.40	2.67							
00:53:26.85	−72:30:21.4			10.20								
00:53:28.66	−72:30:09.4	12.80	7.33									
00:53:28.80	−72:55:22.8	18.32	10.64	13.80	5.39				12.41			−0.38
00:53:33.94	−69:57:09.9		4.60									
00:53:35.83	−69:17:18.4		14.82									
00:53:37.76	−72:31:44.1	140.30	72.14	42.40	14.98	5.92			38.36	15.67		−1.26
00:53:38.87	−73:12:21.5	5.52		26.50								
00:53:41.32	−72:39:31.2			39.90	3.53	5.49						
00:53:47.23	−75:14:41.1	18.50	8.10	1.00	5.31	5.66						
00:53:47.86	−71:49:59.7	16.78	8.90	6.10	4.40							
00:53:48.17	−70:46:01.4		5.71									
00:53:49.35	−71:58:56.3			1.30	3.20				2.46			
00:53:50.76	−69:31:47.8		16.86									
00:53:50.87	−69:31:29.0		15.15									
00:53:51.08	−71:58:48.8	4.83										
00:53:51.84	−70:40:00.3	42.58	23.16	7.80	14.24	14.70		28.09	16.42	10.99		−0.79
00:53:56.25	−70:38:04.7	48.70	43.44	4.00	18.14	3.45			14.38	16.32		−0.67
00:53:57.97	−72:44:00.7	6.36										

Continued on next page

RA (J2000)	DEC	S_{36cm} (mJy)	S_{20cm} (mJy)	S_{13cm} (mJy)	S_{6cm} (mJy)	S_{3cm} (mJy)	Blend Flag	$S_{20cm,matched}$ (mJy)	$S_{13cm,matched}$ (mJy)	$S_{6cm,matched}$ (mJy)	$S_{3cm,matched}$ (mJy)	α
00:54:02.80	−71:09:39.8		3.89									
00:54:03.49	−72:13:48.9	14.82	7.63	9.40	5.21	4.77						
00:54:05.85	−75:34:03.5		58.92									
00:54:08.19	−72:24:21.2	12.36	8.11	6.10	3.83				6.75			−0.58
00:54:09.92	−73:17:09.6			5.30								
00:54:11.67	−73:40:18.4	15.03	10.43	7.70	5.19							
00:54:12.01	−75:08:53.6	8.43										
00:54:16.83	−73:53:06.1	4.07							2.72			−0.39
00:54:22.73	−70:23:53.7		67.41									
00:54:23.50	−70:18:01.1		3.73									
00:54:23.64	−72:52:57.1	58.73	36.39	28.70	14.07	7.29		38.19	27.21			−0.74
00:54:26.22	−74:17:22.5	11.14	7.18	2.50	2.43				4.84			−0.80
00:54:28.89	−69:44:37.3		4.32									
00:54:29.11	−72:01:58.3	10.24	8.27	2.60	3.66							
00:54:29.52	−69:42:24.7		4.11									
00:54:30.78	−71:45:16.2					5.47						
00:54:31.80	−69:42:17.9		6.62									
00:54:33.94	−70:01:12.5		27.54									
00:54:34.53	−73:38:47.5	11.05	10.32	4.10	4.81				7.02			−0.44
00:54:39.63	−72:45:06.6	17.12	11.50	11.10	2.30							
00:54:41.80	−72:29:52.3	11.46	7.16	9.50	2.01							
00:54:42.64	−70:26:41.7		9.33									
00:54:48.74	−72:53:53.4	25.45	14.77	14.60	9.06	5.75				8.69		−0.62

Continued on next page

RA (J2000)	DEC	S_{36cm} (mJy)	S_{20cm} (mJy)	S_{13cm} (mJy)	S_{6cm} (mJy)	S_{3cm} (mJy)	Blend Flag	$S_{20cm,matched}$ (mJy)	$S_{13cm,matched}$ (mJy)	$S_{6cm,matched}$ (mJy)	$S_{3cm,matched}$ (mJy)	α
00:54:49.26	−74:49:36.1	12.58	11.41	8.10	6.88	5.55			9.53			−0.27
00:54:49.52	−70:46:57.4	3.49										
00:54:49.64	−73:16:48.4	19.90	12.21	11.40	8.70	4.43			9.58			−0.70
00:54:50.55	−73:58:59.9	12.28	4.67	1.40								
00:54:53.11	−71:31:36.7	28.93	18.50	11.40	6.38				11.60			−0.88
00:54:56.63	−71:03:40.2	10.48	7.64	1.70	2.68							
00:55:03.90	−71:21:06.0	39.83	20.50	16.70	8.90				16.92			−0.83
00:55:06.40	−72:37:18.7	24.10	9.42	16.20	6.43				8.60	6.68		−0.76
00:55:10.20	−72:37:34.3					5.30						
00:55:10.78	−70:26:23.8		3.71									
00:55:16.77	−75:32:04.4		19.78									
00:55:18.87	−71:44:50.7	25.92	17.19	12.00	4.57							
00:55:21.87	−73:18:26.1	5.25										
00:55:22.72	−72:10:53.0	242.00	76.68	125.40		28.90						
00:55:24.34	−69:51:13.2		3.88									
00:55:24.93	−69:38:08.0		9.00									
00:55:27.08	−71:02:27.6			1.30								
00:55:27.52	−72:10:57.3		13.40					195.20	126.70	74.40	40.07	−0.84
00:55:29.01	−71:02:54.3					4.44						
00:55:29.04	−71:02:39.2		5.00									
00:55:29.94	−72:10:57.6											
00:55:30.60	−70:26:27.3	45.87	25.68									
00:55:31.76	−69:58:59.7		6.58									

Continued on next page

RA (J2000)	DEC	S_{36cm} (mJy)	S_{20cm} (mJy)	S_{13cm} (mJy)	S_{6cm} (mJy)	S_{3cm} (mJy)	Blend Flag	$S_{20cm,matched}$ (mJy)	$S_{13cm,matched}$ (mJy)	$S_{6cm,matched}$ (mJy)	$S_{3cm,matched}$ (mJy)	α
00:55:32.91	−72:31:24.0	29.75	17.58	79.80	6.24				10.89			−0.97
00:55:33.64	−70:39:54.2	4.10			8.19	8.85						
00:55:33.98	−72:10:54.5		21.50									
00:55:36.15	−72:35:14.1	90.00		38.20	12.92	10.54		49.53	35.19	15.29		−0.98
00:55:36.25	−72:35:34.4		19.94									
00:55:37.31	−72:34:53.9		10.80									
00:55:37.32	−74:39:25.9	197.60	86.97	39.20	14.48	5.36			43.74	13.92		−1.52
00:55:39.62	−69:40:24.1		41.84									
00:55:39.65	−72:10:47.8	78.56	27.30	55.00		8.62						
00:55:40.21	−73:13:13.5					4.49						
00:55:44.65	−72:16:08.5			8.90					2.95			
00:55:48.51	−70:13:56.4		5.55									
00:55:53.42	−71:03:22.2	16.74	8.03	9.60	4.55							
00:55:53.79	−74:12:32.9	5.75										
00:55:54.26	−73:03:42.3	4.74										
00:55:54.44	−74:22:35.9	7.44	9.59	7.40	14.34	15.70			8.24			0.10
00:55:57.02	−72:26:04.8	111.95	96.90	79.80	52.37	33.50		100.70	82.17	52.76	35.88	−0.50
00:55:57.14	−72:19:54.8	4.75										
00:56:00.72	−72:09:08.8	10.65	6.53	6.50	3.99				3.63			−1.04
00:56:04.63	−72:19:31.2			26.60								
00:56:04.94	−72:34:50.8	3.24										
00:56:06.98	−75:03:07.2					6.62						
00:56:08.09	−70:38:46.6	150.39	89.69	15.40	25.61	7.61		97.47	31.18			−1.53

Continued on next page

RA (J2000)	DEC	S_{36cm} (mJy)	S_{20cm} (mJy)	S_{13cm} (mJy)	S_{6cm} (mJy)	S_{3cm} (mJy)	Blend Flag	$S_{20cm,matched}$ (mJy)	$S_{13cm,matched}$ (mJy)	$S_{6cm,matched}$ (mJy)	$S_{3cm,matched}$ (mJy)	α
00:56:11.38	−71:07:07.7	875.03	608.60	393.40	211.70	114.00		625.40	435.60	213.30	109.00	−0.89
00:56:16.13	−72:17:32.1	7.13		99.40								
00:56:17.70	−71:25:36.9					3.56						
00:56:20.56	−72:04:17.1			2.78					5.74			
00:56:20.97	−71:25:22.6	4.59										
00:56:22.34	−71:51:11.3	31.88	19.85	10.30	5.48				11.37			−0.99
00:56:25.13	−71:04:53.4		3.59									
00:56:27.74	−70:00:34.9		4.06									
00:56:33.16	−73:57:07.9	22.47	11.63	10.80	8.17	6.41			10.95		5.00	−0.64
00:56:36.83	−74:03:15.8	22.02	27.09	29.60	26.63	18.70			31.12	26.33	20.48	−0.03
00:56:42.84	−70:41:41.8			1.30								
00:56:44.81	−72:52:01.5	112.90	45.42	28.70	23.36	17.40		67.99	46.20	23.76	9.94	−1.00
00:56:45.07	−72:25:05.8	4.89										
00:56:52.62	−71:23:00.6	120.56	79.17	44.70	20.94	20.90		81.33	49.99	21.30	12.49	−0.99
00:56:52.76	−73:16:09.2		3.17									
00:56:55.06	−74:55:47.2	3.24										
00:56:58.24	−74:11:59.9		3.76									
00:56:58.46	−75:29:15.1		26.90									
00:56:59.25	−70:29:24.1		4.15									
00:57:02.05	−70:36:53.6	8.91	7.27									
00:57:02.77	−73:36:54.4		4.45									
00:57:03.34	−72:16:35.9	28.54	17.62	15.70	6.01				11.97			−0.84
00:57:03.73	−70:27:37.9	5.11										

Continued on next page

RA (J2000)	DEC	S_{36cm} (mJy)	S_{20cm} (mJy)	S_{13cm} (mJy)	S_{6cm} (mJy)	S_{3cm} (mJy)	Blend Flag	$S_{20cm,matched}$ (mJy)	$S_{13cm,matched}$ (mJy)	$S_{6cm,matched}$ (mJy)	$S_{3cm,matched}$ (mJy)	α
00:57:04.22	−72:37:57.4	4.76										
00:57:04.97	−73:00:43.1	6.26										
00:57:05.48	−70:40:19.0		3.86			9.32						
00:57:06.94	−74:12:03.3				3.06					3.65		
00:57:12.75	−71:02:09.1	2.97							1.83			−0.47
00:57:14.88	−73:34:50.4	18.38	12.74	9.00	4.97	3.65						
00:57:15.69	−70:40:46.4	81.05	85.26	63.70	74.28	89.60		91.97	130.80	73.87	81.00	−0.05
00:57:15.81	−70:33:28.9	16.52	7.37									
00:57:19.16	−70:38:18.3					4.75						
00:57:20.70	−74:12:26.9		4.86									
00:57:22.44	−74:03:15.6	28.49	14.73	12.60	8.82	4.88			12.78			−0.77
00:57:27.57	−75:14:56.5	6.73	6.91		5.47	3.67						
00:57:28.43	−75:12:58.2	5.28	5.31			5.59			4.29			−0.20
00:57:29.77	−72:32:23.2	4.03	4.55	8.10	4.13					4.55		0.07
00:57:31.05	−74:42:13.6	36.99	20.53	15.10	8.89	5.85			17.16	8.33		−0.85
00:57:32.38	−74:57:48.3	3.32										
00:57:32.47	−74:12:43.3	837.20	429.50	220.90	82.71	34.50		530.30	240.50	82.80	31.31	−1.43
00:57:33.76	−70:35:56.0	4.61										
00:57:36.87	−73:12:58.5	3.34	4.77	1.40	2.23	4.82						
00:57:37.64	−71:59:33.2	16.55	5.75	6.80					4.61			−1.23
00:57:38.39	−71:08:47.7	44.23	27.74	17.30	11.84	10.30			18.44	11.45		−0.78
00:57:40.58	−75:21:53.8		9.45									
00:57:40.88	−73:46:14.7	5.13										

Continued on next page

RA (J2000)	DEC	S_{36cm} (mJy)	S_{20cm} (mJy)	S_{13cm} (mJy)	S_{6cm} (mJy)	S_{3cm} (mJy)	Blend Flag	$S_{20cm,matched}$ (mJy)	$S_{13cm,matched}$ (mJy)	$S_{6cm,matched}$ (mJy)	$S_{3cm,matched}$ (mJy)	α
00:57:41.60	−72:41:55.0	22.99	13.29	18.60	11.04	8.77					8.31	−0.44
00:57:43.13	−71:59:12.9		4.67									
00:57:46.64	−71:17:21.4	8.40	5.51	1.30								
00:57:46.67	−71:20:05.3		5.39									
00:57:48.30	−73:25:51.9	2.62		0.80								
00:57:49.93	−72:30:17.0	4.46										
00:57:50.38	−73:06:01.1	3.06	4.50	5.10								
00:57:50.72	−70:45:54.0	5.58	4.75									
00:57:53.45	−71:18:32.3	13.20	5.56							3.34		−0.79
00:57:54.37	−72:39:11.1					5.09						
00:57:55.35	−70:34:59.7	4.13										
00:57:55.57	−71:56:58.8			9.70					9.11			
00:57:56.59	−72:39:23.1	7.51		26.50	5.72					6.09		−0.12
00:57:56.94	−71:57:19.2		2.87									
00:57:57.60	−74:02:18.7	7.95	6.51	1.30	2.80							
00:57:57.68	−71:56:44.3	10.04	5.26									
00:58:00.00	−72:11:01.4			53.00								
00:58:08.62	−74:56:33.8				3.85							
00:58:10.83	−72:31:09.5	4.16										
00:58:12.09	−71:24:08.5		9.95			4.23						
00:58:12.34	−73:59:49.7	19.88	12.12	8.50	3.36							
00:58:13.15	−70:09:59.6		43.35									
00:58:13.80	−71:35:19.9	4.67	6.96	2.39								

Continued on next page

RA (J2000)	DEC	S_{36cm} (mJy)	S_{20cm} (mJy)	S_{13cm} (mJy)	S_{6cm} (mJy)	S_{3cm} (mJy)	Blend Flag	$S_{20cm,matched}$ (mJy)	$S_{13cm,matched}$ (mJy)	$S_{6cm,matched}$ (mJy)	$S_{3cm,matched}$ (mJy)	α
00:58:15.08	−72:30:03.3	6.29										
00:58:15.35	−73:16:12.0	4.66										
00:58:15.59	−71:23:52.1	38.25		24.10					27.14	12.46		−0.62
00:58:16.82	−72:38:52.6	13.88	6.08	20.10	10.58							
00:58:16.95	−72:18:07.7			59.10	9.13			43.54	40.17	22.24		−0.54
00:58:17.09	−72:37:05.3	3.77										
00:58:17.83	−71:23:34.4		9.86									
00:58:20.46	−71:30:40.6	38.46	32.30	24.60	12.65	3.87			24.79	13.46		−0.59
00:58:20.79	−70:32:00.4	7.56										
00:58:21.56	−73:29:34.8	7.62	5.45	8.10	2.03							
00:58:22.92	−72:00:42.3	21.77	7.91	9.90	3.56							
00:58:27.08	−72:39:54.6	10.30	7.11	21.40	10.22	11.80					8.67	−0.07
00:58:29.62	−72:34:12.9	6.24										
00:58:31.37	−74:01:49.3	18.77	8.99	8.50	5.97	3.20						
00:58:31.95	−71:11:37.9		3.79									
00:58:32.37	−72:14:00.6			18.10								
00:58:32.84	−72:51:12.0	11.34	4.45	28.10	2.26							
00:58:34.73	−75:08:24.0	5.41										
00:58:37.25	−69:44:50.5		3.70									
00:58:37.39	−74:37:46.2				3.70							
00:58:41.27	−70:19:11.3	9.22	6.03									
00:58:42.89	−72:27:16.6				4.80	5.04				5.15		
00:58:44.24	−75:04:21.5	3.52										

Continued on next page

RA (J2000)	DEC	S_{36cm} (mJy)	S_{20cm} (mJy)	S_{13cm} (mJy)	S_{6cm} (mJy)	S_{3cm} (mJy)	Blend Flag	$S_{20cm,matched}$ (mJy)	$S_{13cm,matched}$ (mJy)	$S_{6cm,matched}$ (mJy)	$S_{3cm,matched}$ (mJy)	α
00:58:45.78	−73:05:07.3	5.41		3.40	3.82							
00:58:47.16	−74:04:03.6		3.64									
00:58:47.77	−74:46:54.4	18.74	5.19	6.50	3.86				6.64			−1.00
00:58:48.78	−74:35:14.1	33.29	19.18	12.10	6.44				13.29			−0.89
00:58:51.89	−72:03:25.4	4.17										
00:58:55.15	−72:10:10.0			254.40								
00:58:58.93	−70:19:10.7	5.55										
00:59:01.15	−72:29:49.9	5.85							4.45			−0.26
00:59:04.00	−72:14:46.3			10.40								
00:59:04.44	−70:49:01.3	155.70	64.34	44.90	18.85	11.70		84.20	48.50	16.39		−1.27
00:59:05.13	−75:06:42.7	12.60	6.27									
00:59:06.03	−74:58:49.3	24.63	14.54	8.90	5.57							
00:59:06.60	−73:52:04.2	31.76	29.42	21.20	23.74	25.10			25.00	24.40	21.18	−0.16
00:59:06.72	−74:54:54.4	13.60	9.39	6.30	5.30							
00:59:08.39	−72:10:56.8			204.30								
00:59:09.68	−74:02:39.9	5.24	5.48									
00:59:11.48	−72:24:19.0	3.96							6.16	2.32		−0.25
00:59:12.00	−72:32:41.3	6.71										
00:59:12.84	−74:14:00.6	6.22	3.49									
00:59:13.91	−72:24:25.7			13.00	3.30							
00:59:16.09	−72:10:20.2			210.70								
00:59:16.32	−72:11:20.5			98.60								
00:59:17.73	−72:17:21.6			9.40								

Continued on next page

RA (J2000)	DEC	S_{36cm} (mJy)	S_{20cm} (mJy)	S_{13cm} (mJy)	S_{6cm} (mJy)	S_{3cm} (mJy)	Blend Flag	$S_{20cm,matched}$ (mJy)	$S_{13cm,matched}$ (mJy)	$S_{6cm,matched}$ (mJy)	$S_{3cm,matched}$ (mJy)	α
00:59:18.41	−73:32:00.4	3.79										
00:59:18.82	−75:05:59.7	4.57	3.72									
00:59:26.80	−70:29:47.6	3.58										
00:59:27.21	−73:08:28.3	2.37										
00:59:27.59	−75:12:06.6	8.14	3.42		2.67							
00:59:33.42	−72:10:48.2			307.30								
00:59:34.23	−72:09:42.4			89.80								
00:59:35.77	−71:46:25.9		3.79									
00:59:47.11	−75:02:16.2	3.80										
00:59:48.35	−74:26:28.0		3.51									
00:59:48.50	−71:56:55.5					4.49						
00:59:48.57	−73:21:54.3	4.14										
00:59:48.58	−70:50:28.4	18.87	17.43	14.80	23.35	19.40				22.30	18.30	0.01
00:59:50.38	−74:26:37.6	3.85										
00:59:50.94	−70:52:01.0	17.00	13.17	9.70	6.62					5.57		−0.64
00:59:53.54	−72:08:40.2			183.60								
01:00:01.43	−73:05:55.1					5.72						
01:00:05.79	−69:37:01.1		6.19									
01:00:06.48	−73:26:39.0	7.24	4.43		2.41				3.21			−0.78
01:00:06.85	−69:30:30.8		6.91									
01:00:08.04	−70:52:28.6	4.77										
01:00:10.24	−73:13:16.4	2.79							1.75			−0.45
01:00:11.23	−69:37:17.9		6.30									

Continued on next page

RA (J2000)	DEC	S_{36cm} (mJy)	S_{20cm} (mJy)	S_{13cm} (mJy)	S_{6cm} (mJy)	S_{3cm} (mJy)	Blend Flag	$S_{20cm,matched}$ (mJy)	$S_{13cm,matched}$ (mJy)	$S_{6cm,matched}$ (mJy)	$S_{3cm,matched}$ (mJy)	α
01:00:12.57	−70:40:28.1	16.61	10.82	1.80	5.31			12.16	7.49			−0.77
01:00:14.12	−74:25:27.1	8.25		1.50					3.79			−0.75
01:00:20.19	−71:44:33.5	8.66	3.68	1.50								
01:00:23.26	−71:33:22.6			124.80					179.50	110.10		−0.69
01:00:27.27	−70:51:56.5	2.58										
01:00:29.77	−71:38:26.2	194.30	127.70	82.40	43.50	24.20		132.00	86.98	43.41	23.19	−0.91
01:00:30.56	−73:00:07.3	19.22	12.87	7.40	5.05							
01:00:41.06	−74:05:06.8		13.80									
01:00:41.09	−74:46:29.5			4.40	4.63				4.02			
01:00:42.25	−73:06:16.6	4.25										
01:00:42.93	−74:46:16.9	3.40										
01:00:43.08	−71:21:37.3	13.69	8.99	6.00	3.78				6.63			−0.70
01:00:43.86	−69:53:16.4		18.69									
01:00:46.59	−73:16:13.4	5.36										
01:00:46.72	−74:54:17.9	66.37	21.70	22.90	12.33	3.27			21.47	11.45	5.72	−1.04
01:00:50.80	−75:13:54.0	11.53	4.91		2.49							
01:00:53.00	−70:50:20.3	9.32	8.34	2.70	3.90				5.61			−0.49
01:00:53.80	−73:40:42.0	10.78	7.19	6.40	3.39				9.15			−0.16
01:00:54.71	−73:42:15.7	5.89	4.84	1.30	3.86				2.99			−0.65
01:00:58.19	−71:35:29.3	9.88	6.83	12.80						7.49	7.13	−0.14
01:00:58.61	−73:42:01.9					4.19						
01:00:59.04	−73:45:15.1	3.95			2.50							
01:01:01.00	−74:44:54.4	4.17										

Continued on next page

RA (J2000)	DEC	S_{36cm} (mJy)	S_{20cm} (mJy)	S_{13cm} (mJy)	S_{6cm} (mJy)	S_{3cm} (mJy)	Blend Flag	$S_{20cm,matched}$ (mJy)	$S_{13cm,matched}$ (mJy)	$S_{6cm,matched}$ (mJy)	$S_{3cm,matched}$ (mJy)	α
01:01:02.46	−74:59:29.5	3.37										
01:01:05.65	−70:22:53.9	10.35										
01:01:07.29	−73:28:42.8	3.72										
01:01:07.60	−71:36:43.5	3.12										
01:01:09.83	−72:50:47.2	6.83	3.87									
01:01:09.99	−72:35:49.3	4.01										
01:01:12.03	−70:24:18.2		4.19									
01:01:12.48	−74:41:00.3	25.43	13.06	10.30	5.93	5.28			12.40			−0.69
01:01:16.19	−75:20:21.9		4.68		3.90							
01:01:17.68	−73:31:32.0	5.13							4.00			−0.24
01:01:18.20	−74:13:25.3	2.40										
01:01:25.24	−71:50:54.0			4.20								
01:01:32.12	−69:39:15.5		123.50									
01:01:32.70	−70:57:17.0	3.44										
01:01:33.52	−71:51:32.5					5.38						
01:01:40.71	−72:55:14.2	7.64	4.95	3.40	3.14							
01:01:42.15	−70:32:04.4	6.32	6.70									
01:01:43.31	−72:32:26.8	32.42	13.20	15.00	4.81				11.97			−0.96
01:01:43.40	−74:23:34.7	11.33	3.74	1.60					3.41			−1.16
01:01:47.35	−72:52:39.8	4.37										
01:01:47.41	−72:32:26.8		7.60									
01:01:52.29	−69:56:39.8		4.19									
01:01:52.65	−72:06:01.4		4.18									

Continued on next page

RA (J2000)	DEC	S_{36cm} (mJy)	S_{20cm} (mJy)	S_{13cm} (mJy)	S_{6cm} (mJy)	S_{3cm} (mJy)	Blend Flag	$S_{20cm,matched}$ (mJy)	$S_{13cm,matched}$ (mJy)	$S_{6cm,matched}$ (mJy)	$S_{3cm,matched}$ (mJy)	α
01:01:54.07	−74:45:22.4	5.08							2.31			−0.76
01:01:57.31	−72:06:57.5		4.06									
01:01:57.60	−73:42:48.6	15.39	7.85	5.80	3.35				5.83			−0.94
01:02:01.44	−75:02:36.1			4.10								
01:02:03.29	−70:15:55.2	3.43										
01:02:03.99	−72:24:47.1	13.77	9.30	11.10	3.65	5.43			58.43			1.39
01:02:04.41	−71:03:23.3	7.48	5.10	3.40					7.04			−0.06
01:02:07.28	−74:43:50.9	6.52										
01:02:13.28	−71:20:15.1	4.76							3.40			−0.33
01:02:13.52	−72:04:44.1		4.68									
01:02:14.67	−70:23:31.4	5.24										
01:02:16.46	−72:37:07.7	7.71	4.60									
01:02:16.92	−71:51:40.7			7.40					4.57			
01:02:20.86	−73:53:22.3	29.43	12.28	9.90	6.60	4.97			12.13			−0.85
01:02:21.06	−74:38:06.2	3.53							3.49			−0.01
01:02:21.41	−70:37:17.3	22.96	3.54		2.29							
01:02:21.96	−71:27:21.2	13.14	14.32	12.20	4.94				11.50			−0.13
01:02:23.56	−70:57:10.2	5.13										
01:02:26.64	−74:27:02.0	9.61	5.13	1.30					2.82			−1.18
01:02:27.36	−71:56:35.1	3.05										
01:02:29.35	−73:47:32.8		5.50	1.70	2.00							
01:02:29.56	−75:00:21.8	13.19	8.21	4.20	3.16				4.27			−1.09
01:02:30.61	−73:23:16.8	7.86							2.46			−1.12

Continued on next page

RA (J2000)	DEC	S_{36cm} (mJy)	S_{20cm} (mJy)	S_{13cm} (mJy)	S_{6cm} (mJy)	S_{3cm} (mJy)	Blend Flag	$S_{20cm,matched}$ (mJy)	$S_{13cm,matched}$ (mJy)	$S_{6cm,matched}$ (mJy)	$S_{3cm,matched}$ (mJy)	α
01:02:32.27	−73:47:59.2	11.19							14.04			0.22
01:02:33.40	−74:45:18.3	4.87							3.87			−0.22
01:02:33.97	−69:58:27.9		15.36									
01:02:34.16	−75:21:16.3					3.92						
01:02:34.31	−74:15:34.7	38.75	18.37	15.90	10.26	6.01			18.42	8.23		−0.88
01:02:34.57	−73:48:17.9		5.69									
01:02:37.09	−70:20:19.9	3.36										
01:02:37.67	−72:50:37.3	5.41	4.74		3.48							
01:02:40.23	−71:02:20.7	8.89	5.99	2.60	3.69				2.59			−1.19
01:02:41.40	−69:58:31.5		4.06									
01:02:43.57	−71:59:42.4					5.08						
01:02:44.39	−73:50:10.9	4.50										
01:02:48.51	−75:22:12.6		4.91									
01:02:49.02	−71:53:18.3		9.66	23.30				12.18		15.87	10.33	−0.04
01:02:51.48	−75:35:24.0		64.01									
01:02:53.07	−72:41:12.9	3.22										
01:02:53.95	−72:24:44.6	3.93										
01:02:54.55	−74:37:39.5	6.77										
01:02:54.64	−71:00:44.9			1.60								
01:02:55.45	−71:36:31.6	28.56	19.68	17.70	9.57	5.90			18.58			−0.41
01:02:56.30	−74:34:36.6					4.75						
01:02:56.51	−70:38:53.0				2.34							
01:02:56.87	−74:35:31.2	35.06	18.94	15.20	10.78				17.27	9.37		−0.75

Continued on next page

RA (J2000)	DEC	S_{36cm} (mJy)	S_{20cm} (mJy)	S_{13cm} (mJy)	S_{6cm} (mJy)	S_{3cm} (mJy)	Blend Flag	$S_{20cm,matched}$ (mJy)	$S_{13cm,matched}$ (mJy)	$S_{6cm,matched}$ (mJy)	$S_{3cm,matched}$ (mJy)	α
01:02:57.07	−70:39:52.9		7.99		7.42							
01:02:57.15	−70:39:03.1		8.29							15.65		
01:02:57.29	−70:38:36.4		6.48									
01:02:57.58	−70:39:36.6	30.63										
01:02:58.30	−74:33:44.9	19.06	11.27	4.40					7.65			−0.88
01:02:58.49	−72:25:20.2					6.87						
01:03:01.78	−74:33:52.2					3.99						
01:03:04.99	−70:55:45.4	5.87							3.85			−0.41
01:03:05.00	−71:53:34.3	4.21		14.80	4.04							
01:03:05.30	−75:01:58.4	3.21										
01:03:09.73	−73:10:40.5	4.63										
01:03:13.74	−72:09:58.9			85.90				89.40	77.31	34.43	20.84	−0.83
01:03:15.70	−72:09:48.6	57.17										
01:03:19.10	−70:46:48.4	7.97	9.49	2.90	7.07				9.44			0.16
01:03:19.82	−70:02:35.2		12.11									
01:03:21.31	−72:13:43.8	15.49	3.87	10.30								
01:03:22.84	−74:53:21.7	5.02										
01:03:26.20	−75:09:44.2			2.77								
01:03:26.36	−72:03:08.9			331.40								
01:03:26.92	−73:00:22.8	24.04	13.24	9.30	5.36				9.04	5.80		−0.83
01:03:29.73	−72:47:24.6	25.62	3.50	17.70	6.10				17.45	11.88		−0.44
01:03:30.58	−72:51:52.1			6.10								
01:03:30.89	−74:34:31.2	8.32	5.08	6.70	7.06							

Continued on next page

RA (J2000)	DEC	S_{36cm} (mJy)	S_{20cm} (mJy)	S_{13cm} (mJy)	S_{6cm} (mJy)	S_{3cm} (mJy)	Blend Flag	$S_{20cm,matched}$ (mJy)	$S_{13cm,matched}$ (mJy)	$S_{6cm,matched}$ (mJy)	$S_{3cm,matched}$ (mJy)	α
01:03:31.10	−71:29:19.0			1.30								
01:03:31.73	−70:06:37.0		55.77									
01:03:31.77	−75:07:03.6	135.80	53.33	35.90	21.50	11.20			36.97	19.77	12.80	−1.02
01:03:32.24	−75:27:45.7		8.27									
01:03:33.68	−74:57:31.2	4.52										
01:03:35.25	−75:02:00.5	3.18										
01:03:36.11	−70:39:54.3	9.24										
01:03:39.28	−72:50:41.8	16.39	13.48	10.10	6.72	5.60				7.76		−0.43
01:03:41.13	−70:35:32.1	5.50	3.27									
01:03:44.75	−69:40:52.1		16.40									
01:03:44.77	−69:58:29.8		20.76									
01:03:45.26	−73:20:49.8	6.41	2.97									
01:03:45.89	−69:49:24.1		33.23									
01:03:46.94	−71:24:13.1			2.60					4.22			
01:03:48.80	−71:24:03.7		4.04		3.52							
01:03:56.53	−75:18:45.5			2.60								
01:03:59.12	−71:12:55.0	21.50	9.61	7.60	4.14				10.18			−0.72
01:03:59.33	−75:08:44.9					4.96						
01:04:02.01	−72:01:49.9			222.10				308.70	242.00	151.50	86.99	−0.68
01:04:02.21	−75:08:33.0	5.71	5.42		3.78							
01:04:02.84	−75:08:15.6			3.28					3.87			
01:04:03.58	−75:27:54.3		4.11									
01:04:04.04	−72:02:00.5											

Continued on next page

RA (J2000)	DEC	S_{36cm} (mJy)	S_{20cm} (mJy)	S_{13cm} (mJy)	S_{6cm} (mJy)	S_{3cm} (mJy)	Blend Flag	$S_{20cm,matched}$ (mJy)	$S_{13cm,matched}$ (mJy)	$S_{6cm,matched}$ (mJy)	$S_{3cm,matched}$ (mJy)	α
01:04:05.37	−72:43:43.0	19.37	11.32	8.60	5.24				7.31			−0.94
01:04:06.45	−73:51:27.5	15.27	5.22	6.70	4.30					3.26		−0.89
01:04:07.17	−71:10:07.1		3.85									
01:04:10.49	−73:38:08.4	5.13	6.04	5.90	5.09				6.60			0.24
01:04:11.83	−70:56:02.1	18.49	8.62	5.90	4.25							
01:04:12.63	−75:23:57.4		8.81									
01:04:17.87	−73:07:16.5	3.85										
01:04:20.73	−72:42:41.0	3.19										
01:04:21.81	−70:21:49.4	4.18										
01:04:22.85	−74:49:31.1			2.81	4.88							
01:04:24.63	−71:12:54.6	10.80	6.35		2.16				6.25			−0.53
01:04:25.43	−71:13:05.1			2.00								
01:04:25.59	−74:27:32.5	21.27	15.07	10.50	6.38							
01:04:29.04	−71:24:46.6					5.59						
01:04:31.28	−72:07:25.2	53.04	34.99	37.40	12.11	8.84			22.15	12.94	12.21	−0.66
01:04:32.35	−72:05:08.9			29.60								
01:04:32.87	−72:04:53.6	7.49										
01:04:32.91	−72:07:46.2					4.76						
01:04:34.98	−74:04:10.2	7.23	3.54		1.79				2.30			−1.10
01:04:36.89	−69:58:22.8		34.81									
01:04:39.97	−74:50:28.0	4.10										
01:04:40.68	−75:12:41.0	6.04										
01:04:41.25	−71:31:22.7	19.48	29.69	26.20	18.38	10.70			28.64	17.72		−0.02

Continued on next page

RA (J2000)	DEC	S_{36cm} (mJy)	S_{20cm} (mJy)	S_{13cm} (mJy)	S_{6cm} (mJy)	S_{3cm} (mJy)	Blend Flag	$S_{20cm,matched}$ (mJy)	$S_{13cm,matched}$ (mJy)	$S_{6cm,matched}$ (mJy)	$S_{3cm,matched}$ (mJy)	α
01:04:42.29	−75:01:37.2			3.30					6.56			
01:04:43.01	−74:57:12.5			1.90	1.18							
01:04:44.22	−74:57:03.0	4.71	3.75									
01:04:46.74	−72:22:08.7				5.30					11.74		
01:04:50.83	−70:21:00.4	7.25										
01:04:55.54	−75:29:21.4		5.18									
01:04:57.63	−70:22:40.6	3.08										
01:04:58.05	−70:37:34.5	56.31	52.03	10.50	49.31	53.80		58.50	12.81	47.97	41.39	−0.11
01:05:01.26	−72:10:35.5			83.30								
01:05:03.03	−74:06:55.3	3.28										
01:05:04.09	−71:59:25.0		9.72					93.53		87.80	33.05	−0.48
01:05:05.62	−72:23:19.0			64.90								
01:05:05.77	−71:59:36.3			260.20								
01:05:06.95	−72:18:41.6		3.77						1.89			
01:05:07.00	−71:28:32.8				2.77							
01:05:07.82	−72:38:58.3	5.75	3.83		2.56							
01:05:09.32	−73:20:21.6					3.95						
01:05:09.59	−71:28:38.7	9.36	6.36	2.40					4.16			−0.78
01:05:11.38	−75:34:44.3		26.90									
01:05:13.25	−73:17:10.7	3.31										
01:05:14.82	−70:32:58.7	4.30	2.93									
01:05:16.27	−73:57:39.7	15.81	10.40	7.20	4.95							
01:05:19.41	−71:43:02.3					5.48						

Continued on next page

RA (J2000)	DEC	S_{36cm} (mJy)	S_{20cm} (mJy)	S_{13cm} (mJy)	S_{6cm} (mJy)	S_{3cm} (mJy)	Blend Flag	$S_{20cm,matched}$ (mJy)	$S_{13cm,matched}$ (mJy)	$S_{6cm,matched}$ (mJy)	$S_{3cm,matched}$ (mJy)	α
01:05:20.36	−69:55:11.5		11.82									
01:05:21.09	−70:51:54.5		5.24									
01:05:22.50	−70:52:04.3	16.88		8.00								
01:05:23.88	−75:34:21.4		31.27									
01:05:24.15	−73:15:17.0	43.33	17.90	14.80	7.94	6.31			15.59			−0.99
01:05:24.20	−72:09:23.4			40.40								
01:05:25.08	−72:25:23.1	47.60	25.31	24.10	11.87	6.52		31.29		12.43		−0.76
01:05:25.37	−73:23:18.9	7.27	3.12						1.65			−1.43
01:05:30.97	−72:10:20.9		2.26		3.33							
01:05:32.30	−74:33:30.1	12.09	6.69	1.40								
01:05:32.83	−70:44:44.4					8.24						
01:05:32.88	−72:13:31.1	10.37	11.90	20.70	9.47	9.47			9.96	9.59		−0.04
01:05:36.02	−74:32:01.0	9.38	8.49	10.70	16.55	18.00				15.38	16.13	0.24
01:05:36.31	−75:33:39.9		6.72									
01:05:36.66	−74:00:05.7	26.71	18.09	15.20	11.94	6.78			16.00			−0.49
01:05:38.34	−72:06:43.4			23.50								
01:05:41.26	−72:03:42.0	7.40		39.60	4.51					3.66		−0.40
01:05:43.02	−74:53:26.6	6.56	4.64									
01:05:43.97	−75:05:46.7	29.68	13.22	12.40	8.74	3.17			10.91			−0.96
01:05:48.84	−74:47:10.7	5.38										
01:05:49.27	−70:26:23.4	20.12	13.58									
01:05:51.02	−72:59:36.1	8.34		1.20								
01:05:51.83	−70:38:50.9		3.58									

Continued on next page

RA (J2000)	DEC	S_{36cm} (mJy)	S_{20cm} (mJy)	S_{13cm} (mJy)	S_{6cm} (mJy)	S_{3cm} (mJy)	Blend Flag	$S_{20cm,matched}$ (mJy)	$S_{13cm,matched}$ (mJy)	$S_{6cm,matched}$ (mJy)	$S_{3cm,matched}$ (mJy)	α
01:05:56.56	−71:46:06.9	78.27	36.15	31.90	19.23	12.20		48.10	33.58	17.20		−0.85
01:05:57.49	−71:04:57.0	47.09	30.13	18.80	12.26	8.57			22.76	11.29	8.86	−0.75
01:05:58.43	−70:21:32.8	3.21										
01:05:58.82	−73:25:13.6	18.58	9.57	5.30	4.93							
01:05:58.85	−74:59:04.0			6.80	10.35	5.20						
01:06:01.10	−71:09:28.1	2.80										
01:06:02.25	−72:43:45.3					6.25						
01:06:04.30	−69:31:26.5		13.21									
01:06:07.25	−69:32:07.6		5.87									
01:06:10.39	−73:49:56.8	25.91	4.50	7.90	5.02	4.65	b					
01:06:10.64	−74:41:16.7	15.53	5.13	6.20	3.47				7.33			−0.72
01:06:11.35	−75:04:42.9			1.50								
01:06:14.71	−74:41:28.1		4.88									
01:06:14.83	−73:50:00.1		8.30				b					
01:06:15.08	−72:52:14.7					6.21					10.21	
01:06:17.99	−71:02:30.6	7.22							3.23			−0.78
01:06:19.28	−70:51:13.2	15.38	7.02	2.50	3.62							
01:06:19.49	−72:05:27.8	8.48		18.20						2.64		−0.67
01:06:20.87	−70:41:44.5	33.97	18.43	7.80	6.51				8.02			−1.39
01:06:29.14	−74:51:35.2	8.49	4.30									
01:06:30.72	−70:31:26.0	6.73										
01:06:32.10	−71:48:24.2			2.30								
01:06:33.50	−71:48:07.9	4.80	3.77		1.34							

Continued on next page

RA (J2000)	DEC	S_{36cm} (mJy)	S_{20cm} (mJy)	S_{13cm} (mJy)	S_{6cm} (mJy)	S_{3cm} (mJy)	Blend Flag	$S_{20cm,matched}$ (mJy)	$S_{13cm,matched}$ (mJy)	$S_{6cm,matched}$ (mJy)	$S_{3cm,matched}$ (mJy)	α
01:06:38.21	−69:59:13.6		3.47									
01:06:42.60	−71:20:03.2		4.96	4.50	3.45							
01:06:43.63	−70:30:08.0	10.11	4.74									
01:06:45.48	−71:19:50.4	7.22							7.38			0.02
01:06:46.11	−72:42:27.2	4.91										
01:06:46.34	−74:19:31.2	8.95	5.93	9.40	5.15	5.63						
01:06:47.47	−72:58:14.0	17.74	7.03	7.10	4.27				7.62			−0.81
01:06:47.68	−72:34:53.8	4.04										
01:06:50.97	−75:20:14.4		4.60									
01:06:52.36	−71:19:28.5			2.60								
01:06:52.45	−71:09:56.9	3.95										
01:06:52.71	−72:18:37.0	12.04	7.61	2.50	1.17							
01:06:53.48	−69:39:28.4		15.32									
01:06:57.78	−73:13:20.6	7.22	5.75	3.80	1.21					2.37		−0.64
01:06:59.77	−73:54:54.7	13.19	7.98	4.70	2.72				6.90			−0.62
01:07:02.30	−73:02:02.2	2.70										
01:07:02.65	−70:34:17.8	16.19	9.41									
01:07:04.83	−69:20:13.8		15.44									
01:07:08.48	−71:43:05.9	46.10	24.34	14.50	7.46				16.49	6.28		−1.13
01:07:09.50	−73:07:24.4	1.96							7.58			1.30
01:07:17.36	−73:29:49.2	32.09	13.56	8.80	5.71				10.18			−1.11
01:07:20.23	−74:48:08.3	5.20										
01:07:20.68	−71:17:46.2	7.03		1.80								

Continued on next page

RA (J2000)	DEC	S_{36cm} (mJy)	S_{20cm} (mJy)	S_{13cm} (mJy)	S_{6cm} (mJy)	S_{3cm} (mJy)	Blend Flag	$S_{20cm,matched}$ (mJy)	$S_{13cm,matched}$ (mJy)	$S_{6cm,matched}$ (mJy)	$S_{3cm,matched}$ (mJy)	α
01:07:21.29	−71:37:31.7	5.78		1.30								
01:07:24.73	−74:41:48.3	3.63										
01:07:25.99	−72:16:36.4					5.74						
01:07:30.39	−71:29:14.0	5.58										
01:07:37.76	−71:34:51.4	4.02										
01:07:39.68	−74:22:11.0	3.49		2.13	1.80							
01:07:41.26	−71:53:11.7	5.59	5.48		4.61							
01:07:44.77	−75:15:29.8				5.00	5.94						
01:07:48.34	−70:52:15.5	15.73	9.93	8.30	5.12	5.77			9.20			−0.52
01:07:49.67	−71:45:05.7	6.22	3.90	2.40	3.47							
01:07:56.32	−71:25:34.0	18.80	10.27	9.80	5.34				13.47	6.76		−0.57
01:07:58.84	−70:35:26.9	7.23	3.09									
01:07:59.66	−71:08:22.4	6.34	3.75		8.61	9.96			6.69		7.24	0.06
01:08:01.20	−72:49:53.3	3.59										
01:08:02.83	−71:25:53.5		3.93									
01:08:04.56	−70:39:02.4	5.56			4.30							
01:08:06.04	−70:38:47.2					5.94						
01:08:07.95	−71:39:47.0	23.38	9.90	7.70	3.72	5.80			7.84			−1.05
01:08:09.58	−72:09:13.2	12.63	7.21	2.30	2.72				3.20			−1.32
01:08:11.22	−75:41:55.9		21.16									
01:08:11.65	−72:57:38.1	14.33	9.73	6.20	4.77							
01:08:14.46	−71:05:02.7	3.70										
01:08:15.05	−69:23:56.1		18.56									

Continued on next page

RA (J2000)	DEC	S_{36cm} (mJy)	S_{20cm} (mJy)	S_{13cm} (mJy)	S_{6cm} (mJy)	S_{3cm} (mJy)	Blend Flag	$S_{20cm,matched}$ (mJy)	$S_{13cm,matched}$ (mJy)	$S_{6cm,matched}$ (mJy)	$S_{3cm,matched}$ (mJy)	α
01:08:16.22	−69:36:54.0		2.70									
01:08:17.48	−74:55:20.4	9.99	5.91	6.70	6.70	5.10			6.69			−0.39
01:08:18.55	−69:23:55.5		8.57									
01:08:19.14	−71:14:31.0	3.83										
01:08:19.60	−71:59:56.6			97.00					125.20			
01:08:21.62	−71:49:24.6	7.35	4.72									
01:08:22.80	−74:22:39.8	3.10										
01:08:25.87	−70:05:56.3		5.22									
01:08:26.21	−74:22:17.2					3.55						
01:08:28.97	−75:34:06.6		3.84									
01:08:31.06	−71:47:24.5	3.16										
01:08:31.36	−72:35:31.7					5.87						
01:08:33.15	−70:42:36.0	3.01										
01:08:34.83	−75:16:34.2	5.12										
01:08:36.92	−70:47:01.9		4.62		1.28							
01:08:39.12	−72:47:15.4	38.73	20.23	10.70	5.44				12.10			−1.12
01:08:41.16	−71:27:47.8	4.11										
01:08:42.21	−72:16:01.7	4.76										
01:08:44.07	−70:46:55.5	21.56		9.00					10.85			−0.66
01:08:44.48	−71:24:58.8	5.47										
01:08:46.59	−70:46:53.4		5.23									
01:08:47.63	−75:26:28.2		13.51									
01:08:48.03	−74:19:30.3	11.88		6.80	3.61				8.11			−0.37

Continued on next page

RA (J2000)	DEC	S_{36cm} (mJy)	S_{20cm} (mJy)	S_{13cm} (mJy)	S_{6cm} (mJy)	S_{3cm} (mJy)	Blend Flag	$S_{20cm,matched}$ (mJy)	$S_{13cm,matched}$ (mJy)	$S_{6cm,matched}$ (mJy)	$S_{3cm,matched}$ (mJy)	α
01:08:50.53	−73:11:32.4	3.11										
01:08:51.91	−71:50:18.8	6.82	4.55									
01:08:55.16	−74:05:22.0		4.46									
01:08:57.32	−72:11:40.6	6.29	4.41									
01:08:58.15	−73:11:21.9					5.40						
01:09:01.30	−73:18:15.1	28.72	17.49	25.80	5.54					6.68		−0.84
01:09:01.81	−72:29:03.6		3.53									
01:09:02.06	−71:33:16.6	6.97	4.37	1.90	2.11							
01:09:02.82	−74:30:58.6	4.44										
01:09:03.29	−73:17:51.2					8.22						
01:09:03.75	−73:49:26.2	8.59	4.95	4.60	2.49	5.30			6.02			−0.34
01:09:12.15	−73:17:28.6	9.60	8.00	7.30	6.65	5.30				6.13		−0.26
01:09:13.03	−73:11:38.7	53.77	36.19	54.70	47.23			46.35	64.03	55.03	36.91	−0.10
01:09:14.31	−72:29:39.1	5.49	5.76	2.70	2.29				2.89			−0.62
01:09:17.25	−72:20:39.5	12.10		1.70	4.02					3.70		−0.68
01:09:17.82	−72:05:16.4	3.10										
01:09:19.41	−72:56:00.2	43.00	26.82	18.50	10.14	5.15			19.28			−0.77
01:09:20.58	−73:10:51.0		3.97	6.00		3.56						
01:09:22.33	−72:20:51.2					4.34						
01:09:25.52	−71:37:31.0	3.87										
01:09:27.11	−72:22:24.0	7.59		1.70								
01:09:27.52	−73:15:12.2					5.30						
01:09:28.24	−74:06:08.2					4.95						

Continued on next page

RA (J2000)	DEC	S_{36cm} (mJy)	S_{20cm} (mJy)	S_{13cm} (mJy)	S_{6cm} (mJy)	S_{3cm} (mJy)	Blend Flag	$S_{20cm,matched}$ (mJy)	$S_{13cm,matched}$ (mJy)	$S_{6cm,matched}$ (mJy)	$S_{3cm,matched}$ (mJy)	α
01:09:28.55	−70:42:07.8	25.24	15.69	7.90	7.74	4.47						
01:09:28.89	−74:05:57.5	10.92	8.28	5.30	3.49				7.77			−0.33
01:09:30.04	−72:52:45.1	4.64	3.64									
01:09:31.25	−71:34:54.5	250.40	119.80	76.20	34.83	14.90		134.90	81.88	34.21	12.24	−1.25
01:09:32.30	−69:46:18.9		6.89									
01:09:34.52	−75:36:46.7		3.67									
01:09:35.44	−71:38:23.5	14.09	6.63	5.80	2.49				5.82			−0.85
01:09:36.27	−70:02:11.1		3.26									
01:09:37.78	−74:57:02.0	4.98	4.33		3.72	4.47						
01:09:39.78	−70:50:02.7	9.84	6.13	2.20	8.42	5.33			5.78			−0.51
01:09:40.42	−69:55:57.8		29.20									
01:09:40.58	−69:56:24.0		33.10									
01:09:47.86	−74:58:05.2	3.17										
01:09:48.39	−72:21:30.4	5.57										
01:09:49.94	−70:25:01.4	19.32	8.11									
01:09:51.18	−72:56:17.3	3.27							4.13			0.22
01:09:51.43	−74:43:07.8	3.32										
01:09:54.29	−73:02:01.1	4.54										
01:09:54.66	−72:07:21.9				4.42	5.33						
01:09:55.47	−71:13:46.1	6.19	3.85	2.00					2.12			−1.03
01:09:55.82	−75:00:43.3	2.60										
01:09:58.24	−72:34:40.0	7.65										
01:09:58.79	−71:35:44.1	19.45	9.16	3.80								

Continued on next page

RA (J2000)	DEC	S_{36cm} (mJy)	S_{20cm} (mJy)	S_{13cm} (mJy)	S_{6cm} (mJy)	S_{3cm} (mJy)	Blend Flag	$S_{20cm,matched}$ (mJy)	$S_{13cm,matched}$ (mJy)	$S_{6cm,matched}$ (mJy)	$S_{3cm,matched}$ (mJy)	α
01:10:00.87	−72:08:21.0	5.68			1.42							
01:10:05.34	−72:26:47.9	115.60	127.90	119.30	72.59	41.70		147.60	133.00	73.61	38.16	−0.51
01:10:07.14	−74:10:47.9	5.20	3.68									
01:10:08.04	−74:37:31.4	5.19										
01:10:12.07	−72:55:23.6	8.33										
01:10:13.49	−74:46:33.1	4.21										
01:10:16.63	−71:39:51.6	4.59	4.03	1.90	1.90							
01:10:18.15	−70:48:15.4	10.09	6.91	1.40	3.13				7.84			−0.24
01:10:18.87	−71:47:18.1	3.87										
01:10:20.10	−73:04:25.0		19.20									
01:10:20.84	−73:06:57.6	3.90							1.87			−0.71
01:10:22.52	−73:04:41.4	60.11		39.30	25.47	25.40		52.26	35.37	25.19	15.41	−0.58
01:10:22.93	−70:25:17.5	10.49	6.31									
01:10:23.69	−73:04:50.2		12.60									
01:10:25.36	−69:55:03.8		68.30									
01:10:28.11	−74:51:03.9	28.27	16.67	9.90	5.41				11.24			−0.89
01:10:28.44	−75:00:11.7	3.25										
01:10:29.43	−74:53:58.4	27.51	7.00	12.10	4.71	3.84			15.20	5.24		−0.92
01:10:30.65	−72:33:09.0	14.59	9.36	1.90								
01:10:33.29	−70:03:11.5		4.54									
01:10:33.93	−73:45:51.6	7.20										
01:10:35.16	−72:00:24.3	9.08	6.23	1.70								
01:10:36.39	−72:28:10.7		65.43		36.80	70.50						

Continued on next page

RA (J2000)	DEC	S_{36cm} (mJy)	S_{20cm} (mJy)	S_{13cm} (mJy)	S_{6cm} (mJy)	S_{3cm} (mJy)	Blend Flag	$S_{20cm,matched}$ (mJy)	$S_{13cm,matched}$ (mJy)	$S_{6cm,matched}$ (mJy)	$S_{3cm,matched}$ (mJy)	α
01:10:36.95	−70:10:41.4	6.03	3.91									
01:10:39.08	−70:57:52.9		3.60									
01:10:39.44	−72:28:28.0	346.97		136.20				217.80	154.00	75.57	41.95	−0.89
01:10:39.46	−73:12:57.5					5.79						
01:10:41.08	−73:14:54.3		5.57									
01:10:43.42	−72:53:29.2	3.83										
01:10:44.35	−75:09:53.0	11.20	8.33	2.48	3.87				2.36			−1.50
01:10:45.36	−72:28:53.9				74.95	32.60						
01:10:48.23	−71:14:15.9	15.08	8.09	6.60	2.43	5.03			8.45			−0.56
01:10:49.19	−70:49:53.3	5.53	4.22		6.24							
01:10:49.90	−73:14:27.8	1078.00	497.90	501.60	273.50	146.00		788.40	566.20	299.70	133.90	−0.87
01:10:50.17	−72:10:25.7	16.15	7.62	10.50	8.25	8.25			12.12			−0.28
01:10:53.21	−73:14:16.2					139.18						
01:10:53.53	−70:42:52.7	33.28	13.74	8.20	7.07							
01:10:55.00	−73:32:41.3				3.55							
01:10:56.34	−72:42:54.7			66.90								
01:10:56.56	−73:14:08.2		141.70									
01:10:57.44	−71:19:06.4	3.36										
01:10:58.47	−74:46:17.0	7.62	3.75									
01:11:01.39	−72:35:33.5	7.90	3.61	2.60					1.95			−1.35
01:11:03.79	−72:00:50.4	5.28	4.84									
01:11:06.55	−73:00:31.3	3.76										
01:11:08.26	−69:26:11.6		117.92									

Continued on next page

RA (J2000)	DEC	S_{36cm} (mJy)	S_{20cm} (mJy)	S_{13cm} (mJy)	S_{6cm} (mJy)	S_{3cm} (mJy)	Blend Flag	$S_{20cm,matched}$ (mJy)	$S_{13cm,matched}$ (mJy)	$S_{6cm,matched}$ (mJy)	$S_{3cm,matched}$ (mJy)	α
01:11:08.49	−73:45:27.5	5.20										
01:11:08.50	−72:38:16.5	4.03										
01:11:10.06	−74:43:44.2	5.06										
01:11:11.73	−75:09:38.5					4.53						
01:11:13.98	−74:33:39.7	8.63		1.20								
01:11:15.36	−71:51:37.1	11.98	7.82	2.50	3.58				5.62			−0.73
01:11:15.83	−72:22:47.2			55.70								
01:11:16.22	−70:11:46.9	17.15	21.42									
01:11:16.87	−75:09:37.3	5.17										
01:11:17.10	−73:01:55.5				4.61							
01:11:17.62	−70:21:56.2	3.21										
01:11:18.46	−72:22:54.1	6.79										
01:11:19.75	−75:16:35.8	4.71										
01:11:24.31	−74:00:31.0	3.80										
01:11:25.94	−73:01:32.4					5.37						
01:11:27.25	−69:46:54.9		3.98									
01:11:27.60	−74:16:33.3	2.50										
01:11:28.26	−73:29:37.4	3.53		8.60	9.12	9.97			12.51	6.99	7.17	0.25
01:11:28.96	−75:00:29.7	3.16										
01:11:30.30	−72:46:23.5	3.56										
01:11:30.77	−75:45:03.5		64.20									
01:11:32.47	−73:02:09.4	69.22	66.96	77.40	63.25	63.20		81.32	75.75	63.02	64.28	−0.07
01:11:33.55	−74:50:44.9					4.26						

Continued on next page

RA (J2000)	DEC	S_{36cm} (mJy)	S_{20cm} (mJy)	S_{13cm} (mJy)	S_{6cm} (mJy)	S_{3cm} (mJy)	Blend Flag	$S_{20cm,matched}$ (mJy)	$S_{13cm,matched}$ (mJy)	$S_{6cm,matched}$ (mJy)	$S_{3cm,matched}$ (mJy)	α
01:11:34.08	−75:38:07.9		92.81									
01:11:34.37	−71:14:13.8	62.34	37.90	30.10	20.60	12.20				21.13		−0.62
01:11:36.06	−73:10:23.1		6.95									
01:11:37.48	−74:51:14.5	3.23										
01:11:41.96	−73:09:48.9	4.43										
01:11:45.99	−70:35:30.7	16.67	10.86									
01:11:46.91	−71:18:50.3		6.94						14.76			
01:11:49.38	−71:19:01.2	25.73		10.80								
01:11:52.96	−72:51:19.4	12.47	7.61	3.70	4.27							
01:11:53.66	−71:19:08.3		4.64									
01:11:57.89	−73:41:29.0	34.69	19.95	11.90	7.27	4.48						
01:11:57.97	−69:49:08.6		4.03									
01:12:03.63	−70:59:32.0					10.60						
01:12:04.48	−69:55:31.9		10.61									
01:12:07.41	−73:16:25.6					4.36						
01:12:11.04	−75:35:02.5		3.28									
01:12:11.53	−71:27:15.2	3.27										
01:12:11.92	−74:35:12.1					4.70						
01:12:16.55	−74:23:09.1	10.46		6.60					7.64			−0.30
01:12:18.59	−73:02:53.6	5.06										
01:12:20.87	−73:05:05.5	3.74										
01:12:22.46	−70:39:26.5	7.55	4.63		4.60							
01:12:23.21	−74:12:12.3	47.21	33.91	22.50	13.97	6.96			25.98	13.64		−0.70

Continued on next page

RA (J2000)	DEC	S_{36cm} (mJy)	S_{20cm} (mJy)	S_{13cm} (mJy)	S_{6cm} (mJy)	S_{3cm} (mJy)	Blend Flag	$S_{20cm,matched}$ (mJy)	$S_{13cm,matched}$ (mJy)	$S_{6cm,matched}$ (mJy)	$S_{3cm,matched}$ (mJy)	α
01:12:25.96	−73:27:51.7	51.87	27.16	26.20	13.60	6.52			24.98	12.50	5.57	−0.94
01:12:26.46	−72:48:01.5	21.39	7.11	7.70	4.71				5.95	3.19		−1.10
01:12:31.44	−75:06:17.8	18.45	13.85	8.10	16.03	15.90			11.03	16.12	14.77	−0.06
01:12:33.92	−71:29:44.6	4.68										
01:12:34.71	−73:27:02.1	4.96										
01:12:34.73	−72:09:09.1					5.59						
01:12:46.80	−72:45:18.4	5.88										
01:12:46.82	−73:15:22.8	15.48	7.25	9.00					6.10			−0.90
01:12:48.05	−70:19:28.6	23.79	15.12									
01:12:51.61	−75:25:30.3		12.51		12.28					11.70		
01:12:56.69	−75:35:04.0		3.79									
01:12:58.52	−70:06:20.9		4.11									
01:13:00.88	−70:13:37.3	7.29	8.76									
01:13:01.79	−74:07:11.0	8.38	5.37	4.30	3.72							
01:13:02.45	−71:49:03.3	12.74	5.95	3.60	4.27	4.37						
01:13:03.38	−73:21:07.4		4.95									
01:13:04.24	−70:16:56.9		3.47									
01:13:06.10	−73:17:28.1		4.26									
01:13:18.33	−70:51:09.4					5.48						
01:13:19.13	−74:34:51.9	11.03	8.84	9.00	12.10	12.50				10.82	11.44	0.01
01:13:21.28	−75:25:50.5		37.62									
01:13:21.35	−75:28:20.3		96.25									
01:13:24.00	−74:19:36.9	2.30										

Continued on next page

RA (J2000)	DEC	S_{36cm} (mJy)	S_{20cm} (mJy)	S_{13cm} (mJy)	S_{6cm} (mJy)	S_{3cm} (mJy)	Blend Flag	$S_{20cm,matched}$ (mJy)	$S_{13cm,matched}$ (mJy)	$S_{6cm,matched}$ (mJy)	$S_{3cm,matched}$ (mJy)	α
01:13:25.44	−69:51:02.3		4.03									
01:13:32.46	−69:38:55.4		34.71									
01:13:32.65	−74:07:57.6	53.22	29.13	17.60	10.36	5.43			20.51			−0.92
01:13:33.80	−73:17:04.4			70.10								
01:13:34.74	−72:55:48.7					4.83						
01:13:35.74	−70:44:16.1	3.76										
01:13:36.83	−73:55:46.1	5.94		2.23	3.34							
01:13:38.88	−71:41:19.7	25.16	11.96	7.80	3.97				8.94			−1.00
01:13:40.74	−71:32:23.1	4.56										
01:13:40.83	−71:41:07.0					6.35						
01:13:42.30	−75:04:13.8	5.12										
01:13:44.28	−71:15:20.5	48.00	21.10	21.10	12.10	8.69		29.73			4.89	−0.98
01:13:44.63	−73:21:09.9	5.14										
01:13:47.37	−71:24:09.7	5.28										
01:13:49.79	−73:18:01.4		16.21	170.90		122.00						
01:13:51.19	−75:33:39.0		35.07									
01:13:52.05	−74:26:39.4					7.19						
01:13:52.69	−73:15:51.5			11.10	4.47	5.45						
01:13:54.77	−74:42:10.3	3.31							1.83			−0.57
01:13:56.46	−72:48:05.3	4.88							1.42			−1.19
01:13:56.57	−74:42:51.4					3.91						
01:13:57.27	−74:26:55.3	5.30	4.20	4.10	4.49				5.66			0.06
01:13:57.28	−70:25:30.9	81.48	68.65									

Continued on next page

RA (J2000)	DEC	S_{36cm} (mJy)	S_{20cm} (mJy)	S_{13cm} (mJy)	S_{6cm} (mJy)	S_{3cm} (mJy)	Blend Flag	$S_{20cm,matched}$ (mJy)	$S_{13cm,matched}$ (mJy)	$S_{6cm,matched}$ (mJy)	$S_{3cm,matched}$ (mJy)	α
01:13:57.41	−71:14:24.9	55.13	27.75	22.00	12.47	6.69		33.14				−1.07
01:13:57.50	−73:04:25.1					4.91						
01:13:59.04	−70:16:13.7	4.17										
01:13:59.39	−74:44:51.8	5.39										
01:14:01.38	−70:26:22.6		4.19									
01:14:03.69	−73:20:06.4	128.02	31.40	70.30	30.64	17.30	b	61.53		28.48	17.08	−0.80
01:14:04.11	−74:35:23.5	4.69										
01:14:07.12	−73:20:05.5		28.50				b					
01:14:07.50	−75:17:58.8	7.56										
01:14:12.70	−74:09:12.1	4.41		1.50					3.03			−0.36
01:14:13.57	−72:18:21.1				2.32	2.32						
01:14:13.69	−70:09:44.6	30.77	16.90									
01:14:15.81	−73:27:06.7	5.27		1.50								
01:14:16.92	−73:15:49.3			18.20								
01:14:17.38	−70:09:51.0		7.20									
01:14:18.62	−73:17:29.7	9.30	6.00									
01:14:19.61	−73:15:43.8		5.82									
01:14:23.56	−73:12:45.7					5.48						
01:14:27.10	−72:52:18.1	2.40										
01:14:27.45	−72:17:10.5	4.66							2.62			−0.55
01:14:27.76	−73:33:13.5	8.68	1.97	2.20	3.21				6.21	4.36		−0.39
01:14:30.10	−72:17:16.7					3.89						
01:14:32.77	−73:21:43.1	169.00	132.40	110.10	54.12	28.90		147.60		55.58	27.80	−0.78

Continued on next page

RA (J2000)	DEC	S_{36cm} (mJy)	S_{20cm} (mJy)	S_{13cm} (mJy)	S_{6cm} (mJy)	S_{3cm} (mJy)	Blend Flag	$S_{20cm,matched}$ (mJy)	$S_{13cm,matched}$ (mJy)	$S_{6cm,matched}$ (mJy)	$S_{3cm,matched}$ (mJy)	α
01:14:34.72	−74:52:27.6	4.68										
01:14:34.78	−71:52:59.0		24.30					42.14	27.58	13.42	7.48	−0.94
01:14:35.86	−71:52:44.9	83.88		29.40	14.57	11.90						
01:14:36.90	−71:52:33.1		19.90									
01:14:38.02	−73:18:25.9			85.90		29.30					30.85	
01:14:39.49	−72:49:05.5			2.45					11.54			
01:14:40.16	−72:35:01.6	5.89		2.49								
01:14:46.91	−73:19:48.7		5.82									
01:14:47.09	−73:20:07.0			29.70								
01:14:47.68	−74:20:47.1	4.96		1.30					3.91			−0.23
01:14:48.42	−70:55:08.8	5.36		1.50								
01:14:49.23	−74:18:15.6	5.87										
01:14:49.58	−74:18:04.1			1.80								
01:14:49.77	−70:54:42.0				3.13							
01:14:49.99	−74:20:53.5				3.84							
01:14:50.40	−71:59:48.6	2.90										
01:14:53.46	−73:19:21.0			24.80								
01:14:54.06	−70:14:34.4	35.72	20.67									
01:14:56.35	−74:34:00.9			2.00								
01:14:57.10	−70:00:28.1		4.60									
01:14:57.76	−73:28:11.9	10.60	4.45	3.60	3.41							
01:14:58.44	−74:56:34.5	5.00										
01:14:58.48	−74:33:55.6	6.98										

Continued on next page

RA (J2000)	DEC	S_{36cm} (mJy)	S_{20cm} (mJy)	S_{13cm} (mJy)	S_{6cm} (mJy)	S_{3cm} (mJy)	Blend Flag	$S_{20cm,matched}$ (mJy)	$S_{13cm,matched}$ (mJy)	$S_{6cm,matched}$ (mJy)	$S_{3cm,matched}$ (mJy)	α
01:15:00.23	−70:37:13.7	10.68	9.52	3.10								
01:15:00.70	−70:37:26.4				3.33							
01:15:03.00	−73:11:01.0	1.60										
01:15:05.20	−73:28:26.1					7.44						
01:15:06.56	−74:36:46.8	7.71	6.65	4.30	3.34							
01:15:10.72	−69:46:52.4		3.48									
01:15:15.43	−69:44:03.7		3.29									
01:15:17.75	−70:25:27.6	4.20										
01:15:18.01	−71:59:27.8	8.30	3.77	1.30								
01:15:18.04	−70:44:45.3	5.47	3.99									
01:15:18.37	−71:37:25.4	7.05	3.03		2.66				3.37			−0.71
01:15:22.41	−72:41:17.3	4.37										
01:15:24.80	−71:52:59.8	7.60							1.51			−1.56
01:15:26.11	−73:00:18.3	2.64	3.95	2.40								
01:15:26.83	−72:07:30.7	7.39	4.79									
01:15:27.07	−72:30:01.5			1.80	7.46				5.52			
01:15:27.26	−73:41:37.9					4.34						
01:15:27.52	−72:07:44.8				2.70							
01:15:29.38	−70:01:01.6		4.50									
01:15:29.77	−74:11:11.1	8.77	4.81	1.90								
01:15:34.37	−72:26:36.6	3.48										
01:15:34.86	−71:25:59.2	5.36										
01:15:35.35	−72:00:08.9	30.84	14.15	10.60	6.40				9.90	6.75		−0.89

Continued on next page

RA (J2000)	DEC	S_{36cm} (mJy)	S_{20cm} (mJy)	S_{13cm} (mJy)	S_{6cm} (mJy)	S_{3cm} (mJy)	Blend Flag	$S_{20cm,matched}$ (mJy)	$S_{13cm,matched}$ (mJy)	$S_{6cm,matched}$ (mJy)	$S_{3cm,matched}$ (mJy)	α
01:15:40.50	−74:17:19.3	2.80										
01:15:43.33	−73:50:00.3	3.61										
01:15:43.75	−70:18:43.4	7.89	5.72									
01:15:46.86	−72:46:48.9	3.87										
01:15:48.08	−71:40:07.7			2.40								
01:15:50.38	−71:39:50.6	8.26	3.99		3.51				3.25			−0.90
01:15:50.78	−74:11:01.2	8.80	5.26	1.60	2.01							
01:15:51.65	−72:11:49.9	3.59										
01:15:51.78	−70:04:18.8		48.09									
01:15:52.33	−72:35:52.2	7.48	4.79		2.47							
01:15:53.92	−74:28:22.6			2.80								
01:15:59.29	−70:55:54.5	7.05	4.04		2.15	5.19						
01:15:59.84	−71:04:41.1	37.99	22.68	13.60	6.17				16.38			−0.81
01:16:03.57	−74:43:25.5	36.87	19.56	11.60	7.16				12.81			−1.02
01:16:04.49	−73:53:54.3	17.03	10.09	7.00	4.37							
01:16:05.71	−69:58:49.9		5.55									
01:16:06.38	−74:32:10.4	10.20	6.52	5.40	3.32				5.89			−0.53
01:16:06.61	−74:43:30.5					5.03						
01:16:07.97	−70:41:14.4	8.68							4.34			−0.67
01:16:08.51	−73:10:29.5			32.30								
01:16:09.94	−74:28:14.2	35.57	22.93	15.00	9.93	7.13			17.92	7.96		−0.84
01:16:10.59	−73:39:00.6	150.80	54.50	56.60	26.30	20.10		81.70	59.28	25.91	12.19	−1.04
01:16:11.19	−71:10:28.7	37.56	17.03	14.90	7.95				15.23	5.56		−1.08

Continued on next page

RA (J2000)	DEC	S_{36cm} (mJy)	S_{20cm} (mJy)	S_{13cm} (mJy)	S_{6cm} (mJy)	S_{3cm} (mJy)	Blend Flag	$S_{20cm,matched}$ (mJy)	$S_{13cm,matched}$ (mJy)	$S_{6cm,matched}$ (mJy)	$S_{3cm,matched}$ (mJy)	α
01:16:15.72	−73:38:51.8		34.20									
01:16:15.83	−73:26:57.1	56.70	35.46	29.90	12.40	9.63		44.70	30.40	15.09	9.80	−0.78
01:16:19.66	−75:05:55.6	6.44										
01:16:22.19	−70:06:41.5		6.62									
01:16:22.30	−71:26:23.9	7.20										
01:16:22.98	−70:29:57.2	83.77	47.83	1.80								
01:16:24.46	−73:59:44.1					5.38						
01:16:27.87	−70:32:14.5	5.62										
01:16:28.95	−73:14:38.8	141.30	66.52	170.90	11.35	7.11			38.18	11.30		−1.44
01:16:29.50	−73:16:23.2	1.90										
01:16:32.30	−72:58:03.9	2.10										
01:16:35.72	−71:26:04.0	29.54	15.95	6.00	3.77							
01:16:37.17	−70:14:22.6		3.69									
01:16:37.62	−71:44:33.1	4.01										
01:16:38.10	−73:20:00.3	1.80										
01:16:40.26	−74:32:32.9	3.25										
01:16:46.00	−74:35:30.9	8.81	5.41	13.90	5.23	3.06			15.07			0.52
01:16:48.58	−73:42:40.8	6.21		4.10	2.68							
01:16:50.17	−73:08:51.0					5.92						
01:16:50.40	−72:56:02.8	2.50										
01:16:50.58	−69:53:00.1		3.71									
01:16:52.44	−69:55:40.0		4.16									
01:16:52.84	−70:31:45.5	3.41										

Continued on next page

RA (J2000)	DEC	S_{36cm} (mJy)	S_{20cm} (mJy)	S_{13cm} (mJy)	S_{6cm} (mJy)	S_{3cm} (mJy)	Blend Flag	$S_{20cm,matched}$ (mJy)	$S_{13cm,matched}$ (mJy)	$S_{6cm,matched}$ (mJy)	$S_{3cm,matched}$ (mJy)	α
01:16:58.36	−71:51:40.3	5.51										
01:16:58.40	−73:12:00.1	2.80										
01:17:00.16	−72:48:30.2			2.14					7.45			
01:17:01.45	−71:43:25.4	6.43	4.10									
01:17:01.73	−74:27:24.8	3.30										
01:17:05.41	−69:53:06.6		3.85									
01:17:06.96	−74:04:54.1					4.11						
01:17:08.60	−73:17:09.2	1.90										
01:17:09.00	−70:32:47.1	3.76										
01:17:09.31	−73:36:30.0	2.97										
01:17:17.37	−71:00:39.7	9.82										
01:17:18.13	−70:34:32.0	15.95	9.68	1.90								
01:17:18.48	−75:11:23.3			2.51					3.18			
01:17:19.29	−71:00:43.7			1.60								
01:17:19.60	−71:41:16.1	22.73	7.26	7.80	4.64				6.80			−1.16
01:17:22.17	−73:09:17.2		12.89	9.60	5.10				7.13			
01:17:24.40	−74:47:06.5	7.40	6.28	5.00	5.63	8.49			4.80			−0.42
01:17:24.71	−74:58:37.8			4.10					7.98			
01:17:26.37	−69:53:13.5		6.78									
01:17:26.90	−73:20:08.5	2.00										
01:17:32.31	−74:33:38.1	12.21	7.69	8.60	12.22	9.06			10.83	11.55		−0.04
01:17:32.32	−70:51:10.9		3.73									
01:17:44.27	−71:04:26.3	5.21										

Continued on next page

RA (J2000)	DEC	S_{36cm} (mJy)	S_{20cm} (mJy)	S_{13cm} (mJy)	S_{6cm} (mJy)	S_{3cm} (mJy)	Blend Flag	$S_{20cm,matched}$ (mJy)	$S_{13cm,matched}$ (mJy)	$S_{6cm,matched}$ (mJy)	$S_{3cm,matched}$ (mJy)	α
01:17:44.37	−74:55:50.5	6.98	3.73	3.00	2.77				3.46			−0.68
01:17:47.04	−73:44:45.2	10.53	3.30	2.25					4.59			−0.80
01:17:55.63	−72:19:07.5				4.01							
01:17:57.10	−70:59:31.9					6.31						
01:17:57.25	−73:25:40.8	3.52										
01:17:57.85	−72:19:11.5	18.80	11.79	6.20					8.30			−0.79
01:17:59.64	−74:50:02.2	24.65	13.03	5.60	6.51				7.01			−1.21
01:18:01.60	−71:26:29.1	3.68										
01:18:02.69	−71:38:16.4	6.50										
01:18:03.40	−74:16:26.8	1.90										
01:18:03.86	−72:05:02.5	5.27	4.33									
01:18:05.15	−72:50:33.8			2.71								
01:18:05.25	−73:50:31.4			2.71	4.32	5.89			2.57			
01:18:05.80	−74:58:25.3	36.62	22.22	10.70	7.83				12.04	6.95		−0.96
01:18:08.46	−69:45:59.6		106.60									
01:18:10.04	−70:40:49.0	5.42										
01:18:14.01	−75:08:38.3			2.63								
01:18:16.02	−69:51:47.1		540.50									
01:18:16.14	−71:17:46.2	4.26										
01:18:19.81	−73:07:23.8	6.18	2.51		2.67				4.03			−0.41
01:18:25.11	−73:18:00.1	8.42	3.68	5.80								
01:18:25.81	−75:04:06.4					4.97						
01:18:28.34	−73:24:54.1	5.43							2.12			−0.91

Continued on next page

RA (J2000)	DEC	S_{36cm} (mJy)	S_{20cm} (mJy)	S_{13cm} (mJy)	S_{6cm} (mJy)	S_{3cm} (mJy)	Blend Flag	$S_{20cm,matched}$ (mJy)	$S_{13cm,matched}$ (mJy)	$S_{6cm,matched}$ (mJy)	$S_{3cm,matched}$ (mJy)	α
01:18:29.86	−75:34:02.1		5.72									
01:18:30.43	−72:57:10.1					5.26						
01:18:33.65	−72:50:42.5		3.71									
01:18:34.44	−72:06:47.9	19.50	12.15	5.70	1.77				8.84			−0.76
01:18:37.57	−72:57:26.6	9.02	6.54	5.70	3.83							
01:18:40.17	−71:03:06.4	3.42										
01:18:41.28	−71:52:17.2	18.34	9.53	11.10	6.44				9.51	7.15		−0.55
01:18:44.18	−74:44:39.7		4.14	4.30	4.60				4.35			
01:18:48.51	−74:26:19.2					2.21						
01:18:50.77	−74:26:10.5			3.20								
01:18:53.03	−74:26:04.2	8.09							5.44			−0.38
01:18:54.99	−72:43:01.6	12.31	6.68	1.70								
01:18:56.90	−70:03:10.0		3.64									
01:18:58.80	−74:25:31.1					4.86						
01:19:02.40	−69:29:56.7		21.50									
01:19:09.05	−75:15:36.8			2.25								
01:19:09.24	−74:42:08.1	36.26	15.57	12.60	5.79				13.88	4.65		−1.16
01:19:10.30	−75:01:46.1	12.03	7.57	5.30	3.93							
01:19:10.95	−72:46:47.9	3.99	3.50	2.53		4.17						
01:19:13.45	−71:08:27.2	4.89			2.25				4.35			−0.11
01:19:14.30	−74:18:58.1	2.70										
01:19:14.80	−73:35:43.1					3.94						
01:19:15.58	−75:13:46.7	5.86		2.46								

Continued on next page

RA (J2000)	DEC	S_{36cm} (mJy)	S_{20cm} (mJy)	S_{13cm} (mJy)	S_{6cm} (mJy)	S_{3cm} (mJy)	Blend Flag	$S_{20cm,matched}$ (mJy)	$S_{13cm,matched}$ (mJy)	$S_{6cm,matched}$ (mJy)	$S_{3cm,matched}$ (mJy)	α
01:19:18.34	−70:23:26.7	5.10										
01:19:18.48	−71:05:30.7	179.00	70.39	63.60	31.98	22.30		102.00	63.95	30.79	13.74	−1.07
01:19:19.17	−73:04:36.8					5.23						
01:19:21.76	−75:11:44.9			2.41								
01:19:25.13	−73:01:58.5	4.47										
01:19:26.98	−73:29:21.2					2.59						
01:19:27.04	−73:51:22.9	6.35	4.90									
01:19:29.69	−73:29:08.1				4.25							
01:19:33.41	−72:59:31.8	5.68	3.54	1.60	1.29				2.26			−0.89
01:19:34.75	−75:05:37.8					3.70						
01:19:37.36	−75:05:52.3			3.11								
01:19:39.20	−74:25:58.3	2.60										
01:19:42.08	−74:55:37.2	4.25										
01:19:43.09	−73:28:44.1					4.75						
01:19:43.15	−74:36:56.3	3.92										
01:19:43.92	−69:45:40.1		4.70									
01:19:54.56	−75:03:28.8					4.68						
01:19:56.22	−75:14:31.8	3.98										
01:19:58.72	−75:03:14.5	22.54	12.82	5.90	3.45				6.70			−1.17
01:20:04.57	−74:57:42.8			4.50					10.74			
01:20:06.70	−71:08:13.4	6.59										
01:20:06.78	−72:50:17.5	19.83	11.21	7.10	5.23				8.93			−0.77
01:20:09.61	−71:46:59.2					4.78						

Continued on next page

RA (J2000)	DEC	S_{36cm} (mJy)	S_{20cm} (mJy)	S_{13cm} (mJy)	S_{6cm} (mJy)	S_{3cm} (mJy)	Blend Flag	$S_{20cm,matched}$ (mJy)	$S_{13cm,matched}$ (mJy)	$S_{6cm,matched}$ (mJy)	$S_{3cm,matched}$ (mJy)	α
01:20:11.37	−70:36:05.2	42.09	18.35	10.10	8.07				14.88	9.02		−0.89
01:20:12.16	−74:55:54.0	5.09	3.95									
01:20:12.93	−72:19:34.7		3.45									
01:20:14.61	−75:03:48.6			2.56								
01:20:16.24	−75:04:47.5			2.42								
01:20:20.88	−70:34:24.8	3.83										
01:20:23.75	−72:19:56.2	33.29	19.41	13.60	7.27	6.28			15.50	6.96		−0.89
01:20:24.34	−70:05:38.5		3.75									
01:20:27.04	−71:26:41.2	17.44		3.00								
01:20:30.34	−71:26:40.3		5.72									
01:20:35.84	−75:06:33.5	22.24	22.98	17.20	12.80	18.50			29.84	11.56	15.94	−0.24
01:20:36.63	−73:56:50.2	5.07										
01:20:36.86	−71:33:30.6	7.33	4.26	1.70	2.66	3.98						
01:20:37.17	−71:36:27.9	4.80		1.50					2.50			−0.63
01:20:37.93	−70:38:41.2	125.40	54.38	45.20	36.93	22.50		81.25	61.60	34.85	18.32	−0.79
01:20:48.79	−73:35:13.2		8.48			4.61						
01:20:53.62	−73:49:38.7		3.26									
01:20:55.62	−71:10:43.4	12.10		1.20					4.40			−0.97
01:20:55.90	−73:34:54.2	49.08	27.19	31.60	22.82	19.90		34.69	43.81	21.57	18.27	−0.42
01:20:59.14	−75:38:19.3		22.23									
01:20:59.98	−72:04:23.0					7.16						
01:21:00.96	−73:39:11.9					3.93						
01:21:03.28	−71:43:54.7	3.15										

Continued on next page

RA (J2000)	DEC	S_{36cm} (mJy)	S_{20cm} (mJy)	S_{13cm} (mJy)	S_{6cm} (mJy)	S_{3cm} (mJy)	Blend Flag	$S_{20cm,matched}$ (mJy)	$S_{13cm,matched}$ (mJy)	$S_{6cm,matched}$ (mJy)	$S_{3cm,matched}$ (mJy)	α
01:21:09.52	−69:31:41.7		11.10									
01:21:14.48	−70:27:51.2	5.93	4.85									
01:21:16.22	−70:13:41.8	156.60	103.60									
01:21:20.39	−70:10:13.7	3.41										
01:21:22.83	−69:59:30.4		3.39									
01:21:24.58	−69:32:42.5		23.89									
01:21:26.94	−71:04:48.3	4.03										
01:21:28.66	−71:43:35.2	19.56	10.67	5.30	4.10				7.26			−0.96
01:21:29.23	−72:15:47.8	4.80		1.40								
01:21:30.11	−74:57:45.0	3.85										
01:21:31.60	−71:07:33.3					4.92						
01:21:38.40	−69:43:44.4		7.97									
01:21:40.92	−74:09:30.2	4.81										
01:21:44.19	−69:57:18.7		86.90									
01:21:45.79	−73:16:58.4	9.70	4.70						3.38			−1.02
01:21:46.09	−70:31:26.7		3.54									
01:21:48.24	−72:09:23.8					5.26						
01:21:49.44	−69:56:46.1		101.70									
01:21:50.45	−74:00:05.7	96.41	32.68	40.80	20.91	18.60			46.29	24.20	9.08	−0.98
01:21:52.93	−71:03:04.6	5.62										
01:21:53.83	−71:19:59.6	8.14	4.24	1.70	2.77							
01:21:54.41	−71:55:26.1	19.57	9.47	8.10	5.69				8.65			−0.79
01:21:56.35	−74:46:40.1		4.61			9.41						

Continued on next page

RA (J2000)	DEC	S_{36cm} (mJy)	S_{20cm} (mJy)	S_{13cm} (mJy)	S_{6cm} (mJy)	S_{3cm} (mJy)	Blend Flag	$S_{20cm,matched}$ (mJy)	$S_{13cm,matched}$ (mJy)	$S_{6cm,matched}$ (mJy)	$S_{3cm,matched}$ (mJy)	α
01:22:00.34	−74:46:35.9	31.35	4.69	13.70	5.72				19.87			−0.44
01:22:01.89	−71:32:42.8					6.36						
01:22:05.60	−71:47:35.3	11.35	5.81	2.00					3.19			−1.22
01:22:06.52	−75:08:14.9	11.15										
01:22:07.08	−74:46:38.1		4.80									
01:22:07.78	−70:29:18.3	83.99	51.05	5.30					9.66			−2.08
01:22:09.56	−72:31:19.3	3.65										
01:22:09.75	−71:39:54.1	40.40	24.49	14.90	9.59	10.30			16.21	8.26		−0.91
01:22:10.09	−69:34:02.3		31.13									
01:22:10.13	−70:50:04.1	5.01										
01:22:10.38	−74:55:09.1			2.46								
01:22:15.91	−74:55:00.8					4.35						
01:22:18.29	−73:29:45.9	3.66							2.82			−0.25
01:22:20.49	−75:19:02.4		3.83									
01:22:20.77	−73:03:50.4		5.94	2.90								
01:22:23.68	−71:34:14.6	6.26		1.80					2.55			−0.87
01:22:24.00	−73:11:20.0	3.15			3.85					3.63		0.08
01:22:30.58	−71:14:21.9					6.56						
01:22:31.30	−70:39:16.4	6.04										
01:22:33.89	−71:47:24.2	14.15	12.68	14.80	14.47	13.90			16.34	14.32		0.02
01:22:34.34	−73:38:08.5					4.32			27.36	9.70		−1.47
01:22:35.29	−72:31:51.8	9.84										
01:22:35.87	−73:38:17.0	65.41	27.81	23.40	10.13							

Continued on next page

RA (J2000)	DEC	S_{36cm} (mJy)	S_{20cm} (mJy)	S_{13cm} (mJy)	S_{6cm} (mJy)	S_{3cm} (mJy)	Blend Flag	$S_{20cm,matched}$ (mJy)	$S_{13cm,matched}$ (mJy)	$S_{6cm,matched}$ (mJy)	$S_{3cm,matched}$ (mJy)	α
01:22:38.96	−74:10:13.5	35.14	14.96	14.30	9.34	6.45			17.94	8.14		−0.82
01:22:44.62	−69:29:57.9		21.28									
01:22:44.75	−69:44:15.1		103.00									
01:22:46.64	−74:35:46.0	8.86										
01:22:46.73	−74:26:31.6	13.41	8.37	4.50	4.46							
01:22:47.85	−75:15:33.9					6.67						
01:22:48.61	−74:35:26.6			5.30								
01:22:50.58	−71:50:43.2	63.72	43.95	29.10	18.47	8.97			33.15	19.41		−0.68
01:22:51.22	−70:54:27.2	12.37	9.10	11.10	6.54							
01:22:54.98	−73:14:29.0	3.86	4.12	4.70	3.56							
01:22:55.15	−70:07:08.4		4.68									
01:22:57.09	−75:15:06.5	880.87	580.60	15.20	192.60	96.70				192.80	92.94	−0.94
01:22:58.37	−71:48:42.6	10.91	7.58	1.40								
01:22:58.89	−73:53:59.4	5.28							3.81			−0.32
01:23:01.29	−70:44:35.9	9.18							3.12			−1.04
01:23:01.51	−73:29:43.9	4.47										
01:23:05.59	−73:57:04.9	11.42	3.93						2.45			−1.48
01:23:06.40	−71:11:22.3	14.97	7.43	4.10	2.17				4.97			−1.06
01:23:06.57	−69:55:59.8		42.21									
01:23:08.63	−70:02:11.0		5.36									
01:23:11.07	−74:54:17.4	15.69	12.21	6.10	5.14	4.87						
01:23:11.71	−74:18:12.0	9.35	8.27	5.30	3.61	7.10						
01:23:11.80	−73:28:43.5	5.47	5.67	3.30	10.96	4.23						

Continued on next page

RA (J2000)	DEC	S_{36cm} (mJy)	S_{20cm} (mJy)	S_{13cm} (mJy)	S_{6cm} (mJy)	S_{3cm} (mJy)	Blend Flag	$S_{20cm,matched}$ (mJy)	$S_{13cm,matched}$ (mJy)	$S_{6cm,matched}$ (mJy)	$S_{3cm,matched}$ (mJy)	α
01:23:11.90	−75:16:44.3				4.50					4.52		
01:23:14.90	−74:19:40.1	3.66			3.67							
01:23:15.38	−75:07:20.0		6.95									
01:23:15.50	−75:16:16.6		3.85									
01:23:17.57	−72:36:05.9	12.05	8.23	4.60	4.33				5.81			−0.70
01:23:17.68	−73:45:55.7				3.93							
01:23:17.85	−70:37:31.6		13.10									
01:23:18.47	−75:17:44.6					3.79						
01:23:21.37	−73:45:26.6		6.57	9.00	5.18	6.81			8.57	5.98		−0.51
01:23:21.74	−70:37:40.9	49.08	18.30	18.90	13.84			30.28	26.54	12.27		−0.75
01:23:22.70	−71:47:24.6	6.40										
01:23:23.56	−70:34:37.1	3.77										
01:23:23.96	−73:56:06.4	26.62	29.46	32.10	14.79	4.38			38.82	13.51		−0.33
01:23:24.16	−74:02:43.5	12.44	7.90	5.90	5.76	3.99			6.13			−0.68
01:23:24.19	−71:47:35.7			1.20								
01:23:24.86	−74:22:47.6	3.23										
01:23:30.93	−72:18:14.5	31.81	21.24	15.00	8.45	5.59			16.82			−0.61
01:23:36.59	−70:32:31.8	26.87	16.35	4.90								
01:23:43.59	−70:34:22.9	3.44										
01:23:45.78	−73:54:49.3	3.20										
01:23:45.81	−71:05:20.1	3.48										
01:23:46.10	−73:23:12.7	2.60										
01:23:47.89	−73:54:44.2					5.11						

Continued on next page

RA (J2000)	DEC	S_{36cm} (mJy)	S_{20cm} (mJy)	S_{13cm} (mJy)	S_{6cm} (mJy)	S_{3cm} (mJy)	Blend Flag	$S_{20cm,matched}$ (mJy)	$S_{13cm,matched}$ (mJy)	$S_{6cm,matched}$ (mJy)	$S_{3cm,matched}$ (mJy)	α
01:23:49.68	−73:50:38.1	190.30	79.55	63.80	45.90	30.00		102.00	76.93	46.02	29.96	−0.75
01:23:51.74	−73:46:33.9					3.64			1.59			
01:23:52.88	−74:41:43.7	68.30	28.34	21.10	13.87	9.77			28.06		14.55	−0.66
01:23:54.63	−70:00:39.1		3.54									
01:23:54.80	−72:56:17.7	2.70										
01:23:59.03	−70:34:49.6	3.07										
01:24:04.78	−70:56:27.8	4.94										
01:24:08.01	−73:09:04.1		52.93	92.50				65.19	103.20	98.07	93.95	0.16
01:24:11.35	−71:19:19.3	3.46										
01:24:15.03	−73:41:15.6	6.49		1.50	2.17				2.00			−1.14
01:24:15.95	−70:41:51.9	19.16	11.62	5.80	3.57							
01:24:17.85	−71:12:03.4	27.58	17.71	10.80	7.10	6.58			11.72			−0.83
01:24:24.56	−71:31:38.7	5.71	3.76									
01:24:26.52	−70:34:22.6	5.61	3.37									
01:24:28.78	−70:38:04.4	3.17										
01:24:30.03	−75:22:41.9		61.94		22.38					19.17	13.94	−0.54
01:24:33.37	−71:26:44.6	53.05	29.79	22.10	11.99	7.24			23.58			−0.78
01:24:49.08	−69:22:16.9		17.75									
01:24:49.55	−70:14:21.9		3.97									
01:24:50.84	−74:36:42.0					5.13						
01:24:53.02	−72:25:11.6	2.87										
01:24:55.36	−72:06:30.3			2.70								
01:24:58.23	−72:06:27.9	14.22	8.10						8.45			−0.50

Continued on next page

RA (J2000)	DEC	S_{36cm} (mJy)	S_{20cm} (mJy)	S_{13cm} (mJy)	S_{6cm} (mJy)	S_{3cm} (mJy)	Blend Flag	$S_{20cm,matched}$ (mJy)	$S_{13cm,matched}$ (mJy)	$S_{6cm,matched}$ (mJy)	$S_{3cm,matched}$ (mJy)	α
01:25:06.66	−69:42:16.9		15.89									
01:25:09.64	−72:51:06.0	4.11										
01:25:13.74	−70:02:39.6		8.00									
01:25:15.26	−73:22:57.0			2.71								
01:25:15.93	−75:02:13.6	5.13										
01:25:16.19	−73:16:22.1					4.26						
01:25:18.77	−73:16:33.4	4.39							3.52			−0.21
01:25:20.44	−72:29:15.5	51.23	19.43	26.50	10.46	16.00		43.26	31.70	14.06		−0.74
01:25:24.59	−73:21:54.0			2.82								
01:25:25.11	−71:49:01.6	6.22	6.47	3.60	5.17	6.51						
01:25:27.33	−74:16:17.4					6.09						
01:25:29.69	−72:29:46.9		8.85	11.50	4.90							
01:25:30.50	−70:36:10.3	6.00	2.48									
01:25:30.75	−74:34:58.9	6.64										
01:25:34.16	−71:31:10.4					5.35			2.87			
01:25:35.98	−73:56:33.1	27.23	10.26	9.90	4.76	6.18			11.91		9.98	−0.42
01:25:36.51	−73:22:50.8			62.70								
01:25:39.19	−73:29:46.3	6.25			2.87							
01:25:40.67	−71:29:37.9	9.26	4.91	1.20								
01:25:42.33	−73:43:49.5	5.41										
01:25:46.39	−69:52:10.1		3.54									
01:25:46.88	−73:16:02.6	98.13	45.72	37.80	19.73	7.99		57.13	44.36	17.91		−0.93
01:25:47.27	−72:51:05.9	3.51										

Continued on next page

RA (J2000)	DEC	S_{36cm} (mJy)	S_{20cm} (mJy)	S_{13cm} (mJy)	S_{6cm} (mJy)	S_{3cm} (mJy)	Blend Flag	$S_{20cm,matched}$ (mJy)	$S_{13cm,matched}$ (mJy)	$S_{6cm,matched}$ (mJy)	$S_{3cm,matched}$ (mJy)	α
01:25:48.34	−70:18:18.2	11.67	6.32									
01:25:48.66	−71:51:34.7	33.13	17.62	5.30	3.79				7.64			−1.41
01:25:49.20	−70:57:38.5	5.76	4.24		7.63	4.94						
01:25:50.50	−74:40:22.6	10.02							2.59			−1.31
01:25:51.12	−74:36:41.7	3.98										
01:25:52.62	−74:00:06.8	13.08		4.80	3.56				7.53			−0.53
01:25:54.57	−71:34:23.6	7.53	3.55						4.39			−0.52
01:25:55.47	−74:01:25.4					5.63						
01:26:00.21	−73:54:17.8	32.81	15.02	10.90	6.53	2.19			13.64			−0.85
01:26:03.58	−70:55:47.9	4.32										
01:26:04.76	−69:52:10.1		31.21									
01:26:06.03	−72:48:26.5	3.45										
01:26:11.27	−71:36:01.9	6.40										
01:26:11.42	−69:27:20.6		10.92									
01:26:15.82	−73:08:04.9		18.20			5.82						
01:26:16.89	−73:07:53.5	76.42		32.60	10.94				41.21	13.27		−0.97
01:26:18.07	−70:15:15.1		6.52									
01:26:18.11	−73:12:49.4	11.95	5.23									
01:26:19.43	−73:07:37.2		11.90									
01:26:22.17	−69:33:36.3		16.90									
01:26:22.97	−69:34:17.4		12.30									
01:26:25.19	−70:50:24.0	64.18	33.16	3.70	12.77	4.29			9.27	11.58		−1.05
01:26:29.30	−73:27:14.6	60.47	39.55	31.00	19.94	12.90			37.37	19.81		−0.63

Continued on next page

RA (J2000)	DEC	S_{36cm} (mJy)	S_{20cm} (mJy)	S_{13cm} (mJy)	S_{6cm} (mJy)	S_{3cm} (mJy)	Blend Flag	$S_{20cm,matched}$ (mJy)	$S_{13cm,matched}$ (mJy)	$S_{6cm,matched}$ (mJy)	$S_{3cm,matched}$ (mJy)	α
01:26:33.39	−74:48:52.1	8.39		1.40								
01:26:39.94	−73:15:01.7	103.60	55.80	36.70	17.19	12.70			42.59	16.46	9.72	−1.04
01:26:41.23	−71:37:32.3					6.85						
01:26:41.41	−74:16:25.8	8.01	5.00	2.20		3.96			5.52			−0.36
01:26:45.02	−70:30:29.7	4.03										
01:26:47.23	−73:43:20.6	10.35	7.25	1.30					6.46			−0.45
01:26:49.26	−74:03:13.2	7.04		1.50					4.54			−0.42
01:26:49.38	−73:19:28.7	4.80							2.81			−0.52
01:26:49.98	−73:16:32.6	9.64	3.93	4.60	3.51							
01:26:51.24	−73:52:56.0	4.95										
01:26:52.51	−73:19:30.8					4.00						
01:26:55.54	−75:11:21.8	78.85	49.45	2.20	22.78	12.20			8.30	21.40	11.12	−0.71
01:26:56.99	−71:17:40.1	4.48										
01:26:57.89	−71:34:54.1	3.44		2.85								
01:27:01.17	−71:50:51.2	6.68							5.49			−0.19
01:27:01.24	−74:37:00.1			1.80								
01:27:04.09	−70:05:32.0		10.80									
01:27:05.76	−71:50:51.9			1.40								
01:27:06.27	−70:38:51.6	3.62										
01:27:10.97	−73:09:38.5	5.64										
01:27:11.99	−70:59:29.1			2.25								
01:27:12.04	−73:09:51.9			3.90								
01:27:14.42	−70:59:37.4	26.18	14.77		11.79						5.73	−0.65

Continued on next page

RA (J2000)	DEC	S_{36cm} (mJy)	S_{20cm} (mJy)	S_{13cm} (mJy)	S_{6cm} (mJy)	S_{3cm} (mJy)	Blend Flag	$S_{20cm,matched}$ (mJy)	$S_{13cm,matched}$ (mJy)	$S_{6cm,matched}$ (mJy)	$S_{3cm,matched}$ (mJy)	α
01:27:17.15	−73:49:55.2					6.58						
01:27:18.59	−74:16:40.3	4.30										
01:27:19.09	−69:34:01.4		64.31									
01:27:23.31	−70:10:01.8		7.30									
01:27:25.53	−71:20:49.4	3.96										
01:27:26.50	−70:32:40.8	29.76	17.02									
01:27:27.97	−72:42:07.7	3.53										
01:27:32.49	−69:51:31.3		26.37									
01:27:33.06	−69:38:16.8		60.71									
01:27:33.85	−71:36:39.0	93.87	54.68	18.40	20.58				24.97	19.47		−0.93
01:27:44.30	−71:25:07.7	3.80										
01:27:49.97	−70:56:22.3	64.25	38.63		8.63							
01:27:51.69	−71:28:49.7	4.55										
01:27:52.16	−73:11:03.8	18.58	10.79	9.90	7.62	7.17			12.48			−0.38
01:27:53.14	−69:15:17.4		32.20									
01:27:58.37	−72:05:34.9	25.67	19.12	5.70	7.51				10.32	8.86		−0.63
01:28:02.59	−70:21:25.5	35.09	17.58									
01:28:02.80	−70:50:16.4	4.22										
01:28:05.07	−74:11:05.0	12.53	6.66	4.00	4.12				4.22			−1.05
01:28:08.93	−75:12:49.9	373.90	170.40		60.55	21.08						
01:28:09.97	−75:12:18.0					4.85						
01:28:11.14	−71:53:03.7	3.77										
01:28:11.42	−75:12:53.2									84.60	48.41	−0.95

Continued on next page

RA (J2000)	DEC	S_{36cm} (mJy)	S_{20cm} (mJy)	S_{13cm} (mJy)	S_{6cm} (mJy)	S_{3cm} (mJy)	Blend Flag	$S_{20cm,matched}$ (mJy)	$S_{13cm,matched}$ (mJy)	$S_{6cm,matched}$ (mJy)	$S_{3cm,matched}$ (mJy)	α
01:28:15.57	−74:41:52.5			1.90								
01:28:15.86	−73:07:59.1	15.99	9.74	4.60	3.39							
01:28:16.91	−75:12:57.2		82.50			7.80						
01:28:20.14	−71:22:51.9	14.59	5.13									
01:28:20.68	−71:54:26.7	17.30	7.32									
01:28:23.15	−71:54:37.1			1.90								
01:28:23.66	−74:41:29.3	5.41										
01:28:29.01	−73:41:42.3	12.54	9.04	6.90	6.60	5.22			8.22			−0.41
01:28:31.99	−73:38:11.7	4.13										
01:28:32.93	−70:08:05.6		32.23									
01:28:34.90	−71:57:11.2	7.68	5.47						3.22			−0.84
01:28:41.71	−74:23:21.3	7.97							5.75			−0.31
01:28:42.36	−72:52:07.8	5.41										
01:28:45.69	−69:25:57.7		6.11									
01:28:46.21	−69:36:16.1		354.70									
01:28:49.22	−73:14:03.2	4.95	3.79									
01:28:50.03	−70:50:09.1	4.28										
01:28:51.04	−70:48:37.6	3.12										
01:28:59.67	−71:22:58.6	7.86										
01:29:00.50	−71:51:56.1	20.21										
01:29:00.67	−74:43:02.2	3.46							13.52			1.31
01:29:03.41	−71:52:02.5		5.44									
01:29:07.05	−73:38:51.8					4.70						

Continued on next page

RA (J2000)	DEC	S_{36cm} (mJy)	S_{20cm} (mJy)	S_{13cm} (mJy)	S_{6cm} (mJy)	S_{3cm} (mJy)	Blend Flag	$S_{20cm,matched}$ (mJy)	$S_{13cm,matched}$ (mJy)	$S_{6cm,matched}$ (mJy)	$S_{3cm,matched}$ (mJy)	α
01:29:13.44	−69:27:13.8		8.24									
01:29:17.15	−72:39:56.4	6.75										
01:29:24.22	−73:31:51.7	31.10	15.98	16.10	4.82							
01:29:24.64	−70:34:17.0		11.48									
01:29:26.48	−75:24:37.1		24.08		28.57							
01:29:27.45	−74:28:21.9	4.74										
01:29:28.03	−73:28:35.4					4.46						
01:29:28.04	−74:35:46.2	3.06										
01:29:28.12	−73:06:47.7	10.39	5.62	2.60								
01:29:28.30	−70:34:05.5	47.30										
01:29:30.24	−73:33:10.3	197.80	181.80	110.90	119.10	55.90		206.20	169.00	150.00	71.00	−0.41
01:29:31.20	−70:44:48.7	3.51										
01:29:31.40	−70:34:07.0		9.74									
01:29:32.21	−70:53:53.0	16.75	7.99									
01:29:37.01	−70:11:37.4	8.95										
01:29:40.88	−74:07:45.7	5.83										
01:29:42.99	−70:27:49.0	4.03										
01:29:43.17	−69:26:11.8		5.00									
01:29:45.14	−70:35:30.5	177.40	53.98									
01:29:45.53	−72:32:34.2	7.55	4.57		3.47							
01:29:45.57	−70:35:04.1		17.95									
01:29:47.49	−70:18:10.5	105.10	49.51									
01:29:49.60	−74:37:12.7	3.45										

Continued on next page

RA (J2000)	DEC	S_{36cm} (mJy)	S_{20cm} (mJy)	S_{13cm} (mJy)	S_{6cm} (mJy)	S_{3cm} (mJy)	Blend Flag	$S_{20cm,matched}$ (mJy)	$S_{13cm,matched}$ (mJy)	$S_{6cm,matched}$ (mJy)	$S_{3cm,matched}$ (mJy)	α
01:29:50.50	−70:34:03.4	81.00						29.63				−2.12
01:29:51.17	−70:36:48.5	43.60	25.28									
01:29:51.32	−72:10:31.8	5.88	3.78									
01:29:52.05	−70:33:53.8		18.78									
01:29:54.96	−70:15:25.1	17.27	9.94									
01:29:55.30	−69:20:56.0		5.06									
01:29:58.54	−70:12:57.0	6.80										
01:29:58.57	−72:44:38.1	7.90	4.58									
01:30:02.36	−70:09:08.9	15.66	9.83									
01:30:02.60	−69:50:08.8		6.46									
01:30:02.83	−71:06:42.3	6.59	3.29									
01:30:03.61	−75:12:56.9					5.37						
01:30:06.12	−74:35:55.4	6.80										
01:30:08.79	−71:09:33.7	6.68	4.31									
01:30:12.12	−72:18:22.9	11.59	5.19									
01:30:12.72	−70:37:55.2	4.44										
01:30:13.49	−70:34:23.7		4.16									
01:30:13.70	−74:20:23.7	26.46	25.55	20.70	26.43	24.30			26.62	25.31		−0.02
01:30:16.35	−70:35:53.9		4.80									
01:30:17.30	−74:25:41.0	13.07	4.61	2.50								
01:30:19.79	−70:26:43.2	8.13	4.28									
01:30:20.19	−73:32:34.5					13.40						
01:30:20.86	−73:31:51.2					5.09						

Continued on next page

RA (J2000)	DEC	S_{36cm} (mJy)	S_{20cm} (mJy)	S_{13cm} (mJy)	S_{6cm} (mJy)	S_{3cm} (mJy)	Blend Flag	$S_{20cm,matched}$ (mJy)	$S_{13cm,matched}$ (mJy)	$S_{6cm,matched}$ (mJy)	$S_{3cm,matched}$ (mJy)	α
01:30:24.11	−69:22:29.6		7.57									
01:30:24.76	−74:39:28.9	7.81	7.88	11.90	13.70	8.18			14.68	12.72		0.30
01:30:26.10	−73:11:26.4	2.70										
01:30:27.79	−69:25:14.0		5.08									
01:30:30.72	−71:48:15.3	12.86	6.21									
01:30:31.82	−69:51:15.3		244.40									
01:30:32.34	−73:17:40.9	51.98	29.12	11.30	9.89				12.81			−1.35
01:30:33.19	−74:58:39.7	4.23	3.92	3.02	9.76	5.74				9.16		0.44
01:30:37.35	−73:46:57.3					4.03						
01:30:37.84	−69:52:01.1		3.43									
01:30:40.03	−72:32:22.0	6.47										
01:30:41.08	−73:46:30.0	3.93	3.66		4.81							
01:30:41.77	−72:50:50.5	3.50										
01:30:49.57	−73:46:21.1				3.93							
01:30:53.59	−72:30:50.7	3.84										
01:30:58.49	−70:09:37.5	16.86	10.91									
01:30:59.23	−70:03:53.3		10.26									
01:31:03.53	−70:48:56.1	7.14										
01:31:05.87	−70:06:34.9		3.89									
01:31:06.39	−74:58:40.6	22.59	8.11	1.20	5.62				12.54	5.02		−0.84
01:31:10.35	−71:51:38.5	6.36	4.04									
01:31:12.60	−74:07:15.4	3.77										
01:31:16.51	−73:03:56.7	3.31										

Continued on next page

RA (J2000)	DEC	S_{36cm} (mJy)	S_{20cm} (mJy)	S_{13cm} (mJy)	S_{6cm} (mJy)	S_{3cm} (mJy)	Blend Flag	$S_{20cm,matched}$ (mJy)	$S_{13cm,matched}$ (mJy)	$S_{6cm,matched}$ (mJy)	$S_{3cm,matched}$ (mJy)	α
01:31:20.24	−74:57:43.4	7.40			3.49							
01:31:21.60	−71:11:33.4	3.71										
01:31:21.62	−72:52:46.0	19.10	8.59									
01:31:24.16	−71:33:41.1	25.35	16.92									
01:31:24.28	−74:00:40.5	41.80	18.09	8.30	10.57	6.50			15.94	9.00		−0.88
01:31:29.55	−70:57:26.3	3.32										
01:31:31.14	−71:03:06.0	13.23	5.81									
01:31:33.89	−75:04:44.5	2.91										
01:31:34.76	−75:01:55.2	3.95										
01:31:34.80	−70:00:42.5		28.26									
01:31:38.58	−71:33:53.9	6.40	5.49									
01:31:42.19	−70:10:08.6	61.87	35.71									
01:31:46.05	−73:49:58.1			3.60								
01:31:47.76	−73:49:42.1	34.25	18.04		6.64				5.76	5.86		−1.07
01:31:48.32	−70:00:50.0		7.50									
01:31:50.23	−72:44:52.7	6.18										
01:31:50.72	−72:05:16.6	16.42	9.91									
01:31:51.71	−70:05:27.2		5.09									
01:31:53.05	−70:00:35.2		8.50									
01:31:54.89	−74:17:35.7	8.56	6.59						2.45			−1.21
01:31:56.72	−74:17:26.1			1.90								
01:32:03.79	−70:54:15.9	3.79										
01:32:06.84	−73:08:04.5	3.20	4.16									

Continued on next page

RA (J2000)	DEC	S_{36cm} (mJy)	S_{20cm} (mJy)	S_{13cm} (mJy)	S_{6cm} (mJy)	S_{3cm} (mJy)	Blend Flag	$S_{20cm,matched}$ (mJy)	$S_{13cm,matched}$ (mJy)	$S_{6cm,matched}$ (mJy)	$S_{3cm,matched}$ (mJy)	α
01:32:10.91	−75:03:51.5	8.65										
01:32:12.31	−71:06:12.8	15.23	8.95									
01:32:12.31	−74:20:16.3	9.02		1.40								
01:32:14.36	−75:03:39.3					5.83						
01:32:14.61	−74:20:00.2		3.61									
01:32:14.77	−73:39:03.3	70.34	33.47	4.60								
01:32:18.90	−71:53:48.1	47.75	29.85									
01:32:19.36	−71:55:18.1	3.26										
01:32:21.82	−71:35:51.7	3.72										
01:32:23.73	−72:39:49.7		7.10									
01:32:27.70	−74:25:59.0	3.70										
01:32:29.11	−73:41:22.6	57.17	35.94	5.80					7.42	12.86		−0.94
01:32:29.77	−72:39:57.0	388.00	219.80					243.90				−0.98
01:32:30.66	−74:30:20.7	6.69										
01:32:34.15	−71:00:31.2	9.06										
01:32:36.61	−71:04:15.1	44.11	26.63									
01:32:38.44	−72:21:37.9	35.75	21.34									
01:32:39.47	−74:13:40.8	3.12										
01:32:39.72	−73:44:22.3		11.70									
01:32:43.85	−73:44:12.4	76.84	31.20	5.30					9.51			−2.01
01:32:45.43	−74:33:57.5			3.60								
01:32:46.51	−74:33:48.3	9.27										
01:32:47.41	−71:16:39.2	15.03	9.92									

Continued on next page

RA (J2000)	DEC	S_{36cm} (mJy)	S_{20cm} (mJy)	S_{13cm} (mJy)	S_{6cm} (mJy)	S_{3cm} (mJy)	Blend Flag	$S_{20cm,matched}$ (mJy)	$S_{13cm,matched}$ (mJy)	$S_{6cm,matched}$ (mJy)	$S_{3cm,matched}$ (mJy)	α
01:32:50.83	−71:03:24.6	5.10	2.73									
01:32:56.22	−71:08:51.9	3.18										
01:33:03.70	−73:09:32.2	2.60										
01:33:05.64	−70:02:18.2		4.41									
01:33:06.25	−74:19:31.3	11.15	5.64						1.45			−1.97
01:33:06.38	−74:35:14.9	3.74										
01:33:07.13	−69:30:34.1		25.81									
01:33:07.22	−72:30:06.0	5.69										
01:33:09.35	−74:29:17.2	59.86	36.05	13.10	10.81				13.87	11.38		−0.99
01:33:16.06	−73:16:27.4	2.50	5.00									
01:33:17.61	−71:15:20.5	7.99	3.54									
01:33:23.39	−73:03:24.6		7.13									
01:33:26.47	−70:53:31.0	16.02	8.35									
01:33:27.86	−70:18:20.1	4.66										
01:33:28.24	−74:36:32.4	46.77	28.90	12.10								
01:33:29.75	−73:03:03.9	104.50	54.77									
01:33:30.89	−70:45:19.0	32.04	10.91									
01:33:31.49	−71:16:29.5		45.61									
01:33:32.10	−71:16:16.7	125.70										
01:33:32.56	−71:15:56.1		15.50									
01:33:34.78	−73:36:44.6	17.55	9.35									
01:33:36.79	−73:19:40.5	3.67										
01:33:37.04	−72:02:19.5	10.31	6.21									

Continued on next page

RA (J2000)	DEC	S_{36cm} (mJy)	S_{20cm} (mJy)	S_{13cm} (mJy)	S_{6cm} (mJy)	S_{3cm} (mJy)	Blend Flag	$S_{20cm,matched}$ (mJy)	$S_{13cm,matched}$ (mJy)	$S_{6cm,matched}$ (mJy)	$S_{3cm,matched}$ (mJy)	α
01:33:37.86	−70:32:19.1	3.94										
01:33:38.65	−69:28:36.6		113.13									
01:33:39.38	−74:46:08.5	66.76	22.20	8.50	9.66				10.40			−1.79
01:33:39.90	−72:50:57.3	12.08	7.22									
01:33:41.83	−69:36:51.7		4.26									
01:33:43.12	−73:17:49.5	24.76	7.99									
01:33:44.27	−74:46:13.1		8.80									
01:33:48.76	−69:28:43.8		119.25									
01:33:50.73	−71:23:40.9	3.04										
01:33:50.79	−70:04:19.3		14.16									
01:33:52.40	−69:35:50.2		27.94									
01:33:56.49	−71:10:14.7	19.05	12.83									
01:34:01.86	−70:34:21.0	8.63	4.74									
01:34:03.80	−71:51:18.1	15.48	12.11									
01:34:04.28	−73:11:22.2	4.49	4.00									
01:34:10.94	−75:35:25.9		6.06									
01:34:11.22	−70:08:13.7	8.79										
01:34:13.40	−73:47:56.2	4.07	3.38									
01:34:21.21	−72:20:18.9	5.05										
01:34:21.72	−72:27:17.7	6.74	6.97									
01:34:22.93	−73:18:09.2	12.71	6.04									
01:34:26.43	−70:39:40.9	3.70										
01:34:26.58	−70:14:14.7		4.26									

Continued on next page

RA (J2000)	DEC	S_{36cm} (mJy)	S_{20cm} (mJy)	S_{13cm} (mJy)	S_{6cm} (mJy)	S_{3cm} (mJy)	Blend Flag	$S_{20cm,matched}$ (mJy)	$S_{13cm,matched}$ (mJy)	$S_{6cm,matched}$ (mJy)	$S_{3cm,matched}$ (mJy)	α
01:34:27.57	−70:14:01.6	4.71										
01:34:30.49	−72:07:26.1	3.40										
01:34:31.47	−71:40:18.4	6.26										
01:34:34.53	−72:38:37.1	5.14										
01:34:35.77	−73:15:39.7	9.37										
01:34:36.41	−75:24:12.8		5.37									
01:34:36.71	−70:47:38.8	4.11										
01:34:39.09	−72:21:25.8	18.33	10.41									
01:34:40.00	−72:12:46.6	24.14	12.22									
01:34:40.67	−70:58:03.6	74.84	80.42									
01:34:41.32	−72:24:32.9		3.92									
01:34:43.88	−70:56:26.0	4.13	5.64									
01:34:46.36	−72:36:40.0	7.25										
01:34:46.87	−73:23:40.7	4.78										
01:34:48.80	−69:21:42.6		23.82									
01:34:50.34	−75:23:59.5		5.98									
01:34:53.45	−72:24:44.2	160.20	91.77									
01:34:55.41	−72:54:57.7	4.02										
01:34:59.49	−70:16:44.3	6.84	3.21									
01:35:00.23	−71:12:58.0	4.22	6.66									
01:35:00.50	−70:22:11.4	15.16	8.27									
01:35:06.79	−71:01:55.7	53.32	38.45									
01:35:10.25	−72:13:17.8	3.22										

Continued on next page

RA (J2000)	DEC	S_{36cm} (mJy)	S_{20cm} (mJy)	S_{13cm} (mJy)	S_{6cm} (mJy)	S_{3cm} (mJy)	Blend Flag	$S_{20cm,matched}$ (mJy)	$S_{13cm,matched}$ (mJy)	$S_{6cm,matched}$ (mJy)	$S_{3cm,matched}$ (mJy)	α
01:35:11.03	−75:12:00.5	12.21	7.49									
01:35:27.31	−74:41:37.3	21.81	9.60									
01:35:29.99	−70:48:24.1	18.85	10.02									
01:35:42.63	−69:44:28.9		5.30									
01:35:42.63	−74:05:28.9	8.65										
01:35:45.84	−69:30:29.9		24.64									
01:35:45.94	−73:32:02.6	12.53	3.91									
01:35:47.90	−74:13:32.5	4.90										
01:35:48.22	−69:30:12.6		16.38									
01:35:51.30	−72:09:16.6	3.85										
01:35:51.81	−74:29:19.1	5.44	5.98									
01:35:51.84	−71:26:03.7	10.23	6.25									
01:35:56.51	−75:39:05.9		25.30									
01:35:58.90	−74:12:48.0	16.66	8.45									
01:35:59.89	−72:02:59.0	17.84	10.10									
01:36:00.86	−71:55:10.7	11.11	7.48									
01:36:01.32	−72:50:57.9	7.14	5.13									
01:36:08.46	−71:35:02.8	3.66										
01:36:18.34	−72:07:23.0	15.04	9.63									
01:36:18.86	−70:29:01.8		93.40									
01:36:22.55	−70:34:12.7		56.76									
01:36:23.48	−74:32:50.1	9.08	6.28									
01:36:27.68	−69:18:40.2		16.34									

Continued on next page

RA (J2000)	DEC	S_{36cm} (mJy)	S_{20cm} (mJy)	S_{13cm} (mJy)	S_{6cm} (mJy)	S_{3cm} (mJy)	Blend Flag	$S_{20cm,matched}$ (mJy)	$S_{13cm,matched}$ (mJy)	$S_{6cm,matched}$ (mJy)	$S_{3cm,matched}$ (mJy)	α
01:36:32.24	−74:06:59.1	60.30	30.47									
01:36:34.68	−73:36:53.8	19.04	12.66									
01:36:34.98	−74:43:33.2	6.05	3.85									
01:36:35.92	−71:16:47.4		3.79									
01:36:43.92	−71:17:20.1	9.34										
01:36:44.43	−70:56:08.3	47.63	28.65									
01:36:44.77	−75:23:14.1		4.25									
01:36:45.96	−71:17:25.2		3.60									
01:36:49.36	−72:12:52.3	3.16										
01:36:51.99	−69:16:43.7		39.47									
01:36:52.17	−71:37:19.6	21.05	14.87					143.90				4.05
01:36:52.18	−69:39:38.3		7.34									
01:36:53.33	−70:08:36.7		16.67									
01:36:53.37	−69:26:10.3		11.02									
01:36:58.88	−70:57:23.5	40.88	29.28									
01:37:03.04	−73:04:14.1	258.20	121.00									
01:37:03.27	−74:02:58.4	5.10										
01:37:03.99	−71:59:39.4	3.11										
01:37:04.28	−69:21:37.9		15.25									
01:37:09.99	−73:27:35.5	14.52	3.32									
01:37:10.18	−71:31:16.4	7.78										
01:37:15.46	−74:44:04.3	3.78										
01:37:18.79	−72:06:11.8	3.31										

Continued on next page

RA (J2000)	DEC	S_{36cm} (mJy)	S_{20cm} (mJy)	S_{13cm} (mJy)	S_{6cm} (mJy)	S_{3cm} (mJy)	Blend Flag	$S_{20cm,matched}$ (mJy)	$S_{13cm,matched}$ (mJy)	$S_{6cm,matched}$ (mJy)	$S_{3cm,matched}$ (mJy)	α
01:37:20.79	−70:07:31.8		5.94									
01:37:23.99	−73:16:55.0	3.52										
01:37:24.12	−74:53:33.7	18.87	12.16									
01:37:24.23	−70:06:58.5		5.41									
01:37:28.33	−73:06:21.3	10.15	7.26									
01:37:30.64	−71:30:42.8	2.92										
01:37:37.73	−73:28:02.2	6.21	4.72									
01:37:41.72	−72:01:03.3	3.87										
01:37:42.42	−73:30:49.4	73.16	53.03									
01:37:54.54	−71:56:04.2	5.47										
01:37:57.88	−71:22:40.5		4.53									
01:37:58.59	−73:27:47.1	9.62										
01:38:00.36	−74:13:51.1	69.44	42.06									
01:38:00.47	−72:03:29.2	14.97	8.85									
01:38:03.71	−72:32:02.7	6.34	4.89									
01:38:05.77	−72:14:34.7	4.80										
01:38:11.44	−71:03:08.2		15.93									
01:38:12.20	−70:44:14.2		5.15									
01:38:13.28	−73:23:38.7	27.29	14.62									
01:38:13.39	−74:43:28.5	6.96										
01:38:17.01	−72:35:49.1	11.60	4.24									
01:38:17.98	−71:14:48.2		17.73									
01:38:21.49	−72:57:03.5	12.64	7.67									

Continued on next page

RA (J2000)	DEC	S_{36cm} (mJy)	S_{20cm} (mJy)	S_{13cm} (mJy)	S_{6cm} (mJy)	S_{3cm} (mJy)	Blend Flag	$S_{20cm,matched}$ (mJy)	$S_{13cm,matched}$ (mJy)	$S_{6cm,matched}$ (mJy)	$S_{3cm,matched}$ (mJy)	α
01:38:23.37	−72:36:52.1	17.83	7.05									
01:38:23.65	−74:30:13.3	4.98										
01:38:25.15	−74:41:15.6	17.65	7.55									
01:38:25.37	−74:41:35.8		4.59									
01:38:35.60	−72:36:54.3	14.40										
01:38:37.61	−69:12:35.8		64.52									
01:38:37.68	−69:52:21.6		4.57									
01:38:42.06	−73:37:50.5	39.10	5.79									
01:38:45.28	−71:59:12.5	18.69	8.99									
01:38:46.29	−73:38:06.1		4.80									
01:38:53.80	−74:30:27.9	2.80										
01:39:02.55	−74:18:50.6	3.20										
01:39:05.52	−72:56:28.3	122.00	66.63									
01:39:05.91	−74:16:39.7	3.90	4.02									
01:39:10.20	−72:10:26.4	4.97										
01:39:13.36	−75:00:40.7	60.22	32.41									
01:39:13.56	−71:46:06.9		6.32									
01:39:15.25	−71:04:45.7		5.95									
01:39:15.64	−69:55:43.2		5.98									
01:39:19.61	−73:16:55.7	94.18	41.84									
01:39:24.69	−72:41:44.3	23.33	7.11									
01:39:25.18	−74:55:48.4	11.07	8.88									
01:39:25.28	−70:06:13.1		8.99									

Continued on next page

RA (J2000)	DEC	S_{36cm} (mJy)	S_{20cm} (mJy)	S_{13cm} (mJy)	S_{6cm} (mJy)	S_{3cm} (mJy)	Blend Flag	$S_{20cm,matched}$ (mJy)	$S_{13cm,matched}$ (mJy)	$S_{6cm,matched}$ (mJy)	$S_{3cm,matched}$ (mJy)	α
01:39:26.97	−73:57:55.0	8.78										
01:39:29.05	−72:38:29.4	4.64										
01:39:30.87	−73:09:55.0	9.64	8.23									
01:39:33.60	−70:32:35.6		11.08									
01:39:37.51	−71:44:09.4		6.25									
01:39:40.17	−73:45:16.6	14.06										
01:39:41.35	−70:20:51.0		7.26									
01:39:46.73	−69:33:24.4		30.56									
01:39:50.58	−73:10:00.2	71.39	27.10									
01:40:00.24	−70:24:10.3		5.84									
01:40:01.09	−75:00:41.4	7.35										
01:40:05.87	−70:28:42.1		4.78									
01:40:06.02	−69:21:58.2		9.76									
01:40:06.65	−69:39:15.6		43.64									
01:40:08.65	−69:38:46.0		18.58									
01:40:10.00	−74:22:49.2		5.35									
01:40:11.76	−74:23:02.2	16.50										
01:40:13.09	−74:23:12.7		5.18									
01:40:22.43	−73:30:49.0	5.88	4.25									
01:40:22.98	−73:25:57.7	5.76										
01:40:23.52	−69:28:30.1		14.22									
01:40:25.03	−70:57:15.9		10.24									
01:40:25.03	−74:39:18.7	5.60										

Continued on next page

RA (J2000)	DEC	S_{36cm} (mJy)	S_{20cm} (mJy)	S_{13cm} (mJy)	S_{6cm} (mJy)	S_{3cm} (mJy)	Blend Flag	$S_{20cm,matched}$ (mJy)	$S_{13cm,matched}$ (mJy)	$S_{6cm,matched}$ (mJy)	$S_{3cm,matched}$ (mJy)	α
01:40:25.16	−71:13:12.0		8.18									
01:40:27.56	−72:48:12.9	16.64	13.74									
01:40:39.62	−72:50:59.2	28.38	15.22									
01:40:50.00	−73:58:06.6	6.08										
01:40:50.32	−72:40:59.1		15.89									
01:40:53.12	−74:48:03.9	4.25										
01:40:56.04	−70:42:32.6		7.04									
01:40:56.89	−69:44:37.7		40.37									
01:40:57.99	−70:42:45.9		8.02									
01:40:58.68	−74:49:05.7	6.11										
01:41:05.80	−71:58:28.5		25.09									
01:41:06.37	−72:27:50.0		90.41									
01:41:10.01	−71:40:47.0		4.76									
01:41:10.84	−71:49:29.8		6.70									
01:41:13.30	−74:49:12.9	4.83										
01:41:14.81	−74:07:31.8	109.40	52.58									
01:41:15.23	−70:14:55.2		19.66									
01:41:19.29	−70:41:18.3		34.99									
01:41:21.29	−74:40:15.3	4.18										
01:41:22.82	−73:24:50.0	3.74										
01:41:26.10	−75:30:47.7		9.52									
01:41:27.12	−73:03:58.9	9.18										
01:41:28.88	−70:16:36.4		45.95									

Continued on next page

RA (J2000)	DEC	S_{36cm} (mJy)	S_{20cm} (mJy)	S_{13cm} (mJy)	S_{6cm} (mJy)	S_{3cm} (mJy)	Blend Flag	$S_{20cm,matched}$ (mJy)	$S_{13cm,matched}$ (mJy)	$S_{6cm,matched}$ (mJy)	$S_{3cm,matched}$ (mJy)	α
01:41:28.91	−71:25:40.3		5.10									
01:41:31.42	−73:38:07.7	7.53										
01:41:36.03	−73:31:17.6	13.67	6.20									
01:41:38.97	−73:35:36.7	7.84										
01:41:39.18	−71:24:34.6		5.24									
01:41:42.96	−72:26:23.3		40.06									
01:41:54.11	−70:15:30.6		9.88									
01:41:55.06	−69:41:27.7		498.49									
01:42:04.20	−74:07:56.1	6.47	5.68									
01:42:11.34	−70:06:40.4		29.31									
01:42:23.79	−73:02:14.9		9.02									
01:42:23.93	−72:11:12.9		9.35									
01:42:28.34	−73:02:00.0		14.97									
01:42:32.94	−71:38:41.2		5.30									
01:42:33.01	−73:36:57.1	18.46	10.26									
01:42:35.99	−72:30:01.3		36.71									
01:42:41.98	−74:33:19.3	4.06										
01:42:42.95	−71:12:16.5		4.58									
01:42:49.26	−73:58:37.2	36.44	19.73									
01:42:49.90	−74:34:44.8	70.84	40.57									
01:42:53.62	−74:38:43.0	17.10	6.23									
01:42:55.62	−70:09:19.0		8.30									
01:43:02.42	−70:15:14.0		22.38									

Continued on next page

RA (J2000)	DEC	S_{36cm} (mJy)	S_{20cm} (mJy)	S_{13cm} (mJy)	S_{6cm} (mJy)	S_{3cm} (mJy)	Blend Flag	$S_{20cm,matched}$ (mJy)	$S_{13cm,matched}$ (mJy)	$S_{6cm,matched}$ (mJy)	$S_{3cm,matched}$ (mJy)	α
01:43:03.23	−74:26:34.2	3.54										
01:43:05.10	−73:16:16.7		10.68									
01:43:10.57	−74:34:32.5	3.58										
01:43:11.57	−71:29:32.6		5.99									
01:43:15.54	−73:38:00.1		6.74									
01:43:16.25	−71:36:42.7		14.01									
01:43:18.92	−71:36:28.9		12.85									
01:43:20.17	−74:26:38.4	3.08										
01:43:25.78	−74:43:06.4	5.20	3.87									
01:43:39.14	−73:18:48.1		5.59									
01:43:51.94	−72:22:20.2		18.26									
01:43:55.85	−74:47:18.4	5.44										
01:43:58.55	−74:31:32.6		30.75									
01:44:01.20	−74:31:34.6	76.60										
01:44:02.53	−71:41:24.8		5.32									
01:44:05.98	−69:55:56.2		7.79									
01:44:08.92	−75:09:18.2	12.88	6.28									
01:44:09.97	−70:36:34.0		12.99									
01:44:10.46	−72:55:22.8		4.60									
01:44:16.89	−70:27:46.7		5.43									
01:44:24.40	−73:09:44.4		6.21									
01:44:33.64	−74:31:10.4	4.63										
01:44:33.66	−74:33:08.3	116.10										

Continued on next page

RA (J2000)	DEC	S_{36cm} (mJy)	S_{20cm} (mJy)	S_{13cm} (mJy)	S_{6cm} (mJy)	S_{3cm} (mJy)	Blend Flag	$S_{20cm,matched}$ (mJy)	$S_{13cm,matched}$ (mJy)	$S_{6cm,matched}$ (mJy)	$S_{3cm,matched}$ (mJy)	α
01:44:36.09	−75:07:49.6	4.86										
01:44:36.93	−74:33:12.9		26.26									
01:44:39.99	−70:19:19.2		75.28									
01:44:46.43	−70:09:02.7		10.81									
01:45:03.31	−71:25:16.1		15.55									
01:45:12.52	−73:02:47.7		30.43									
01:45:14.69	−74:04:49.1		4.28									
01:45:15.78	−70:48:42.8		100.39									
01:45:20.23	−74:21:24.2		6.92									
01:45:23.47	−75:17:58.4		13.45									
01:45:24.92	−73:08:22.0		12.26									
01:45:41.11	−69:53:57.6		8.82									
01:45:46.74	−75:16:17.8		132.51									
01:46:08.54	−70:19:38.1		16.00									
01:46:09.07	−74:08:17.9		12.81									
01:46:11.57	−74:51:15.3	8.23	6.05									
01:46:28.49	−72:48:38.1		4.60									
01:46:36.97	−74:04:28.9		12.49									
01:46:43.92	−72:44:04.3		20.09									
01:47:00.09	−72:57:33.7		37.82									
01:47:02.62	−74:27:16.3		8.15									
01:47:03.86	−75:10:28.8	7.77										
01:47:40.26	−73:03:00.7		9.17									

Continued on next page

RA (J2000)	DEC	S_{36cm} (mJy)	S_{20cm} (mJy)	S_{13cm} (mJy)	S_{6cm} (mJy)	S_{3cm} (mJy)	Blend Flag	$S_{20cm,matched}$ (mJy)	$S_{13cm,matched}$ (mJy)	$S_{6cm,matched}$ (mJy)	$S_{3cm,matched}$ (mJy)	α
01:47:49.68	−74:46:49.1		8.89									
01:47:54.36	−75:25:35.5		16.79									
01:47:58.73	−74:48:33.4		70.06									
01:48:00.09	−72:57:33.7		37.82									
01:48:10.04	−74:43:44.2		71.07									
01:48:58.79	−75:07:24.7		6.37									
01:48:59.64	−72:49:50.0		27.88									
01:49:03.30	−75:06:39.9		14.19									
01:49:06.08	−73:12:53.2		29.47									
01:49:18.49	−74:01:11.1		10.26									
01:49:24.88	−73:02:29.2		26.57									
01:49:28.19	−73:02:26.0		41.50									